Dissertation

Mesons in Nuclei and Nuclear Reactions with Elementary Probes

by

Pascal Mühlich

Justus-Liebig-Universität
Giessen

Institut für Theoretische Physik I, Prof. Dr. Ulrich Mosel

Pascal Mühlich

Mesons in Nuclei and Nuclear Reactions with Elementary Probes

Inaugural-Dissertation zur
Erlangung des Doktorgrades
der Naturwissenschaftlichen Fakultät
der Justus-Liebig-Universität Gießen
Fachbereich 07 – Mathematik, Physik, Geographie

Gießen, 2007

Dekan: Prof. Dr. Bernd Baumann
1. Berichterstatter: Prof. Dr. Ulrich Mosel
2. Berichterstatter: Prof. Dr. Volker Metag

To

Sinje

Preface

Many people have contributed to the success of this work. I refuse to mention them in a particular order as the importance of their individual contributions, however direct or indirect they might have been, can and should hardly be evaluated. One exception from this general precept is my supervisor

Prof. Dr. Ulrich Mosel

whom I owe very special thanks not only due to accepting me as a member of his Institute but also due to his enduring interest in the progress of this work, our frequent and constructive discussions, and, at least equally important, his open and friendly kind. His experience as a physicist was a major resource driving the detailed scientific investigations which have lead to the numerous results presented throughout this Thesis. Moreover, I am particularly indebted to (in alphabetic order)

Luis	Alvarez-Ruso
Oliver	Buss
Thomas	Falter
Frank	Frömel
Elke	Jung
Alexei	Larionov
Stefan	Leupold
Thierry	Mertens
Volker	Metag
Markus	Post
Vitaliy	Shklyar
David	Trnka

In this place I apologize to all those people I might have forgotten to mention explicitely and express my gratidue for their help. Furthermore, I thank the computer crew of the Institute for Theoretical Physics I for providing and maintaining the technical basis for producing the numerical results. The pleasant atmosphere among all members of the Institute certainly also supported my will and ability to bring this work to a happy ending. Finally, I am very greatful to my parents who substantially helped to facilitate my life outside of the Institute. Above all, I thank you for your love, Sinje.

Giessen, April 2007 *Pascal Mühlich*

Contents

Appendix

Chapter 1

Introduction

1.1 Introduction and Motivation

Atomic nuclei are undoubtedly more than just an assembly of protons and neutrons. This is already obvious from the observation that their total mass is not exactly the same as the sum of the proton and neutron masses. This discrepancy is ascribed to the interaction energy that phenomenologically can be split into several components. The relevant degrees of freedom which mediate the nuclear force depend on the resolution in space and time by which the nucleus is probed. High resolution snapshots can reveal short range components of the interaction corresponding to quark and gluon structures, the elementary building blocks of all hadronic matter. In contrast, low energy probes resolve larger spatial distances corresponding to the lowest states of the hadronic spectrum. In this energy regime the effective degrees of freedom besides the nucleons and their excited states are the scalar, pseudoscalar and vector mesons. Concerning the nuclear force their lightest representatives, namely the $\pi(138)$ in the pseudoscalar sector, the scalar $\sigma(600)$ meson, and the $\rho(770)$ and $\omega(782)$ vector mesons, play a central role.

To our present knowledge, the phenomenology of strong interactions can be described successfully by quantum chromodynamics (QCD). Consequently, the inner structure, observable properties, and interaction of baryons and mesons should be explained by this theory. However, due to the non-abelian character of QCD, manifest in the confining property of the interaction at small momentum transfers, QCD appears to be poorly suited to investigate phenomena at moderate energies. Whereas perturbative methods have proven the validity of QCD at high energies, the only possibility to study QCD in its confining regime is to numerically solve a discretized version on the lattice. However, whereas one can hope that in the future such calculations will be possible without the rather drastic approximations applied today, they give little insight into the mechanisms behind the observable quantities. Consequently, other methods have to be applied in order to arrive at an understanding of the properties and interactions of the observable hadron spectrum.

The partonic substructure of the experimentally explored low-lying hadron multiplets is quite settled by now. It is less clear, however, if some meson and baryon resonances are generic multi quark states or rather can be understood as hadronic molecules. The knowledge that the nucleon is built from three constituent quarks raises the immediate question why the nucleon mass is much larger than the sum of the constituent quark

masses. Compared to nuclei built from individual nucleons the interaction energy seems to play an even more important role in this case. Having accepted that quarks confined in hadrons appear to be much heavier than in free space (even though quarks never can be isolated) immediately a second question has to be raised, namely why the pion is so much lighter than all other hadrons. To our present understanding, the answer is given by the spontaneous breakdown of chiral symmetry, a symmetry that is approximately present in the SU(3) QCD Lagrangian but is broken in the QCD ground state. A special property of the symmetry breaking mechanism is the appearance of a massless mode that is identified with the pion. Thus, important features of the hadron spectrum are dictated by chiral symmetry, an intriguing property of strong interactions.

At high densities or temperatures one expects that chiral symmetry will be restored. That means, that, unlike the ground state, the state of strongly interacting matter at high density or temperature possesses the same (approximate) symmetry as the Lagrangian. Consequently, also the masses of hadrons – or, more precisely, their spectral functions – that are strongly affected by the symmetry breaking mechanism are expected to change in such a dense or hot environment. Unlike the chiral phase transition at finite temperature the transition from the chirally broken to the restored phase at finite baryon density is expected to set in already at rather moderate densities smaller than nuclear matter density leading to the partial[1] restoration of chiral symmetry inside ordinary nuclei by up to 30% [1, 2, 3, 4]. Thus, it appears to be a reasonable concept to investigate hadron properties in nuclear reactions in order to learn about the symmetry properties of strong interactions. These reactions can be relativistic heavy ion collisions that explore the phase structure of strong interactions by creating new states of matter as well as nuclear reactions with elementary probes such as protons, pions, photons or electrons.

One rather prominent example of experimentally observed medium modifications, which demonstrates the quite substantial in-medium changes that can be expected already in photonuclear reactions, is displayed in Fig. 1.1. It shows the total photoabsorption cross section from protons, Deuterium and heavier target nuclei. The cross section from nuclei represents an average over a variety of target materials from Li to Pb. Both the cross sections from the proton and Deuterium show two resonance structures in the displayed energy interval, called the first and second resonance region. They are created by the excitation of the $\Delta(1232)$ and a composition of the $P_{11}(1440)$, $D_{13}(1520)$ and $S_{11}(1535)$ nucleon resonances. The second resonance peak is not seen at all in the nuclear data. Whereas Fermi motion certainly contributes to the broadening of the structures it cannot explain the complete disappearance of the peak. Collisional broadening of the resonances due to resonance nucleon collisions has been considered as a possible source of the observed depletion of the second resonance structure. This issue, however, is still far from settled. More exclusive reactions have to be studied in order to obtain more information on the individual resonance components. One such reaction to be discussed throughout this work could be η photoproduction in nuclei which can provide exclusive information on the $S_{11}(1535)$ nucleon resonance properties.

[1] In this work we understand *partial restoration* in the sense that the symmetry at finite density is only restored to a certain extent, namely by about 30% at normal nuclear matter density. In its original meaning, however, the attribute *partial* refers to the fact that the chiral $U_A(3) = U_A(1) \times SU_A(3)$ symmetry is only restored *partially*, namely in its $SU_A(3)$ sector.

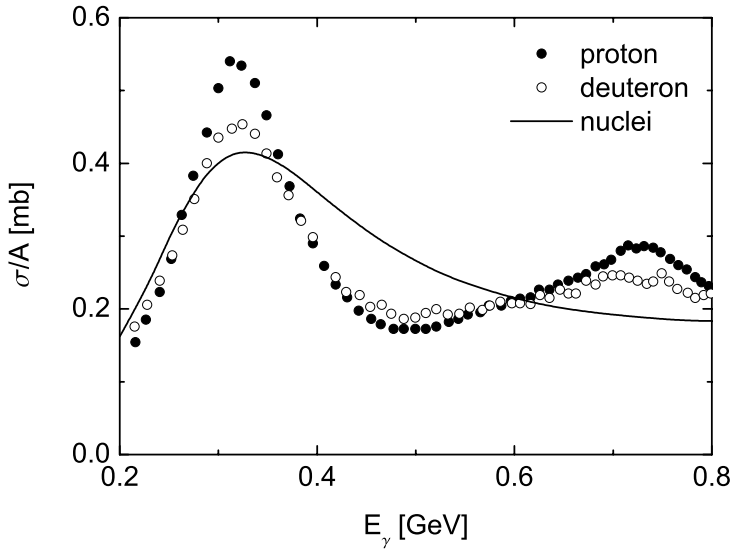

Figure 1.1: Excitation function for total photoabsorption off the proton [5] and Deuteron [6] and the average for nuclei [7].

Various experiments have also reported indications for mesonic medium modifications. Particular effort has been directed to the investigation of the light neutral vector mesons mainly for two reasons: First, the rather simple scaling laws suggested theoretically [8, 9] directly relate their in-medium masses to the degree of chiral symmetry breaking. Second, they couple to virtual photons that in turn decay into dileptons. The latter leave the nuclear medium almost untouched and, thus, carry the in-medium information to the detectors. In-medium changes of the ρ and ω properties have been reported from heavy ion experiments [10, 11, 12, 13, 14], proton induced dilepton production [15, 16, 17] and photonuclear reactions [18, 19]. Even if the models [8, 9] have stimulated most of the experimental activities in the field one should be aware that they are based on rather controversial postulates. In a more modern approach these scaling laws are replaced by much more sophisticated sum rule analyses [20, 21, 22, 23] that, albeit their ultimate statement is weaker, relate partonic and hadronic information in an almost model independent way.

Chiral symmetry dictates that the masses of chiral partners, hadronic states with equal spin but opposite parity, are the same. The non-existence of such parity duplets in vacuum is a major clue that chiral symmetry is broken there. However, if chiral symmetry was restored partially in a dense medium, the masses of chiral partners should approach each other. One particular example is the chiral duplet formed by the $\pi(138)$ and $\sigma(600)$ mesons. Theoretical studies suggest a downward shift of the $\pi\pi$ interaction strength in nuclear matter closely correlated with the spectral distribution in the σ channel. Moreover, in contrast to its questionable nature as a proper quasiparticle in vacuum, the σ meson might develop a much narrower peak at finite baryon density due to phasespace suppression for the $\sigma \rightarrow \pi\pi$ decay, hence making it possible to explore its properties when embedded in a nuclear many-body system [24, 25, 26, 27]. The $\pi\pi$ interaction

strength in matter is most effectively studied via $\pi\pi$ production experiments. This has been done in pion [28, 29, 30] and photon [31] induced reactions off complex nuclear targets. In both cases observable signals for a modification of the σ meson in the dense region of nuclei have been reported.

The aim of the present work is twofold: On the one hand we calculate the expected medium modifications of mesons from our knowledge on elementary meson nucleon interactions. Here, we essentially concentrate on the ω meson at zero temperature and moderate baryon density. On the other hand, we study nuclear reaction mechanisms with the aim to interpret experimental results connected to mesonic in-medium changes. The main emphasis of this work is placed on the latter topic. In particular we study photon and pion induced reactions on nucleons and nuclei as these have the essential advantage over heavy ion collisions to proceed under well-defined conditions. Whereas in heavy ion reactions the observables represent integrated quantities over various stages of the collision with different densities and temperatures, nuclear reactions initiated by elementary projectiles occur in a nuclear system close to its ground state. In this respect nuclear targets can be understood as micro laboratories utilized to investigate the properties and interactions of mesons in nuclear matter. Almost all theoretical approaches to hadronic in-medium changes emanate from the assumption that the surrounding strongly interacting medium is in equilibrium, an assumption that proves to be true as long as the nuclear target is perturbed by a single particle probe only. Here, electromagnetic projectiles are to be preferred over hadronic ones as they deposit their energy at one single place in the nucleus which makes the theoretical treatment easier. Also their ability to penetrate deep into the nuclear target is an advantage regarding the observation of density dependent effects.

One of the present great challenges of nuclear theory is to be able to disentangle new phenomena like in-medium modifications from more conventional nuclear effects such as Fermi motion, absorption and rescattering of the final state particles. In this respect, the relation of theoretical results connected to the intrinsic properties of the QCD excitation spectrum to experimental observables is an important and frequently undervalued issue. In this work we take the position that first all possible explanations by traditional nuclear mechanisms have to be ruled out before the observed effects are ascribed to modifications of intrinsic particle properties generated by the presence of the medium. To this end we study the production and propagation of mesons in nuclei in a semiclassical approximation using vacuum matrix elements but taking into account binding energies, Fermi motion and Pauli blocking of the produced final state. If this approach consistently fails to reproduce the experimental measurements, one confidently might introduce new ideas going beyond what has been established in the past. In this respect, the presented studies can be understood as a crosscheck regarding the observation of medium modifications in photon and pion induced nuclear reactions.

1.1.1 Primer on nuclear reaction theory

Presently there exist two different theoretical approaches to inclusive nuclear reactions. The first – and more sophisticated – one is semiclassical transport theory. In this work

we utilize a relativistic transport model based on a numerical solution of the BUU equation containing a coupled channel treatment of final state interactions. Owing to its semiclassical nature it provides a rather appealing and transparent interpretation of nuclear reactions which, thus, elapse in space and time apparently similar as in experiment. Another more simplistic approach is Glauber theory that reduces the nuclear reaction to more elementary interactions with individual nucleons. It regards the target as a homogeneous medium wherein the final state is produced in one place and absorbed according to its mean free path on the way out of the nucleus. The Glauber approach is both conceptionally and numerically much less expensive than the transport model and is used in the present work basically as a crosscheck for the transport results. Both approaches are introduced in the Appendices of this work together with a rather extended list of references where both their derivation and application is treated in more detail. Due to the semiclassical nature of the transport approach and the various approximations going into the Glauber formalism both models are expected to work well for high bombarding energies. Despite the long wave length of low energetic particles and, thus, the close simultaneous overlap of their extended wave functions with the nucleonic wave functions of the target, in particular the transport approach in some cases has proven to produce quite reasonable results also in the low energy regime. One, however, has to keep in mind that this success is not guaranteed from first principles and, thus, a careful interpretation of the results for low energy nuclear reactions seems to be advisable.

Let us prefix some general aspects connected to the calculations within the semiclassical transport model performed throughout this work. The general concept and some selected details of the applied transport model are given in Appendix A. We advise the interested reader not familiar with transport theory and its application to nuclear reactions to first read Appendix A before proceeding in this paragraph. In the present work we study particle production in photon and pion induced nuclear reactions at rather moderate energies. In this domain the semiclassical transport calculations are performed in the following modus operandi: in all calculations we use the so-called parallel ensemble method in order to numerically solve the coupled channel transport equations. Moreover, we also apply the perturbative particle method which is expected to work well for the case of nuclear reactions where the target nucleus stays close to its ground state. Both methods are purely numerical procedures in order to allow the computation of relatively rare events produced with small cross sections. In particular the parallel ensemble method is only an approximation to the exact solution of the transport equations which has proven to be well applicable. Since the target nucleus is expected to stay in its ground state we calculate all density dependent quantities as function of an analytical Woods-Saxon density distribution which is kept constant in time. Also Pauli blocking is accounted for by means of the corresponding analytical blocking factors calculated within a local Thomas-Fermi approximation. The assumption that the nucleus stays in its equilibrium configuration throughout the relevant time scale of the reaction is inspected in Appendix A.5. If not mentioned differently, collisions are simulated explicitly corresponding to a numerical solution of the collision integral. Special in this respect is only the $\Delta(1232)$ isobar which acquires an additional in-medium width due to three-body collisions not included in the BUU collision term. This three-body contribution as calculated in [32] is treated as an optical potential for the Δ and also gives rise to a broadening of the resonance propagator. More details on the applied transport model

and the solutions of the BUU equation can be found in Appendix A. The treatment of the π and Δ dynamics in nuclei will be discussed in some detail in Chapter 3.

1.2 Overview and Abstracts

This work is divided in two parts: First, we investigate meson production in the low-energy regime, namely center of mass energies starting from the two pion threshold. Here, the production of scalar and pseudoscalar mesons in strongly interacting systems is studied. Second, nuclear reactions at intermediate energies above the typical hadronic mass scale of ~ 1 GeV are considered. Here the main emphasis is placed on the production and decay of vector mesons in nuclear environments. The single Chapters of this work can be read more or less independently (if not referenced explicitly) and are essentially the result of distinct publications. In the following we give a list of short abstracts for all these Chapters in order to provide an overview over their structure and content.

Part I – Scalar and Pseudoscalar Mesons

Chapter 2: Primer Part I – Chiral symmetry and the σ meson. Some basic properties of the theory of strong interactions are recalled. Special emphasis is placed on the role of chiral symmetry and its spontaneous breaking and restoration. The relation of hadronic medium modifications and the change of the symmetry properties of the underlying theory are discussed. To this end a very simple toy model is constructed that connects the in-medium changes of the π and σ mesons in strongly interacting matter. Finally, the relation of these medium modifications to incoherent πN final state interactions as treated in the semiclassical BUU transport approach is discussed.

Chapter 3: The reaction $\gamma A \to \pi\pi X$. In this Chapter we investigate $\pi^0\pi^0$ and $\pi^0\pi^\pm$ photoproduction off complex nuclei at incident beam energies between of 400 and 550 MeV. Simulations of two pion photoproduction on protons and nuclei are performed by means of the semiclassical BUU transport model including a full coupled channel treatment of the final state interactions. Different treatments of the pion nucleon interaction are discussed. Elastic scattering of the final state pions from the nucleons in the medium is found to yield a downward shift of the $\pi\pi$ mass distributions. We show that the target mass dependence of the $\pi^0\pi^0$ invariant mass spectrum as measured experimentally can be explained without introducing medium effects going beyond absorption and quasi-elastic scattering of the final state particles. Parts of this Chapter have been published in Refs. [33, 34, 35, 36].

Chapter 4: The reaction $\pi A \rightarrow \pi\pi X$. The investigation of $\pi\pi$ production of the previous Chapter is pursued for the case of pion nucleus reactions. A microscopic model with the aim to describe the elementary $\pi N \rightarrow \pi\pi N$ transition process is constructed and applied to all isospin channels. In a second step the double pion production reaction from Deuterium is calculated in a simple spectator model and compared to experimental data serving as a reference measurement for the nuclear reactions. Finally the $\pi N \rightarrow \pi\pi N$ amplitude is implemented into the coupled channel BUU transport code and the impact of final state interactions is studied. Similar as in the case of photon induced double pion production a downward shift of spectral strength is found that, at least in parts, accounts for the experimentally observed effects.

Chapter 5: The reaction $\gamma A \rightarrow \eta X$. Photoproduction of η mesons off complex nuclei in the photon energy range $E_\gamma = (0.6 - 2.2)$ GeV is investigated. The calculations are performed to match the conditions of an ongoing experiment at ELSA. Important issues to be studied are the elementary η photoproduction cross sections off neutrons, the properties of the $S_{11}(1535)$ resonance in nuclei and the η nucleus final state interactions. To this aim results for proton, Deuterium and heavy target nuclei are compared to preliminary data. Nuclear reactions are calculated by means of the semiclassical BUU model and using elementary ηN cross sections from a coupled channel $K-$matrix analysis to be tested against experiment as input. Albeit we find qualitative agreement of our results to the data, some quantitative features are not reproduced on a satisfactory level. Parts of this Chapter will be published in Ref. [37].

Part II – Vector Mesons

Chapter 6: Primer Part II – Dileptons as a signal for chiral restoration. In the high energy regime the in-medium properties of the neutral vector mesons are of special interest. As they couple to dileptons nuclear dilepton production has been considered as a unique method to obtain the in-medium information. In the present Chapter we consider the photoproduction of dilepton pairs from nuclear targets. In particular, we discuss some special properties of dilepton production in nuclei that are of interest also to the remainder of this work. Finally, the relation of the vector meson spectra to the more fundamental properties of quark and gluon operators and their changes in the nuclear medium are discussed. Parts of this Chapter have been published in Ref. [38].

Chapter 7: The reaction $\gamma A \rightarrow \phi X$. In this Chapter medium modifications of the ϕ meson and possibilities to detect these modifications are considered. In particular, the $A-$dependence of the nuclear ϕ production cross section is studied. The calculations are done to match the conditions of an experiment where the K^+K^- final state has been observed. Whereas no valuable information can be extracted from the invariant mass distributions, the attenuation of the total ϕ meson yield seems to suggest a rather drastic change of the ϕ properties in the nuclear medium. Parts of this Chapter have been published in Ref. [39, 40].

Chapter 8: The ω spectral function in nuclear matter. The ω spectral function in nuclear matter at zero temperature is calculated by means of the low density theorem. We obtain the ωN forward scattering amplitude for energies up to $\sqrt{s} = 2$ GeV employing a unitary coupled channel effective Lagrangian model that has been applied successfully to the combined analysis of pion and photon induced reactions with the final states γN, πN, $2\pi N$, ηN, ωN, $K\Lambda$ and $K\Sigma$. The model includes all known nucleon isobar resonances with spin 1/2, 3/2 and 5/2 and masses below 2 GeV. While the peak of the ω spectral distribution is shifted only slightly, we find a considerable broadening of the ω meson due to resonance-hole excitations. For ω mesons at rest we find an additional width of about 60 MeV at saturation density. Parts of this Chapter have been published in Refs. [41, 42].

Chapter 9: The reaction $\gamma A \to \omega X$. We investigate inclusive ω photoproduction off complex nuclei, concentrating on the feasibility to examine a possible in-medium change of the ω meson properties by the observation of the $\pi^0\gamma$ decay spectrum. To this end both the differential and total production rates are calculated. Whereas the differential cross sections proof to be only moderately sensitive to the in-medium broadening of the ω, the total production rate yields important information on the inelastic collision width. The experimental data on the $\pi^0\gamma$ invariant mass spectrum from finite nuclei suggest a rather drastic downward shift of the in-medium ω mass. However, since this statement depends on the subtracted backgrounds and the tails of the spectral distributions the situation remains controversial. Parts of this Chapter have been published in Refs. [43, 44, 45, 46, 47].

In Chapter 10 the most important results of this work are summarized and a short discussion of possible improvements is given.

1.3 Abbreviations

The following abbreviations are used frequently throughout this work:

QCD	Quantum Chromo Dynamics
BUU	Boltzmann Uehling Uhlenbeck (transport model)
EM	Electro Magnetic (interaction)
CM	Center of Mass (frame)
LA	Laboratory (frame)
ISI	Initial State Interactions
FSI	Final State Interactions
CC	Coupled Channel
OM	Optical Model

Part I

Scalar and pseudoscalar mesons

Chapter 2

Primer Part I – Chiral symmetry, the σ meson and final state interactions

2.1 Introduction

This Section serves to introduce the general physical concepts and ideas relevant to the remainder of the first part of this work. All the research presented in the following is covered by one central keyword, namely *chiral symmetry*. More precisely, its spontaneous breaking in the QCD vacuum and at least partial restoration inside strongly interacting environments are the issues to be investigated in detail. Consequently, in the first Section of this Chapter we will introduce briefly the concepts of chiral symmetry and its breaking. In spite of the fact that chiral symmetry is a symmetry of the underlying strong interaction Lagrangian, we will discuss it in an effective chiral model, the *linear σ model*. Albeit this model does not provide a precise low-energy representation of QCD, it is able to reproduce πN observables at low energies (e. g. [48]) and has been used frequently to explore phenomena related to chiral symmetry breaking and its spontaneous restoration at finite density and temperature (e. g. [49, 50, 51, 52]).

As will be detailed later, in the low energy sector of non-perturbative QCD, with the scalar and pseudoscalar meson nonet being the relevant degrees of freedom, chiral symmetry breaking becomes apparent in the non-degeneracy of the $\pi(138)$ and $\sigma(600)$ modes. Therefore, the partial restoration of chiral symmetry manifests itself through the modification of these modes until degeneracy is reached eventually in the chiral restored phase at several times nuclear matter density. Since the most dominant decay mode of the scalar σ meson is the $\sigma \to \pi\pi$ decay, the spectral density in the scalar channel can be observed via the $\pi\pi$ final state with the $\pi\pi$ pair being in a relative $S = I = 0$ state. The softening (spectral shift towards lower masses) of the σ mode in turn causes a decrease of the $\sigma \to \pi\pi$ phasespace. This leads to the conjecture that the σ might appear as a much sharper resonance when embedded in a strongly interacting medium. This situation has to be contrasted to the vacuum one, where the σ appears at most as a very broad resonance-like structure with its width being of the order of the σ mass.

Spontaneous chiral symmetry breaking and its restoration are features of the strong interaction. However, due to confinement, the relevant degrees of freedom in the low-energy sector of QCD are not quarks and gluons but mesons and baryons. Their dynamics and interaction are described most effectively by effective Lagrangians with meson and

baryon degrees of freedom that respect the relevant symmetries of QCD. Consequently, the medium modifications of these hadrons are accounted for by hadronic interactions – renormalization of their pion clouds, short-range correlations, and resonance-hole excitations. One, however, has to keep in mind that these particles are made out of quarks and gluons and, hence, it is the quark and gluon operators that are modified by the presence of the hadronic medium. These in-medium changes give rise to the restoration of chiral symmetry signaled by the medium modification of quark and gluon condensates. In Section 2.3 we study the properties of the pion in nuclear matter within an extremely simple hadronic model, namely the $\Delta-$hole one. Thereafter we study the connection of the nuclear pion dynamics and the mechanism of partial symmetry restoration. With the discussion of this toy model we intend to introduce some basic properties of in-medium changes of hadrons in cold nuclear matter that form the background to our studies presented in this work.

Experimentally $\pi\pi$ production has been investigated in pion- and photon-induced reactions on nuclear targets [28, 29, 30, 31, 53, 54, 55]. These experiments will be studied in great detail in the forthcoming Chapters. In photon induced reactions the observed medium effects have been described most successfully within the model of [56, 57] where the low-energy $\pi\pi$ dynamics is treated via a chiral unitary approach. We will discuss this approach briefly in the final Section of this Chapter and we will argue that the included πN interactions are not complete. In the following Chapters we will then show that the ignored part of in-medium changes gives rise to effects equally strong as the included renormalization of the 2π propagators and, hence, equally capable to reproduce the experimental data.

2.2 Chiral symmetry

In this Section we will introduce the concept of chiral symmetry in QCD. Moreover, its spontaneous and explicit breaking will be discussed also in the framework of a chirally invariant effective model, the linear σ model.

2.2.1 QCD and chiral symmetry

Quantum chromo dynamics. The phenomenology of strong interactions is described by the non-abelian gauge field theory of **Q**uantum **C**hromo **D**ynamics (QCD) [58]. On top of the symmetry requirements [59] this theory has to account for the known phenomena of *asymptotic freedom* and *confinement*. The latter one becomes manifest in the fact that no isolated quarks can be observed. Asymptotic freedom has the consequence that the quarks inside hadrons behave as pointlike non-interacting particles. Displaying

explicitly all summation indices the QCD Lagrangian has the following form

$$\begin{aligned}\mathcal{L}_{\mathrm{QCD}} &= -\frac{1}{4}\sum_{i=1}^{8} G^i_{\mu\nu}G^{\mu\nu}_i + \sum_{c,c'=1}^{3}\sum_{f,f'=1}^{6}\sum_{s,s'=1}^{4} \\ &\qquad \bar{\psi}_{cfs}\left[i(\gamma_\mu)_{ss'}\delta_{ff'}\left(\delta_{cc'}\partial_\mu - ig\sum_{i=1}^{8} G^\mu_i t^i_{cc'}\right) - \delta_{ss'}\delta_{cc'}M_{ff'}\right]\psi_{c'f's'} \quad (2.1)\end{aligned}$$

where $M_{ff'}$ is the quark mass matrix (6×6 matrix in flavor space), t_i are the 8 linearly independent, hermitian and traceless generators of SU(3) (3×3 matrices in color space), and $G_{\mu\nu}$ is the gauge field tensor. In terms of the gauge field operator G_μ it can be written as

$$G^k_{\mu\nu} = \partial_\mu G^k_\nu - \partial_\nu G^k_\mu + g f_{ijk} G^i_\mu G^j_\nu \quad (2.2)$$

with the completely antisymmetric structure constants $f_{ijk} = -2i\mathrm{Tr}\left([t_i, t_j]t_k\right)$. A special property of this theory is the universality of the coupling constant g that accounts both for the quark-gluon and gluon-gluon couplings. The non-vanishing coupling between the gauge bosons is a consequence of the non-abelian property of the theory. Gauge invariance dictates that the coupling constants for both interactions coincide.

Chiral limit. In the low-energy sector of QCD the heavy quark degrees of freedom of the theory can be frozen. Thus, one works with a limited number of quark flavors, usually $N_f = 2$ ($\psi = (u, d)^T$) or $N_f = 3$ ($\psi = (u, d, s)^T$). In the following we will consider the case $N_f = 2$ only. As compared to typical hadronic energy scales the masses of the up and down quarks are very small $m_u \approx m_d \approx 5 - 10$ MeV. Thus, it appears reasonable to neglect these masses in the Lagrangian (2.1). This approximation is called the *chiral limit*.

Chirality. Massless fermions have a well-defined chirality. Chirality or handiness describes the projection of the spin on the particle moving direction. Thus, for a massless spin$-1/2$ particle the chirality can have a positive or a negative eigenvalue. Since for massless states chirality is a good quantum number one can project on well-defined chirality eigenstates

$$\psi_{R,L} = \frac{1}{2}\left(1_{4\times 4} \pm \gamma_5\right)\psi. \quad (2.3)$$

Applying this definition to the quark fields in the Lagrangian (2.1) with $m_u = m_d = 0$ the Lagrangian splits into two independent parts, namely one describing the dynamics of right-handed quarks and one describing left-handed ones. Note, that ψ_R and ψ_L appear as independent fermion field operators. Nonetheless these fermions can interact via the exchange of the gauge bosons.

Symmetry transformations. Now we consider the following SU(2) transformations of the quark field operators [60]:

$$\begin{aligned} \lambda_V: \quad & \psi \longrightarrow e^{-i\frac{\boldsymbol{\tau}}{2}\boldsymbol{\theta}_V}\psi \qquad \bar{\psi} \longrightarrow e^{+i\frac{\boldsymbol{\tau}}{2}\boldsymbol{\theta}_V}\bar{\psi} \\ \lambda_A: \quad & \psi \longrightarrow e^{-i\gamma_5\frac{\boldsymbol{\tau}}{2}\boldsymbol{\theta}_A}\psi \qquad \bar{\psi} \longrightarrow e^{-i\gamma_5\frac{\boldsymbol{\tau}}{2}\boldsymbol{\theta}_A}\bar{\psi} \end{aligned} \tag{2.4}$$

where $\boldsymbol{\tau} = (\tau_1, \tau_2, \tau_3)^T$ are the generators of SU(2) (the Pauli spin matrices) and $\boldsymbol{\theta}_{V,A} = (\theta_1, \theta_2, \theta_3)^T$ are arbitrary rotation angles. These transformations are known as chiral transformations. In the massless limit the Lagrangian (2.1) is invariant under both transformations λ_V and λ_A. As a consequence of this invariance the vector and axial vector currents

$$V_\mu^k = \bar{\psi}\gamma_\mu\frac{\tau^k}{2}\psi \tag{2.5}$$

$$A_\mu^k = \bar{\psi}\gamma_\mu\gamma_5\frac{\tau^k}{2}\psi \tag{2.6}$$

are conserved. Consequently, also the linear combinations

$$\begin{aligned} (j_R^\mu)_k &= \tfrac{1}{2}(V_k^\mu + A_k^\mu) = \bar{\psi}_R\gamma^\mu\tfrac{\tau_k}{2}\psi_R \\ (j_L^\mu)_k &= \tfrac{1}{2}(V_k^\mu - A_k^\mu) = \bar{\psi}_L\gamma^\mu\tfrac{\tau_k}{2}\psi_L \end{aligned} \tag{2.7}$$

which are the right- and left-handed quark charge currents are conserved separately. In other words, assuming massless quarks the chirality is conserved in processes involving strong interactions.

2.2.2 Symmetry breaking

Spontaneous symmetry breaking. Hadronic states that can be rotated into each other by symmetry operations should have identical eigenvalues. As a consequence of the chiral symmetry of the Lagrangian one thus expects mass degenerate eigenstates with equal spin but opposite parity. However, these parity partners are not observed in the QCD vacuum. Examples of candidates of such chiral duplets are $\pi(138) \leftrightarrow \sigma(600)$, $\rho(770) \leftrightarrow a_1(1260)$ and $N(938) \leftrightarrow S_{11}(1535)$. Obviously there is a mass split between chiral partners that itself is of the order of typical hadron masses. Hence, one is led to the conclusion that chiral symmetry is broken spontaneously in the QCD vacuum. That means that the Lagrangian of QCD is invariant under this symmetry transformation whereas the QCD ground state is not. According to Goldstone's theorem the spontaneous symmetry breaking is responsible for the appearance of massless Goldstone modes [61]. Within flavor SU(2) they are identified with the pion isospin triplet. Indeed the pion has a much smaller mass than all other hadrons.

Explicit symmetry breaking. The small but finite quark mass term in the flavor SU(2) Lagrangian (2.1) is still invariant under the transformation λ_V but not under λ_A. This is known as the explicit breaking of chiral symmetry since the symmetry is already not

present in the underlying Lagrangian. This explicit symmetry breaking is responsible for the finite mass of the pion. Since the explicit symmetry breaking term in the Lagrangian is small as compared to typical hadronic mass scales, λ_A is still an approximate symmetry of the theory. The slight symmetry breaking is the basis of the so-called partial conserved axial current hypothesis (PCAC) [60, 62]. It provides a direct connection of the divergence of the axial current and the pion mass:

$$\partial_\mu A_k^\mu = -f_\pi m_\pi^2 \phi_k \tag{2.8}$$

where f_π is the weak pion decay constant which has been determined experimentally to be $f_\pi = 93.2$ MeV [63]. In the chiral limit $m_\pi \to 0$, this Equation implies the conservation of the axial current.

2.2.3 Linear σ model

Now we briefly introduce the linear σ model that – in a very intuitive way – displays the spontaneous symmetry breaking mechanism. Moreover, we will use it in order to at least qualitatively explore the link of hadronic interactions and its symmetry properties. The linear σ model is an effective chirally invariant model involving π, σ and nucleon degrees of freedom [58, 59, 60, 64]. It contains both the vector and axial vector SU(2) symmetries of QCD. Within the linear σ model observables in $s-$wave πN scattering up to energies of roughly 1 GeV have been described successfully [48]. The Lagrangian of this model can be written as follows [59]

$$\begin{aligned} \mathcal{L}_\sigma &= \bar{\psi} i\gamma^\mu \partial_\mu \psi - g\bar{\psi}(\sigma + i\gamma_5 \boldsymbol{\tau}\cdot\boldsymbol{\pi})\psi \\ &\quad + \frac{1}{2}(\partial_\mu \boldsymbol{\pi})^2 + \frac{1}{2}(\partial_\mu \sigma)^2 \\ &\quad - \frac{1}{4}\lambda^2(\boldsymbol{\pi}^2 + \sigma^2 - f_\pi^2)^2. \end{aligned} \tag{2.9}$$

The first line contains the kinetic energy and interaction terms of massless nucleons, whereas the second line gives the kinetic energy terms of the $\boldsymbol{\pi}-$ and $\sigma-$fields. The last line defines the $\pi-\sigma$ potential $V(\sigma, \boldsymbol{\pi})$. This potential is frequently referred to as the Mexican hat potential due to its typical shape. It has a minimum at $\sigma = f_\pi$ for $\boldsymbol{\pi} = 0$. The σ field has a mass of $m_\sigma^2 = 2\lambda f_\pi^2$ whereas the pion stays massless. As there is no explicit mass term for the nucleon it gains its mass exclusively through the interaction with the σ field. Its mass therefore is $m_N = g f_\pi$.

The chiral symmetry transformation λ_A (2.4) rotates the $\boldsymbol{\pi}$ and σ fields into each other. If chiral symmetry were to hold both fields should carry equal mass. This is obviously not the case. In the ground state the expectation value of the pion vanishes $\langle \boldsymbol{\pi} \rangle = 0$ whereas the σ, that carries the quantum numbers of the vacuum, has a finite expectation value $\langle \sigma \rangle = \sigma_0 = f_\pi$. In the language of QCD the σ expectation value has to be proportional to the scalar quark condensate $\langle \bar{q}q \rangle$. Thus, we expect a finite value of the scalar quark condensate in the chirally broken (Nambu-Goldstone) phase. Moreover, if chiral symmetry under some conditions were restored the finite expectation value $\langle \sigma \rangle \sim \langle \bar{q}q \rangle$ has to melt away. In this chirally restored (Wigner-Weyl) phase the chiral partners (π, σ) and (ρ, a_1) should become degenerate. Also the pion, that looses its identity as a

Goldstone boson, has to become massive. We will come back to this discussion later after having introduced a simple and transparent model for the nuclear π and σ dynamics.

Explicit chiral symmetry breaking can be introduced by adding a pion mass term to the Lagrangian (2.9) of the form [60]

$$\delta\mathcal{L} = f_\pi m_\pi^2 \sigma. \tag{2.10}$$

This term has a very similar form as the explicit symmetry breaking term in the original QCD Lagrangian (2.1). It has the effect of slightly tilting the originally symmetric potential $V(\sigma, \pi)$. The nucleon mass is unchanged by this symmetry breaking term. However, it now can be split into a contribution from the symmetric part of the σ potential and one from the symmetry breaking part. The latter one defines the pion-nucleon sigma term $\Sigma_{\pi N}$ that we will refer to in a later Section of this work. The σ mass slightly changes due to the pion mass; it now reads $m_\sigma^2 = 2\lambda f_\pi^2 + m_\pi^2$.

The spontaneous breaking of chiral symmetry becomes manifest in the non-vanishing expectation value of the σ field $\sigma_0 = f_\pi$. As said earlier, this expectation value defines the nucleon vacuum mass. This situation illustrates the importance of the chiral symmetry breaking mechanism. Apart from the small current quark mass contribution the dominant part of the nucleon mass is due to spontaneous chiral symmetry breaking that, consequently, accounts for most of the energy of all visible matter.

2.3 The pion in nuclear matter

At first our topic now completely changes. It is the aim of this Chapter to explore the general mechanism that gives rise to modifications of particle properties in strongly interacting matter. More specifically, we study the connection between hadronic properties and their changes due to many body dynamics on the one hand and the change of more fundamental properties of the underlying theory of strong interactions on the other hand. In the previous Section we have already seen that in systems where chiral symmetry is partially restored the masses of the π and σ mesons should approach each other. Moreover, the expectation value of the σ field, connected to the scalar quark condensate, has to decrease if chiral symmetry were partially restored. Now we explore these issues from a different point of view: we start with an effective hadronic model and calculate the in-medium changes of the pion at finite baryon density. Then we employ the linear σ model to obtain a link to the σ properties and calculate its mass spectrum and expectation value when the density increases. To this end we will use a rather simple toy model that gives some insight into important mechanisms that modify hadronic particle properties at finite density. These mechanisms will also be relevant for the remainder of this work.

The medium modifications of any hadron arise through its interactions with the surrounding medium. These interactions modify the particle propagator $D(p)$ (we restrict ourselve to spin-0 particles throughout this discussion) that is the Fourier transform of the two point function $\langle \mathcal{T}\phi(x)\bar{\phi}(y)\rangle$ where $\mathcal{T}$ is the time-ordering symbol [58, 65]. In

(a) (b)

Figure 2.1: Feynman diagrams representing the resonance hole excitation. (a) $s-$channel contribution, (b) $u-$channel contribution.

graphical language, the propagator is represented by an internal line carrying the four-momentum p. In the medium this plain line can be interrupted by self energy insertions that arise through the interactions with the medium. The self energy is given as a sum over all one-particle-irreducible[1] diagrams with two external lines (corresponding to the incoming and outgoing hadron) [58]. As an infinite number of these interactions can occur, it is appropriate to perform a partial[2] resummation of the self energy insertion. This leads to the typical structure of the full propagator with the self energy in the denominator that gives rise to corrections of both the mass and width of the hadron inside a medium, see Eq. (2.11) in the following.

The model for the π in-medium self energy we adopt from [66]. Since it is our aim to explore some fundamental properties of pion and sigma propagation in the medium we keep the model as simple as possible. A quantitative evaluation of these effects is clearly beyond the scope of this work. To this end we consider the in-medium change of the pion due to its coupling to the $\Delta(1232)$ resonance only. This is motivated by the observation, that the excitation of the Δ resonance gives the most important contribution to pion nucleon scattering at moderate energies. However, we simplify the treatment of the Δ applying certain approximations that will be specified below. The formation of resonance-hole states is an important mechanism that introduces additional branches in the spectral function. Strictly speaking, the dispersion relation has no longer one unique solution, namely the free energy-momentum relation, but multiple solutions are possible. Quantum mechanically the particle is split into several contributions with individually reduced probabilities to obey one particular energy-momentum relation. In [66] it is shown that this mechanism forms a crucial part of the π in-medium self energy. Here, we neglect the decay width of the Δ resonance as well as Fermi motion. In the following we briefly summarize the model presented in [66], see also [63]. The interested reader is referred to [66], Chapter 2, where pion propagation in matter is discussed in detail.

In terms of the $\Delta-$hole self energy Π_Δ the resummed π in-medium propagator is defined as

$$D_\pi(q_0, \mathbf{q}) = \frac{i}{q_0^2 - \mathbf{q}^2 - m_\pi^2 - \Pi_\Delta(q_0, \mathbf{q})}. \tag{2.11}$$

[1] These are all those diagrams that can *not* be split into two diagrams by removing a single line. This condition has to be imposed in order to prevent double counting when resumming the self energy.

[2] The attribute *partial* is to be understood in that sense that in spite of the resummation not all possible contributions to the self energy are obtained. As these are higher order in the interaction one can hope that these contributions are of minor importance.

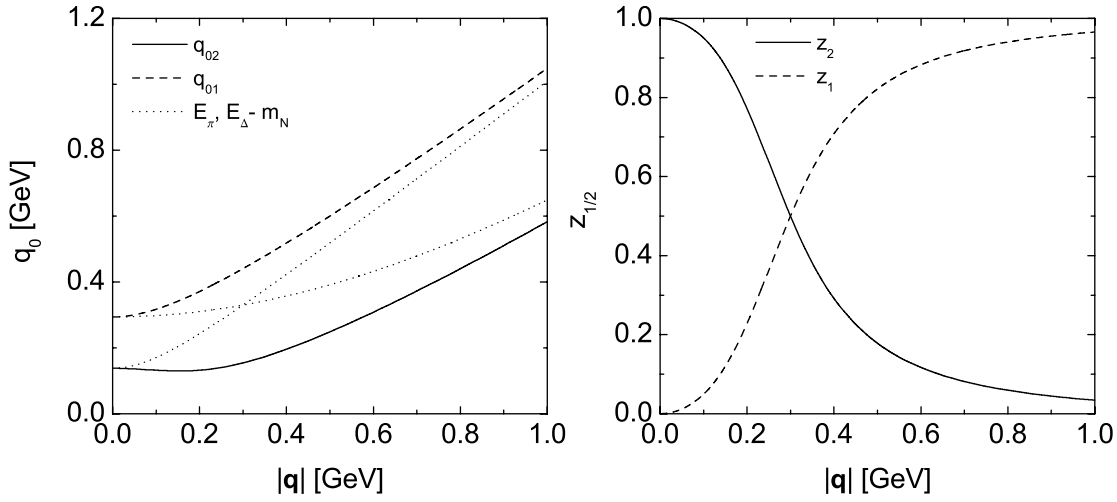

Figure 2.2: *Left*: Dispersion relation of the interacting (*solid, dashed*) and free (*dotted*) modes in the $\pi N\Delta$ system. *Right*: Strength of the interacting modes. The results are shown for density $n_N = n_0$.

where $q = (q_0, \mathbf{q})$ denotes the π four-momentum. Within a non-relativistic framework applying the assumptions mentioned above, the π self energy taken as the sum of the $s-$ and $u-$channel contributions shown in Fig. 2.1 is given by [66]

$$\Pi_\Delta(q_0, \mathbf{q}) = C_\Delta \frac{\mathbf{q}^2 n_N}{q_0^2 - \bar{E}^2} \quad \text{with} \quad \bar{E} = \sqrt{m_\Delta^2 + \mathbf{q}^2} - m_N, \tag{2.12}$$

where the $\pi N\Delta$ coupling as specified in Eq. (D.18), Appendix D has been used. The prefactor C_Δ is given by

$$C_\Delta = \frac{8}{9}\left(\frac{f_\Delta}{m_\pi}\right)^2 \bar{E} \tag{2.13}$$

with the $\pi N\Delta$ coupling constant $f_\Delta = 2.13$. We multiply the self energy with a form factor

$$F^2(\mathbf{q}) = \left(\frac{\lambda_\Delta^2 + q_\Delta^2}{\lambda_\Delta^2 + \mathbf{q}^2}\right)^2. \tag{2.14}$$

where the parameter q_Δ is the momentum of an on-shell pion from the decay of an on-shell Δ. For the cutoff we take $\lambda_\Delta = 1.1$ GeV.

Inserting the self energy (2.12) in the propagator (2.11) one finds two poles. The position of these poles can be determined analytically by searching the zeros of the denominator. One finds

$$q_{01}^2 = \frac{\bar{E}^2 + E_\pi^2 + \sqrt{(\bar{E}^2 - E_\pi^2)^2 + 4\mathbf{q}^2 n_N C_\Delta}}{2} \tag{2.15}$$

$$q_{02}^2 = \frac{\bar{E}^2 + E_\pi^2 - \sqrt{(\bar{E}^2 - E_\pi^2)^2 + 4\mathbf{q}^2 n_N C_\Delta}}{2}. \tag{2.16}$$

The in-medium propagator can then be recast in the following form

$$D_\pi(q_0, \mathbf{q}) = i\left(\frac{z_1}{q_0^2 - q_{01}^2} + \frac{z_2}{q_0^2 - q_{02}^2}\right) \tag{2.17}$$

where we now have introduced the strength factors z_1 and z_2. They are given by

$$z_1 = \frac{1}{2} - \frac{\Delta E}{2\sqrt{\Delta E^2 + \mathbf{q}^2 n_N C_\Delta}} \tag{2.18}$$

$$z_2 = \frac{1}{2} + \frac{\Delta E}{2\sqrt{\Delta E^2 + \mathbf{q}^2 n_N C_\Delta}} \tag{2.19}$$

with the abbreviation $\Delta E = \bar{E}^2 - E_\pi^2$.

Both the solutions of the dispersion relation and the strength factors are shown in Fig. 2.2 at density $n_N = n_0 = 0.16$ fm^{-3}. Also the free dispersion relations of the π and the $\Delta-$hole mode are shown. At a three-momentum of $\mathbf{q} = 0.3$ GeV the free solutions cross each other. As a consequence, the solution q_{02} corresponds to the pion mode at small momenta, but resembles the $\Delta-$hole mode at high momenta and vice versa for the solution q_{01}. At the same time also the strength factors cross. They obey the sum rule $z_1 + z_2 \equiv 1$ which corresponds to the proper normalization of the pion spectral function. In particular at momenta around 300 MeV also the effect of level repulsion can be seen nicely in the left plot in Fig. 2.2. It has the consequence that the solutions of the dispersion relation represented by both branches of the spectral function move away from each other on the real energy axis. This issue is discussed in detail in [66].

2.4 $\pi\pi$ scattering

In vacuum the σ meson is seen as a very broad resonance-like structure in the $\pi\pi$ scattering amplitude. Thus, it appears reasonable to investigate $\pi\pi$ scattering inside a system of strongly interacting matter in order to study the σ properties at finite density. To this end we use an expression for the $\pi\pi$ amplitude obtained within the linear σ model [52] that contains the σ meson as an explicit degree of freedom. Medium modifications of the scattering amplitude are then introduced by means of the interaction of the pions with the surrounding medium. The in-medium propagation of the σ meson in the energy domain near the 2π threshold has been the object of several investigations using phenomenological approaches [25], the linear σ model (e. g. [25, 49, 51, 67]), the NJL model (e. g. [68]), or effective chiral field theory (e. g. [25, 57, 69]).

2.4.1 Scattering amplitude

The expression for the $s-$wave $\pi\pi$ scattering amplitude within the tree-level approximation (without rescattering effects) we adopt from [52] where the scalar susceptibility in the nuclear medium has been investigated. To this end the linear σ model as introduced

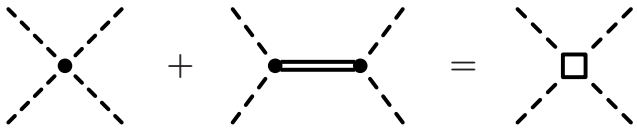

Figure 2.3: Lowest order $\pi\pi$ rescattering kernel in the linear σ model consisting of a 4π contact interaction and a $s-$channel scattering graph containing a σ propagator.

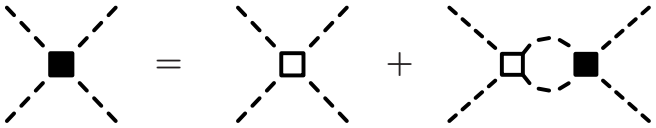

Figure 2.4: Lippman-Schwinger equation for the $\pi\pi$ scattering amplitude.

in a previous Section has been employed. Applying the Feynman rules for the σ model as given for instance in [58] the tree-level $\pi\pi$ potential has the following form

$$V(k) = 6\lambda + 24(\lambda f_\pi)^2 \frac{1}{k^2 - m_\sigma^2} = 6\lambda \frac{k^2 - m_\pi^2}{k^2 - m_\sigma^2} \tag{2.20}$$

where $k = (k_0, \mathbf{k})$ is the total four-momentum of the pion pair. In the following we concentrate on pion pairs with vanishing total three-momentum $k = (k_0, 0) = (E, 0)$. The first term in (2.20) corresponds to a 4π contact interaction whereas the second one is generated by $s-$channel σ propagation. This is illustrated in Fig. 2.3. In [52] it has been argued that the $t-$ and $u-$channel terms are of minor importance and therefore negligible. With this potential the Lippman-Schwinger equation $T = V + VGT$ (see Fig. 2.4) can be solved algebraically. One finds

$$T(k) = \frac{6\lambda(k^2 - m_\pi^2)}{k^2 - m_\sigma^2 - 3\lambda(k^2 - m_\pi^2)\mathcal{G}_{\pi\pi}(k)} \tag{2.21}$$

where $\mathcal{G}_{\pi\pi}(k)$ is the two-pion propagator. It is given by

$$\mathcal{G}_{\pi\pi}(k_0) = i \int \frac{d^3q}{(2\pi)^3} \int \frac{dq_0}{2\pi} D_\pi(q_0, \mathbf{q}) D_\pi(k_0 - q_0, -\mathbf{q}) \tag{2.22}$$

with the single pion propagator $D_\pi(q_0, \mathbf{q})$ that in vacuum is given by $D_\pi = [q_0^2 - \mathbf{q}^2 - m_\pi^2 + i\epsilon]^{-1}$. The imaginary part of $\mathcal{G}_{\pi\pi}$ can be readily evaluated using Cutkosky's cutting rules, see e. g. [58, 66]. We find

$$\mathcal{I}\mathrm{m}\mathcal{G}_{\pi\pi}(E) = \frac{1}{8\pi} \sqrt{\frac{1}{4} - \frac{m_\pi^2}{E^2}}\, \Theta(E^2 - 4m_\pi^2) \tag{2.23}$$

with $E^2 = k^2$ since $\mathbf{k} = 0$. The real part can be obtained by means of a dispersion relation [65, 70]

$$\mathcal{R}\mathrm{e}\mathcal{G}_{\pi\pi}(k) = \mathcal{P} \int \frac{dq^2}{\pi} \frac{\mathcal{I}\mathrm{m}\mathcal{G}_{\pi\pi}(q)}{q^2 - k^2}. \tag{2.24}$$

By inspecting this expression we realize that the integral does not converge. Thus, the loop integral needs to be regularized. In the spirit of our toy model we regularize it by introducing a cutoff at the vertices:

$$F(k) = \frac{\lambda^4}{\lambda^4 + (k^2 - m_\sigma^2)^2} \tag{2.25}$$

with $\lambda = 1.03$ GeV taken from [56]. Equation (2.21) can again be rewritten in order to display explicitly the σ propagator:

$$T(k) = 6\lambda \frac{k^2 - m_\pi^2}{1 - 3\lambda \mathcal{G}_{\pi\pi}(k)} D_\sigma(k) \tag{2.26}$$

$$D_\sigma(k) = \left[k^2 - m_\sigma^2 - \frac{6\lambda^2 f_\pi^2 \mathcal{G}_{\pi\pi}(k)}{1 - 3\lambda \mathcal{G}_{\pi\pi}(k)} \right]^{-1} \tag{2.27}$$

The last term in (2.27) represents the σ self energy $\Pi_\sigma(k_0, \mathbf{k})$. It is due to the coupling of the σ to the 2π state that is dressed by rescattering processes. These rescattering processes are driven exclusively by the 4π contact interaction, the first term in (2.20).

2.4.2 Medium modifications

Going to the nuclear medium we replace the free pion propagator in (2.22) by the in-medium propagator determined previously (2.11). Applying again Cutkosky's rules we find for the imaginary part of the in-medium two-pion propagator after a short calculation

$$\begin{aligned} \mathcal{I}\mathrm{m}\mathcal{G}_{\pi\pi}(E = \sqrt{s}, n_N) = \frac{1}{4\pi} \Bigg[& \frac{z_1^2}{q_{01}} k_{11}^2 \left| \frac{\partial f_{11}}{\partial |\mathbf{q}|} \right|^{-1}_{|\mathbf{q}| = k_{11}} + \frac{z_2^2}{q_{02}} k_{22}^2 \left| \frac{\partial f_{22}}{\partial |\mathbf{q}|} \right|^{-1}_{|\mathbf{q}| = k_{22}} + \\ & \frac{z_1 z_2}{q_{01}} k_{12}^2 \left| \frac{\partial f_{12}}{\partial |\mathbf{q}|} \right|^{-1}_{|\mathbf{q}| = k_{12}} + \frac{z_1 z_2}{q_{02}} k_{21}^2 \left| \frac{\partial f_{21}}{\partial |\mathbf{q}|} \right|^{-1}_{|\mathbf{q}| = k_{21}} \Bigg] \end{aligned} \tag{2.28}$$

with the abbreviations

$$f_{11}(E, \mathbf{q}) = E^2 - 2E q_{01}(\mathbf{q}) \tag{2.29}$$

$$f_{22}(E, \mathbf{q}) = E^2 - 2E q_{02}(\mathbf{q}) \tag{2.30}$$

$$f_{12}(E, \mathbf{q}) = (E - q_{01}(\mathbf{q}))^2 - q_{02}^2(\mathbf{q}) \tag{2.31}$$

$$f_{21}(E, \mathbf{q}) = (E - q_{02}(\mathbf{q}))^2 - q_{01}^2(\mathbf{q}). \tag{2.32}$$

The momenta k_{ij} are defined by the equation

$$f_{ij}(E, |\mathbf{q}| = k_{ij}(E)) \equiv 0. \tag{2.33}$$

According to these different terms we also split the σ self energy into four components:

$$\Pi_\sigma = \Pi_{11} + \Pi_{12} + \Pi_{21} + \Pi_{22}. \tag{2.34}$$

The contribution Π_{11} is due to the situation where both pions obey the solution q_{01} of the in-medium pion dispersion relation. Consequently, k_{11} is the three momentum that

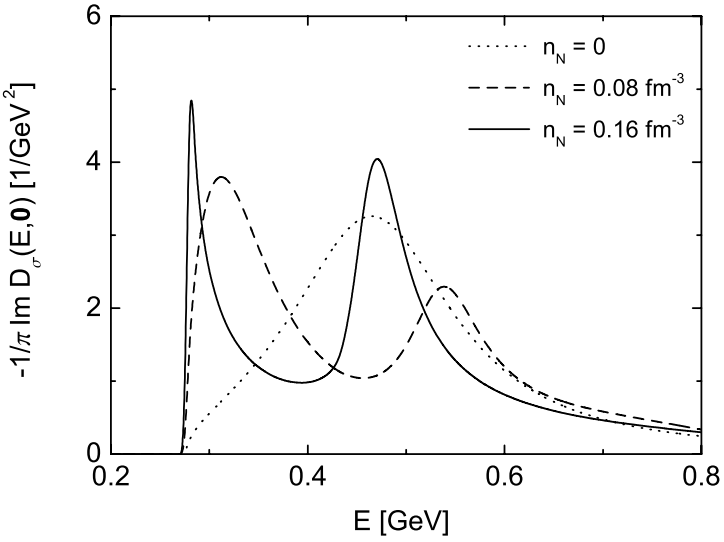

Figure 2.5: Imaginary part of the in-medium σ propagator at densities $n_N = 0$ (*dotted line*), $n_N = 0.5\,n_0$ (*dashed line*) and $n_N = n_0$ (*solid line*) for a σ at rest $E = q_0(\mathbf{q} = 0) = \sqrt{q^2}$.

allows to both fullfill the particular enrergy/momentum relations and four momentum conservation. Equivalent considerations hold for the remaining contributions. In total there are four solutions since either of the two pions can propagate in the π or the Δh branch of the π spectral function. Since both pions cannot be distinguished from each other it is clear that $\Pi_{12} \equiv \Pi_{21}$. The real part of the propagator $\mathcal{G}_{\pi\pi}$ can again be obtained from the dispersion relation (2.24), resulting in an analytical expression for the σ self energy and, hence, a normalized spectral function [66].

In Fig. 2.5 the imaginary part of the σ propagator as defined in Eq. (2.27) for different nuclear densities is shown. In vacuum the imaginary part of the propagator exhibits a broad single peak structure. The physical mass of the σ in vacuum, defined by the zero of the real part of the propagator, is given by the sum of its bare mass and the real part of the vacuum self energy. It amounts to roughly 470 MeV. The total width of the σ spectral distribution is larger than 200 MeV.

In the medium the situation changes. Due to the dressing of the pion propagators in the rescattering kernel additional structures are created. Some spectral strength is moved towards the 2π threshold. There the 2π phasespace becomes small, resulting in a dramatical enhancement of the σ spectral function at low σ masses. This enhancement is created by the Π_{11} component of the self energy what means that both intermediate pions propagate in the pion mode (q_{02} at low three-momentum). The pion mode is pushed to lower q^2 values in the medium due to level repulsion. Consequently, the strength generated by this component moves to smaller invariant masses. The second peak in the spectrum at around the σ vacuum mass is created by the mixed contributions $\Pi_{12} = \Pi_{21}$. Here, one pion is in the π and the other one in the Δh mode. Due to the applied zero-width approximation ($\Gamma_\Delta = 0$) the threshold of this component is fixed at

$\sqrt{q^2} = m_\pi + m_\Delta - m_N = 432$ MeV and the structure created in the σ spectral function is rather narrow. The Π_{22} component contributes only at larger q^2 values due to the high mass of the Δh mode. It has no great effect on the σ propagator since it becomes significant only at masses above the σ pole. In summary, we have made two important observations: First, the medium modifications of the two-pion propagator due to the insertion of resonance-hole excitations leads to spectral strength moving to smaller σ masses. Second, this change of the σ spectrum gives rise to a substantial enhancement of the spectral function close to the 2π threshold.

A very similar behavior of the in-medium $\pi\pi$ scattering amplitude or, alternatively, the σ propagator has been found by various more sophisticated approaches. Also in the model of [27, 49, 50, 71, 72] the σ spectral function has been studied in the framework of the linear σ model. Assuming a partial restoration of chiral symmetry in the medium the chiral order parameter f_π^* has been reduced with increasing density. This is related to a melting of the scalar quark condensate at finite density

$$m_\pi^2 f_\pi^2 = -(m_u + m_d)\langle\bar{q}q\rangle. \tag{2.35}$$

This Equation is known as the **G**ell-Mann-**O**akes-**R**enner (GOR) relation. As a consequence of the reduced f_π^* the complex pole of the σ propagator moves towards smaller masses and generates a strong enhancement at the 2π threshold due to the smaller phase-space for the $\sigma \to \pi\pi$ decay there. In [52] the scalar and pseudoscalar susceptibilities have been studied. They are defined via the σ and π propagators at zero energy. The authors of [52] have found that their values approach each other when the density in the system becomes high in agreement with partial symmetry restoration. In [57, 69] the $\pi\pi$ scattering amplitude has been investigated within a different framework. The $\pi\pi$ scattering amplitude has been calculated from chiral perturbation theory, an effective low energy expansion of QCD in terms of pion masses and momenta. The lowest order term giving rise the $\pi\pi$ scattering is a 4π contact interaction. Through the iteration of this interaction the σ meson, seen as a complex pole in the scattering amplitude, is dynamically generated. As in our simple minded model, the pion propagators in the rescattering kernel have been dressed by particle-hole and $\Delta-$hole excitations. On top of that also vertex corrections have been included. As a result again a downward shift of the complex pole in the scattering amplitude, identified with the σ meson, has been reported.

2.4.3 Chiral order parameter

The chiral transition towards the Wigner-Weyl phase is signaled not only by the approaching degeneracy of the chiral partners but also by the melting of the scalar quark condensate. In the σ model the only mechanism leading to chiral restoration in cold matter is the nuclear pion cloud. The two pion propagator is the correlator of a scalar quantity, namely the squared pion field. Thus, one can expect a link of the two scalar correlators, the quark density and the two pion propagator. Such a link has been obtained in [52, 73]

$$\langle\bar{q}q\rangle_\rho = \langle\bar{q}q\rangle_0 \left(1 - \frac{\langle\boldsymbol{\pi}^2\rangle}{2f_\pi^2}\right) \equiv \langle\bar{q}q\rangle_0 \Sigma(n_N) \tag{2.36}$$

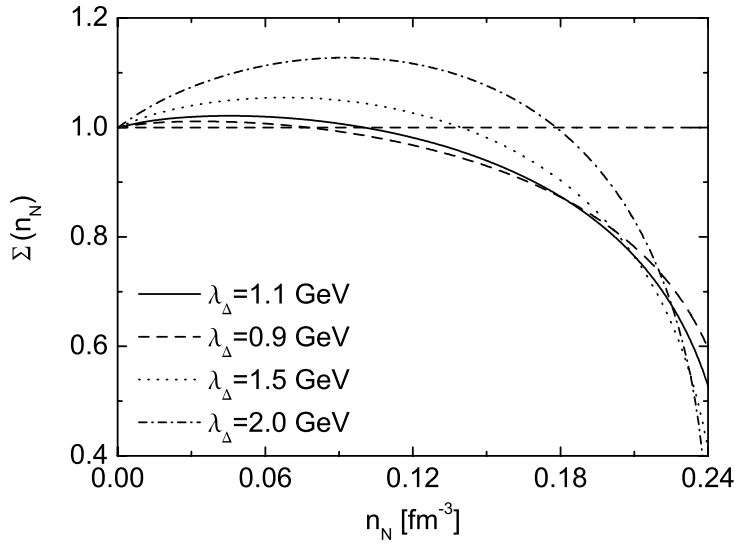

Figure 2.6: Density dependence of the σ expectation value. Ignoring the effects of the medium $\Sigma(n_N)$ is constant at $\Sigma = 1$. The different lines belong to various cutoff values λ_Δ, see legend.

where the second identity defines the function $\Sigma(n_N)$. The two pion condensate is understood to contain the contributions of the medium only. It can be expressed in terms of the single pion propagator [74]

$$\langle \boldsymbol{\pi}^2 \rangle = 3i \int \frac{d^4q}{(2\pi)^4} \left[D_\pi^{\rm med}(q_0, \mathbf{q}) - D_\pi^{\rm vac}(q_0, \mathbf{q}) \right] \tag{2.37}$$

$$= -\frac{3}{\pi} \int \frac{d^3q}{(2\pi)^3} \int_0^\infty dE \; \mathcal{I}\mathrm{m} \left[D_\pi^{\rm med}(E, \mathbf{q}) - D_\pi^{\rm vac}(E, \mathbf{q}) \right] \tag{2.38}$$

where the second line has been obtained by expressing the pion propagators via a dispersion relation and performing a contour integration in the complex q_0 plane. The in-medium propagator contains the effects of the pion polarization function Π. Inserting again the simple form derived previously (2.12) we obtain the approximate expression for the pion condensate

$$\langle \boldsymbol{\pi}^2 \rangle = \frac{3}{4\pi^2} \int_0^\infty |\mathbf{q}|^2 d|\mathbf{q}| \left[\frac{z_1(\mathbf{q})}{q_{10}(\mathbf{q})} + \frac{z_2(\mathbf{q})}{q_{20}(\mathbf{q})} - \frac{1}{\sqrt{m_\pi^2 + \mathbf{q}^2}} \right] \tag{2.39}$$

where the last term in the parenthesis subtracts the effects of the free space propagator. Using this expression for $\langle \boldsymbol{\pi}^2 \rangle$ in Eq. (2.36) we can now calculate numerically the density dependence of the quark condensate in nuclear matter.

The result is shown in Fig. (2.6). For large densities we find a substantial lowering of the function $\Sigma(n_N)$ that translates into the onset of chiral symmetry restoration. Note, that these results are not quantitatively reliable as important contributions to the in-medium

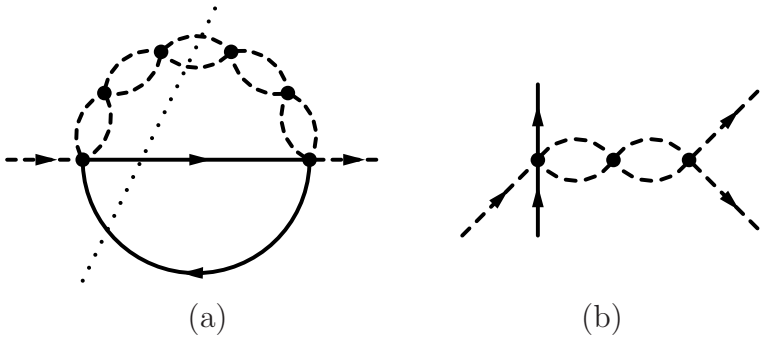

Figure 2.7: (a) $\pi\pi$ production in terms of the $\pi\pi Nh$ self energy diagram. The outer dashed lines represent either a pion or a photon. (b) The process $(\gamma/\pi)N \rightarrow \pi\pi N$ corresponding to the cut (dotted line) in diagram (a).

σ propagator have been left out and rude approximations to the pion polarization function have been done (e. g. the zero-width approximation; omission of Landau-damping, $s-$wave πN interactions and short-range correlations). From Eq. (2.39) one can read off that for instance nucleon-hole excitations will reduce the quark condensate already at moderate densities since strength at space-like momenta creates large positive contributions to the integral. In Fig. 2.6 also the impact of different cutoff values for the $\pi N\Delta$ vertices is shown. The results – at least in our basic model – are obviously very sensitive to the choice of this parameter. For large densities, however, the common feature of a sizable reduction of the order parameter is maintained.

In summary the following picture emerges: In the QCD vacuum chiral symmetry is broken spontaneously. As a consequence chiral partners are not degenerate and the scalar quark condensate, that directly couples left- and right-handed quarks and, thus, explicitely breaks the chiral invariance, develops a non-vanishing expectation value. In a nuclear medium, the dispersion relation of the pion becomes strongly modified due to the large pion-nucleon interaction. The low-energy $p-$wave part of this interaction is dominated by the excitation of the $\Delta(1232)$ resonance. The reshuffling of strength in the pion spectral function generates a redshift of the spectral function in the scalar-isoscalar channel that is dominated by the coupling to two-pion states. Also the expectation value of the scalar quark condensate decreases due to the same mechanism. Consequently, one can interpret these modifications as signals for the onset of chiral symmetry restoration driven by the pion-nucleon interaction at finite density.

2.5 Final state interactions

Pion-pion scattering inside nuclear environments cannot be measured directly. Thus, one has to relie on alternative processes that are linked to the $\pi\pi$ scattering amplitude and that can be measured inside nuclear targets. These are preferably nuclear $\pi\pi$ production experiments using elementary projectiles as pions or photons. Both reactions have been studied experimentally and also some theoretical effort has been invested in

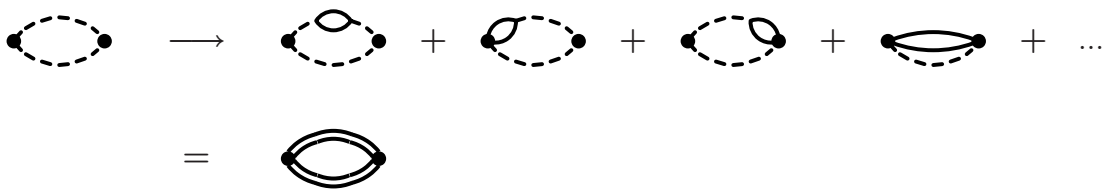

Figure 2.8: Medium modifications of the 2π loop accounting for particle-hole and resonance-hole excitations. The double lines indicate full in-medium propagators.

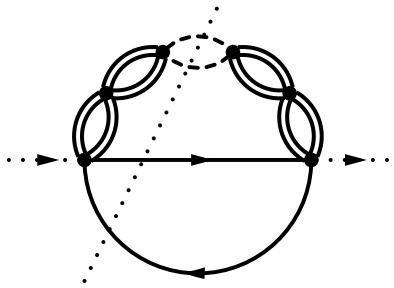

Figure 2.9: Cut in the VO model with full in-medium propagators.

order to interpret the outcome of these experiments in terms of partial chiral symmetry restoration. One prominent model that has been used to study both types of reactions is the Vicente Vacas-Oset (VO) model [57]. Results have been presented in [75] for the case of pion induced reactions and in [76] for the case of photon induced reactions. In the following we will comment briefly on this approach and the relation to the studies in this work.

Both the $\pi \to \pi\pi$ and $\gamma \to \pi\pi$ reactions can be discussed in a very intuitive way by means of the $\pi\pi Nh$ self energy diagram, shown in Fig. 2.7. In terms of this self energy the cross section for nuclear $\pi\pi$ production is obtained by cutting the self energy diagram as indicated by the dotted line. By rearranging the external lines of the cutted diagram one can see easily that it corresponds to the reaction $\pi(\gamma)N \to \pi\pi N$. In the VO model the rescattering of the pions has been accounted for by solving the Bethe-Salpeter equation for the outgoing pions with a $\pi\pi$ potential obtained within a chiral unitary approach. In a second step the medium modifications of the $\pi\pi$ scattering amplitude have been introduced by dressing the internal single pion propagators with particle-hole and resonance-hole excitations. This is indicated in Fig. 2.8. However, when going back to the cut in the original self energy diagram, we note that in the VO model the dressing of the pions in the cutted loop has been omitted to a large extend. This is shown in Fig. 2.9. The inelasticity due to the decay of particle-hole and resonance-hole states to unobserved final states has been at least approximately accounted for by a phenomenological absorption factor. However, the inclusion of all possible cuts through the self energy diagram gives rise not only to modifications of the internal pion propagators but also to final state interactions (FSI) of the asymptotic pion states. The blobs in Fig. 2.9 contain all possible processes and also introduce

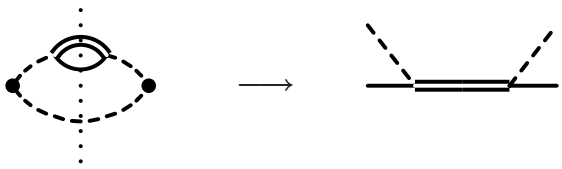

Figure 2.10: Self energy (*left*) and $s-$channel πN scattering (*right*) diagram accounting for FSI of the asymptotic pion states. Here, the double line represents a $\Delta(1232)$ resonance.

non-linear orders in the nucleon density. A particular example, the elastic $s-$channel scattering process via the excitation of a resonance, is shown in Fig. 2.10. Apart from absorption, these processes have been omitted in the VO model. The dressing of the π propagator with a Δh excitation for instance gives rise to the elastic scattering process $\pi(k)N(p) \to \Delta(k+p) \to \pi(q)N(k+p-q)$ with k, p and q being the four momenta of the inital π, inital nucleon and final π, respectively. As elastic scattering processes change the pion momenta, the $\pi\pi$ invariant mass spectrum is reshaped. This clearly has some impact on the extraction of the σ properties in nuclear targets and, thus, has to be accounted for properly.

Whereas the link of the dressing of the internal pion propagators to chiral symmetry restoration has been established, there is no such connection of the FSI of the asymptotic pion states to symmetry restoration. However, if the internal pions experience modifications due to the presence of the strongly interacting medium also the external pion states participate in the same types of processes. It is the aim of the following Chapters to quantitatively calculate the impact of ordinary FSI on the $\pi \to \pi\pi$ and $\gamma \to \pi\pi$ reactions in nuclei. Imposing classical FSI but no renormalization of in-medium particle properties the consistency of the experimental data will be tested without introducing explicitely the effects of chiral symmetry restoration.

Chapter 3

The reaction γA $\longrightarrow \pi\pi$X

3.1 Introduction

The conjecture that a partial restoration of chiral symmetry inside a nuclear medium causes a softening and narrowing of the $f_0(600)$ – or σ – meson [49, 77] has led to the idea of measuring the $\pi\pi$ invariant mass distributions near the 2π threshold in photon induced reactions on nuclei [78]. In contrast to its questionable nature as a proper quasiparticle in vacuum, the σ meson might develop a much narrower peak at finite baryon density due to phasespace suppression for the $\sigma \rightarrow \pi\pi$ decay, hence making it possible to explore its properties when embedded in a nuclear many-body system [24, 25, 26, 27]. The σ meson can decay in either $\pi^0\pi^0$ or $\pi^+\pi^-$ pairs but not to the $\pi^\pm\pi^0$ channels which, therefore, can serve as a reference for the observation of in-medium effects. Experimentally this has been investigated by the TAPS collaboration at the **Ma**inz **Mi**crotron (MAMI) accelerator facility [31, 79, 80, 81, 82, 83].

In the following Sections we will investigate the photoproduction and propagation of pion pairs in nuclei. We will do so employing the coupled-channel BUU transport model introduced briefly in Appendix A that provides a rather complete and intuitive description of nuclear reactions. In particular we study the influence of conventional final state effects on the $\gamma A \rightarrow \pi\pi X$ reaction. These FSI are included in the transport calculations by means of explicit scattering processes modelled according to experimentally known cross sections. On the other hand, we do not introduce any softening of the scalar spectral function connected to the modification of in-medium condensates. In this respect, the present study can be understood as a crosscheck regarding the observation of a modification of the σ meson in two pion photoproduction off nuclei. To analyze the TAPS experiment we need to consider pions with very low kinetic energies. The validity of discussing pions with long wave length in the semiclassical BUU picture has been studied in Refs. [35, 36, 84] and will be commented on briefly in the present context.

The authors of Refs. [76, 85] studied double pion photoproduction off nuclei in a many-body approach, achieving quite impressive agreement with the TAPS data. Their results imply a modification of the $\pi\pi$ interaction in the medium that can be related to an in-medium change of the properties of the σ meson. Within the model of Ref. [76], the σ meson is generated dynamically through the underlying chiral dynamics of the $\pi\pi$ interaction, which is treated in a chiral-unitary approach. However, the FSI of the pions with the nucleons in the surrounding nuclear medium have been treated as purely

absorptive by means of a Glauber-type damping factor calculated along straight line trajectories. In fact, rescattering of the final pions affects the charge of the detected final state (by charge exchange processes) and changes the trajectories. Therefore, FSI could considerably distort the observed invariant mass spectra.

This Chapter is structured in the following way: First we report briefly on the present experimental status and introduce the model used for double pion photoproduction from elementary targets. Next, we discuss the interaction of pions with nuclear matter within our semiclassical approach. Hereafter we present results of our calculations, discussing first the influence of different final state processes on the nuclear cross section in detail. Finally we compare to experimental data and summarize our findings.

3.2 Experimental status

Double pion production in γA collisions in the invariant mass range of the σ meson has been studied at the tagged photon facility MAMI using the **T**wo-**A**rm-**P**hoton-**S**pectrometer TAPS [31, 80, 81, 82, 83, 86, 87]. In the TAPS spectrometer neutral pions are detected via their $\gamma\gamma$ decay with BaF_2 scintillation detectors arranged in the horizontal plane around the target cell as shown in Fig. 3.1. Neutral/charged particle identification can be derived from thin plastic scintillators in front of the BaF_2 crystals. This setup allows to disentangle neutral and charged pions, but it does not offer the possibility to separate positive from negative particles. Thus, the two pion channels $(\gamma, \pi^0\pi^0)$ and $(\gamma, \pi^\pm\pi^0)$ can be measured independently. In the analyzing procedure the multi-differential cross sections are extrapolated to the full 4π geometry by means of an iteration procedure starting from simple phasespace distributions.

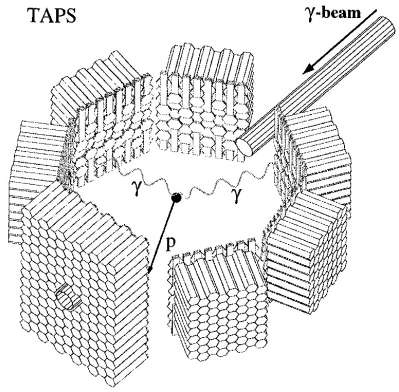

Figure 3.1: Setup of the TAPS detector at the **Ma**inz **Mi**crotron (MAMI) accelerator. The picture is taken from [80].

In the first publication on double pion photoproduction off nuclei [31] the TAPS collaboration presented results for the target nuclei ^{1}H, ^{12}C and ^{208}Pb. They concentrated on the photon energy interval from 400 MeV to 460 MeV in order to focus on low energy

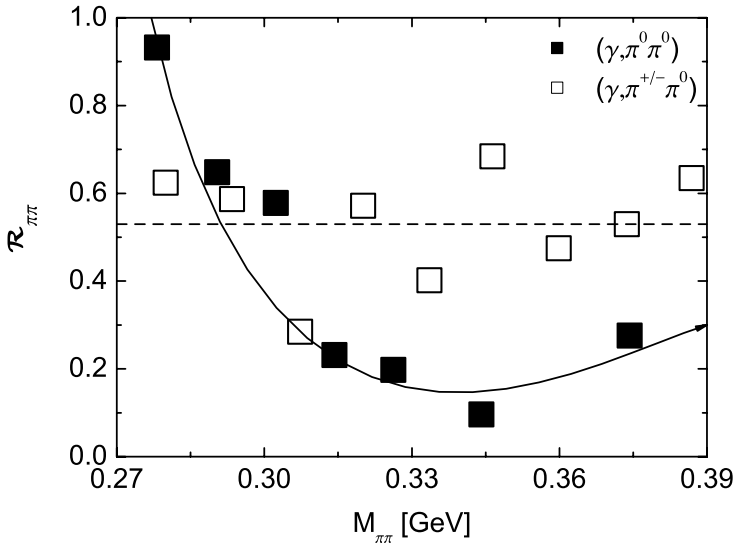

Figure 3.2: Ratios between differential cross sections from ^{208}Pb and ^{12}C targets according to Eq. (3.1) for the double pion production channels $A(\gamma, \pi^0\pi^0)$ (solid symbols) and $A(\gamma, \pi^\pm\pi^0)$ (open symbols) measured by the TAPS collaboration [31] at $E_\gamma \in [400, 460]$ MeV. The solid and dashed lines are just to guide the eye and have no physical meaning.

pions that interact less strongly with nuclear matter than pions with higher kinetic energies. As their most important observation a shift of spectral strength towards the two pion threshold with increasing target mass number was reported. This accumulation of strength has been observed in the $\pi^0\pi^0$ but not for the $\pi^\pm\pi^0$ channel. This effect can be visualized by the ratio of the mass differential cross sections

$$\mathcal{R}_{\pi\pi} = \left(\frac{d\sigma_{\gamma A\to\pi\pi X}}{dM_{\pi\pi}}\right)_{A=208} \left(\frac{d\sigma_{\gamma A\to\pi\pi X}}{dM_{\pi\pi}}\right)^{-1}_{A=12} \tag{3.1}$$

which we show in Fig. 3.2. These data sets, however, have recently been reanalyzed by the TAPS collaboration, now extending the photon energy interval from 400 MeV to 820 MeV in order to enhance statistics. So far preliminary analysis of two pion data in the energy intervals $E_\gamma \in [400, 460]$ MeV, $E_\gamma \in [400, 500]$ MeV, $E_\gamma \in [500, 550]$ MeV and $E_\gamma \in [740, 780]$ MeV have been performed. The preliminary results of this analysis can be found in [81, 82, 83] and a comparison of the former results to the new analysis is given in [87]. The old analysis is re-evaluated, especially in the $\pi^\pm\pi^0$ channel. Presently, new sets of data, taken with a 4π setup with Crystal Ball and TAPS at MAMI, are being analyzed.

A second experiment for $\pi^0\pi^0$ photoproduction in nuclei has been proposed using the multi-GeV **L**aser **E**lectron **P**hoton beam at **S**Pring8 (LEPS) [88, 89, 90]. There the σ mesons could be produced with photons of 2.4 GeV energy, i. e. CM energies considerably above the nucleon resonance region. A backward scintillation detector can be employed to detect the four photons from the $\pi^0 \to \gamma\gamma$ decay, thus focusing on pion pairs produced

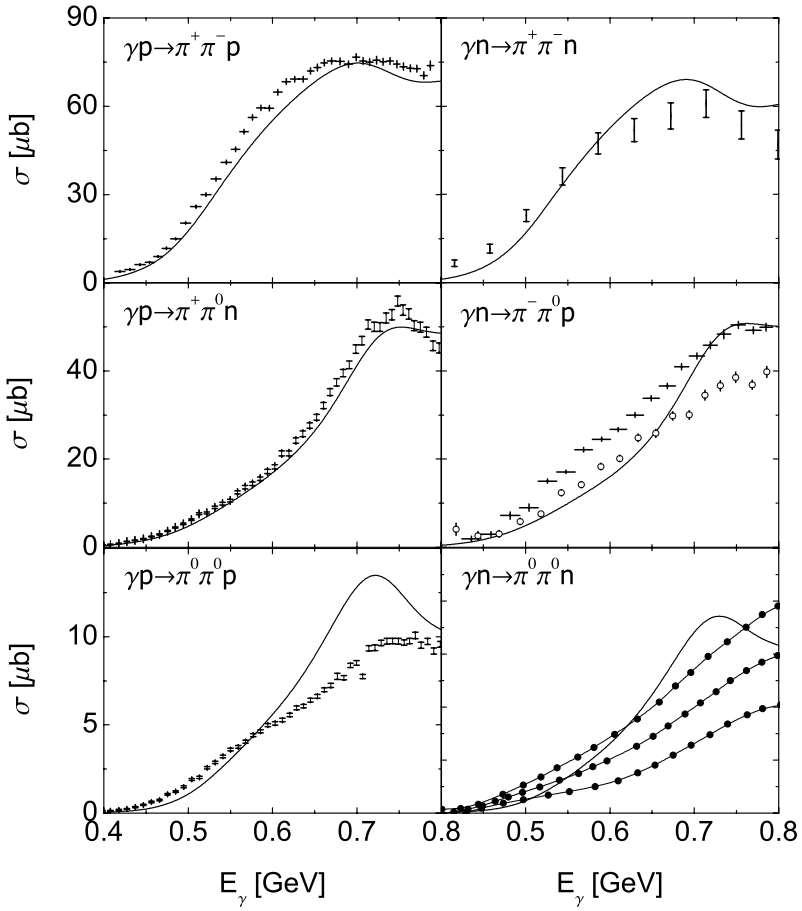

Figure 3.3: Total double pion photoproduction cross sections from nucleons for all isospin channels. Experimental data from Refs. [91, 92, 93, 94, 95, 96]. The three data sets in the lower right panel correspond to the minimum, mean, and maximum cross section determined experimentally.

with high momentum transfers $|t| > 1.5$ GeV^2. Up to the present, no results of this experiment have been reported.

3.3 The γN $\to$ $\pi\pi$N reaction

There are six possible pion pair production channels which occur in the collision of photons with nucleons. They are

$$\gamma p \;\; \to \;\; \left\{ \begin{array}{l} \pi^+\pi^- p \\ \pi^+\pi^0 n \\ \pi^0\pi^0 p \end{array} \right. \tag{3.2}$$

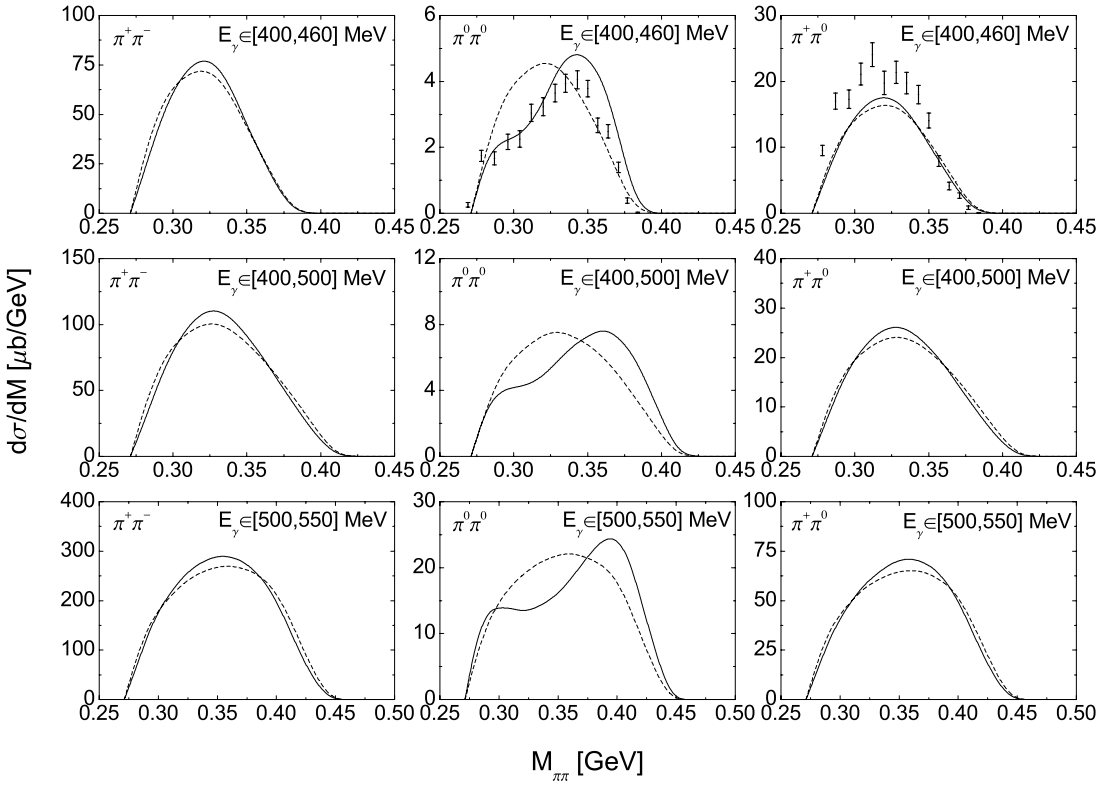

Figure 3.4: Two pion invariant mass distributions from γp collisions for different isospin channels and bombarding energies calculated with the NO model. The normalization of the cross sections is obtained as described in the text. Dashed lines are calculated using three-body phasespace distributions. Experimental data from Ref. [31].

for proton targets and

$$\gamma n \;\; \to \;\; \left\{ \begin{array}{l} \pi^+\pi^- n \\ \pi^-\pi^0 p \\ \pi^0\pi^0 n. \end{array} \right. \tag{3.3}$$

for neutron targets. For the description of double pion photoproduction from nucleons for beam energies of up to 800 MeV we employ the Nacher-Oset (NO) model from [97]. The NO model is an update of the Gómez Tejedor-Oset (GTO) model presented in [98] that has been extended by the inclusion of additional mechanisms. This has been stimulated by new experimental information, especially on the $\gamma p \to \pi^+\pi^0 n$ reaction, obtained with the large acceptance detector DAPHNE [91, 92]. The GTO model describes double pion photoproduction based on a set of tree-level diagrams which involve pions, nucleons and nucleonic resonances as intermediate states. The baryon resonances are $P_{33}(1232)$, $P_{11}(1440)$ and $D_{13}(1520)$. The NO model in addition includes ρ mesons and $P_{33}(1700)$ states. The improvements of the NO model result in a much better agreement with the experimental data in all isospin channels over the complete range of photon energies from threshold up to 800 MeV.

In Fig. 3.3 we show the total cross section for all channels calculated with the NO model

compared to a compilation of experimental data. The level of agreement is high, recalling that no parameters have been fitted to the data. Rather standard values for the coupling constants known from decay widths and scattering lengths have been used. In some channels, however, the calculated cross sections in the threshold region are predicted too small. In [76] this has been compensated by the inclusion of the $\pi\pi$ final state interaction. Pion rescattering, included by means of a separable Bethe-Salpeter kernel, strongly modifies the isoscalar ($I = 0$) part of the scattering amplitude. As an effect the total cross section in the $\pi^0\pi^0$ channel is almost doubled in the energy interval of interest (400 MeV $-$ 460 MeV) whereas the shapes of the differential distributions remain almost unchanged. This is due to the strong $s-$wave interaction of the final state pion pair. In the $\gamma p \to \pi^0\pi^0 p$ channel the data is overestimated from roughly $E_\gamma = 600$ MeV on. In [97] it was speculated that this mismatch comes from uncertainties concerning the parameters of the $D_{13}(1520)$ nucleon resonance which contributes in this channel dominantly through the $D_{13}(1520) \to \Delta\pi$ decay chain and turns out to be of minor importance for the other isospin channels. For the present purpose we, thus, directly use the data measured by the TAPS and DAPHNE collaborations [91, 92, 93, 94, 95] to normalize the calculated cross sections except for the $\gamma p \to \pi^+\pi^0 n$ and $\gamma n \to \pi^+\pi^- n$ channels. In the other channels either the presence of the σ meson is expected to only slightly modify our model results or the level of agreement with the data is not good enough. Note, that in Fig. 3.3 also the most recent data for the $\gamma n \to \pi^-\pi^0 p$ channel from [96] is shown (open symbols). This measurement, which deliveres a cross section roughly 20% smaller than the older one, was not available at the time when our calculations have been done and, thus, is not included in the simulations. This recipe provides us with a reasonable input not only for the total cross sections but also for the differential distributions. This is illustrated in Fig. 3.4 where the invariant mass distributions for all γp channels are shown and compared to the data from the TAPS collaboration [31] where available.

3.4 Pion interaction with nuclear matter

In the present investigations the pion nucleus FSI play a central role. Thus, we start with a formulation of the relevant processes and a discussion of their implementation into the transport framework. Let us first specify our notation. We classify the pion nucleon interactions in different categories according to their impact on the pion flux in the individual isospin channels:

$$\pi^a N^b \quad \longrightarrow \quad \pi^a N^b \tag{3.4}$$

$$\pi^a N^b \quad \longrightarrow \quad \pi^{c\neq a} N^{d\neq b} \tag{3.5}$$

where a, b, c and d are isospin indices. The first process separately conserves the isospin $z-$components of the individual particles. It is called *elastic collision* since the particles in the initial and the final state are identical. The second process (3.5) only conserves the total isospin $z-$component but explicitly changes the individual ones. This process is called a *charge exchange collision*. Furthermore, we have

$$\pi N \quad \longrightarrow \quad \pi X (\neq N) \tag{3.6}$$

$$\pi N \quad \longrightarrow \quad X (\not\ni \pi). \tag{3.7}$$

The reaction (3.6) is referred to as an *inelastic collision* since intrinsic excitation energy is transfered to the final state X. In the low energy sector the only relevant one is again $X = \pi N$ such that the total reaction (3.6) reads $\pi N \to \pi\pi N$. The process (3.7) corresponds to pion *absorption* since the pion in the initial state is erased from the flux. It is not relevant here since the lightest hadronic final state accounting for pion absorption on a single nucleon is $X = \eta N$. The process $\pi N \to \eta N$ has a threshold of about $p_\pi \simeq 680$ MeV and, thus, becomes relevant only at pion energies far above the relevant energy regime considered in the present investigations. In the low energy sector, pion absorption is introduced only via the three-body process

$$\pi(NN) \quad \longrightarrow \quad NN. \tag{3.8}$$

which can also proceed via intermediate resonance excitation. This will also be subject to the discussions in the following Section.

The pion mean free path in nuclear matter and pion absorption on nuclear targets in the BUU model have been studied in [35, 36, 84]. These observables are used to validate our semiclassical approach for the low pion kinetic energies corresponding to long pionic wave lengths we have to account for in the present context. We will comment briefly on these calculations later in this Section.

3.4.1 The πNΔ dynamics

In order to describe the pion nucleus FSI in the transport simulation via the above introduced reactions we follow two different recipes. On one hand, we explicitly simulate pion nucleon collisions including the excitation of intermediate resonances. This is done applying the so-called parallel ensemble solution to the BUU collision term. This method is described briefly in Appendix A and in more detail in the References given there. On the other hand, we use an optical model approach in order to simulate pion absorption. Thus, the pion is associated with an optical potential which determines the time evolution of the pion densities. The relation of this method to the numerical solution of the BUU collision term is motivated also in Appendix A. Both approaches will be introduced briefly in the following. In particular the use of an pion optical potential relies on the assumption that the target nucleus stays close to its equilibrium state. The validity of this assumption is investigated in Appendix A.5.

BUU collision term (CC)

Here we use the full BUU collision term in order to describe the pion nucleus FSI. Thus, all particles including the excited resonances are propagated explicitly and their collisions among each other are simulated numerically according to collision probabilities determined from their total cross sections. This corresponds to a full coupled channel (CC) treatment of the FSI. The numerical realization of the collision term has been discussed quite in detail in Ref. [99]. Elastic and charge exchange pion nucleon collisions dominantly proceed via the excitation of intermediate resonances

$$\pi N \to R \to \pi N \tag{3.9}$$

where R can be any of the nucleon isobar resonances listed in Table A.1 obeying the conservation of the relevant quantum numbers. In the present context only the $\Delta(1232)$ is relevant. The cross sections for these processes are obtained by means of resonance fits to experimental data which include Breit-Wigner parameterizations of the individual resonance contributions. In addition, a non-resonant background is introduced whenever the sum of the resonance contributions is not sufficient to reproduce the data. This is described in detail in Ref. [100]. There also Figures of the calculated cross sections compared to experiment can be found. For the charge exchange collisions, the background components to the cross sections have been redetermined recently in [35] stimulated by new experimental information. The inelastic and absorptive two-body processes (3.6) and (3.7) are implemented on the very same footing as the elastic and charge exchange ones. However, they play a minor role in the present studies.

Apart from the pion itself also the excited nucleon resonances can collide with nucleons from the medium and, thus, can be reabsorbed. Such resonance nucleon collisions give rise to medium modifications of the resonance properties and also of the pion nucleon cross sections. A typical reaction chain is

$$\pi N \to R \quad \hookrightarrow \quad RN \to NN. \tag{3.10}$$

Due to the pion-less in-medium decay channel of the resonance ($R \to NNh$) an additional contribution to pion absorption arises. This reaction chain, however, contributes to the three-body absorption process (3.8) since two different nucleons are involved in the pion and nucleon resonance absorption processes. The parameterizations of the resonance nucleon cross sections used in the BUU model are also given in [100], Appendix A. These cross sections have been constrained via detailed balance from measured reactions such as $NN \to NR \to NN\pi$.

Special attention has to be paid to the $\Delta(1232)$ resonance. In the BUU model, the self energy of the $\Delta(1232)$ arises exclusively through the processes

$$\Delta N \longrightarrow \Delta N \tag{3.11}$$
$$\Delta N \longrightarrow NN \tag{3.12}$$

since the processes $\Delta N \to R(\neq \Delta)N$ are neglected because of their minor importance [100]. However, the processes (3.11) and (3.12) generate a collision width of the $\Delta(1232)$ which is about a factor of 2 smaller than results of a microscopic state-of-the-art calculation [32], see Fig. 3.5. Also phenomenological fits to experimental data on elastic pion nucleus scattering yield a much larger value. This deficiency can be ascribed to the missing three-body processes $\Delta NN \to \Delta NN$ and $\Delta NN \to NNN$. Note, that the latter one contributes to pion absorption.

We cure this problem by associating an optical potential with the $\Delta(1232)$ resonance whose imaginary part accounts for the absorptive processes $\Delta N \to NN$ and $\Delta NN \to NNN$. In the denominator of the $\Delta(1232)$ propagator, however, the full width including also the quasi elastic contributions enters. Thus, consistency of the Δ width entering the propagator and the collision rates is guaranteed except for the $\Delta NN \to \Delta NN$ contribution which is not included in the collision term. For testing purposes we also

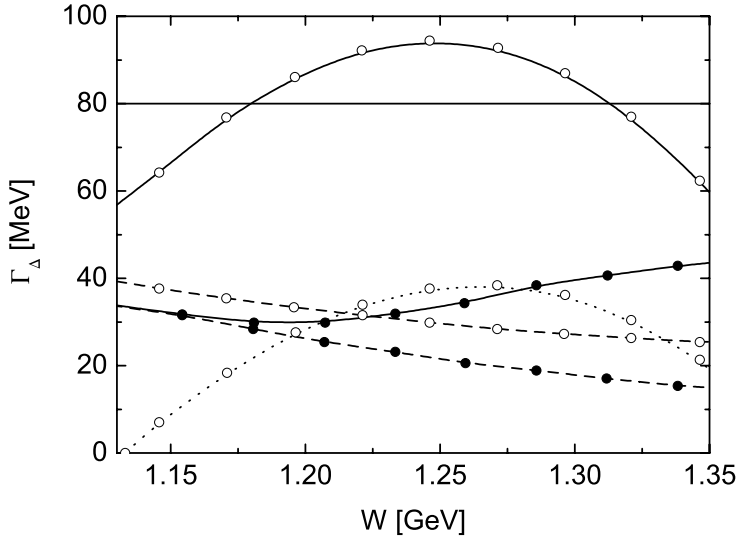

Figure 3.5: Collision width of the $\Delta(1232)$ resonance at nuclear matter density n_0. *Filled symbols*: Total (solid line) and absorptive (dashed line) BUU collision rates, *open symbols*: parameterization from [32] (solid line) decomposed into two-body (dashed line) and three-body (dotted line) absorption. The horizontal line corresponds to the phenomenological value $\mathcal{I}\mathrm{m}U_\Delta = -40$ MeV. The momentum of the resonance is taken to be the resonance momentum after its photoproduction from a free nucleon at rest, i. e. $p_\Delta = (W^2 - m_N^2)/(2m_N)$.

introduce different parameterizations for the real part of the Δ nucleus potential. We consider the following scenarios:

$$\begin{aligned}
&\text{(A)} \quad U_\Delta(\mathbf{r},\mathbf{p}) &&= \quad U_N(\mathbf{r},\mathbf{p}) &&- \quad i\,\frac{1}{2}\,(\Gamma_{\Delta N} + \Gamma_{\Delta NN}) \\
&\text{(B)} \quad U_\Delta(\mathbf{r},\mathbf{p}) &&= \quad \frac{2}{3}U_N(\mathbf{r},\mathbf{p}) &&- \quad i\,\frac{1}{2}\,(\Gamma_{\Delta N} + \Gamma_{\Delta NN}) \\
&\text{(C)} \quad U_\Delta(\mathbf{r},\mathbf{p}) &&= \quad \frac{2}{3}U_N(\mathbf{r},\mathbf{p}) &&- \quad i\ 40\ \text{MeV}\ \frac{n_N}{n_0}
\end{aligned} \tag{3.13}$$

where $\Gamma_{\Delta N}$ and $\Gamma_{\Delta NN}$ are the in-medium two-body and three-body contributions to the absorptive $\Delta(1232)$ width. In case (A) the real part of the optical potential just equals to the nucleon mean field whose parameterization in the BUU model is given in [100]. In cases (B) and (C) the depth of the potential is reduced motivated by the empirical value of the Δ potential of $\mathcal{R}\mathrm{e}U_\Delta \simeq -30$ MeV at density n_0 deduced from πA data where it was found to be almost independent of energy throughout the whole resonance region, see Ref. [63]. Also the imaginary part in case (C) has been well established for elastic πA scattering off small nuclear systems. Later the imaginary part of the nuclear Δ potential has been calculated in a microscopic framework in [32]. We include the imaginary part of this microscopic potential in scenarios (A) and (B) by means of the parametrization given in Ref. [32]. The imaginary parts of the optical $\Delta(1232)$ potential are illustrated

in Fig. 3.5. See also [100], Chapter 4 for a detailed discussion of Δ propagation in the BUU model. Unless otherwise stated, we are working by default with parametrization (B) for the Δ nucleus potential.

In addition to pion absorption via the excitation of the $\Delta(1232)$ resonance, low-energy $s-$wave contributions to the absorptive pion self energy are needed in order to properly account for pion propagation in nuclear matter below kinetic energies of ~ 80 MeV. To this end a phenomenological non-resonant three-body absorption process

$$\pi(NN) \longrightarrow NN \tag{3.14}$$

is included. Since our calculations are done in the perturbative mode (see Appendix A) this corresponds to an additional pion optical potential accounting for non-resonant three-body absorption processes. This contribution has been fixed via detailed balance from the inverse reaction $NN \to \pi NN$, see Ref. [100]. More recently, refinements to these cross sections have been implemented paying special attention to the low energy behavior [84].

Pion optical potential (OM)

In the optical model (OM) approach, we modify the original implementation of the BUU model in the fact, that baryonic resonances are not propagated explicitly. In addition, low energy pion absorption is accounted for by means of the absorptive part of the pion optical potential developed in [101, 102]. This recipe allows to disentangle the effects of absorption and elastic and inelastic pion nucleon scattering. Moreover, the same absorption mechanism has been incorporated by the authors of [76] which makes a meaningful comparison to our results possible. The pion potential used in our calculations is an extrapolation for low energy pions of the one obtained previously [103] for the case of pions at rest using microscopic many-body techniques with the aim to calculate pionic atoms. Details of this potential can be found in [101] and in Appendix D of [84]. There also the implementation into our semiclassical model is described.

At pion kinetic energies above $T_\pi = 85$ MeV the potential of Ref. [102] is used. It is meant to describe the region dominated by the $\Delta(1232)$ resonance and matches well with the low energy one. Both potentials have been separated into absorptive and quasi elastic contributions. They include two-body and three-body absorption mechanisms and pion quasi elastic scattering on the level of $1p1h$ and $2p2h$ excitations. In this model the same quasi elastic and Δ absorption processes from [32] as in the optical potential for the Δ, which is used with the BUU collision term as discussed previously, are included. Here we should mention that already in Section 2.3 we have calculated the $\Delta-$hole self energy of the pion in a simplified model. However, the self energy calculated earlier accounted for quasi elastic pion nucleon scattering only since the only final state the Δ could decay to was again $\Delta \to \pi N$. In addition, the Δ width in the resonance propagators was neglected. However, apart from these approximations, the general structure of $\Delta-$hole self energy in the model of [102] is quite the same.

In our transport simulations we only use the absorptive part of the pion optical potential. Elastic scattering and charge exchange reactions are always implemented by means of

the cross sections obtained from the resonance fit to the pion nucleon scattering data. Note, that within our previously specified notation a charge exchange collision is not regarded as an absorptive process. The important difference to the previously discussed full coupled channel treatment, however, is, that the resonances are not propagated explicitley. The resonance contributions to the pion nucleon cross sections are calculated using vacuum resonance properties and are treated in the simulation as non-resonant pion nucleon scattering processes.

3.4.2 Self energy in the BUU model

In order to compare both approaches to the pion nucleus FSI, we investigate the imaginary part of the total and the absorptive self energy of the pion within our semiclassical transport model. In [36, 84] it was shown, that the real part of the pion in-medium self energy has only very little impact on the double pion photoproduction cross sections. Thus, we neglect it in our present calculations and take

$$\mathcal{R}\mathrm{e}\Pi_\pi \equiv 0 \tag{3.15}$$

evaluating the imaginary part of the self energy at the on-shell point

$$\mathcal{I}\mathrm{m}\Pi_\pi(q = (q_0, \mathbf{q}), n_N(\mathbf{r})) \equiv \mathcal{I}\mathrm{m}\Pi_\pi(E_\pi = \sqrt{m_\pi^2 + \mathbf{q}^2}, n_N(\mathbf{r})), \tag{3.16}$$

where $n_N(\mathbf{r})$ is the local nucleon density at the spatial coordinate $\mathbf{r}$. Now we calculate

$$\mathcal{I}\mathrm{m}\Pi_{\mathrm{abs}}(E_\pi, n_N) = E_\pi \frac{d(\ln(N_\pi^{\mathrm{tot}}(t)))}{dt} \tag{3.17}$$

$$\mathcal{I}\mathrm{m}\Pi_{\mathrm{tot}}(E_\pi, n_N) = E_\pi \frac{d(\ln(N_\pi^{\mathrm{non-int}}(t)))}{dt} \tag{3.18}$$

where N_π denotes the number of pions at the time t. In practice, we obtain these self energies by performing a Monte Carlo simulation with pions and nucleons initialized in a sphere with constant density n_N and periodic boundary conditions. In this calculation we include all potentials and collision rates. The number $N_\pi^{\mathrm{tot}}(t)$ denotes the total number of pions at the time t and $N_\pi^{\mathrm{non-int}}(t)$ the number of pions that did not interact at all, i. e. in the second case pions that participated in a quasi elastic collision are excluded. In this way we obtain the total and the absorptive part of the pion in-medium self energy. Moreover, we calculate only one fixed time step but repeat this simulation several times in order to collect statistics. This allows to let all excited resonances decay at the end of each simulation according to their actual decay branching ratios. Only then the correct separation into the absorptive and non-absorptive components of the pion self energy is possible.

In Fig. 3.6 the pion decay rates $\Gamma_\pi = -\mathcal{I}\mathrm{m}\Pi_\pi / E_\pi$ for both scenarios, i. e. the optical model (OM) approach and the full coupled channel (CC) BUU calculation using the different assumptions on the real and imaginary part of the $\Delta(1232)$ self energy, are shown. The calculations have been done for the case of symmetric nuclear matter neglecting electromagnetic forces, thus the self energies of π^+ and π^- are identical. In the low energy regime the self energy is dominated by the three-body channel $\pi NN \to NN$. For

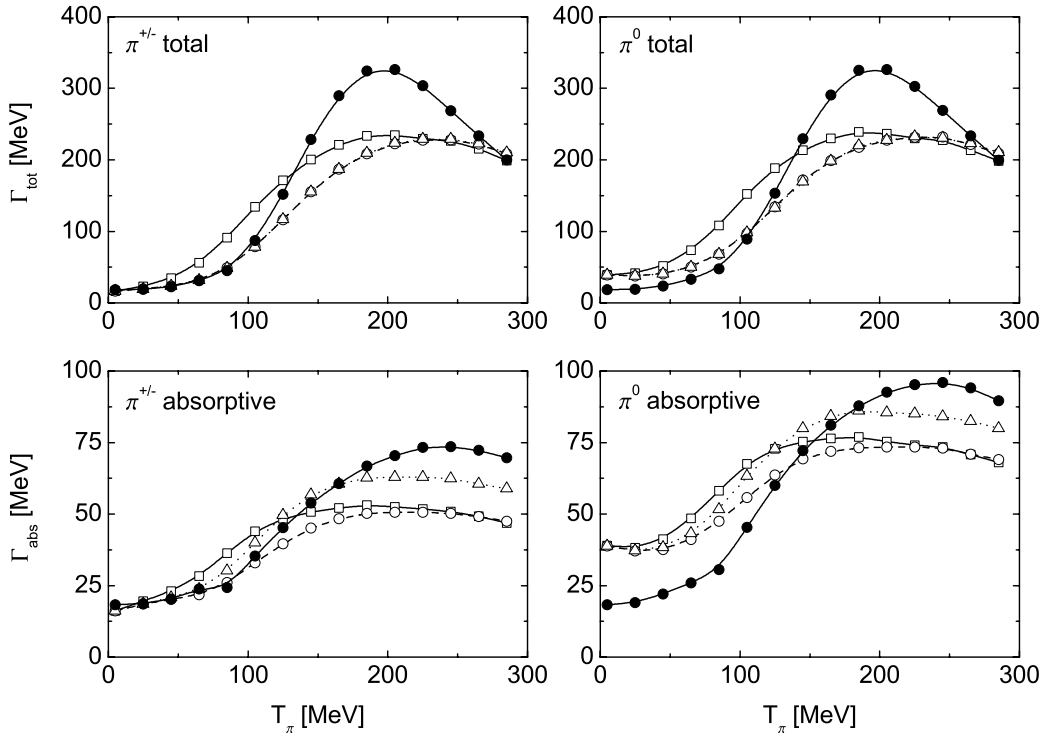

Figure 3.6: Total and absorptive width of the pion in symmetric nuclear matter extracted from the BUU model. *Open squares–solid lines*: coupled-channel CC calculation with $\Delta-$potential parametrization (A), *open circles–dashed lines*: CC calculation with Δ potential (B), *open triangles–dotted lines*: CC calculation with Δ potential (C), *solid circles–full lines*: optical model OM calculation.

higher energies both the absorptive and total self energies are dominated by the $\Delta(1232)$ resonance via the reactions $\pi N \to \Delta$ followed by $\Delta N \to NN$ or $\Delta NN \to NNN$ and $\pi N \to \Delta \to \pi N$.

The CC self energy with the Δ potential (A) deviates from the other scenarios in the fact that the Δ peak is shifted to lower pion kinetic energies. This is due to the more attractive Δ potential when parametrization (A) is used. For the cases (B) and (C) the total pion self energies are almost identical, but the separation into the elastic and absorptive contributions differs in the vicinity of the Δ peak by about 20%. This is due to the fact that off-shell the energy dependent width in parametrizations (A) and (B) drops substantially as compared to the constant width used in parametrization (C). Moreover, in parametrization (C) no quasi elastic component has been separated and, thus, the total Δ collision width is ascribed to Δ absorption. This results probably in an overestimation of the pion absorption strength.

In the relevant energy region for the TAPS experiment ($T_\pi \leq 100$ MeV), the charged pion self energies in the OM and the default CC-B calculation (Δ potential (B) according to Eq. (3.13)) are almost identical, whereas the neutral pion self energy turns out to be smaller within the OM approach as compared to the CC-B calculation. In the pion optical

model we use for the π^0 an isospin symmetrized absorption rate as in Refs. [84, 101]

$$\Gamma_{\rm OM}(\pi^0) = \frac{1}{2}\left[\Gamma_{\rm OM}(\pi^+) + \Gamma_{\rm OM}(\pi^-)\right]. \tag{3.19}$$

In contrast, in the BUU approach the decay rate at low energies due to the non-resonant $\pi NN \to NN$ process is determined from the cross section for the process $NN \to \pi NN$ using detailed balance. Due to conservation of the $z-$component of the total isospin in this three-body process one either needs two neutrons or a proton-neutron pair in the initial state to absorb a π^+ (total $I_z = 0$ or $I_z = 1$). Accordingly, one needs either two protons or a proton-neutron pair to absorb a π^- (total $I_z = -1$ or $I_z = 0$). On the other hand, neutral pions can be absorbed by all possible nucleon-nucleon combinations ($I_z = -1, 0, 1$). Hence, the decay rate of the π^0 at very low energies is larger than the π^+ and π^- decay rates. The isospin average of the decay rates (3.19) is thus not valid for three-body absorption processes. Rather than this simple recipe, which is valid at least for the nucleon-hole components of the self energy in symmetric nuclear matter [63], a complete isospin decomposition of the pion self energy in matter is required. As a consequence of the simplifying assumption (3.19), the absorptive self energy in the CC approach is larger than the OM self energy. As we shall see later, this results in substantially larger cross sections for the $\gamma A \to \pi\pi X$ reaction when the optical model is employed.

An additional observation is the higher peak value of both the total and absorptive pion decay rates in the OM and CC calculations. At first glance this is surprising since at least in the CC-A and CC-B scenarios the very same Δ absorption rates as in the pion optical potential (OM) are included. However, this can be due to the following reasons. First, the elastic and charge exchange collisions in the OM calculations have been included by means of the resonance fits also used in the CC scenario. However, in the OM calculation these cross sections are ascribed to non-resonant processes and are calculated using vacuum resonance properties. Second, in these calculations charge exchange collisions count for the absorptive decay rates. Since the corresponding cross sections in the OM scenario are calculated in vacuum, deviations already in the absorptive pion decay rates can be expected. In finite nuclei, however, additional considerations have to be made. In the OM calculation the pion self energy is purely local, thus all density dependent collision rates are taken at the same fixed nucleon density. In contrast, in the CC calculations the excited resonances are propagated explicitely and thus can move to regions with smaller or larger nucleon densities. This mechanism has the consequence of an explicitely non-local pion self energy.

3.4.3 Mean free path

In [35, 36, 84] results for the pion mean free path obtained within the BUU model have been compared to results obtained within a quantum mechanical framework. The pion mean free path is given by

$$\lambda_\pi = \frac{v}{\Gamma_\pi} \tag{3.20}$$

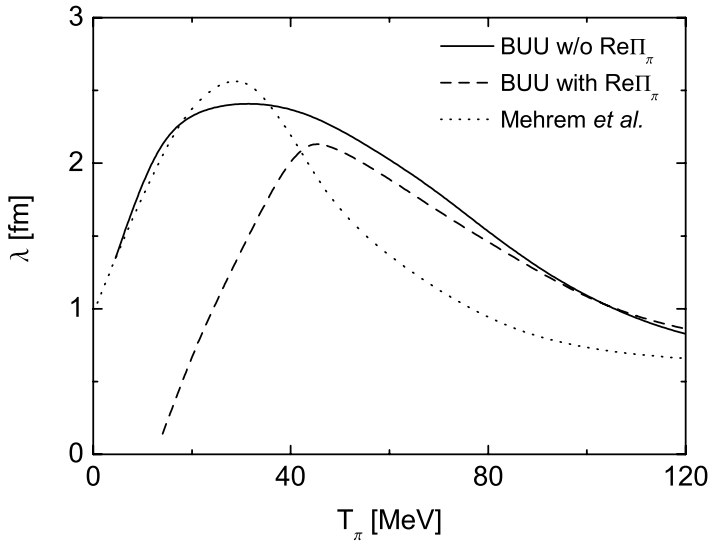

Figure 3.7: Mean free path of a neutral pion in symmetric nuclear matter at $n_0 = 0.168$ fm^{-3}. *Solid line*: BUU calculation without $\mathcal{R}\mathrm{e}\Pi_\pi$, *dashed line*: BUU calculation with $\mathcal{R}\mathrm{e}\Pi_\pi$, *dotted line*: result from [104]. The picture is taken from [36].

where v is the pion velocity in the medium and Γ_π is its total width, that in turn is connected to the self energy via $\Gamma_\pi = -\mathcal{I}\mathrm{m}\Pi_\pi/E_\pi$. The results from [36] are shown in Fig. 3.7 in comparison to the mean free path obtained in a quantum mechanical framework in [104]. An important outcome of the study in [35, 36, 84] is the non-linear dependence of the mean free path on the nucleon density. This non-linearity is generated by the three-body process $\pi NN \to NN$, that goes to first order quadratically with density, the implicit density dependence of the nucleon and $\Delta(1232)$ potentials and Pauli blocking. Thus, the low-density approximation $\lambda \sim 1/(n_N\sigma)$, that a priori neglects multi(≥ 3)-body processes, is neither quantitatively nor qualitatively applicable in the energy regime of $T_\pi \leq 70$ MeV where these effects turn out to be important.

As a benchmark for the BUU results, the mean free path obtained in the quantum mechanical framework of [104, 105] has been used. It turns out that in the quantum mechanical framework solving the full dispersion relation including the real part of the pion optical potential is very important. On the other hand, if one includes the real part of the pion optical potential in the semiclassical model, the description of pions with kinetic energies $T_\pi \leq 40$ MeV is not possible due to the presence of tunneling effects. For higher energies the mean free path is quite insensitive to the real part of the in-medium pion self energy. In fact, the best agreement to the mean free path calculated in [105] is obtained by using the full BUU collision term including two- and three-body processes, but omitting $\mathcal{R}\mathrm{e}\Pi_\pi$. One should, however, keep in mind that the mean free path is not directly observable and a test of our semiclassical model can, therefore, only be given by experiment.

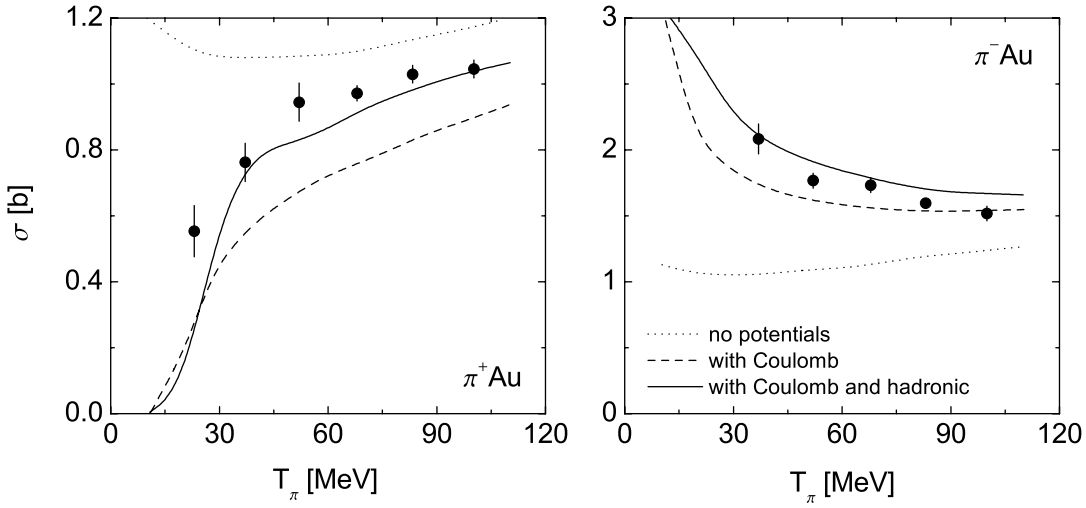

Figure 3.8: Total absorption cross section on a gold target for positive and negative pions. *Dotted lines*: without potentials, *dashed lines*: with Coulomb potential, *solid lines*: with Coulomb and hadronic pion potential. Data points from Ref. [106]. The picture is taken from [36].

3.4.4 Pion nucleus reactions

In [35, 36, 84] total π^+A and π^-A absorption cross sections have been studied in order to test our semiclassical model at low pion kinetic eneriges. In these calculations the BUU collision term including the explicit propagation of resonances has been used. As a showcase for the results obtained, we display in Fig. 3.8 the total cross section for the Gold target. For both reactions π^+A and π^-A excellent agreement down to pion kinetic energies of $T_\pi \approx 30$ MeV is obtained. It is critical to include the Coulomb potential. The absorption cross sections are also sensitive to the real part of the pion in-medium self energy. A detailed discussion of these results can be found in [36]. In summary, these results show, that despite the large wave length of the pions, the semiclassical model yields reasonable results for both the pion mean free path and pion absorption. Moreover, the pion interaction with nuclear matter seems to a large extent to be saturated by the included $1 \leftrightarrow 2$, $2 \leftrightarrow 2$ and $2 \leftrightarrow 3$ body processes.

The main effect of the hadronic pion potential is not a change in the pion mean free path, but a change of the pion trajectories as discussed in detail in Refs. [36]. Also the important effect of the Coulomb potential is to attract negative and to repell positive pions. This effect, however, is less important for reactions where the pions are produced inside the medium. This is in contrast to πA reactions where the pions already feel the potentials before penetrating into the nucleonic matter. Thus, double pion photoproduction is rather insensitive to the real part of the pion in-medium self energy. This insensitivity of the photoproduction cross sections to the real part of the hadronic pion potential and the good description of the nuclear absorption cross section makes us quite confident to be able to account for the physical effects relevant to double pion production

in nuclei within our semiclassical model.

3.5 Final state interactions in the γA $\to \pi\pi$X reaction

In the following we adopt the coupled channel BUU transport model in a Monte Carlo simulation to examine the influence of the FSI on two pion photoproduction off nuclei. To this aim we separate the FSI in absorption, elastic and charge exchange collisions of the produced pions with the nucleons of the target nucleus. Throughout this Section we use the optical model (OM) approach to the pion FSI since only then this separation is possible. In the end we will then compare calculations including the full set of FSI obtained within the OM and coupled channel (CC) scenarios. In these calculations we do not use the real part of the pion in-medium self energy assuming therefore that the pions move along straight lines between collisions. We also neglect the Coulomb potential that gives only marginal corrections to observables involving charged pions in the final state.

3.5.1 Absorption

Two pion invariant mass distributions for the incoherent $A(\gamma, \pi^0\pi^0)$ and $A(\gamma, \pi^\pm\pi^0)$ reactions are shown in Fig. 3.9. To get an impression on the strength of the FSI, we also show results without any FSI. For the solid curves we assumed purely absorptive FSI, implying that the final state pions do not undergo elastic or charge exchange collisions. These curves can be compared to the dashed lines that represent the theoretical results of Refs. [76] and [31] [1] involving the $\pi\pi$ interaction in the vacuum. Within the theoretical uncertainties of both models these results can be regarded as identical in the $\pi^0\pi^0$ channel. However, in the $\pi^\pm\pi^0$ channel we obtain larger differential cross sections for both nuclei, especially at high invariant masses. Since we are using almost the same input for the elementary reaction and the same absorption mechanism as in [76] we would have expected a similar level of agreement as in the $\pi^0\pi^0$ channel.

As a crosscheck for our results we also calculate the incoherent $\gamma A \to \pi\pi X$ reaction employing the semi-analytical Glauber model. Using the Glauber eikonal approximation to describe the FSI of the outgoing pions (see Appendix B) the total cross section for the reaction $\gamma A \to \pi\pi X$ can be written in the following form

$$\begin{aligned}\sigma_{\gamma A\to\pi\pi X} &= \int d^3r \frac{d^3p_1}{(2\pi)^3} d^3q_1 d^3q_2 \left(\frac{d\sigma_{\gamma N_1\to\pi\pi N_2}}{d\mathbf{q}_1 d\mathbf{q}_2}\left(\sqrt{s}_f\right)\right) \\ &\quad \times f_0(\mathbf{r},\mathbf{p}_1)\Theta(|\mathbf{k}+\mathbf{p}_1-\mathbf{q}_1-\mathbf{q}_2|-p_F)F_\pi(\mathbf{r},\mathbf{q}_1)F_\pi(\mathbf{r},\mathbf{q}_2) \quad (3.21)\end{aligned}$$

where $\sigma_{\gamma N_1\to\pi\pi N_2}$ is the $\pi\pi$ photoproduction cross section on a single nucleon in the LA frame, $f_0(\mathbf{r},\mathbf{p})$ is the nucleon momentum distribution according to Eq. (A.2), p_F the

[1] The results of the calculation for the $\pi^\pm\pi^0$ channel given in Ref. [31] are wrong by a factor of 2 [107]. This has been corrected in the present work.

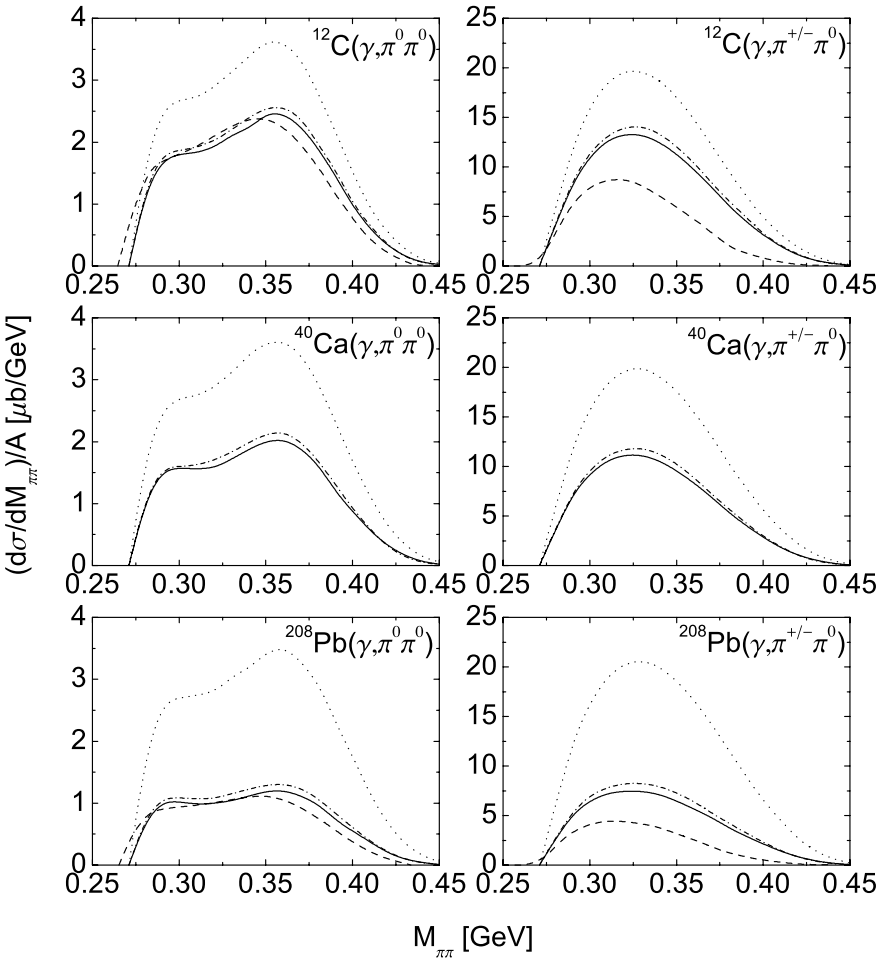

Figure 3.9: Two pion mass distributions for $\pi^0\pi^0$ (left) and $\pi^\pm\pi^0$ (right) photoproduction off ^{12}C, ^{40}Ca and ^{208}Pb in the photon energy interval $E_\gamma \in [400, 460]$ MeV. *Dotted lines*: no FSI, *solid lines*: pion absorption but no quasi elastic scattering, *dashed lines*: results from Refs. [31, 76, 107] without medium modifications of the $\pi\pi$ interaction, *dash-dotted*: Glauber results.

local Fermi momentum according to Eq. (A.3) and $F_\pi(\mathbf{r}, \mathbf{q}_i)$ is a pion absorption factor that is given by

$$F_\pi(\mathbf{r}, \mathbf{q}_i) = \exp\left[\int_{\mathbf{r}}^{\infty} dl_i \frac{1}{|\mathbf{q}_i|} \mathcal{I}\mathrm{m}\Pi(\mathbf{r}_i)\right] \tag{3.22}$$

$$\mathbf{r}_i = \mathbf{r} + l_i \frac{\mathbf{q}_i}{|\mathbf{q}_i|}. \tag{3.23}$$

Π is the optical model self energy of the pion discussed previously in Section 3.4. Here only the absorptive part of this self energy has been included. $\sqrt{s}_f$ is the free photon nucleon CM energy corrected for the nuclear potential, see Appendix A Eq. (A.4). Since we are evaluating the integrals in Eq. (3.21) by means of a Monte Carlo quadrature method, we are able to obtain all kinds of differential cross sections from just one calculation

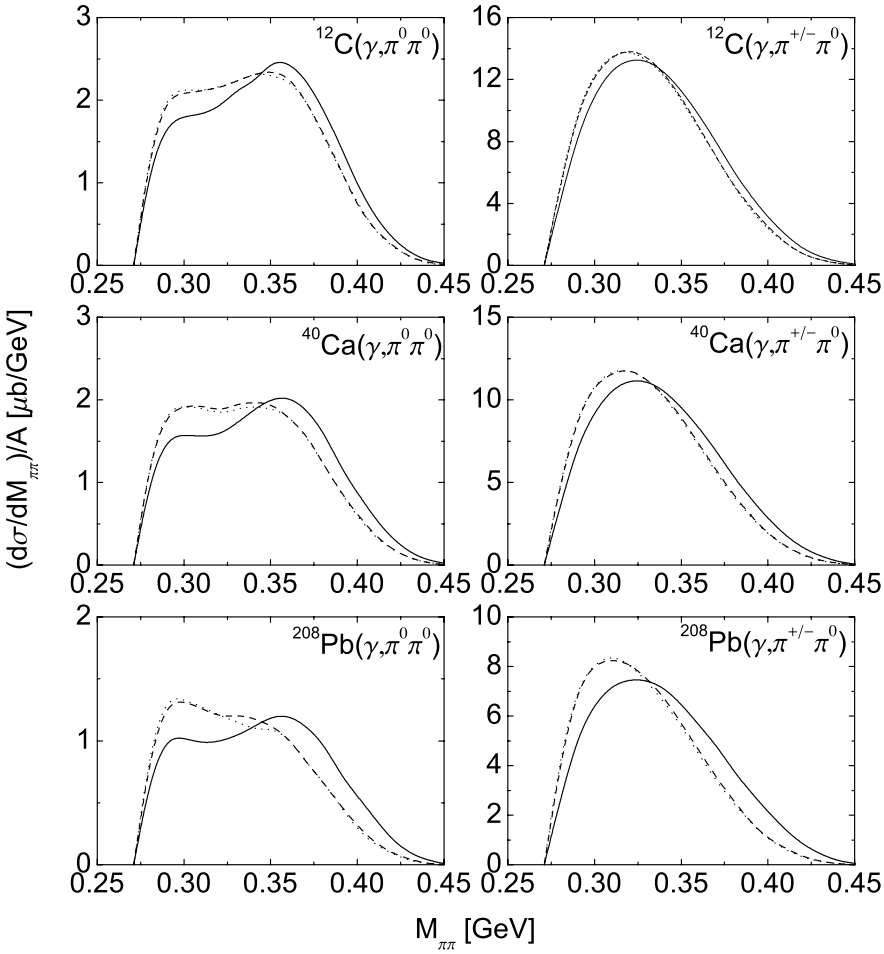

Figure 3.10: Two pion invariant mass distribution for $\pi^0\pi^0$ (left) and $\pi^\pm\pi^0$ (right) photoproduction off ^{12}C, ^{40}Ca and ^{208}Pb in the energy interval $E_\gamma \in [400, 460]$ MeV. *Solid lines*: purely absorptive FSI, *dashed lines*: absorption and elastic scattering with isotropic angular distributions, *dotted lines*: absorption and elastic scattering with realistic angular distributions.

by projecting on the respective kinematical variables. The results obtained employing Eq. (3.21) are shown in Fig. 3.9 as dash-dotted lines. They agree very well with our BUU model results including pion absorption in the FSI only. This, however, is not surprising as the same physics is included in both types of calculations. Thus, we are confident to have evaluated the theoretical models correctly. The disagreement with the results from [76], however, is not understood.

3.5.2 Elastic scattering

As a next step we investigate the influence of elastic πN scattering on the $\gamma A \to \pi\pi X$ reaction. In Fig. (3.10) the results with purely absorptive FSI are compared to results

including elastic πN scattering events. Still we do not allow for charge exchange reactions, i. e. we include processes like $\pi^+ p \to \pi^+ p$ but we do not allow for processes like $\pi^+ n \to \pi^0 p$. The cross sections for these reactions are obtained from a resonance fit to experimental data and are discussed in detail in Ref. [100]. Nontheless, in the present OM calculations these processes are treated as non-resonant scattering events since we do not propagate nucleon resonances. Most noticeable, we observe a shift of strength towards the two pion threshold with increasing target mass. This effect becomes stronger for larger nuclei since in large nuclear systems there is a higher probability for the pion to scatter elastically. This shift can be attributed to the energy loss of the pions that undergo elastic collisions, in most cases yielding a smaller invariant mass of the respective pion pair.

This can at least partially be understood as follows. In general, the two pions of the primary produced $\pi\pi$ pair have unequal momenta. For the relevant kinematics the mean value of the single pion momenta ranges somewhere between 100 MeV and 150 MeV. In this energy domain the elastic cross section for πN scattering varies dramatically due to the increasing importance of the Δ resonance, leading to a high probability for the pion with the higher momentum, say above 150 MeV, to scatter elastically. The invariant mass of the pair is a function of the absolute value of the two pion momenta and the angle between the pion moving directions. Keeping the momentum of the slow moving pion and the angle constant, this function rises monotonously with the value of the larger pion momentum. In an elastic πN collision the fast pion in average will lose some of its kinetic energy, hence leading to a downward shift of the invariant mass of the pion pair. The change of the angle between the pion directions does not have a net effect, since this angle is changed more or less isotropically, hence leading in some cases to higher and in other cases to lower invariant masses. The kinetic energy loss of the pions is demonstrated in Fig. 3.11. There the kinetic energy differential cross sections for various nuclear target materials with respect to the two pion kinetic energy sum is shown. Imposing different scenarios of FSI the degradation of the pions generated by elastic and charge exchange collisions can be observed.

In our standard BUU implementation, the probability of a meson-baryon collision is determined using the experimental values of the vacuum cross sections for the available channels and assuming isospin symmetry for the rest. If an elastic scattering process occurs, then the momenta of the final particles are sorted assuming isotropic angular distributions in the meson-baryon CM frame. In case of a forward peaked angular distribution the simplified isotropic prescription could lead to an overestimation of the stopping power of the respective meson in the medium due to the generally too high momentum transfer in meson-baryon collisions. Moreover, if collisions with low momentum transfer were dominant, they could be enormously reduced in the medium due to Pauli blocking. Since the pion energy loss by quasi elastic collisions is essential in the present context we include realistic angular distributions for the $\pi N \to \pi N$ reaction.

In principle, the angular distribution of the outgoing particles in pion-nucleon scattering is modified due to the presence of the $P_{33}(1232)$ resonance already at rather low energies. We include realistic angular distributions for all elastic and charge exchange reactions in terms of the phase-shifts and inelasticities obtained from the SAID analysis [108, 109]. Details are given in Appendix C and can also be found in Ref. [63]. In this way angular

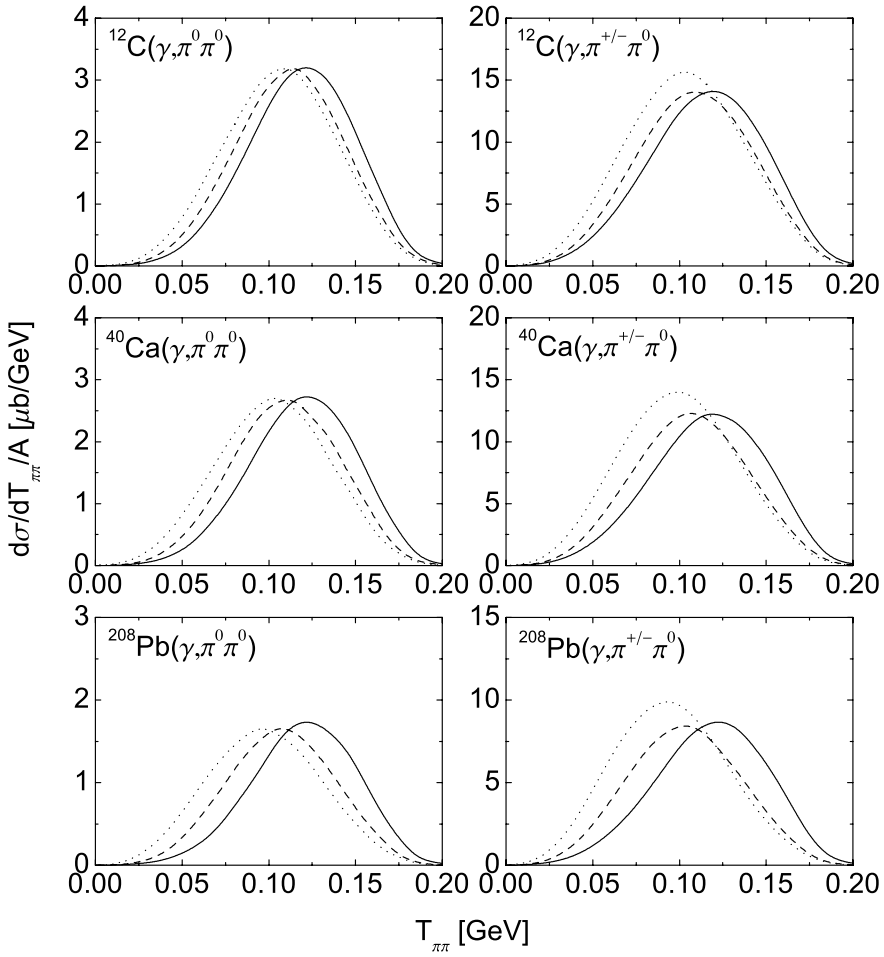

Figure 3.11: Two pion kinetic energy spectra for $\pi^0\pi^0$ (left) and $\pi^\pm\pi^0$ (right) photoproduction off ^{12}C, ^{40}Ca and ^{208}Pb in the energy interval $E_\gamma \in [400, 460]$ MeV as function of the pion kinetic energy sum $T_{\pi\pi} = T_{\pi_1} + T_{\pi_2}$. *Solid lines*: purely absorptive FSI, *dashed lines*: absorption and elastic scattering, *dotted lines*: absorption, elastic scattering and charge exchange.

differential cross sections for the quasi elastic $\pi N \to \pi N$ process, that agree well with experiment, are obtained.

Implementing these realistic cross sections into our BUU simulations, we obtain the results for the mass differential cross sections indicated by the dotted lines in Fig. 3.10. These cross sections hardly deviate from the results obtained with the isotropic $\pi N \to \pi N$ angular distributions. As a matter of fact, some of the cross sections for quasi elastic πN scattering have even more strength under backward angles, thus leading to high momentum transfers in πN collisions. As a consequence no net effect on the $\pi\pi$ mass distributions can be observed. We note, that this observation is in line with the results obtained earlier in Ref. [110].

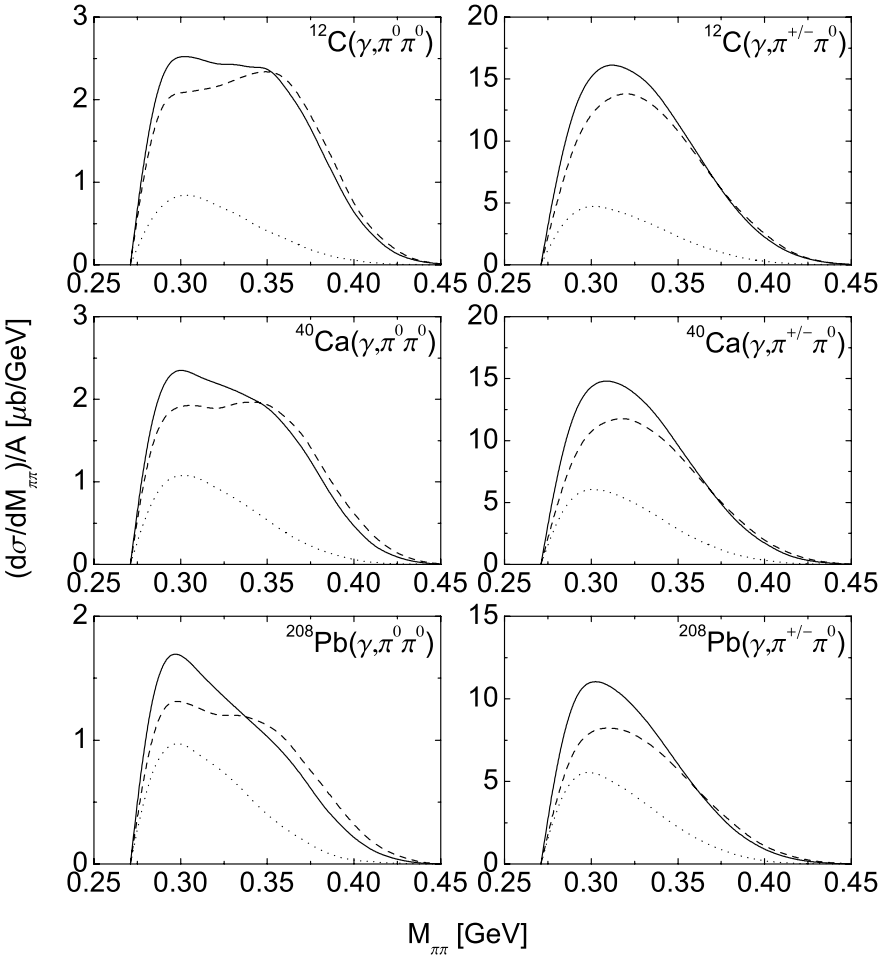

Figure 3.12: Two pion mass spectra for $\pi^0\pi^0$ (left) and $\pi^\pm\pi^0$ (right) photoproduction off ^{12}C, ^{40}Ca and ^{208}Pb in the energy interval $E_\gamma \in [400, 460]$ MeV. *Solid lines*: total mass differential cross section, *dashed lines*: without charge exchange collisions , *dotted lines*: charge exchange contribution.

3.5.3 Charge exchange

In Fig. 3.12 we show the invariant mass distributions including also charge exchange pion nucleon collisions. The corresponding charge exchange cross sections are obtained from a resonance fit to the data. This is shown in detail in Ref. [100] and in [35] where additional background contributions were introduced. The total photoproduction cross section is enhanced by these reactions. In the $\pi^0\pi^0$ channel, this enhancement is due to the fact that the cross section for photoproduction of $\pi^\pm\pi^0$ pairs is much larger than the cross section for $\pi^0\pi^0$ photoproduction, hence leading to more side-feeding by the $\pi^+ n \to \pi^0 p$ and $\pi^- p \to \pi^0 n$ reactions as compared to the loss of neutral pion flux by the inverse reactions. An equivalent effect is observed in the $\pi^\pm\pi^0$ channel because the cross section for $\pi^+\pi^-$ photoproduction is much larger than the cross sections of any of the other channels, hence leading to considerable side-feeding by means of the charge exchange reactions. For the

charge exchange collisions, the same kinematic considerations as in the purely elastic case hold, therefore leading to an even more pronounced shift of strength to the low invariant mass region as can be seen from the solid line in Figure 3.12. This is corroborated by the observation that the pions are even more slowed down when charge exchange collisions are included, see Fig. 3.11. We have also calculated the contribution from single pion photoproduction via inelastic $\pi N \to \pi\pi N$ collisions. Within the considered energy range, those pion pairs give an additional correction of about 5% to the total cross sections and, therefore, have been omitted in the present calculations.

3.6 Results

After having discussed the influence of ordinary final state interactions on the $\gamma A \to \pi\pi X$ reaction, we will now present our final results. These will be shown for both the optical model OM and the coupled-channel CC scenario for the pion final state interactions. Even if a clear separation of absorption, quasi elastic and charge exchange collisions is not possible in the CC model, these processes lead to the same effects on the nuclear cross sections as in the OM calculations.

3.6.1 Total cross section

We have calculated the total cross section for the $\gamma A \to \pi\pi X$ reaction for photon energies up to 800 MeV. We note, however, that in most of the channels (3.2) to (3.3) the elementary 2π photoproduction cross section is known experimentally only up to energies of around 800 MeV. In our BUU calculations, the cross section is kept constant for higher values of the photon energy. In reactions on finite nuclear systems the photon energy in the rest frame of the respective nucleon, that incoherently absorbs the incoming photon, can exceed the photon laboratory energy due to Fermi motion. Therefore, our calculations at the highest energies shown are afflicted with large theoretical error bars.

In Fig. 3.13 we show results obtained within both the OM and the CC scenario for the pion FSI. In case of the CC calculations results using the parameterizations (A) and (B) for the $\Delta-$nucleus potential are shown. The cross sections are normalized by $A^{2/3}$ implying a surface dominated production mode, i. e. strong absorption of the final state pions. Our results are compared to the preliminary data given in [87]. These data sets clearly favor the parametrization (B) for the real part of the $\Delta-$nucleus potential. Still in the $\pi^{\pm}\pi^0$ channel our results are roughly 20% above the data. This behavior, however, seems not to be created by pion absorption, since the effect becomes *less* pronounced with increasing target mass. This is illustrated also in Fig. 3.14 where we show the parameter α according to a fit $\sigma \propto A^{\alpha}$ using the symmetric nuclei ^{12}C and ^{40}Ca ($Z = N = A/2$). Experimentally we observe even stronger absorption in the $\pi^0\pi^0$ channel ($\alpha_{\pi^0\pi^0} < \alpha_{\pi^{\pm}\pi^0}$) whereas our calculations show the same behavior for both isospin channels ($\alpha_{\pi^0\pi^0} \simeq \alpha_{\pi^{\pm}\pi^0}$). This is clear theoretically as we are considering symmetric nuclei only and use isospin symmetry to obtain the π^0 absorption cross sections [100]. A source of uncertainty, however, is the elementary two pion photoproduction cross section from neutrons, that can be determined experimentally only with large error bars, see Fig. 3.3.

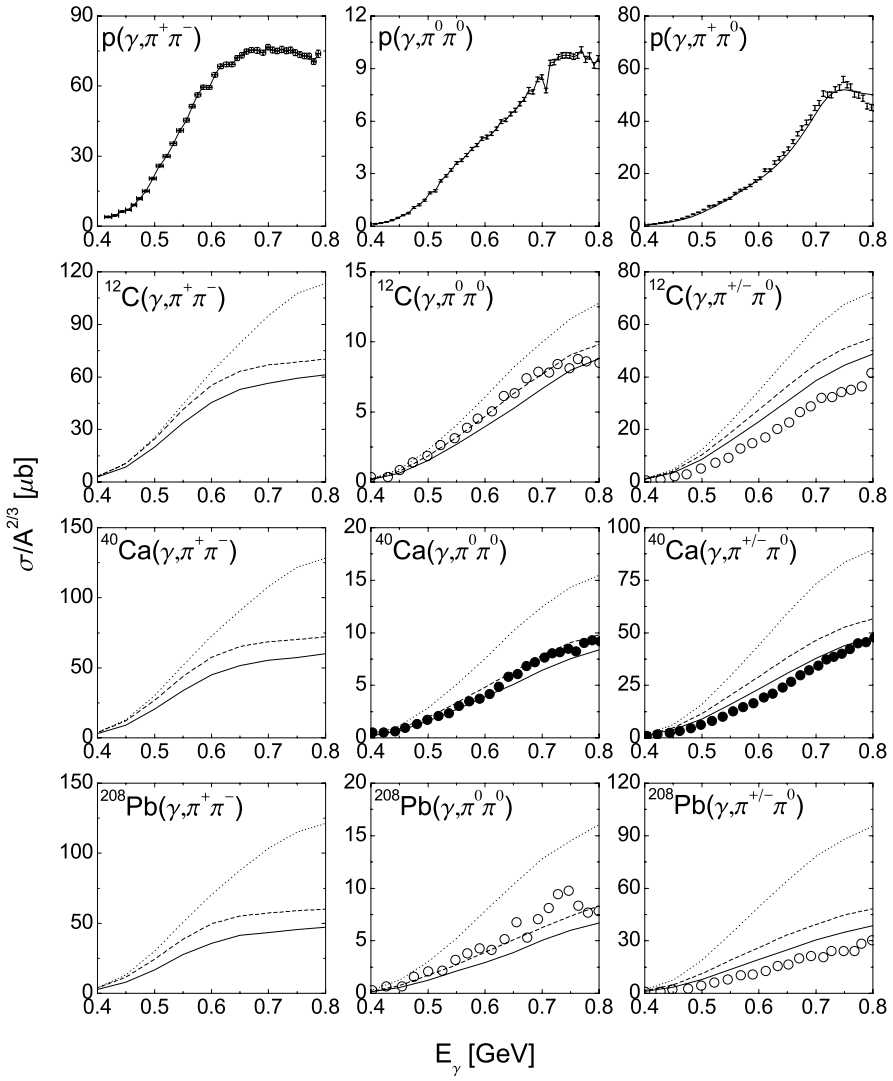

Figure 3.13: Total cross sections for double pion photoproduction of various nuclear targets. *Solid lines*: CC calculation with $\Delta-$potential (A), *dashed lines*: CC calculation with $\Delta-$potential (B), *dotted lines*: OM calculation. Experimental data from [87] (open symbols) and [111] (solid symbols).

3.6.2 Differential cross sections

In Fig. 3.15 we present our results for the mass differential cross sections in the photon energy range $E_\gamma \in [400, 460]$ MeV in comparison to the experimental data from the TAPS collaboration [31]. In the $\pi^0\pi^0$ channel we find excellent agreement with the experimental data within the OM scenario. Our curves also look qualitatively similar to the results of Ref. [76] despite the different physics involved. The downward shift in the invariant mass spectrum, that in Ref. [31] was taken as an indication for the medium modification of the $\pi\pi$ correlation and, thus, for the onset of chiral symmetry restoration, is reproduced solely by traditional incoherent final state interactions of the two outgoing

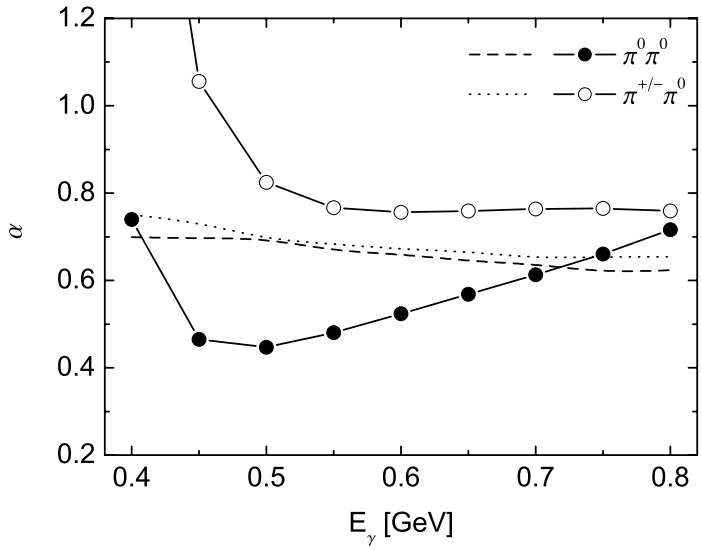

Figure 3.14: Parameter α for $\pi^+\pi^-$, $\pi^0\pi^0$ and $\pi^\pm\pi^0$ photoproduction extracted from ^{40}Ca and ^{12}C data. *Lines*: BUU (CC) calculation with Δ potential parametrization (A), *symbols*: α extracted from data taken from Ref. [87].

pions. However, whereas in [76] the backcoupling of the pion-nucleon interaction on the $\pi\pi$ correlation in the medium has been calculated in our model it just gives rise to incoherent final state interactions.

In the $\pi^\pm\pi^0$ channel our results are considerably higher than the data and also above those obtained in Ref. [76]. The difference of the theoretical curves can – at least partially – be understood by the incomplete set of FSI incorporated in the model of Ref. [76]. Side-feeding has been omitted in Ref. [76] by restricting the interactions of the produced pions with the nuclear medium to purely absorptive FSI. The discrepancy with the experimental data is a standing problem because the apparently stronger pion absorption in the $\pi^\pm\pi^0$ channel than in the $\pi^0\pi^0$ channel, as indicated by the experimental measurements, is not understood. However, as mentioned earlier there have been experimental problems due to the only limited acceptance of the TAPS setup at MAMI-B. As can be judged from the comparison with the more recent analysis of Ref. [87] (open circles in Fig. 3.15) the data especially in the $\pi^\pm\pi^0$ channel are afflicted with large error bars. Thus, we are unable to draw any robust conclusion from the confrontation of our results and the data. The preliminary results for the Calcium target from [81] disagree in size also in the $\pi^0\pi^0$ channel (open triangles in Fig. 3.15). However, in the higher energy intervals the preliminary data from [81] have been renormalized in the final version [111] and now agree rather well with our calculations, see Figs. 3.16 and 3.17. Thus, we speculate that also for the lower energies the overall normalization was not obtained correctly in the preliminary analysis of Ref. [81]. In Fig. 3.15 also results obtained using the BUU (CC) scenario are shown. Apart from the overall normalization they are almost identical to the OM calculations.

Recently double pion photoproduction off nuclei has been investigated using the BUU

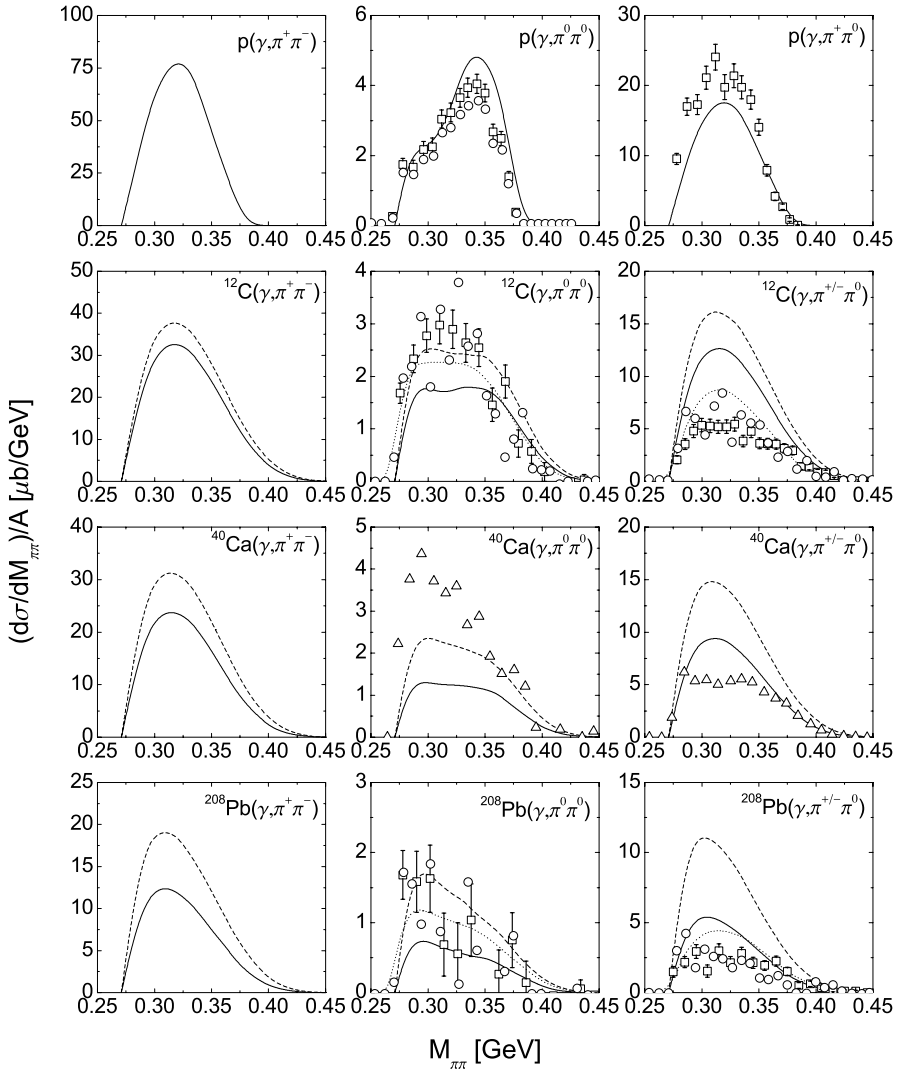

Figure 3.15: Two pion mass spectra for $\pi^+\pi^-$ (left), $\pi^0\pi^0$ (center) and $\pi^\pm\pi^0$ (right) photoproduction off ^{1}H, ^{12}C, ^{40}Ca and ^{208}Pb in the energy interval $E_\gamma \in [400, 460]$ MeV. *Solid lines*: BUU (CC) calculation, *dashed lines*: BUU (OM) calculation, *dotted lines*: results from Ref. [76] with the in-medium $\pi\pi$ interaction. Data from Ref. [31] (squares), [87] (circles) and [81] (triangles).

transport model in [36]. Special attention has been paid to the impact of the in-medium pion dispersion relation and uncertainties in the elementary production amplitude. The in-medium pion dispersion was investigated by means of a simplified $\Delta-$hole model similar to the one discussed in Section 2.3. However, the observable effects of this medium modification on the two pion photoproduction cross sections off nuclei were found to be only marginal. More substantial are the effects due to changes of the elementary $\gamma \to \pi\pi$ cross section. Uncertainties in the experimental determination of these cross sections from neutron targets generate relative theoretical errors in the overall normalization of the photoproduction cross section which are of the order of 20%, see Fig. 21 in [36].

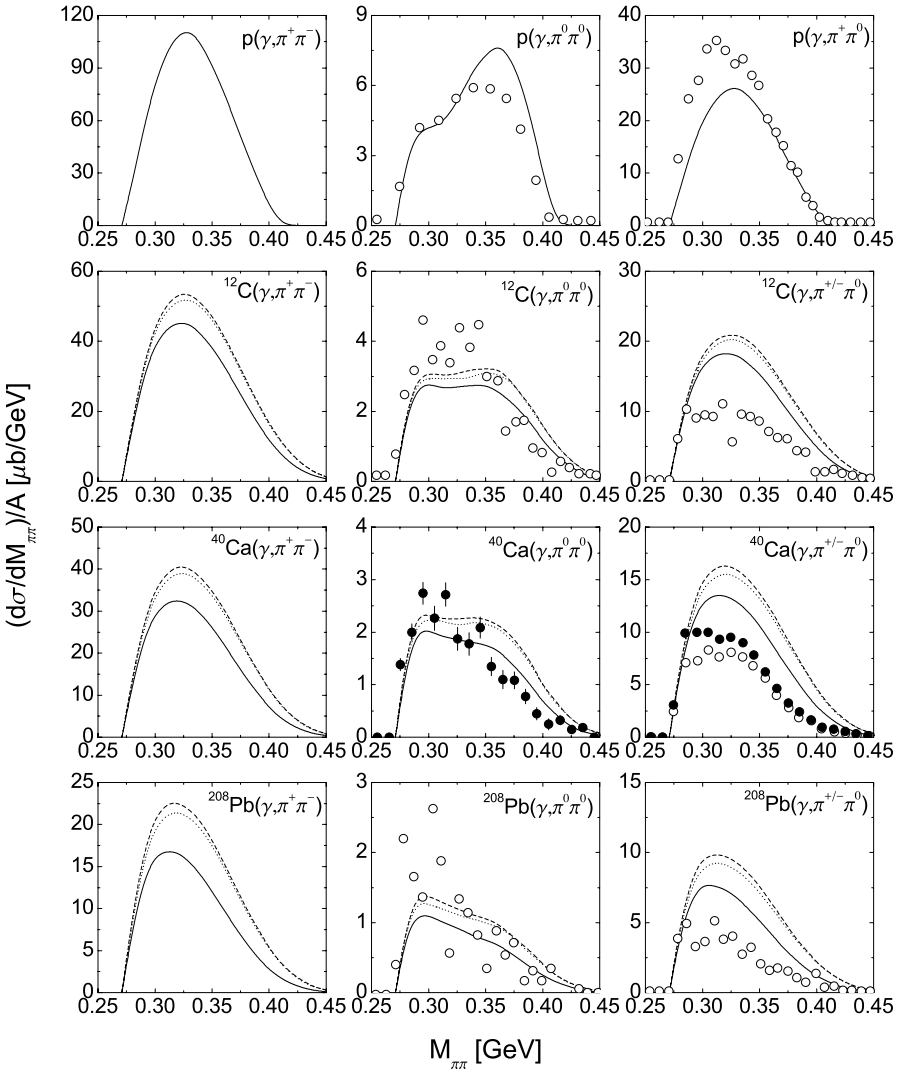

Figure 3.16: Two pion mass spectra for $\pi^+\pi^-$ (left), $\pi^0\pi^0$ (center) and $\pi^\pm\pi^0$ (right) photoproduction off ^{1}H, ^{12}C, ^{40}Ca and ^{208}Pb in the energy interval $E_\gamma \in [400, 500]$ MeV. *Solid lines*: BUU (CC) calculation with $\Delta-$potential parametrization (A), *dashed lines*: parameter set (B), *dotted lines*: parameter set (C). Data from Ref. [87] (open symbols) and [111] (solid symbols).

In order to investigate the persistence of the observed softening of the $\pi\pi$ spectra, double pion mass distributions have been analyzed by the TAPS collaboration also for the energy intervals $E_\gamma \in [400, 500]$ MeV and $E_\gamma \in [500, 550]$ MeV. Our results obtained within the CC scenario using the three different parameterizations for the $\Delta(1232)$ potential (3.13) are shown in Figs. 3.16 and 3.17. Still, our results in the $\pi^\pm\pi^0$ channel are up to 50% higher than the data. We display the data sets from [87] without error bars since on the one hand the analysis is only preliminary and on the other hand the dispersion of the data points gives an idea about the errors. The data from [111] are, however, closer to our theoretical curves. Note also, that the normalization of our calculations depends on the cross sections for the elementary $\gamma N \to \pi\pi N$ reactions used as input to our simulations.

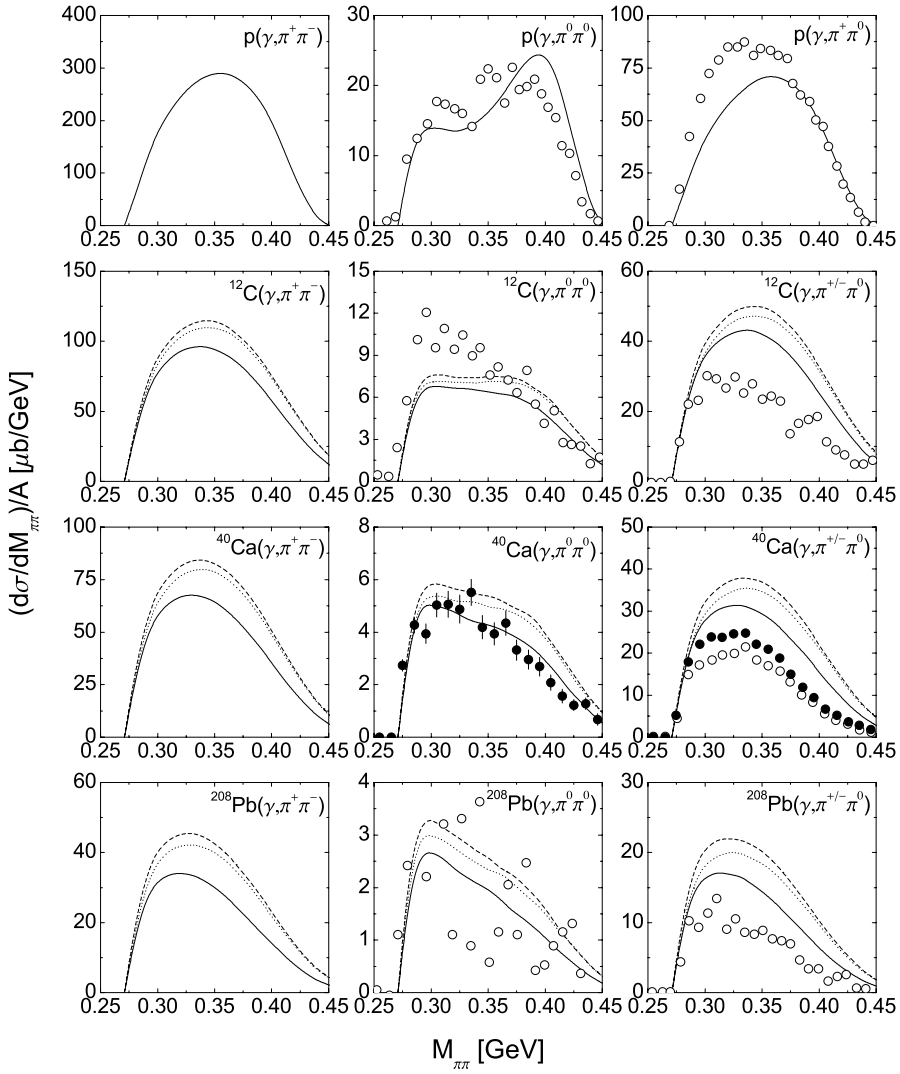

Figure 3.17: Two pion mass spectra for $\pi^+\pi^-$ (left), $\pi^0\pi^0$ (center) and $\pi^\pm\pi^0$ (right) photoproduction off ^{1}H, ^{12}C, ^{40}Ca and ^{208}Pb in the energy interval $E_\gamma \in [500, 550]$ MeV. *Solid lines*: BUU (CC) calculation with $\Delta-$potential parametrization (A), *dashed lines*: parameter set (B), *dotted lines*: parameter set (C). Data from Ref. [87] (open symbols) and [111] (solid symbols).

As mentioned earlier, the most recent measurement of the $\gamma n \to \pi^-\pi^0 p$ reaction delivered a cross section about 20% smaller than the one included in our calculations, see Fig. 3.3. For heavy nuclear targets which have a large neutron excess, this can lead to an up to 15% smaller nuclear photoproduction cross section in the $\gamma A \to \pi^0\pi^\pm X$ channel. The new input cross section for the $\gamma n \to \pi^-\pi^0 p$ reaction has been included in our most recent calculations shown in [111]. These results match well with the experimental data points. However, the shapes of the experimental mass distributions, that are taken as an indicator for the in-medium effect on the $\pi\pi$ interaction, are in all cases consistent with the theoretical ones. So far the quality of the data is not good enough to rule out our classical interpretation of the downward shift of the $\pi\pi$ strength in the $\gamma A \to \pi\pi X$

reaction. The strength of this shift becomes most pronounced in the $\pi^0\pi^0$ channel due to the particular form of the elementary distribution in this channel, see Figs. 3.15 to 3.17. Thus, a seperate measurement of the $\gamma A \to \pi^+\pi^- X$ reaction, that should exhibit similar features concerning the in-medium $\pi\pi$ correlation but follows closely a phasespace distribution in vacuum, would be desireable.

Chapter 4

The reaction πA $\longrightarrow \pi\pi$X

4.1 Introduction

The study of $\pi\pi$ production in nuclei has been stimulated by the expectation to observe significant effects that signal the onset of chiral symmetry restoration at the rather moderate densities inside ordinary nuclei. The information about the degree of symmetry breaking is mediated by the spectral density in the scalar-isoscalar channel that should exhibit a substantial enhancement close to the 2π threshold if chiral symmetry were restored partially. First experiments of 2π production with pion beams have been reported in [28] and later in [29, 30] where indeed such an enhancement has been found in the $\pi^+\pi^-$ channel but not in the $\pi^+\pi^+$ channel. The latter one can not be influenced by the isoscalar σ meson since the pions have total isospin $I = 2$. Thus, the observed nuclear mass number dependence of the $\pi\pi$ spectra could indeed be related to a spectral change in the scalar-isoscalar σ channel.

In the previous Chapter we have discussed in detail similar effects in the $\gamma N \to \pi\pi N$ reaction in nuclei. However, the observed effects could also be explained by traditional incoherent final state interactions that slow down the pions and, consequently, rearrange the strength in the $\pi\pi$ spectrum such that the low mas region increases. These effects were very similar as those generated by the medium modification of the $\pi\pi$ interaction in the scalar-isoscalar channel that ultimately can be connected to the partial restoration of chiral symmetry. However, as we have shown in the last Section of Chapter 2 both traditional final state interactions and in-medium changes of the scalar spectral function can be generated by identical physical processes, namely the rescattering of the pions from the nucleons in the medium. Consequently, it is the aim of our studies presented in this Chapter to investigate the continuation of our results for the $\gamma N \to \pi\pi N$ reaction to pion-induced nuclear reactions.

The $\pi A \to \pi\pi X$ ($\pi \to \pi\pi$ in the following) reaction has been studied theoretically both in Refs. [112] and [75]. In [112] the $\pi\pi$ interaction using the chirally improved Jülich model [113] has been implemented. On the other hand the production process $\pi N \to \pi\pi N$ as well as nuclear effects as Fermi motion and traditional final state interactions were described in a simplified manner. The results indeed show some enhancement in the $\pi^+\pi^-$ channel close to threshold that agrees well with the experimental data. In [75] the same reaction has been studied in much more detail, treating both the initial

production and final state interactions in a more realistic way. Consequently, the substantial enhancement present in the experimental data [29] could not be reproduced even including explicitly the in-medium change of the $\pi\pi$ interaction. However, also in [75] important components of the final state interactions have been omitted. This issue has been discussed already in Section 2.5.

We will start our discussion with a short report of the experimental situation. The following Section then will deal in some detail with the elementary reaction $\pi N \to \pi\pi N$ for that a microscopic model will be extended and improved in order to describe the data in the relevant energy interval. Using this microscopic input we show in Section 4.4 a calculation of 2π production from Deuterium and compare to the data of [114] that has been used as a reference measurement regarding the observation of density dependent effects [29]. Similar as in the previous Chapter we finally investigate in detail the effects of traditional final state interactions on the $\pi \to \pi\pi$ reaction in nuclei. To this end we again use the semiclassical BUU model that accounts for the FSI within an incoherent coupled channel treatment. In the end we compare to the experimental data [29, 54] and to the model results from [75, 112].

4.2 Experimental status

Pion-induced double pion production has been measured both from elementary targets and complex nuclei. For the case of the elementary reaction total cross section data for all five experimental accessible isospin channels (see the following Section) have been obtained [115]. In some cases also differential distributions are available [116, 117]. The investigation of two pion production from complex nuclei has been driven by the expectation to gather information on the in-medium scalar spectral density. First data on these reactions has been made available about ten years ago [28]. Because of the interest in the σ channel one has concentrated on the $\pi^+ \to \pi^+\pi^-$, $\pi^- \to \pi^0\pi^0$ and – as a reference measurement – $\pi^+ \to \pi^+\pi^+$ isospin channels. The emphasis has been put to the study of the spectral shapes of the two pion mass distributions. These measurements have been done by the CHAOS [29, 30, 55] and Crystal Ball [54] collaborations.

CHAOS. The CHAOS spectrometer has a cylindrical geometry and consists of several layers of concentric wire chambers, a constant magnetic field and an outer ring of scintillation detectors [118]. With this setup the $\pi^+\pi^+$ and $\pi^+\pi^-$ final states have been measured simultaneously. The results of CHAOS have been criticized because of the extremely small angular coverage. The geometry of the detector is shown schematically in Fig. 4.1 where we have taken the $z-$axis as the beam direction and y and z forming the horizontal plane. Then the pions are detected only if $\varphi \in [-7^\circ, 7^\circ]$ where φ is the angle between the pion momentum and the $yz-$plane and $\theta \in [10^\circ, 170^\circ]$ with θ being the angle between the pion momentum and the $z-$axis. In addition, the spectrometer has a kinetic energy threshold of $T_\pi > 11$ MeV. From the geometrical constraints it follows that only $\Delta\Omega \simeq 1.36$ sr of 4π, or $\frac{\Delta\Omega}{4\pi} \simeq 11\%$ of the total solid angle are covered. Since both pions have to be detected only about $\left(\frac{\Delta\Omega}{4\pi}\right)^2 \simeq 1.2\%$ of all $\pi \to \pi\pi$ events are identified. Apart from substantially decreasing the statistics the spatial inhomogeneity of

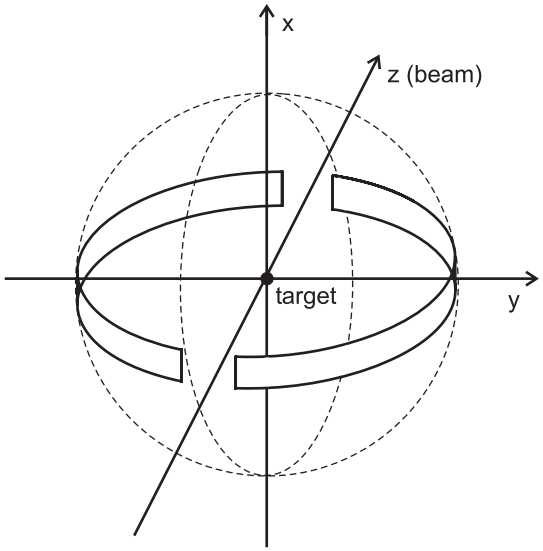

Figure 4.1: Geometrical acceptance of the CHAOS detector. The active area is indicated by the horizontal band.

the CHAOS spectrometer also deforms the two pion differential distributions. This can be seen in our results presented in the later Sections. In our calculations to be compared to the CHAOS data we include the above discussed acceptance constraints.

Crystal Ball. In contrast to CHAOS the Crystal Ball detector covers about 93% of the total solid angle [119]. It consists of a multiplicity of scintillation crystals. In this detector neutral final states can be isolated from charged ones whereas positive and negative particles cannot be distinguished from each other. Consequently, one has concentrated on the measurement of the $\pi^0\pi^0$ final state via the detection of the four photons from the $\pi^0 \to \gamma\gamma$ decay. The published data from Crystal Ball are corrected for the acceptance limitations. Thus, we do not have to apply any corrections to our calculated cross sections.

Elementary reactions. The total $\pi \to \pi\pi$ cross section from proton targets has been measured in all five isospin channels. These data can be found in Refs. [120, 121, 122, 123, 124, 125, 126] and a compilation of the data obtained before 1995 is given in Ref. [115]. We will later control the outcome of our model for the elementary process by a comparison to these data. For the channels $\pi^{\pm}p \to \pi^{+}\pi^{\pm}n$ and $\pi^{-}p \to \pi^0\pi^0 n$ also mass differential distributions have been obtained. These have been taken by the CHAOS [116] and Crystal Ball [117, 127] collaborations. In spite of the extremely limited CHAOS acceptance these data have been extrapolated to the full 4π geometry. Thus, we are only able to compare to these acceptance corrected data sets that comprise additional uncertainties due to the extrapolation procedure that cannot be reconstructed or judged from the original publication [116].

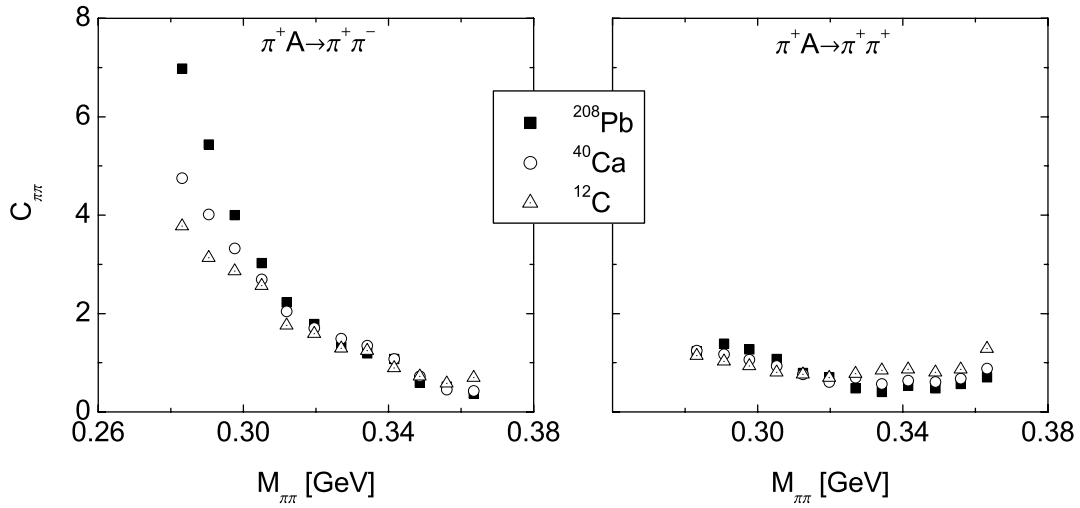

Figure 4.2: Ratio $\mathcal{C}_{\pi\pi}$ for the $\pi^+\pi^-$ and $\pi^+\pi^+$ isospin channels measured in the CHAOS experiment [53].

Nuclear reactions. The first measurement of the $\pi^+ \to \pi^+\pi^\pm$ reaction in nuclei with CHAOS at TRIUMF has been reported in [29, 30]. This measurement has been done at a pion kinetic energy of $T_\pi = 280$ MeV using the nuclear target materials ^{2}H, ^{12}C, ^{40}Ca and ^{208}Pb. As a result a dramatic enhancement of the $\pi^+\pi^-$ mass distribution at the 2π threshold has been reported. Albeit some strength was also seen in the $\pi^+\pi^+$ channel, it was already present in vacuum whereas in the $\pi^+\pi^-$ case it was not. Later, this different $A-$dependence of the 2π mass spectra has been visualized by the differential ratio [53]

$$\mathcal{C}_{\pi\pi} = \frac{d\sigma_A(M_{\pi\pi})/\sigma_A}{d\sigma_N(M_{\pi\pi})/\sigma_N} \tag{4.1}$$

that was expected to be less sensitive to the CHAOS acceptance constraints and traditional rescattering effects. This ratio is shown in Fig. 4.2. Indeed a substantial enhancement of this ratio at the 2π threshold is observed in the $\pi^+\pi^-$ channel whereas it stays almost flat in the $\pi^+\pi^+$ channel. However, such ratios always have to be taken with care since only small changes in the reference measurement, that enters the denominator of (4.1), induce large changes in the composite ratio. Later new data have been taken by the CHAOS collaboration for a range of beam energies $T_\pi = 243, 264, 284$ and 305 MeV using ^{45}Sc as target material [55, 128]. Albeit much more carefully analyzed, the results of the first measurement [29] have been confirmed.

Motivated by the encouraging but debated result from the CHAOS experiment the $\pi^- \to \pi^0\pi^0$ reaction from the nuclear target materials ^{2}H, ^{12}C, ^{27}Al and ^{64}Cu at $T_\pi = 293$ MeV has been measured with Crystal Ball at SLAC [54]. The $\pi^0\pi^0$ channel has the advantages that it cannot be in a $p-$state, it cannot have odd isospin and there are no Coulomb corrections. In contrast to the CHAOS results no such dramatic enhancement close to the 2π threshold has been found. Nevertheless a change of the $\pi^0\pi^0$ mass spectrum was observed. As the nuclear mass number becomes high, the 2π mass distributions measured with Crystal Ball approach a pure phasespace distribution whereas in vacuum

they substantially deviate from phasespace. Both the CHAOS and Crystal Ball results will be analyzed and discussed in the final Section of this Chapter.

4.3 The πN $\to$ $\pi\pi$N reaction

An important ingredient to our calculations of pion-induced double pion production in nuclei is the elementary process $\pi N \to \pi\pi N$. In particular reactions with more than two particles in the final state require some microscopic input. The matrix element for the reaction $2 \to 3$ independently depends on five kinematical variables which makes the use of interpolations or parameterizations unfeasible also from the practical point of view. Here we start from the model for the $\pi^- p \to \pi^+\pi^- n$ reaction presented in [129] and extend it to all possible isospin channels. In addition, we include new Feynman diagrams that were not considered in [129] and that improve the agreement with the experimental data. These are the diagrams $4a - c$ in Fig. 4.3 in the following. Moreover, for the diagrams already included in [129] we had to add additional time-orderings which did not contribute to the $\pi^- p \to \pi^+\pi^- n$ reaction exclusively studied in [129]. Pion-induced double pion production from protons has also been studied within similar approaches in Refs. [130, 131, 132, 133, 134, 135, 136, 137].

4.3.1 Isospin analysis

In total there are ten different $\pi N \to \pi\pi N$ reactions with charged pions in the initial state. There are five channels for proton targets

$$\pi^+ p \to \pi^+\pi^+ n \tag{4.2}$$
$$\pi^+ p \to \pi^+\pi^0 p \tag{4.3}$$
$$\pi^- p \to \pi^+\pi^- n \tag{4.4}$$
$$\pi^- p \to \pi^0\pi^0 n \tag{4.5}$$
$$\pi^- p \to \pi^0\pi^- p \tag{4.6}$$

and five channels for neutron targets

$$\pi^- n \to \pi^-\pi^- p \tag{4.7}$$
$$\pi^- n \to \pi^-\pi^0 n \tag{4.8}$$
$$\pi^+ n \to \pi^+\pi^- p \tag{4.9}$$
$$\pi^+ n \to \pi^0\pi^0 p \tag{4.10}$$
$$\pi^+ n \to \pi^0\pi^+ n \tag{4.11}$$

Out of these only the first five channels are directly accessible for experimental observation. In the isospin symmetric limit $m_u = m_d$ the amplitudes for these reactions are not independent but can be expressed in terms of isospin amplitudes. The initial state of one pion and one nucleon can have total isospin $I = \frac{1}{2}$ or $I = \frac{3}{2}$. Due to isospin conservation final states with $I = \frac{5}{2}$ are not possible. To unambiguously specify the three particle final

process	T_{01}	T_{11}	T_{31}	T_{32}
$\pi^+ p \to \pi^+\pi^+ n$	0	0	0	$\frac{2}{\sqrt{5}}$
$\pi^+ p \to \pi^+\pi^0 p$	0	0	$\frac{1}{\sqrt{2}}$	$-\frac{1}{\sqrt{10}}$
$\pi^- p \to \pi^+\pi^- n$	$-\frac{\sqrt{2}}{3}$	$-\frac{1}{3}$	$\frac{1}{3}$	$\frac{\sqrt{5}}{15}$
$\pi^- p \to \pi^0\pi^0 n$	$\frac{\sqrt{2}}{3}$	0	0	$\frac{2\sqrt{5}}{15}$
$\pi^- p \to \pi^0\pi^- p$	0	$\frac{\sqrt{2}}{3}$	$\frac{1}{3\sqrt{2}}$	$-\frac{1}{\sqrt{10}}$
$\pi^- n \to \pi^-\pi^- p$	0	0	0	$-\frac{2}{\sqrt{5}}$
$\pi^- n \to \pi^-\pi^0 n$	0	0	$\frac{1}{\sqrt{2}}$	$\frac{1}{\sqrt{10}}$
$\pi^+ n \to \pi^+\pi^- p$	$\frac{\sqrt{2}}{3}$	$-\frac{1}{3}$	$\frac{1}{3}$	$-\frac{\sqrt{5}}{15}$
$\pi^+ n \to \pi^0\pi^0 p$	$-\frac{\sqrt{2}}{3}$	0	0	$-\frac{2\sqrt{5}}{15}$
$\pi^+ n \to \pi^0\pi^+ n$	0	$\frac{\sqrt{2}}{3}$	$\frac{1}{3\sqrt{2}}$	$\frac{1}{\sqrt{10}}$

Table 4.1: Isospin amplitudes for $\pi N \to \pi\pi N$ processes. The notation is $T_{I,I_{\pi\pi}}$

state one further isospin of two of the three final state particles is needed. Frequently the isospin $I_{\pi\pi}$ of the two pion system with the possible values $I_{\pi\pi} = 0, 1, 2$ is used. Consequently, we find four different isospin channels $(I, I_{\pi\pi}) = (\frac{1}{2}, 0)$, $(\frac{1}{2}, 1)$, $(\frac{3}{2}, 1)$ and $(\frac{3}{2}, 2)$. The decomposition of the $\pi N \to \pi\pi N$ reactions into these isospin amplitudes is given by the following relation:

$$\begin{aligned} T_{I_\pi m_\pi I_{N_1} m_{N_1} \to I_{\pi_1} m_{\pi_1} I_{\pi_2} m_{\pi_2} I_{N_2} m_{N_2}} \;=\; & \sum_{I=\frac{1}{2}}^{\frac{3}{2}} \sum_{I_{\pi\pi}=0}^{2} \mathcal{C}(I_\pi I_{N_1} m_\pi m_{N_1} | I m) \\ & \times \mathcal{C}(I_{\pi_1} I_{\pi_2} m_{\pi_1} m_{\pi_2} | I_{\pi\pi} m_{\pi\pi}) \\ & \times \mathcal{C}(I_{\pi\pi} I_{N_2} m_{\pi\pi} m_{N_2} | I m) T_{I,I_{\pi\pi}} \end{aligned} \tag{4.12}$$

where I_π, m_π is the isospin of the initial pion and its $z-$component, I_{N_1} refers to the initial nucleon, etc. The total isospin $z-$component is $m = m_{N_1} + m_\pi$ and the $\pi\pi$ isospin $z-$component is $m_{\pi\pi} = m_{\pi_1} + m_{\pi_2}$. The isospin factors for the individual reaction channels as defined by Eq. (4.12) are given in Table 4.1. From this Table we can immediately read off that some cross sections are identical, namely for the processes $\sigma(\pi^+ p \to \pi^+\pi^+ n) = \sigma(\pi^- n \to \pi^-\pi^- p)$ and $\sigma(\pi^- p \to \pi^0\pi^0 n) = \sigma(\pi^+ n \to \pi^0\pi^0 p)$. Hence, we are left with the task to calculate eight independent $\pi N \to \pi\pi N$ reactions. The construction of the tree-level amplitude will be discussed in the following Section. The isospin coefficients of the individual contributions to the amplitude are given explicitly in Appendix D.

4.3.2 Model

Our model is based upon that developed in [129]. In [129] the reaction $\pi^- p \to \pi^+\pi^- n$ was calculated at pion kinetic energies close to threshold. The influence of diagrams including the Δ and $N^*(1440)$ resonances on the threshold behavior of the total cross section was studied. However, only those N^* terms that couple in relative $s-$wave and, thus, did not vanish at threshold, were included. In particular the omission of the $N^*\Delta\pi$ Lagrangian induced a cross section about 50% below the data. In addition, the chiral symmetry breaking parameter ξ, present in the Weinberg chiral Lagrangian $\mathcal{L}_{\pi\pi\pi\pi}$, was determined to be in the range of $\xi = -0.5 - 0$. However, today it is known that only the value $\xi = 0$ is consistent with QCD [138].

The complete set of Feynman diagrams of the present model is shown in Fig. 4.3. The model includes the contributions from the lowest order pion-nucleon Lagrangian as well as the excitation of $\Delta(1232)$ and $N^*(1440)$ resonances. The pion-nucleon Lagrangians $\mathcal{L}_{NN\pi}$, $\mathcal{L}_{NN\pi\pi\pi}$, $\mathcal{L}_{\pi\pi\pi\pi}$ and $\mathcal{L}_{NN\pi\pi}$ can be derived from the leading order expansion of the effective low energy field theory for strong interactions. This effective theory again is expanded in powers of the pion field, keeping only terms up to four pion fields in the pion-pion and up to three fields in the pion-nucleon Lagrangian, see [139]. It was shown [140] that higher order terms are related to resonance exchange. Since our model explicitly includes the Δ, $N^*(1440)$ and ρ resonances in the intermediate states we do not have to consider higher order contributions to the pion-pion and pion-nucleon Lagrangians.

The model for the reaction $\pi^- p \to \pi^+\pi^- n$ including a reduced set of Feynman diagrams, namely the diagrams $1-3$ in Fig. 4.3 with the time-orderings contributing to the $\pi^- p \to \pi^+\pi^- n$ reaction, has been presented quite in detail in [129]. Thus, we forgo to repeat these details in the present context and refer the interested reader to the literature [129]. However, the important pieces necessary for the calculation of the $\pi N \to \pi\pi N$ reaction are given also in Appendix D. In addition, there also the isospin factors needed to obtain the amplitudes for all other isospin channels and the additional amplitudes are given. In the following we only briefly describe one particularly important process that has been omitted completely in [129].

The diagram 4(b) of Fig. 4.3 requires to take into account the $N^*\Delta\pi$ vertex. Due to the relatively large $N^* \to \Delta\pi$ branching ratio $(20 - 30\%)$ [141] one expects its contribution to be significant, in particular in the kinematic region where the Roper ($N^*(1440)$) resonance can be on-shell. In analogy to the $N\Delta\pi$ coupling the non-relativistic Lagrangian for this vertex reads

$$\mathcal{L}_{N^*\Delta\pi} = \frac{g_{N^*\Delta\pi}}{m_\pi}\psi^\dagger_\Delta S^\dagger_i(\partial_i\boldsymbol{\phi})\mathbf{T}^\dagger\psi_{N^*} + h.c. \tag{4.13}$$

where $\mathbf{S}^\dagger$ and $\mathbf{T}^\dagger$ are the spin and isospin $1/2 \to 3/2$ transition operators, defined such that their matrix elements simply becomes Clebsh-Gordan coefficients, see Appendix D. In [129] the $N^*(1440)$ decay width was implemented only approximately in analogy to the Δ width by taking $\Gamma_{N^*} \propto q^3(W)$ where q is the $N\pi$ CM momentum and W is the Roper invariant mass. In order to be more accurate in the evaluation of the N^* width we also have to include the $N^* \to \Delta\pi$ decay with the realistic width of the Δ resonance. The

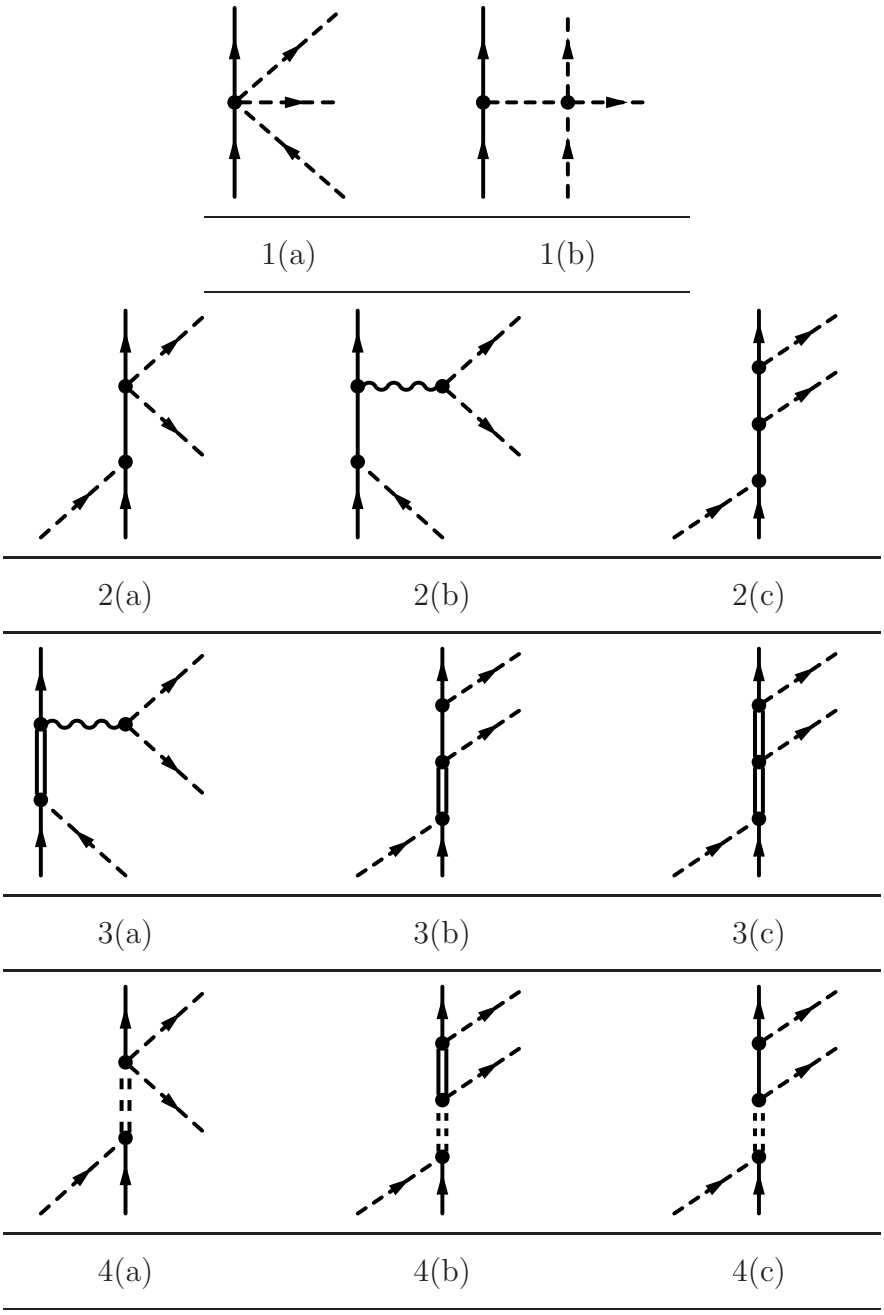

Figure 4.3: Complete set of Feynman diagrams included in the calculation of the $\pi N \to \pi\pi N$ transition amplitude. *Single solid lines*: nucleons, *single dashed lines*: pions, *double lines*: $\Delta(1232)$ resonances, *double dashed lines*: Roper $N^*(1440)$ resonances, *wiggly line*: $\rho(770)$ mesons. In addition, we consider all possible time orderings, resulting in the total amount of 74 diagrams included in the calculations.

fact that the Δ width is not small compared to the mass difference between the Roper

and the Δ makes this correction advisable. The $N^* \to \Delta\pi$ width is given by [139]

$$\Gamma_{\Delta\pi}(W) = \frac{1}{3\pi^2}\left(\frac{g_{N^*\Delta\pi}}{m_\pi}\right)^2 \int_0^{p_{\max}} dp \frac{p^4}{\sqrt{p^2+m_\pi^2}} |D_\Delta(W_\Delta)|^2 \Gamma_\Delta(W_\Delta) \tag{4.14}$$

with the Δ energy in the N^* rest frame

$$W_\Delta^2 = W^2 - 2W\sqrt{p^2+m_\pi^2} + m_\pi^2 \tag{4.15}$$

and the maximum possible $\Delta\pi$ CM momentum

$$p_{\max} = \left[\left(\frac{W^2 - m_N^2 - 2m_N m_\pi}{2W}\right)^2 - m_\pi^2\right]^{\frac{1}{2}}. \tag{4.16}$$

D_Δ is the (non-relativistic) Δ propagator given by Eq. (D.28) in Appendix D and Γ_Δ the total Δ decay width (D.29). The $N^*\Delta\pi$ coupling constant has a value of $g_{N^*\Delta\pi} = 2.07$ [139]. The remaining contributions to the Roper width are given in Appendix D. We use this parametrization for the Roper width also in all other diagrams including intermediate N^* resonances. On top of these contributions we also include the three point diagrams 4(c) from Fig. 4.3 with nucleons and Roper resonances in the intermediate states. The contribution of these, however, is only marginal.

4.3.3 Results

In Fig. 4.4 we show the total cross section for all isospin channels obtained by a coherent summation of all contributions from Fig. 4.3. Experimental data is only available in those channels where a proton is in the initial state. In most cases the agreement is quite good recalling that no parameters have been fitted to the data but rather standard values for the coupling constants as obtained from different experimental analyses have been used. However, in some cases the cross sections are too high at the largest pion kinetic energies. This is observed mainly in the $\pi^- p \to \pi^+\pi^- n$ and $\pi^- p \to \pi^-\pi^0 p$ channels and can be attributed to an overestimation of the Roper resonance terms. This behavior could be cured possibly by using an off-shell cutoff at the $N^*\Delta\pi$ vertices. However, we are not interested in such high kinetic energies that anyway would require to consider additional contributions to the $\pi N \to \pi\pi N$ amplitude.

The agreement of our model and the data also extends to the differential distributions. This can be seen in Fig. 4.5 where the differential cross sections with respect to the two pion invariant mass squared is shown for three different isospin channels where experimental data is available. In addition to the model results also pure phase distributions normalized to the calculated cross sections are shown. In the $\pi^- p \to \pi^+\pi^- n$ and $\pi^- p \to \pi^0\pi^0 n$ channels the cross sections substantially deviate from phasespace whereas in the $\pi^+ p \to \pi^+\pi^+ n$ channel the m^2-distribution is quite close to the phasespace distribution. This fact will be important later when we investigate the effect of final state interactions on the two pion production process inside extended nuclear targets. In contrast to the other channels the agreement to the shape of the differential distribution in

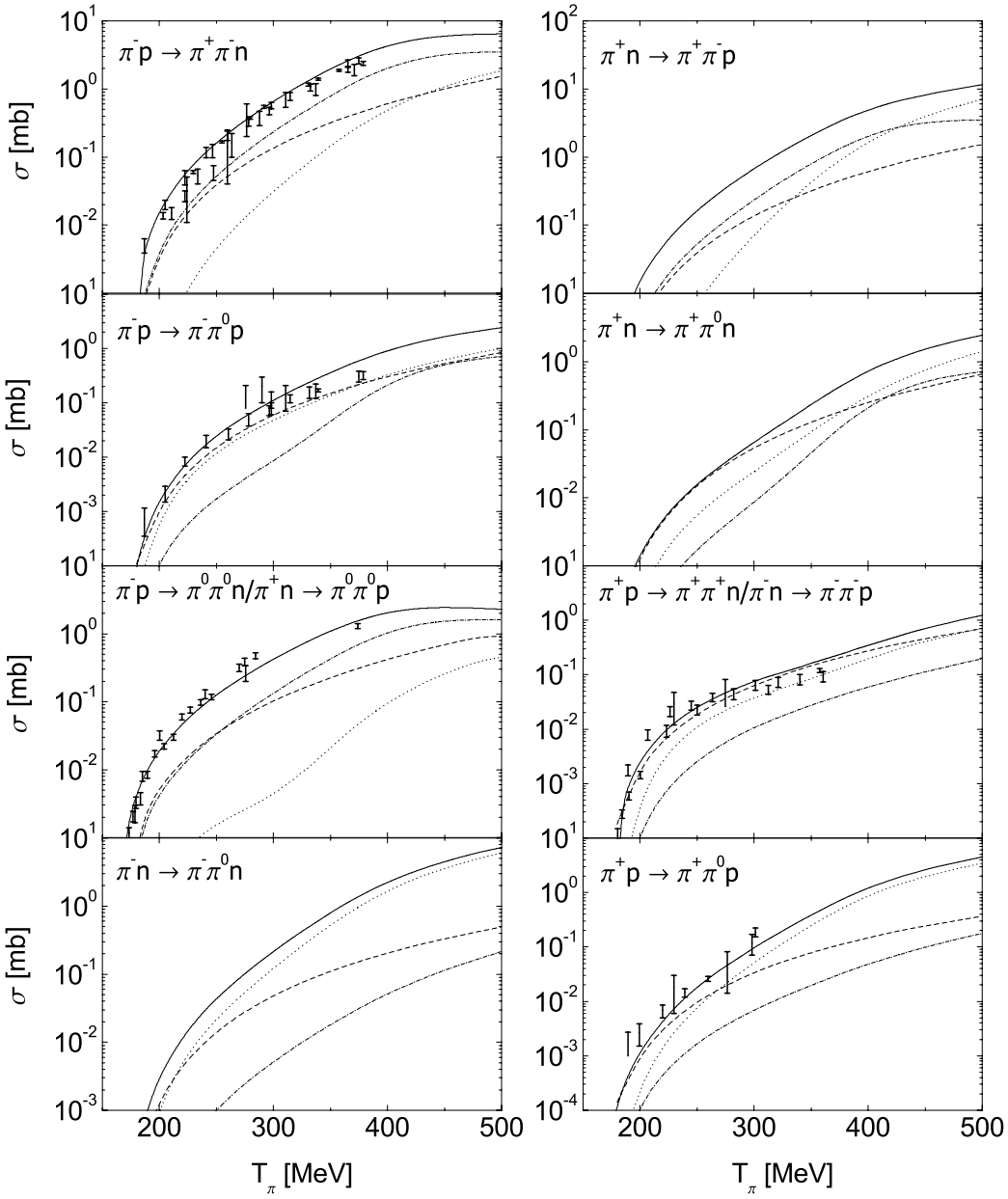

Figure 4.4: Total cross sections for the different isospin channels in the reaction $\pi N \to \pi\pi N$ as function of the initial pion kinetic energy. *Solid lines*: coherent sum of all amplitudes, *dashed line*: only nucleon and pion pole terms, *dotted lines*: $\Delta(1232)$ excitation terms only, *dash-dotted lines*: Roper resonance terms only. The compilation of experimental data has been taken from Ref. [115].

the $\pi^+p \to \pi^+\pi^+n$ channel is rather poor. However, this feature is not unexpected as we have it in common with other models [137]. As discussed previously, these data have been obtained with the CHAOS spectrometer that has an extremely limited geometrical acceptance concerning the azimuthal angular coverage. Consequently, the data shown in Fig. 4.5 have been obtained by extrapolating a differential distribution from the only

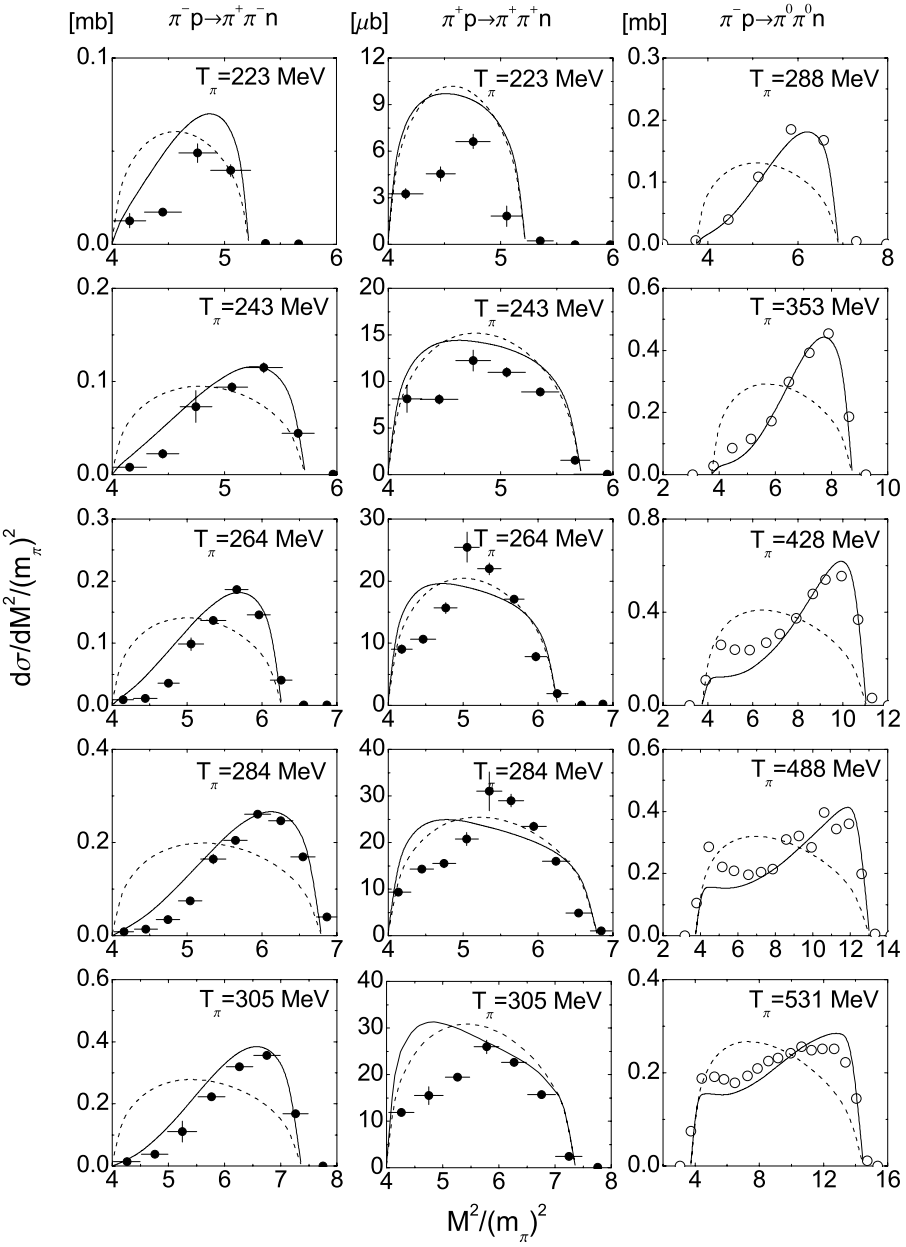

Figure 4.5: Mass distributions for the processes $\pi^- \to \pi^+\pi^- n$, $\pi^+ p \to \pi^+\pi^+ n$ and $\pi^- p \to \pi^0\pi^0 n$. *Solid lines*: model results, *dashed lines*: three-body phasespace normalized to the model predictions. Data from Refs. [116] (bars) and [117] (open circles). In the $\pi^- p \to \pi^0\pi^0 n$ the data have been obtained without normalization.

1.2%, that are actually seen (!), to the full 100%. This cannot be done unambigously and, thus, model dependencies that cannot be reconstructed from the published data, already enter the experimental result. Consequently, we do not consider the comparison to these data as being very meaningful. Further differential distributions will be discussed for the Deuteron case in the following Section.

4.4 The πd $\to \pi\pi$(NN) reaction

Model. We calculate the $\pi d \to \pi\pi(NN)$ process in the simple spectator approximation. This means that we assume a quasifree reaction mechanism and neglect any rescattering processes. Thus, the cross section from Deuterium is given as a sum over the proton and neutron cross sections. In addition, Fermi motion is introduced by assigning an initial momentum to the nucleon involved in the reaction. In this calculation we treat the nucleon as an off-shell particle with its energy being equal to the free nucleon mass, thus neglecting the Deuteron binding energy, and its momentum chosen randomly according to the Fourier transform of the Deuteron wave function. The total photoproduction cross section is thus given by

$$\sigma_D(E) = \int \frac{d^3p}{(2\pi)^3} \left(|u(p)|^2 + |d(p)|^2\right) \left(\sigma_{\gamma p}(s) + \sigma_{\gamma n}(s)\right) \tag{4.17}$$

where $u(p)$ and $d(p)$ are the $s-$ and $d-$wave components of the Deuteron wave function. The invariant energy is given by $s = (k+p)^2$ with $p_0 = m_N$ and $k_0 = E_\gamma$. In the actual calculation we neglect the small $d-$wave admixture in the wave function and use the Hulthen nucleon momentum distribution that is obtained as an exact solution to the Deuteron problem assuming a Yukawa-type nucleon-nucleon potential [142]. The expression for the wave function in momentum space has the following form [139, 142]

$$u(p) = \sqrt{8\pi \frac{\alpha\beta(\alpha+\beta)}{(\alpha-\beta)^2}} \left(\frac{1}{\alpha^2+p^2} - \frac{1}{\beta^2+p^2}\right) \tag{4.18}$$

with the parameters $\alpha = 45$ MeV and $\beta = 7\alpha$, that have been adjusted in order to fit the observed properties of the Deuteron system. We obtain the Deuteron cross section within a Monte Carlo program that calculates the reaction amplitudes kinematically allowed for a given CM energy. The initial nucleon momentum is obtained by Monte Carlo sampling from the probability distribution

$$w(|\mathbf{p}|) = \frac{\mathbf{p}^2 |u(\mathbf{p})|^2}{(2\pi)^3} \tag{4.19}$$

that is normalized to one. Consequently, the CM energy varies from event to event. The distribution is centered around the energy value of the free process and is slightly asymmetric with a longer tail on the low-energy side. Thus, the kinematic ranges of the free process are smeared and broadened for the Deuterium case.

Results. In Fig. 4.6 we show the resulting differential cross sections compared to the data from [114]. We have approximately implemented the experimental acceptance cuts as discussed previously. The channels $\pi^+ \to \pi^+\pi^-$ and $\pi^+ \to \pi^+\pi^+$ are compared through the distributions in the kinematical observables $M_{\pi\pi}$ (two pion invariant mass), $\Theta_{\pi\pi}$ ($\pi\pi$ opening angle) and $T_{\pi\pi}$ (pion kinetic energy sum). In the $\pi^+ \to \pi^+\pi^+$ channel the final state $\pi\pi$ distribution is very close to a pure phasespace distribution. The particular shape of the invariant mass distribution is created by the geometrical acceptance

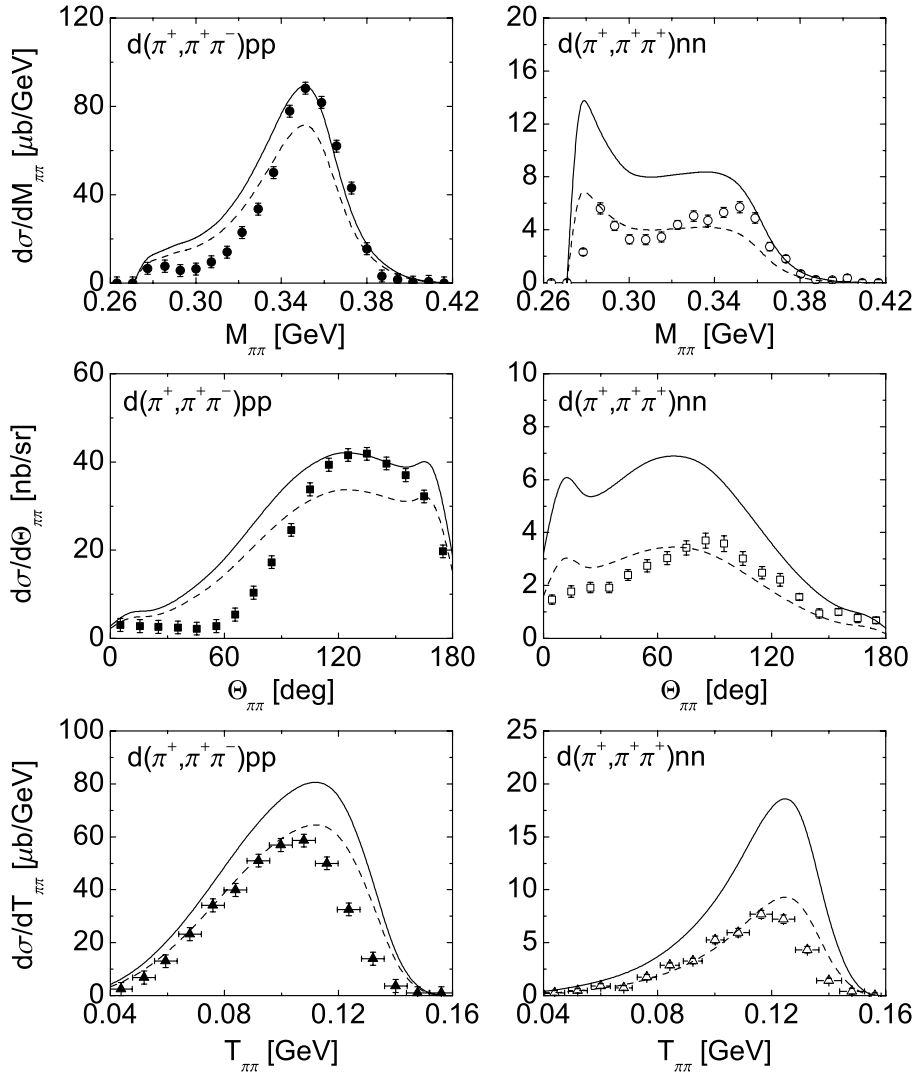

Figure 4.6: Differential cross sections for the reactions $\pi^+ d \to \pi^+\pi^- pp$ and $\pi^+ d \to \pi^+\pi^+ nn$. Shown are the differential distributions with respect to the two pion invariant mass $M_{\pi\pi}$, the $\pi\pi$ opening angle $\Theta_{\pi\pi}$ and the pion kinetic energy sum $T_{\pi\pi}$. *Solid lines*: results of the present model, *dashed lines*: the same as before but multiplied with 0.75(left) respectively 0.5(right). Data from Ref. [114].

constraints of the experimental apparatus that favors the situations where the pions either go together or in opposite directions. These situations correspond to low and high invariant two pion masses, thus creating the two peaks in the mass distribution. In the $\pi^+ \to \pi^+\pi^-$ channel the non-existence of the low mass peak reflects the non-uniformity of the production amplitude that due to destructive interference possesses only little strength in the regime of low two pion masses.

Overall the agreement in both channels is satisfactory regarding the fact that we have calculated the production amplitude on tree-level only and also the extension of the elementary process to the Deuterium case has been kept very simple. In the $\pi^+ \to \pi^+\pi^-$

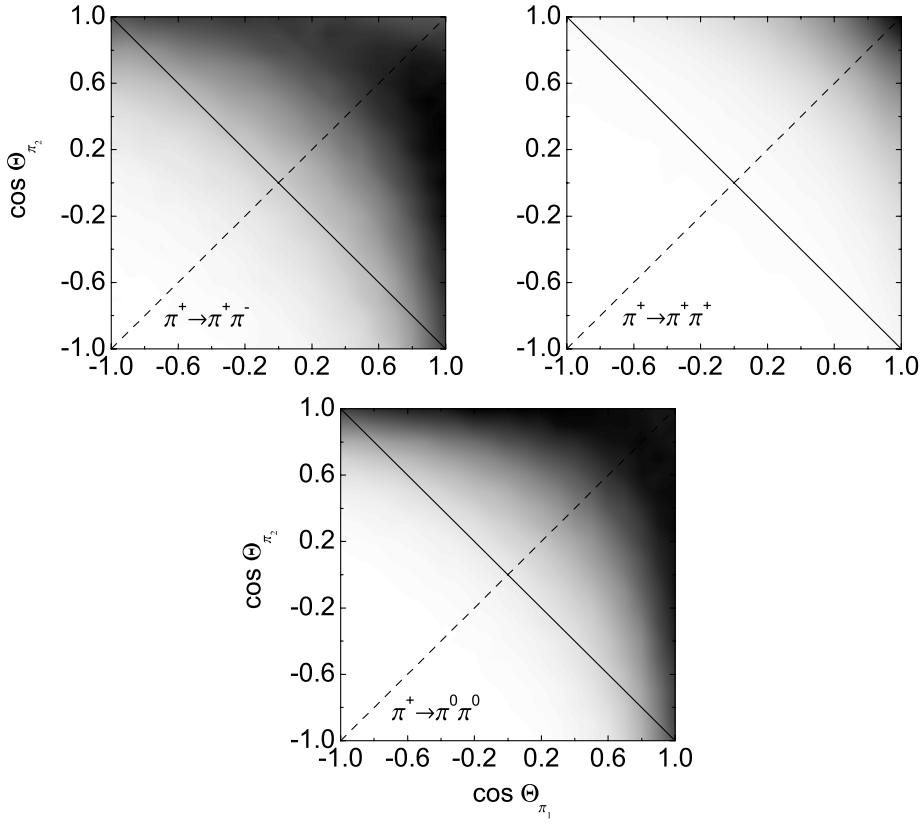

Figure 4.7: LA angular distribution $d\sigma/d\Omega_1 d\Omega_2$ from Deuterium at $T_\pi = 284$ MeV ($\pi^+ \to \pi^+\pi^+$ and $\pi^+ \to \pi^+\pi^+$) and $T_\pi = 293$ MeV ($\pi^- \to \pi^0\pi^0$), respectively. The vertical gray scale is a linear one.

channel our model overestimates the normalization of the cross section. Reducing it by 25% as indicated by the dashed line, better agreement for all differential distributions is obtained. Partly this could be due to the omittance of any final state interactions that, albeit weak, are already present in the Deuteron system. As discussed in much detail in the previous Chapter for the case of photon-induced pion production in nuclei charge exchange reactions tend to equally distribute the flux to the various isospin channels. Thus, initially large channels as $\pi^+\pi^-$ are reduced in favor of smaller channels such as for instance $\pi^+\pi^0$. However, the same disagreement has also been found in [75] where the $\pi^+ \to \pi^+\pi^-$ channel has been reduced by 20% in order to fit the experimental data. Furthermore, we note that in the $\pi^+ \to \pi^+\pi^+$ case we overestimate the cross section at low $M_{\pi\pi}$. This is also reflected by the second peak in the opening angle distribution for the situation where both pions go together. This we have to keep in mind when comparing the nuclear cross sections to experimental data.

Since we are aiming at an investigation of the influence of FSI on the two-pion differential distributions, an interesting quantity to look at is the LA angular distribution of the pions which to some extend determines the strength of the FSI effects. In Fig. 4.7 we show the differential cross sections $d\sigma/d\Omega_1 d\Omega_2$ with Ω_1 and Ω_2 the LA angles of both pions.

The solid diagonal line corresponds to the situation where both pions go in opposite directions and, thus, have high invariant mass whereas the dashed line corresponds to the opposite situation. In the $\pi^+ \to \pi^+\pi^+$ channel almost the entire strength is concentrated to forward angles. In contrast, in both the $\pi^+\pi^-$ and $\pi^0\pi^0$ channels also pions under backward LA angles are produced. If the pions are produced inside a finite target nucleus, quasi elastic scattering can change their directions and, hence, the invariant mass of the pair. The $\pi\pi$ opening angle can only become smaller if the pions initially are produced back-to-back but can become larger if they are produced with the same moving directions. Moreover, the pion nucleus interaction dominantly proceeds at the front side of the target nucleus due to the strong initial pion absorption. Thus, pions produced under forward angles have to cross the nuclear volume whereas pions going backward rapidly leave the strongly interacting region. This can have the consequence that the influence of the FSI is different in the $\pi^+\pi^+$ channel as compared to the $\pi^+\pi^-$ and $\pi^0\pi^0$ isospin channels due to the different angular distributions. The quantitative simulation of these effects will be subject to the following discussions.

4.5 Transport simulations

After having judged the capabilities of our model on the elementary level we move on to the calculation of nuclear observables. To this end we again employ the semiclassical transport approach with exactly the same type of final state interactions as investigated in detail in the previous Chapter. However, in contrast to the photon-induced reactions we now in addition have to account for the initial state interaction of the incoming pion. Also the static EM potential of the target can have a larger impact in the present case with the emphasis on charged pions only. Finally, we will compare our results to experimental data and the model results of [75].

4.5.1 Initial state interactions

The reaction probability of any particle with nucleons inside an extended nuclear target is high on the front side of the nucleus and smaller on the backside with respect to the incoming beam direction. This is very intuitive because of the absorption of the projectiles when penetrating the nuclear medium that causes the incoming flux to be attenuated. For the case of photon-induced reactions this effect becomes sizable only at energies above $\sim$ 1 GeV where the photon-nucleon interaction starts to be dominated by the hadronic compound of the photon represented by the light vector mesons, see e. g. [143, 144]. In contrast this effect is much more important for the case of hadronic particle beams as pions or protons that interact more strongly also at low energies.

The attenuation of the incoming pion beam could be simulated realistically in the transport approach by initializing the projectile outside the region of the nuclear forces and solving the transport equations including the full coupled-channel collision term for the time evolution of the reaction. This straightforward method, however, is very inefficient in the present case for the study of the $\pi N \to \pi\pi N$ reaction at low pion kinetic energies. In this energy domain the $2\pi N$ channel accounts only for roughly $\sim$ 1% of the total

pion-nucleon cross section. Consequently, in only 1 out of 100 pion-nuleon reactions a $2\pi N$ final state is produced. In addition we have seen previously that the geometrical CHAOS acceptance allows to only detect about 1% of all produced $\pi\pi$ pairs. Not even considering the absorption of the final state particles we, consequently, find that only a fraction of 10^{-4} of the initialized πA reactions contribute to the cross section we are aiming at.

On the other hand, the beam energy of $T_\pi = 280$ MeV is still quite close to the reaction threshold $T_\pi = m_\pi + \frac{3}{2}\frac{m_\pi^2}{m_N} \simeq 168$ MeV. Due to the loss of kinetic energy in quasi elastic πN events the probability that the $2\pi N$ final state is created in a secondary interaction is enormously reduced. We, therefore, simulate the low-energy pion-nucleus reaction in complete analogy to the photon-induced reactions. This means, that the incoming projectile only reacts once with a target nucleon and produces the $2\pi N$ final state. The attenuation of the incoming flux is accounted for by calculating an initial state attenuation factor. Defining the $z-$direction as the incoming pion beam direction the attenuation factor is given by

$$s_\pi(\mathbf{r}) = \exp\left[\int_{-\infty}^{z} d\xi \frac{\mathcal{I}\mathrm{m}\Pi(E_\pi(\mathbf{k}), n_N(\sqrt{\mathbf{b}^2+\xi^2}))}{|\mathbf{k}|}\right] \tag{4.20}$$

where $\mathcal{I}\mathrm{m}\Pi$ is the imaginary part of the on-shell π self energy. Here, we use the complete self energy that is a sum of both absorptive and quasi elastic contributions because of the energy loss of scattered pions that reduces the probability of subsequent 2π production. For the self energy we use two different parameterizations: On one hand we use the $\Delta-$hole self energy from Ref. [102] introduced in the previous Chapter which contains components corresponding to up to $3p3h$ excitations. This pion optical potential is meant to describe the energy regime dominated by the $\Delta(1232)$ resonance. On the other hand we approximate the on-shell self energy by the total vacuum πN cross section in the $T\rho-$approximation $\mathcal{I}\mathrm{m}\Pi = -n_N|\mathbf{k}|\sigma_{\pi N}$. This recipe accounts for two-body collisions and includes effects up to linear order in density only.

The energy and coordinate dependent attenuation factor (4.20) is multiplied to the elementary cross section for the individual πN reactions. The total nuclear cross section is obtained by integrating over the nuclear volume. Neglecting final state interactions as well as Fermi motion and Pauli blocking the total cross section reads

$$\sigma_{\pi A} = \int d^3r\, n_N(\mathbf{r}) s_\pi(\mathbf{r}) \sigma_{\pi N}. \tag{4.21}$$

In order to illustrate the effect of the attenuation factor we show in Fig. 4.8 the integrand of Eq. (4.21):

$$I(z) = n_N(\mathbf{r} = (\mathbf{b} = \mathbf{0}, z)) s_\pi(\mathbf{r} = (\mathbf{b} = \mathbf{0}, z)) \tag{4.22}$$

where $\mathbf{b} = (x, y)$ is the 2-dimensional coordinate perpendicular to the $z-$direction. In Fig. 4.8 we have considered the case of ^{208}Pb. It displays the density of those nucleons that effectively contribute to the nuclear reaction when the beam is coming at zero impact parameter. The downstream nucleons are substantially shadowed. This effect becomes particularly large at pion momenta around 300 MeV due to the πN kinematics

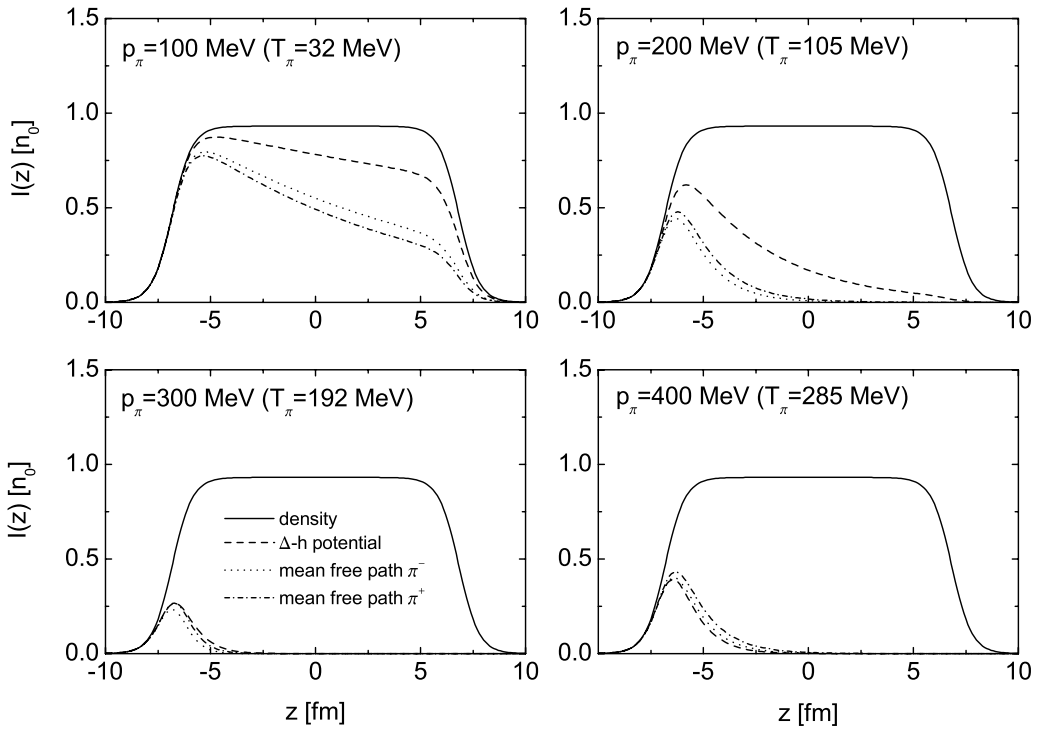

Figure 4.8: Effective active nuclear volume of a ^{208}Pb nucleus in pion-induced reactions for various bombarding energies. *Solid line*: nuclear density profile, *dashed line*: pion absorption according to optical potential (both π^+ and π^-), *dotted line*: pion absorption according to total πN vacuum cross section (π^-), *dash-dotted line*: the same but for π^+.

and the dominance of the $\Delta(1232)$ resonance. Positive and negative pions are attenuated differently since the considered nucleus is not isospin symmetric. At extremely low pion kinetic energies the $\Delta-$h potential does not match with our recipe using the total vacuum cross sections. This is clear since at low pion energies both recipes are not sufficient to properly describe the pion interaction with nuclear matter, see also Section 3.4. However, at the higher energies we are interested in (T_π = 280 MeV) both approaches almost coincide.

Finally, we show in Fig. 4.9 the effect of the initial state attenuation factor on the $\pi^+ \to \pi^\pm\pi^+$ reaction in nuclei. To this end no final state interactions have been included. We have considered ^{40}Ca as target nucleus. The cross sections are reduced by roughly a factor of 2/3. Apart from this reduction we do not observe any modifications, neither with nor without implying the CHAOS acceptance constraints. The shapes of the mass distributions are obviously unaffected by initial state interactions.

4.5.2 Coulomb correction

In the case of the $\gamma \to \pi^\pm\pi^0$ reaction the EM potential has turned out to be of minor importance and we, therefore, have neglected it in our calculations of the previous Chap-

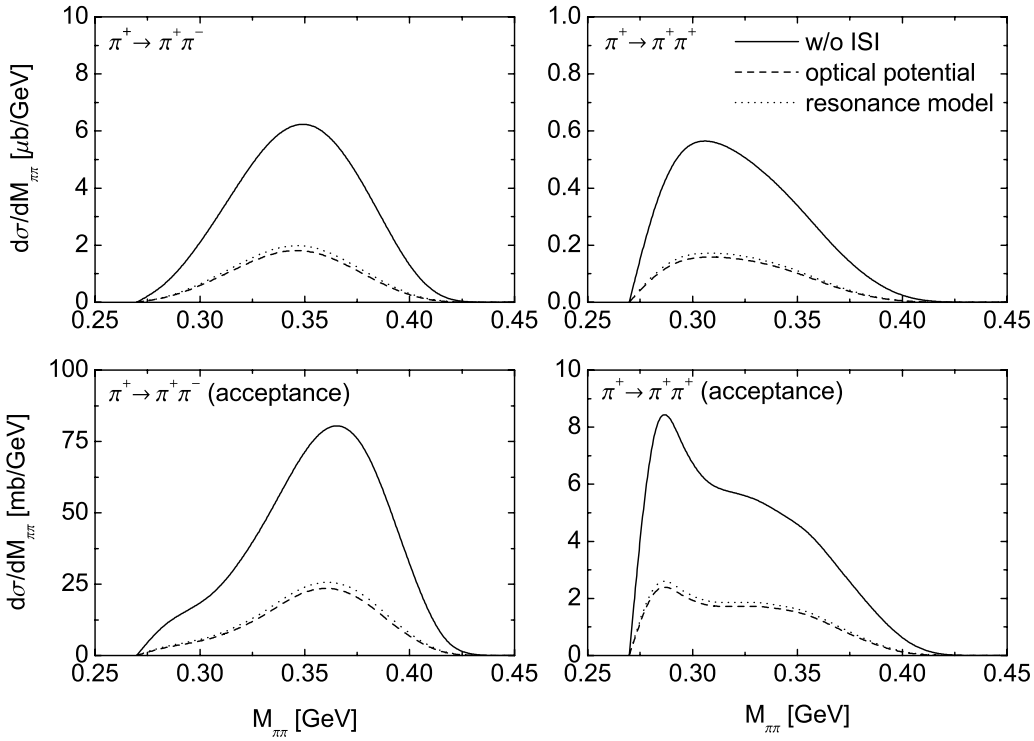

Figure 4.9: Effect of initial state interactions (ISI) on the $\pi^+ \to \pi^\pm\pi^+$ reaction in nuclei. *Solid line*: without ISI, *dashed line*: with ISI using the pion optical potential, *dotted line*: with ISI using the total vacuum πN cross section. The lower panels include the CHAOS acceptance constraints.

ter. However, in the study at hand both the initial and the final state particles carry electrical charge and, consequently, couple to the static EM field of the target nucleus. This static potential can become as deep as 25 MeV for the case of Lead targets. The inclusion of EM forces into our semiclassical treatment of incoherent nuclear reactions cannot be done without approximations. In principle, the EM coupling of charged particles would have to be added to the hadronic interaction Lagrangian. This coupling then gives rise to additional diagrams that have to be considered in those scattering processes involving charged particles. However, in the derivation of the collision term entering the semiclassical transport equations the assumption enters that the forces are short-ranged and, thus, subsequent scattering processes can be regarded as independent with the involved particles streaming freely in between. This assumption cannot be made when EM interactions are included.

Therefore EM interactions are rather included on the mean field level. Instead of considering single scattering graphs the real valued potential created by the exchange of virtual photons with the surrounding particles is determined. This potential enters the transport equations and, thus, the classical equations of motion, see e. g. [145, 146]. The hadronic contributions to the interaction are treated identical as in free space but with the energies and momenta of the initial and final state particles modified according to the

local EM potential. This treatment is particularly simple in the case at hand since our calculations are done in the perturbative mode, see Appendix A and [100]. That means that the nuclear background (the nucleons forming the target nucleus) is not influenced by the only small distortion created by the single pion probe. Consequently, the nuclear density is kept constant according to the initial Woods-Saxon density distribution. We comment on this approximation in Appendix A.5. A positive effect of this approximation is that the EM potential does not depend on time and also its spatial components vanish, i. e. $A_\mu = (V_C, \mathbf{0})$.

In order to approximately include the effects of the EM forces we follow the following recipe: Energy and momentum of the incoming pion with the original four-momentum $(k_0, \mathbf{k})$ are corrected according to

$$k^* = (k_0^*, \mathbf{k}^*) \quad = \quad (k_0 \pm eV_C(\mathbf{r}), \frac{\mathbf{k}}{|\mathbf{k}|}\sqrt{k_0^{*2} - k^2}) \tag{4.23}$$

where $V_C(\mathbf{r})$ is the local EM potential. The sign of the potential term changes according to the charge of the incoming pion. Then the hadronic cross section for the $\pi N \to \pi\pi N$ reaction is evaluated from the vacuum matrix element but with the initial in-medium pion four-momentum $k^* = (k_0^*, \mathbf{k}^*)$. Also the hadronic nucleon mean field is accounted for in the calculation of the CM energy as explained in Appendix A. The momenta of the final state particles are first sorted according to the vacuum matrix element and later on rescaled according to the local Coulomb potential. The outgoing pions are propagated inside the static EM mean field. Outside of the nucleus instead of numerically solving the equations of motion the pions are propagated on classical Coulomb trajectories (see e. g. [147]) until eventually the impact of the nuclear potential vanishes. In the case where the total energy of a pion becomes smaller than the pion vacuum mass this particle is erased from the flux since it cannot reach the detector. We will come back to the discussion of Coulomb effects on the observables after having studied the hadronic final state interactions.

4.5.3 Final state interactions

On exactly the same lines as in the previous case of double pion photoproduction off nuclei we now adopt the coupled-channel BUU model in order to study the influence of ordinary hadronic final state interactions (FSI) on the $\pi \to \pi\pi$ reaction in nuclei. Again we start by using the optical model approach to the pion FSI as introduced in the previous Chapter that allows for a clear separation of absorption, elastic scattering and charge exchange processes. Only in the end we also employ the full coupled-channel BUU collision term and compare the results of both approaches. In the following we present results for the nuclear target materials ^{2}H, ^{12}C, ^{40}Ca and ^{208}Pb at a pion kinetic energy of $T_\pi = 280$ MeV in order to compare our final results to the data taken by the CHAOS [29] and Crystal Ball [54] collaborations. In all these calculations – except for the cross sections to be compared to the Crystal Ball data – we approximately include the CHAOS acceptance constraints as discussed in a previous paragraph.

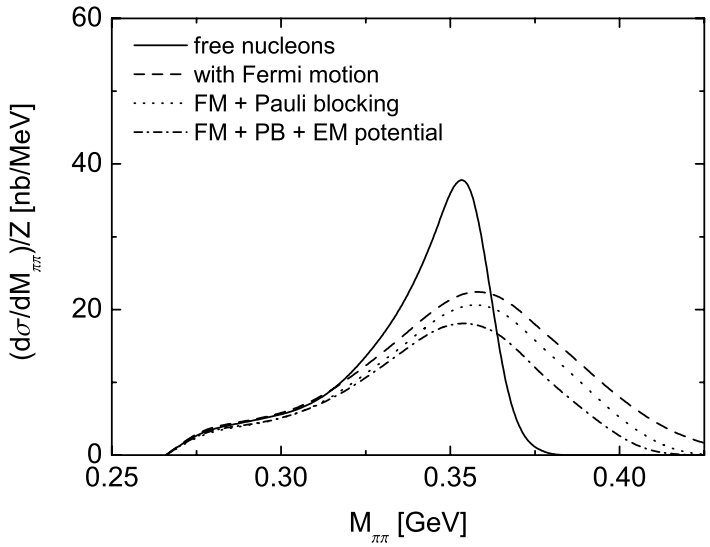

Figure 4.10: Two pion mass spectrum for the $\pi^+ \to \pi^+\pi^-$ reaction off ^{40}Ca at a pion kinetic energy of $T_\pi = 280$ MeV. *Solid line*: free nucleons at rest, *dashed line*: with Fermi motion (FM), *dotted line*: with FM and Pauli blocking (PB), *dash-dotted line*: with FM, PB and EM potential.

Fermi motion. First we examine the effects of Fermi motion, Pauli blocking and the EM potential. Fermi motion and Pauli blocking do not belong to the final state interations but they directly influence the phasespace distribution of the particles in the final state via the smearing of the CM energy and the blocking of certain phasespace areas. Both effects are included in our calculations by means of a local density approximation, see Appendix A. The treatment of the EM potential has been discussed previously. The two pion invariant mass distribution for the $\pi^+ \to \pi^+\pi^-$ reaction off Calcium can be seen in Fig. 4.10 which shows various curves corresponding to different nuclear scenarios. Most obvious we observe a substantial broadening of the mass distribution due to the larger phasespace area which can be populated with the help of Fermi motion. Even more important, however, is the observation that the peak at initially high invariant masses is strongly depleted due to Fermi motion whereas at low two pion massses hardly any effect is visible. This is, however, evident from the fact that the populated phasespace area is enlarged towards higher values of the two pion invariant mass but has an unshiftable lower threshold at twice the pion mass.

Pauli blocking and the EM potential slightly reduce the cross section. For better visibility of the invariant mass dependence of the particular effects we display the ratio of the differential cross sections including various nuclear mechanisms in Fig. 4.11. The solid squares are obtained by dividing the cross section calculated with Fermi motion by the one calculated without accounting for Fermi motion. Here it becomes even more obvious that Fermi motion suppresses the high invariant mass components in the spectrum which are spread over a wider range of two pion invariant masses when Fermi motion is included whereas the low mass components are almost unaffected. The effect of Pauli blocking,

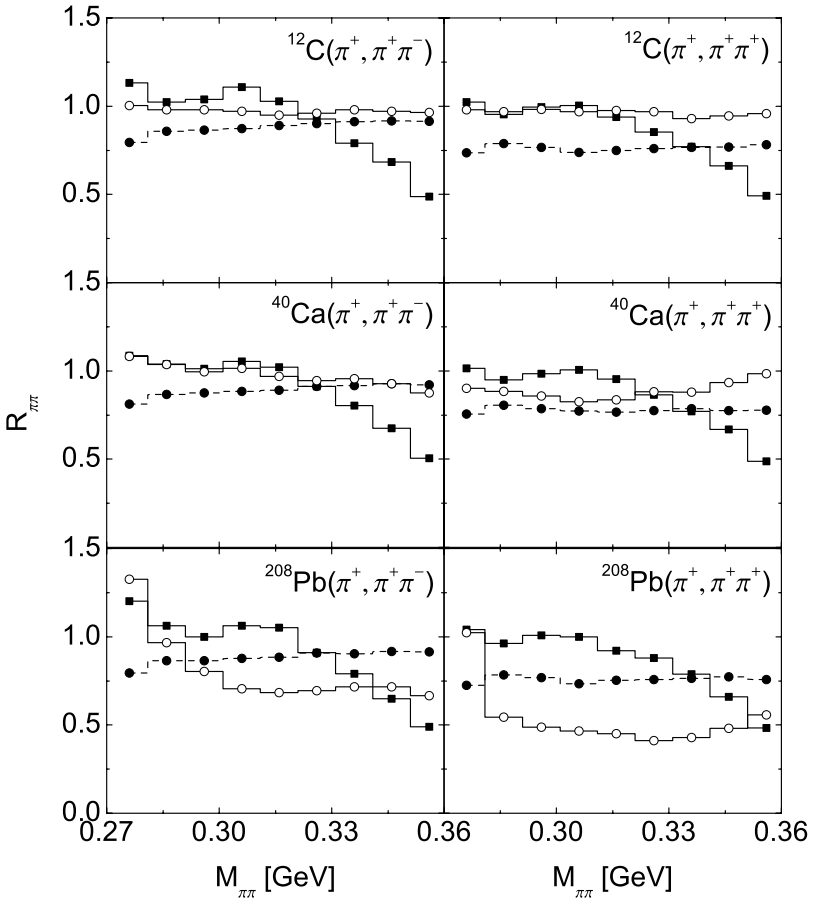

Figure 4.11: Ratio of mass differential cross sections including different nuclear effects. *Filled squares*: cross section with Fermi motion (FM) divided by cross section without FM, *filled circles – dashed lines*: with FM divided by FM and Pauli blocking (PB), *open circles*: FM and PB divided by FM, PB and EM potential.

exclusively responsible for the deviation of the dashed curve (solid circles) from unity, shows no pronounced invariant mass dependence. For the heavy targets it reduces the cross section over the entire invariant mass range. The EM potential, however, has little impact in the small target nuclei but produces a strong effect in the Lead target. It again tends to enhance the invariant mass region close to the two pion threshold and to decrease the cross section at higher masses. Overall the EM potential reduces the cross section due to the smaller total energy available because of the positively charged π^+ which is repelled from the nucleus. Due to the same reason the range of two pion masses which are populated is limited to smaller masses, thus producing a slight redshift of the spectrum. In addition, the momenta of the outgoing pions are modified by the spatial gradients of the potential such, that pion pairs with small invariant masses accumulate and higher mass components in the spectrum are depleted. The influence of the EM potential will again be reduced when also FSI are considered which change the effective nuclear densities probed. We will come back to the disucssion of Coulomb effects at the end of this Section.

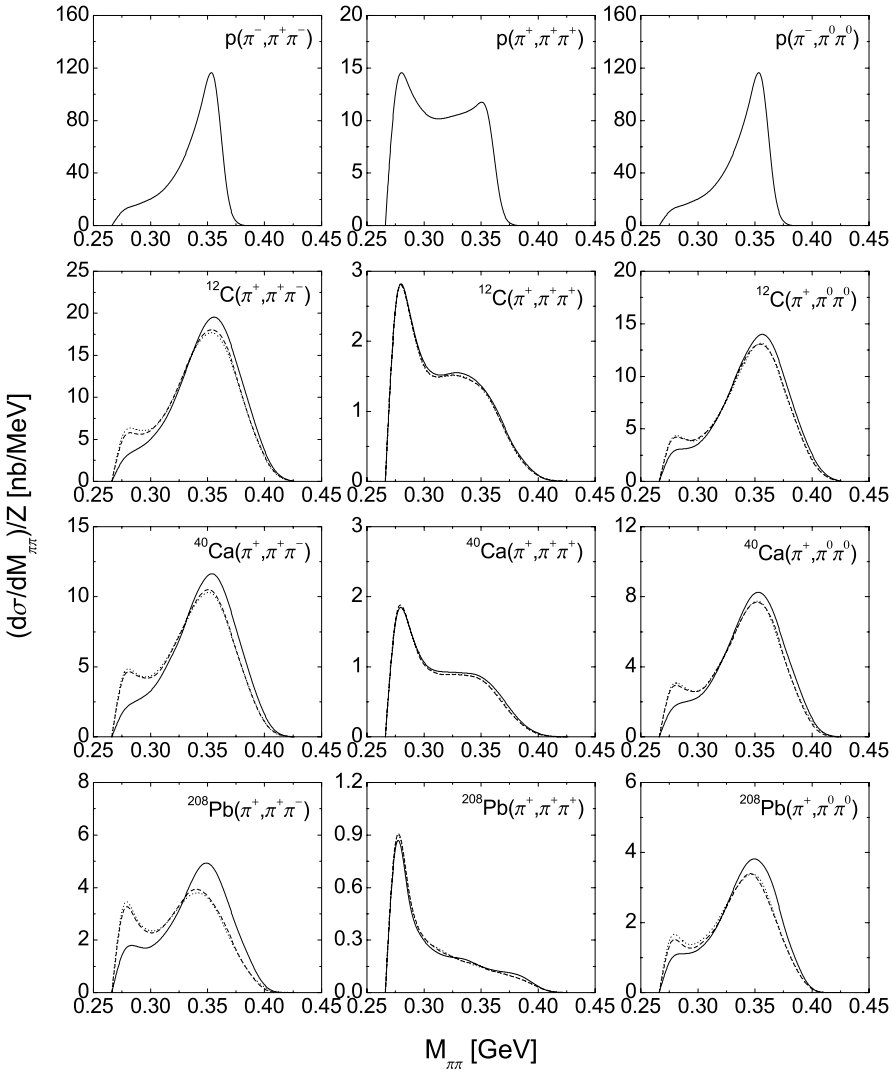

Figure 4.12: Two pion mass spectra for the $\pi^+ \to \pi^+\pi^-$ (left), $\pi^+ \to \pi^+\pi^+$ (center) and $\pi^+ \to \pi^0\pi^0$ (right) reactions off ^{2}H, ^{12}C, ^{40}Ca and ^{208}Pb at a pion kinetic energy of $T_\pi = 280$ MeV. *Solid line*: purely absorptive FSI, *dashed line*: absorption and elastic scattering with isotropic angular distributions, *dotted line*: as before but with realistic angular distributions.

Absorption. Fig. 4.12 shows the two pion invariant mass distributions in the $\pi^+\pi^-$, $\pi^+\pi^+$ and $\pi^0\pi^0$ channels. Here, the effects of absorption and elastic πN scattering are studied. The two peak structure in the central Figure of the upper row ($\pi^+ p \to \pi^+\pi^+ n$) is created by the CHAOS acceptance constraints which favors high and low two pion invariant masses. These acceptance cuts are applied to all spectra in both the $\pi^+ \to \pi^+\pi^-$ and $\pi^+ \to \pi^+\pi^+$ channels which later on will be compared to the CHAOS data. The effects of Fermi motion and Pauli blocking are included in all the following finite nuclear target calculations. Even if the pion nucleon interaction is rather weak at these low energies, pion absorption has the consequence to reduce the total cross section. This can be seen by comparing the curves in Figs. 4.10 and 4.12. This reduction amounts to

roughly 50% for the case of the Calcium target. On the other hand the shapes of the spectra are hardly affected. The softening of the spectra as compared to the Deuterium case is mainly generated by Fermi motion as discussed in the previous paragraph. This was also observed by the authors of Ref. [75]. Contrary to the authors of [148] we do not observe a substantially different pion absorption strength at high and low invariant masses due to the geometrical peculiarities of the pion pairs going together or in opposite directions, respectively.

Elastic collisions. Including elastic collisions more strength is moved down towards the 2π threshold. This effect again can be attributed to the energy loss of the pions in the elastic collisions. The very same effect was also observed and discussed in great detail in the $\gamma \rightarrow \pi\pi$ reaction in nuclei, see Chapter 3. Using realistic angular distributions for the $\pi N \rightarrow \pi N$ scattering events instead of the hitherto used isotropic description yields only a minor change of the mass distributions. The experimental angular distributions lead to a somewhat higher stopping power of the pions in the medium. Thus, the redshift of the spectrum becomes slightly more pronounced. However, this effect is not significant recalling the theoretical uncertainties due to our semiclassical treatment of the nuclear reaction. Very similar effects as in the $\pi^+\pi^-$ channel are also observed in the $\pi^0\pi^0$ channel shown in the right most column of Fig. 4.12 that already on the elementary level shows very similar features as the $\pi^+\pi^-$ one.

The second column of Fig. 4.12 shows the results in the $\pi^+\pi^+$ channel. The two peak structure of the vacuum cross section is generated by the geometrical constraints imposed by the CHAOS acceptance that favors the situation where the pions either go together or in opposite directions. Going to finite nuclear targets this structure is modified due to Fermi motion such, that the high mass peak becomes blurred whereas the low mass one increases its relative strength. This effect becomes more and more pronounced for large target nuclei and has nothing to do with pion rescattering. It is interesting to note that the impact of quasi elastic pion rescattering in the medium is extremely small here as compared to the $\pi^+\pi^-$ and $\pi^0\pi^0$ channels. This can be understood as follows: Neglecting the energy loss of the pions in the elastic collisions, pion elastic scattering in an infinite nuclear system would have the effect of distributing the pions randomly in phasespace since their correlation is lost in the collisions. This means that however the initial pion distribution looked like after some relaxation time the pions resemble approximately a phasespace distribution. In the case at hand the initial distributions in the $\pi^+\pi^-$ and $\pi^0\pi^0$ channels strongly deviate from phasespace whereas the $\pi^+\pi^+$ distribution does not. Ultimately this leads to the conjunction, that the $\pi^+\pi^-$ and $\pi^0\pi^0$ mass distributions will be modified by elastic pion rescattering whereas in the $\pi^+\pi^+$ channel the pions are just permuted in phasespace what does not generate substantial changes in the mass distribution. This explanation is corroborated by the observation of the Crystal Ball collaboration which found that the two pion distribution in the $\pi^- \rightarrow \pi^0\pi^0$ reaction becomes much closer to phasespace for large target masses as compared to small targets [54]. The pion energy loss, however, creates also in the $\pi^+\pi^+$ case a slight but negligible redshift of the two pion mass spectrum.

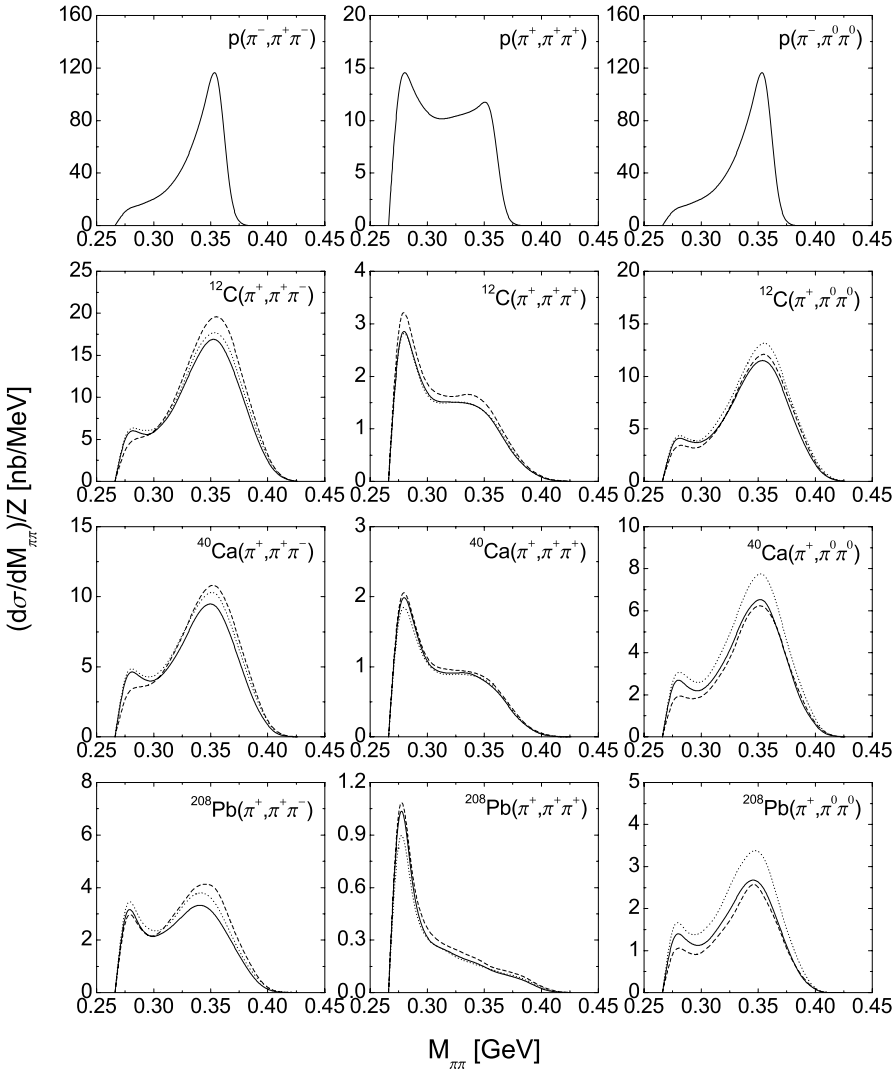

Figure 4.13: Two pion mass spectra for the $\pi^+ \to \pi^+\pi^-$ (left), $\pi^+ \to \pi^+\pi^+$ (center) and $\pi^+ \to \pi^0\pi^0$ (right) reactions off ^{2}H, ^{12}C, ^{40}Ca and ^{208}Pb at a pion kinetic energy of $T_\pi = 280$ MeV. *Solid line*: full FSI OM (pion optical potential), *dashed line*: full FSI CC (BUU resonance model), *dotted line*: absorption and elastic collisions only.

Charge exchange. In Fig. 4.13 the effects of additional charge exchange reactions is shown. In all isospin channels these collisions intensify the redshift of the spectrum. As typical for nuclear effects the changes in the spectra become more substantial for large target masses since then the probability of secondary scattering events is high. As in the elastic case this effect is more pronounced in the $\pi^+\pi^-$ and $\pi^0\pi^0$ channels as compared to the $\pi^+\pi^+$ channel due to the same arguments as given above. In addition, we also show a calculation using the coupled channel collision term of the BUU model including the explicit propagation of baryonic resonances. Whereas the spectral shape is very close to the calculations using the pion optical potential, the overall normalization in some cases deviates more obviously. This is due to the smaller absorptive self energy of the pion in the optical model approach. This issue has been discussed in the previous Chapter and

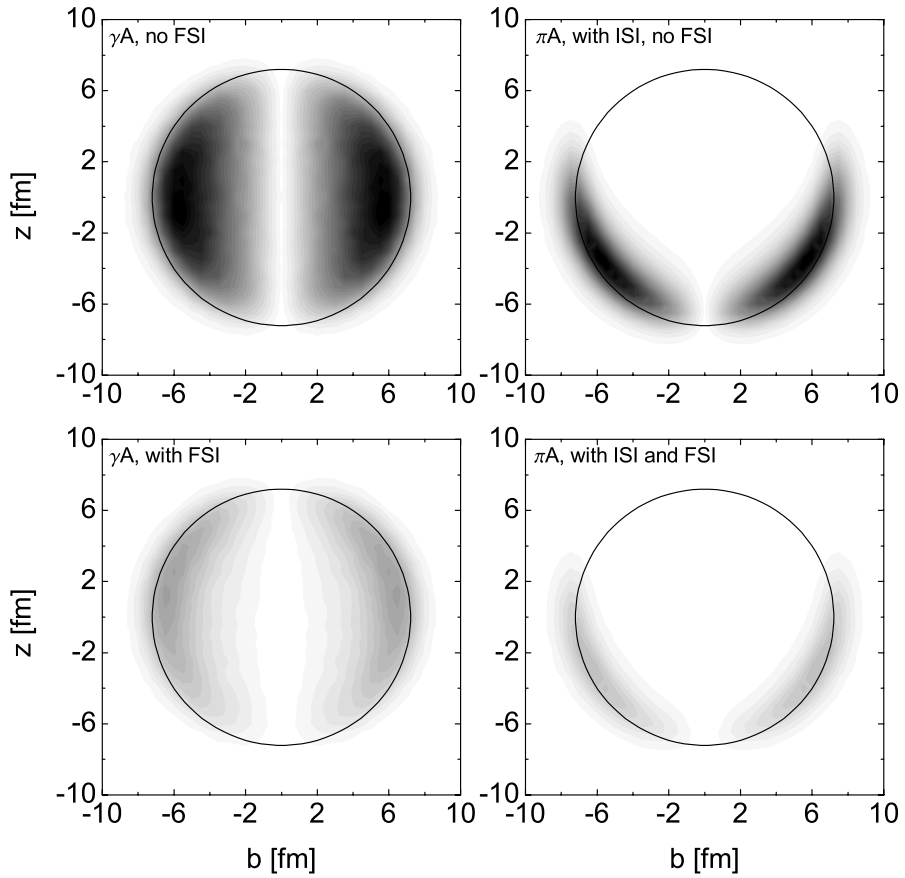

Figure 4.14: Spatial distributions of the elementary $\gamma/\pi \to \pi\pi$ transitions in the $\gamma \to \pi\pi$ (left) and $\pi \to \pi\pi$ (right) reactions in ^{208}Pb at $E_\gamma = 500$ MeV and $T_\pi = 280$ MeV, respectively. The upper panels are calculated without FSI whereas the lower calculations include also FSI. The projected vertical grey scale is a linear one and is in the upper and lower plots the same. The circle has a radius of 7.2 fm.

also similar results have been found for the case of photo-induced two pion production.

When comparing photon and pion-induced nuclear reactions it is also interesting to observe the spatial distribution of the creation points of the detected pion pairs. This distribution is shown in Fig. 4.14 in terms of the cross section $d\sigma/(dbdz)$ where b is the radial coordinate perpendicular to the photon beam direction which defines the $z-$axis. The radial coordinate is defined via $b = \sqrt{x^2 + y^2} \cdot \mathrm{sign}(x)$ owing to the cylindrical symmetry of the reaction. Even without FSI the pions come from positions deeper inside the nucleus in the photon-induced case because of the initial state pion absorption. Thus, pion-induced double pion production dominantly happens at the front side of the target nucleus. FSI in both cases reduce the number of pion pairs which reach the detector. In the pion-induced case a much smaller spatial area of the target also at lower densities is probed. Consequently, the likeliness that an observed target mass dependence is generated by density dependent modifications of the $\gamma/\pi \to \pi\pi$ transition

amplitude is much smaller for the case of pion-induced reactions. On the other hand, in many cases still one of the pions has to cross at least parts of the nuclear volume and, thus, undergoes FSI. Therefore, FSI are nonetheless very important and can account for features of the nuclear cross sections depending on the nuclear volume or, respectively, the target mass.

Comparison to data

Now we compare our results to the data obtained by the CHAOS [29] and Crystal Ball collaborations [54]. This comparison is shown in Fig. 4.15. The data have been obtained without overall normalization, hence we scale them arbitrarily and just compare the spectral shapes. In the $\pi^+\pi^-$ channel the data develop a pronounced peak close to the 2π threshold. This has been taken as an indication for a substantial redshift of the scalar spectral function in systems with non-vanishing baryon density. However, without touching the properties of the initial $\pi\pi$ distribution we also get a peak very similar as the one observed experimentally. Whereas the peak in the data is very pronounced already for rather moderate target masses the peak in our calculations only becomes substantial in large nuclei.

The $\pi^+ \to \pi^+\pi^+$ reaction has been used in order to obtain a reference measurement that does not exhibit the same in-medium changes as in the $\pi^+\pi^-$ channel since it cannot be influenced directly by the scalar spectral density. In the $\pi^+\pi^+$ channel also a substantial peak near the 2π threshold has been found. However, this peak was already present in the vacuum whereas in the $\pi^+\pi^-$ channel it was not. Our calculations somewhat overestimate this peak and, on the other hand, are to low at two pion masses around 350 MeV. This behavior, however, was already present on the elementary level and has to be attributed to shortcomings in the vacuum $\pi^+p \to \pi^+\pi^+n$ transition amplitude, see also Fig. 4.5. Overall, the evolution of the 2π mass spectra from elementary targets to heavy nuclei as observed experimentally in the $\pi^+\pi^-$ and $\pi^+\pi^+$ channels is qualitatively reproduced by our semiclassical calculation including Fermi motion, Pauli blocking and traditional final state interactions. These results point into the same direction as in the case of the $\gamma \to \pi\pi$ reaction in nuclei. The understanding of both reactions in terms of standard nuclear mechanisms anticipates the more tempting explanation related to the onset of chiral symmetry restoration.

Since our results also depend on the EM potential that, however, is included in our calculations only with certain approximations, we show in Fig. 4.16 the influence of the EM potential on the $\pi\pi$ spectra. In particular in the $\pi^+\pi^-$ channel we find a quite strong dependence of the overall normalization on the EM potential. This is due to the reduced invariant energy available when the EM potential is turned on since the positively charged π^+ is repelled from the nucleus. In the $\pi^+\pi^+$ channel this effect is less important owing to the fact that the elementary cross section in this channel rises less steeply in the relevant energy interval, see Fig. 4.4. The redshift of the two pion mass spectra becomes less substantial when the EM potential is omitted. Consequently, also the description of the data in the $\pi^+ \to \pi^+\pi^+$ channel is getting better without the potential. Albeit we believe that the EM potential is crucial in pion-nucleus reactions at such low energies, the approximate treatment within our semiclassical model asks for

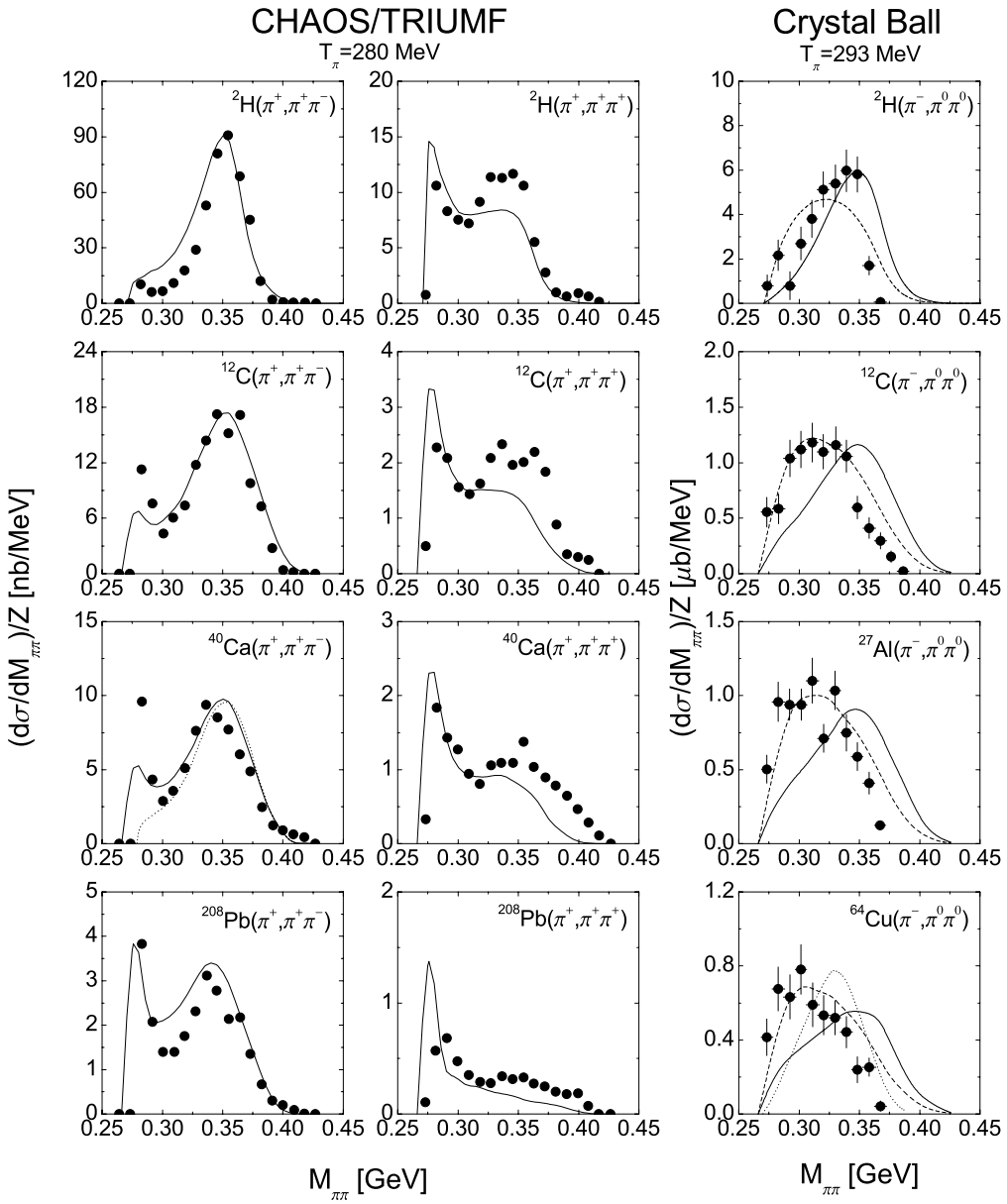

Figure 4.15: Two pion mass spectra for the $\pi^+ \rightarrow \pi^+\pi^-$ (left) and $\pi^+ \rightarrow \pi^+\pi^+$ (center) reactions off ^{2}H, ^{12}C, ^{40}Ca and ^{208}Pb at a pion kinetic energy of $T_\pi = 280$ MeV and mass spectra for the $\pi^+ \rightarrow \pi^0\pi^0$ reaction (right) off ^{2}H, ^{12}C, ^{27}Al, and ^{64}Cu at $T_\pi = 293$ MeV. The experimental data both from Refs. [29] (left and central column) and [54] (right column) are freely normalized. *Solid lines*: results of the present study using the microscopic $\pi \rightarrow \pi\pi$ amplitude, *dashed lines*: BUU results using just phasespace distributions as input, *dotted lines*: results from Refs. [54, 75].

a careful interpretation of the results. Even though the long wave length of the pions in principle requires a calculation regarding quantum effects one still can hope that the dominance of the "classical path" justifies a calculation following classical trajectories. This treatment, however, eventually breaks down if the classical path is forbidden by

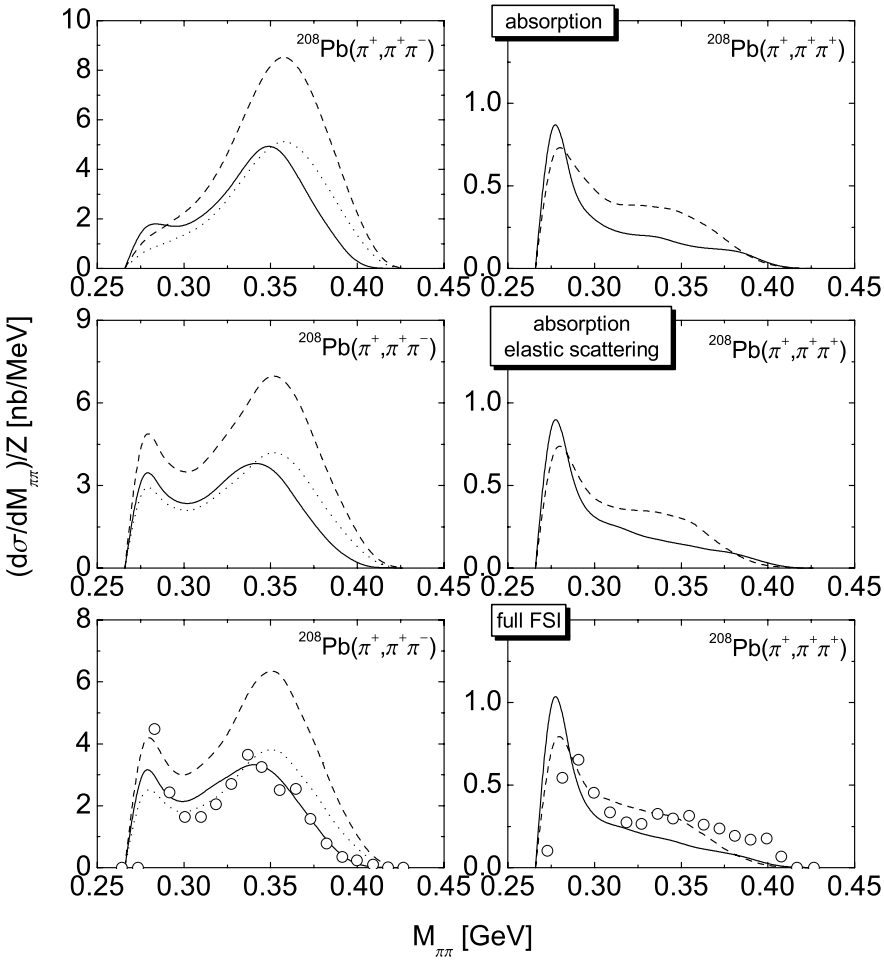

Figure 4.16: Two pion mass spectra for the $\pi^+ \to \pi^+\pi^-$ (left) and $\pi^+ \to \pi^+\pi^+$ (right) reactions off ^{208}Pb at a pion kinetic energy of $T_\pi = 280$ MeV including different assumptions on the pion final state interactions. *Solid lines*: With EM potential, *dashed lines*: without EM potential, *dotted lines (left column only)*: without EM potential, rescaled. The experimental data from Ref. [29] are freely normalized.

energy conservation and tunneling effects become important.

In the right column of Fig. 4.15 our results on the $\pi^- \to \pi^0\pi^0$ reaction are compared to the data obtained in the Crystal Ball experiment. The cross sections in this channel are about two orders of magnitude larger than in the $\pi^+\pi^-$ channel because of the much larger geometrical acceptance of the Crystal Ball spectrometer. Moreover, the Crystal Ball data have been corrected for the experimental acceptance limitations. Here the agreement of our full calculations (solid lines) and the data is rather poor. Whereas the data do not develop a peak close to the 2π threshold a shape change of the mass spectra with increasing target mass is anyhow observed. Indeed, the data become close to a pure phasespace distribution for complex nuclei whereas in vacuum the $\pi^0\pi^0$ mass distribution substantially deviates from phasespace, see also Fig. 4.5. Albeit weaker, also our calculations show such a behavior.

As compared to our model results the shape change in the data is much more substantial already for small target nuclei. In fact, our transport calculations are very well able to describe the data for complex nuclei when pure phasespace distributions are used as input for the inital $\pi N \to \pi\pi N$ production process, see the dashed lines. In contrast, for the Deuterium target phasespace fails to describe the differential distribution. From this we deduce that a substantial change in the $\pi^- p \to \pi^0\pi^0 n$ production amplitude occurs inside nuclei. Still, there is one caveat since already for the Deuterium target the data basically drop to zero at $M_{\pi\pi} = 370$ MeV whereas the region kinematically allowed extends to about $M_{\pi\pi} \simeq 445$ MeV, at least for larger nuclei. Also for heavy nuclear targets the experimental cross sections are limited to smaller two pion invariant masses than expected theoretically. Thus, more experimental and theoretical work is needed in order to extend our understanding of the $\pi \to \pi\pi$ reaction in nuclei. In particular multi-differential distributions from elementary targets are needed in order to allow to control the vacuum production amplitudes.

Comparison to other models

In the end we also want to comment briefly on the calculations done in [75] and [112]. The results of Ref. [75] are also shown in Fig. 4.15 for ^{40}Ca in the case of the $\pi^+ \to \pi^+\pi^-$ channel[1] and for ^{64}Cu in the case of the $\pi^- \to \pi^0\pi^0$ channel. In [75] the medium modification of the $\pi\pi$ interaction as discussed in some detail in the previous Chapters has been included. Despite the shift of the $\pi\pi$ interaction strength towards low values of the 2π invariant mass the data in both the $\pi^+\pi^-$ and $\pi^0\pi^0$ channels could not be reproduced by the calculations in [75]. This has been attributed to the rather moderate densities probed by the strongly interacting projectile and the absorptive final state interactions that further reduce the sensitivity of the observables to the high density regions. In contrast to these findings, in [112] a spectral enhancement very similar to the one observed experimentally could be reproduced using a rather simple model. These calculations, however, have been analyzed by the authors of [75] with the result that the good agreement found is entirely due to the crude approximations made. In particular the assumed average density at which the reaction takes place was estimated to be much too high in [112]. In summary, the outcome of these calculations yields the important result that the spectral enhancement in the $\pi \to \pi\pi$ reactions in nuclei can not be explained by a modification of the in-medium $\pi\pi$ interaction alone. Even more pronounced as in the $\gamma \to \pi\pi$ process the $\pi \to \pi\pi$ reaction is dominated by incoherent final state interactions that – at least in parts – account for the observed spectral enhancement close to the 2π threshold.

[1] For some reasons, however, in [75] results have been presented for the $\pi^- \to \pi^+\pi^-$ reaction, whereas the data to which they compare to has been taken for the $\pi^+ \to \pi^+\pi^-$ reaction. Albeit both processes in principle do not coincide (see for instance Table 4.1), at the rather low energies one is looking at here the differential distributions indeed are quite close to each other, see e. g. Fig. 4.5.

Chapter 5

The reaction $\gamma A \longrightarrow \eta X$

5.1 Introduction

Not only the spectral distributions of mesons but also the properties of the nucleon itself and its excited states can change inside a medium of strongly interacting matter. This is suggested experimentally by the disappearance of the second and third resonance region in the total photoabsorption cross section off nuclei, see Fig. 1.1 in the introduction to this work. Even in vacuum the excitation spectrum of the nucleon is far from being understood. In particular the total number of states as expected from quark model calculations is not found experimentally and also the position of the observed states in the excitation scheme is not predicted correctly. Nucleon resonances in free space and in nuclei are studied most effectively via their excitation with pions and, more recently, with photons. Many different hadronic final states have to be observed in order to arrive at a most complete understanding of the resonance masses and widths. The excitation function of η photoproduction throughout the second resonance region is completely dominated by the excitation of the $S_{11}(1535)$ resonance because of the particularly large $S_{11} \rightarrow \eta N$ branching ratio. Thus, η photoproduction from nucleons and nuclei provides a unique means to study the $S_{11}(1535)$ properties in free space as well as inside strongly interacting media.

The in-medium changes of nucleon resonance properties are created both from resonance nucleon collisions and medium modifications of the resonance decay products. Since the resonance properties in turn also affect the self energies of the particles they decay to, a coupled channel problem arises. In addition, the resonances feel the hadronic potential generated by the presence of the medium. Both effects are summarized in the resonance in-medium self energy. It generates a renormalization of the resonance mass and width inside nuclei which may in turn produce visible modifications of the resonance excitation function measured from nuclear targets. The sensitivity of the total cross section for the $\gamma A \rightarrow S_{11}(1535)(A-1) \rightarrow \eta X$ reaction to the $S_{11}(1535)$ self energy has been studied theoretically in Ref. [149]. From a microscopic calculation, using the resonance parameters from [150], a net broadening of 35 MeV at normal nuclear matter density was found for an on-shell $S_{11}(1535)$ resonance. However, the use of this broadening in a BUU simulation of η photoproduction in nuclei provided the result, that the observables are not sensitive to changes of the S_{11} in-medium width. On the other hand, more pronounced effects were found due to the nuclear binding energy. The

experimental data available at the time favored a medium momentum dependent nuclear equation of state over a hard momentum independent one.

Another interesting aspect connected to η production in nuclei is the η nucleus final state interaction. The production of η mesons in nuclei is the only source of information on the ηN interaction since no η beam can be produced due to the unstable nature of the η meson. Even in vacuum the knowledge on the ηN interaction is restricted to the analysis of the inverse $\pi N \rightarrow \eta N$ reaction. In [151] the attempt has been made to extract the energy dependence of the elastic and absorptive ηN cross sections via a confrontation of experimental results with BUU calculations. Data, however, were only available in a rather narrow energy interval below the $S_{11}(1535)$ pole. For η kinetic energies from threshold up to 200 MeV the ηN cross section was found to be independent of the η energy. In addition, also the isospin dependence of the η photoproduction cross section is presently a heavily debated issue. This is driven by recent measurements of η photoproduction off Deuterium [152] which suggest a rather large resonance contribution in the neutron channel that is not seen in the proton channel.

The following Chapter is structured in the following way: first we will briefly summarize the experimental results on η photoproduction from nuclear targets. Then we introduce the physical quantities which are used as input to our BUU transport calculations. In Section 5.4 the η photoproduction cross section from neutrons is discussed. In Section 5.5 we study the η nucleus final state interactions using both the Glauber model and the transport approach. Finally, we discuss medium modifications both of the η and the $S_{11}(1535)$ resonance.

5.2 Experimental status

In the past, experiments of η photoproduction from nuclei were performed at rather moderate beam energies. The TAPS group covered the energy range from threshold up to photon energies of 800 MeV [153]. As target materials they considered C, Ca, Nb and Pb. Measurements at KEK, using C, Al and Cu as target nuclei, produced data at photon energies up to 1 GeV [154, 155]. Thus, both experiments covered only the low energy half of the $S_{11}(1535)$ line shape. More recently, η photoproduction off nuclei has been measured at ELSA using the combined Crystal Barrel and TAPS detectors [152, 156, 157]. This setup provides an almost 4π coverage and, thus, acceptance corrections are only of minor importance. Energies from threshold up to 2.2 GeV were covered. This energy range clearly exceeds the region of the $S_{11}(1535)$ resonance and also the inclusive production threshold. Here, the nuclear materials D, C, Ca, Nb and Pb were measured. Besides the inclusive data, also exclusive ones, applying an appropriate missing mass cut, were analyzed. In addition to the total cross sections also missing mass, kinetic energy, and angular differential distributions including overall normalization were produced. These results are still preliminary but a final version will be available soon [37]. In the later Sections we will compare our calculations to these observables.

5.3 Parametrization of physical quantities

This Section serves to introduce details of the η and $S_{11}(1535)$ dynamics implemented into our transport simulations. The main source of η mesons is the elementary γN interaction. Besides these processes, η mesons can also be produced via secondary interactions as for instance in the reaction chain $\gamma N \to \pi N, \pi N \to S_{11} \to \eta N$. We start with a discussion of the photon nucleon interaction.

5.3.1 Photon nucleon cross section

Total cross section

It is well known that in the second resonance region the reaction $\gamma p \to \eta p$ is entirely saturated by the excitation and subsequent decay of the $S_{11}(1535)$ resonance, see e. g. [158]. In our transport model we use the resonance parameter set as obtained in the coupled channel analysis of [150]. Within these parameters the η couples to three resonances only, namely the $S_{11}(1535), S_{11}(1650)$ and $F_{17}(1990)$ with pole mass branching ratios to ηN of 0.43, 0.03 and 0.94, respectively. In the photoproduction process we neglect the two higher lying resonances since the $S_{11}(1650)$ contribution is extremely small and the parameters of the $F_{17}(1990)$, including its coupling to the ηN and γN channels, are known only poorly.

For the total $S_{11}(1535)$ photoproduction cross section we use the following Breit-Wigner parametrization [100]:

$$\sigma_{\gamma p \to R} = \left(\frac{k_0}{k}\right)^2 \frac{s\Gamma_\gamma(s)\Gamma_R(s)}{(s-m_R^2)^2 + s\Gamma_R^2(s)} \frac{2m_N}{m_R\Gamma_0} |A_{1/2}^p|^2 \tag{5.1}$$

with $\Gamma_\gamma = \Gamma_0(k/k_0)$ and the pole mass decay width $\Gamma_0 = 151$ MeV. The momenta k and k_0 are the photon nucleon CM momenta at the total energy $\sqrt{s}$ and m_R, respectively. The total resonance width Γ_R is the sum of the individual decay widths to the πN, ηN and $2\pi N$ channels which are parametrized as in Refs. [100, 159]. The ηN partial width is given by

$$\Gamma_{S_{11}\to\eta N}(s) = \Gamma_0 \frac{m_R}{\sqrt{s}} \frac{q(\sqrt{s})}{q(m_R)} \tag{5.2}$$

where $\Gamma_0 = 65$ MeV is the $S_{11} \to \eta N$ on-shell width and $q(\sqrt{s})$ is the ηN CM momentum. In addition to [159] we multiply the $S_{11} \to \eta N$ decay width with an additional form factor

$$F(s) = \frac{\lambda^4}{\lambda^4 + (s-m_R^2)^2} \tag{5.3}$$

with $\lambda = 0.9$ GeV. This is necessary in order to be able to describe the recent data for η photoproduction on the proton at energies above the resonance pole [160]. This is illustrated in the insert of Fig. 5.1. We speculate that this correction is needed because of

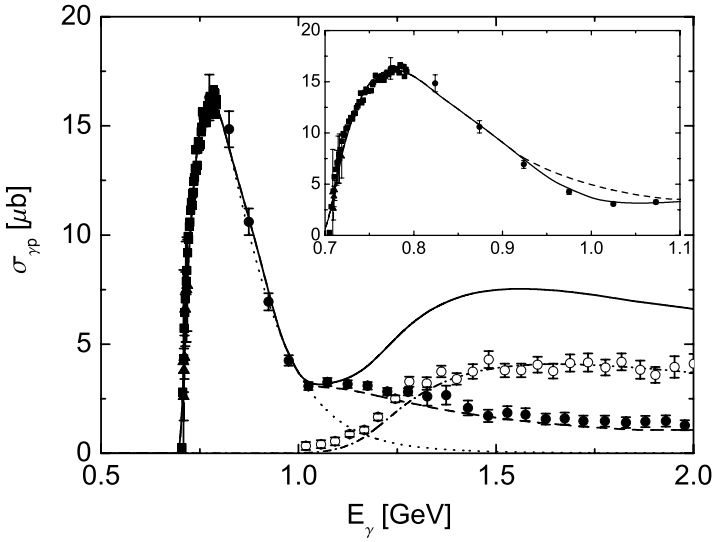

Figure 5.1: Total cross section $\gamma p \to \eta X$. *Dotted line*: Contribution from $S_{11}(1535)$, *dashed line*: exclusive cross section $\gamma p \to \eta p$, *dash-dotted line*: $\gamma p \to \eta \pi^0 p$, *solid line*: sum of all contributions. Data for the $\gamma p \to \eta p$ process from [160] (filled circles), [161] (filled squares), [162] (filled triangles) and for the $\gamma p \to \eta \pi^0 p$ process from [163, 164] (open circles). The insert shows a magnification of the resonance region. Here, the dashed line is calculated without the form factor (5.3).

the interference of the $S_{11}(1535)$ and $S_{11}(1650)$ resonance contributions which is known to be responsible for the steep drop of the cross section above the $S_{11}(1535)$ pole. This interference is not accounted for in our incoherent model and, thus, has to be mimiced by a reduction of the individual contributions. Consequently, we use the form factor (5.3) only in the calculation of the $\gamma N \to S_{11}(1535)$ photoproduction cross section. For the photocoupling helicity amplitude we have

$$A^p_{1/2} = 0.109 \text{ GeV}^{-1/2} \tag{5.4}$$

from Ref. [161].

The cross section for η photoproduction off the proton via the excitation of the $S_{11}(1535)$ resonance is given by

$$\sigma_{\gamma p \to S_{11} \to \eta p} = \sigma_{\gamma p \to S_{11}} \frac{\Gamma_{S_{11} \to \eta p}}{\Gamma_{S_{11}}} \tag{5.5}$$

with the total resonance photoproduction cross section from (5.1). This cross section is shown in Fig. 5.1 as dotted line in comparison to the experimental data. Up to photon energies of roughly 1 GeV the data is described entirely by the resonance contribution. For higher beam energies, however, additional contributions to the photoproduction process have to be considered. In [160] the exclusive cross section above 1 GeV has been ascribed to a sum of various higher lying resonance contributions. This is corroborated by the $\eta-$MAID analysis [165] that provides an excellent description of the elementary

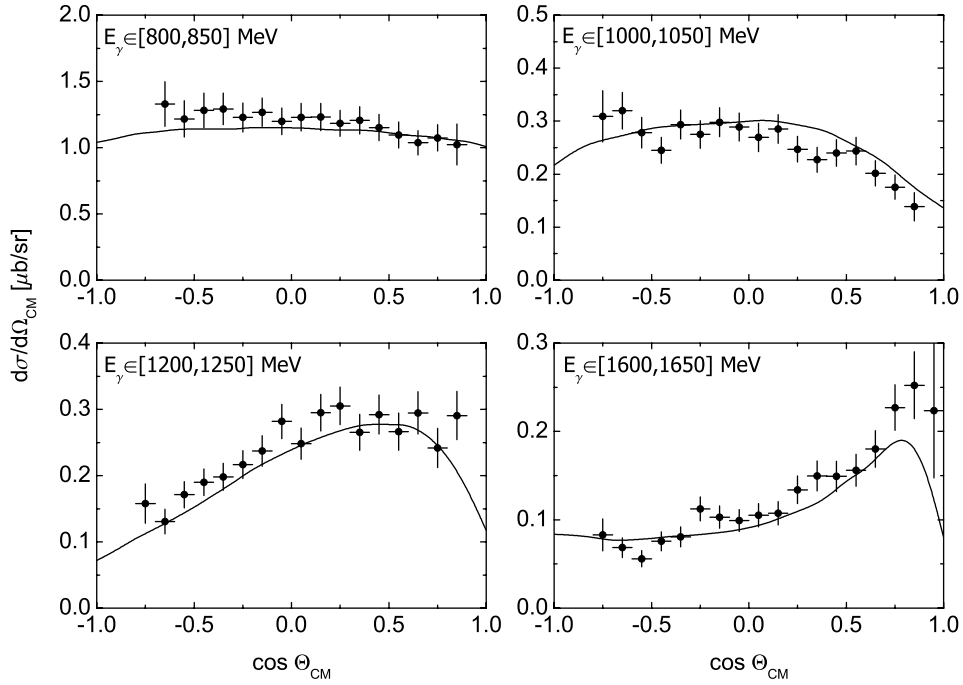

Figure 5.2: Angular differential cross section for the exclusive process $\gamma p \rightarrow \eta p$. Data from [160]. The lines show the cross sections from the $\eta-$MAID analysis [165].

η photoproduction cross section. Thus, we consider the difference of the MAID cross section [165] and the $S_{11}(1535)$ contribution as a background to the η photoproduction process

$$\sigma^{\mathrm{bg}}_{\gamma p \rightarrow \eta p} = \sigma^{\mathrm{MAID}}_{\gamma p \rightarrow \eta p} - \sigma_{\gamma p \rightarrow S_{11} \rightarrow \eta p}. \tag{5.6}$$

The total cross section for the $\gamma p \rightarrow \eta p$ reaction, given by the sum of the resonance contribution and the background, is also shown in Fig. 5.1. It agrees well with the experimental data over the complete photon energy range.

Differential cross section

In the photon energy range where the cross section is saturated by the $S_{11}(1535)$ contribution the CM angular distribution is basically flat. For higher energies where other resonances start to play a role and also interferences between the various contributions can occur, the angular differential cross section starts to show anisotropies. This is shown in Fig. 5.2. Since the angular distribution of the elementary production process influences, via Pauli blocking and final state interactions, the total and differential nuclear photoproduction cross sections we include realistic CM angular distributions into our simulations. This is done again by means of the cross sections provided by the $\eta-$MAID analysis [165] also shown in Fig. 5.2. Since we explicitly propagate the $S_{11}(1535)$ resonance we include an anisotropic differential decay width of the S_{11} to the ηN channel

whenever the resonance has been produced via photoexcitation. The CM angular distribution is measured with respect to the initial CM photon direction which, thus, also depends on the initial nucleon momentum. In the transport simulation these additional informations, namely the components of the CM nucleon three momentum, have to be remembered by the S_{11} testparticles. In this way the correct angular distributions for the $\gamma p \to \eta p$ process extended in a systematic way to nuclear reactions can be obtained. However, if the S_{11} interacts with the nuclear medium before it decays to an ηN final state, the correlation with the initial photon is lost. In this case the CM decay distribution is again taken to be isotropic.

Inclusive channels

At a threshold energy of $E_\gamma = 935$ MeV the inclusive η photoproduction channels open. This photon energy corresponds to the opening of the phasespace for the lightest inclusive channel, namely $\gamma N \to \eta\pi N$. In [164] the total cross section of the $\gamma p \to \eta\pi^0 p$ reaction has been determined experimentally. It becomes sizable only at energies of about $E_\gamma = 1.2$ GeV, see Fig. 5.1. This suggests a dominance of the reaction chain $\gamma p \to \eta\Delta^+$ and subsequent decay of the Δ to $N\pi$. We parametrize the total cross section for the photoproduction of the $\eta\Delta$ final state as

$$\sigma_{\gamma p\to\eta\Delta^+} = \frac{1}{16\pi s|\mathbf{k}_{\rm cm}|}\int\limits_{(m_N+m_\pi)^2}^{(\sqrt{s}-m_\eta)^2} dW_\Delta^2 \mathcal{A}_\Delta(W_\Delta)|\mathbf{p}_{\rm cm}(W_\Delta)||\mathcal{M}_{\eta\Delta}|^2, \tag{5.7}$$

with $\mathbf{k}_{\rm cm}$ and $\mathbf{p}_{\rm cm}$ the initial and final CM momenta, respectively, and $\mathcal{M}_{\eta\Delta}$ the invariant matrix element which we fit to the total cross section data from [164]. We find

$$|\mathcal{M}_{\eta\Delta}|^2 = \frac{4.52\ \text{GeV}^4\text{mb}}{(\sqrt{s}-0.9\ \text{GeV})^2 + (0.9\ \text{GeV})^2/4}. \tag{5.8}$$

Furthermore, $\mathcal{A}_\Delta$ is the (vacuum) spectral function of the Δ resonance. We parametrize it in form of a relativistic Breit-Wigner distribution, see Appendix A, with the energy dependent decay width $\Delta \to N\pi$ from Refs. [100, 159] which is similar to Eq. (D.29) multiplied with an appropriate from factor. The cross section for the $\gamma p \to \eta\pi^0 p$ process is then given by

$$\sigma_{\gamma p\to\eta\pi^0 p} = \sigma_{\gamma p\to\eta\Delta^+} \cdot \frac{\Gamma_{\Delta^+\to\pi^0 p}}{\Gamma_\Delta} \tag{5.9}$$

with Γ_Δ the total Δ decay width. Since we assume the total Δ width to be saturated by the decay into the $N\pi$ channel, the branching ratio to the $\pi^0 p$ final state is given by the isospin matrix element

$$\frac{\Gamma_{\Delta^+\to\pi^0 p}}{\Gamma_\Delta} = |\langle p\pi^0|\mathbf{T}\cdot\boldsymbol{\phi}|\Delta^+\rangle|^2 \tag{5.10}$$

$$= |\langle p|\mathrm{T}_0|\Delta^+\rangle\langle\pi^0|\phi_0|0\rangle|^2 = (\tfrac{1}{2}\,\tfrac{1}{2}\,1\,0\,|\,\tfrac{3}{2}\,\tfrac{1}{2})^2 = \frac{2}{3} \tag{5.11}$$

where $\mathbf{T}$ is the isospin $1/2 \to 3/2$ transition operator and $\boldsymbol{\phi}$ is the pion field operator, see Appendix D. Correspondingly, also the reaction $\gamma p \to \eta\Delta^+ \to \eta\pi^+ n$ occurs. It has not been measured experimentally, but isospin symmetry dictates

$$\sigma_{\gamma p\to\eta\Delta^+\to\eta\pi^0 p} : \sigma_{\gamma p\to\eta\Delta^+\to\eta\pi^+ n} = \left|\langle p\pi^0|\mathbf{T}\cdot\boldsymbol{\phi}|\Delta^+\rangle\right|^2 : \left|\langle n\pi^+|\mathbf{T}\cdot\boldsymbol{\phi}|\Delta^+\rangle\right|^2 \quad (5.12)$$

$$= 2:1. \quad (5.13)$$

Both the total cross section for the $\gamma p \to \eta\pi^0 p$ reaction and the total inclusive η photoproduction cross section, that is given by the sum of the exclusive and inclusive channels, are shown in Fig. 5.1. The data is reproduced very well. Note, that also the reaction $\gamma p \to \eta\pi^+ n$ – not measured experimentally and, thus, not included in the data points shown in Fig. 5.1 – contributes to the total inclusive cross section shown as solid line in Fig. 5.1.

5.3.2 Secondary interactions

In addition to the direct photoproduction reaction, in nuclei η mesons can also be produced from secondary interactions. Most important are the reaction chains $\gamma N \to \eta N$ followed by $\eta N \to \eta N$ and $\gamma N \to \pi N$ followed by $\pi N \to \eta N$. The first one does not enhance the η multiplicity in the outgoing channel since it corresponds to a quasifree η production process with subsequent elastic rescattering. The latter one, however, feeds additional flux from the π into the η channel. Besides the $\gamma N \to \eta N$ channel our model includes a variety of other hadronic final states that can be produced in the elementary γN interaction, namely $\gamma N \to \pi N$, $\pi\pi N$, $P_{33}(1232)$, $D_{13}(1520)$, $F_{15}(1680)$, VN, $VP_{33}(1232)$, $V\pi N$. In the low energy sector, the cross sections for these processes are obtained in terms of resonance fits to the data similar to Eq. (5.1) and are given explicitly in [100]. The cross sections for vector meson production have also been adjusted to experimental vector meson photoproduction data and are given in [166] and, in parts, will be discussed in the later Chapters. In the present context they are, however, of minor importance. In addition, also strange meson baryon final states can be produced. Due to strangeness conservation in strong interaction processes, they do not contribute to the η photoproduction reaction.

In the case at hand the only important secondary η production channel is $\pi N \to \eta N$. The corresponding cross section will be discussed in the following. More interesting, however, are the elastic and inelastic ηN scattering processes which give rise to final state interactions. These will also be discussed in this Section.

Pion induced η production

The three resonances $S_{11}(1535)$, $S_{11}(1650)$ and $F17(1990)$ which couple to the ηN channel also couple to the πN channel. Thus, their excitation via pion nucleon collisions gives rise to the reaction $\pi N \to R \to \eta N$. The total cross section for this process takes the form [100]

$$\sigma_{\pi^- p\to R\to\eta n} = \frac{4\pi}{|\mathbf{k}_{\rm cm}|^2}\frac{2J_R+1}{2}\frac{s\Gamma_{R\to\pi^- p}(s)\Gamma_{R\to\eta n}(s)}{(s-m_R^2)^2+s\Gamma_R^2(s)} \quad (5.14)$$

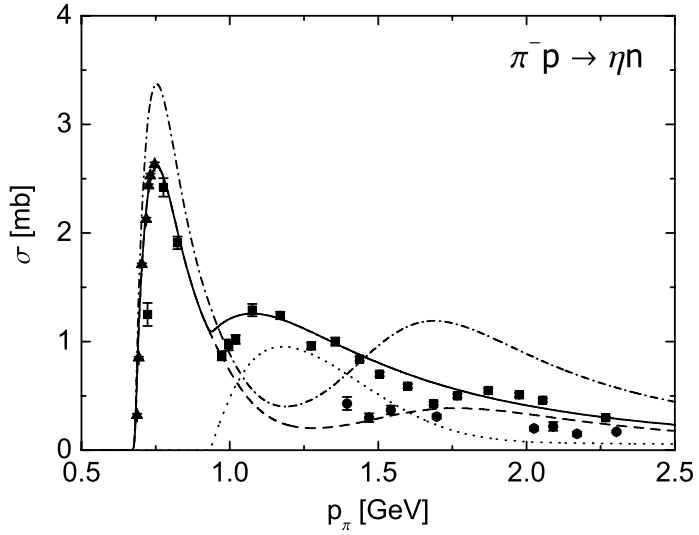

Figure 5.3: Total cross section for the $\pi^- p \to \eta n$ reaction. *Dash-dotted line*: resonance contributions with old parameter set, *dashed line*: resonance contributions with new parameters, *solid line*: total cross section, *dotted line*: background. Data from [167] (squares), [168] (circles) and [169] (triangles).

where J_R is the total spin of the resonance. The partial decay widths of the resonances are given by the parametrization from [100, 159]. Note, however, that the resonance widths are not multiplied with the form factor (5.3) since it was introduced only in order to account for a peculiarity of the photoproduction cross section. Using the Manley parameter set [150] we obtain the cross section shown in Fig. 5.3 by the dash-dotted line. For pion momenta above 1.5 GeV this cross section is obviously much larger than the data. Also on the $S_{11}(1535)$ resonance peak we obtain a too large cross section. In contrast, for pion momenta between 1 GeV and 1.5 GeV the cross section is too small. The excess at high energies is due to the extremely large coupling of the $F_{17}(1990)$ resonance to the ηN channel in the Manley analysis [150]. This large coupling was not directly constrained by data but was rather invented to absorb the inelastic flux in the F_{17} channel. Thus, we reduce the $F_{17}(1990) \to \eta N$ branching ratio such that the resonance contribution stays just below the data. We use $\Gamma_{F_{17}\to\eta N}/\Gamma_{F_{17}} = 0.32$ instead of $\Gamma_{F_{17}\to\eta N}/\Gamma_{F_{17}} = 0.94$ and put the remaining flux into the $F_{17} \to 2\pi N$ channel. In addition, we reduce the $S_{11}(1535)$ contribution by 23% which results in a good description of the cross section at the resonance pole.

In order to compensate for the missing strength at intermediate energies, we introduce an additional background to the $\pi N \to \eta N$ reaction. For energies above the $S_{11}(1535)$ resonance we parametrize the total $\pi N \to \eta N$ cross section as

$$\sigma^{\text{fit}} = \Omega \frac{1}{s} \frac{|\mathbf{q}_{\text{cm}}|}{|\mathbf{k}_{\text{cm}}|} \frac{30\ \text{GeV}^2\text{mb}|\mathbf{q}_{\text{cm}}|^2}{s(\sqrt{s} - 1.75\ \text{GeV})^2 + |\mathbf{q}_{\text{cm}}|^2} \exp\left(-1.5 \frac{\sqrt{s}}{m_N + m_\eta}\right) \tag{5.15}$$

where $s = (k_\pi + k_N)^2$ is the total CM energy squared, $\mathbf{k}_{\text{cm}}$ is the initial and $\mathbf{q}_{\text{cm}}$ is the final CM three-momentum. Moreover, Ω is an isospin factor that is $\Omega = 2/3$ for the

reactions $\pi^- p \to \eta n$ and $\pi^+ n \to \eta p$, and $\Omega = 1/3$ for the reactions $\pi^0 p \to \eta p$ and $\pi^0 n \to \eta n$. In order to obtain the background cross section we have to subtract the resonance contributions:

$$\sigma^{\rm bg} \;=\; \max\left[0, \max\left(\sigma^{\rm fit}, \sigma^{\rm res}\right) - \sigma^{\rm res}\right] \tag{5.16}$$

where $\sigma^{\rm res}$ is the sum of all resonance cross sections according to Eq. (5.14) obtained with the modified Manley parameter set as explained above. This cross section is shown as dashed line in Fig. 5.3. Via a comparison to the more recent coupled channel analysis [170] the background cross section $\sigma^{\rm bg}$ can be ascribed to a sum of various higher-lying resonance contributions which have not been resolved by the Manley analysis [150]. The cross section for the $\pi^- p \to \eta n$ reaction decomposed into the resonance and background contributions is shown also in Fig. 5.3.

The ηN cross section

An important ingredient to the η dynamics in nuclear matter are the ηN vacuum and in-medium cross sections. They are, however, not accessible for experimental study. Only one particular channel, namely the $\eta N \to \pi N$ one, is constrained experimentally by its inverse. Within a coupled channel analysis of elementary scattering processes including as many observables as possible in all hadronic final states, additional information on such scattering processes can be obtained. A particular example would be the previously discussed $\pi N \to \eta N$ reaction. If this interaction turns out to be mediated by some resonance R which is also known to also couple to the $2\pi N$ channel, a certain contribution to the $\eta N \to 2\pi N$ cross section can be fixed from the partial decay widths obtained from the $\pi N \to R \to 2\pi N$ and $\pi N \to R \to \eta N$ reactions. Such coupled channel analyses have been performed for a long time by various authors and on quite different levels of sophistication. Particular examples are the Manley analysis [150] which is used within the BUU model to account for low energy meson nucleon collisions, the one from Vrana et al. [171], or the more recent and rather sophisticated $K-$matrix analysis from [158, 172, 173, 174] that has been applied lately to η photoproduction on the nucleon [170].

Since the η photoproduction cross section from nuclei is also sensitive to the ηN interaction, one can further constrain the knowledge on the ηN cross sections by a careful analysis of the nuclear data. To this end we consider three different models for the η nucleus final state interactions. First, we assume the η FSI to be mediated by the reexcitation of resonances with the resonance parameters from the Manley analysis. This is identical to the FSI included in the earlier BUU calculations in Refs. [149, 151]. Second, we use the (non-resonant) cross section parameterizations also used in [151] with

$$\sigma_{\eta N \to \eta N} \;=\; \frac{45}{s}\ {\rm GeV}^2{\rm mb} \tag{5.17}$$

$$\sigma_{\eta N \to X \neq \eta N, \pi N} \;=\; 10\ {\rm mb}. \tag{5.18}$$

For the reaction $\eta N \to \pi N$, however, we keep the cross section as obtained via detailed balance from the inverse process. The inelastic cross section (5.18) is lower than the one in [151] since a larger cross section has proven to be incompatible with the data.

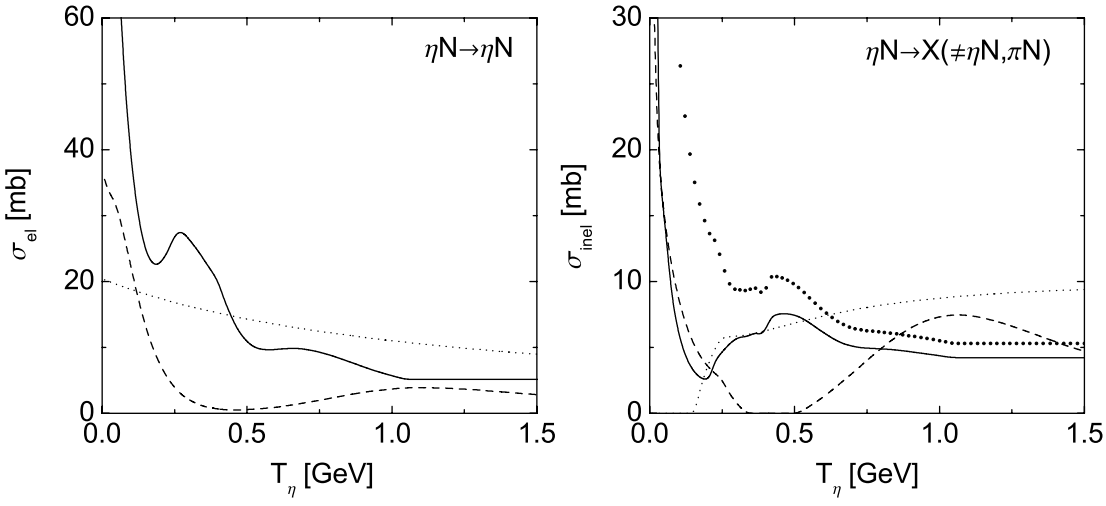

Figure 5.4: Total elastic and inelastic ηN cross sections. *Dashed line*: BUU resonance model (modified Manley parameters), *dotted line*: parameterizations (5.17) and (5.18), *solid line*: $K-$matrix cross sections, *dots*: total inelastic $K-$matrix cross section including the πN final state.

As a third recipe we use the ηN cross sections as obtained from the coupled channel $K-$matrix analysis in Ref. [170].

All these cross sections are shown in Fig. 5.4. The cross sections obtained from the Manley parameter set have very little strength at η kinetic energies around 400 MeV. This is due to the fact that there is no intermediate mass nucleon resonance with a sizable coupling to the ηN channel. This is in contrast to the $K-$matrix analysis that shows rather prominent resonance structures at these energies. In a certain energy interval the non-resonant cross sections from [151] are comparable in size to the $K-$matrix ones. However, they represent energy averages as they do not exhibit the strong energy variation due to the resonance excitation mechanism.

5.4 The $\mathrm{n}(\gamma, \eta)$ cross section

Due to the non-availability of free neutron targets, photoproduction off light nuclei must be explored in order to investigate η photoproduction off neutrons. Of particular interest is Deuterium, since nuclear effects as Fermi motion, Pauli blocking, final state interactions and binding effects are minimal. We calculate quasifree η photoproduction off Deuterium in the simple spectator approximation. That is, we neglect any final state interactions and assign an initial momentum to the nucleons obtained in a probabilistic way in a Monte Carlo simulation from the $s-$wave part of the Deuteron wave function. This is done on the very same lines as in Section 4.4 for the case of double pion production. For the proton we take the cross sections as introduced in the previous Section. The neutron cross sections will be discussed in some detail in the following.

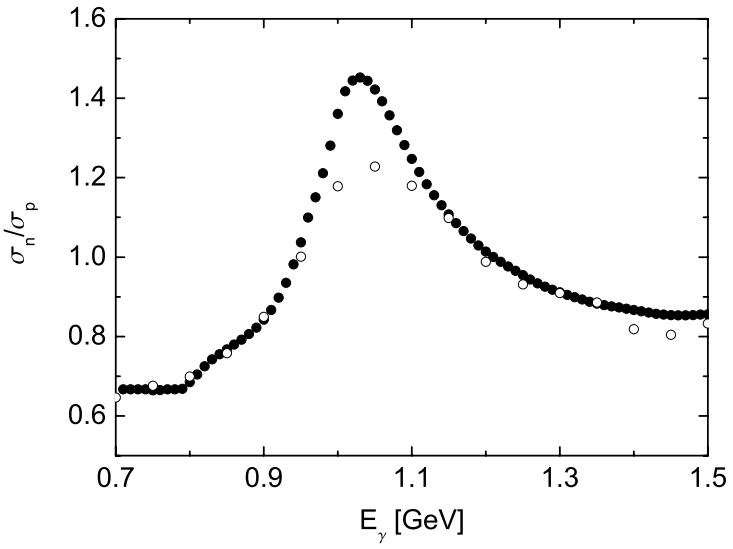

Figure 5.5: Ratio of exclusive photoproduction cross sections from protons and neutrons. *Full symbols*: cross section ratio as predicted from the $\eta-$MAID [165] model, *open symbols*: ratio obtained from the Deuterium calculation.

In the energy region of the $S_{11}(1535)$ resonance the ratio of the neutron to the proton cross section is almost constant around a value of roughly 2/3. This value has been obtained from a resonance fit to η photoproduction data on Deuterium [175, 176] and ^{4}He [177] targets. It corresponds to the photocoupling helicity amplitude of

$$A^n_{1/2} = 0.089 \text{ GeV}^{-1/2} \tag{5.19}$$

to be used with Eq. (5.1). Adopting this value for the $\gamma n \to S_{11}(1535)$ cross section we find reasonable agreement to the most recent η photoproduction data from Deuterium [152]. Consequently, we keep this contribution to the η photoproduction cross section off neutrons fixed.

Similar as in the proton case, at energies above the $S_{11}(1535)$ higher lying resonances start to play a role. These processes have been investigated by means of the $\eta-$MAID model [165]. The MAID analysis predicts a significant rise in the ratio of the neutron to the proton cross section above the $S_{11}(1535)$ resonance due to a significant ηN coupling of the $D_{15}(1675)$ resonance which is known to have a much stronger electromagnetic coupling to the neutron than to the proton. This is shown in Fig. 5.5. Also other models as the chiral soliton model [178] or the coupled channel $K-$matrix analysis [170] find such a resonance, albeit with different quantum numbers, in the ηN channel.

At energies around ~ 1 GeV the inclusive η production channels open. Experimentally, this background can be suppressed successfully by imposing the condition that not more than six photons from the η decay are found in the detector combined with an appropriate missing mass cut. This method has been tested by a measurement of the exclusive channels $\gamma d \to \eta pn$ with the coincident detection of the participant proton or neutron

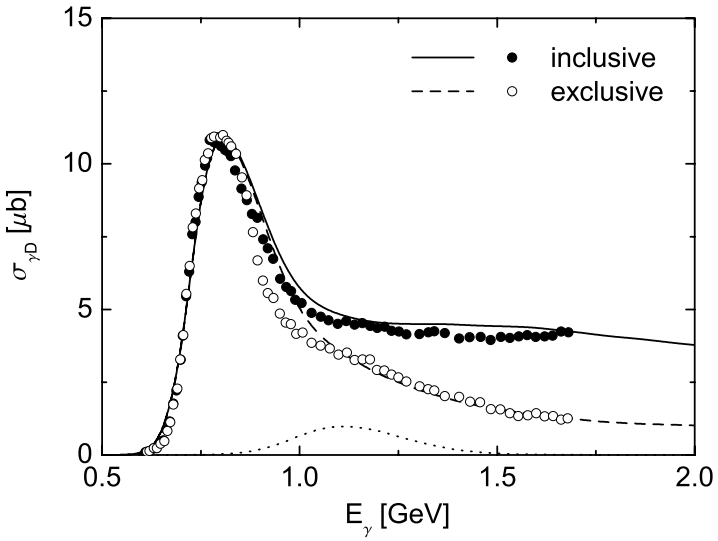

Figure 5.6: Total η photoproduction cross section from Deuterium. *Solid line/filled symbols*: inclusive cross section, *dashed line/open symbols*: exclusive cross section, *dotted line*: contribution from inclusive channel $n(\gamma, \eta\pi)$. Both data sets from [152].

and was found to work perfectly well. In Fig. 5.6 the data obtained in this way together with our calculations including the exclusive channels $\gamma p \to \eta p$ and $\gamma n \to \eta n$ only are shown. The level of agreement is high in both the low energy half of the $S_{11}(1535)$ and at energies clearly above the S_{11} resonance. A mismatch of our calculations and the data occurs only at the high energy tail of the S_{11} where the data drop faster than our results. In case of the free proton target a similar behavior could be cured by inventing the additional form factor (5.3) which is included in the present calculations anyway. In Fig. 5.5 also the effect of the initial nucleon momentum distribution on the ratio of the neutron to the proton cross section as extracted from the Deuterium results is shown. Here, the peak appears to be lower because of the Fermi smearing generated by the nucleon momentum distribution. Fermi motion affects the ratio of the neutron to proton cross section measured from Deuterium because of the different energy dependence of both elementary cross sections.

Next, we also have to fix the inclusive production channels from the neutron. To this end we make the ansatz

$$\sigma_{\gamma n \to \eta \Delta^0} = \kappa_\Delta \cdot \sigma_{\gamma p \to \eta \Delta^+} \tag{5.20}$$

with the proton cross section from Eq. (5.7) and compare our calculations including all channels to the full inclusive Deuteron data. At photon energies from 1.3 GeV on the $\eta\Delta$ channel gives the dominant contribution to η photoproduction from the proton. In this energy regime our calculations are only consistent with the Deuteron data by putting

$$\kappa_\Delta \simeq 0. \tag{5.21}$$

This is quite surprising. Obviously, the electromagnetic excitation of the neutron couples much less strongly to the $\eta\Delta$ channel than the excitations of the proton. On the

other hand, with the choice (5.20) and (5.21) we cannot reproduce the Deuteron data at intermediate energies $E_\gamma = (1 - 1.2)$ GeV. The missing strength is indicated in Fig. 5.6 by the dotted line. It can have various origins, namely different energy dependences of the $\gamma n \to \eta\pi N$ and $\gamma p \to \eta\pi N$ cross sections (not taken into account by means of the ansatz (5.21)), a modification of the exclusive cross section in the compound Deuteron system due to a change of interference patterns, or a two-body photoabsorption process such as $\gamma(NN) \to S_{11}(1535)N$ which has also been considered to be responsible for the strong modification of the total photoabsorption process on nuclei in the energy range between the first and second resonance regions [179, 180].

In the spirit of our quasifree incoherent model, the first possibility seems to be most reasonable. Consequently, we introduce an additional contribution $\gamma n \to \eta\pi n$ which does not proceed via an intermediate Δ and adjust the corresponding cross section to the inclusive Deuteron data shown as solid symbols in Fig. 5.6. We parametrize it in the following way:

$$\sigma_{\gamma N\to\eta\pi N} = \left(\frac{k}{k_0}\right)^2 \frac{s\Gamma_\gamma(s)\Gamma_{R\to\eta\pi N}(s)}{(s-m_R^2)^2 + s\Gamma_R^2(s)} \frac{2m_N}{m_R\Gamma_0}\left(|A^N_{1/2}| + |A^N_{3/2}|\right) \tag{5.22}$$

with

$$\Gamma_\gamma(s) \;=\; \Gamma_0 \frac{k}{k_0}\left(\frac{k_0^2+X^2}{k^2+X^2}\right)^2 \tag{5.23}$$

where k and k_0 are the initial CM momenta at total energy $\sqrt{s}$ and m_R, respectively. For the electromagnetic cutoff we take $X = 0.3$ GeV from [181]. The hadronic partial width we parametrize as

$$\Gamma_{\eta\pi N}(s) \;=\; \Gamma_0 \frac{m_R}{\sqrt{s}} \frac{R_3(\sqrt{s})}{R_3(m_R)} F^2 b_{\eta\pi N} \tag{5.24}$$

where $R_3(E)$ is the three-body phasespace volume at the total CM energy E. The remaining contributions to the resonance width are summarized in the $R \to \pi N$ channel with a decay width given by an expression similar to (5.2). F is a form factor identical to (5.3) with $\lambda = 0.6$ GeV. This restrictive cutoff value is needed in order to suppress the cross section at photon energies where the total $\gamma d \to \eta X$ cross section is already saturated by the $\gamma N \to \eta N$ and $\gamma N \to \eta\Delta$ channels.

We use the parameters of the $D_{15}(1675)$ resonance with a mass $m_R = 1.675$ GeV and total width $\Gamma_0 = 150$ MeV [141] that fits well to the phenomenology of the needed cross section. For the photocoupling helicity amplitudes we have [141]

$$\begin{array}{rclrcl} A^p_{1/2} &=& 0.019 & A^n_{1/2} &=& -0.043 \\ A^p_{3/2} &=& 0.015 & A^n_{3/2} &=& -0.058 \end{array} \tag{5.25}$$

For the pole mass branching ratio we take $b_{\eta\pi N} = 0.088$ which is fitted to the η photoproduction data from the Deuteron. In Fig. 5.6 the resulting contribution to the total η photoproduction cross section off Deuterium is shown as dashed line. The total inclusive cross section agrees rather well with the experimental data points.

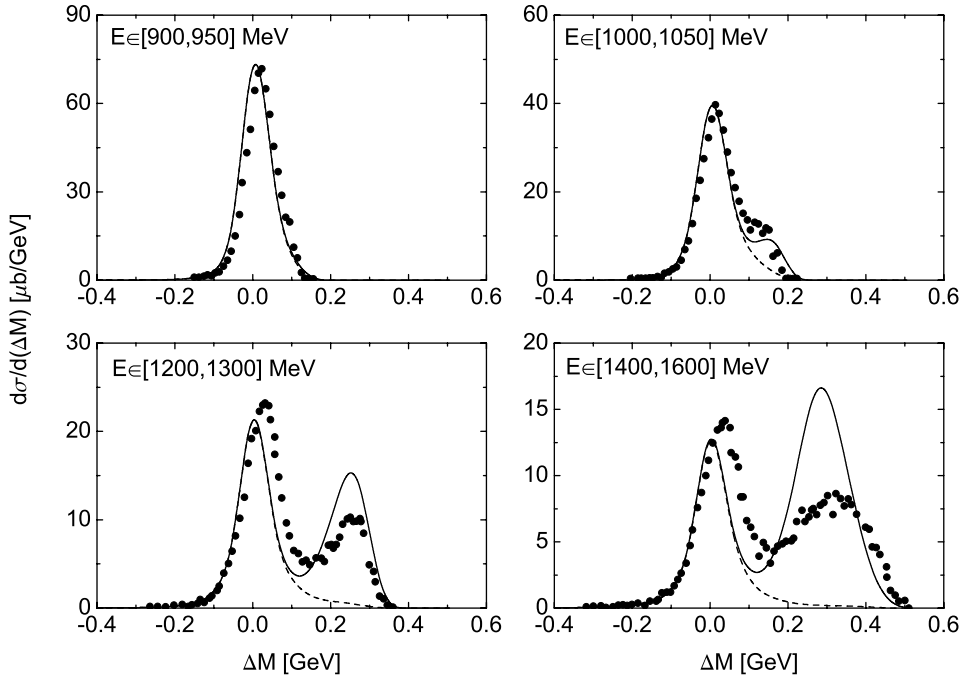

Figure 5.7: Missing mass distributions from Deuterium. *Dashed line*: exclusive final state ηN, *solid line*: total. Preliminary data from [156].

Finally, we also calculate missing mass distributions and compare to the still preliminary data from [37, 156]. The missing mass is defined as

$$\Delta M = \sqrt{(E_\gamma + m_N - E_\eta)^2 - (\mathbf{k}_\gamma - \mathbf{q}_\eta)^2} - m_N \tag{5.26}$$

where $\mathbf{k}_\gamma$ is the initial photon momentum and $(E_\eta, \mathbf{q}_\eta)$ are the η energy and three-momentum. This expression assumes a quasifree production mechanism. On a free unbound nucleon the missing mass ΔM would be equal to zero if the final state consists of an η and a nucleon only. In nuclear targets, however, the missing mass distributions will be broadened due to Fermi motion. For inclusive channels ΔM acquires finite positive values due to the additional undetected massive particle(s) in the final state.

For the case of η photoproduction off Deuterium missing mass distributions are shown in Fig. 5.7. According to Eqs. (4.17) and (5.26) these are given by

$$\begin{aligned} \frac{d\sigma}{d(\Delta M)} &= \int d^3q \int \frac{d^3p}{(2\pi)^3} |u(p)|^2 \left(\frac{d^3\sigma_p}{dq^3} + \frac{d^3\sigma_n}{dq^3} \right) \times \\ &\quad \delta\left(\sqrt{(E_\gamma + m_N - E_\eta)^2 - (\mathbf{k}_\gamma - \mathbf{q}_\eta)^2} - m_N - \Delta M \right) \end{aligned} \tag{5.27}$$

where $u(p)$ is the $s-$wave Deuteron wave function in momentum space (see Chapter 4) and $d^3\sigma_{p(n)}/d^3q$ is the momentum differential η photoproduction cross section off protons (neutrons). In this calculation we have included a mass resolution of $\delta(\Delta M) = 25$ MeV.

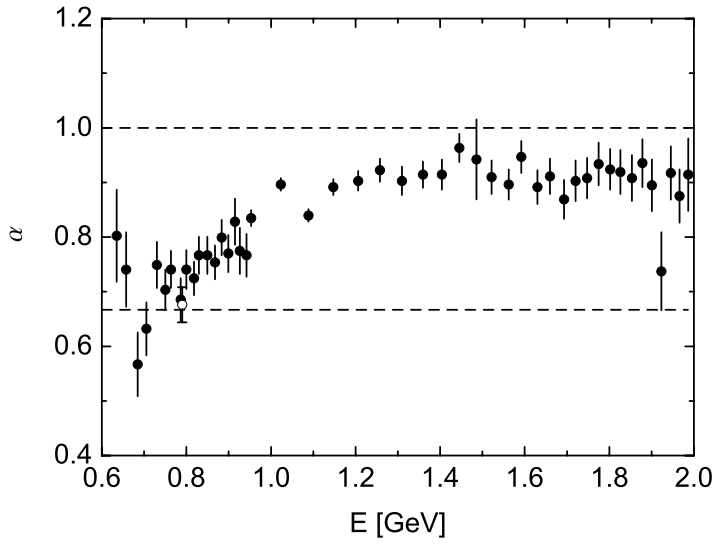

Figure 5.8: Scale factor α as function of the photon beam energy. Data from [160] (open symbol) and [157] (filled symbols).

This is done as described in Section 7.3. The preliminary data is given without normalization [156]. In Fig. 5.7 we choose the normalization such, that the integrated missing mass distributions match with the total inclusive cross section shown in Fig. 5.6. In the lower energy intervals the data is reproduced very well. For higher energies, however, too much strength sits in the right peak which corresponds to the inclusive η production channels with one additional pion in the final state. This strength is undoubtedly coming from the $\gamma p \to \eta\Delta$ reaction that has been fixed in our model using the experimental data from [164], see Fig. 5.1. In turn, too little strength sits in the exclusive peak. In particular in the highest energy interval both peaks are broader in the experimental data as compared to our theoretical results. This broadening could be generated by collective effects which are not included in our simple spectator calculations.

5.5 The ηN cross section

Now we turn to the photoproduction of η meson off nuclei. As said earlier, nuclear η photoproduction can be a useful tool to study the ηN interaction. Qualitative information on the absorptive part of the η nucleus interaction can be obtained already from a fit of the total photoproduction cross section with a simple scaling law:

$$\sigma_A(E) \sim A^{\alpha(E)} \tag{5.28}$$

where A is the nuclear mass number. If final state interactions are weak one can expect a scaling close to $\alpha = 1$ since all nucleons contribute to the total η production cross section. In contrast, strong absorption implies $\alpha \simeq 2/3$ which means that the nuclear cross section scales with the size of the nuclear surface. This conjunction can be derived

in a quite intuitive way using the Glauber formalism and is discussed in Appendix B. In Fig. 5.8 the α parameter extracted from the experimental data over a broad photon energy range in Ref. [157] is shown. For low energies the photoproduction cross section scales indeed like $\sigma \sim A^{2/3}$ implying a rather large η absorption cross section. This situation seems to change for photon energies above the $S_{11}(1535)$ pole. This issue and its implications for the η nucleus final state interactions are subject to the discussions of the following Section. We start with a Glauber analysis of the photoproduction data in order to obtain information on the η absorption cross section.

5.5.1 Glauber analysis

In the following we use the Glauber formalism in order to extract the ηN interaction strength. To this end we calculate the kinetic energy differential η photoproduction cross section in the eikonal approximation given by Eqs. (B.26) and (B.30). In order to minimize uncertainties concerning the photoproduction cross section from neutrons we analyze the ratio

$$\mathcal{R}(A,T) = \left(\frac{d\sigma_A}{dT}\right)_A \left(\frac{d\sigma_A}{dT}\right)^{-1}_{A=12}. \tag{5.29}$$

where T is the η kinetic energy. Using Equation (B.26) this ratio is given by

$$\mathcal{R}(A,T) = \frac{A_{\text{eff}}(A)}{A_{\text{eff}}(12)}. \tag{5.30}$$

where A_{eff} is the effective mass number according to Eq. (B.30). We evaluate the ratio $\mathcal{R}$ numerically and vary the reabsorption cross section σ_η, which enters Eq. (B.30) and which will be specified further below, until agreement with the experimental data is obtained. This is done for different values of the η kinetic energy. Note, that the effective mass number according to Eq. (B.30) only implicitly depends on the η kinetic energy via the reabsorption cross section σ_η. The results of the fitting procedure in terms of the cross section σ_η are shown in Fig. 5.9. Apart from single outliers the ηN cross section varies only smoothly over the η kinetic energy range. The energy dependence of σ_η can be parametrized as

$$\sigma_\eta(T) = \frac{32 \text{ mb}}{1 + \frac{T}{0.68 \text{ GeV}}} \tag{5.31}$$

which is a fit to the data omitting the low energy ($T < 100$ MeV) region where the dispersion of the analyzed data points becomes substantial.

So far we have avoided to further specify the cross section σ_η. Within the Glauber picture the answer to this question is straightforward: σ_η is equal to the total η absorption cross section including all processes which take η mesons out of the flux. However, in reality also elastic ($\eta N \to \eta N$) and inelastic ($\eta N \to \eta X$) collisions occur which do not reduce the η multiplicity in the final state. On the other hand, these processes slow down the η mesons and, thus, shuffle strength from the high to the low energy part of the spectrum. This can be seen in our transport calculations to be discussed in the following Sections,

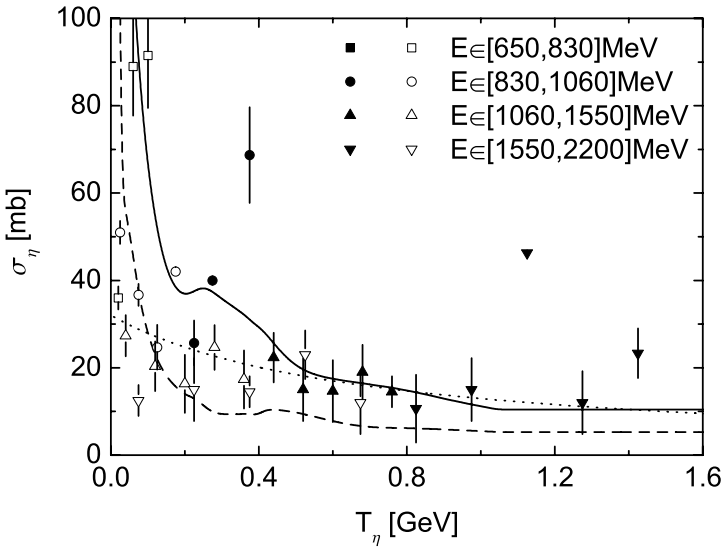

Figure 5.9: Total ηN cross section extracted from the kinetic energy differential η photoproduction cross section from [157] using the Glauber formalism. *Dashed line*: inelastic ηN cross section from the coupled channel model [170], *solid line*: total ηN cross section from [170], *dotted line*: fit to the data (5.31) omitting the low energy ($T < 100$ MeV) region. *Solid symbols*: $T > 0.5\,T_{\rm max}$, *open symbols*: $T < 0.5\,T_{\rm max}$.

see for instance Fig. 5.18. Consequently, we expect the cross section σ_η extracted from data in a given photon energy interval at the highest kinetic energies to be close to the total ηN cross section including also elastic channels and at low kinetic energies to be *smaller* than the absorptive one. This is due to the fact, that at low kinetic energies the η flux is reduced according to the absorptive cross section and enhanced due to elastic processes occurring at initially higher kinetic energies. Consequently, for each photon energy interval analyzed only the data points at the highest kinetic energies give a reliable estimate for the total ηN cross section whereas the Glauber analysis breaks down for the lower kinetic energies.

In Fig. 5.9 the data points for the cross section σ_η obtained at kinetic energies larger and smaller $0.5\,T_{\rm max}$ ($T_{\rm max} = E_\gamma - m_\eta$) are indicated by the solid and open symbols, respectively. Also shown are the absorptive and total ηN cross sections obtained in the coupled channel $K-$matrix analysis [170]. Indeed, the ηN cross section extracted from the kinetic energy differential photoproduction cross section at kinetic energies $T > 0.5\,T_{\rm max}$ agrees rather well with the total ηN cross section from [170]. This is a nice confirmation of our understanding of the ηN dynamics from a more macroscopic point of view. Moreover, these results rule out the ηN cross sections as obtained from the Manley analysis [150]. Both the absorptive and total ηN cross sections are much too small in the relevant energy interval in order to be consistent with the extracted ηN cross section data, see Fig. 5.4.

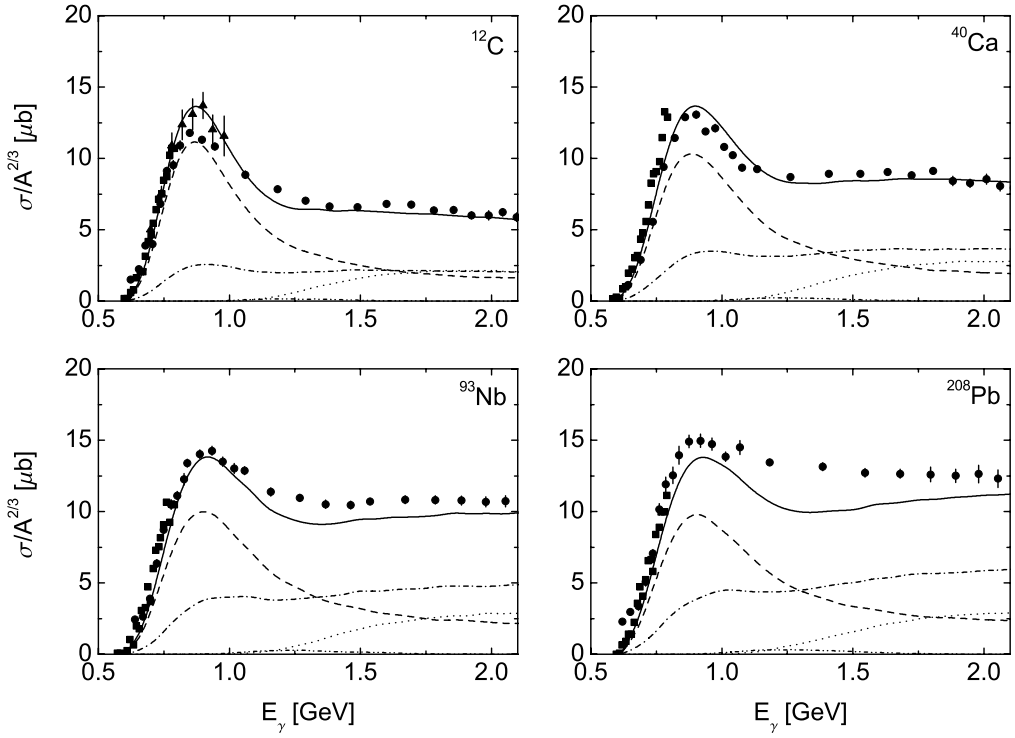

Figure 5.10: Total η photoproduction cross section off different target nuclei as a function of photon energy. *Solid line*: total cross section, *dashed line*: exclusive ηN channel, *dotted line*: $\eta\Delta$ contribution, *dash-dotted line*: secondary η production, *dash-dot-dotted line*: $\eta\pi N$ contribution according to (5.22). Data from [152] (circles), [153] (squares) and [154, 155] (triangles).

5.5.2 Transport simulations

Now we perform BUU transport simulations of η photoproduction off various target nuclei. In these calculations the initialization of the elementary photon nucleon interactions is done according to the cross sections discussed in a previous Section. The η final state interactions are described by means of the elastic and inelastic ηN cross sections obtained from the $K-$matrix analysis [170], see Fig. 5.4. In spite of the fact that these cross sections are obtained from a resonance fit, in the simulations they give rise to non-resonant scattering processes and are entirely ascribed to the final states $\eta N \rightarrow \eta N$, πN and $\pi\pi N$. This is necessary in order to be able to modify the cross sections implemented into the BUU simulation in terms of the Manley resonance model [150]. More consistent, however, would be the implementation of a new resonance parameter set which is able to reproduce all hadronic cross sections at once. The present modus operandi neglects a priori medium modifications to the η absorption cross section due to resonance nucleon collisions as for instance in the reaction chain $\eta N \rightarrow S_{11}$ followed by $S_{11}N \rightarrow NN$. In Ref. [149] the influence of such contributions was, however, found to be extremely small.

In Fig. 5.10 the inclusive η excitation function over a wide range of photon energies

is shown for various target nuclei. At small energies clearly the exclusive ηN channel dominates. For the highest beam energies the $\eta\Delta$ channel becomes equally important. Over almost the complete energy range we also observe a substantial contribution from η mesons produced via secondary interactions. This component in the η excitation function is more important for the case of heavy nuclear targets and can become as large as about 50% of the total cross section in the Lead target. The contribution of the $\gamma N \to R \to \eta\pi N$ reaction, however, is very small and hardly visible in Fig. 5.10. Since it was more important in case of the Deuterium target, this could be due to Pauli blocking or FSI. Note, that we do not propagate the resonance R but rather consider this contribution as a phenomenological background with the $\eta\pi N$ final state initialized according to three body phasespace. Consequently, the reaction $\gamma N \to \eta\pi N$ is subject to the Pauli principle. This could be different if a resonance would be produced which first propagates to a region with a smaller nucleon density before it eventually decays to the $\eta\pi N$ final state. Moreover, the η mesons produced via this reaction have quite small kinetic energies and, thus, undergo strong FSI since the ηN cross sections are particularly large there.

The agreement of our calculations and the data is quite satisfactory for the Calcium target whereas it is less good for the other nuclei. In the case of Carbon the resonance peak is about 10% higher than the recent data from [152]. However, the older data from [154, 155] agree very well with our theoretical curves. For the heavy targets our cross sections are lower than the data especially at energies above the $S_{11}(1535)$ peak. This situation becomes more pronounced for Lead as compared to the Niobium target. This obvious mismatch could be due to the only insufficient description of the relevent η production processes in the energy region above the $S_{11}(1535)$ resonance. Remember, that we invented a phenomenological $\gamma N \to \eta\pi N$ contribution in order to cure the deficiency of our calculations in the total η production cross section off Deuterium. The disagreement of the calculations and the data in Fig. 5.10 reminds of the total photoabsorption cross section from nuclei just above the first resonance region. In [179, 180] this was healed by inventing the two photon absorption process $\gamma NN \to N\Delta$. In contrast to the single nucleon processes which scale $\sim A$ the two nucleon processes contain components $\sim A^2$ and, thus, become even more important for heavy nuclear targets. This is in line with the observation that can be made in Fig. 5.10, namely the increasing descrepancy between calculations and data with the nuclear mass number A. On the other hand, also single nucleon processes with a strong isospin dependence could produce such a behavior since the heavy target nuclei have a substantial neutron excess. Moreover, also FSI give rise to nuclear mass number dependent effects. However, whereas the theoretically too small photoproduction cross section for heavy targets indicates a smaller reabsorption cross section, the agreement for light nuclei would worsen by a reduction of the η absorption strength.

More information about the individual contributions to the η photoproduction reaction from nuclei can be obtained from the differential distributions. In Fig. 5.11 missing mass spectra for various photon energy ranges and target nuclei are shown together with preliminary data [182]. These data sets have been obtained without overall normalization and, thus, have been scaled to the peak value of our calculated distributions. Again we include a mass resolution of $\delta(\Delta M) = 25$ MeV. In the lowest energy interval we observe a single peak structure since one is essentially below the inclusive production threshold.

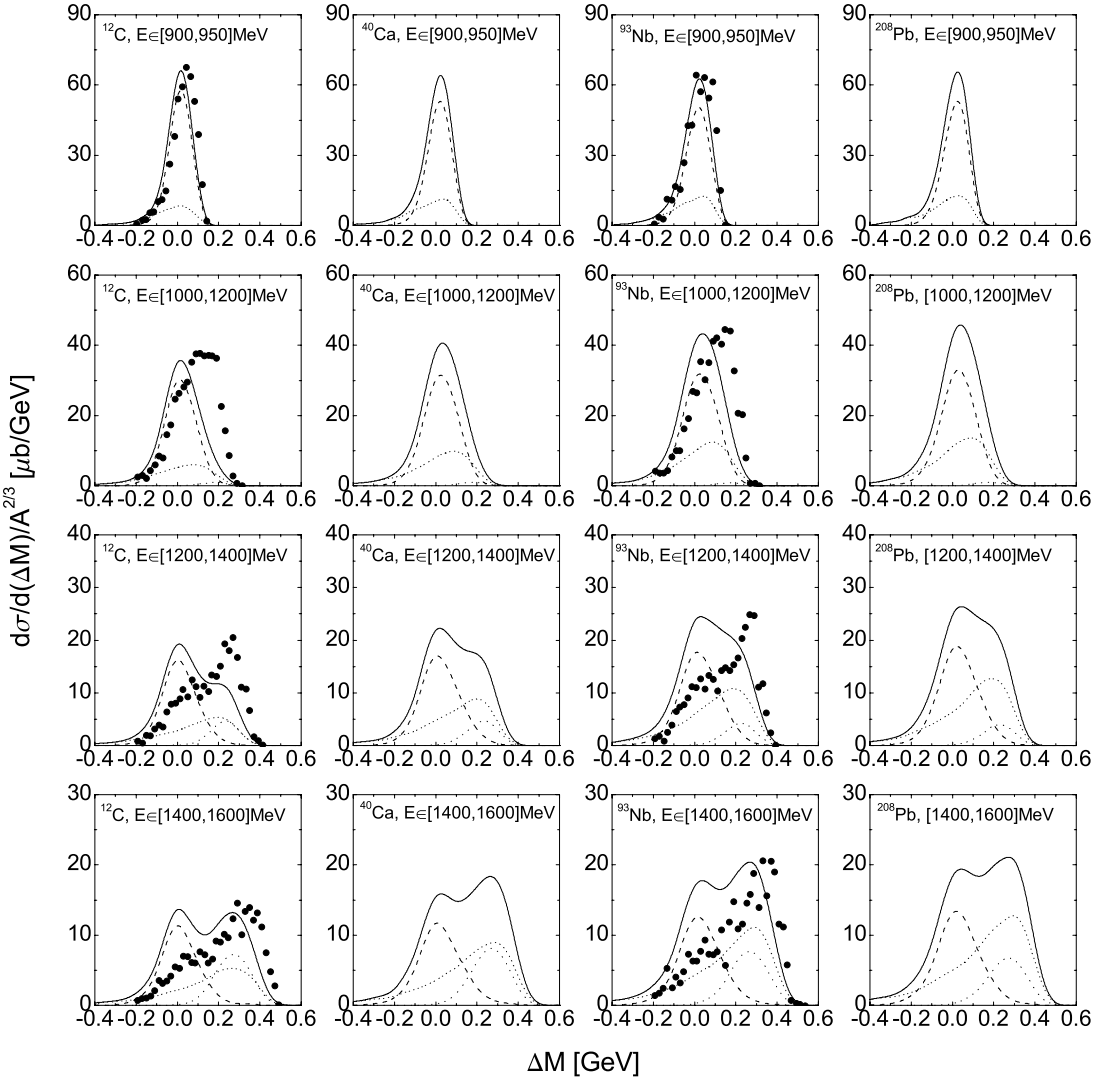

Figure 5.11: Missing mass spectra for various target nuclei and different beam energies. *Solid line*: all events, *dashed line*: exclusive events, *dotted line*: inclusive $\eta\Delta$ events, *dash-dotted line*: secondary events. Preliminary data without normalization from [182].

From $\sim$ 1 GeV on the data already starts to show a broadening of the peak towards high missing masses corresponding to the production of inclusive $\eta\pi N$ final states. This becomes more pronounced with increasing photon energy and eventually a two peak structure can be observed. This effect is also present in the calculations and can be ascribed to a composition of the $\eta\Delta$ final state and secondary η production during the FSI. However, in the data the inclusive peak is stronger throughout the whole energy region. This is in contrast to the Deuterium data which showed an opposite behavior. Thus, again the question after the physical mechanisms behind this effect arises. In principle, the missing strength in the inclusive peak could be produced already initially ($\gamma N \to \eta\pi N$) as well as during the FSI via processes like $\eta N \to \eta\pi N$. The latter ones are not included at all in our calculations. A more thorough theoretical treatment of the

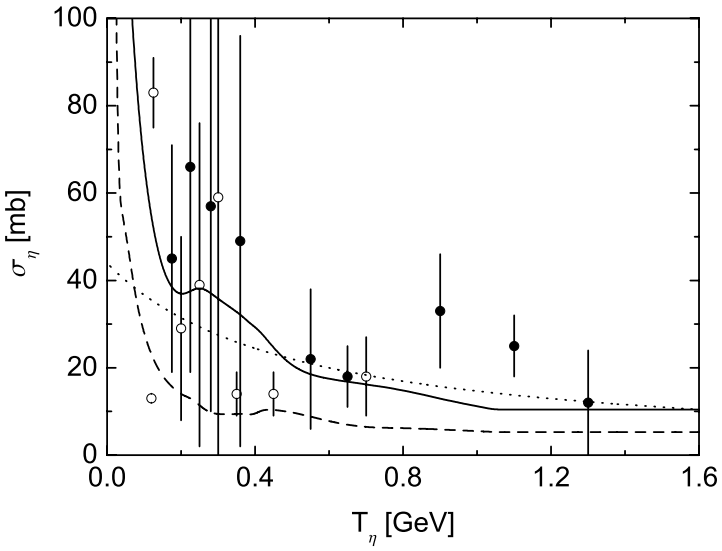

Figure 5.12: Total ηN cross section extracted from the kinetic energy differential η photoproduction cross section from [157] with the missing mass cut $\Delta m < 140$ MeV using the Glauber formalism. *Dashed line*: inelastic ηN cross section from the coupled channel model [170], *solid line*: total ηN cross section from [170], *dotted line*: fit to the data (5.32) omitting the low energy ($T < 100$ MeV) region.

elementary photoproduction cross section from protons and Deuterium is thus required to illuminate this issue.

Both η mesons produced via inclusive photon nucleon reactions and η mesons produced during the FSI obscure the line shape of the $S_{11}(1535)$ resonance above photon energies of about 800 MeV. Also the extraction of the ηN cross section from the photoproduction data can be hampered by these processes as discussed in the previous Section. Thus, it appears to be a reasonable concept to suppress these contributions by an appropriate missing mass cut. A possible choice is $\Delta M < 140$ MeV as can be seen in Fig. 5.11. However, one should keep in mind that this cut does not suppress the entire background from η rescattering. This can also be seen in Fig. 5.11. At low energies also the background from secondary η production peaks below $\Delta M = 140$ MeV. Only for high photon energies this contribution is shifted towards large positive missing masses.

5.5.3 Glauber analysis revisited

We repeat the Glauber analysis from Section 5.5.1 using the energy differential cross section data with the previously discussed missing mass cut. The results are shown in Fig. 5.12 again together with the ηN cross sections from the $K-$matrix analysis [170]. Now the extracted data points can be fitted with

$$\sigma_\eta(T) = \frac{44 \text{ mb}}{1 + \frac{T}{0.5 \text{ GeV}}} \tag{5.32}$$

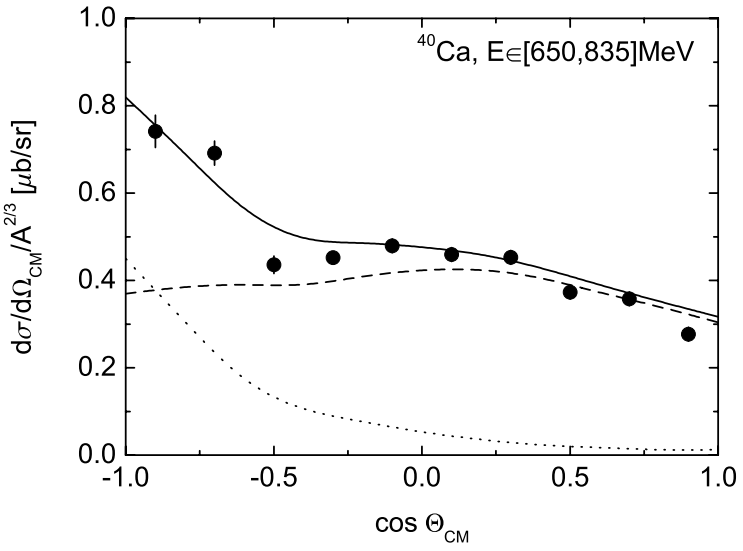

Figure 5.13: Angular differential cross section from Carbon. *Solid line*: total cross section, *dashed line*: exclusive quasifree events, *dotted line*: secondary/rescattering contribution. Preliminary data from [157].

for $T_\eta > 100$ MeV where T is the η kinetic energy. This cross section is slightly larger than the one extracted previously without the missing mass cut, compare to Eq. (5.31). The spread of the data points is much more substantial now due to the lower statistical significance of the photoproduction data with the missing mass cut.

At low kinetic energies the error bars are such large that no cross section can be assigned here. At higher energies the extracted values are somewhat larger than in the previous case without the missing mass cut. This could be due to scattering processes of the type $\eta N \to \eta N$ or $\eta N \to \eta\pi N$ which do not lead to η absorption. On the other hand, these processes can lead to larger values of the missing mass. Thus, these events would be eliminated when the missing mass cut is applied and, consequently, contribute to the effective ηN absorption cross section extracted via the Glauber analysis. The missing mass cut delivers an additional argument for the fact that the extracted cross section is equal to the total ηN cross section rather than just to the inelastic one. In summary, both analyses suggest that the ηN cross section amounts to roughly 30 mb at low kinetic energies ($T \simeq 300$ MeV) and drops smoothly towards higher kinetic energies where it reaches a value of roughly 10 mb for $T > 1.2$ GeV.

5.5.4 Rescattering

In [157] also angular distributions have been obtained. One particular example for the Calcium target is shown in Fig. 5.13. The differential cross section is shown with respect to the CM emission angle of the η meson assuming its production from a free nucleon at rest. In the looked at photon energy interval the photoproduction process is clearly

dominated by the excitation and subsequent decay of the $S_{11}(1535)$ resonance. This contribution gives an almost flat angular distribution as is obvious also from Fig. 5.2. Here, this contribution is shown by the dashed line. However, the data show some depletion for very forward angles ($\cos\theta \simeq 1$) and a quite substantial enhancement for backward angles ($\cos\theta \simeq -1$). The depletion in forward direction is due to Pauli blocking which suppresses particle production at small momentum transfers. Our calculations also give an explanation for the enhancement under backward angles, it is generated by final state interactions. The η mesons produced via secondary interactions ($\eta N \to \eta N$ or $\pi N \to \eta N$) contribute mainly at backward CM angles since their kinetic energy is smaller than the energy of η mesons produced in the initial photon nucleon interaction without rescattering. Consequently, their angular distribution in the CM frame, which itself is moving with the velocity $(1 + m_N/E_\gamma)^{-1}$ along the incoming beam direction, is concentrated at backward angles. This clearly visible contribution of secondary η production events opens the possibility to study the elastic ηN scattering cross section.

In Fig. 5.14 we show the CM angular distributions for all target nuclei and various beam energy ranges. Besides the calculation with the $K-$matrix ηN cross sections we also show results obtained with the absorptive cross section from the $K-$matrix analysis and the elastic one according to Eq. (5.17). Except for the Lead target, the calculation with the cross section from the $K-$matrix model agrees reasonably well with the data. For the case of Lead, however, the experimental cross sections show an even stronger rise towards backward CM angles. For photon energies below $\sim$ 1 GeV the elastic cross section from Eq. (5.17) obviously produces too little elastic scattering events. As can be seen in Fig. 5.4 for η kinetic energies below 500 MeV it is much smaller than the $K-$matrix cross section. For photon energies above $\sim$ 1 GeV, however, both recipes give almost identical results. This could be due to the fact that for $T_\eta > 500$ MeV the parametrization (5.17) gives a larger cross section than the $K-$matrix one. This can compensate for the smaller cross section at low kinetic energies. Overall, the data seem to favor the elastic ηN cross section as obtained from the $K-$matrix analysis [170]. This statement, however, also depends on the understanding of the elementary η production mechanisms at photon energies above the $S_{11}(1535)$ resonance.

5.6 Medium modifications

Finally, we want to discuss briefly possible medium modifications of the $S_{11}(1535)$ resonance and the η meson.

5.6.1 Resonance self energy

The influence of medium modifications of the $S_{11}(1535)$ resonance on η photoproduction off nuclei has been investigated within the framework of the BUU model already in Ref. [149]. In these calculations the collisional broadening of the $S_{11}(1535)$ of roughly 35 MeV at normal nuclear matter density obtained in a coupled channel model was implemented. Later a net broadening of 30 MeV relative to the Pauli blocked vacuum

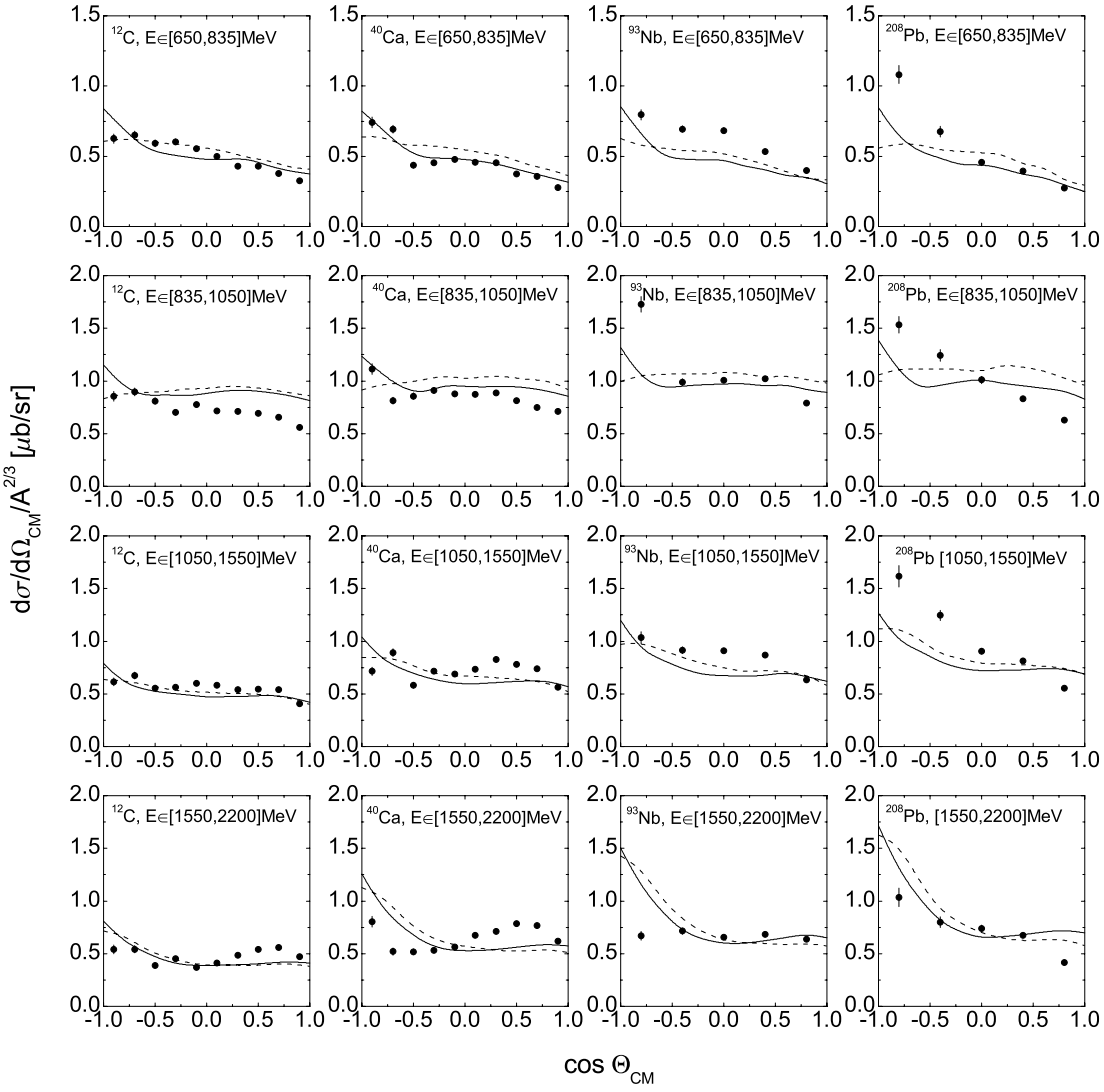

Figure 5.14: Angular differential cross section for all target nuclei and various beam energy ranges. *Solid line*: ηN cross section from $K-$matrix analysis [170], *dashed line*: elastic cross section parametrization (5.17).

width almost independent of the S_{11} momentum was found using the same framework [70]. In the BUU model the nucleon resonances undergo FSI by means of the processes

$$RN \longleftrightarrow RN \tag{5.33}$$
$$RN \longleftrightarrow R'N,\ R' \neq R \tag{5.34}$$
$$RN \longleftrightarrow NN \tag{5.35}$$

which also give rise to collisional broadening. These collision rates explicitly included in our transport simulations by means of the collision integral are consistent with a broadening of $30 - 35$ MeV. In the present calculations we thus use

$$\Gamma_{\text{coll}} = 30 \text{ MeV} \frac{n_N}{n_0} \tag{5.36}$$

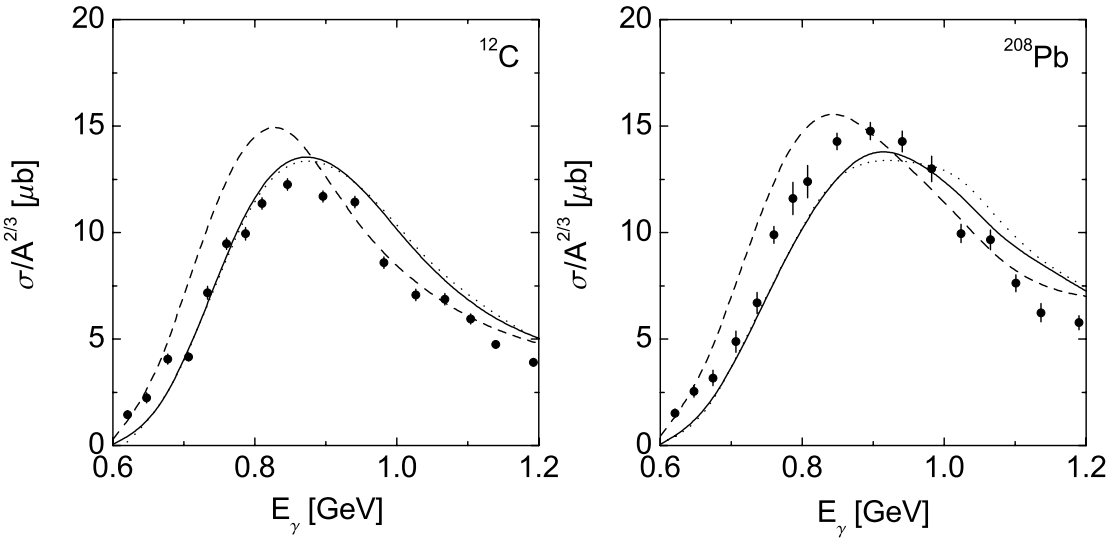

Figure 5.15: Total cross section for η photoproduction off Carbon (left panel) and Lead (right panel) with a cut on the missing mass $\Delta m < 140$ MeV. *Solid line*: standard calculation with momentum dependent resonance self energy (medium equation of state), *dashed line*: momentum independent resonance self energy (hard equation of state), *dotted line*: momentum dependent self energy and collisional broadening. Preliminary data from [152].

where n_N is the local nucleon density. In Fig. 5.15 the total η photoproduction cross section in the $S_{11}(1535)$ resonance region with the missing mass cut $\Delta M < 140$ MeV is shown. The dotted line, which is calculated with the collisional broadening of the $S_{11}(1535)$ resonance and which has to be compared to the solid one, shows no visible modifications due to the in-medium broadening. This is in line with the earlier calculations presented in [149].

In addition we also show a curve in Fig. 5.15 calculated with a hard momentum independent nuclear equation of state in contrast to the hitherto used medium momentum dependent one. The parameterizations of the nuclear mean field potential implemented into our transport model are given explicitly for instance in Refs. [100, 149]. In the BUU model the nucleon resonances feel the very same nuclear potential as the nucleons themselves. Consequently, the use of the momentum dependent nuclear mean field leads to an effective resonance mass which is close to the free one whereas the momentum independent mean field leads to an effective mass about ~ 60 MeV smaller than the resonance vacuum mass. This is due to the fact that the S_{11} produced at photon energies of around 800 MeV has itself a momentum of about 800 MeV. For this momentum, however, the momentum dependent mean field almost vanishes whereas the momentum independent one does not. The calculation with the momentum independent equation of state is incompatible with the data. Again, this was also found in [149]. For the Lead target the results obtained with the momentum dependent potential are somewhat lower than the data. This, however, could also be generated by a too large η absorption cross section or

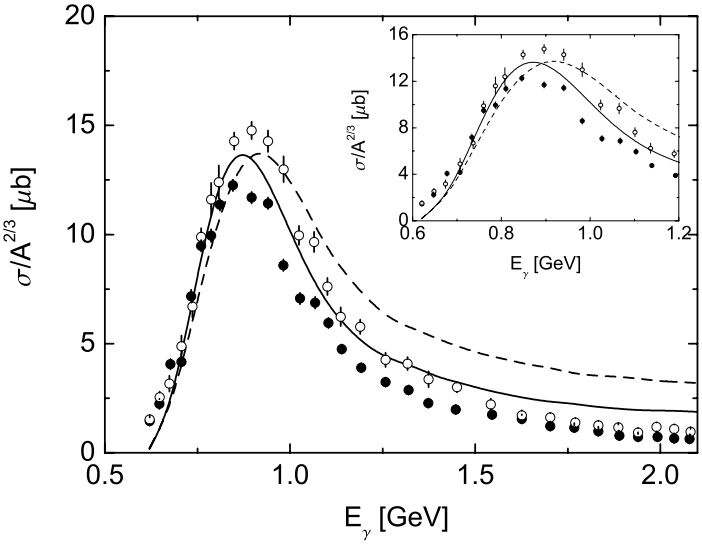

Figure 5.16: Total cross section for η photoproduction off Carbon (solid line, filled symbols) and Lead (dashed line, open symbols) with a cut on the missing mass $\Delta m <$ 140 MeV. Preliminary data from [152]. The insert shows a magnification of the threshold region.

missing background contributions to the elementary η photoproduction process. Thus, in the following we keep the medium momentum dependent nuclear equation of state corresponding to an almost vanishing $S_{11}(1535)$ potential as seen in the photoexcitation function and neglect the collisional broadening.

In Fig. 5.16 the total η photoproduction cross sections off Carbon and Lead including the missing mass cut $\Delta M < 140$ MeV are shown. For high energies the calculated cross sections are too large by a factor of about two. This corresponds to the excess of strength in the missing mass spectrum in the $\Delta M \simeq 0$ peak, see Fig. 5.11. In the energy region of the $S_{11}(1535)$ the deviations are smaller. An important observation is that at least the qualitative features of the data can be reproduced without introducing any medium modifications of the resonance. The broadening of the $S_{11}(1535)$ peak is even overestimated by our calculations which do not include any collisional broadening. Also the slight shift of the peak when going from small nuclei to heavy targets is found in the calculations. This behavior is exclusively created by Fermi motion and the strong energy dependence of the ηN absorption cross section. In summary the comparison of the data and our calculations shows that the experimental results for the total η photoproduction cross section off nuclei do not suggest any medium modifications of the $S_{11}(1535)$ resonance.

5.6.2 η nucleus potential

Finally, we study the influence of the real part of the η nucleus potential on the observables. To this end we implement a scalar η potential U_η which renormalizes the effective η mass at finite density according to

$$\mathcal{H}_\eta = \sqrt{(m_\eta^o + U_\eta(\mathbf{q}, n_N))^2 + \mathbf{q}^2} \tag{5.37}$$

which is the Hamiltonian to be used for the η testparticles in the transport calculations and $m_\eta^o = 547$ MeV is the η vacuum mass. We adopt the η potential from the coupled channel model in Ref. [66, 70]. There, the η potential was found to be attractive at small momenta and repulsive for high momenta. This is due to the sizable coupling of the η to the $S_{11}(1535)$ resonance which sits slightly above the ηN threshold and, thus, pushes the genuine η branch in the spectral function down. A detailed discussion of such effects will be given in Chapter 8 for the case of the ω meson. In [70] also effects going beyond the low density approximation were considered. For the case of the η meson, however, they were found to have almost no net effect on the real part of the η potential. On the other hand, they lead to a reduced collisional broadening of the η as compared to the low density limit. The effect of short range correlations was found to be negligible. In the present work we parametrize the real part of the η potential in the following way:

$$U_\eta(\mathbf{q}, n_N) = -50 \text{ MeV} \left(1 - \frac{|\mathbf{q}|}{0.6 \text{ GeV}}\right) \frac{n_N}{n_0} \tag{5.38}$$

where $\mathbf{q}$ is the η three momentum and n_N is the nuclear density. This potential is attractive for small η momenta and turns repulsive from $\mathbf{q} = 600$ MeV on and, thus, approximately resembles the real part of the η potential calculated in [66, 70]. Here we neglect the in-medium broadening of the η which, however, can become as large as about 140 MeV at n_0 and $|\mathbf{q}| = 400$ MeV [66, 70]. Its implementation into the transport model requires more expenses and, thus, goes beyond the scope of the present study.

The density and momentum dependent effective η mass has the consequence to modify the phasespace for all processes with η mesons in the final state. In particular it has a backcoupling on the $S_{11}(1535) \to \eta N$ decay width. This width is given by

$$\Gamma_{S_{11}\to\eta N}(s, n_N) = \Gamma_0 \frac{m_R}{\sqrt{s}} \int \frac{d\Omega_{\text{cm}}}{4\pi} \frac{|\mathbf{q}_{\text{cm}}(\sqrt{s}, m_N, m_\eta^*)|}{|\mathbf{q}_{\text{cm}}(m_R, m_N, m_\eta^o)|} \tag{5.39}$$

with

$$m_\eta^* \equiv m_\eta^*(n_N, |\mathbf{q}|) = m_\eta^o + U_\eta(n_N, |\mathbf{q}|) \tag{5.40}$$

where $\mathbf{q}$ is the LA momentum of the η. Since the CM momentum $\mathbf{q}_{\text{cm}}$ depends on the η mass and the η mass in turn depends on the CM and LA momenta, Eqs. (5.39) and (5.40) have to be solved iteratively. As a starting point we use $m_\eta^* = m_\eta^o$ and calculate the η LA momentum $\mathbf{q}_1$ under the CM angle Ω. In the second step we obtain $m_1 = m_\eta^*(|\mathbf{q}_1|, n_N)$. This procedure is repeated until $|m_i - m_{i-1}| \leq 0.1$ MeV. In Fig. 5.17 the resulting $S_{11} \to \eta N$ width is shown. Due to the energy dependence of the effective η mass, the S_{11} width now also becomes momentum dependent. For masses below the resonance pole the

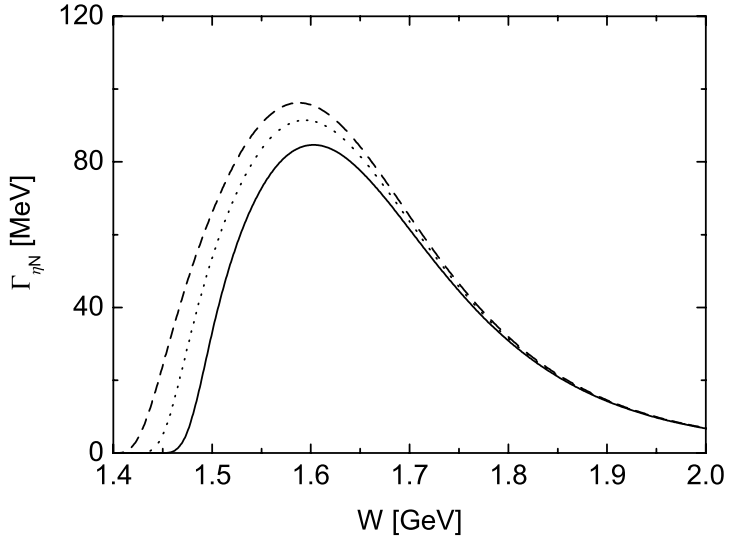

Figure 5.17: Partial decay width of the $S_{11}(1535)$ resonance to the ηN channel. *Solid line*: without η nucleus potential, *dashed line*: with η nucleus potential, $|\mathbf{k}_{\rm res}| = 0$ MeV, *dotted line*: with η nucleus potential, $|\mathbf{k}_{\rm res}| = 900$ MeV.

decay width can increase by up to 30 MeV. Also the ηN threshold moves down by about 50 MeV due to the attractive η potential at low energies. Moreover, we also modify the phasespace factors for the background contributions to the η photoproduction process. This is done in the same way as in Eq. (5.39). As a consequence the η photoproduction cross sections acquire sightly larger values in the threshold regions.

In Fig. 5.18 results calculated with and without the scalar η potential from Eq. (5.38) in terms of the kinetic energy differential η photoproduction cross sections from various nuclei are shown. Qualitatively these results show the same behavior as the CM angular distributions, see Fig. 5.14. For light nuclei the experimental cross sections are well reproduced. At low kinetic energies a sizable contribution from η mesons produced via secondary interactions during the FSI can be observed. However, for Niobium and Lead targets we are missing strength at low kinetic energies. This missing strength is seen as well in the total inclusive η excitation function from about $E_\gamma \simeq 1.1$ GeV on, in the missing mass spectra in the inclusive $(\eta\pi N)$ peak and under backward angles in the CM angular distributions. It could be generated both from inclusive photoproduction channels (e. g. $\gamma N \to \eta\pi N$, $\gamma NN \to S_{11}\Delta$), via FSI (e. g. $\eta N \to \eta\Delta$) or additional side feeding (e. g. $\gamma N \to \zeta N$, $\zeta N \to \eta N$) contributions. The effect of the η nucleus potential, however, is only marginal. The total normalization as well as the shapes of the kinetic energy differential distributions are only slightly affected. Whereas the in-medium change is visible at small energies, at high energies the effect is entirely lost since there the change in the phasespace factors is small and also the impact of the potential on the η propagation can be neglected. Whereas the η photproduction reaction off nuclei provides quite an amount of information on the nuclear reaction dynamics, its sensitivity to the η and $S_{11}(1535)$ in-medium properties is rather limited. Some questions

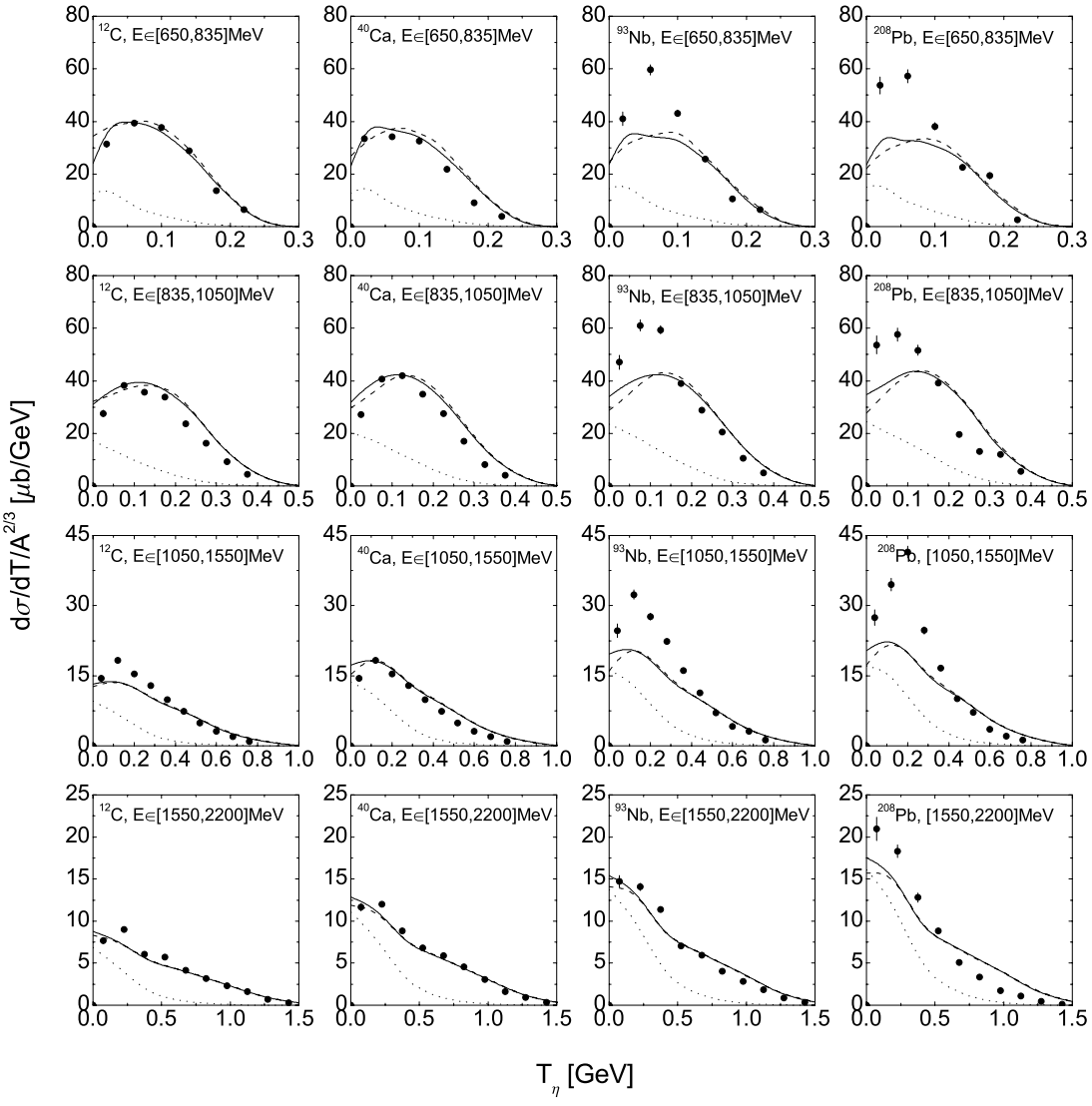

Figure 5.18: Kinetic energy differential cross sections for all target nuclei and various beam energy ranges. *Solid line*: total cross section, *dotted line*: secondary/rescattering contribution, *dashed line*: total cross section with η potential (5.38).

concerning the production and interaction of the η meson in nuclei remain open and ask for more refined investigations.

Part II

Vector mesons

Chapter 6

Primer Part II – Dileptons as a signal for chiral restoration

6.1 Introduction

The second part of this work is devoted to the investigation of the properties of the light neutral vector mesons in nuclear media. In this respect this first Section serves to generally introduce the idea of how one can obtain experimental information on the in-medium spectral distributions. The calculation of the reaction considered here, $\gamma A \to e^+e^-X$, has already been discussed in detail in Refs. [100, 159]. Here some special aspects will be highlighted, namely some typical experimental considerations connected with the proposed techniques and implications of the in-medium information obtained for the underlying theory of strong interactions.

In the language of non-perturbative QCD, the quantities one is interested in are the QCD vector currents. According to the valence quark picture, the vector current can be split into individual components carrying the quantum numbers of the light vector mesons:

$$j_\mu^\rho = \frac{1}{2}(\bar{u}\gamma_\mu u - \bar{d}\gamma_\mu d) \tag{6.1}$$

$$j_\mu^\omega = \frac{1}{6}(\bar{u}\gamma_\mu u + \bar{d}\gamma_\mu d) \tag{6.2}$$

$$j_\mu^\phi = -\frac{1}{3}(\bar{s}\gamma_\mu s). \tag{6.3}$$

The vector mesons ρ, ω and ϕ are seen as resonances in the current-current correlation function which in turn is related to the vector meson spectral functions. It is defined as

$$\Pi_{\mu\nu}(q) = i \int d^4x e^{iqx} \langle 0|\mathcal{T} j_\mu^{\rm em}(x) j_\nu^{\rm em}(0)|0\rangle \tag{6.4}$$

which is the four-dimensional Fourier transform of the propagator of the QCD electromagnetic current $j_\mu^{\rm em}$. $\mathcal{T}$ denotes the time-ordered product. Owing to the Lorentz structure of the vector current and current conservation the correlation function is a Lorentz tensor which is four-transverse, i. e. $q^\mu \Pi_{\mu\nu} \equiv 0$. In the vector meson dominance

picture it is assumed that the interaction of the electromagnetic current with hadrons in the energy domain considered here is saturated by the light vector meson components

$$j_\mu^{\rm em} = j_\mu^\rho + j_\mu^\omega + j_\mu^\phi. \tag{6.5}$$

Additional contributions have to be considered only for invariant energies above the charm threshold $\sqrt{s} > 2m_c \simeq 3$ GeV.

It is the aim to investigate the properties of the current-current correlator inside a surrounding of strongly interacting matter. Since the vector mesons are not asymptotic states but resonances only their decay products can be seen in the detectors. The particular advantage of the neutral vector mesons is that they can decay into dileptons. If such a decay happens inside the nuclear medium the dileptons leave the strongly interacting system untouched and carry the in-medium information to the detectors. From the dilepton invariant mass distributions the in-medium spectral densities in the isovector (ρ), isoscalar (ω) and the ϕ channel can be reconstructed. A specific difficulty is that in particular the narrow vector mesons ω and ϕ are long-lived and, therefore, most likely decay outside the strongly interacting region. Moreover, the measurement of dielectron spectra offers no possibility to distinguish the individual vector meson components. As we will see in the later Chapters, in some cases individual information on the single channels can be obtained from either hadronic or semi-hadronic decay modes.

6.2 Experiment

Experimentally dilepton production in strongly interacting systems has been looked at mainly in heavy ion experiments [10, 11, 12, 13, 14, 183], see [184] for a comprehensive overview. In these reactions dileptons are emitted predominantly in the hot and dense phases from thermal annihilation processes such as $\bar{q}q \to l^+l^-$ and $\pi^+\pi^- \to l^+l^-$ and possibly from Dalitz decays of baryon resonances $\pi N \to N^*/\Delta^* \to e^+e^-N$. However, the dilepton signal probes all stages in the course of the heavy ion reaction and, thus, the extracted quantities always represent integrals over various densities and temperatures passed through during the reaction. More recently, heavy ion experiments are accompanied by elementary reactions on nuclei. These can provide in-medium information from nuclear systems close to equilibrium, see also Appendix A.5 for a discussion of this issue. In this case the kinematical situation has to be chosen such that the produced vector mesons decay inside the strongly interacting matter. Whereas the generally large momenta of the vector mesons produced with elementary projectiles hamper this condition, complementary in-medium information on the high-momentum components in the vector meson spectra can be obtained from these reactions.

First experimental observations of a significant reshaping of dilepton invariant mass spectra in heavy-ion reactions as compared to elementary collisions have been made by the NA45 [10, 11, 12, 13] and HELIOS [14] collaborations. The obtained spectra showed a serious enhancement over the elementary ones consistent with spectral strength moving downward to smaller masses [186, 187, 188, 189]. More recently dielectron spectra in proton-nucleus collisions have been studied at KEK [15, 16, 17]. Albeit under much

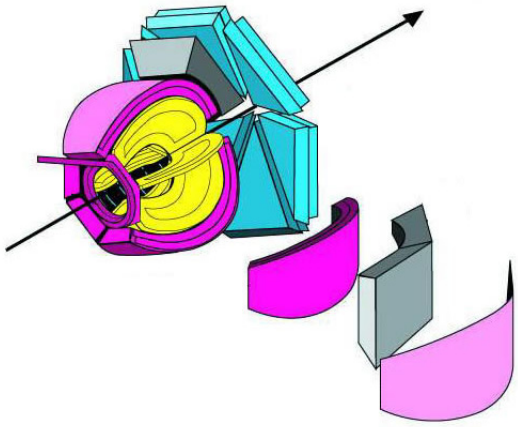

Figure 6.1: Schematic view of the CLAS detector setup at Jefferson Lab. The arrow indicates the beam direction. The triangular calorimeters in forward direction form the central detection device for electrons and positrons. The picture is taken from [185].

debate, again a downward mass shift of the ρ and ω mesons for nuclear targets has been reported.

At Jefferson Lab the reaction $\gamma A \to e^+e^-X$ has been measured for the first time. The g7 experiment was designed to study effects of the medium on the properties of the light vector mesons ρ, ω and ϕ. A bremsstrahlung photon beam with an energy range of roughly $E_\gamma = (0.8 - 3.5)$ GeV was sent on a target cell containing the nuclear materials ^{2}H, ^{12}C, ^{48}Ti, ^{56}Fe, and ^{208}Pb. The dilepton pairs have been measured in coincidence with the **C**EBAF **L**arge **A**cceptance **S**pectrometer (CLAS) that is shown schematically in Fig. 6.1. The unique mass resolution of this detector setup allows for an impressive identification of the free ω and ϕ peaks. As a first result a strong depletion of the ω and ϕ peaks was claimed for increasing target masses. In the shapes of the spectral distributions, however, no medium effects could be observed. Due to the lack of statistics and the missing full background simulation the results of this pioneering experiment are inconclusive. A follow-up experiment has been proposed with statistics superior to the g7 data taken in 2002. Nonetheless the results of g7 represent the first observation of the photoproduction of the light neutral vector mesons close to threshold via their rare decay into dileptons.

6.3 Dielectron spectra in γA reactions

6.3.1 Hadronic cocktail

In nuclear targets dilepton pairs can be produced from various hadronic sources. The whole of these sources are known as the *hadronic cocktail*. In particular one has to distinguish the direct $h \to l^+l^-$ decays and the Dalitz decays $h \to l^+l^- + X$. In case of a direct decay the invariant mass of the hadron can be reconstructed from the dilepton

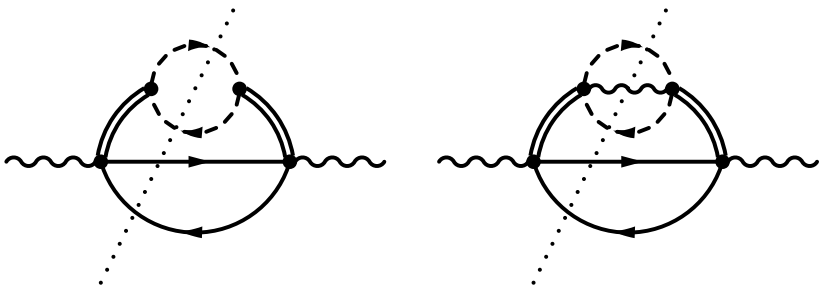

Figure 6.2: Self energy diagram corresponding to the photoproduction of the e^+e^- final state via the excitation of a vector meson and its direct $V \to e^+e^-$ decay (a) and Dalitz decay contribution (b).

four-momenta whereas the Dalitz decays contribute a broad l^+l^- background from that no information on the vector meson mass distributions can be extracted. Both types of processes are illustrated in Fig. 6.2. In order to simulate dilepton production in our Monte Carlo transport code we consider the following direct decays

$$\rho \to e^+e^- \tag{6.6}$$
$$\omega \to e^+e^- \tag{6.7}$$
$$\phi \to e^+e^-. \tag{6.8}$$

The decay rates of the vector mesons are obtained under the assumption of strict vector meson dominance. Thus, they are assumed to directly resemble the electomagnetic current-current correlator. Formulas can be found in [100]. The $V \to e^+e^-$ decay widths are proportional to $1/q^3$ where $q = (q_0, \mathbf{q})$ is the vector meson four-momentum. This proportionality comes from the product of the virtual photon propagator squared ($\sim 1/q^4$) and a phasespace factor ($\sim (q^2)^{1/2}$). In addition we consider the decay of the pseudoscalar η meson

$$\eta \to e^+e^- \tag{6.9}$$

which is assumed to be infinitely narrow, thus its e^+e^- width is taken to be constant. Theoretically, this width has been estimated to be roughly $\Gamma_{\eta\to e^+e^-} \simeq 2.7 \cdot 10^{-6}$ eV [190, 191]. Experimentally, however, the upper limit has been determined to be $\Gamma_{\eta\to e^+e^-} = 9.09 \cdot 10^{-2}$ eV [141, 191] with a 90% confidence level. We include it in our calculations according to this upper limit in order to estimate its effect on the dilepton spectra. For the Dalitz decays we include

$$\Delta \to e^+e^-N \tag{6.10}$$
$$\pi^0 \to e^+e^-\gamma \tag{6.11}$$
$$\eta \to e^+e^-\gamma \tag{6.12}$$
$$\omega \to e^+e^-\pi^0. \tag{6.13}$$

Parameterizations for the Dalitz decay widths can be found in [100]. Potentially the

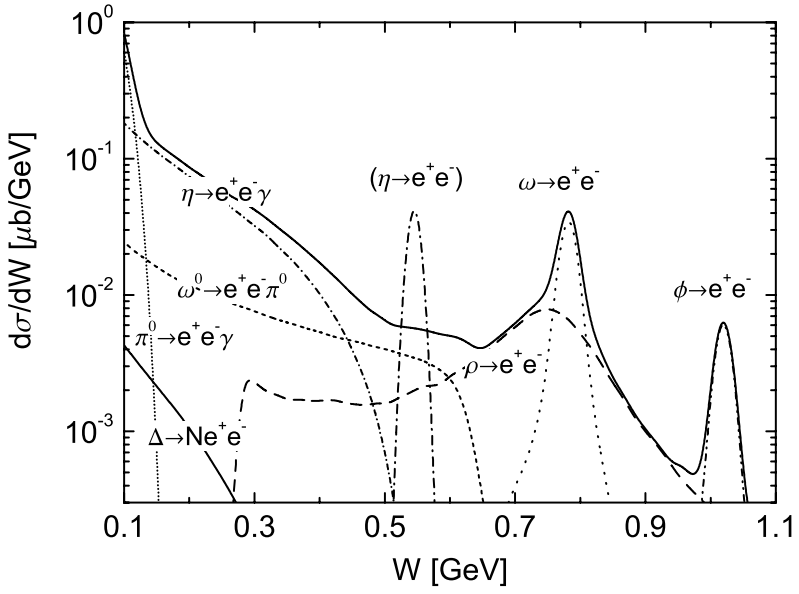

Figure 6.3: Dilepton invariant mass spectrum from proton target at $E_\gamma = 2.5$ GeV. *Solid line*: total yield (without $\eta \to e^+e^-$ decay), *others*: individual contributions, see labels. The spectra are convoluted with an experimental resolution of $\Delta W = 10$ MeV. The contribution of the $\eta \to e^+e^-$ decay corresopnds to the experimental upper limit for the $\eta \to e^+e^-$ width.

Dalitz decays of higher baryon resonances could also generate sizable contributions to the dilepton spectrum. In particular, they could give rise to an accumulation of some spectral strength at low dilepton masses, an issue that should be subject to future investigations.

For the case of a free proton target the contributions to the e^+e^- yield from the individual vector meson components are given by

$$\frac{d\sigma}{dW} = \sigma_{\gamma N \to VX}(s) 2W \mathcal{A}_V(W) \frac{\Gamma_{V \to e^+e^-}}{\Gamma_V} \tag{6.14}$$

where W is the vector meson invariant mass and $\sigma_{\gamma N \to VX}(s)$ is the total inclusive vector meson photoproduction cross section at invariant energy squared $s = m_N^2 + 2m_N E_\gamma$. In vacuum, the vector meson spectral function depends on one suitable energy variable only. It can be parameterized by

$$\mathcal{A}_V(W) = \frac{W}{\pi} \frac{\Gamma_V(W)}{(W^2 - m_V^2)^2 + W^2 \Gamma_V(W)^2} \tag{6.15}$$

with the vector meson pole mass m_V and the total vector meson width Γ_V. The spectral function can be interpreted as a probability distribution which determines the probability to find a particular particle with mass $W = \sqrt{q^2}$ where $q = (q_0, \mathbf{q})$ is its four-momentum. The analytical form of (6.15) is motivated by the relation of spectral function and prop-

agator:

$$\mathcal{A}_V(q) = -\frac{1}{\pi}\mathcal{I}\mathrm{m}D_V(q) = -\frac{1}{\pi}\mathcal{I}\mathrm{m}\frac{1}{q^2 - m_V^2 - i\sqrt{q^2}\Gamma_V(q)}. \tag{6.16}$$

Due to the analytical properties of the propagator, the spectral function has to fullfill the normalization condition [66]

$$1 \equiv \int dq^2 \mathcal{A}_V(q). \tag{6.17}$$

In the above expressions we have neglected the spin structure of propagator and spectral function. In addition, the real part of the vector meson self energy has been ignored. Note, that in the latter Equations we have expressed the spectral function as a function of the vector meson four-momentum q. This is more general since in particular at finite density the spectral function depends on both energy and momentum independently. This will be detailed more precisely in Chapter 8.

The Dalitz decay contributions to the dilepton yield are given by

$$\frac{d\sigma}{dW} = \int dW_Q^2 \mathcal{A}_Q(W_Q)\frac{1}{\Gamma_Q}\frac{d\Gamma_{Q\to e^+e^-X}}{dW}\sigma_{\gamma N\to QX}(s) \tag{6.18}$$

where $\mathcal{A}_Q$ is the spectral function of the hadronic source Q and Γ_Q is its total width. The spectral function $\mathcal{A}_Q$ is given by an expression similar to (6.15). $d\Gamma_{Q\to e^+e^-X}/dW$ is the differential partial Dalitz decay width of the source Q into dileptons with invariant mass W. Explicit expressions for these decay widths and parametrizations of the photon nucleon cross sections can be found in [100].

The sum of the dielectron sources given above as obtained from a Monte Carlo simulation is shown in Fig. 6.3 for an elementary γp collision at $E_\gamma = 2.5$ GeV. Whereas the Dalitz decays generate a broad background that is dominant at small dilepton masses below $W = 500$ MeV, the η, ω and ϕ peaks clearly stick out of the spectrum. The ρ, however, has a very broad shape already in vacuum that is almost hidden below the ω meson. In the summed spectrum the ρ and ω components can hardly be isolated.

6.3.2 Dilepton radiation from ρ mesons

The strong dependence of the vector meson decay widths on the invariant mass (squared) q^2 distorts their spectral shapes as measured from the e^+e^- distribution. This can be seen nicely in Fig. 6.3 for the case of the $\rho \to e^+e^-$ component. Since experimental analyses frequently undervalue this effect, we demonstrate it for the particular example of the ρ decay. Similar considerations also hold for the other vector meson decay channels. The invariant mass (squared) differential dielectron rate is given by

$$\frac{dR_{e^+e^-}}{dq^2}(q) \simeq \mathcal{A}_\rho(q_0, \mathbf{q})\frac{\Gamma_{\rho\to e^+e^-}(q^2)}{\Gamma_{\mathrm{tot}}(q^2)}, \tag{6.19}$$

where $\mathcal{A}_\rho$ is the ρ spectral function. For simplicity we consider no medium modifications here and, thus, the spectral function depends on q_0 or $W = \sqrt{q_0^2 - \mathbf{q}^2}$, respectively, only.

It is given by Eq. (6.15). The total width $\Gamma_{\rm tot}(W)$ is given by the sum over the hadronic and electromagnetic ρ meson self energies

$$\Gamma_{\rm tot}(W) = \Gamma_{\rm had}(W) + \Gamma_{\rm em}(W) \approx \Gamma_{\rho\to\pi\pi}(W) + \Gamma_{\rho\to e^+e^-}(W). \tag{6.20}$$

These widths are given by

$$\Gamma_{\rho\to\pi\pi}(W) = \frac{f_\rho^2}{48\pi} W \left[1 - 4\left(\frac{m_\pi}{W}\right)^2\right]^{\frac{3}{2}} \Theta(W - 2m_\pi) \tag{6.21}$$

$$\Gamma_{\rho\to e^+e^-}(W) = C_\rho \frac{m_\rho^4}{W^3} \tag{6.22}$$

with $f_\rho = 6.14$ and $C_\rho = 8.814 \cdot 10^{-6}$ and m_π and m_ρ are the π and ρ vacuum masses. We study two limiting cases:

1. $\underline{W \to 0}$:

$$\frac{dR_{e^+e^-}}{dW}(W) = 2W \frac{dR_{e^+e^-}}{dq^2}(W = \sqrt{q_0^2 - \mathbf{q}^2}) \tag{6.23}$$

$$= \frac{2C_\rho m_\rho^4}{\pi} \frac{1}{W\left((W^2 - m_\rho^2)^2 + W^2\Gamma_{\rm tot}(W)^2\right)} \tag{6.24}$$

$$\overset{\Gamma\to 0}{=} \frac{2C_\rho m_\rho^4}{\pi} \frac{1}{W\left(W^2 - m_\rho^2\right)^2} \tag{6.25}$$

$$\overset{W\ll m_\rho}{=} \frac{2C_\rho}{\pi}\frac{1}{W} \tag{6.26}$$

That is, for low invariant masses the dielectron rate is proportional to $1/W$. Note that in Fig. 6.3 the $\rho \to e^+e^-$ spectrum only starts at $q^2 = 4m_\pi^2$. This is due to a cutoff of the vacuum ρ spectral function in our Monte Carlo code due to purely numerical reasons. For ρ masses below two times the pion mass the population probability becomes too small for a probabilistic simulation.

2. $\underline{W \to m_\rho}$:

In the vicinity of the free ρ meson mass the dielectron rate is characterized by the position and width of the ρ meson peak. In order to simplify our considerations we neglect the small pion masses in the expression for the total ρ width. We set $\Gamma_{\rm tot}(W) = \gamma W$. The parameter γ can be determined at the on-shell point via $\gamma = \Gamma_0/m_\rho \simeq 0.2$ with $\Gamma_0 = \Gamma_{\rm tot}(m_\rho)$. The position of the peak is determined by a zero of the first derivative of the denominator of the dilepton rate. The derivative is given by

$$\frac{dN}{dW} = (W^2 - m_\rho^2)^2 + \gamma^2 W^4 + W\left[4W(W^2 + m_\rho^2) + \gamma^2 W^4\right]$$

$$\overset{W^2=s}{=} 5(1+\gamma^2)s^2 - 6m^2 s + m^4 \overset{!}{=} 0. \tag{6.27}$$

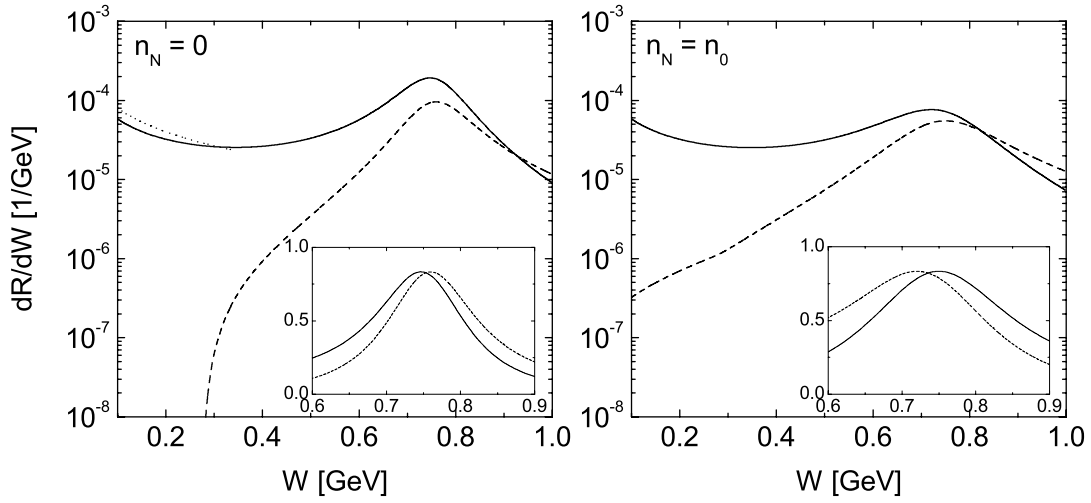

Figure 6.4: Dilepton yield from the ρ meson (solid line) and ρ spectral function (dashed line) with arbitrary normalization. The dotted line (left panel) is $\sim 1/W$ and is also normalized arbitrarily. The insert shows a magnification of the peak region on a linear scale. *Left*: vacuum ρ properties, *right*: with collisional broadening at $n_N = n_0$.

With the abbreviation $\beta^2 = (1+\gamma^2)^{-1}$ the relevant solution to this Equation can be written as

$$s_0 = \frac{3}{5}\beta^2 m_\rho^2 + \sqrt{\left(\frac{3}{5}\beta^2 m_\rho^2\right)^2 - \frac{1}{5}\beta^2 m^4} \tag{6.28}$$

$$= \frac{3}{5}\beta^2 m_\rho^2 \left[1 + \frac{2}{3}\sqrt{1 - \frac{5}{4}\gamma^2}\right] \tag{6.29}$$

$$\simeq \beta^2 m_\rho^2 = \frac{m_\rho^4}{m_\rho^2 + \Gamma_0^2} \tag{6.30}$$

and, thus, the peak of the dilepton rate is shifted with respect to the free vector meson mass by

$$\delta W = m_\rho \left(1 + \frac{\Gamma_0^2}{m_\rho^2}\right)^{-1/2} - m_\rho \simeq -\frac{\Gamma_0^2}{2m_\rho}. \tag{6.31}$$

The second solution to the quadratic Equation (6.27) determines the position of a maximum of the denominator, it gives the position of the minimum of the dilepton rate in the transition region between the ρ pole and the low-energy $1/W$ increase. If we plug in numbers ($m_\rho = 770$ MeV, $\Gamma_0 = 150$ MeV) in Eq. (6.31) we find the actual position of the local maximum of the dilepton rate at $W = 755$ MeV.

We have seen that even the vacuum dilepton mass distribution does not resemble the ρ vacuum spectral function. In particular the peak of the e^+e^- mass distribution does not coincide with the free ρ pole mass. This is visualized in the left panel of Fig. 6.4 where the

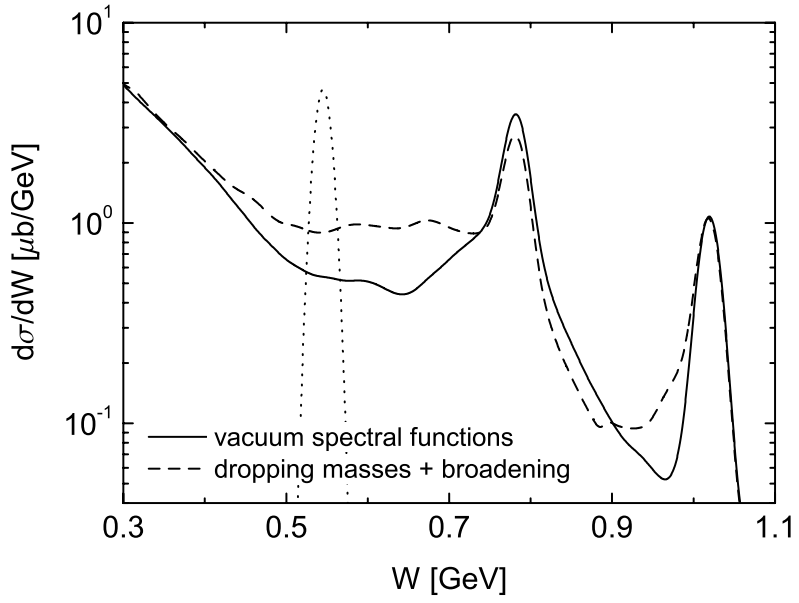

Figure 6.5: Dielectron invariant mass spectrum from lead target at $E_\gamma = 2.5$ GeV. The events are convoluted with a mass resolution of 10 MeV. *Solid line*: without medium modifications, *dashed line*: with dropping masses and collisional broadening, *dotted line*: upper limit for the contribution of the $\eta \to e^+e^-$ decay.

free ρ spectral function and the corresponding dilepton yield without any approximations is shown. Only after dividing out the corresponding decay width the genuine ρ spectrum can be recurred. This also shows a complication in the determination of in-medium masses since also the total and partial decay widths can be modified due to the presence of the medium. The effect of a collisional width which enters both the spectral function and the $\rho \to e^+e^-$ branching ratio is demonstrated in the right panel of Fig. 6.4. Here, we have used the phenomenological ρ collision width of $\Gamma_{\rm coll} = 100$ MeV n_N/n_0 independent of the ρ invariant mass. Changes of the in-medium branching ratios will be discussed in more detail for the case of the ω meson in Chapter 9. Due to the density dependent medium modifications the separation of spectral function and decay width is not longer possible and the bare properties of the vector meson cannot be extracted. However, without treating properly the vector meson partial decay widths, no in-medium modifications of the spectral shapes as compared to the vacuum situation can be confirmed.

6.3.3 Effects of the medium

The ultimate question is if the invariant mass distributions measured from nuclear targets are sensitive to in-medium changes of the vector meson spectral functions. Such changes can be realized by a broadening of the in-medium spectral distributions as well as shifts of the peak or even the creation of additional bumps caused by collective resonance-hole excitations, see also Chapter 2 and Chapter 8 in the following. In Fig. 6.5 we show the

result of a Monte Carlo simulation of the reaction $\gamma + \mathrm{Pb} \to e^+e^- + X$ at $E_\gamma = 2.5$ GeV using the semiclassical BUU model, see Appendix A. The in-medium contributions to the dilepton yield are given by similar expression as (6.14) and (6.18). However, for the case of finite nuclear targets the time evolution of the reaction has to be considered explicitely respecting the time dependence of the particle densities and the density dependence of the spectral functions. More details on the treatment of dilepton production within the BUU model can be found in Refs. [100, 159].

Fig. 6.5 shows two different curves, namely one without any medium modifications and one with a typical scenario of in-medium changes. In the latter case the vector meson spectral functions are broadened in the medium due to vector meson nucleon collisions. The broadening is calculated by means of the low density theorem

$$\Gamma_{\mathrm{coll}} = n_N \langle v_{\mathrm{rel}} \sigma_{VN} \rangle \tag{6.32}$$

where n_N is the nuclear density, v_{rel} is the vector meson nucleon relative velocity, and σ_{VN} is the total vector meson nucleon cross section. This cross section also enters the BUU collision term and, thus, consistency of the collision rates and the broadening is guaranteed. The brackets indicate an average over the nucleon momentum distribution. A formal derivation of this formula will be given in Chapter 8 and the resulting collision widths for the ω and ϕ mesons will be discussed in Chapters 7 and 9. A typical feature of a collision width calculated according to (6.32) is a linear rise with increasing three-momentum because of the proportionality to the relative velocity v_{rel}. This, however, is in particular not the case for the ρ meson since nucleon resonances play an important role in the ρN scattering process which strongly influence the energy dependence of σ_{VN}. The collision width of the ρ meson has been calculated in Ref. [100] and is shown there in Fig. 6.1. For on-shell ($q^2 = m_V^2$) vector mesons at rest ($\mathbf{q} = 0$) we find collision widths of 100 MeV for the ρ, 37 MeV for the ω, and 18 MeV for the ϕ meson. Note, that the previously discussed change of the in-medium branching ratios is automatically contained in the BUU simulation by means of the collison term. This issue is discussed briefly in Appendix A.4. In addition we include dropping vector meson masses which scale linearly with the nuclear density according to the widely used scaling law $m_V^* = m_V^o(1-0.16\,n_N/n_0)$. A detailed discussion of such effects will follow in the later Chapters. The dynamical treatment of density and momentum dependent spectral functions in the transport approach is introduced briefly in Appendix A and in some more detail in Refs. [39, 100, 159].

We observe substantial effects generated by the in-medium change of the vector meson spectral functions. These are most pronounced in the intermediate mass region 550 MeV $< W <$ 750 MeV. Between the η and ω peaks we find a strong enhancement of the mass spectrum due to the smaller ρ and ω masses in the medium. Since the in-medium strength is shifted away from the ω pole mass, we observe a substantial depletion of the ω peak. This effect has also been seen – albeit much stronger – in the preliminary analysis of the g7 experiment. The modifications of the ϕ meson are significant on a level that will hardly be observable in experiment due to the extremely small cross section. The intermediate mass dilepton enhancement is generated by the composite ρ and ω sources and thus does not provide individual information in the isoscalar and isovector channels. The contribution of the $\eta \to e^+e^-$ decay shown in Fig. 6.5 corresponds to the

experimental upper limit for the $\eta \to e^+e^-$ decay width. The non-existence of this peak in experimental dilepton spectra can, thus, impose a new more severe constraint on this decay mode.

6.4 The e^+e^- final state

Even the detection of the weakly interacting e^+e^- final state is not a priori without problems. In this short Section we discuss some particular questions that arise in this context and argue why these effects do not hamper the observation of in-medium changes.

6.4.1 Combinatorial background

Typical dilepton experiments are carried out at energies of several GeV. The g7 Experiment at Jefferson Lab has been performed with a photon beam of up to 3.5 GeV energy. Thus, not only exclusive final states but a bunch of hadrons can be produced in one single γA reaction. In particular vector meson production at GeV energies is accompanied by multi pion emission via resonance excitations like $\gamma N \to V\Delta \to V\pi N$ and final state interactions. Consequently not only one single e^+e^- pair can be produced but several pairs emerge from the same elementary interaction. However, the $V \to e^+e^-$ branching ratios are extremely small. Whereas the genuine vector meson contributions to the dilepton spectrum are proportional to this branching ratio, off-diagonal background terms are proportional to the branching ratio squared (if we consider, for simplicity, the combinatorial background from the production of two vector mesons of the same kind). This is obvious as both vector mesons have to decay to the e^+e^- final state in order to be visible in the detector. Consequently this contribution is suppressed by another four to five orders of magnitude. Of course the situation can be more involved for hadronic decay modes that typically have larger branching ratios.

6.4.2 Coulomb distortion

The particular advantage of the $V \to e^+e^-$ decay mode is the absence of any hadronic final state interactions that distort the e^+e^- invariant mass spectrum. However, since the leptons carry electrical charge they couple to the static electromagnetic field of the target nucleus. Thus, they propagate not on straight lines but on twisted Coulomb trajectories. In Chapter 4 we have encountered quite substantial effects on the observables generated by the EM interaction of charged pions and the static nucleus. The aim of this paragraph is to estimate the effect of Coulomb distortion on the dilepton invariant mass.

The invariant mass squared of the dilepton pair is given by

$$\begin{aligned} s \;=\; W^2 \;&=\; (p_+ + p_-)^2 \\ &\overset{m_e \ll |\mathbf{p}|}{\approx} (|\mathbf{p}_+| + |\mathbf{p}_-|)^2 - |\mathbf{p}_+|^2 - |\mathbf{p}_-|^2 - 2\mathbf{p}_+ \cdot \mathbf{p}_- \\ &=\; 2|\mathbf{p}_+||\mathbf{p}_-|(1 - \cos\theta) \end{aligned} \tag{6.33}$$

If the pair propagates from the interior of a nucleus with Coulomb Potential V_C to the vacuum $V_C = 0$ the change of the momenta is approximately given by

$$|\mathbf{p}_+^\infty| = |\mathbf{p}_+| + \Delta p \tag{6.34}$$
$$|\mathbf{p}_-^\infty| = |\mathbf{p}_-| - \Delta p \tag{6.35}$$
$$\Delta p \approx V_C. \tag{6.36}$$

If the dielectron pair is created from a vector meson decaying at rest, the initial momenta of e^+ and e^- are the same ($|\mathbf{p}_+| = |\mathbf{p}_-| = p$). If, in addition, they are created close to the center of a spherically symmetric nucleus (in the high density region one is interested in) one can neglect the bending of their trajectories due to the non-zero potential gradients. Note that here also the potential is deepest and, thus, the change of the momenta becomes maximal. Under these assumptions we find for the invariant mass squared of the pair in vacuum

$$s_\infty = 2(p^2 - (\Delta p)^2)(1 - \cos\theta). \tag{6.37}$$

The change of the invariant mass of a dilepton pair that has been generated from the decay of a vector meson of mass m_V at rest is

$$\Delta W = W_\infty - W \tag{6.38}$$
$$\approx \frac{s_\infty - s}{2m_V} \tag{6.39}$$
$$\approx \frac{2(\Delta p)^2}{2m_V}(1 - \cos\theta) \tag{6.40}$$
$$\leq 2\frac{(\Delta p)^2}{m_V} \tag{6.41}$$

If we insert typical numbers ($V_C = 20$ MeV, $m_V = 770$ MeV) we find

$$\Delta W \leq 1 \text{ MeV}. \tag{6.42}$$

This is indeed a very small number as compared to the vector meson vacuum masses and widths. Moreover, the experimental resolutions that can be obtained with present detector setups typically exceed $\mathcal{O}(10$ MeV). Thus, the effect of Coulomb distortion on the dilepton mass spectra can safely be neglected. This statement, however, is not universal and depends on the masses and energies of the final state particles. Therefore similar considerations have to be done for each experimental situation. If hadronic final states are observed, strong interaction potentials have to be considered in addition that anyhow could lead to a substantial distortion of the invariant mass spectra.

6.4.3 Bethe-Heitler process

There is also a purely electromagnetic process that produces the same e^+e^- final state as the hadronic $h \to e^+e^- + X$ decays. Since in the detector both contributions cannot be distinguished from each other they interfere. This electromagnetic process consists of the conversion of the incoming photon to a real and a virtual lepton followed by

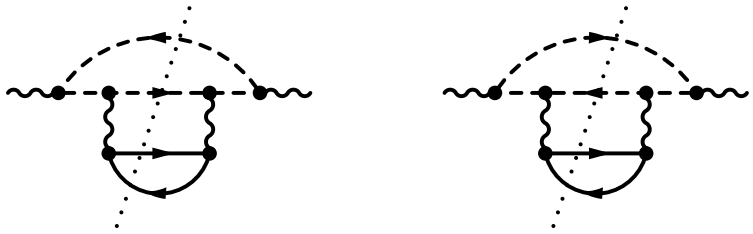

Figure 6.6: Feynman diagrams for the Bethe-Heitler process in terms of the l^+l^-Nh self energy of the photon. *Dashed lines*: leptons, *solid lines*: nucleons.

the exchange of a virtual photon with a nucleon from the target nucleus that puts the virtual lepton on its mass shell. This is shown in Fig. 6.6. In this scattering process the nucleon can be split into its strongly interacting components and several hadrons can be produced. This process is known as the Bethe-Heitler process. For the case at hand only the elastic contribution is relevant what means that the hadronic final state again consists of a nucleon in its ground state only. The pair production process accompanied by the excitation of the target is greatly suppressed for kinematical reasons and therefore negligible. Apart from this incoherent reaction also a coherent Bethe-Heitler process is possible. In this case the virtual photon couples to the entire charge of the target nucleus. This contribution, however, can easily be suppressed by an appropriate missing mass cut and, thus, does not spoil the investigation of the vector meson components in the dielectron spectrum [100, 159].

The Bethe-Heitler contribution to the $\gamma + A \to e^+e^- + X$ has been studied already in [159] and more recently in [192] where also formulas and a comprehensive derivation can be found. The latter results slightly deviate from the previous ones. We speculate that this disagreement is due to numerical reasons because of the large variations in the integrated matrix element. However, the results obtained in [192] agree with the results presented here that have been obtained independently and, thus, give us confidence that our evaluation of the Bethe-Heitler cross section is correct. The Bethe-Heitler matrix element is proportional to the intermediate electron (positron) propagator

$$((k-p)^2 - m_e^2)^{-1} = -(2k \cdot p)^{-1}, \tag{6.43}$$

where k is the four-momentum of the incoming photon and p is the four-momentum of the positron (electron). Thus, a lower cut on the product $k \cdot p$ can effectively suppress the Bethe-Heitler contribution. Moreover, the product $k \cdot p$ is small if the lepton three-momentum $\mathbf{p}$ is directed to forward angles. The CLAS detector, shown schematically in Fig. 6.1, that forms the central part of the g7 experimental setup, actually has a hole in forward direction. Therefore the Bethe-Heitler contribution anyway should be small for this particular experiment. However, the admixture of Bethe-Heitler events in the data sample has to be studied thoroughly in order to fully understand the detected backgrounds. In Fig. 6.7 the Bethe-Heitler contribution is compared to the hadronic cocktail for $E_\gamma = 2.5$ GeV. The effects of Fermi motion, Pauli blocking and a cut of $k \cdot p > 0.1$ GeV^2 are shown. In fact, the Bethe-Heitler cross section still is sizable in the region where interesting phenomena are expected. Thus, this contribution has to

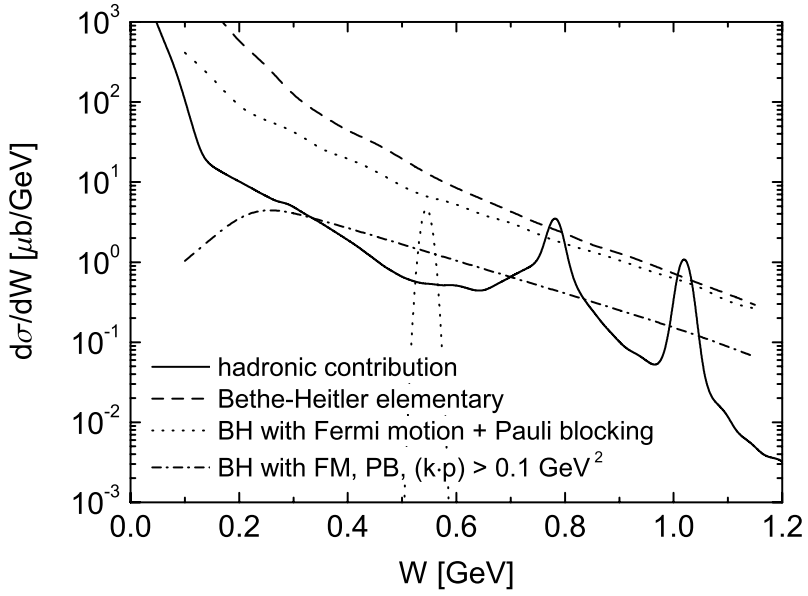

Figure 6.7: Bethe-Heitler (BH) contribution to the dilepton invariant mass spectrum at $E_\gamma = 2.5$ GeV. *Solid line*: Hadronic cocktail, *dashed line*: Bethe-Heitler contribution from 208 independent free nucleons, *dotted line*: incoherent Bethe-Heitler contribution from lead target including the effects of Fermi motion (FM) and Pauli blocking (PB), *dash-dotted line*: the same as before but with the cut $k \cdot p > 0.1$ GeV^2. The upper limit for the $\eta \to e^+e^-$ contribution is also shown.

be considered carefully in the analysis of dilepton data. The genuine hadronic dilepton sources are almost unaffected by the cut on the intermediate lepton propagator as was shown already in [100, 159]. Even larger cutoff values are possible without losing much information in order to further suppress the Bethe-Heitler contribution.

6.5 Physics impact

From the considerations presented here we have seen that the reaction $\gamma + A \to e^+e^- + X$ can indeed yield information on the vector meson in-medium spectral distributions. Neither strong nor electromagnetic final state interactions hamper the observation of the e^+e^- invariant mass distributions generated from in-medium vector meson decays. Typical nuclear background sources either are small anyway or can be suppressed by appropriate kinematic cuts. However, mandatory conditions for the observation of any in-medium changes are the possibility to detect dilepton pairs with small total three momenta and a complete understanding of the residual background. Together with complementary information from hadron induced πA and pA reactions and heavy-ion experiments presumably different scenarios of medium modifications can be discriminated. What these information tell about in-medium QCD will be subject to the following short overview.

6.5.1 Vector mesons and QCD

The ultimate goal of all theoretical and experimental effort undertaken to investigate the behavior of hadrons in nuclear media is to explore the phase structure of the underlying theory of strong interactions. At the same time where quarks and gluons are liberated – or deconfined – from their hadronic compounds the quarks are expected to loose their constituent masses leading to the restoration of chiral symmetry that is spontaneously broken in the QCD vacuum. Note that both phase boundaries, i. e. the transition from the chirally broken to the restored phase and the hadron-quark gluon plasma transition, only incidentally appear to coincide[1]. Their equivalence, however, is strongly suggested by QCD lattice calculations. Once the quarks have lost their masses, left and right handed quarks decouple (in the sense that they are described by *independent* fermion fields) leading to a degeneracy of hadronic states (the concept of hadrons might, however, be useless if the quarks indeed have entered a deconfined phase) with opposite parity. The non-existence of such parity doublets in vacuum is one of the major clues that chiral symmetry is spontaneously broken there, see also Chapter 2. From the degeneracy in the chirally symmetric phase it follows that at the phase boundary the vector and axial vector current-current correlators must become identical. This could be realized by either a mixing of the vector and axial vector channels, a modification of the individual spectral shapes or an admixture of both possibilities.

The QCD sum rule approach aims at a connection of hadronic spectral functions with a QCD expansion of the current-current correlator in terms of quark and gluon condensates. Originally it was introduced for the vacuum but later on generalized to in-medium situations. By means of an operator product expansion the current-current correlator can be related to a series of various condensates such as $\langle\bar{q}q\rangle$, $\langle G^2\rangle$ or $\langle(\bar{q}q)^2\rangle$. Of particular interest is the relation to the two-quark condensate $\langle\bar{q}q\rangle$ that has the role of an order parameter that measures the strength of the chiral symmetry breaking. It is closely related to the pion decay constant by the Gell-Mann-Oakes-Renner relation (2.35). Taking an average $\bar{m} = \frac{1}{2}(m_u + m_d) = 6$ MeV yields a vacuum value for the quark condensate of $\langle\bar{q}q\rangle = -(240\text{ MeV})^3$. Concerning vector mesons it turned out that their in-medium changes are not directly related to changes of the two-quark condensate, but to specific moments of the nucleon structure function and to changes of the four-quark condensate. The authors of [20, 21] have proposed a quite stringent connection of the in-medium ω spectrum and the density dependence of the four-quark condensate. More recently a new type of sum rule has been established [23] that, in contrast to the earlier approaches, relates only in-medium hadronic and partonic information and is essentially free of the problem how to determine a reliable Borel window – a mass scale that is introduced in order to improve the convergence of the involved dispersion integrals. The authors of [23, 193] have shown that QCD sum rules cannot determine the spectral shape of vector mesons but rather constrain or correlate specific parameters of a given hadronic model. Turning this argumentation around the measurement of modified vector meson spectra in the medium can give important information on the density and temperature dependence of certain two- and four-quark condensates.

First investigations of in-medium vector mesons within the framework of QCD sum

[1] This issue, however, is not settled as yet.

rules have been done in [9]. There the vector mesons where assumed to remain infinitely narrow and also possible additional structures in the spectral function where disregarded. These crude approximations resulted in the conjunction that the vector meson in-medium masses drop drastically. Moreover, the authors of [9] found identical results for ρ and ω mesons since the Landau-damping contribution – the depletion of the genuine vector meson branch due to the shift of strength to the space-like region generated by the collective excitation of nucleon-holes – was underestimated by a factor of nine for the case of the ω meson. An expansion up to linear order in density and factorization of the four-quark condensate resulted in a direct conjunction of the in-medium chiral condensate and the vector meson masses. From a completely different point of view the vector meson in-medium masses were addressed at around the same time by the authors of [8]. Based on quite general scaling arguments an approximate link of the in-medium condensates and the vector meson mass was proposed

$$\left(\frac{m_V^*}{m_V}\right)^3 = \frac{\langle\bar{q}q\rangle_\rho}{\langle\bar{q}q\rangle_0}. \tag{6.44}$$

Albeit both approaches are based on assumptions that have proven to be not well justified, these results have triggered most of the theoretical and experimental interest in the field. Dilepton spectroscopy in heavy-ion experiments has mainly been stimulated by the hypothesis of dropping vector meson masses in nuclear media as a signal for the partial restoration of chiral symmetry.

6.5.2 In-medium condensates

In the vacuum quarks and gluons condense giving rise to non-vanishing vacuum expectation values for the condensates $\langle\bar{q}q\rangle$ and $\langle G^2\rangle$. A precise definition of the two-quark or *chiral* condensate can be given in terms of the quark propagator

$$\langle\bar{q}q\rangle = -\lim_{y\to x^+} \mathrm{Tr}\langle 0|\mathcal{T}q(x)\bar{q}(y)|0\rangle \tag{6.45}$$

where $\mathcal{T}$ indicates the time-ordered product. In the vacuum the scalar quark condensate mixes right and left handed quarks. Thus, the nonzero value of this quark operator product indicates that chiral symmetry is spontaneously broken in the QCD vacuum.

Now the question arises how this condensate changes as the nuclear density increases. Since the condensate has the role of an order parameter of the symmetry breaking mechanism, a reduced value of the condensate can be regarded as a signal for the starting restoration of this symmetry. In the following derivation we basically follow [62]. In order to obtain an estimate for the density-dependence of the two-quark condensate one starts from the chirally symmetric QCD Hamiltonian and considers the symmetry breaking quark mass terms as a perturbation

$$\mathcal{H}_{QCD} = \mathcal{H}^{(0)}_{QCD} + m_q(\bar{u}u + \bar{d}d). \tag{6.46}$$

Here we have neglected the small difference in the light quark masses $m_u = m_d \equiv m_q$ (which, however, is as large as the quark masses themeselves). Using the Hellmann-Feynman theorem [62] one finds a relation between the expectation value of the quark

condensates and the energy density

$$\langle\psi|\bar{u}u + \bar{d}d|\psi\rangle = \frac{d\epsilon_\psi}{dm_q} \tag{6.47}$$

where ψ is an eigenstate of the QCD Hamiltonian and ϵ_ψ is the corresponding energy density. Examples for such eigenstates are the QCD vacuum or nuclear matter at density n_N. Using the GOR relation (2.35) and $\langle\bar{u}u\rangle = \langle\bar{d}d\rangle \equiv \langle\bar{q}q\rangle$ the above equation can be recast in the following form

$$\frac{\langle\bar{q}q\rangle}{\langle\bar{q}q\rangle_0} = 1 - \frac{m_q}{m_\pi^2 f_\pi^2}\frac{\partial}{\partial m_q}(\epsilon - \epsilon_0). \tag{6.48}$$

Thus, the density-dependence of the quark condensate is given by the variation of the energy density with the current quark mass. If we consider nuclear matter as a non-interacting nucleon gas, the energy density relative to the QCD vacuum is given by

$$\epsilon - \epsilon_0 = 4 \int\limits_{|\mathbf{p}|<p_f} \frac{d^3p}{(2\pi)^3}\sqrt{\mathbf{p}^2 + m_N^2} \tag{6.49}$$

where p_f denotes the nucleon Fermi momentum. For the derivative with respect to the quark mass we find

$$m_q\frac{\partial}{\partial m_q}(\epsilon - \epsilon_0) = \underbrace{4 \int\limits_{|\mathbf{p}|<p_f} \frac{d^3p}{(2\pi)^3}\frac{m_N}{\sqrt{\mathbf{p}^2 + m_N^2}}}_{\rho_s} \underbrace{\left(m_q\frac{\partial m_N}{\partial m_q}\right)}_{\Sigma_{\pi N}}. \tag{6.50}$$

The latter term is equal to the pion-nucleon sigma term. It measures the contribution from explicit chiral symmetry breaking to the nucleon mass m_N. The sigma term can be deduced from experimental data on low-energy pion-nucleon scattering using e. g. the linear σ model or chiral perturbation theory in order to relate it to measurable quantities. Its empirical value is $\Sigma_{\pi N} \simeq 45$ MeV. The first term in (6.50) is equal to the scalar nucleon density ρ_s. For small nucleon densities ($|\mathbf{p}| \ll m_N$) it can be approximated by the zeroth component of the nucleon current $\rho_s \simeq n_N$. Finally we obtain the leading order result for the density-dependence of the two-quark condensate:

$$\frac{\langle\bar{q}q\rangle_\rho}{\langle\bar{q}q\rangle_0} = 1 - \frac{\Sigma_{\pi N}}{m_\pi^2 f_\pi^2}n_N. \tag{6.51}$$

Thus, at normal nuclear matter density the condensate is reduced as compared to its vacuum value by roughly 1/3. Note, that we have neglected the effects of the nuclear interaction energy. It has been included in various more elaborate approaches, see e. g. [1, 2, 4]. However, its impact becomes important only at nuclear densities which exceed normal nuclear matter density. Then also the low-density approximation $\rho_s = n_N$ breaks down. The astonishing fact about this simple derivation is the fact that the terms in the Hamiltonian due to *explicit* chiral symmetry breaking are exploited in order to estimate the effects of *spontaneous* chiral symmetry breaking. The parameter of explicit chiral symmetry breaking – the current quark mass m_q – appears as a coupling constant in the Hamiltonian in front of the symmetry breaking term $\bar{q}q$. The strong interaction energy density given by the expectation value of the Hamiltonian in the chirally broken phase, however, is dictated mainly by the spontaneous breakdown of the symmetry that becomes evident in the finite expectation value of $\langle\bar{q}q\rangle$.

6.5.3 Conclusion

In the previous paragraph we have seen that the chiral quark condensate drops in the center of ordinary nuclei by roughly 1/3. This drop is connected with at least partial restoration of chiral symmetry in nuclei. The dropping quark condensate has the consequence that the mass distributions of the vector mesons are modified in the medium. Albeit this conjunction is not as direct as implied by the pioneering results of [8, 9] a modification of the spectral functions connected with in-medium condensates is also seen in recent more elaborate approaches. Dilepton spectroscopy has proven to be a useful tool to investigate vector meson mass spectra in nuclei. Not only heavy-ion experiments but also nuclear production experiments with elementary projectiles as the photon can yield important in-medium information. However, the dilepton channel offers no possibility to isolate the individual vector meson components. Therefore, dilepton experiments have to be accompanied by the investigation of hadronic and semi-hadronic decay modes. Only the entirety of such experiments can eventually determine the degree of chiral symmetry breaking at finite baryon density and temperature.

Chapter 7

The reaction $\gamma A \longrightarrow \phi X$

7.1 Introduction

The properties of the ρ and ω mesons and possible experimental signatures for their changes in nuclear media have been thoroughly studied in the literature, see Chapters 6, 8 and 9 or [184] for a review. Comparatively, the ϕ meson has received much less attention. Nevertheless, the ϕ meson turns out to be an extremely interesting probe since it exhibits a very sharp resonance structure in vacuum that a priori allows to determine smallest deviations of its spectral shape in the medium from the situation in free space. Moreover, the ϕ meson properties are strongly correlated to the renormalization of kaons and antikaons in the nuclear medium, a subject that attracts much interest by itself [194, 195, 196, 197, 198, 199].

The changes of the ϕ properties in a medium with finite density or temperature have been studied with approaches as effective Lagrangians and QCD sum rules [200, 201, 202, 203, 204]. As a general picture these studies find a quite small shift of the ϕ pole mass but a sizable renormalization of its width as temperature or density increase. Particular numbers for these changes are a width of $\delta\Gamma = 28$ MeV and a mass shift of $\delta m = -6$ MeV found in [203, 204] and $\delta\Gamma = 40$ MeV and $\delta m = -10$ MeV obtained in [200, 201]. These calculations have been performed for ϕ mesons at rest with respect to cold nuclear matter at saturation density $n_N = 0.16$ fm^{-3}. Compared to the free ϕ width of only 4.4 MeV [141], the important feature is that the width of the ϕ meson in nuclei increases substantially by up to one order of magnitude.

In the following Chapter we investigate a means to study the ϕ in-medium properties via photoproduction from nuclear targets at energies close to the reaction threshold. First we discuss the possibility to directly observe the spectral shape of the ϕ meson via a measurement of the invariant mass spectrum of its most important decay products, namely K^+K^- pairs. Another more indirect method to learn about the ϕ width in nuclei will be introduced in a following Section. In Section 7.4 we discuss how we model inclusive ϕ photoproduction in free space and in Section 7.5 we consider ϕ meson propagation in nuclear matter. Finally, we will examine the photoproduction of ϕ mesons in finite nuclei and the implications of the experimentally obtained cross sections for the ϕ properties at finite nuclear density.

7.2 Observables

In the following we will discuss two different possibilities to learn about the ϕ in-medium properties via photonuclear reactions. The first one – the direct observation of the K^+K^- invariant mass spectrum – will be discussed only briefly since we will show that no valuable information can be obtained from this observable. The investigation of the nuclear transparency ratio will be pursued in the following Sections and finally results will be compared to experimental data.

7.2.1 Invariant mass spectrum

Decay length. The possibility to study modifications of the ϕ meson in photon nucleus reactions has first been proposed by the authors of [205]. Their idea has been to measure the K^+K^- invariant mass spectrum from ϕ mesons produced in finite nuclei with total three momenta smaller than $100-150$ MeV. The restriction to small total momenta is a mandatory condition in order to learn about the ϕ in-medium properties via the invariant mass distribution of its decay products. The idea behind this is that only those K^+K^- pairs created from ϕ decays inside the target carry information on the ϕ in-medium spectral density. An estimate for a sensible momentum cutoff can be obtained from the distance λ which a ϕ meson propagates from its creation vertex until it eventually decays:

$$\lambda(q_0, \mathbf{q}) \simeq \lambda(q_0 = \sqrt{m_0^2 + \mathbf{q}^2}) = v\gamma\tau = \frac{|\mathbf{q}|}{m_0 \Gamma_0}, \tag{7.1}$$

where m_0 and Γ_0 are the mass and total width of the ϕ meson in its rest frame, $q = (q_0, \mathbf{q})$ is its four-momentum and $\tau = \Gamma_0^{-1}$ the lifetime. In order to probe the interior of the nucleus in which a ϕ meson has been produced, the three-momentum has to be limited to values of about $100-150$ MeV, corresponding to distances $\lambda = 4.4-6.6$ fm. These numbers have to be compared to typical nuclear radii which are roughly given by the empirical formula $R = 1.21\ \text{fm} \cdot A^{1/3}$ [206]. For Lead ($A = 208$), which is the largest stable nucleus typically used as target material in nuclear experiments, we find $R \simeq 7.2$ fm.

Production cross section. One of the drawbacks of using the ϕ meson as a probe in photon nucleus reactions is the small photoproduction cross section [210]. Due to the only small virtual strangeness content in the nucleon wave function the ϕ photoproduction cross section is about two orders of magnitude smaller than that of the ρ meson. As a consequence of the diffractive production mechanism the angular differential cross section for the exclusive process $\gamma p \to \phi p$ is sharply peaked in forward direction [207, 208, 209]. In Fig. 7.1 we show the momentum differential cross section for various photon energies. Here we have used a parametrization for the photoproduction amplitude from [207] that has been obtained in terms of $t-$channel Regge- and Pomeron-exchanges, see also [211]. In the momentum spectrum the forward peaked angular distribution is reflected by a strong peak for the highest ϕ momenta and a rapidly dropping cross section for small momenta. This situation illustrates the problems of the proposed measurement: First,

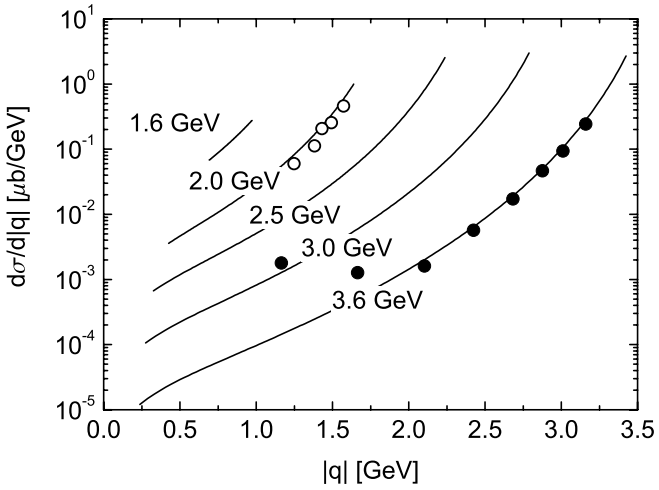

Figure 7.1: Momentum differential cross section for the process $\gamma p \to \phi p$ using the Regge parametrization of the photoproduction amplitude from [207]. Shown are the cross sections for various photon energies from 1.6 to 3.6 GeV. Data from [208] (open symbols) and [209] (filled symbols).

the cross section will be incredibly small due to the mandatory restriction to very small ϕ momenta[1] and second, the inclusive nuclear cross section at low total momenta could be dominated by inelastic production channels ($\gamma N \to \phi X$) or even background reactions ($\gamma N \to K^+K^-X$) that a priori do not show the same exponential decrease and that are hard to control theoretically.

Final state interactions (FSI). One of the most critical arguments against studying the $\gamma \to \phi \to K^+K^-$ reaction chain in nuclei is the strong kaon FSI. In the semiclassical transport picture, these FSI can be divided into two different classes: First, the K^+K^- mass spectrum will be distorted by elastic and inelastic K^+N and K^-N collisions which change the K^+ or K^- momentum in one instantaneous interaction. Second, the K^+ and K^- trajectories will be modified as compared to the free solutions of the equations of motion by the spatial gradients of the kaon-nucleus potential. This potential is generated by electromagnetic and strong interaction forces. If one understands an elastic collision as the destruction of a particle with given energy and momentum, the first class of FSI corresponds to the imaginary part of an optical potential whereas the second class of FSI finds an analogon in its real part. Note that the real part of an optical potential does a priori not lead to a loss of flux but changes the particle position in phasespace. Eventually this can spoil the possibility to correctly identify the genuine final state. Throughout this work we refer to the effects of the imaginary part of the meson nucleus potential as the FSI, whereas the real parts are addressed as the (classical and real valued) potentials.

The distortion of the K^+K^- invariant mass spectrum by collisions can be handled easily.

[1]Note, however, that Fig. 7.1 has been calculated on a free unbound proton. In nuclei, with the help of Fermi motion, even ϕ momenta below $100 - 150$ MeV are populated as we have shown in [211].

On one hand, the invariant mass distributions of those events is very different from the undistorted spectrum as we have shown in [211] and, therefore, can be separated from the resonant part. On the other hand, absorptive processes as $K^- N \to X$ dominate the FSI and, thus, the component of ϕ decays inside the nucleus in the final observables will anyway be small. This has the positive effect that only a small contribution of events is distorted by FSI. In turn, however, also the sensitivity to the ϕ in-medium decays is substantially reduced by the small K^- mean free path [39]. In contrast to $K^- N$ and $K^+ N$ collisions the ϕN collisions do not distort the $K^+ K^-$ mass spectrum. Quasi elastic ϕN collisions rather slow down high energetic ϕ mesons and, thus, increase the low-momentum component in the ϕ meson spectrum. Consequently, the relative amount of decays inside the target increases what leads to more substantial observable in-medium effects. We have proven that the yield of low-momentum ϕ mesons ($\mathbf{q} < 500$ MeV) increases by up to one order of magnitude due to these collisions, see our calculations presented in [39].

Coulomb distortion. The phasespace for the $\phi \to K^+ K^-$ decay is rather small since the sum af the kaon masses ($2m_K = 992$ MeV) is only slightly smaller than the ϕ mass itself ($m_V = 1020$ MeV). Thus, kaons created in ϕ decay processes have rather low kinetic CM energies. Moreover, as we have discussed previously, one has to trigger on those $K^+ K^-$ pairs with very small total three momenta. The propagation of charged particles with low energies requires to account for the electromagnetic (EM) potential in the equations of motion. Already in Chapter 4 we have found that the EM potential can be crucial in nuclear reactions involving charged particles in either the inital or final state.

As the single particle energies are constants of motion, the absolute values of the K^+/K^- three momenta in vacuum far away from the nucleus are given by

$$|\mathbf{p}_\pm| = \left[\left(\sqrt{{\mathbf{p}^*_\pm}^2 + m_K^2} \pm V(\mathbf{r}_{\rm cr}) \right)^2 - m_K^2 \right]^{\frac{1}{2}}, \tag{7.2}$$

where $\mathbf{p}^*_\pm$ are the K^+/K^- three momenta at their creation point $\mathbf{r}_{\rm cr}$, $V(\mathbf{r}_{\rm cr})$ is the absolute value of the EM potential and $m_K = 496$ MeV is the charged kaon mass. If W denotes the asymptotic value of the invariant mass of the pair in vacuum and W^* the invariant mass at the creation point, the variance of this quantity can be expressed as

$$\Delta W = W - W^* \approx \frac{s - s*}{2m_V} \tag{7.3}$$

with the ϕ meson mass $m_V = 1020$ MeV and $s = W^2$. Most substantial in-medium effects can be observed if the ϕ meson is at rest with respect to the target and decays in the center of the nucleus where the density is high. In this case the kaons are produced

back-to-back and we find

$$\begin{aligned}\Delta W &\approx -\frac{(\mathbf{p}_+ + \mathbf{p}_-)^2}{2m_V} \\ &\approx \frac{p_0^2}{m_V}\left(\sqrt{1-4\frac{(p_0^2+m_K^2)V_0^2}{p_0^4}}-1\right) \\ &\simeq -2\left(\frac{V_0}{p_0}\right)^2\frac{p_0^2+m_K^2}{m_V},\end{aligned} \tag{7.4}$$

where $p_0 = \sqrt{m_V^2/4 - m_K^2} \simeq 119$ MeV is the kaon three-momentum in the CM frame right after the ϕ decay. For the case of a Calcium target the Coulomb potential has a depth of $V_0 \approx -11$ MeV. Inserting numbers we find a downward shift of the K^+K^- invariant mass of $\Delta W = -5$ MeV. As this effect will act differently depending on the position and momentum of the decaying ϕ meson, Coulomb distortion will eventually result in a broadening of the reconstructed mass spectrum. This broadening effect, however, is at least of the same order as the medium effects that can be expected for ϕ production inside common nuclei.

In addition to that we also encounter the effect, that very low energetic antikaons do not have enough energy to leave the nucleus. This yields an additional reduction of the in-medium decay contribution to the K^+K^- spectrum. Note also that the above estimate has been done for the relatively small Calcium nucleus ($A = 40$, $V_C \simeq -11$ MeV). Consequently, the effect will be even more dramatic for heavier nuclei ($A = 208$, $V_C \simeq -25$ MeV). From this situation we have to conclude that it will be impossible to obtain any sensible information about the in-medium spectral shape of the ϕ meson from a measurement of the K^+K^- invariant mass spectrum. We have proven that an explicit simulation within the BUU transport model including a careful treatment of the electromagnetic forces indeed does not show an experimentally measurable sensitivity to an in-medium broadening of the ϕ meson. The nature of this problem has its origin in the different ranges of the strong and electromagnetic forces. The strong interaction phenomenon to be probed is of short range, whereas the superimposed electromagnetic force is long ranged and therefore still sizable in the nuclear surface that can be probed with the hadronic final state.

7.2.2 Transparency ratio

In spite of this somewhat discouraging situation there is another possibility to investigate the changes of the ϕ width in nuclei first considered in [204]. The method is to look for the attenuation of the ϕ flux in nuclear ϕ photoproduction. Much earlier this method has been used to extract the ρN cross section from photoproduction experiments [212]. The observable under consideration is the so-called nuclear transparency ratio

$$T_A = \frac{\sigma_{\gamma A\to\phi X}}{A\sigma_{\gamma N\to\phi X}} \tag{7.5}$$

that is the ratio of the nuclear ϕ production cross section divided by A times the cross section on a free nucleon. It can be interpreted as the momentum and position space

averaged probability of a ϕ meson to get out of the nucleus. The dependence of the loss of flux on the target mass number is related to the ϕ width in the nuclear medium. This can be seen as follows: In a simple Glauber model, neglecting Fermi motion, Pauli blocking, coupled-channel effects, nuclear shadowing and quasi elastic scattering processes, the nuclear cross section for K^+K^- photoproduction via the exclusive incoherent production of ϕ mesons can be written as[2] (see also Appendix B)

$$\sigma_{\gamma A} = \int d\Omega \int d^3r\, n_N(\mathbf{r}) \frac{d\sigma_{\gamma N}}{d\Omega} \exp\left[-\int_0^{|\delta\mathbf{r}|} dl\, \frac{dP}{dl} \right] F_K(\mathbf{r}+\boldsymbol{\delta}) \tag{7.6}$$

with the ϕ absorption probability per unit length dP/dl,

$$\mathbf{r}' = \mathbf{r} + l\frac{\mathbf{q}}{|\mathbf{q}|} \quad \text{and} \quad \delta\mathbf{r} = \frac{v}{\gamma}\frac{1}{\Gamma_0}\frac{\mathbf{q}}{|\mathbf{q}|}. \tag{7.7}$$

Moreover, F_K is a K^- absorption factor that is obtained by integrating the K^- absorption probability from the decay vertex of the ϕ at $\mathbf{r}+\delta\mathbf{r}$ to infinity and averaging over the possible K^- directions. In the low density limit it is given by

$$F_K(\mathbf{r}+\delta\mathbf{r}) = \frac{1}{4\pi}\int d\Omega_{\rm cm} \exp\left[-\sigma_{K^-N} \int_0^{\infty} dl' n_N(\mathbf{r}'') \right] \tag{7.8}$$

with $\mathbf{r}'' = \mathbf{r}+\delta\mathbf{r}+l'\mathbf{k}/|\mathbf{k}|$ where $\mathbf{k}$ is the LA momentum of the K^-, $\Omega_{\rm cm}$ is its CM emission angle and σ_{K^-N} is the K^-N absorption cross section. Note, that positive kaons cannot be absorbed in non-strange nuclear matter. The Lorentz factor γ transforms the ϕ width from the ϕ rest frame to the ϕ moving frame. The exponential in Eq. (7.6) contains the ϕ absorption probability per unit length dP/dl. In the limit of $\Gamma_0 \to 0$ and a vanishing absorption probability $dP/dl \to 0$ the exponential as well as the K^- absorption factor become equal to unity. We then obtain the intuitive result

$$\sigma_{\gamma A} = A \cdot \sigma_{\gamma N}. \tag{7.9}$$

In this limit the total incoherent nuclear cross section is equal to A times the nucleonic cross section. This also implies a transparency ratio of one as can be seen from the definition (7.5).

If we consider the propagation of the ϕ meson in an optical potential (of which the real part is neglected[3]) the ϕ self energy Π_ϕ can be introduced as

$$\frac{dP}{dt} = -\frac{\mathcal{I}\mathrm{m}\Pi}{\omega} = \gamma\Gamma_{\rm coll}, \tag{7.10}$$

[2] At least the effects of Fermi motion, Pauli blocking and nuclear shadowing can be incorporated easily in this model. We neglect it here in order to keep our considerations as simple as possible.

[3] This approximation is well justified. As mentioned earlier, state-of-the art models find a real part of the nuclear ϕ potential that leads to a renormalization of the ϕ mass in the nuclear medium by at most 10 MeV which indeed is a negligible number as compared to the free mass of the ϕ of roughly 1 GeV.

where dP/dt is the ϕ absorption probability per unit time. The second equality defines the collisional ϕ decay width Γ_{coll} corresponding to nuclear quasi elastic and absorption channels. From this we obtain the probability of loss of flux per unit length by

$$\frac{dP}{dl} = \frac{dP}{vdt} = \frac{\omega}{q}\frac{dP}{dt} = -\frac{\mathcal{I}\text{m}\Pi}{q}. \tag{7.11}$$

Using this relation one can rewrite the exponential in Eq. (7.6) as

$$\exp\left[\frac{1}{q}\int_0^{|\delta\mathbf{r}|} dl\,\mathcal{I}\text{m}\Pi\left(q, n_N(\mathbf{r}')\right)\right] \tag{7.12}$$

which, however, is a quite general expression that does not rely on the low-density approximation since the self energy $\Pi(q)$ may contain components going beyond two-body collisions. From this expression one can now read off how two different mechanisms will affect the nuclear transparency ratio: First, if the ϕ collision width becomes large because of the opening of inelastic nuclear channels, the nuclear cross section and the transparency ratio will become smaller because of the exponential suppression factor. Second, if the ϕ decay width to the K^+K^- channel increases e. g. due to kaon self energies in the medium, the ϕ decay vertex at $\mathbf{r} + \delta\mathbf{r}$ lies with higher probability inside the radius of the target nucleus. Antikaons produced inside a strongly attractive nuclear potential will be confined for a longer time to the nuclear volume or may even be bound. Due to the large imaginary part of the nuclear K^- potential these antikaons will be absorbed to inelastic nuclear channels.

In principle a measurement of the transparency ratio on different target nuclei can yield valuable information on the imaginary part of the ϕ in-medium self energy. Nevertheless, this statement is not without problems. First, one has to rely on a proper theoretical treatment of the nuclear cross section that has to relate the ϕ medium properties to observable cross sections. Second, such a measurement provides no possibility to disentangle the various scenarios of medium modifications. In-medium changes of the ϕ self energy can be generated through ϕ baryon collisions or from a modification of the K^+K^- decay channel by means of in-medium kaon self energies. In fact, the transparency measurement directly only allows for the extraction of the absorptive part of the ϕ nucleus potential. The relation to the absorptive ϕN cross section, however, has to rely on the low density theorem whose validity cannot be guaranteed. Still one has to keep in mind that also this quantity is an averaged in-medium quantity, that comprises the effects of the nuclear medium at various densities passed through during the course of the reaction.

7.3 Experimental setup

Nuclear photoproduction of ϕ mesons has been investigated experimentally using the **L**aser **E**lectron **P**hoton facility at **S**Pring-8 (LEPS) [213, 214, 215, 216]. In this experiment the incident photon beam is produced by means of backward Compton scattering of photons produced with an ultra violet laser from 8 GeV electrons. To determine the

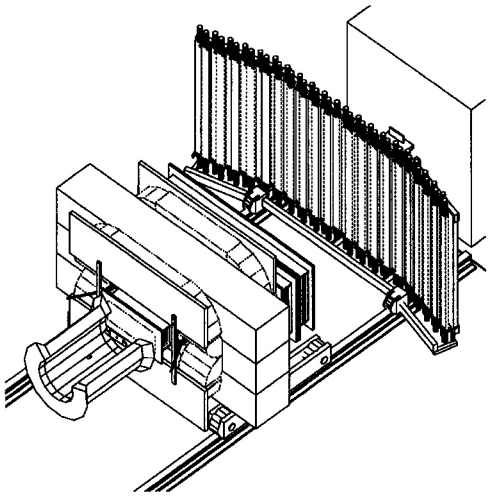

Figure 7.2: Setup of the **L**aser **E**lectron **P**oton **S**pectrometer (LEPS) at the SPring-8 accelerator facility. The picture is taken from [214].

photon energy the recoil electrons are detected and momentum analyzed by a bending magnet. With this setup photons with a maximum energy of 2.4 GeV can be obtained. In contrast to $\gamma-$ray spectra from bremsstrahlung photons, the photon spectrum does not show the typical $1/E$ fall-off, but is more or less constant over the full energy range with a small peak at the highest energies. The transparency measurement has been done over the finite photon energy range from 1.5 to 2.4 GeV. As target materials ^{7}Li, ^{12}C, ^{27}Al and Cu have been considered.

The LEPS spectrometer is optimized for the measurement of ϕ mesons at forward angles by detecting the K^+K^- pairs. It consists of a dipole magnet, three drift chambers and a forward **T**ime **o**f **F**light (ToF) wall, see Fig. 7.2. This detector system has only a limited angular coverage. In our simulations this limited acceptance can be accounted for by counting only particles leaving the reaction vertex with momenta that obey the following conditions:

$$\sin(\pi - 0.4) \leq \frac{p_x}{|\mathbf{p}|} \leq \sin(\pi + 0.4) \tag{7.13}$$

$$\sin(\pi - 0.2) \leq \frac{p_y}{|\mathbf{p}|} \leq \sin(\pi + 0.2). \tag{7.14}$$

That is, the angular coverage is limited in the horizontal and vertical plane due to the rectangular detector geometry. As the ToF acceptance focuses on forward directions, the detector is unable to observe very low-momentum ϕ mesons. This, on the other hand, would be mandatory to observe the in-medium ϕ properties via the K^+K^- invariant mass spectrum. Since very low-energetic ϕ mesons decay almost back-to-back in the LA frame, not both the K^+ and the K^- can go in forward direction. Most likely one of the final state particles will miss the forward ToF wall.

The finite mass and momentum resolution for the K^+/K^- detection generates also a finite invariant mass resolution that has been estimated for the present experiment to be roughly 2 MeV. To account for this effect, we smear each physical event in our simulation with a Gaussian distribution. In summing up the individual events this corresponds to the replacement

$$\delta(W - W_i) \to \frac{1}{\sqrt{2\pi(\delta W)^2}} \exp\left[-\frac{(W - W_i)^2}{2(\delta W)^2}\right] \tag{7.15}$$

with $\delta W = 2$ MeV for the individual testparticle contributions to the final observables. This is important when cuts to the K^+K^- invariant mass are applied.

Experimentally, the selection of the ϕ events from the total data sample is done in the following way: First, one is gating on the K^+K^- events in the invariant mass region from 1005 MeV to 1035 MeV. Then the background is subtracted by fitting a phasespace distribution to the invariant mass region from 1050 MeV to 1100 MeV that is subtracted from the total spectrum. By tracing back the origin of the K^+K^- pairs in our simulations we have checked that this method works reasonably well.

7.4 The reaction γN $\to$ ϕX

The most important ingredients to our transport simulations are the ϕ photoproduction cross sections on elementary targets, i. e. protons and neutrons. These elementary processes can be divided into two different classes, namely the elastic[4] processes $\gamma p \to \phi p$ and $\gamma n \to \phi n$ and the inelastic ones $\gamma N \to \phi X$ with $X \neq N$ and $N \in \{p, n\}$. The elastic processes are characterized by a final state consisting of only one ϕ meson and a nucleon that is not intrinsically excited. These reactions can, at least in principle, be calculated from Feynman diagrams using effective hadronic Lagrangians. The situation is more subtle for the inelastic processes where the final state consists of a ϕ meson and either an excited nucleon or – more general – a bunch of hadrons with total baryon number $B = 1$. First, depending on the available energy, there can be a huge amount of possible processes as all existing hadrons obeying the conservation of the relevant quantum numbers with masses $\sum_h M_h \leq \sqrt{s} - m_V$ can be produced in the final state. Second, one has to consider a large number of diagrams contributing to these reactions containing unknown parameters as coupling constants and cutoffs which makes the calculation unfeasible from the practical point of view. Moreover, there is not any guidance from experiment as so far none of these reactions has been measured. In the following we will first discuss the model we use for the elastic ϕ photoproduction processes. After that we also discuss the inelastic processes and show how we obtain at least a rough constraint on the parameters by experimental input.

[4]The name 'elastic' is inspired by the **V**ector **M**eson **D**ominance (VMD) picture, in which the photon-hadron interaction takes place merely over the hadronic components of the photon, namely the light vector mesons ρ, ω and ϕ. Photoproduction of ϕ mesons is then described by the elastic scattering of the massless ϕ component of the photon into an on-shell ϕ meson.

7.4.1 Elastic ϕ photoproduction

To evaluate the cross section for the elastic ϕ photoproduction process we follow the model of Ref. [217] that gives a very good description of the data in the low $-t$ region, where $-t$ is the four-momentum transfer from the photon to the ϕ meson squared. The aim of the work [217] has been to determine quantitatively the contribution of the non-strange amplitude to ϕ photoproduction. It has been suggested that through interference polarization observables in ϕ photoproduction can be highly sensitive to an even rather small strangeness admixture in the nucleon wave function, an issue that still remains controversial. To this end different scenarios have been considered, e. g. the exchange of a second Pomeron trajectory with negative intercept $\alpha(0) < 0$ and the additional contribution of scalar meson exchange. For the present purpose, however, it has turned out to be sufficient to consider the pseudoscalar exchange amplitude, direct ϕ meson radiation via the nucleon Born terms and the standard Pomeron exchange.

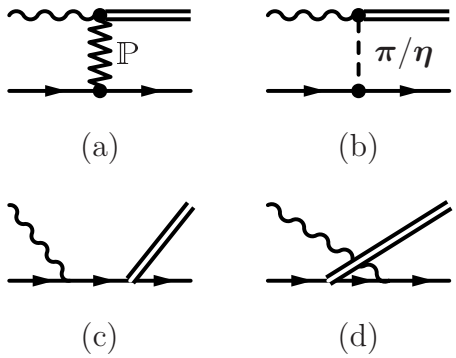

Figure 7.3: Tree level diagrams considered in the calculation of elastic ϕ photoproduction.

These different contributions are shown diagrammatically in Fig. 7.3. The Pomeron exchange (a) gives the dominant contribution at high energies, which allows to determine its parameters by fitting the differential cross section at large $\sqrt{s}$. At low energies $\sqrt{s} < 5$ GeV the predictions based on this Pomeron trajectory appear to be lower than the data. This discrepancy can be healed by inventing the pseudoscalar exchange terms (b) with parameters that have been predetermined using SU(3) and the ϕ decay widths. Moreover, the nucleon Born terms (c) give a more flat angular distribution and, hence, serve to explain the more recent data at high momentum transfer. Precise data under CM backward angles in principle allow to determine not just the ϕNN coupling constant but rather the product of coupling and form factor at the ϕNN vertex.

In principle, the ϕNN vertex in the Born diagrams has to be dressed by a form factor for off-shell nucleons in order to account for the compositness of these particles. However, using a $s-$dependent form factor for the $s-$channel diagram and an $u-$dependent form factor for the $u-$channel diagram would result in a violation of gauge invariance with respect to the photon and vector meson fields alike[5]. As a consequence the authors of

[5]This can be seen easily by contracting the Born amplitude, which is sum of the $s-$ and $u-$channel

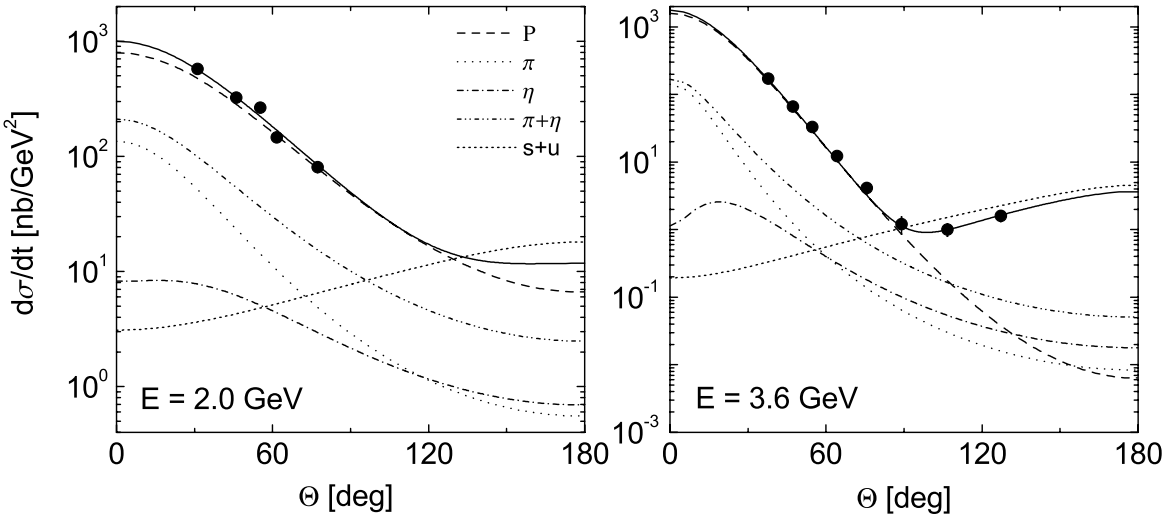

Figure 7.4: Angular differential cross section for elastic ϕ photoproduction. Data from [208] (2 GeV) and [209] (3.6 GeV).

Ref. [217] used a constant form factor $F = F_s = F_u = 1$ for both contributions, resulting in an overestimation of the angular differential cross section for high momentum transfers, where the $s-$ and $u-$channel contributions become dominant, see Fig. 7.4. Following the suggestion of Ref. [218], we therefore introduce an overall form factor for the $s-$ and $u-$channel nucleon exchange diagrams ((c) and (d) in Fig. 7.3) that keeps the gauge invariance of the amplitude as well:

$$\left(\tilde{\mathcal{M}}_s + \tilde{\mathcal{M}}_u\right) = F(s,u)\left(\mathcal{M}_s + \mathcal{M}_u\right). \tag{7.16}$$

This form factor is composed as follows:

$$F(s,u) = z_s f(s) + z_u f(u), \quad f(x) = \frac{\Lambda^4}{\Lambda^4 + (x - m_N^2)^2}. \tag{7.17}$$

In order to allow a unique definition of the coupling constants, the prefactors have to fulfill the constraint $z_s + z_u \equiv 1$. We fix the parameters z_s, z_u and Λ using the data on the angular differential cross section at 2 GeV from Ref. [208] and at 3.6 GeV from Ref. [209]. We find

$$z_s = 0.9 \tag{7.18}$$
$$z_u = 1 - z_s = 0.1 \tag{7.19}$$
$$\Lambda = 1.87 \text{ GeV}. \tag{7.20}$$

As can be seen from Fig. 7.4 an excellent description of the data can be obtained. Some details of the model needed for the evaluation of the total and differential cross sections are given in Appendix E.

terms, with either k_μ or q_μ. Without form factor the $s-$ and $u-$channel terms cancel each other, whereas if they have different prefactors the gauge condition $k_\mu \mathcal{M}^{\mu\nu} = q_\nu \mathcal{M}^{\mu\nu} \equiv 0$ is not fulfilled.

7.4.2 Inelastic ϕ photoproduction

We describe inclusive particle production in γN interactions above energies of $\sqrt{s} = 2$ GeV employing the hadronic event generator FRITIOF. In Appendix A a brief description of the implementation of FRITIOF together with some References providing an extensive description of the model are given.

In order to check the inclusive cross section for ϕ production generated by the FRITIOF routine we compare the outcome of simulations on elementary targets with the only existing and published data on inclusive ϕ photoproduction. These data on the angular differential cross section $d\sigma/dt$ are available only for photon energies between 4.85 GeV and 5.85 GeV [219]. They are also limited to invariant masses of the hadronic remnants in the range of 1.2 GeV $\leq M_X \leq$ 2.1 GeV. In the calculation of this cross section one problem of the FRITIOF event generator becomes apparent, namely that FRITIOF produces too many $\gamma N \to V\Delta$ events. This might be due to the fact, that the $\Delta(1232)$ is the only nucleon resonance that is produced as a product of the fragmentation process and, hence, to compensate for the missing higher resonances, too much strength is put to the channels including the Δ in the final state.

We cure this problem by also treating the $\gamma N \to V\Delta$ reaction independent of the FRITIOF routine, i. e. the unphysical events generated by FRITIOF are rejected and the cross section for the $\gamma N \to V\Delta$ process, that is calculated externally, is subtracted from the total γN cross section parametrization used as input to the FRITIOF routine. For the case at hand we make the following ansatz for the total cross section:

$$\sigma_{\gamma p\to\phi\Delta^+} = \frac{1}{16\pi s|\mathbf{k}_{\rm cm}|}\int\limits_{m_\pi^2}^{(\sqrt{s}-m_N-m_\pi)^2} dW_V^2\mathcal{A}_V(W_V,n_N)\int\limits_{(m_N+m_\pi)^2}^{(\sqrt{s}-W_V)^2} dW_\Delta^2\mathcal{A}_\Delta(W_\Delta)\times \\ \times|\mathbf{p}_{\rm cm}(\sqrt{s},W_V,W_\Delta)|\,|\mathcal{M}_{\gamma p\to\phi\Delta^+}|^2, \tag{7.21}$$

where $\mathcal{A}_\Delta$ and $\mathcal{A}_V$ denote the spectral functions of the Δ and the ϕ, $\mathbf{k}_{\rm cm}$ and $\mathbf{p}_{\rm cm}$ are the initial and final CM momenta according to Eq. (E.5) and W_Δ and W_V are the invariant masses of the Δ and the ϕ, respectively. We fit the matrix element $\mathcal{M}_{\gamma p\to\phi\Delta^+}$ to the inclusive ϕ production data [219]. For the angular distribution we make the ansatz of an exponential form factor typical to $t-$channel processes times a propagator assuming a dominant contribution from π exchange:

$$\frac{d\sigma}{dt} \propto e^{Bt}\left(\frac{1}{t-m_\pi^2}\right)^2 \tag{7.22}$$

with the slope parameter B that again has to be adjusted to experiment. In Fig. 7.5 we show the results of our calculations. The parameters determined from the fitting procedure are

$$|\mathcal{M}_{\gamma p\to\phi\Delta^+}|^2 = 0.374 \tag{7.23}$$

$$B = 6.5\ \text{GeV}^{-2}. \tag{7.24}$$

From our recipe we find quite good agreement at the lower energies, whereas the data are less well reproduced at higher energies. Note, however, that the energy regime we

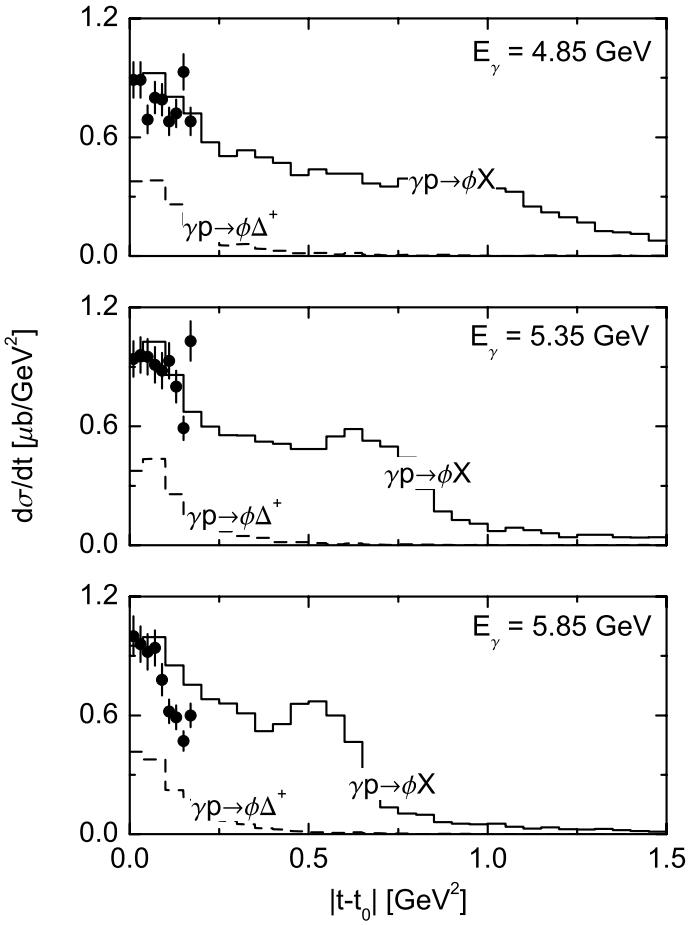

Figure 7.5: Differential cross section for the process $\gamma p \to \phi X$ with 1.2 GeV $\leq M_X \leq$ 2.1 GeV. *Solid line*: total yield, *dashed line*: contribution from $\gamma p \to \phi \Delta^+$. Data from Ref. [219].

are interested in is lower than these data sets. Moreover, the comparison is also limited concerning the invariant mass of the unobserved final state X. More and precise data also at lower energies would certainly be desirable.

7.5 The ϕ meson in nuclear matter

The calculation of ϕ meson production from finite nuclei as well as a theoretical determination of the ϕ properties in a surrounding with finite baryon density require the knowledge of the ϕN interaction. Unfortunately the cross sections for ϕN collisions are not accessible by experiment as the ϕ meson is a short-lived particle and, hence, no ϕ meson beam can be produced. The only indirect method to determine the total ϕN cross section considered so far is the attenuation measurement discussed previously. However, such a measurement will always give information about effective in-medium quantities

including already higher-order corrections, e. g. Fermi motion, Pauli blocking and multi particle collisions. Moreover, starting from some assumption on the ϕN cross section, an enhancement of ϕ meson absorption originating from a renormalization of the $K\bar{K}$ self energy cannot be distinguished from the opening of additional inelastic nuclear channels as both effects will act in the same direction, namely towards a reduction of the nuclear production cross section.

7.5.1 The ϕN interaction

For the use with our transport model we have to rely on educated guesses for the ϕN interaction strength. Total hadronic cross sections can be parametrized in a simple and useful form employing Regge theory, see for instance [211]. Assuming an additive quark model the total ϕ proton cross section can be parametrized as [220, 221]

$$\sigma_{\phi p}^{\mathrm{tot}} \simeq \sigma_{K^+p} + \sigma_{K^-p} - \sigma_{\pi^+p} \tag{7.25}$$

$$\simeq \left(10.01 s^{\epsilon} - 1.52 s^{-\eta}\right) \text{ mb} \tag{7.26}$$

with s in GeV^2 and the Regge intercept parameters

$$\epsilon = 0.0808 \qquad \eta = 0.4525. \tag{7.27}$$

Because of isospin symmetry, the cross section on the neutron is the same as the cross section on the proton. This parametrization is expected to work at energies sufficiently above the nucleon resonance region. Due to the lack of experimental information and the fact that the ϕ meson is not known to couple strongly to any nucleon resonance we also use it down to the ϕN threshold. This cross section is shown in Fig. 7.6.

An estimate for the elastic cross section $\phi N \to \phi N$ can be obtained using the **V**ector **M**eson **D**ominance (VMD) model. Within the strict VMD picture [222, 223] one finds the following relation between the vector meson photoproduction cross section with real photons and the elastic VN scattering process:

$$\sigma_{VN}^{\mathrm{el}} \approx \left(\frac{g_V}{e}\right)^2 \sigma_{\gamma N \to VN} \tag{7.28}$$

with the photon vector meson coupling constants e/g_V. A mean value for this coupling from the numbers obtained in the literature is $g_\phi^2/4\pi = 18.4$, taken from Ref. [143]. Sufficiently above threshold the exclusive ϕ meson photoproduction cross section has been determined experimentally to be roughly 4 μb. Hence we obtain $\sigma_{\phi N}^{\mathrm{el}} \approx 10$ mb. Throughout our transport calculations we use the parametrization from Ref. [224]

$$\sigma_{\phi N}^{\mathrm{el}} = \frac{10}{1 + |\mathbf{q}|} \text{ mb} \tag{7.29}$$

with $\mathbf{q}$ in GeV, that is in accordance with the above estimate.

For CM energies above $\sqrt{s} = 2.2$ GeV we again rely on the FRITIOF routine to simulate meson baryon collisions. It was shown in Ref. [166] that the FRITIOF routine does not generate enough elastic VN scattering events. We cure this deficiency by extending the

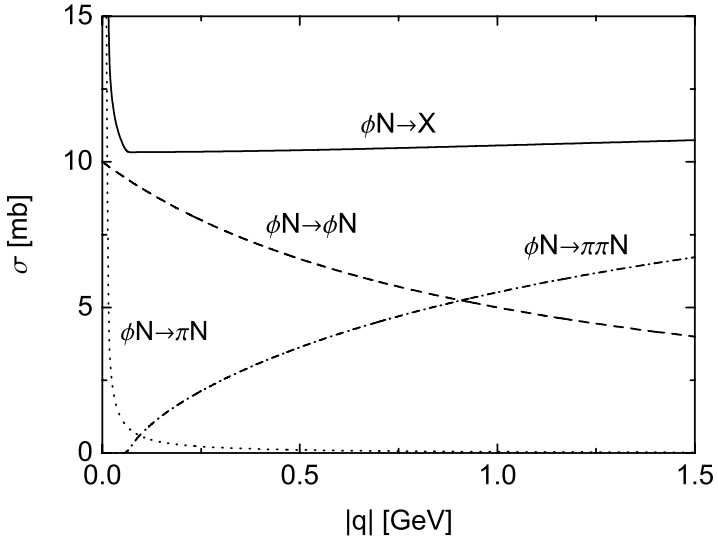

Figure 7.6: Total ϕ nucleon cross sections on a free nucleon at rest as function of the ϕ LA momentum.

use of the parametrization (7.29) to high energies and simulating the high energy elastic scattering events externally. The FRITIOF routine is then used only to determine the final states of the inelastic ϕN collisions.

In the low energy region $\sqrt{s} < 2.2$ GeV we treat the inelasticity $\sigma^{\rm inel} = \sigma^{\rm tot} - \sigma^{\rm el}$ as being purely due to ϕ meson absorption. This is justified because the phasespace for inelastic channels as $\phi N \to \phi X$ with $M_X \geq m_N + m_\pi$ is extremely small below the threshold energy. The absorptive process $\phi N \to \pi N$ is constrained by its inverse via detailed balance. The cross section for pion induced ϕ production has been fitted to experimental data in Ref. [225]

$$\begin{aligned} \sigma_{\phi N \to \pi N} &= |\,(\tfrac{1}{2}1 z_{N_1} z_\pi | \tfrac{1}{2}1 \tfrac{1}{2} z_{N_2})\,|^2 0.00882 \text{ mb GeV}^3 \times \\ &\quad \frac{(0.99 \text{ GeV})^2}{(\sqrt{s} - 1.8 \text{ GeV})^2 + (0.99 \text{ GeV})^2/4} \frac{\pi^2}{12} \frac{p_f}{p_i s} \end{aligned} \tag{7.30}$$

with z_N and z_π being the $z-$components of the nucleon and pion isospin. The remaining inelasticity we put entirely to the channel $\phi N \to \pi\pi N$. This again should be a reasonable approximation as coupled channel effects, e. g. ϕ meson regeneration through the chain $\phi N \to m N' \to \phi' N''$, are expected to be extremely small because of the extremely small branching ratios involved ($\sigma_{\pi N \to \phi N}/\sigma_{\pi N \to X} = \mathcal{O}(10^{-3})$). All cross sections discussed above are illustrated in Fig. 7.6.

7.5.2 The ϕ self energy from ϕN collisions

Before we calculate the $\phi \to \bar{K}K$ vacuum self energy we first discuss the in-medium contribution to the ϕ width due to ϕ nucleon collisions. A single particle state that propagates through an environment with non-zero density acquires the additional probability

to be destroyed by collisions with the particles from the medium. The destruction of such a state with given momentum and quantum numbers can happen through a change of direction and energy or the absorption into inelastic nuclear channels. By the uncertainty principle the reduced lifetime of such a state also causes a larger uncertainty of its energy, or – in other words – a larger width of its spectral distribution. Taking into account two-body collisions only, the collisional broadening can be calculated from the low density theorem that relates the collision rate ($R \sim n_N \sigma \sim$ number of collisions per unit time) to the lifetime ($\tau \sim (Rv)^{-1}$) and, hence, to the width of the single particle probe. A formal derivation of the low density theorem will be given in Chapter 8. The collisional self energy of the ϕ meson in cold nuclear matter ($T = 0$, $n_\pi = 0$) is given by

$$\mathcal{I}\mathrm{m}\Pi_{\mathrm{coll}}(q_0 = \sqrt{m_V^2 + \mathbf{q}^2}, \mathbf{q}, n_N(\mathbf{r})) = -4 \int \frac{d^3p}{(2\pi)^3} \Theta(|\mathbf{p}| - p_F) \frac{|\mathbf{k}_{\mathrm{cm}}|\sqrt{s}}{E_N(\mathbf{p})} \sigma_{VN}(s) \quad (7.31)$$

with $\mathbf{k}_{\mathrm{cm}}$ the CM momentum of nucleon and ϕ, E_N the nucleon on-shell energy in the LA frame and p_F the local Fermi momentum as given in Eq. (A.3). The cross section σ_{VN} is the total ϕ nucleon cross section containing all quasi elastic and absorption channels. Note that Eq. (7.31) does not account for Pauli blocking what in principle could be easily incorporated in such a framework. In the case at hand, however, we are using a parametrization of the total cross section, whereas to account properly for Pauli blocking a microscopic model that allows to calculate angular distributions would be mandatory. Also the dependence of the width on the invariant mass has been neglected by fixing the ϕ energy to $q_0 = E(\mathbf{q}) = \sqrt{m_\phi^2 + \mathbf{q}^2}$ since the parametrization (7.25) is valid for on-shell ϕ mesons. This parametrization contains no information about the off-shell behavior of the ϕN interaction that again could only be determined within a microscopic framework.

In Fig. 7.7 we show the on-shell collision width of the ϕ in the ϕ rest frame

$$\Gamma_{\mathrm{coll}} = -\frac{\mathcal{I}\mathrm{m}\Pi_{\mathrm{coll}}}{m_\phi} \quad (7.32)$$

as function of the ϕ laboratory momentum. The linear rise comes because of the almost constant total cross section and the rising relative velocity of ϕ and nucleon. The non-linear behavior at small momenta is due to Fermi motion. Also the dependence on the nucleon density is linear which, however, is a premise for the use of Eq. (7.31). For the ϕ meson at rest we find a collisional broadening of roughly 18 MeV at saturation density, which is in line with the results of the more sophisticated models presented in Refs. [200, 201, 203, 204] taking into account that no modification of the kaon loop has yet been considered.

7.5.3 Modification of the ϕ width from kaon self energies

The vacuum self energy of the ϕ meson is almost entirely given by its coupling to kaon-antikaon pairs. The remaining part due to the $\phi \to \rho\pi$ decay we treat in our simulations as constant above the 3π threshold and zero otherwise. The kaon-antikaon decay width can be calculated from the imaginary part of the diagram shown in Fig. 7.8, where the particles in the loop are either K^+ and K^- or K^0 and $\bar{K}^0$.

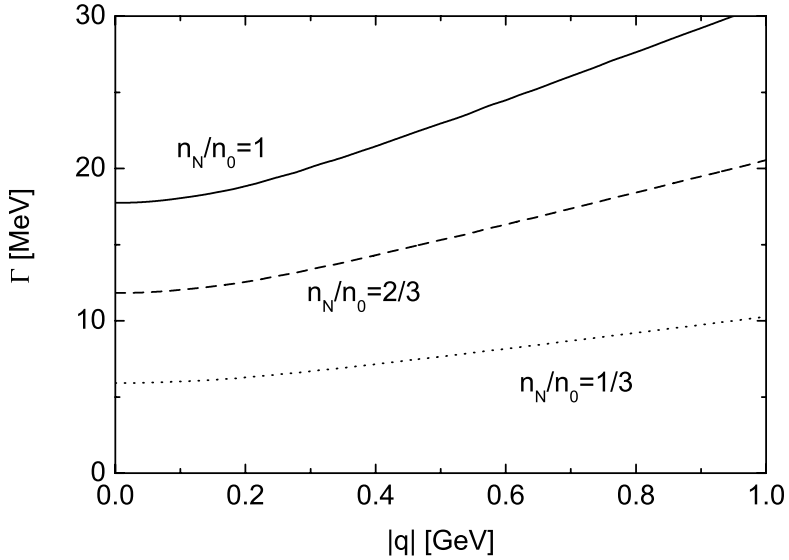

Figure 7.7: In-medium width of the ϕ meson in the ϕ rest frame generated by ϕN collisions according to Eq. (7.31) for various nuclear densities.

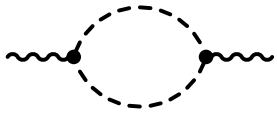

Figure 7.8: Vacuum self energy graph of the ϕ meson due to the fluctuation to kaon-antikaon pairs.

The Lagrangian density that describes the coupling of the ϕ meson to charged kaons is given by

$$\mathcal{L} = -ig_\phi \phi_\mu \left(K^- \partial^\mu K^+ - K^+ \partial^\mu K^- \right). \tag{7.33}$$

The Lagrangian for the neutral kaons has an analogous form. The relative minus sign emerges from the commutator which is part of the gauge-covariant derivative that couples the vector mesons as massive gauge bosons into the pseudoscalar SU(3) chiral Lagrangian [226]. Applying standard Feynman rules we find for the charged kaon loop

$$\Pi_\phi = 4ig_\phi^2 \int \frac{d^4k}{(2\pi)^4} \frac{1}{k^2 - m_K^2 + i\epsilon} \frac{1}{(q-k)^2 - m_K^2 + i\epsilon} \epsilon_i k_i \epsilon_j k_j \tag{7.34}$$

where q is the ϕ four-momentum and $\boldsymbol{\epsilon}$ is the vector meson polarization vector. The imaginary part of the loop integral can be readily evaluated using Cutkosky's cutting rules [58, 66]. Finally one obtains for the free $\phi \to K^+K^-$ decay width

$$\Gamma_\phi(s) = -\frac{\mathcal{I}\mathrm{m}\Pi_\phi(s)}{\sqrt{s}} = \frac{g_\phi^2}{6\pi} \frac{|\mathbf{k}_{\mathrm{cm}}|^3}{s} \tag{7.35}$$

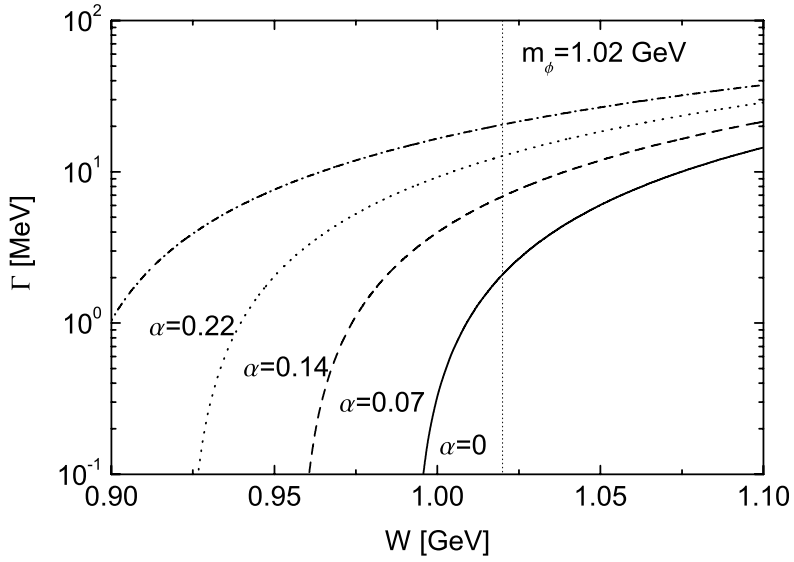

Figure 7.9: K^+K^- decay width of the ϕ meson for different values of the Brown/Rho mass shift parameter α as function of the invariant mass of the ϕ meson at normal nuclear matter density n_0. The vertical line highlights the free ϕ mass of 1.02 GeV.

where $|\mathbf{k}_{\rm cm}|$ is the kaon CM momentum which is given by

$$|\mathbf{k}_{\rm cm}| = \frac{\sqrt{s}}{2}\left(1 - 4\frac{m_K^2}{s}\right)^{1/2} . \tag{7.36}$$

Eq. (7.35) requires $g_\phi = 4.57$ to obtain agreement with the experimental value of the ϕ decay width at the on-shell point of $\Gamma = 2.18$ MeV.

Going to the nuclear medium, the leading density modification of the kaon self energies results in a strong attractive mass shift for the antikaon as will be discussed in more detail in a later Section. The dressing of the internal lines of the loop diagram 7.8 with this self energy then also leads to a modification of the ϕ decay width. If one – as frequently done – sticks to the quasiparticle picture, i. e. the imaginary part of the kaon self energy in the spectral function is neglected, the evaluation of the loop integral remains straightforward. Basically the vacuum expression holds whereas the masses of kaon and antikaon have to be replaced by their shifted in-medium values at given density. The dependence of the ϕ width on these effective kaon masses is given by

$$\Gamma^*_\phi(s, n_N) = \Gamma_\phi(s)\left[\frac{(s - (m^*_{K^+} + m^*_{K^-})^2)(s - (m^*_{K^+} - m^*_{K^-})^2)}{(s - 4m_K^2)s}\right]^{3/2} . \tag{7.37}$$

In Fig. 7.9 we show the K^+K^- decay width of the ϕ as function of the ϕ mass. The mass modification of the antikaon we express via a density-dependent scalar potential

$$m^*_{K^-} = m_K + S_K(\mathbf{r}) \tag{7.38}$$

$$m^*_{K^+} = m_K \tag{7.39}$$

where m_K is the free kaon mass and $\mathbf{r}$ is its spatial coordinate. In this place we neglect the effects of the nuclear medium on the K^+ mass since they are of minor importance. For the scalar potential we use a Brown/Rho type parametrization [8]

$$S_K(\mathbf{r}) = \alpha m_K \frac{n_N(\mathbf{r})}{n_0} \tag{7.40}$$

with the nuclear saturation density $n_0 = 0.16$ fm^{-3}. The ϕ decay width rises substantially for large attractive mass shifts due to the increasing phasespace. Using a strength parameter of $\alpha = -0.22$ that has been obtained by a relativistic mean field approach in Ref. [195] the ϕ width reaches a value of 20 MeV at the on-shell point and normal nuclear matter density.

7.6 Photoproduction of ϕ mesons in nuclei

In the following we will use our Monte Carlo transport model in order to study the properties of the transparency ratio in nuclear ϕ meson photoproduction. The transport model is presented briefly in Appendix A. In particular, we study the impact of known nuclear effects and the sensitivity of the attenuation measurement to the inelastic ϕN cross section. The kaon nucleus FSI are described by means of the BUU collision integral using vacuum K^+N and K^-N cross sections. The latter ones are obtained in terms of resonance fits to the data plus additional background contributions, see Ref. [100].

A modified spectral function in the nuclear environment has also some impact on the production cross sections inside the medium. In general, a larger width will smear the cross section in the threshold region, whereas at higher energies only minor modifications will be observed due to the smooth energy dependence of the cross section. Moreover, for the ϕ meson the in-medium broadening is still small as compared to its mass that defines the production threshold, hence leading only to small modifications of the phasespace integrals. The issue of modified in-medium cross sections will be discussed in more detail in Chapter 9 for the case of ω photoproduction in nuclei where larger effects will be encountered. In Appendix F the corresponding formulas are given.

7.6.1 From protons to finite nuclei

We start our calculations with including only collisional broadening of the ϕ meson as an in-medium effect while maintaining the vacuum properties for all other mesons (in particular the kaons). For the ϕN interaction we use the cross sections as given in the previous Section. The open triangles (dotted line) in Fig. 7.10 show the nuclear transparency ratio, defined in Eq. (7.5), as function of the target mass number. The deviation of T_A from unity is created mainly by two effects: First, the ϕ meson or its decay products (if the ϕ decays inside the nucleus) are absorbed on their way out of the nucleus. Second, the transparency ratio is reduced by Pauli blocking and Fermi motion. This is important as the ϕ photoproduction cross section is strongly forward peaked, hence the momentum transfer to the hit nucleon in general is quite small. As a

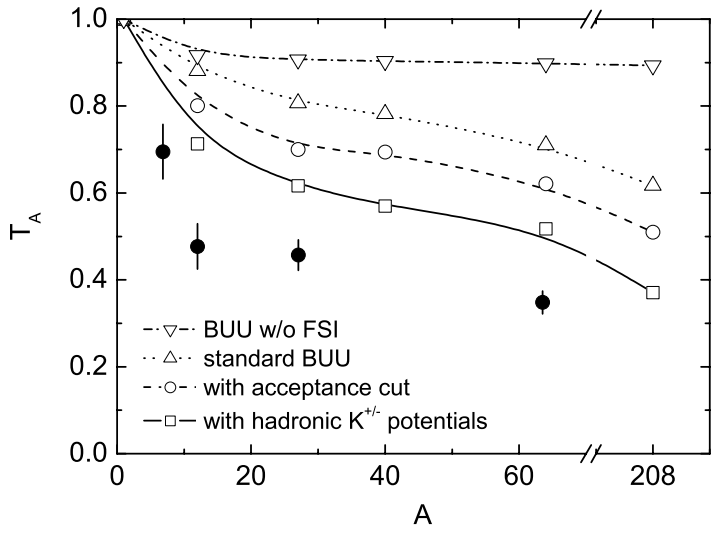

Figure 7.10: Nuclear transparency ratio from BUU simulations (open symbols) in comparison to the data (solid symbols) from Ref. [213]. The lines are spline interpolations and are meant to guide the eye.

consequence the momentum of the outgoing nucleon lies with high probability within the Fermi sphere, what leads to Pauli blocking of this reaction. Fermi motion reduces the nuclear photoproduction cross section due to the energy dependence of the elementary cross section which is still rising at the near threshold energies considered here. These effects are illustrated via the dash-dotted line in Fig. 7.10 which shows the transparency ratio calculated without any FSI. A much smaller effect is due to nuclear shadowing. In the considered energy regime the coherence length[6] of the ϕ component in the incoming photon ($E_\gamma = 2$ GeV $\Rightarrow$ $l_\phi \simeq 0.7$ fm) is still small as compared to the ϕ mean free path ($\lambda_\phi \simeq 6$ fm), hence leading only to a marginal correction of the cross section. Nevertheless, we include this small effect into our calculations.

The results depicted by the open circles (dashed line) take into account also the limited detector acceptance that has been discussed already in Section 7.3. We observe a further reduction of the transparency ratio. This can be attributed to the effect of Fermi motion of the initial nucleon in the incoherent photon nucleus interaction. The transverse momentum of the hit target nucleon leads to a broadening of the angular distributions in the photon nucleus reaction as compared to the reaction on a free nucleon at rest that is forward peaked. Hence, more of the produced particles do not fall into the acceptance window, leading to the observed reduction of the nuclear cross section when the geometrical acceptance constraint is turned on. This reduction is thus not connected to the absorptive part of the ϕ meson self energy as some of the ϕ mesons just go into another direction that is not covered by the forward detector setup.

So far, we have assumed that the branching ratio for the decay of the ϕ meson into

[6]This is the distance that a particular hadronic compound of the photon with given energy and momentum propagates. It is usually estimated as $l_h \approx ||\mathbf{k}_\gamma| - |\mathbf{q}_h||^{-1}$ [143].

K^+K^- is the same as in vacuum. However, the strong kaon and antikaon potentials in the medium lead to a considerable renormalization of the antikaon mass whereas in case of the kaon a cancellation of scalar and vector potentials results in an at most slight repulsive mass shift. To explore qualitatively the implications of these in-medium changes we include the in-medium kaon mass renormalization as given by Eqs. (7.38) and (7.40). Before we discuss the effects of the modified kaon dispersion on the total ϕ production rate and the transparency, we want to look at the differential cross section. Similar as in the case of the electromagnetic potential the kaon momenta will be changed during the propagation by means of the finite gradients. As a consequence also the invariant mass of the ϕ meson, reconstructed from the K^+ and K^- four-momenta, takes slightly different values than in the instant of the ϕ decay. Qualitatively this can be seen as follows.

As the single particle energies are constants of motion, the momentum of a K^- produced at finite density has to decrease when this K^- propagates to the vacuum because its mass is rising according to Eq. (7.38). The absolute value of its three-momentum in vacuum is then given by

$$|\mathbf{p}| = \sqrt{\mathbf{p}^{*2} + {m^*_{K^-}}^2 - m_K^2} \tag{7.41}$$

where $\mathbf{p}^*$ and $m^*_{K^-}$ are the momentum and effective mass of the antikaon at its production point in the medium and m_K is the kaon vacuum mass. The invariant mass squared of the K^+K^- pair is given by

$$s = (E_+ + E_-)^2 - |\mathbf{p}_+|^2 - |\mathbf{p}_-|^2 - 2\mathbf{p}_+ \cdot \mathbf{p}_- \tag{7.42}$$

where $E_+, \mathbf{p}_+$ and $E_-, \mathbf{p}_-$ are the energies and momenta of the K^+ and the K^-, respectively. For the K^- three-momentum we can write $|\mathbf{p}_-| = |\mathbf{p}^*_-| - \Delta p$ with $\Delta p \geq 0$, given by Eq. (7.41). Assuming for simplicity that the directions of kaon and antikaon remain unchanged, we obtain for the modification of the invariant mass squared

$$s - s^* = \Delta p \left(|\mathbf{p}_-| + |\mathbf{p}_+| + 2\frac{\mathbf{P}^2 - \mathbf{k}^2}{|\mathbf{p}^*_-|} \right), \tag{7.43}$$

where s^* is the invariant energy squared of the pair at its creation point inside the nucleus and s is the invariant energy squared after the propagation to the vacuum. $\mathbf{P}$ denotes the ϕ three-momentum in the nuclear rest frame and $\mathbf{k}$ is the kaon three-momentum in the ϕ rest frame. If the ϕ is at rest inside the nucleus, i. e. $\mathbf{P} = 0$, then $|\mathbf{p}^*_+| = |\mathbf{p}^*_-| = |\mathbf{k}|$. We then immediately find $s - s^* = -(\Delta p)^2 \leq 0$, i. e. the invariant mass after the propagation is lower than the mass of the decayed ϕ meson. If the ϕ momentum increases, the expression inside the brackets of Eq. (7.43) at some point turns positive, anyway when $|\mathbf{P}| \geq |\mathbf{k}| \simeq 130$ MeV. This means that the invariant mass reconstructed from the K^+K^- pair is larger then the mass of the decayed ϕ meson.

As ϕ mesons with a broad momentum spectrum contribute to our observables (see Fig. 7.15 in the following), we will encounter a broadening of the mass spectrum due to the attractive K^- potential. This is exactly what we observe in Fig. 7.11 which shows the K^+K^- invariant mass distribution together with experimental data off a Copper target. Both the data and the calculations are freely normalized. The shape of the measured mass distribution almost exactly follows the vacuum distribution. The width

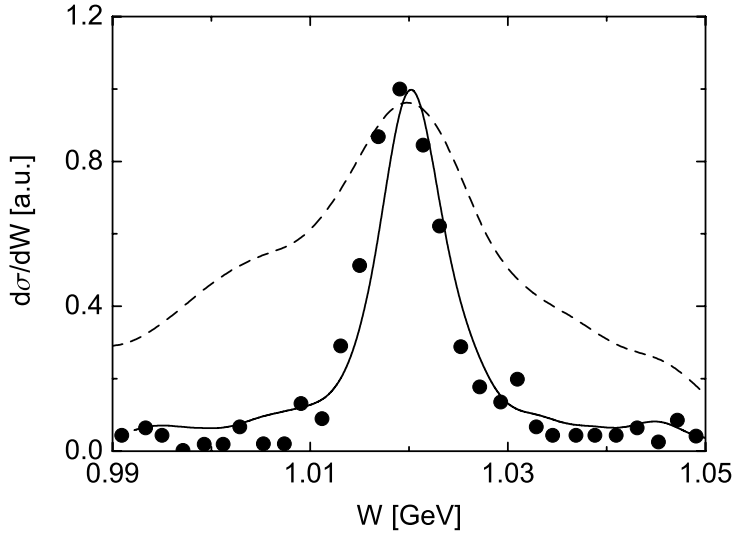

Figure 7.11: K^+K^- invariant mass spectrum from ^{64}Cu in the photon energy intervall $E_\gamma \in [1.5, 2.4]$ GeV applying the LEPS acceptance constraints, see Section 7.3. *Dashed line*: Brown/Rho parametrization (7.38) of in-medium kaon mass, *solid line*: kaon dispersion relation (7.47). The fluctuations are due to statistics. Data from Ref. [213].

of the spectrum is dictated by the ϕ vacuum width and the finite detector resolution. The broadened spectrum whose particular shape is created by the hadronic scalar kaon potentials is obviously incompatible to the data. The implementation of a more refined model will be discussed in the following Section.

7.6.2 Covariant kaon dynamics

For the implementation of the nuclear kaon and antikaon potentials we adopt the approach of Ref. [227] where the influence of a relativistically correct description of the kaon dynamics on the K^+ flow in heavy ion reactions has been investigated. The model of Ref. [227] relies upon the chiral Lagrangian set up by Kaplan and Nelson [194, 228]. Applying the mean field approximation, the following Euler-Lagrange field equations for the $K^\pm$ mesons have been derived:

$$\left[\partial_\mu\partial^\mu \pm \frac{3i}{4f_\pi^{*2}} j_\mu \partial^\mu + \left(m_K^2 - \frac{\Sigma_{KN}}{f_\pi^2}\rho_s\right)\right] \phi_{K^\pm} = 0, \tag{7.44}$$

where ρ_s is the scalar baryon density, j_μ is the baryon vector current and Σ_{KN} is the kaon nucleon sigma term for which we adopt the value of $\Sigma_{KN} = 450$ MeV from the mean field approach of Ref. [229]. Further parameters of the model are the vacuum pion decay constant $f_\pi = 93$ MeV and the in-medium pion decay constant at normal nuclear matter density $f_\pi^* = \sqrt{0.6} f_\pi$. Introducing the effective kaon mass as

$$m_K^* = \sqrt{m_K^2 - \frac{\Sigma_{KN}}{f_\pi^2}\rho_s + V_\mu V^\mu} \tag{7.45}$$

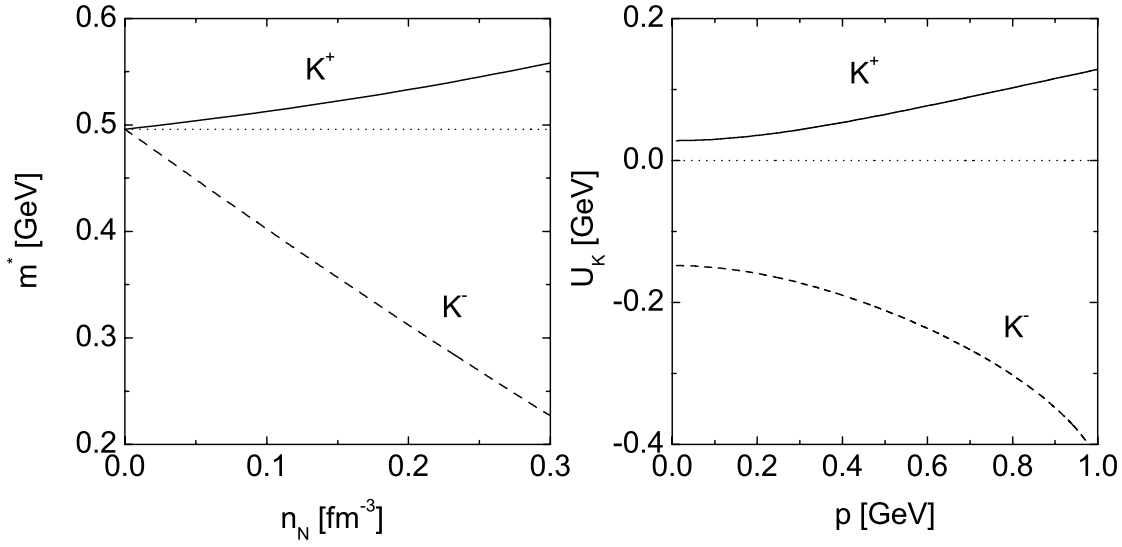

Figure 7.12: *Left*: Kaon and antikaon energy at zero momentum as function of the nuclear density. *Right*: Effective scalar potential according to Eq. (7.52) at normal nuclear matter density as function of the kaon three-momentum.

with the vector potential

$$V_\mu = \frac{3}{8 f_\pi^{*2}} j_\mu \tag{7.46}$$

the kaon dispersion relation in nuclear matter reads

$$E_{K^\pm} = \sqrt{m_K^{*\,2} + (\mathbf{p} \pm \mathbf{V})^2} \pm V_0. \tag{7.47}$$

Note that the effective mass given by Eq. (7.45) is *not* the kaon/antikaon energy at zero momentum frequently denoted as in-medium mass that defines the in-medium production thresholds. A discussion of this approach to the nuclear kaon potential and implications for the kaon flow in relativistic heavy ion collisions can also be found in Refs. [230, 231].

Due to the point-like interaction of the incoming photon with a single nucleon of the target the nucleus stays close to its ground state. This issue is discussed in Appendix A.5. Thus, the spatial components of the baryon four-vector current vanish, which also implies a vanishing vector potential $\mathbf{j} = \mathbf{V} = 0$. As one encounters nuclear densities smaller than n_0 only, the difference of scalar and vector density can safely be neglected as can be seen for instance from Fig. 1 in Ref. [230]. Thus, we have

$$j_0 = n_N \simeq \rho_s. \tag{7.48}$$

The left panel of Fig. 7.12 shows the kaon and antikaon energies at zero momentum $E_{K^\pm}(\mathbf{p} = 0)$ according to Eq. (7.47) as function of the nuclear density.

In the BUU implementation we solve the Hamilton equations of motion for the kaon and antikaon testparticles. In the static approximation (the nucleon phasespace density is

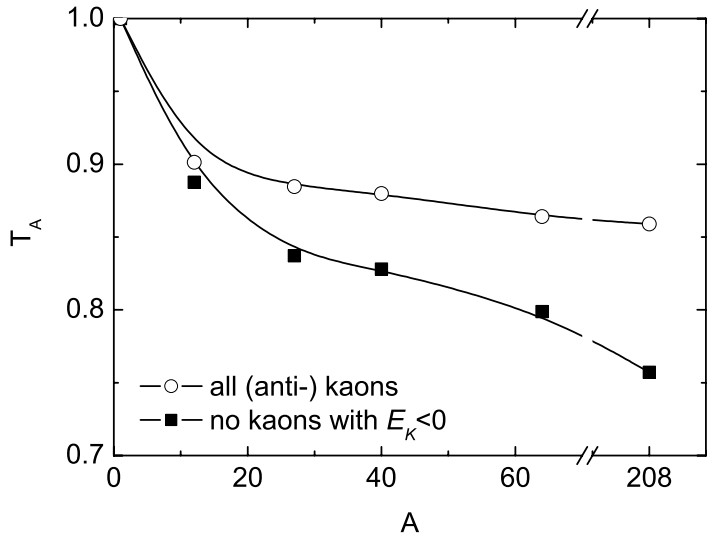

Figure 7.13: Nuclear transparency ratio as function of the target mass from BUU simulations. No acceptance constraints are applied. *Open symbols*: all (anti-) kaon testparticles are counted to obtain the final particle yield, *solid symbols*: antikaons with total energy $E_K < 0$ are subtracted from the final yield.

kept constant in time) the kaon vector field and effective mass just depend on the spatial coordinates $V_\mu = (V_0(\mathbf{r}), 0)$ and $m_K^* = m_K^*(\mathbf{r})$. We then obtain the following equations of motion:

$$\dot{\mathbf{r}} = \partial_{\mathbf{p}} \mathcal{H}_\pm = \frac{\mathbf{p}}{p_0} \tag{7.49}$$

$$\dot{\mathbf{p}} = -\partial_{\mathbf{r}} \mathcal{H}_\pm = -\frac{m_K^*}{p_0} \partial_{\mathbf{r}} m_K^* \mp \partial_{\mathbf{r}} V_0(\mathbf{r}) \tag{7.50}$$

where $\mathcal{H}_\pm$ are the K^+ and K^- Hamilton functions, respectively, given by the single particle energies (7.47). Thus, the spatial gradients of the scalar and vector potentials give rise to attractive/repulsive forces which bend the kaon and antikaon trajectories.

Effectively, both the scalar and vector potential can be summarized in one effective scalar potential U_K. The kaon dispersion relation then reads

$$E_{K^\pm} = \sqrt{(m_K + U_K)^2 + \mathbf{p}^2}. \tag{7.51}$$

In terms of the effective mass and the vector potential discussed previously this effective scalar potential is defined as

$$U_K(\mathbf{r}, \mathbf{p}) = \left[\left(\sqrt{{m_K^*}^2 + \mathbf{p}^2} \pm V_0(\mathbf{r}) \right)^2 - \mathbf{p}^2 \right]^{\frac{1}{2}} - m_K. \tag{7.52}$$

Note, that in contrast to the vector potential V_μ and the kaon effective mass m_K^* the scalar potential U_K also depends on the kaon/antikaon three-momentum. This effective

potential can now be compared directly to the scalar potential S_K introduced earlier in Eq. (7.40). At zero three-momentum we find that the depth of the potential U_K corresponds to the use of $\alpha_{K^-} \simeq -0.3$ and $\alpha_{K^+} \simeq +0.06$ in Eq. (7.40) which is at least roughly comparable to the previously used values of $\alpha_{K^-} \simeq -0.22$ and $\alpha_{K^+} \simeq 0$. However, in contrast to U_K the potential S_K depends on the spatial coordinates only. The momentum variation of the effective potential U_K is illustrated in the right panel of Fig. 7.12. Since this variation is rather substantial we are certainly missing important features of the kaon nucleus dynamics by the use of the approximation (7.40). Consequently, we adopt the more refined vector potential and effective mass according to the kaon/antikaon disperison relation (7.47) in our following calculations. Using this recipe we obviously obtain much better agreement also in the differential K^+K^- photoproduction cross sections. This can be seen again in Fig. 7.11. The solid line shows the result obtained under the same conditions as previously with the potential S_K from Eq. (7.40) (dashed line), however, using the covariant description of the nuclear kaon dynamics as described above. Thus, it turns out to be important to thoroughly account for the relativistic structure of the kaon and antikaon potentials.

As a consequence of the larger ϕ decay width generated by the attractive K^- potential, more of the produced ϕ mesons decay inside the target nucleus. The antikaons produced inside the strongly attractive potential can be confined to the nuclear volume leading to an increase of K^- absorption. Alternatively, their trajectories are distorted due to the propagation through the nonzero potential gradients. These K^+K^- pairs are likely to be found outside the experimentally imposed acceptance window. The results for the nuclear transparency ratio including the kaon/antikaon dispersion relation according to Eq. (7.47) are shown in Fig. 7.10 by the open squares. Indeed the expected reduction is observed. We illustrate the effect of the antikaon potential in Fig. 7.13. In one curve shown there the antikaons with negative total energy are subtracted from the data sample, whereas for the second curve also these not detectable particles are counted to obtain the total antikaon yield.

7.6.3 The ϕN cross section in nuclei

Even including the effects of Pauli blocking, ϕ meson and K^- absorption, kaon/antikaon quasi elastic scattering, nuclear shadowing, the nuclear kaon/antikaon potentials as well as the limited detector acceptance, the strength of the experimentally measured attenuation can still not be reproduced, see Fig. 7.10. This discrepancy implies an additional in-medium effect. A further reduction of the nuclear ϕ photoproduction cross section could in principle be caused by either a modification of the K^+K^- decay width going beyond our simple approach, a modified ϕN absorption cross section or even a change of the primary production processes. Moreover, the renormalization of the kaon properties in the medium could also cause a modification of the K^+N and K^-N cross sections. Such effects have, for instance, been studied in Refs. [232, 233]. However, for the time being we disregard the effects of such additional medium corrections and consider the whole attenuation effect as being created by ϕ meson absorption. The comparison to the experimental data then fixes a value for the total ϕN absorption cross section. Possible changes of the involved initial and final state processes, as discussed, introduce

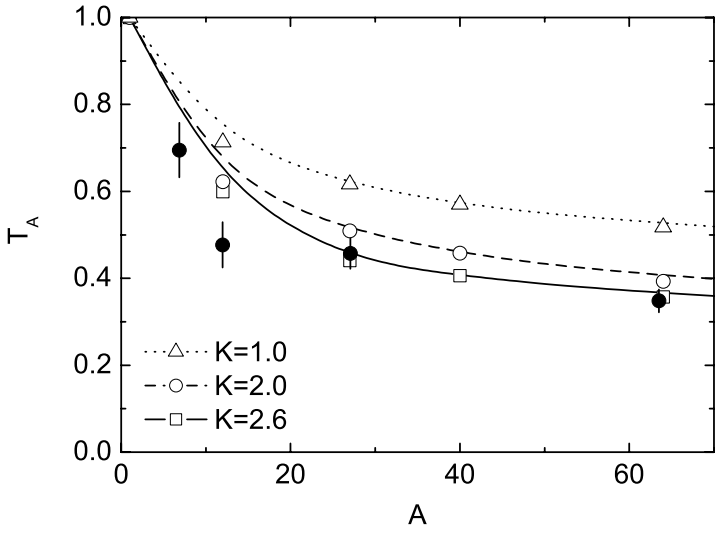

Figure 7.14: Nuclear transparency ratio as function of the target mass. Shown are BUU calculations (open symbols) in comparison to the data (solid squares) from Ref. [213]. The lines are spline interpolations and are meant to guide the eye. Calculations have been done for different $K-$factors, see text.

considerable ambiguities in the extraction of this quantity.

In order to fit the ϕN cross section to the experimental transparency data we make the following ansatz: We multiply the total ϕN cross section given by Eq. (7.25) with a constant normalization $K-$factor

$$\tilde{\sigma}_{\phi N} = K \cdot \sigma_{\phi N}. \tag{7.53}$$

In doing so we keep the partial channels $\phi N \to \phi N$ and $\phi N \to \pi N$, which are at least roughly constrained by experimental data, untouched. Thus, the modification of the ϕ in-medium cross section is entirely moved into the absorptive channel $\phi N \to 2\pi N$. The results of these calculations are shown in Fig. 7.14. Best agreement is obtained with a $K-$factor of $K = 2.6$.

In order to relate this number to the total ϕN cross section we need to know the momentum of the detected ϕ mesons. This momentum, however, is not fixed but rather a broad spectrum of ϕ mesons emerges from the photon nucleus interaction. As a showcase we illustrate the momentum differential ϕ photoproduction cross section off Calcium in Fig. 7.15. The $A-$dependence of the momentum distribution has turned out to be rather weak. Without any acceptance constraints the momentum distribution is almost symmetrically distributed around a mean value of roughly 1 GeV. This is in contrast to the elementary cross sections shown in Fig. (7.1) which exhibit a strong peak for the highest momenta. The reasons for this difference are the inclusive production channels ($\gamma N \to \phi X$), ϕ meson rescattering ($\phi N \to \phi X$), and the broad photon energy range which is integrated over ($E_\gamma \in [1.5, 2.4]$ GeV). Turning the acceptance constraints on,

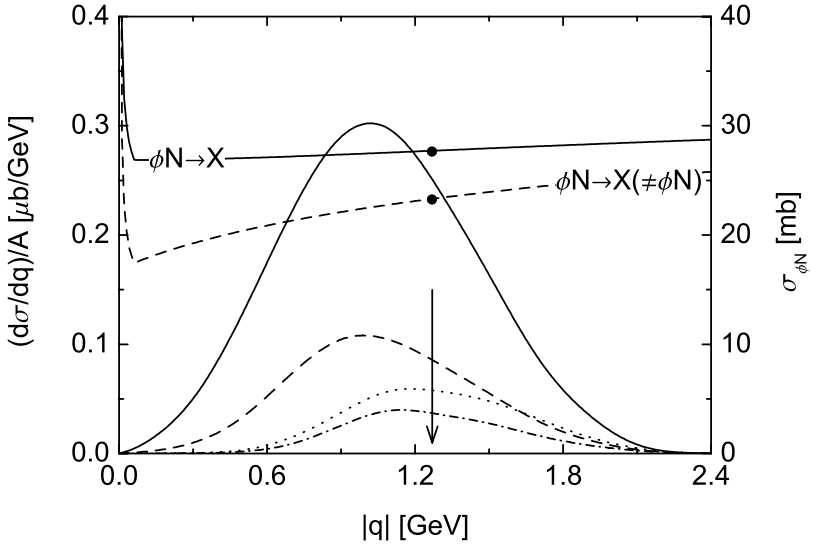

Figure 7.15: Momentum differential cross section for the reaction $\gamma\mathrm{Ca} \to K^+K^-X$ in the photon energy range $E_\gamma = (1.5 - 2.4)$ GeV with $K = 2.6$. *Solid line*: total K^+K^- yield, no acceptance constraints, *dashed line*: resonant ($\phi \to K^+K^-$) contribution, *dotted line*: total yield with acceptance constraints, *dash-dotted line*: resonant ($\phi \to K^+K^-$) contribution with acceptance constraints. The arrow indicates the mean value of the ϕ momentum inside the acceptance window $|\overline{\mathbf{q}}| = 1.26$ GeV. The upper horizontal curves have to be read with the vertical axis on the right and show the total (solid) and absorptive (dashed) ϕN cross sections used in the calculation with $K = 2.6$.

the low momentum components in the spectrum are depleted in favor of the high momentum parts. This is due to the detector geometry which favors the situation where the ϕ mesons go forward and, thus, have relatively high momenta. The mean value of the ϕ three-momentum inside the acceptance window is $|\overline{\mathbf{q}}| = 1.26$ GeV which is indicated in Fig. 7.15 by the vertical arrow. The total and absorptive ϕN cross sections used in these calculations thus amount to

$$\sigma_{\phi N}^{\mathrm{tot}}(|\bar{\mathbf{q}}| = 1.26 \text{ GeV}) \simeq 27 \text{ mb} \tag{7.54}$$

$$\sigma_{\phi N}^{\mathrm{abs}}(|\bar{\mathbf{q}}| = 1.26 \text{ GeV}) \simeq 23 \text{ mb}. \tag{7.55}$$

These values are suggested by the experimental measurements of the nuclear transparency ratio. In particular the total cross section is afflicted with large error bars since the transparency measurement is quite insensitive to the elastic components of the ϕN interaction. This issue will be studied in Chapter 9 along with the determination of the ω nucleus interaction strength.

A further quantity extracted from the experimental data in Ref. [213] is the $A-$dependence of the total ϕ meson yield. A scaling close to $\sigma \sim A^{2/3}$ implies strong absorption as the total cross section scales with the size of the nuclear surface. On the other hand a scaling close to $\sigma \sim A$ implies weak absorption as all nucleons of the target contribute

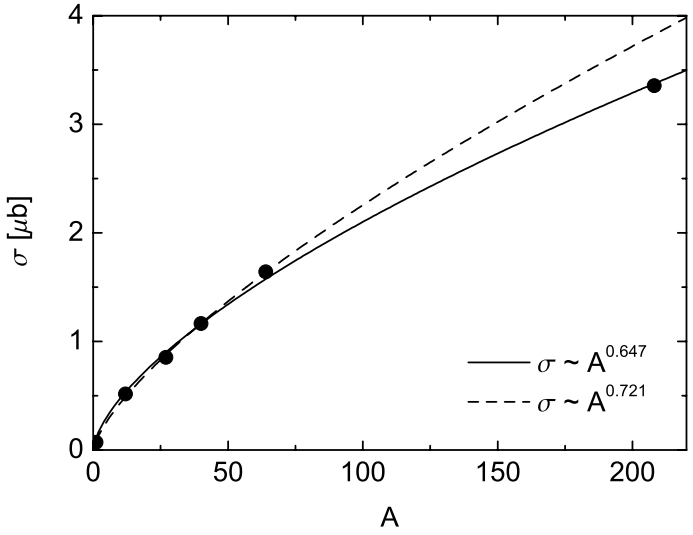

Figure 7.16: $A-$dependence of the total cross section. The open symbols are the results of our BUU calculations with $K = 2.6$ in Eq. (7.53). The solid line is a fit to all calculations, whereas for the dashed line the ^{208}Pb nucleus has been omitted from the fit.

to the total cross section. Considering only the incoherent events the authors of [213] have fitted the total yield with the ansatz

$$\sigma(A) \propto A^{\alpha} \tag{7.56}$$

with a value of $\alpha = 0.72 \pm 0.07$. The nuclear cross section as function of the target mass number from our BUU calculations that agree best with the experimental transparency ratio ($K = 2.6$) is shown in Fig. 7.16. Fitting the ansatz (7.56) to all calculated nuclei we find a value of $\alpha \simeq 0.65$. Omitting the Lead target in the fit, that also has not been considered experimentally, we obtain the value $\alpha \simeq 0.72$. This is in perfect agreement with experiment. Anyway, both values clearly show that the production of ϕ mesons on nuclei is surface dominated. In passing we, however, note that even in the simple Glauber model the total cross section does not strictly scale like $\sigma \sim A^{\alpha}$. Consequently, also the fitted parameter α depends on the mass numbers of the target nuclei included in the fit. See also Fig. B.1 and the formulas given in Appendix B.3. This should be kept in mind when the attempt is made to extract an inelastic meson nucleon cross section from photoproduction data. Here, instead of the α parameter, always the transparency data should be compared directly to either Glauber or transport calculations.

Chapter 8

The ω spectral function in nuclear matter

8.1 Introduction

A lot of theoretical effort has already been put into the determination of the isoscalar spectral density in nuclear matter [200, 234, 235, 236, 237, 238, 239, 240, 241, 242, 243, 244, 245]. The results of these models are, however, controversial. A variety of models predict a lowering of the in-medium ω mass [235, 237, 238, 239, 242]. At normal nuclear matter density and zero temperature a drop of the ω mass by up to 150 MeV has been predicted. On the other hand even slight upwards shifts and the appearance of additional peaks in the spectral function have been suggested [20, 23, 240, 241, 246]. The situation is less uneven for the in-medium broadening of the ω meson. Here, values at normal nuclear matter density of up to 70 MeV have been obtained. A quite dramatical effect, recalling that the free ω width amounts to 8.4 MeV only.

Most of these approaches use the fact that to lowest order in the nuclear density the ω in-medium self energy is proportional to the ωN forward scattering amplitude. Due to the unstable nature of the ω meson already in vacuum this reaction is not accessible for experimental study. Therefore, results are very sensitive to the theoretical assumptions on the ωN scattering dynamics. One solution to this problem is to use a unitary coupled channel approach to constrain the ωN amplitude. That is, one uses all available experimental information on hadronic and electromagnetic scattering processes that are connected to the ωN channel via rescattering processes in order to fix the open parameters of the model. To this end we extract the ωN scattering amplitude from the coupled channel $K-$matrix approach developed in Refs. [158, 172, 173, 247, 248]. Recently this model has been applied successfully to the study of the (γ, ω) and (π, ω) reactions on the nucleon [174, 249].

In the following Chapter we will first examine how the ω in-medium spectrum is influenced by the resonance scattering mechanism. To this end we construct a simple non-relativistic model from which we obtain the ω spectral function in the low-density limit. Taking over the resonance parameters and couplings from the coupled channel $K-$matrix analysis we then calculate the ω in-medium spectrum within a tree-level model, using Breit-Wigner parameterizations of the resonance propagators that emerge

due to the rescattering mechanism within the coupled channel framework. In the following we will argue why this approach is still insufficient to correctly reproduce the ωN scattering process. In a further Section we then show our results obtained by taking over the full off-shell ωN scattering amplitude directly from the coupled channel $K-$matrix model. Finally a discussion and comparison to other approaches will be given.

8.2 Framework

In the following Section we will introduce the physical framework that will be relevant to the remainder of this Chapter. To begin with, we recall the vacuum properties of the ω meson. After the introduction of some general aspects of vector mesons in nuclear matter we construct a simple non-relativistic model that illuminates the role of the formation of resonance-hole states. As a result of this Section the low-density theorem will emerge.

8.2.1 The ω meson in vacuum

The properties of any vector meson in vacuum as well as in medium are encoded in the spectral function $\mathcal{A}_{\mu\nu}$ which is basically the imaginary part of its retarded propagator. The latter is related to the retarded self energy $\Pi_{\mu\nu}$. As long as the vector meson couples to conserved currents only (as we will presume throughout this work), the three-longitudinal part of the vacuum propagator vanishes (for an introduction to the Lorentz-structure of the spin-1-propagator and the corresponding projectors see e. g. [66]). The imaginary part of the three-transversal mode of the vacuum propagator has the form

$$\begin{aligned} \mathcal{A}^T(q) = -\frac{1}{\pi}\mathcal{I}\mathrm{m}\, D^T(q) &= -\frac{1}{\pi}\mathcal{I}\mathrm{m}\, \frac{1}{q^2 - {m_V^o}^2 - \Pi^T(q)} \\ &= -\frac{1}{\pi}\frac{\mathcal{I}\mathrm{m}\Pi^T(q)}{\left[q_0^2 - \mathbf{q}^2 - {m_V^o}^2 - \mathcal{R}\mathrm{e}\Pi^T(q)\right]^2 + \left[\mathcal{I}\mathrm{m}\Pi^T(q)\right]^2}, \end{aligned} \tag{8.1}$$

where $q = (q_0, \mathbf{q})$ is the four-momentum of the vector meson and m_V^o is its bare pole mass. The imaginary part of the self energy can be related to the decay width by means of Cutkosky's cutting rules [58, 66]:

$$\mathcal{I}\mathrm{m}\Pi^T(q) = -i\sqrt{q_0^2 - \mathbf{q}^2}\,\Gamma(q^2). \tag{8.2}$$

The corresponding real part can be obtained by means of a (subtracted) dispersion relation, see e. g. Refs. [66, 70] and Chapter 9, Section 9.3.2.

The dominant part of the ω self energy in vacuum is given by the processes $\omega \to 2\pi$, $\omega \to 3\pi$ and $\omega \to \pi^0\gamma$. For the decay width to the semi-hadronic $\pi^0\gamma$ channel we adopt the expression derived in Ref. [226]:

$$\Gamma(\omega \to \pi^0\gamma) = \frac{9}{24\pi}\left(\frac{d}{f_\pi}\right)^2 \left(\frac{q^2 - m_\pi^2}{\sqrt{q^2}}\right)^3 \Theta(q^2 - m_\pi^2) \tag{8.3}$$

where $q = (q_0, \mathbf{q})$ is the ω four-momentum, $f_\pi = 92.4$ MeV is the pion decay constant and $d \simeq 0.1$ is a coupling parameter that has been fitted in order to obtain agreement with the experimental value of $\Gamma_0(\omega \to \pi^0\gamma) = (717 \pm 42)$ keV.

The rather small $\omega \to 2\pi$ contribution to the ω self energy is due to $\rho - \omega$ mixing. The ω decay width to this channel can be derived from the phenomenological interaction Lagrangian

$$\mathcal{L}_{V\pi\pi} = -g_{V\pi\pi}\boldsymbol{\pi}(\partial_\mu \boldsymbol{\pi})V^\mu. \tag{8.4}$$

Thus we have

$$\Gamma(\omega \to 2\pi) = \Gamma_0(\omega \to 2\pi)\frac{m_\omega^2}{q^2}\left(\frac{q^2 - 4m_\pi^2}{m_\omega^2 - 4m_\pi^2}\right)^{\frac{3}{2}}\Theta(q^2 - 4m_\pi^2) \tag{8.5}$$

where $\Gamma_0(\omega \to 2\pi) = 142.8$ keV is the decay width at the physical ω mass.

The $\omega \to 3\pi$ self energy is a sum of a direct $\omega \to 3\pi$ contribution and the so-called GSW (Gell-Mann, Sharp, Wagner) process, a twostep process in which the ω first converts into a $\rho\pi$ state followed by the decay of the virtual ρ into two pions. However, for simplicity we neglect the direct contribution, which – as we shall see later – results in a good description of the free ω spectrum. The GSW contribution to the $\omega \to 3\pi$ width is given by a convolution of the $\omega \to \rho\pi$ width and the ρ vacuum spectral function $\mathcal{A}_\rho$

$$\Gamma(\omega \to 3\pi) = \int_{(2m_\pi)^2}^{(\sqrt{q^2} - m_\pi)^2} ds\ \bar{\Gamma}_{\omega\to\rho\pi}(q^2, s)\mathcal{A}_\rho(s)\frac{\Gamma_{\rho\to\pi\pi}(s)}{\Gamma_{\rho\to X}(s)} \tag{8.6}$$

where s is the mass of the virtual ρ meson squared and $\bar{\Gamma}(\omega \to \rho^*\pi)$ is the ω decay width to a π and a virtual ρ meson. From the $\omega\rho\pi$ interaction Lagrangian we find

$$\bar{\Gamma}(\omega \to \rho\pi) = \frac{3}{4\pi}\left(\frac{g}{m_\pi}\right)^2\left[\frac{(q^2 - s - m_\pi^2)^2 - 4sm_\pi^2}{4q^2}\right]^{\frac{3}{2}}\Theta(q^2 - 9m_\pi^2). \tag{8.7}$$

The $\omega\rho\pi$ coupling constant g is determined by the postulate that at the on-shell point the experimental width of 7.5 MeV [141] is retained. The expression for the decay width $\Gamma(\rho \to 2\pi)$ is identical to Eq. (8.5) but with the replacement $m_\omega \to m_\rho$ and $\Gamma_0(\rho \to 2\pi) = 149.2$ MeV.

Finally we obtain the vacuum self energy of the ω meson by summing up the individual contributions:

$$\Pi(q_0, \mathrm{q}) = -i\sqrt{q_0^2 - \mathbf{q}^2}\left[\Gamma(\omega \to \pi^0\gamma) + \Gamma(\omega \to 2\pi) + \Gamma(\omega \to 3\pi)\right]. \tag{8.8}$$

Note, that we have neglected here to derive the real part of the ω vacuum self energy. Therefore, the physical ω mass, that on-shell is given by the sum of the bare mass and the real part of the self energy, has to be inserted in the denominator of the vacuum spectral function (8.1): $m_V^o \to m_V = 782$ MeV. This approximation is justified because of the small vacuum width of the ω meson – thus the variation of the real part within the relevant energy region around the ω pole is expected to be small. The individual contributions to the ω decay width in vacuum are shown in Fig. 8.1.

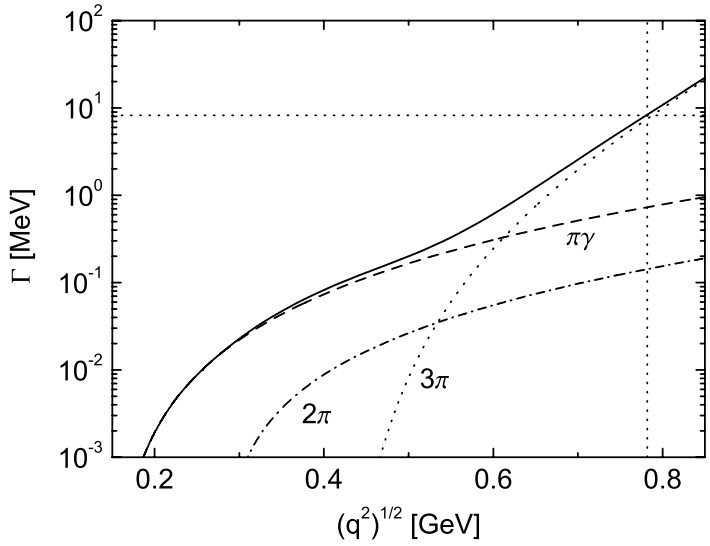

Figure 8.1: Total and partial decay widths of the ω meson in vacuum. *Solid line*: total summed width. The vertical dotted line illustrates the physical ω mass $m_0 = 782$ MeV and the horizontal one the total vacuum width $\Gamma_0 = 8.4$ MeV.

8.2.2 Vector mesons in nuclear matter

In the presence of a nuclear medium, the description of a vector meson requires besides the four-momentum $q_\mu = (q_0, \mathbf{q})$ a second four-vector n_μ, characterizing the medium. A convenient choice is to evaluate this vector in the rest frame of nuclear matter:

$$n_\mu = (m_N, \mathbf{0}) \tag{8.9}$$

where m_N is the nucleon mass. Besides q^2 two other Lorentz invariant structures can be built up from n_μ and q_μ. With the choice (8.9) the self energy depends independently on the two variables q^2 and q_0 or, alternatively, on q_0 and $|\mathbf{q}|$. In addition, the vector meson self energy now also depends on the projection of the spin on the vector meson three-momentum, i. e. the polarization. With the use of the four-vectors q_μ and n_μ a three-longitudinal and a three-transversal projector, $P_L^{\mu\nu}$ and $P_T^{\mu\nu}$ respectively, can be defined. Due to current conservation, the terms proportional to q_μ and q_ν vanish when $P_L^{\mu\nu}$ is contracted with the self energy tensor. Therefore the self energy of the longitudinal mode is given by

$$\Pi^L(q_0, q^2) = -\frac{q^2}{(n.q)^2 - n^2 q^2} \frac{n_\mu n_\nu}{m_N^2} \Pi^{\mu\nu}(q_0, q^2) \overset{(8.9)}{=} -\frac{q^2}{\mathbf{q}^2} \Pi^{00}(q_0, q^2). \tag{8.10}$$

Having calculated the longitudinal projection, the transversal one can be obtained from the helicity averaged self energy $\bar{\Pi}$ by subtracting the longitudinal part

$$\Pi^T(q_0, q^2) = \frac{1}{2} \left(\bar{\Pi}(q_0, q^2) - \Pi^L(q_0, q^2) \right). \tag{8.11}$$

Here, $\bar{\Pi}$ is given by the average over both polarizations. More details on the Lorentz structure of the in-medium self energy and a definition of the projectors can be found in Ref. [66].

8.2.3 Toy model

In order to calculate the collisional self energy of the ω meson in nuclear matter we start with one assumption, namely that the vector meson nucleon scattering process is dominated by the excitation of baryon resonances. This can be motivated from our experimental knowledge on low-energy pion nucleon scattering where indeed an approximate saturation of the cross section by the resonance excitation mechanism is seen. In turn the restriction to $s-$channel scattering processes provides us with the possibility to construct the in-medium self energy in a rather simple manner using the optical theorem. This has been worked out quite in detail in Refs. [66, 70, 250, 251] for the case of the π, η and ρ mesons. Moreover, in [252] it was shown by a leading order expansion in the number of quark colors N_c that the only surviving mesonic medium modification in the limit $N_c \to \infty$ is the excitation of resonance-hole states.

In order to study the properties of our model we consider in the following the coupling of the ω meson to one single resonance only. As a particular example we choose the $D_{13}(1700)$ resonance with the quantum numbers $J^P = 3/2^-$, rest mass $m_R = 1.743$ GeV, and total width $\Gamma_R = 67$ MeV. This resonance sits close to the ωN threshold and has a sizable coupling to the ωN channel, thus its effect on the ω self energy is expected to be crucial. The resonance parameters are taken from the coupled channel resonance analysis [158, 173]. The relativistic Lagrangian that describes the $RN\omega$ coupling is given by [248]:

$$\mathcal{L}_{RNV} = \bar{u}^{\mu}_{R} \left[\frac{g_1}{2m_N} \gamma^{\nu} + i \frac{g_2}{4m_N^2} \partial^{\nu}_{N} + i \frac{g_3}{4m_N^2} \partial^{\nu}_{V} \right] u_N V_{\mu\nu} \tag{8.12}$$

with the antisymmetric field tensor $V^{\mu\nu} = \partial^{\mu}_{V} V^{\nu} - \partial^{\nu}_{V} V^{\mu}$ that automatically ensures current conservation. In order to keep our preliminary considerations as simple as possible we only keep the coupling proportional to g_1 and drop the other ones in the remainder of this Section.

Non-relativistic reduction

In order to further simplify our model we perform a non-relativistic reduction of (8.12). That is, we expand the Lagrangian in terms of the nucleon and vector meson momenta

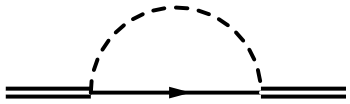

Figure 8.2: Self energy of a baryon resonance from the decay into scalar (ς), pseudoscalar (φ) or vector (V) meson and nucleon.

and keep only the leading terms:

$$\begin{aligned}
\mathcal{L}_1 &= \frac{g_1}{2m_N}\bar{u}^{\mu}_R\gamma^{\nu}u_N V_{\mu\nu} \\
&= \frac{g_1}{2m_N}\bar{u}_R S^{\mu\dagger}\gamma^{\nu}u_N V_{\mu\nu} \\
&= \frac{g_1}{2m_N}N_R N_N(\chi_S^{\dagger},0)\gamma_0 S^{\mu\dagger}\gamma^{\nu}\begin{pmatrix}\chi_S \\ \frac{\sigma\mathbf{p}}{E_p+m_N}\chi_S\end{pmatrix}V_{\mu\nu} \\
&\approx \frac{g_1}{2m_N}N_R N_N\chi_S^{\dagger}S_i^{\dagger}\chi_S V_{0i},
\end{aligned} \tag{8.13}$$

where in the second step we have used the fact that in the rest frame of the resonance the zeroth component of the spin $3/2 \to 1/2$ transition operator (Eq. D.45) vanishes: $S_0 = 0$. N_R and N_N are the normalization constants of resonance and nucleon spinor, respectively. Going from line three to four, we have neglected the vector component $\nu = 0$. It has the consequence to mix the upper and lower components of the nucleon and resonance spinors such that an additional power of the nucleon momentum is introduced. Rewriting the vector meson field tensor, we finally obtain the non-relativistic Lagrangian for the coupling of the ωN channel to $J^P = 3/2^-$ resonances

$$\mathcal{L}^{\mathrm{NR}}_{RNV} = \frac{g_1}{2m_N}\,\psi_R^{\dagger}S_i^{\dagger}\left(\partial_0 V_i - \partial_i V_0\right)\psi_N \tag{8.14}$$

where we have considered a vertex with an incoming ω and nucleon creating the outgoing resonance state. Here, p_0 denotes the energy of the nucleon and q_0 is the energy of the ω, both taken in the ωN CM frame.

Resonance self energy

The vacuum self energy of baryon resonances arises from the coupling to meson nucleon channels. In our framework these channels are $\pi N, 2\pi N, \eta N, \omega N, K\Lambda$ and $K\Sigma$. In principle, the self energy of a spin$-1/2$ resonance is a matrix in Dirac space. In this work, however, we replace it by an averaged quantity that is obtained by averaging the exact self energy over the resonance spins. We then have again the simple relation (8.2) that relates the averaged self energy and the decay width.

Once again we simplify our toy model by – besides $R \to \omega N$ – including one additional vacuum decay channel only, namely $R \to \pi N$. The non-relativistic Lagrangian that

(a) (b)

Figure 8.3: Lowest order contribution to the vector meson self energy in nuclear matter (a) and vector meson nucleon scattering via excitation and decay of a $s-$channel resonance (b).

describes the coupling of a $3/2^-$ resonance to pseudoscalar meson nucleon channels is given by [248]

$$\mathcal{L}_{RN\varphi} = -\frac{g}{2m_N m_\pi}\psi_R^\dagger(\mathbf{S}^\dagger\cdot\mathbf{q})(\boldsymbol{\sigma}\cdot\mathbf{p})\psi_N \tag{8.15}$$

where $\mathbf{q}$ and $\mathbf{p}=-\mathbf{q}$ are the meson and nucleon CM momenta in the resonance rest frame. Following standard Feynman rules, the decay width of a $J^P=3/2^-$ nucleon resonance with mass $\sqrt{s}$ into a pseudoscalar $\varphi(=\pi)$ or vector $V(=\omega)$ meson and nucleon in the resonance rest frame is given by

$$\Gamma_{\varphi,V} = \frac{1}{8\pi}\frac{|\mathbf{q}|}{s}\frac{1}{2J_R+1}\Omega_{\varphi,V} \tag{8.16}$$

with the non-relativistic spin traces

$$\Omega_{\varphi,V} = 4m_N m_R \mathrm{Tr}\left[\Gamma_{\varphi,V}^\dagger\Gamma_{\varphi,V}\right]. \tag{8.17}$$

The vertex functions $\Gamma_{\varphi,V}$ are obtained from the interaction Lagrangians (8.14) and (8.15). The trace arises from the summation over the outgoing nucleon spins. Explicitly, the traces are given by

$$\Omega_\varphi = \frac{16}{3}m_N m_R|\mathbf{q}|^4\left(\frac{g}{2m_N m_\pi}\right)^2 \tag{8.18}$$

$$\Omega_V = \frac{16}{3}m_N m_R\left(\frac{g_1}{2m_N}\right)^2(3q_0^2-\mathbf{q}^2). \tag{8.19}$$

Vector meson self energy

From the coupling of the vector meson to baryon resonances the contribution to the in medium self energy $\Pi_{\mu\nu}$ is given to lowest order by the diagram shown in Fig. 8.3(a). The application of standard Feynman rules leads to the following expression for the vector meson self energy:

$$-i\Pi^{T/L}(q_0,\mathbf{q}) = -\int\frac{d^4p}{(2\pi)^4}(-i)^2\mathrm{Tr}\left[G_N(p)\Gamma_\mu^\dagger G_R(k)\Gamma_\nu\right]P_{L/T}^{\mu\nu} \tag{8.20}$$

$$\Rightarrow \Pi^{T/L}(q_0,\mathbf{q}) = -i\int\frac{d^4p}{(2\pi)^4}n(\mathbf{p})\frac{\Omega_{T/L}}{(p_0-E(\mathbf{p}))(k_0-E_R(\mathbf{k})+\frac{i}{2}\Gamma_R(k))} \tag{8.21}$$

where $\Omega_{T/L}$ denotes the projection of the spin trace on the three-transversal/longitudinal mode of the vector meson field that is calculated according to the relations (8.10) and (8.11). The non-relativistic propagators of nucleon and resonance are given by:

$$-iG_N(p) = \frac{n(\mathbf{p})}{p_0 - E(\mathbf{p}) - i\epsilon} \tag{8.22}$$

$$-iG_R(k) = \frac{1}{k_0 - E_R(\mathbf{k}) + \frac{i}{2}\Gamma_R(k)}. \tag{8.23}$$

Here $E_N(p)$ and $E_R(k)$ are the nucleon and resonance on-shell energies, respectively, and $\Gamma(k)$ is the vacuum decay width of the resonance calculated as discussed in the previous paragraph. For the Fermi distribution function one has $n(\mathbf{p}) = \Theta(p_F - |\mathbf{p}|)$. For the non-relativistic spin traces we find

$$\Omega_L = \frac{16}{3} m_N m_R \left(\frac{g_1}{2m_N}\right)^2 q^2 \tag{8.24}$$

$$\Omega_T = \frac{16}{3} m_N m_R \left(\frac{g_1}{2m_N}\right)^2 q_0^2. \tag{8.25}$$

Using Cutkosky's cutting rules [58, 66] the imaginary part of the self energy can be evaluated further:

$$\begin{aligned}
\mathcal{I}\mathrm{m}\Pi(q_0, \mathbf{q}) &= \frac{1}{2}\int \frac{d^4p}{(2\pi)^4} n(\mathbf{p})(-2\pi i)\delta(p_0 - E(\mathbf{p}))(-2\pi i)\mathcal{A}_R(k)\Omega_{T/L} \\
&= \int \frac{d^3p}{(2\pi)^3} n(\mathbf{p})\mathcal{I}\mathrm{m}\frac{\Omega_{T/L}}{k_0 - E_R(\mathbf{k}) + \frac{i}{2}\Gamma_R(k)} \\
&\approx \frac{n_N}{4}\mathcal{I}\mathrm{m}\frac{\Omega_{T/L}}{k_0 - E_R(\mathbf{k}) + \frac{i}{2}\Gamma_R(k)} \\
&\equiv n_N \mathcal{I}\mathrm{m}T_{T/L}.
\end{aligned} \tag{8.26}$$

Going from line two to three we have made the approximation that the trace only weakly depends on the nucleon three-momentum $\mathbf{p}$. This assumption is valid at small densities and allows to pull the trace out of the integral. In spin-isospin symmetric nuclear matter the remaining integral gives the factor of $n_N/4$. Going to the last line we have identified the product of the trace and the resonance propagator with the forward scattering amplitude for the process $V_r(q) + N_s(p) \to R(k+p) \to V_r(q) + N_s(p)$ where r and s denote polarization and spin of vector meson and nucleon, respectively. This process is shown diagrammatically in Fig. 8.3(b). The last line of (8.26) is called the *low density theorem* that is – for obvious reasons (using rather ρ instead of n_N) – often referred to as the $T\rho-$approximation.

Even more generally the low density theorem is expressed in terms of the ωN scattering tensor $T_{\mu\nu}$:

$$\Pi_{\mu\nu} = n_N T_{\mu\nu}, \tag{8.27}$$

which is a very general expression that is not restricted to the formation of resonances. It holds basically for all processes involving one nucleon line at a given time. To get the

m_R	Γ_R	$\Gamma_{\pi N}$	$\Gamma_{\omega N}$	g_1
1.743 GeV	0.067 GeV	0.029 GeV	0.038 GeV	4.294

Table 8.1: Parameters of the $D_{13}(1700)$ resonance in our toy model.

complete self energy one needs the complete ωN scattering amplitude in (8.27). Note, that we have extended Eq. (8.27) to yield the imaginary and real part of the in-medium self energy. This can be done if the self energy has well defined analytic properties. However, if some contributions to the self energy are multiplied with form factors in order to cut the off-shell contribution of individual resonances, analyticity is destroyed. In order to restore analyticity in this case the real part of the self energy could be calculated using dispersive methods. As was shown in [66] in most cases both methods yield quite similar results.

In general, (8.26) is not a mandatory approximation to hadronic in-medium self energies. In particular (but not only) for nuclear densities larger than n_0 the $T\rho$ approximation is not valid and higher order density effects have be accounted for, see Refs. [66, 70]. In this case the full in-medium self energy of the resonance has to be inserted in the denominator of Eq. (8.21). This is obtained by evaluating diagram 8.2 with full in-medium meson propagators that in turn are obtained by inserting the self energies calculated from Eq. (8.21). Thus, a self-consistency problem arises that has to be solved in an iterative scheme. This has been done for the case of the π, η and ρ mesons in Ref. [70]. In the present work, however, we will stick to the approximation (8.26) what, as we shall see in a later Section, is mandatory when the $K-$matrix coupled channel solution to the $N\omega$ scattering problem is used.

Spectral function

Now we can calculate the ω spectral function in nuclear matter according to Eq. (8.1), assuming that the ω couples to nucleons via the excitation of one single $s-$channel resonance only. In Table 8.1 the parameters of our simple model are given; they are chosen such as to reproduce the vacuum properties of the $D_{13}(1700)$ resonance obtained in the coupled channel analysis [158, 173]. The ω spectral function at normal nuclear matter density is shown in Fig. 8.4. The spectral function is characterized by the formation of an additional peak that arises from the excitation of the resonance-hole loop. At given three-momentum $\mathbf{q}$ the energy of a resonance-hole state with a resonance of mass m_R is approximately determined by the equation

$$\begin{aligned} (q+p)^2 &= q^2 + m_N^2 + 2m_N\sqrt{q^2+\mathbf{q}^2} = m_R^2 \\ \Rightarrow q^2 &= m_N^2 + m_R^2 - 2m_N\sqrt{m_R^2+\mathbf{q}^2}. \end{aligned} \tag{8.28}$$

This is not exact, since through the real part of the self energy the position of the peak is influenced by level repulsion. This phenomenon can be observed in each quantum mechanical two level system with a perturbation coupling both levels, for a discussion

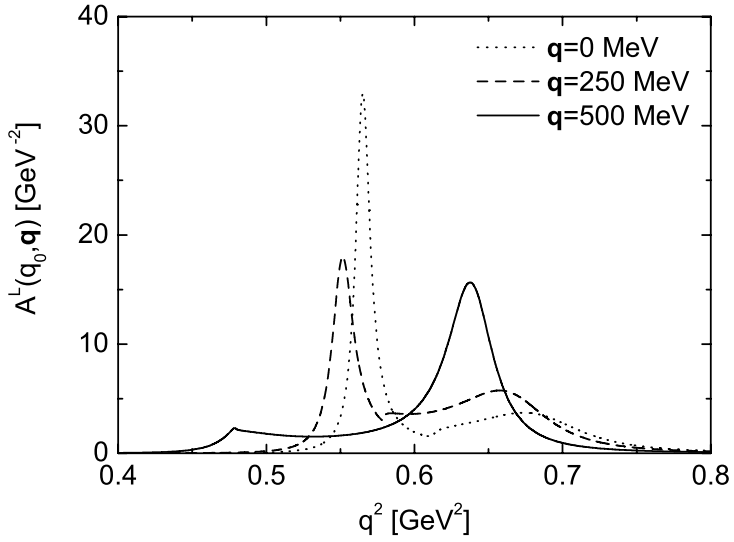

Figure 8.4: Transverse spectral function of the ω meson at normal nuclear matter density. The in-medium self energy is calculated in a non-relativistic approximation and consists of a single $3/2^- h$ excitation only. Shown are curves for different ω three-momenta.

of this effect see for instance Ref. [66]. At rest, the resonance-hole peak appears at $q^2 \simeq 0.67$ GeV^2 since the considered resonance sits slightly above the $N\omega$ threshold ($m_R = 1.743$ GeV $> m_N + m_\omega = 1.72$ GeV). Due to level repulsion the genuine ω peak has a mass of $\sqrt{q^2} \simeq 755$ MeV. Going to higher ω three-momenta the resonance-hole branch moves to smaller energies according to Eq. (8.28) and also pushes the ω peak further down. At three-momenta around 0.3 GeV the picture dramatically changes as both the genuine ω and the RN^{-1} branches cross. Thus, for $|\mathbf{q}| = 0.5$ GeV the resonance-hole branch appears at much smaller energy and – again due to level repulsion – pushes the ω peak to higher masses $\sqrt{q^2} \simeq 800$ MeV. Now also the broadening of the ω peak becomes substantial. The broadening will again be reduced for higher three-momenta when the RN^{-1} excitation moves further down and, thus, its influence in the vicinity of the ω peak becomes small again.

This situation demonstrates the general properties of our model. Resonance-hole excitations introduce additional branches in the spectral function. If their position in energy is close to the genuine ω mass, the ω peak is broadened via the imaginary part of the self energy. The real part of the self energy has the consequence to shift the position of the generic peak. This shift always pushes the peak away from the position of the resonance-hole component. This phenomenon is known as level repulsion. Consequently, at high three-momenta where most resonances have passed the on-shell point, see Eq. (8.28), no attractive mass shift can be generated in our approach. For low momenta the direction of a mass shift in particular depends on the coupling of the ω to subthreshold resonances. These couplings are, however, a priori hard to constrain experimentally.

8.3 Tree-level model

Pursuing the evaluation of the ω self energy with the model sketched in the previous Section we now construct the self energy from the summation of the individual resonance contributions. The parameters – couplings, resonance masses and widths, cutoffs – we take over from a recent fit to the (γ, ω) and (π, ω) reactions using the coupled channel resonance model [158, 173, 248].

8.3.1 Model

The coupled channel resonance model of Ref. [174, 249] is based on a solution of the Bethe-Salpeter equation within the $K-$matrix approximation. A brief overview will be given in a later Section. The particular solution of the coupled channel problem used has been obtained within the Pascalutsa coupling scheme that introduces a reduced number of parameters as compared to the conventional scheme since so-called off-shell projectors in the $J = 3/2$ sector are absent (see [248, 253]). The parameters of the included spin$-1/2$ and spin$-3/2$ resonances are given explicitly in the following and will be referred to as parameter set A. This solution, however, is not the most recent one obtained and will be replaced in the final Section of this Chapter by an updated version (parameter set B) including conventional couplings and a proper treatment of $J^P = 5/2^{\pm}$ resonances.

We calculate the ωN forward scattering amplitude needed for the evaluation of the self energy according to Eq. (8.27) in a completely relativistic manner. The relativistic Lagrangians for the coupling of the $J^P = 1/2^{\pm}$ and $J^P = 3/2^{\pm}$ resonances to the $N\omega$ system are given explicitly in Appendix G. The relativistic propagators of the interacting spin$-1/2$ and spin$-3/2$ resonances are given by

$$\mathcal{G}_{1/2}(k) = i\frac{\not{k} + \sqrt{k^2}}{k^2 - m^2 - \Sigma(k)} \tag{8.29}$$

and

$$\mathcal{G}^{\mu\nu}_{3/2}(k) = -i\frac{\not{k} + \sqrt{k^2}}{k^2 - m^2 - \Sigma(k)}\left[g^{\mu\nu} - \frac{1}{3}\gamma^\mu\gamma^\nu - \frac{2}{3k^2}k^\mu k^\nu + \frac{1}{3\sqrt{k^2}}(k^\mu\gamma^\nu - k^\nu\gamma^\mu)\right] \tag{8.30}$$

where $k = (k_0, \mathbf{k})$ is the four-momentum of the resonance and $\Sigma(k)$ is the averaged resonance self energy. It is given by

$$\Sigma(k) = -i\sqrt{k^2}\sum_f \Gamma_{R\to f}(k)F^2(k). \tag{8.31}$$

where $\Gamma_{R\to f}$ are the partial energy dependent vacuum decay widths of the resonance to meson nucleon channels. The use of $\sqrt{k^2}$ in the nominators in Eqs. (8.29) and (8.30) has been motivated in detail in Ref. [66]. The relativistic self energy of the ω according to Eq. (8.26) is given by

$$\Pi^{L/T}(q_0, \mathbf{q}) = \frac{n_N}{4m_N}\sum_R \frac{\Omega_R^{L/T}}{k^2 - m_R^2 - \Sigma(k)}F^2(k) \tag{8.32}$$

where n_N is the nuclear density and $k = p + q$ is the resonance four-momentum. The form factor cuts the off-shell contributions of the individual resonance contributions. We parametrize it as

$$F(k) = \frac{\Lambda_R^4}{\Lambda_R^4 + (k^2 - m_R^2)^2}. \tag{8.33}$$

In [249] universal values for the cutoffs Λ_R have been used for resonances with spin J. They are

$$\Lambda_{1/2} = 4.29 \text{ GeV} \tag{8.34}$$
$$\Lambda_{3/2} = 1.02 \text{ GeV}. \tag{8.35}$$

The sum in Eq. (8.32) runs over all included spin$-1/2$ and spin$-3/2$ resonances. The traces $\Omega_R^{L/T}$ are obtained from the evaluation of the following expressions

$$\Omega_{1/2}^{L/T} = \frac{k^2}{m_R^2}\text{Tr}\left[(\not{p} + m_N)\mathcal{V}_\mu^\dagger(\not{k} + \sqrt{k^2})\mathcal{V}_\beta\right] P_{T/L}^{\nu\beta} \tag{8.36}$$
$$\Omega_{3/2}^{L/T} = \frac{k^2}{m_R^2}\text{Tr}\left[(\not{p} + m_N)\mathcal{V}_{\mu\nu}^\dagger P_{3/2}^{\mu\alpha}(k)\mathcal{V}_{\alpha\beta}\right] P_{L/T}^{\nu\beta} \tag{8.37}$$

with the three longitudinal and three transverse projectors $P_L^{\mu\nu}$ and $P_T^{\mu\nu}$. In the second line we have used the spin 3/2 projector, it is given explicitely in Eq. (G.12). The vertex functions are determined from the interaction Lagrangians given in Appendix G. In total we include ten nucleon resonances. Their properties and $RN\omega$ coupling constants are given in Table 8.2. In practice we obtain the spin traces by means of the `Mathematica` package `FeynCalc` [254]. Due to the interference of the different couplings, their analytic structure is rather involved and, therefore, not given explicitly in this work. In order to get a handle on the accuracy of our calculations we also calculate the complete self energy in a non-relativistic manner as done previously in the derivation of the formalism. Also the non-relativistic couplings and traces are given explicitly in Appendix G.

8.3.2 Results

In Fig. 8.5 the results for the ω spectral function at normal nuclear matter density for three-momenta of $\mathbf{q} = 0$ GeV, 0.4 GeV and 0.8 GeV are shown. At $\mathbf{q} = 0$ GeV the longitudinal and transverse spectral functions are degenerate. Qualitatively they exhibit very similar features as in our simple toy model, where we considered a single resonance-hole excitation only. Due to the large width of most of the included resonances and their close overlap, in many cases the individual resonance-hole peaks cannot be distinguished. However, in the present parameter set A the $D_{13}(1700)$ couples strongly to the $N\omega$ channel and its structure in the spectral function is clearly seen. As its mass is only slightly above the $N\omega$ threshold, the excitation of the $D_{13}(1700)h$ loop produces a second peak in the spectral function slightly above the generic ω peak. Due to level repulsion the ω peak is pushed down to q^2 values of roughly $q^2 = 0.55$ GeV^2. The importance of the $D_{13}(1700)$ excitation is also visualized clearly in Fig. 8.6 where the real and imaginary parts of the ω self energy are shown. The $D_{13}(1700)h$ excitation

$L_{2I,2S}$	status	mass	width	J	P	$g^1_{RN\omega}$	$g^2_{RN\omega}$	$g^3_{RN\omega}$
$P_{11}(1440)$	****	1516	644	1/2	+	−6.73	8.21	−
$P_{11}(1710)$	***	1704	408	1/2	+	4.87	−11.76	−
$S_{11}(1535)$	****	1548	125	1/2	−	3.59	6.85	−
$S_{11}(1650)$	****	1703	294	1/2	−	0.56	2.09	−
$S_{11}(1820)$		1929	682	1/2	−	−2.15	0.0	−
$P_{13}(1720)$	****	1694	152	3/2	+	26.48	−5.88	13.56
$P_{13}(1900)$	**	1948	792	3/2	+	6.0	13.0	−30.0
$D_{13}(1520)$	****	1509	93	3/2	−	−7.15	1.12	3.78
$D_{13}(1700)$	***	1743	67	3/2	−	14.97	−7.59	−16.57
$D_{13}(1800)$		1946	703	3/2	−	−14.28	12.83	4.64

Table 8.2: Parameter set A. Properties of the $J^P = 1/2^\pm$ and $3/2^\pm$ resonances that couple to the $N\omega$ channel. Masses and widths are given in MeV. The current status is quoted as in Ref. [141]. In addition, also the $RN\omega$ coupling constants entering the Lagrangians (Appendix G) are given.

generates the dominant part of the self energy in the relevant q^2 region around the ω pole.

For the longitudinal mode the dominance of the $D_{13}(1700)$ persists over the complete momentum range considered. However, for high momenta the resonance-hole peak moves away from the ω pole and, thus, its importance decreases. Moreover, its $s-$wave coupling is proportional to q^2 and therefore becomes smaller as the three-momentum increases until it eventually vanishes when the resonance-hole excitation reaches the photon point. The transverse spectral function and self energy exhibit rather rich resonance structures for finite three-momenta. At three-momentum values around $\mathbf{q} = 0.4$ GeV the sub-threshold resonances $D_{13}(1520)$, $D_{13}(1700)$ and $P_{13}(1720)$ push the ω peak slightly up in energy. However, due to the pronounced resonance-hole peaks, considerable strength is moved down to smaller q^2 values. At high momentum the transverse spectral function is clearly dominated by the excitation of the $P_{13}(1720)$ resonance that produces a peak at small q^2 values. In both the transverse and longitudinal spectral function the generic ω peak gets broadened by the overlap of the high-lying resonances. At $\mathbf{q} = 0$ GeV the broadening amounts to roughly 23 MeV and increases for $\mathbf{q} = 0.8$ GeV to 71 MeV for the longitudinal mode and 89 MeV for the transverse mode. In Fig. 8.5 also the impact of the real part of the self energy is visualized. The effect of level repulsion is introduced through the real part of the self energy and pushes the ω branch of the spectral function to q^2 values where the imaginary part is smaller as in the vicinity of the resonance-hole excitation, see also Fig. 8.6. Thus, the width of the ω peak is smaller there and its strength is more concentrated. For high three-momenta, where most of the resonance-

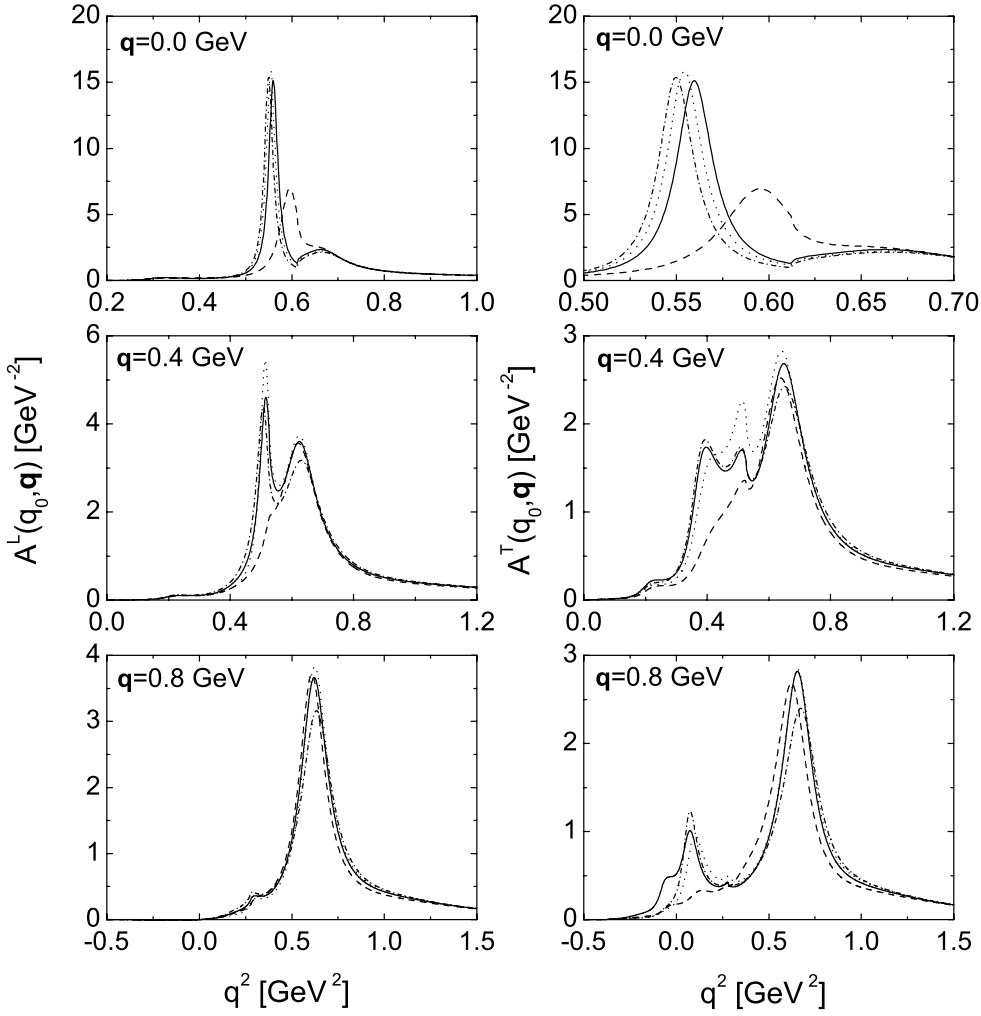

Figure 8.5: Spectral function of the ω meson at normal nuclear matter density. Shown are the longitudinal (*left*) and transverse (*right*) spectral functions which are degenerate at $\mathbf{q} = 0$ GeV. *Solid line*: relativistic calculation, *dashed line*: relativistic, without $\mathcal{R}\mathrm{e}\Pi$, *dotted line*: non-relativistic calculation, *dash-dotted line*: non-relativistic calculation with coupling constants fitted to the relativistic amplitudes.

hole excitations have passed the point $q^2 = m_\omega^2$, the impact of the real part of the self energy becomes small again.

At this point we stop the discussion of our results. In the following paragraph we rather discuss the shortcomings of our approach and how one can obtain a more complete model for the ω in-medium spectrum. Implications of our results for the experimental study of ω production in nuclear targets and a comparison to other approaches from the literature will be given at the end of this Chapter.

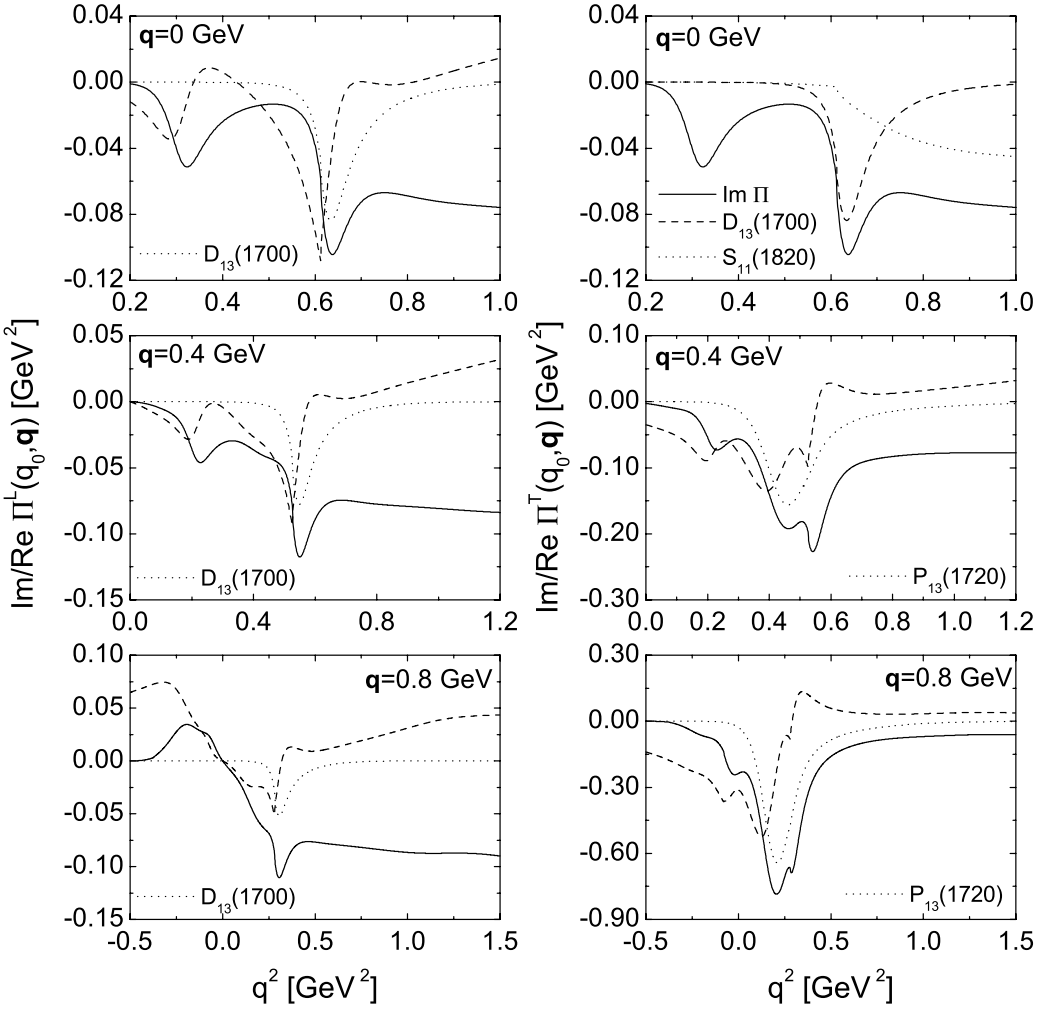

Figure 8.6: Real and imaginary part of the collisional self energy of the ω meson at normal nuclear matter density. Shown are the longitudinal (*left*) and transverse (*right*) modes. *Solid line*: imaginary part of the self energy, *dashed line*: real part of the self energy (not for the upper right plot, here: $D_{13}(1700)$ contribution to the imaginary part), *dotted line*: important single resonance contribution to $\mathcal{I}\mathrm{m}\Pi$, details see legend.

8.3.3 Shortcomings

This paragraph is devoted to a brief discussion of the shortcomings of the previously presented model. To some extent these shortcomings could be healed in a straightforward way whereas others are connected to more fundamental issues.

Analytic structure of the propagator. In the evaluation of the forward scattering amplitude we do not keep the full analytic structure of the intermediate spin$-1/2$ and spin$-3/2$ propagators. In vacuum the self energy of a spin$-1/2$ particle is given by [58]

$$\Sigma(p) = \not{p} I_1(p) + I_2(p) \tag{8.38}$$

with the scalar strength functions

$$I_1(p) = \frac{1}{4p^2}\mathrm{Tr}\left[\not{p}\Sigma(p)\right] \quad \text{and} \quad I_2(p) = \frac{1}{4}\mathrm{Tr}\left[\Sigma(p)\right]. \tag{8.39}$$

In terms of this self energy the vacuum propagator has the form

$$\mathcal{G}(p) = \frac{i}{\not{p} - m - \Sigma(k)} \equiv i\frac{\not{p}(1-I_1) + (m+I_2)}{p^2(1-I_1)^2 - (m+I_2)^2}. \tag{8.40}$$

However, throughout this work we use an averaged self energy instead. Thus the propagator can again be cast into the simple form (8.29). Indeed this choice does not influence the calculation of the squared matrix element whereas the forward scattering amplitude, needed for the evaluation of the imaginary part of the ω self energy, is not invariant under the replacement (8.40) $\rightarrow$ (8.29). In case of spin$-3/2$ resonances the situation is even more involved owing to the fact that spin$-3/2$ fields are matrices in both Dirac- and Lorentz-space, see e. g. Ref. [255]. The quality of the approximation (8.29) can be judged from a comparison of the total ωN cross section calculated from the squared matrix element and – via the optical theorem – from the imaginary part of the forward scattering amplitude. In some cases we have found rather substantial deviations.

Interference of resonances. In nuclear matter different particle states can mix by the scattering of nucleons. For the case at hand processes like $\omega N \rightarrow R_1 \rightarrow \pi N \rightarrow R_2 \rightarrow \omega N$ can lead to interference terms if the quantum numbers of resonance R_1 and R_2 are identical. This effect is particularly important if the masses of the mixing resonance states are close to each other. Formally the Dyson-Schwinger equation can be extended to a matrix structure due to the contributing different resonance states with identical quantum numbers. The diagonal terms of the self energy matrix correspond to the usual resonance diagrams already included in our model whereas the off-diagonal terms have been omitted for simplicity.

Background terms and off-shell parameters. Apart from $s-$channel resonance contributions the ωN scattering amplitude can also be influenced by non-resonant $t-$channel terms. There is no straightforward way to include such contributions within the present framework. Moreover, within the conventional coupling scheme (in contrast to the Pascalutsa coupling scheme, see e. g. [248, 253, 255]) the propagation of spin$-3/2$ resonances away from their mass shell involves on top of the spin$-3/2$ components also spin$-1/2$ contributions. These components generate background contributions to the forward scattering amplitude and self energy that, by construction, are omitted in our approach. The results of the coupled channel resonance model clearly favor the conventional coupling scheme over the Pascalutsa scheme as a much better description of the experimental data base can be achieved.

High-spin resonances. Already the inclusion of spin$-3/2$ resonances is rather involved and is not treated in a rigorous way in the present model. Even more complicated is the formalism for spin$-5/2$ resonances. The authors of [174, 249] have, however, found

important contributions to the ω photoproduction reaction from spin$-5/2$ resonances already at threshold through background contributions. In order to cure this deficiency we would have to pay rather high expenses going beyond the scope of the present work.

Coupled channel effects. The ωN channel is connected to other hadronic final states such as $\pi N, 2\pi N, \eta N, K\Lambda, K\Sigma, ...$ by the coupling of these multi-particle states to nucleon resonances. Thus, the ωN scattering amplitude involves rescattering processes like $\omega N \to R \to \pi N \to R \to \omega N$. Such processes are automatically included in the calculation of the ωN scattering amplitude if a Bethe-Salpeter equation including all relevant final states is solved. The relevance of this rescattering mechanism can only be judged from the actual solution of the coupled channel problem. If these processes turn out to be important our tree-level calculation is not able to account for large parts of the ωN scattering dynamics and, thus, most probably fails to give sensible results for the ω in-medium self energy.

Analyticity. The real part of the self energy can be calculated by means of a dispersion relation. The unsubtracted dispersion integral reads

$$\mathcal{R}\mathrm{e}\Pi(q_0, \mathbf{q}) = \mathcal{P} \int_0^\infty \frac{d\omega^2}{\pi} \frac{\mathcal{I}\mathrm{m}\Pi(\omega, \mathbf{q})}{\omega^2 - q_0^2}. \tag{8.41}$$

The use of such a dispersion integral produces a self energy that is analytic in the upper complex energy half plane. In this case the spectral function is automatically normalized. In the present work, however, we have calculated the real part of the self energy directly from the evaluation of the corresponding Feynman diagrams. Whereas this is in principle possible, analyticity is destroyed due to the multiplication with form factors that have no proper analytic properties. In [66] both approaches have been compared for the case of the ρ meson and the $D_{13}(1520)$ and $S_{11}(1535)$ nucleon resonances. Whereas quantitative differences have been found the gross features of both self energy and spectral function come out quite similar using both methods. In particular the ρ spectral function does not differ much under this choice. The extension of our model to analytic self energies by the use of the dispersion method is, however, straightforward.

Non-linear density contributions. In Eq. (8.21) the width of the excited resonances in the ωN scattering process enters. Due to the presence of a nuclear medium also the resonance widths will be modified. This in-medium change is partly due to the modified properties of intermediate ωN states that make up part of the resonance self energy. Thus, a self consistency problem arises that in principle can be solved in an iterative scheme, see for instance Ref. [66, 70]. The use of a medium modified resonance self energy in (8.21) introduces higher order ($\sim n_N^n$, $n \geq 2$) terms in the ω self energy. These terms are expected to be small if the nuclear density is small, see also the derivation of Eq. (8.26) in Section 8.2.3. However, in [66, 70] some cases have been found where already at rather moderate densities ($n_N \simeq 0.5\, n_0$) the low-density limit fails.

Altogether, extensive work has to be done in order to improve our model such, that a reliable calculation of the ω in-medium spectrum becomes possible. An alternative

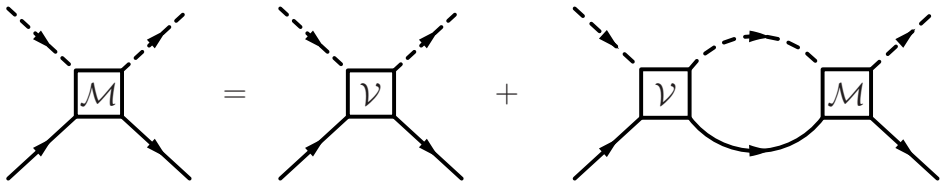

Figure 8.7: Bethe-Salpeter equation for the two-particle scattering amplitude.

approach that eliminates most of the above issues is to use directly the results for the ωN scattering amplitude from the coupled channel $K-$matrix model [249]. Apart from the last two items (analyticity and higher order contributions in the nuclear density) all shortcomings of our tree-level calculation will be avoided. The restoration of analyticity via the use of dispersion relations, however, requires the knowledge of the scattering amplitude up to rather high energies that are not accessible within this model. Also to go beyond the low density limit is so far not feasible due to the coupled channel rescattering mechanism.

8.4 Coupled channel calculation

An extensive description of the coupled channel approach has been given in [158, 173, 174, 248, 249] and References therein. Here we briefly outline some of the main features of the model focusing mainly on the ωN scattering tensor.

8.4.1 The ωN scattering amplitude

The $2 \to 2$ scattering amplitude is obtained by summing the two-body interaction potential to all orders, while the physical constraints as relativistic invariance, unitarity and gauge invariance are preserved. This corresponds to a solution of the Bethe-Salpeter equation that is shown graphically in Fig. 8.7. Formally, i. e. dropping the arguments and the integration/summation over the intermediate states, the Bethe-Salpeter equation can be written as

$$\mathcal{M} = \mathcal{V} + \mathcal{V}\mathcal{G}_{\rm BS}\mathcal{M} \tag{8.42}$$

with the two-body interaction potential $\mathcal{V}$ and the Bethe-Salpeter propagator $\mathcal{G}_{\rm BS}$ that is the product of the intermediate state nucleon and meson propagators. $\mathcal{M}$ is the full two-body scattering amplitude containing also rescattering effects. To solve this equation the so-called $K-$matrix approximation is applied. Here the real part of the propagator $\mathcal{G}_{\rm BS}$ is neglected, which corresponds to putting all intermediate particles on their mass shell. The asymptotic particle states considered in our approach are γN, πN, $2\pi N$, ηN, ωN, $K\Lambda$ and $K\Sigma$.

The interaction potential $\mathcal{V}$ entering the Bethe-Salpeter equation is built up as a sum of the $s-$, $u-$ and $t-$channel contributions corresponding to the tree-level diagrams shown in Fig. 8.8. The internal lines in the diagrams (a) and (b) represent either a nucleon

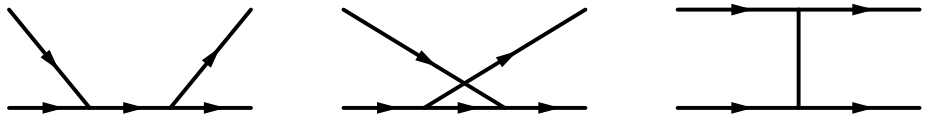

(a) (b) (c)

Figure 8.8: $s-$, $u-$ and $t-$channel contributions to the interaction kernel.

or a baryon resonance. In the $t-$channel exchange diagram (c) the contributions from scalar, pseudoscalar and vector mesons are taken into account, see e.g. [249]. Thus, resonance and background contributions are generated consistently from the same interaction Lagrangians. The Lagrangians used to construct the $K-$matrix kernel are given in the literature [158, 173, 174, 249]. For completeness, the resonance $RN\omega$ couplings are summarized in Appendix G. Applying a partial wave decomposition of the scattering amplitudes, Eq. (8.42) can be rewritten in the $K-$matrix approximation in the form

$$T_{ij}^{J^\pm,I} = K_{ij}^{J^\pm,I} + i\sum_k T_{ik}^{J^\pm,I} K_{kj}^{J^\pm,I}, \tag{8.43}$$

where $T_{ij}^{J^P,I}$ is a scattering amplitude for the total spin J, parity P and isospin I. The indices i, j, k denote the various final states $i, j, k = \pi N$, $2\pi N$, ωN, etc.

In such a treatment of the scattering problem the transition amplitudes $T_{\omega N\to\omega N}^{J^\pm}$ are the result of solving the coupled channel equation (8.43) where resonance contributions and rescattering effects are included in a selfconsistent way. In a previous calculation [249] the updated solution to the $\pi N \to \gamma N$, πN, $2\pi N$, ηN, ωN, $K\Lambda$, $K\Sigma$ and $\gamma N \to \gamma N$, πN, ηN, ωN, $K\Lambda$, $K\Sigma$ reactions in the energy region $\sqrt{s} \leq 2\,\mathrm{GeV}$ has been obtained. The a priori unknown resonance coupling constants have been obtained from the fit to all available experimental reaction data in the energy region under discussion. As a result of these calculations the elastic ωN scattering amplitudes of interest have been extracted. Here, we use these amplitudes as an input for the calculation of the ω spectral function at finite nuclear density by means of the low-density theorem.

For the case at hand we have extended our coupled channel model in order to allow for arbitrary four-momenta of the ω meson as required by Eq. (8.1). Thus, we are interested in the forward scattering amplitude as a function of the two independent variables $|\mathbf{q}|$ and q_0 or, alternatively, q^2. The extension is achieved by introducing an additional final state into the Bethe Salpeter equation (8.43) that we call $N\omega^*$. Such an additional effective ω meson is characterized by completely identical properties as the physical ω meson apart from its mass $(q^2)^{1/2}$ that can take arbitrary values. To calculate the amplitude $T_{\omega^* N}$ as a function of $q_{\omega^*}^2 = m_{\omega^*}^2 \neq m_\omega^2$ we follow the procedure used in [158] to describe photon-induced reactions on the nucleon. With the amplitudes from Eq. (8.43) we obtain

$$T_{\omega^* N,i}^{J^\pm,I} = K_{\omega^* N,i}^{J^\pm,I} + i\sum_{j\neq\omega^* N} K_{\omega^* N,j}^{J^\pm,I} T_{j,i}^{J^\pm,I}, \tag{8.44}$$

$$T_{\omega^* N,\omega^* N}^{J^\pm,I} = K_{\omega^* N,\omega^* N}^{J^\pm,I} + i\sum_{j\neq\omega^* N} K_{\omega^* N,j}^{J^\pm,I} T_{j,\omega^* N}^{J^\pm,I}, \tag{8.45}$$

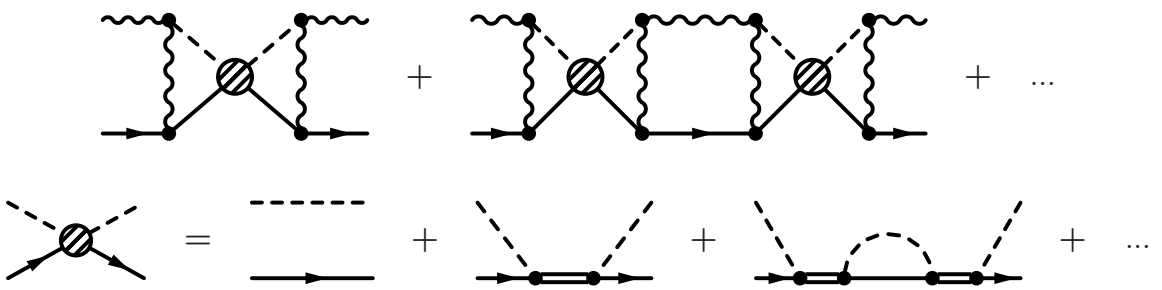

Figure 8.9: Simplified model for ωN scattering to explore the effect of resonance excitations. $T_{\omega N}$ is a sum of an infinite series of diagrams (upper panel) with the $S_{11}(1650)$ resonance excitation in the intermediate πN channel.

where the amplitudes $T_{j,i}^{J^\pm,I}$ are solutions of the coupled channel problem taken from [249]. The matrices $K_{\omega^* N,i}^{J^\pm,I}$ contain the interaction potential for the transitions $\omega^* N \to \omega^* N$, ωN, πN, etc., and are chosen to be the same as $K_{\omega N,i}^{J^\pm,I}$ but with $m_{\omega^*} \neq m_\omega$. It is easy to see that for $q_{\omega^*}^2 = m_{\omega^*}^2 = m_\omega^2$ the amplitudes $T_{\omega^* N}$ from Eq. (8.45) and $T_{\omega N}$ in Eq. (8.43) become equal. Note, that introducing the $\omega^* N$ final state does not destroy the unitarity of $T_{\omega N}$ since the $\omega^* N$ channel does not appear in the intermediate state in Eq. (8.45). In this way we obtain the vacuum scattering amplitude entering the low density theorem: The in-medium ω meson (the outer legs) can take arbitrary four-momenta $(q_0, \mathbf{q})$, whereas the internal lines maintain the vacuum properties of the ω and all other mesons, i. e. the four-momentum of the internal ω is constrained by the on-shell condition $q_0 = E_\omega(\mathbf{q}) = \sqrt{m_\omega^2 + \mathbf{q}^2}$. This corresponds to a first order expression in the nuclear density, taking into account only interactions with one nucleon at a time.

8.4.2 The role of coupled channel dynamics

The ωN scattering amplitude derived in [249] and used in the present calculations is a coherent sum of resonance and background contributions including multi-rescattering effects in a number of intermediate channels: πN, $2\pi N$, etc. In contrast, the work of [200, 237] uses only Born and mesonic box diagrams with the Δ being the only resonance excitation considered. In this Section we, therefore, illustrate the importance of a single resonance excitation at ~ 1.65 GeV and coupled channel effects. To this end we construct a simplified model for ωN scattering where the transition amplitude under discussion is a sum of the infinite series of diagrams shown in Fig. 8.9. It corresponds to solving the coupled channel Bethe-Salpeter equation in the $K-$matrix approximation with the ωN and πN channels including also the transitions $\pi N \to \omega N$. As a showcase we take into account the excitation of the $S_{11}(1650)$ resonance in the intermediate πN channel. The choice of this resonance is motivated by its mass which is close to the ωN threshold. Note that here this resonance contributes to ωN scattering only indirectly via the rescattering in the intermediate πN channel.

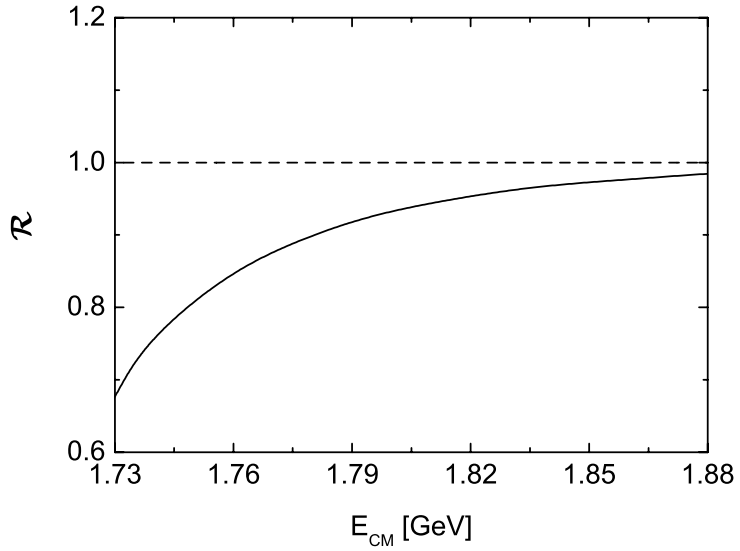

Figure 8.10: Ratio $\mathcal{R}$ of total cross sections calculated within the simplified model displayed in Fig. 8.9 without resonance contributions to that including the $S_{11}(1650)$ state.

To explore the role of the $S_{11}(1650)$ resonance excitation we calculate the total cross sections $\sigma_{\omega N}$ using $\Gamma^{\pi N}_{N(1650)} = 0$ and $\sigma^{N(1650)}_{\omega N}$ using $\Gamma^{\pi N}_{N(1650)} = 95$ MeV, respectively. Thus, in the first case the resonance contributions are absent. The non-resonance couplings are chosen in accordance with [249]. Form factors are neglected for the sake of simplicity. To minimize the dependence on the choice of the coupling constants at the non-resonance vertices we calculate the ratio of the total cross sections $\mathcal{R} = \sigma_{\omega N}/\sigma^{N(1650)}_{\omega N}$ that is shown in Fig. 8.10 as a function of the CM energy. One can see a dramatic change of the ωN scattering once the contribution from the $S_{11}(1650)$ resonance is included. As was expected the main difference between the two calculations is found in the energy region close to the resonance pole. At higher energies the contribution from the $S_{11}(1650)$ vanishes and both results coincide. Note, that no direct resonance couplings to the ωN channel are allowed in these calculations. We conclude that for a realistic description of the ωN scattering amplitude coupled channel effects must be taken into account. The contributions from nucleon resonances cannot be neglected even for vanishing resonance couplings to the ωN final state.

8.4.3 Results

According to the low-density theorem, the ω spectral function is entirely determined by the forward scattering amplitude $T_{\omega N}$. At zero momentum the latter reduces to the scattering length. Hence, the ωN scattering length $a_{\omega N}$ defines the ω meson self energy at the physical mass. In [249] the scattering lengths and effective radius have been extracted from the ωN scattering amplitude. Here, we follow [237] and define $a_{\omega N}$ in a slightly different way which is useful for the present calculations (see Appendix H). For

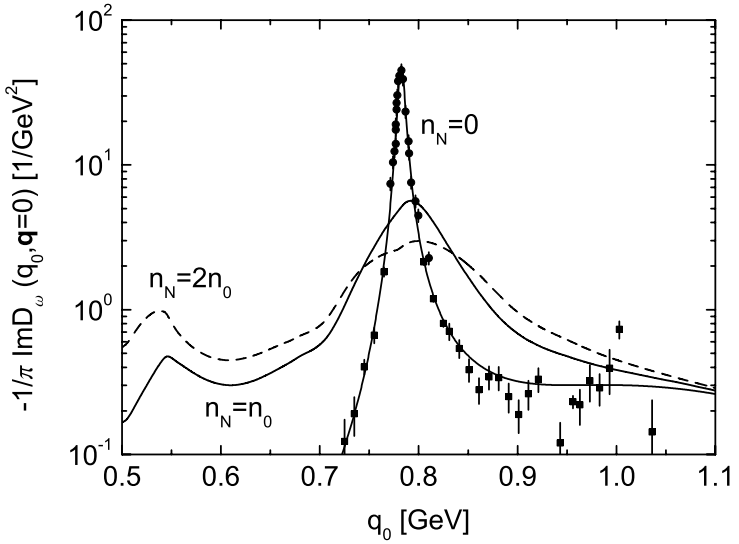

Figure 8.11: The ω spectral function for an ω meson at rest, i. e. $q_0 = \sqrt{q^2}$. The appropriately normalized data points correspond to the reaction $e^+e^- \to \omega \to 3\pi$ in vacuum, taken from Refs. [256, 257]. Shown are results for densities $n_N = 0$, $n_N = n_0 = 0.16$ fm^{-3} (solid) and $n_N = 2n_0$ (dashed).

the ωN scattering length we obtain the values

$$\begin{aligned} a_{\omega N} &= a_{\omega N}^{\frac{1}{2}^-} + a_{\omega N}^{\frac{3}{2}^-} = (-0.17 + i0.31) \text{ fm}, \\ a_{\omega N}^{\frac{1}{2}^-} &= (-0.27 + i0.16) \text{ fm}, \\ a_{\omega N}^{\frac{3}{2}^-} &= (+0.11 + i0.15) \text{ fm}, \end{aligned} \tag{8.46}$$

where $a_{\omega N}^{\frac{1}{2}^-}$ and $a_{\omega N}^{\frac{3}{2}^-}$ are the contributions from the spin$-1/2$ (S_{11}) and spin$-3/2$ (D_{13}) sector, respectively. While we find an attraction in the D_{13} wave the contribution from S_{11} dominates the real part leading to the slight overall repulsion in the ωN system. This result has to be compared with $a_{\omega N} = (1.6 + i0.3)$ fm obtained in [237] and $a_{\omega N} = (-0.44 + i0.2)$ fm obtained in [241]. While the imaginary parts in all three calculations are similar, there is a spread of values in the real part; we will comment later on this variation.

In Fig. 8.11 the ω spectral function at finite nuclear densities $n_N = 0$, $n_N = n_0 = 0.16$ fm^{-3} and $n_N = 2n_0$ is shown for an ω meson that is at rest with respect to the surrounding nuclear matter. The appropriately normalized data points correspond to the process $e^+e^- \to \gamma^* \to \omega \to \pi^+\pi^-\pi^0$ that directly resembles the ω vacuum spectral function. Most noticeable the ω meson survives as a quasi particle at nuclear saturation density which is in agreement with all competing approaches known by the authors. The main effect of the in-medium self energy is a considerable broadening of the peak that amounts to roughly 60 MeV at $n_N = n_0$. This value is in line with a recent attenuation analysis [47]. The peak position is shifted upwards only slightly by about 10 MeV. Due

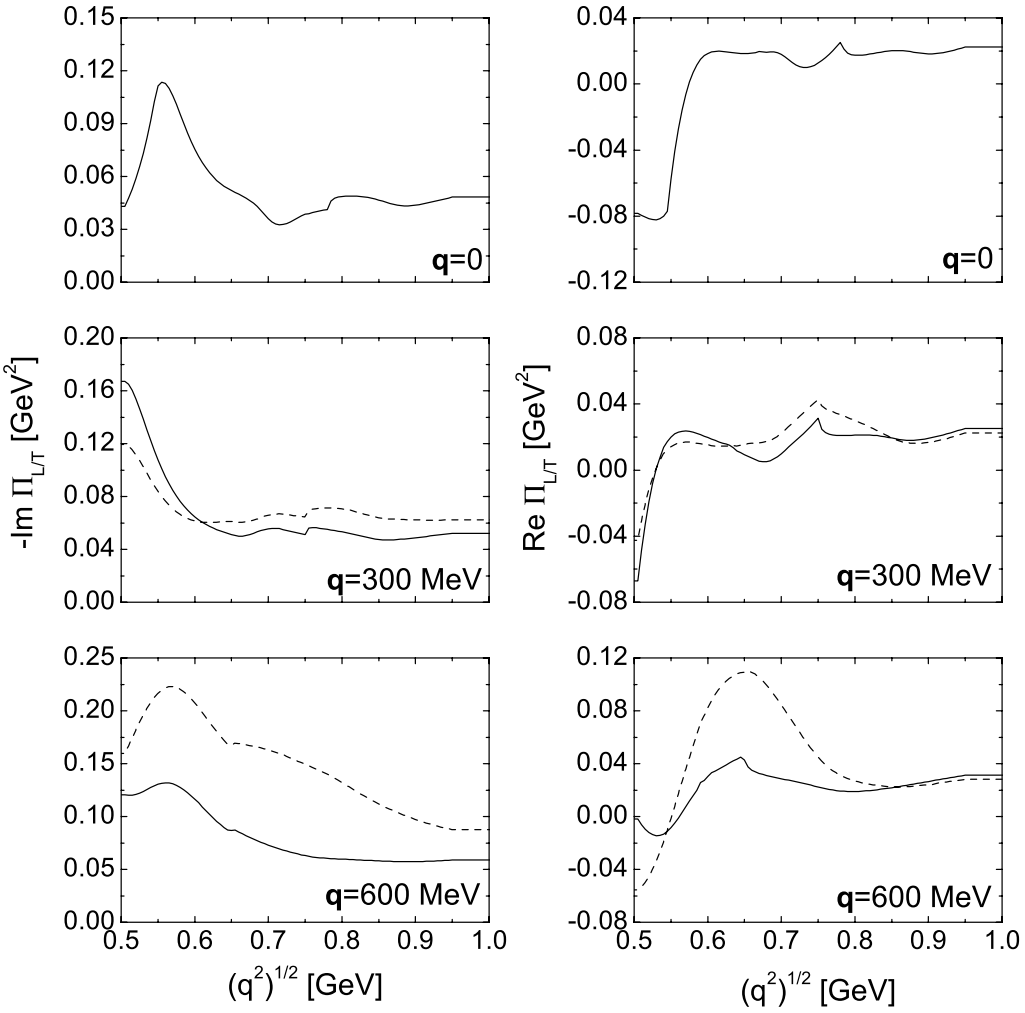

Figure 8.12: Real (right panel) and imaginary (left panel) part of the ω self energy in nuclear matter at saturation density $n_0 = 0.16$ fm^{-3}. Shown are the longitudinal (solid) and transverse (dashed) modes for ω three-momenta $|\mathbf{q}| = 0$, $|\mathbf{q}| = 300$ MeV, $|\mathbf{q}| = 600$ MeV with respect to nuclear matter at rest.

to the collective excitation of resonance hole loops the spectral function shows a second peak at low values of the ω energy q_0.

The ω in-medium self energy including the excitation of resonance-hole pairs exhibits a remarkably rich structure, see Fig. 8.12, where we show the real and imaginary part of the ω self energy of both the longitudinal and transverse mode for three-momenta $|\mathbf{q}| = 0$ MeV, 300 MeV and 600 MeV at normal nuclear matter density. In the limit of very small resonance widths, each resonance-hole pair generates an additional branch in the spectral distribution which leads to a multi peak structure. As the widths of most of the involved resonances for the case at hand are large, see Table 8.3, almost no individual peaks can be distinguished and the resonance excitations add up to a background-like structure.

$L_{2I,2S}$	status	mass	$\Gamma_{\rm tot}$	$R_{\pi N}$	$R_{2\pi N}$	$R_{\eta N}$	$R_{\omega N}$	$g^1_{RN\omega}$	$g^2_{RN\omega}$	$g^3_{RN\omega}$
$S_{11}(1535)$	****	1526	136	34.4	9.5	56.1	–	3.79	6.50	–
$S_{11}(1650)$	****	1664	131	72.4	23.1	1.4	–	−1.13	−3.27	–
$P_{11}(1440)$	****	1517	608	56.0	44.0	2.82	–	1.53	−4.35	–
$P_{11}(1710)$	***	1723	408	1.7	49.8	43.0	0.2	−1.05	10.5	–
$P_{13}(1720)$	****	1700	152	17.1	78.7	0.2	–	−6.82	−5.84	−8.63
$P_{13}(1900)$	**	1998	404	22.2	59.4	2.5	14.9	5.8	14.8	−9.9
$D_{13}(1520)$	****	1505	100	56.6	43.4	0.012	–	3.35	4.80	−9.99
$D_{13}(1950)^a$	**	1934	859	10.5	68.7	0.5	20.1	−10.5	−0.6	17.4
$D_{15}(1675)$	****	1666	148	41.1	58.5	0.3	–	109	−99.00	83.5
$F_{15}(1680)$	****	1676	115	68.3	31.6	0.0	–	12.40	−35.99	−78.28
$F_{15}(2000)$	**	1946	198	9.9	87.2	2.0	0.4	−19.6	19.3	23.14

Table 8.3: Parameter set B. Properties of the $J^P = 1/2^\pm$, $3/2^\pm$ and $5/2^\pm$ resonances that couple to the $N\omega$ channel. Masses and widths are given in MeV and the on-shell decay ratios R are given in percent. The current status is quoted as in Ref. [141]. In addition, also the $RN\omega$ coupling constants entering the Lagrangians (Appendix G) are given. ^{a}: in Ref. [141] listed as $D_{13}(2080)$.

However, for the ω meson at rest one additional peak in both the imaginary part of the self energy and the spectral function can be identified at ~ 0.55 GeV (see Figs. 8.12 and 8.11). This branch of the ω spectral function is due to the excitation of the $S_{11}(1535)$ resonance. This resonance couples in relative $s-$wave to the $N\omega$ channel and dominates the spectrum at low ω momenta and low q^2. Note, that the authors of [241] come to the same conclusion on the role of the $S_{11}(1535)$ state. However, contrary to [241] we see no prominent effect from $D_{13}(1520)$ because of the smaller coupling of this resonance to the ωN final state. The invariant mass $\sqrt{q^2}$ of the $S_{11}(1535)$ resonance-hole branch moves to smaller values as the three-momentum increases what can approximately be determined by the kinematical relation (8.28). Therefore, in Fig. 8.12 the resonance-hole peak visible at a mass of $\sqrt{q^2} \approx 550$ MeV for zero momentum moves down to $\sqrt{q^2} \approx 500$ MeV for a momentum of 300 MeV.

Another interesting structure is visible in Fig. 8.12 at masses of 782 MeV ($|\mathbf{q}| = 0$ MeV), 750 MeV ($|\mathbf{q}| = 300$ MeV) and 649 MeV ($|\mathbf{q}| = 600$ MeV). This cusp structure is due to the opening of the elastic channel $\omega^*(\sqrt{q^2})N \to \omega(782)N$, i. e. the scattering of the off-shell ω^* into the on-shell ω becomes energetically possible. The position of this threshold is determined by the equation

$$q^2 = m_N^2 + (m_N + m_\omega)^2 - 2m_N\sqrt{(m_N + m_\omega)^2 + \mathbf{q}^2}. \tag{8.47}$$

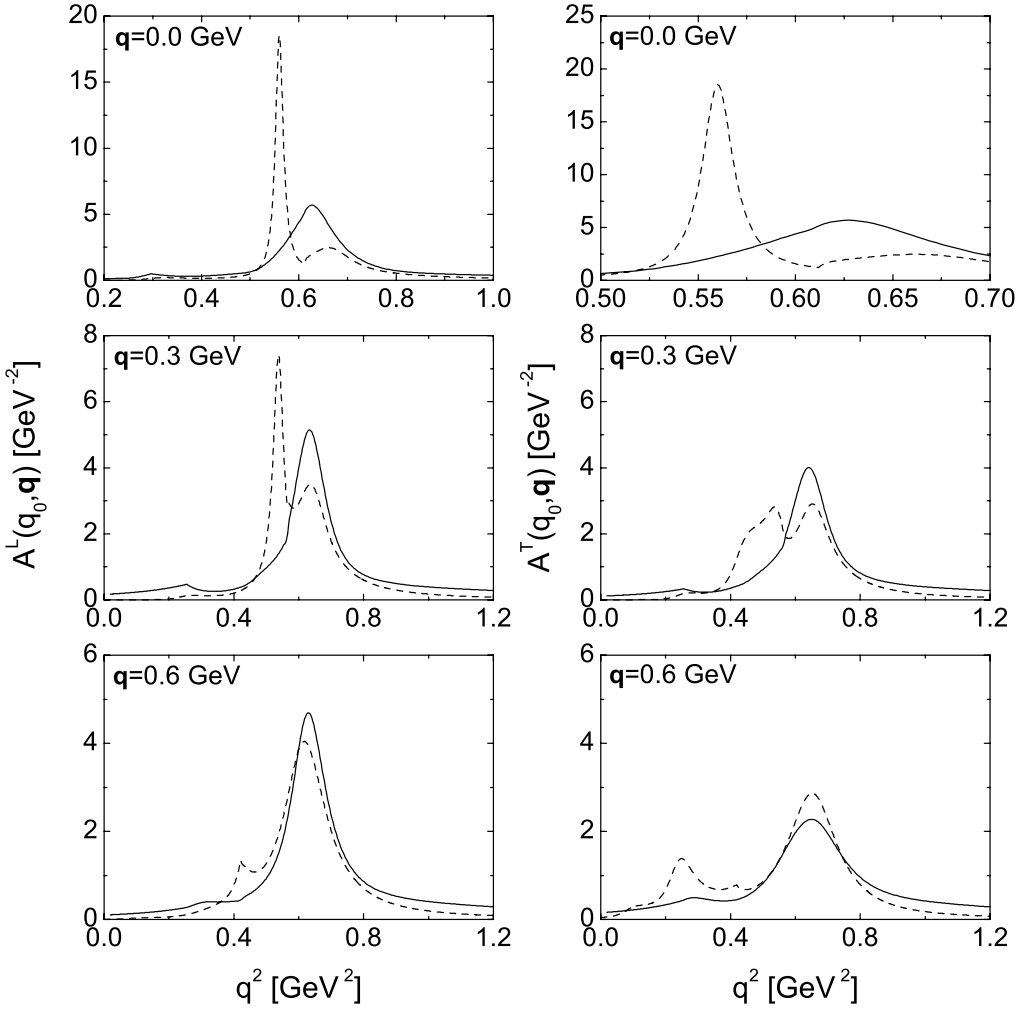

Figure 8.13: The longitudinal (*left*) and transverse (*right*) modes of the ω spectral function at nuclear saturation density $n_0 = 0.16$ fm^{-3}. Shown are results for ω three-momenta $|\mathbf{q}| = 0$, $|\mathbf{q}| = 300$ MeV, $|\mathbf{q}| = 600$ MeV with respect to nuclear matter at rest. *Solid lines*: coupled channel results, parameter set B, *dashed lines*: tree-level results, parameter set A.

We should note that this threshold effect is an artifact of the applied low-density approximation. If the self energy was obtained in an iterative scheme, i. e. taking into account higher order density effects, this cusp structure would be smeared out.

In Fig. 8.13 we show the longitudinal and transverse mode of the ω spectral function for momenta of $|\mathbf{q}| = 0$ MeV, 300 MeV and 600 MeV. Also shown is the spectral function obtained from the tree-level model presented in the previous Section using the parameter set A. A comparison and discussion of these results will be given in a later Section. We observe a significantly different momentum dependence of the two helicity states: $\mathcal{A}^T$ is strongly affected at large ω momenta whereas $\mathcal{A}^L$ remains almost unchanged. This is expected from the breaking of Lorentz invariance due to the presence of the nuclear medium. We note in passing that this resembles qualitatively the spectral functions for

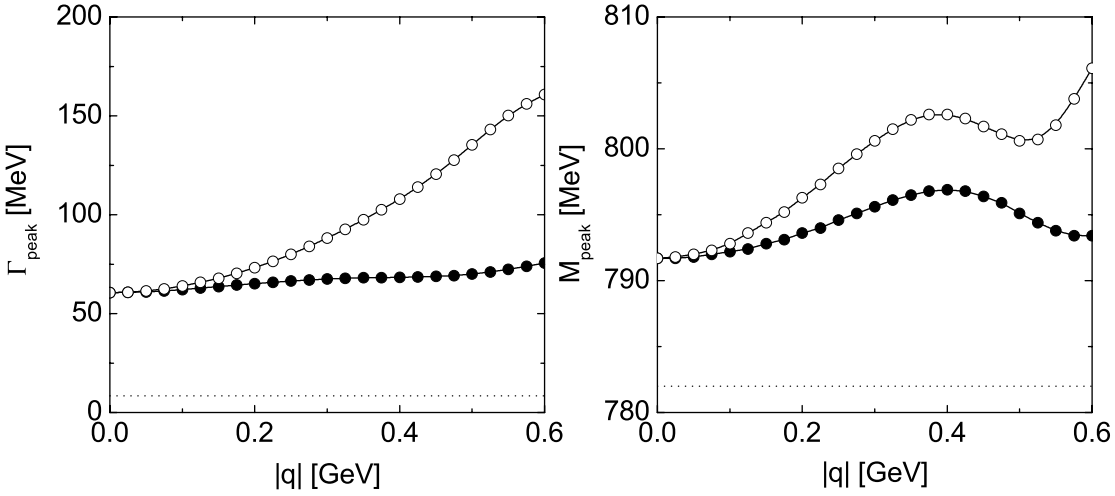

Figure 8.14: Position (*right*) and width (*left*) of the generic ω peak at nuclear matter density n_0 as function of the ω LA momentum. *Open symbols*: transversely polarized ω mesons, *solid symbols*: longitudinally polarized ω mesons. The dotted horizontal lines illustrate the free values $m_\omega^0 = 782$ MeV and $\Gamma_0 = 8.4$ MeV.

the in-medium ρ meson calculated in [70].

The same effect is visible in the calculation of the ω width evaluated at the actual peak position of the ω branch. It is given by the expression

$$\Gamma^{L/T}_{\rm peak}(\mathbf{q}) = -\frac{\mathcal{I}m\Pi^{L/T}\left(q_0 = (m^2_{\rm peak} + \mathbf{q}^2)^{\frac{1}{2}}, \mathbf{q}\right)}{m_{\rm peak}}. \tag{8.48}$$

In the left panel of Fig. 8.14 we show $\Gamma^L_{\rm peak}(\mathbf{q})$ and $\Gamma^T_{\rm peak}(\mathbf{q})$ as a function of the ω three-momentum. For an ω meson at rest the collisional broadening amounts to roughly 60 MeV at normal nuclear matter density. For finite three-momentum this width more or less stays constant for the longitudinal branch whereas it drastically rises for the transverse modes. From Eqs. (8.27) and (8.48) follows that the widths of the longitudinal and transverse modes, $\Gamma^{L/T}_{\rm peak}(\mathbf{q})$, are entirely defined by the imaginary parts of the ωN scattering amplitudes $\mathcal{I}m\,T(0, +\frac{1}{2})$ and $\mathcal{I}m\left[T(1, -\frac{1}{2}) + T(1, +\frac{1}{2})\right]/2$, correspondingly (see Appendix H). The lower subscript denotes the helicities of the ω meson and the nucleon. Note, that at the ωN threshold only the $J = 1/2^-$ and $J = 3/2^-$ partial waves contribute. Since the ωN scattering is dominated by the resonance mechanism the helicity amplitudes are governed by the $RN\omega$ coupling constants extracted in [249]. They are given in Table 8.3 for completeness. The different $RN\omega$ coupling constants correspond to various helicity combinations of the ωN final state, see [173, 249] for details. With increasing ω momentum the resonance contributions become more important giving main contributions to the $(1, -1/2)$ and $(1, +1/2)$ helicity amplitudes. As a result the transverse mode is strongly modified with increasing ω momentum.

The peak position of the genuine ω branch in both spectral functions moves only slightly to higher q^2 values as can be seen also in the right panel of Fig. 8.14. This is due to level repulsion as the most important resonance-hole states are subthreshold with respect to the $N\omega$ channel. Since the scattering amplitude $T_{\omega N}$ used in our calculations is a coherent sum of a number of resonance contributions including coupled channel effects the separation of individual resonance contributions is difficult. However, several conclusion can be drawn. First, over the full energy range under consideration the self energy is dominated by resonance hole excitations, whereas the nucleon Born terms give only marginal contributions. Although the excitation of resonance-hole states leads to additional branches in the spectral functions, no clearly distinguishable peak structures emerge due to the large widths and the only moderate coupling to the $N\omega$ channel of the individual resonances. This is also suggested by pion- and photon-induced ω production data which do not show any prominent resonance structures. The ωN amplitude at threshold is dominated by the $S_{11}(1535)$ resonance and – through background ($u-$channel) contributions – by the $D_{15}(1675)$ and $F_{15}(1680)$ states. At zero momentum the $S_{11}(1535)$ resonance generates strength at low invariant masses. The $u-$channel contributions of the $P_{11}(1710)$ and $F_{15}(1680)$ resonances that lie only slightly subthreshold to the $N\omega$ channel due to level repulsion push the ω branch to higher q^2 values.

8.5 Discussion

Now we discuss some special aspects connected to our previously presented results, namely the theoretical uncertainties and the comparison to other models from the literature. The relation of the present results to recent ω production experiments will be discussed at the end of the following Chapter.

8.5.1 Theoretical uncertainties

In Fig. 8.13 we have shown a comparison of the spectral functions obtained from our coupled channel and tree-level models. The differences are most pronounced for low ω three-momenta. This is most probably due to a deficiency of the tree-level calculation. In the coupled channel model, the ω photoproduction amplitude at threshold is strongly affected by spin$-5/2$ resonances through background contributions. Such background components are absent in our tree-level calculation. In the parameter set A the ωN coupling strength is directed to other partial waves, thus giving a rather strong coupling of the $D_{13}(1700)$ resonance that generates a clearly visible resonance-hole component in the ω spectrum. In contrast, background contributions do not show up as resonant structures in the spectral function. Furthermore we feel that the coupled channel mechanism tends to reduce the importance of individual processes, i. e. thresholds are smeared out and resonances contribute through external partial waves and through the indirect coupling to intermediate states as $\pi N, \eta N$ etc. For high three-momenta both models give quite similar results. This is due to the decreasing importance of the real part of the ωN scattering amplitude as the resonance-hole components move away from the physical ω mass. In contrast to the imaginary part, the real part is not very well constrained by

experimental data as we have seen already in the comparison of the scattering length to values from the literature.

The main point of uncertainty in our coupled channel results is the treatment of the $2\pi N$ final state. In the solution of the Bethe Salpeter equation the $2\pi N$ state cannot be treated in a rigorous way. Rather a scalar meson with mass $m = 2m_\pi$ is introduced that absorbs the total inelastic flux that goes to multi(≥ 3)-particle final states. This method could a priori cause a more smooth energy dependence of the $\omega \to 2\pi$ cross section. If the real part of the ωN scattering amplitude was obtained by means of a dispersion relation, a different energy dependence of the total cross section could lead to rather different results since the dispersion integral is particularly sensitive to the energy variation of the cross section. However, neither the $\omega \to 2\pi$ nor the inverse reaction is experimentally accessible which leads to large ambiguities in particular due to the chosen form factors. Eventually we are also unable to go beyond the low density approximation within the coupled channel approach. On top of the coupled channel mechanism, higher order density contributions could further smear out resonance structures. However, we also did not include Pauli blocking for the intermediate resonance self energies. In contrast to collisional broadening Pauli blocking tends to reduce the in-medium resonance widths. In case of the $\Delta(1232)$ resonance both mechanisms almost cancel each other, resulting in almost identical vacuum and in-medium widths of this resonance [100].

8.5.2 Comparison to other models

We now compare our results to those obtained from other models. Very close in spirit to our approach is the work of [241] that is also based on a solution of a coupled channel Bethe Salpeter equation. The in-medium self energy of the ω meson is driven by the collective excitation of particle hole and resonance hole loops. However, this analysis is restricted to ω mesons at rest as no $p-$wave resonances have been incorporated. At least qualitatively the results of [241] compare very well to our findings: Due to resonance-hole excitations an additional peak in the spectral function at low invariant masses was found. In [241] this component of the ω spectrum has been ascribed to the unresolved contributions of the $D_{13}(1520)$ and $S_{11}(1535)$ nucleon resonances. Whereas this low-mass component contributes much stronger as in our model the genuine ω peak is also shifted only slightly upwards in energy.

The model of Refs. [200, 237] is based on an effective Lagrangian which combines chiral SU(3) dynamics and vector meson dominance. There the main contribution to the ω medium modification comes from a change of the $\rho\pi$ self energy generated by the ρN and πN interactions. Whereas the on-shell broadening obtained by the authors of Ref. [237] compares very well to our value of roughly 56 MeV, they find an extremely strong attractive mass shift that is not found in our calculations. In [200, 237] the real part of the in-medium self energy, that determines the peak position of the spectral function, is obtained by a dispersion relation. The magnitude and in particular the energy dependence of this real part can be attributed to the strong energy variation of the $\omega N \to 2\pi N$ cross section which in [237] is dominated by the scattering into an intermediate ρN state. We note that the $2\pi N$ final state is not constrained by any data in the calculations of [237]. In contrast, in our approach the $2\pi N$ final state is constrained by

the coupled channel mechanism. In particular, it has to account for the inelasticity in the pion-induced reaction channels. This results in a more moderate energy dependence of the corresponding cross sections and, hence, via dispersion, in a smaller real part of the scattering amplitude.

We also stress, that the self energy in [237] is obtained from a pure tree-level calculation using the heavy-baryon approximation whose application is not at all justified, see [258]. In particular, the heavy-baryon approximation has the consequence, that diagrams including a direct ωN interaction do not contribute to the forward scattering amplitude. On the other hand, in the reanalysis [258] these diagrams were found to produce the largest contribution to the imaginary part of the ωN scattering amplitude. Dropping the heavy-baryon approximation to obtain the ω self energy, an extremely strong attractive mass shift, not consistent with recent experimental data on ω production in nuclei [18], is found within the same model as constructed in [237]. This strong mass shift can be attributed to the relativistic tree-level treatment of the $2\pi N$ channel. We have illustrated earlier that the coupling of the ωN and πN channels to nucleon resonances yields important contributions to the ω in-medium spectrum that are absent in the calculation of [237]. However, as also in our approach the three-body state $2\pi N$ is not treated rigorously, some room for theoretical improvements remains open.

Chapter 9

The reaction γA $\longrightarrow$ ωX

9.1 Introduction

In this Chapter we concentrate on experimental signatures for the ω in-medium changes in the $\gamma A \rightarrow \pi^0\gamma X$ reaction. This reaction has been investigated experimentally at ELSA [18, 19]. The essential advantage of the $\omega \rightarrow \pi^0\gamma$ decay channel is its particular large branching ratio that is three orders of magnitude larger than the branching ratio of the ω into dileptons. Moreover, the $\pi^0\gamma$ channel allows for the exclusive study of the ω properties since at least in vacuum the $\rho \rightarrow \pi^0\gamma$ decay is suppressed by two orders of magnitude relative to the $\omega \rightarrow \pi^0\gamma$ decay. Skepticism about this study arises because of the small total decay width of the ω on one hand and the final state interactions of the semi-hadronic $\pi^0\gamma$ final state on the other hand. Due to the small width most ω mesons leave the nucleus before they decay in an $\omega \rightarrow \pi^0\gamma$ process. The invariant mass of the remaining $\pi^0\gamma$ pairs created inside the nucleus can be distorted by quasi elastic πN scattering processes. Thus, the question arises if and – if yes – under which conditions it is possible to gain valuable information on the ω properties from the $\gamma A \rightarrow \pi^0\gamma X$ reaction.

Numerous theoretical results for the ω in-medium spectral function have been obtained on the basis of rather different methods [200, 234, 237, 240, 241]. In parts, these have been discussed at the end of the last Chapter. A drop of the ω mass at normal nuclear matter density by up to 150 MeV and a broadening of its width by up to 70 MeV have been predicted. These substantial effects explain the large attention paid to the experimental determination of the ω in-medium changes, recalling that its free width amounts to 8.4 MeV only. The origin of the ω medium modifications at finite density and zero temperature have been attributed to collective resonance-hole excitations [240, 241], that lead to additional structures in the spectral function, or a renormalization of the pion cloud [200, 237], that results in a rather drastic shift of spectral strength to the low mass region. The microscopic calculations within the $K-$matrix coupled channel model presented in the previous Chapter predict a substantial broadening but only a moderate upwards shift of the generic ω peak mass. In addition, rather weak resonance-hole components are found which shift some spectral strength to the low mass region.

This Chapter is structured as follows: First we will briefly introduce the CBELSA/TAPS experiment to which the conditions of our calculations have been adjusted. Up to the present the results of this experiment represent a unique source of information on ω meson

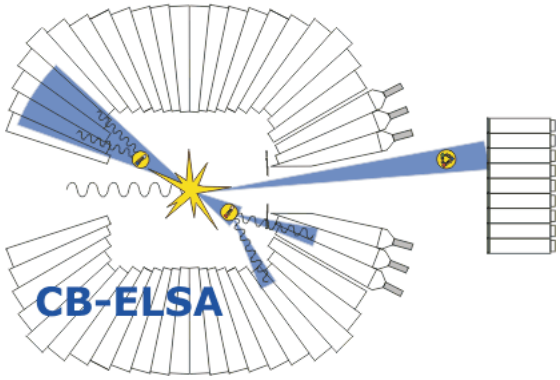

Figure 9.1: Sketch of the combined Crystal Barrel/TAPS detector setup at ELSA. Here, TAPS is mounted as a forward wall, thus closing the detector coverage almost to the 4π geometry.

production from nuclear targets. After that we discuss some details of our calculations, namely the interaction of the ω with nuclear matter and its elementary photoproduction cross sections. Then we will study the feasibility to learn about the ω in-medium changes via the $\gamma A \to \pi^0 \gamma X$ reaction resulting in the suggestion of a procedure to extract the ω in-medium properties from the experimental results obtained up to the present. The results of this study are presented in Sections 9.5 and 9.6. First the total and then also differential cross sections will be the subject of the discussion. At the end we confront the microscopic results for the ω spectral function and self energy obtained in the previous Chapter with our analysis of the experimental CBELSA/TAPS data.

9.2 Experimental status

Experimentally the reaction $\gamma A \to \omega X \to \pi^0 \gamma X'$ has been investigated by the CBELSA/TAPS collaboration at the **El**ectron **S**tretcher and **A**ccelerator (ELSA) in Bonn [18, 19]. The photon beam with an energy range of $E_\gamma = (0.64 - 2.53)$ GeV is produced via bremsstrahlung from a 2.8 GeV electron beam. The photon energy is determined by means of a magnetic spectrometer. In the case at hand the incident beam energies have been limited to the interval 900 MeV $< E_\gamma <$ 2200 MeV. This choice represents a compromise between sufficiently low energies for ω production in nuclear targets and sufficient discrimination of background sources which strongly increase with decreasing beam energies. As target materials the nuclei ^{1}H, ^{12}C, ^{40}Ca, ^{93}Nb, and ^{208}Pb have been considered. Our calculations which cover a finite photon beam interval are weighted with $f(E_\gamma) = E_\gamma^{-1}$ which is typical for bremsstrahlungs beams.

The $\pi^0\gamma$ pairs are identified via the detection of three photons from the $\pi^0\gamma \to 3\gamma$ decay and the requirement that the invariant mass of the two photons from the $\pi \to \gamma\gamma$ decay are consistent with the neutral pion mass. The detector consists of the combined setup of the **C**rystal **B**arrel (CB) detector and the **T**wo-**A**rm-**P**hoton-**S**pectrometer TAPS. The Crystal Barrel detector is a photon spectrometer consisting of CsI scintillation crystals

with an angular coverage from 30° to 168° in the polar plane and full coverage in the azimuthal plane. The TAPS detector is build from BaF_2 and is mounted as a forward wall. Thus, an almost 4π coverage could be obtained, see Fig. 9.1. The invariant mass resolution obtained with this detector is roughly $\delta W \simeq 55$ MeV which is the FWHM (full width half maximum) of a $\delta-$like signal propagated through the complete detector machinery. In our simulations this resolution can be accounted for by using the convolution (7.15) with $\delta W \simeq 25$ MeV.

Results of the CBELSA/TAPS experiment have been reported first in [18] and more recently in [19]. In [18] only data from ^{1}H and ^{93}Nb targets in the full photon energy range have been presented. The huge experimental background has been subtracted by fitting the invariant mass distributions far outside the ω vacuum mass where the ω contribution was expected to be negligible. This fitted curve has been interpolated in the ω region and has been subtracted from the total yield. In [19] the attempt has been made to understand this background quantitatively. Whereas the shape and magnitude can be reproduced rather well it has also exposed that the exact trend of the background curve can be sensitive to rather small changes in some of the cross section of the background sources. The results on the invariant mass distributions can be extremely sensitive to the background subtraction. The ambiguity of the background subtraction and the consequences on the extracted properties of the ω spectrum have been reexamined also in [259]. A complete quantitative background simulation, similar to the hadronic cocktail calculations for case of dilepton spectroscopy, would certainly be desirable.

When gating on ω momenta smaller than 500 MeV an accumulation of strength in the $\pi^0\gamma$ mass spectrum below the ω peak mass in the $\gamma\mathrm{Nb} \to \pi^0\gamma X$ reaction has been reported [18]. The authors considered the extreme scenario that all events in the peak at $m_\omega^o = 782$ MeV stem from ω vacuum decays. The spectrum obtained from the ^{1}H was normalized to the peak value of the ^{93}Nb spectrum and, thus, the difference of both spectra was expected to represent the component of ω in-medium decays to the total $\pi^0\gamma$ yield. This contribution was fitted with a Breit-Wigner-like curve resulting in an in-medium ω mass of $m_\omega^* = (722^{+39}_{-9})$ MeV. The averaged probed density was estimated by means of a Monte Carlo simulation in Ref. [260] to be $\sim 0.6 n_0$. This result, however, should be considered with care. First, there is no model independent way to determine the relative amount of in-medium and vacuum decays. Also the average probed density is no observable quantity. Second, this method to extract the ω in-medium mass implies a single peak structure of the ω in-medium spectrum. Moreover, it is assumed that the vacuum decay component in the $\pi^0\gamma$ spectrum has a shape identical to the free invariant mass spectrum. This is not necessarily true as we will see in a forthcoming Section.

The experimental results [18, 19] obviously contradict our calculation of the ω in-medium properties within the coupled channel $K-$matrix model presented in the previous Chapter. In the following we will analyze the experimental results by means of BUU transport calculations which provide a unique means to account for FSI and the dynamical evolution of momentum and density dependent spectral functions. To this end the in-medium self energy of the ω meson will be parametrized in a way consistent with the ωN interaction which enters the BUU collision integral. Using both the measurements of the total and differential ω photoproduction cross sections we will try to find a scenario of in-medium changes consistent with the data. Finally, these parameters suggested by

the combination of transport simulation and experiment will be compared again to the microscopic coupled channel calculation of the ω in-medium properties.

9.3 Preliminaries

This Section serves to present some details of our Monte Carlo transport calculations that are of special interest to the discussion at hand. Important components of these calculations are the elementary photoproduction cross sections, the processes giving rise to final state interactions and the modeling of the ω in-medium changes. The latter ones are implemented rather in a phenomenological way than using microscopic techniques as applied in the previous Chapter. In the end, however, we will discuss how the cross sections and self energies implemented in the transport code match with the microscopic ones.

9.3.1 The ω in nuclear matter

Final state interactions. In the very same spirit as in the case of ϕ photoproduction we use parameterizations for the ωN total cross sections. For ωN elastic scattering we have

$$\sigma_{\omega N}^{\rm el} = [5.4 + 10 \exp{(-0.6\ |\mathbf{q}|)}]\ \ {\rm mb} \tag{9.1}$$

where $\mathbf{q}$ is the laboratory momentum of the ω meson in GeV. This expression has been obtained in [261] by an interpolation of the low energy cross section, calculated from a microscopic model, and the high energy limit obtained within an additive quark model. Also for the inelastic cross section we use the parametrization from [261]

$$\sigma_{\omega N}^{\rm inel} = \left[20 + \frac{4}{|\mathbf{q}|}\right]\ {\rm mb}, \tag{9.2}$$

that again interpolates the low energy cross section, given by the sum of the individual contributions $\omega N \to \pi N, 2\pi N, \sigma N, \rho N$ and $\rho\pi N$, and the high energy limit, estimated within the strict vector meson dominance model (SVMD). For high energies ($\sqrt{s} > 2.2$ GeV) inelastic scattering events are simulated within the FRITIOF model [262]. Both the cross sections (9.1) and (9.2) are obviously only estimates. However, more recent coupled channel analysis of pion- and photon-induced ω production cross sections on the nucleon [249] yield results that are comparable in magnitude with those of [261] although they fall of with momentum more quickly than (9.2). Ultimately, attenuation experiments as will be discussed in this Chapter can help to determine at least the inelastic cross section.

Collisional broadening. We obtain the collisional width of the ω via the low density theorem according to Eq. (7.31). According to the optical theorem, the ω collisional self energy is proportional to the total ωN cross section $\sigma^{\rm tot}_{\omega N} = \sigma^{\rm el}_{\omega N} + \sigma^{\rm inel}_{\omega N}$ containing all quasi elastic and absorption channels. For ω mesons at rest we find a collisional width of 37 MeV at normal nuclear matter density, a value that lies within the range of most of the more elaborate approaches [237, 240, 241]. This width rises to more than 100 MeV at $|\mathbf{q}| = 1$ GeV. We note, however, that we assume in our calculations a Breit-Wigner shape for the spectral function of the ω and thus do not allow for a multi-humped structure as obtained in our calculations in the previous Chapter and in Refs. [240, 241]. Effects of resonance-hole components in the spectral function will be discussed at the end of this Chapter.

Real part of the self energy. Regardless of the fact that a shift of spectral strength in either direction can be realized by different mechanisms we parametrize the real part of the ω self energy by a density dependent in-medium mass shift

$$m_V(\mathbf{r}) = m_V^o \left(1 + \alpha_V \frac{n_N(\mathbf{r})}{n_0}\right) \tag{9.3}$$

where m_V^o is the vacuum pole mass and α_V is an open parameter that determines the relative strength of the mass shift at normal nuclear matter density. The form of this mass shift is motivated by the early studies of Hatsuda and Lee [9], who investigated mass shifts of vector mesons at rest where within the QCD sum rule approach, and Brown and Rho [8], who suggested a universal scaling law of hadron masses in nuclear matter. Values of $\alpha_\omega \approx -(0.14 - 0.18)$ are frequently found in the literature, see for instance [200]. If not mentioned differently, we use $\alpha_\omega = -0.16$ throughout this study. However, we keep in mind that apart from attractive/repulsive mean field potentials the real part of the ω in-medium self energy can also be affected by different mechanisms as the creation of resonance-hole states. These mechanisms can not be parametrized in the simple form (9.3) but lead also to a reshuffling of spectral strength.

In-medium decay. As for the ω also the spectral function of the ρ meson is expected to change in the nuclear medium [70, 200, 250, 251]. Such a modification of the in-medium ρ spectrum has also an impact on the ω self energy as the most important decay channel of the ω in vacuum is $\omega \to 3\pi$ that is dominated by the Gell-Mann-Sharp-Wagner (GSW) process, a process where the ω first converts into an intermediate $\rho\pi$ state followed by the decay of the virtual ρ into two pions. The analytical expression for the $\omega \to 3\pi$ decay width has been given in Eq. (8.6). Due to the $\Theta-$function in Eq. (8.7) only the low-energy tail of the ρ spectral function contributes to the integral in Eq. (8.6). Therefore the $\omega \to 3\pi$ width increases substantially for higher ω masses as more and more of the ρ strength is picked up by the integral. This can be seen in Fig. 8.1 where the ω vacuum decay widths are shown.

Going to the nuclear medium, the ρ spectral distribution is broadened due to elastic and inelastic ρN collisions that lead to a shorter lifetime of the interacting ρ state. We

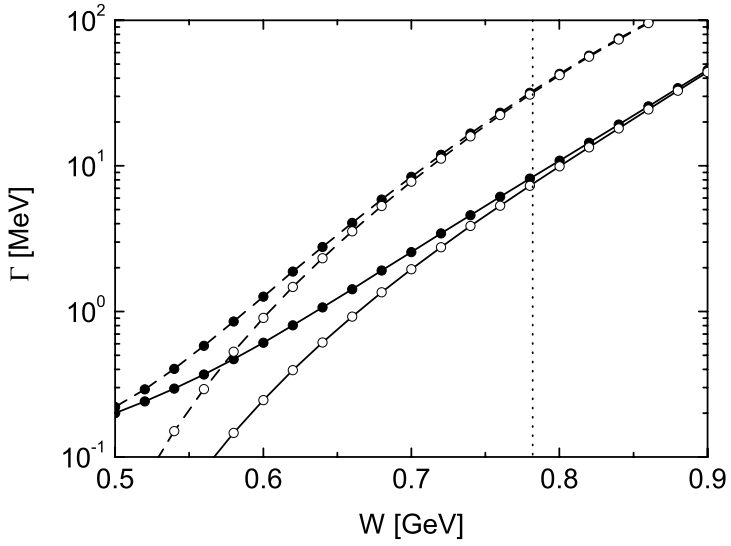

Figure 9.2: Total ω decay width (solid symbols) and $\omega \to \rho\pi$ partial width (open symbols) in vacuum (solid lines) and at normal nuclear matter density imposing collisional broadening and an attractive mass shift for the ρ meson (dashed lines). The ω collisional width is not included. At the on-shell point the $\rho\pi$ decay width amounts to 7.5 MeV in vacuum and increases to 31.8 MeV at n_0 with the ρ in-medium changes.

include this broadening by adding the phenomenological collisional width of roughly 100 MeV at normal nuclear matter density [159] to get the total ρ width in the medium:

$$\Gamma_{\rm tot}(W, n_N) = \Gamma_{\rho\to\pi\pi}(W) + 0.1 \text{ GeV} \cdot \frac{n_N}{n_0}. \tag{9.4}$$

where W is the invariant ρ meson mass. Note, however, that (9.4) is only a rough parametrization. In general, the in-medium width also depends on the three-momentum, see for instance Chapter 8 for the case of the ω meson. On top of that we also consider a dropping ρ mass analogous to the ω mass in matter, compare Eq. (9.3), with $\alpha_\rho = -0.16$. We note, that not only a shift of the ρ pole mass but also a very general reshuffling of spectral strength to the low energy part of the ρ spectral function would result in a similar effect on the ω decay width. Such a shift of strength could be caused by the excitation of subthreshold nucleon resonances as for instance obtained in the sophisticated approach of Ref. [70]. Our result at normal nuclear matter density excluding the ω collisional width is shown in Fig. 9.2. Due to the fact that more of the spectral strength of the ρ meson lies inside the bounds of the integration in Eq. (8.6), the $\omega \to \rho\pi$ on-shell width increases from 7.5 MeV in vacuum to 31.8 MeV at normal nuclear matter density.

In the CBELSA/TAPS experiment the ω is reconstructed from the $\pi^0\gamma$ final state. Thus, the measured spectra always contain the $\omega \to \pi^0\gamma$ branching ratio

$$BR(\omega \to \pi^0\gamma) = \frac{\Gamma_{\omega\to\pi^0\gamma}(W)}{\Gamma_{\rm tot}(W)}. \tag{9.5}$$

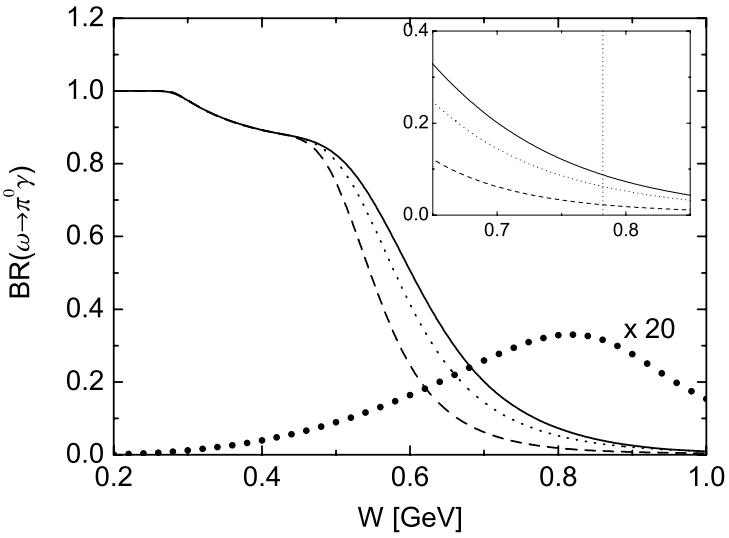

Figure 9.3: Branching ratio $\omega \to \pi^0\gamma$. *Solid line*: vacuum ρ properties, *dotted line*: with collisional broadening of the ρ meson at n_0, *dashed line*: with ρ collisional broadening and dropping ρ mass, *symbols (÷20)*: with collisional broadening for the ω and vacuum ρ properties. The insert shows a magnification of the energy interval around the physical ω mass.

This branching ratio depends on the invariant ω mass W. As can be seen in Fig. 8.1, the $\omega \to \pi^0\gamma$ width varies only smoothly over the available phasespace whereas the total width that is dominated by the $\omega \to \rho\pi$ decay channel increases strongly. As a consequence, the branching ratio (9.5) drops substantially in the vicinity of the ω vacuum mass since there the $\rho\pi$ phasespace starts to become sizable. This is shown in Fig. 9.3. Moreover, this quickly changing branching ratio becomes sensitive to the ρ properties at finite nuclear densities. This is also indicated in Fig. 9.3 by the dashed and dotted lines which include collisional broadening and an attractive shift for the in-medium ρ meson. Note, however, that the branching ratio is also affected by the collisional decay channels of the ω in the medium. This is indicated by the symbols in Fig. 9.3 which have been multiplied with a factor of 20 for visualization. Due to the opening of additional in-medium decay channels the relative strength going into the $\pi^0\gamma$ channel is reduced. Note, that the collisional width calculated according to the low density theorem (7.31) with the cross section parametrizations (9.1) and (9.2) does not depend on the ω mass. Nonetheless, the energy variation of the branching ratio is different in the medium due to the much smoother behavior of the total ω in-medium width in the denominator of the branching ratio as compared to the vacuum one. For low ω masses the branching ratio increases since the total width in the denominator is almost constant ($\Gamma_{\rm tot} \simeq \Gamma_{\rm coll}$) and the $\pi^0\gamma$ width in the numerator rises with energy. For high invariant masses the $\omega \to \rho\pi$ width in the denominator starts to become relevant and brings the branching ratio down again. This in-medium change of the decay branching ratio is automatically contained in our BUU transport calculations via the inclusion of the same collision rates in the BUU collision term and the spectral function. This issue is discussed in some more detail in

Appendix A.4.

9.3.2 Real part of the ω nucleus potential

In the previous paragraph we have introduced a phenomenological parametrization of the in-medium ω mass whereas the in-medium width of the ω meson has been calculated from the total ωN cross section using the low density theorem (7.31). The collisional width is directly proportional to the imaginary part of the collisional on-shell self energy. The real part of the self energy which is related to the in-medium mass (defined as the zero of the real part of the in-medium propagator), however, is connected to the imaginary part by analyticity [65, 66]. Thus, one can use dispersion relations in order to relate the imaginary and real parts by the numerical evaluation of the principle value integral. Since in the case of vector meson self energies standard dispersion integrals do not converge, one needs to employ at least once subtracted dispersion relations. In this case the high energy contribution is suppressed which improves the convergence of the integral and reduces the sensitivity to the high energy behavior of the imaginary part. This, however, requires one additional information, namely the value of the real part of the self energy at the subtraction point. Note, that this approach to the in-medium properties of the ω differs from the one presented in detail in Chapter 8. In Chapter 8 both the real and imaginary parts of the in-medium self energy were calculated using microscopic interaction kernels but dropping its analytic properties for practical reasons. In the case at hand, however, we start out from a phenomenological parametrization of the ωN interaction which is then extended to the (on-shell) in-medium self energy using again the low density theorem and imposing analyticity of the ωN scattering amplitude.

Within the low density approximation the ω self energy is directly proportional to the ωN forward scattering amplitude $f_{\omega N}$. A formal derivation of this relation was given in Section 8.2.3. For the in-medium ω mass one thus finds the following expression:

$$m^{*2} = m^2 - 4\pi \mathcal{R}e f_{\omega N}(E, \theta = 0) n_N, \tag{9.6}$$

where $E = q_0$ is the ω energy. For the case where all external particles are on their mass shell, the two particle forward scattering amplitude is a function of a suitable energy variable E only.

A necessary condition for the applicability of the dispersion method is that the amplitude is an analytic (or, in mathematical terms, *holomorphic*) function of the complex energy E except for certain single singularities. This condition, however, is fulfilled whenever the scattering amplitude is obtained from a convergent perturbation series. The property of analyticity of any complex function can be shown via the proof that it is differentiable throughout the whole complex plane. From a mathematical point of view we do not have to care about this problem in the case at hand since the parameterizations (9.1) and (9.2) lead to holomorphic scattering amplitudes for on-shell ω mesons anyway. Physically we do not have any handle on the analyticity of the amplitude since we do not obtain it from a consistent theory. Moreover, we have to demand that there are no singularities in the amplitude for $\mathcal{I}\mathrm{m}E > 0$. This condition is related to causality of the scattering

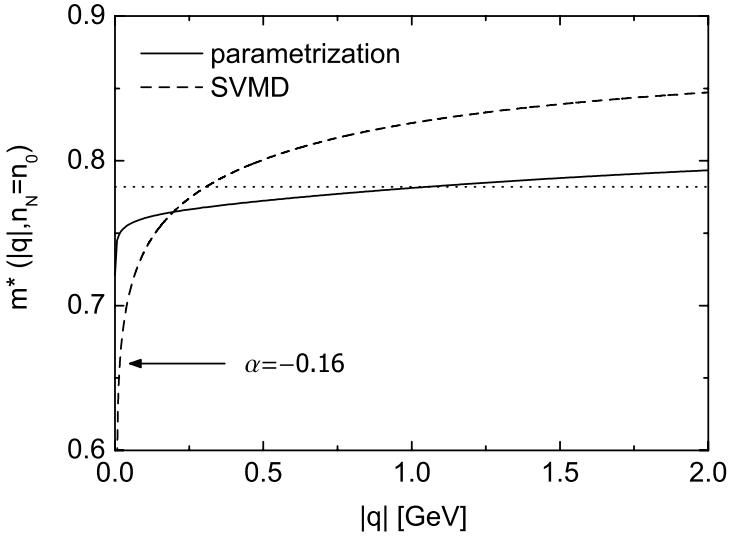

Figure 9.4: Effective ω mass according to Eq. (9.6) at normal nuclear matter density. *Solid line*: dispersion using the cross section parametrizations (9.1) and (9.2), *dashed line*: cross section obtained via VMD, *dotted line*: vacuum mass.

amplitude and has been proven only for some special cases as for instance pion nucleon scattering [63].

Under these assumptions the real part of the forward scattering amplitude $f_{\omega N}(E, \theta = 0)$ can be calculated from its imaginary part via a once subtracted dispersion relation [65]

$$\mathcal{R}\mathrm{e}f(E,0) = \mathcal{R}\mathrm{e}f(E_0,0) + \frac{(E^2 - E_0^2)}{\pi}\,\mathcal{P}\int\limits_{E_{\min}^2}^{\infty} \frac{d\nu^2\,\mathcal{I}\mathrm{m}f(\nu,0)}{(\nu^2 - E_0^2)(\nu^2 - E^2)}, \tag{9.7}$$

where $E_{\min}$ is the threshold energy, E_0 is the subtraction point and $\mathcal{P}$ denotes the principle value. The imaginary part of the forward scattering amplitude is connected to the ωN total cross section via the optical theorem

$$\mathcal{I}\mathrm{m}f_{\omega N}(E,0) = \frac{|\mathbf{q}|}{4\pi}\,\sigma_{\omega N}^{\mathrm{tot}}(E), \tag{9.8}$$

where $\mathbf{q}$ is the ω momentum in the nucleon rest frame. Thus, we obtain the real and imaginary parts of the ωN forward scattering amplitude for on-shell ω mesons as a function of the ω energy or, alternatively, the ω three-momentum in the nucleon rest frame. Via Eq. (9.6) this yields the momentum dependent on-shell mass shift of the ω in nuclear matter. Similar investigations have been done earlier for the case of the ρ meson in nuclear matter in Refs. [263, 264].

In Fig. 9.4 we show the effective ω mass as a function of the ω momentum in the nuclear rest frame. For the ratio of the real to the imaginary part of the forward scattering amplitude at the subtraction point $E_0 = 4$ GeV we use $\alpha(E_0) = \mathcal{R}\mathrm{e}f(E_0,0)/\mathcal{I}\mathrm{m}f(E_0,0) = -0.1$, which on one hand is motivated by measurements of the ρN and ϕN forward

scattering amplitudes [265, 266, 267] and on the other hand yields a result that is consistent with the canonical parametrization of the in-medium ω mass at zero momentum ($\alpha = -0.16$, see e. g. [8, 9, 237]). Besides the calculation employing the parametrization of the total ωN cross section according to Eqs. (9.1) and (9.2) that we also use to obtain the interaction probability for ωN collisions throughout the FSI in our transport code, we also show a curve for which the total ωN cross section has been obtained via vector meson dominance (VMD). Within the strict VMD model (SVMD) the ω photoproduction cross section extrapolated to zero momentum transfer can be related to the total ωN cross section using the optical theorem:

$$\left(\frac{d\sigma_{\gamma N\to\omega N}}{dt}\right)_{t=0} = \frac{\alpha_{\rm em}}{16 g_\omega^2}\frac{|\mathbf{q}_{\rm cm}|^2}{|\mathbf{k}_{\rm cm}|^2}\left(1+\alpha^2\right)\sigma_{\omega N}^2 \tag{9.9}$$

where g_ω is the VMD ω photon coupling constant and $\mathbf{k}_{\rm cm}$ and $\mathbf{q}_{\rm cm}$ are the photon nucleon and ω nucleon CM momenta, respectively. Here, a value of $\alpha(E_0) = -0.3$ is used as determined for the ρN forward scattering amplitude in Ref. [267]. The SVMD result shows a much stronger momentum dependence of the effective ω mass. However, the dispersion integral is dominantly sensitive to the low energy part of the cross section and one does not expect that the SVMD model is valid for these energies. A similar result, i. e. a rising vector meson mass with increasing vector meson momentum, has been found in a more refined study in Ref. [263] for the ρ meson.

These results differ both qualitatively and quantitatively from the ω self energy obtained earlier in Chapter 8. Indeed in Chapter 8 analyticity of the scattering amplitude was discarded due to the fact that form factors, which introduce additional poles in the amplitude were multiplied to the $RN\omega$ vertices. However, in [66] it was shown that only small deviations are to be expected by the direct calculation of the real part of the self energy from such a non-analytic scattering amplitude. The restoration of analyticity via the dispersive evaluation of the real parts of the scattering amplitude was not possible due to the only limited applicability of the $K-$matrix approach in the total CM energy. However, the present analysis of the in-medium ω mass comprises more severe problems. On one hand the subtraction point is basically unknown and has been fixed here only using an argument based on the similarity of the ρN, ωN and ϕN interactions. On the other hand, the dispersion integral is particularly sensitive to the energy variation of the ωN cross section at low energy. The phenomenological parametrizations (9.1) and (9.2) can not at all raise the claim to correctly represent the low-energy ωN scattering dynamics. Nevertheless it is interesting to note that already for very small finite three-momenta the attractive mass shift basically vanishes and turns into a repulsive shift for higher momenta. Such a behavior is also produced by the resonance-hole excitation mechansim as demonstrated in the previous Chapter.

It is, however, clear that the in-medium ω mass calculated here has no observable consequences in the ω photoproduction reaction. In photon-nucleus collisions the ω mesons are produced with high momenta where the in-medium mass again is close to the free ω mass. We have checked that by including the above result in our Monte Carlo simulations. To this end the in-medium ω mass can be parametrized in the following way:

$$m_\omega^* = m_\omega^o\left(1-\beta\left(1-\gamma\left[\frac{|\mathbf{q}|}{\rm GeV}\right]^\delta\right)\frac{n_N}{n_0}\right) \tag{9.10}$$

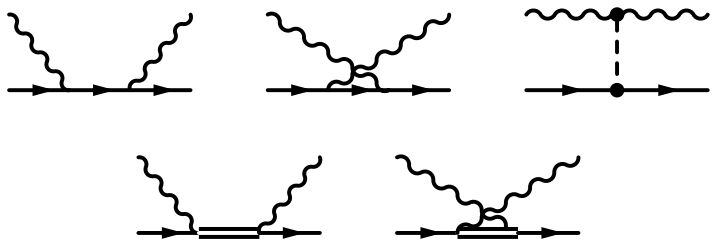

Figure 9.5: Feynman diagrams included in the calculation of the differential cross section for the process $\gamma N \to \omega N$. *Solid lines*: nucleons, *double lines*: nucleon resonances, *wiggly lines*: photons (incoming) or vector mesons (outgoing).

with the constants $\beta = 0.16$, $\gamma = 1.0$, and $\delta = 0.11$. This parameterization reproduces the canonical value of the ω mass at zero momentum (9.3) with $\alpha = -0.16$ and then goes over into the result for the momentum dependent ω mass using the ωN cross sections (9.1) and (9.2). Indeed, the use of this parametrization yields results that are identical to the vacuum case.

9.3.3 The γN $\to$ ωN reaction

The experimental data for exclusive ω photoproduction on the proton show rather prominent structures that are absent for the case of ρ and ϕ photoproduction [268]. It may be speculated that these structures are due to the excitation of nucleon resonances. However, so far the coupling of the ω meson to such resonance states is a widely unexplored aspect of hadron physics. The extraction of resonance properties and their coupling to the hadronic final states is the main emphasis of the coupled channel resonance model developed in [158, 172, 173, 247, 174, 249]. Within this framework the total ω photoproduction cross section owes its appearance to a complicated interference of resonant amplitudes and rescattering processes [158]. Such rescattering processes generate a sensitivity of the ω production cross section also to the elastic and inelastic ωN scattering amplitudes. In a successor work [249] an excellent description of the $\gamma p \to \omega p$ and $\pi p \to \omega p$ reactions could be obtained by extending the model to higher-spin resonances.

For the use with our Monte Carlo code we, however, need an analytical expression for the ω photoproduction amplitude. Only then the effects of Fermi motion and in-medium changes of the ω properties can be treated consistently. Thus, following the calculation of the $\gamma N \to \phi N$ process in Chapter 7, we construct a tree-level model by taking over the most important contributions from the coupled channel model of [158]. We refit the used cutoffs and $RN\omega$ coupling constants in order to describe the experimental database. This is necessary since these parameters depend on background terms and the rescattering mechanism that cannot be incorporated on this level.

We include the $t-$channel $\pi-$exchange as well as the $s-$ and $u-$channel nucleon diagrams shown in the upper row of Fig. 9.5. The Lagrangians used to construct the amplitude are given in Appendix E. In order to ensure gauge invariance of the amplitude we use the form-factor prescription invented by Haberzettl et al. in Ref. [218]. Since the

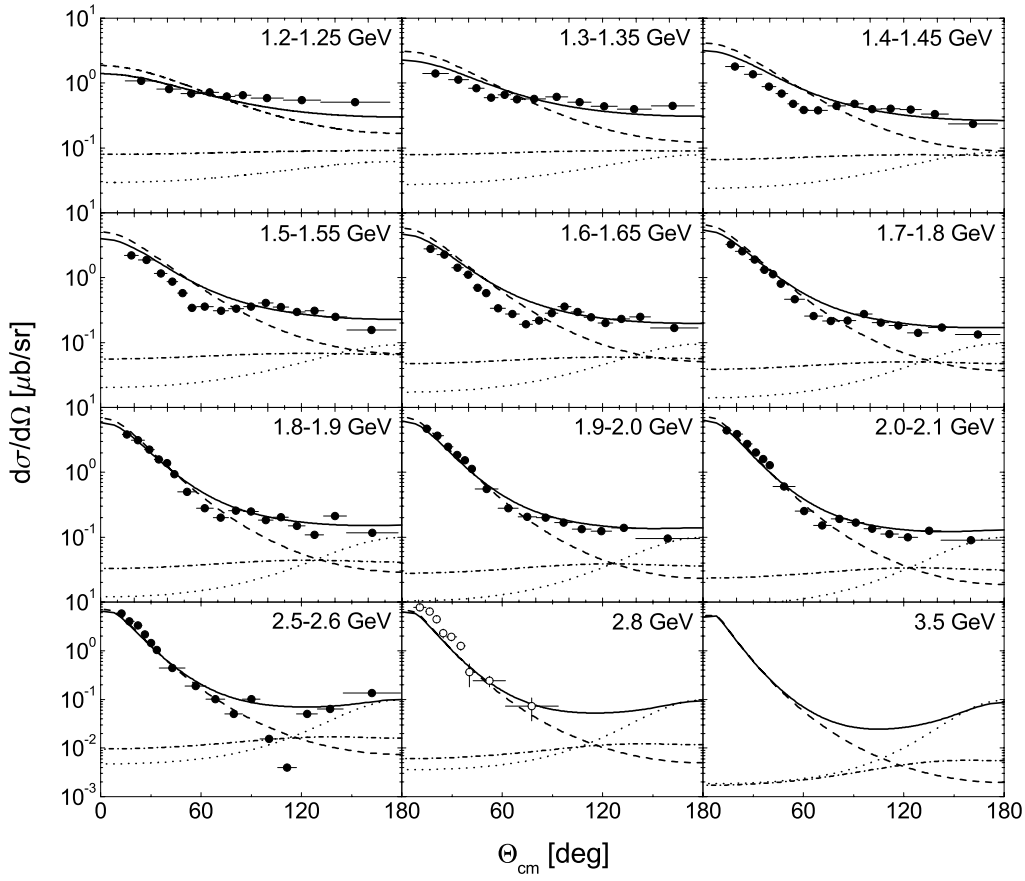

Figure 9.6: Angular differential cross section for the process $\gamma p \to \omega p$. Data from [268] (*solid symbols*) and [269] (*open symbols*). *Dashed lines*: $\pi-$exchange, *dotted lines*: resonance contributions, *dash-dotted lines*: $s-$ and $u-$channel born diagrams, *solid lines*: coherent sum.

authors of Ref. [158] found important contributions of the $P_{11}(1710)$ nucleon resonance, we also include the $s-$ and $u-$channel resonance contributions shown in the lower row of Fig. 9.5. At the $RN\omega$ vertices we apply the same form factors as on the corresponding nucleon vertices. The results for the angular differential cross section, that is obtained by a coherent summation of the individual contributions, are shown in Fig. 9.6. A satisfactory description of the data can be achieved.

The overall normalization of the cross section, however, is not obtained correctly in the energy range of $E_\gamma = (1.3-1.6)$ GeV where the total cross section shows a dip, see Fig. 9.7 in the following and Fig. E.1 in Appendix E. Such structures cannot be reproduced within our simple approach. In order to obtain the cross section normalization used as input to our Monte Carlo simulations we, therefore, employ the following recipe. We make the ansatz

$$\sigma_{\gamma N\to VN} = \frac{1}{16\pi s|\mathbf{k}_{\rm cm}|} \int\limits_{m_\pi^2}^{(\sqrt{s}-m_N)^2} dW^2 |\mathcal{M}_{\gamma N\to VN}\left(Q(W)\right)|^2 \mathcal{A}_V(W,n_N)|\mathbf{q}_{\rm cm}(W)| \quad (9.11)$$

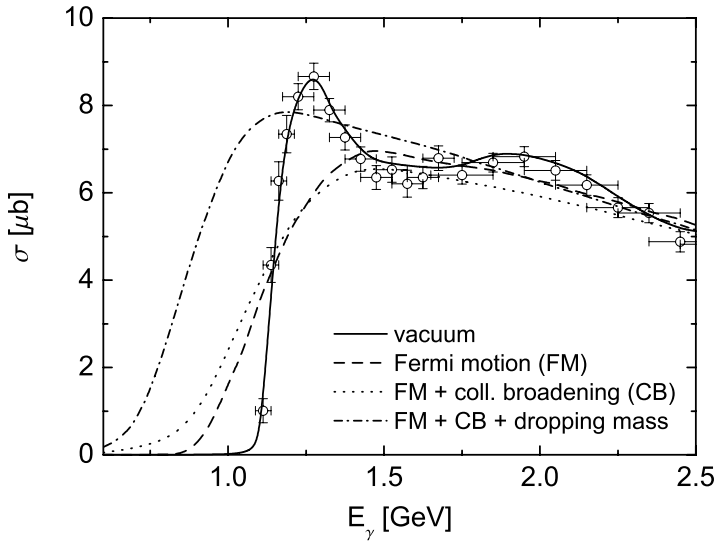

Figure 9.7: Total exclusive ω photoproduction cross section. Curves including medium modifications are calculated at normal nuclear matter density n_0. The data, showing the vacuum cross section, are taken from [268].

where $W = \sqrt{q_0^2 - \mathbf{q}^2}$ is the ω mass, $\mathcal{A}_V$ is the ω spectral function, and $\mathbf{k}_{\rm cm}$ and $\mathbf{q}_{\rm cm}$ are the initial and final state CM momenta, respectively. The lower bound of the integration arises from the fact that the $\pi^0\gamma$ final state is the lightest decay mode of the ω included in our calculations. The squared matrix element $|\mathcal{M}|^2$ is obtained from the experimental data under the assumption, that in vacuum the dependence of the matrix element on the invariant ω mass W can be neglected. In vacuum this is well justified since the spectral function $\mathcal{A}_V$ in Eq. (9.11) selects only masses close to the ω pole mass. Thus, we have

$$|\mathcal{M}_{\gamma N\to VN}(\sqrt{s})|^2 = 16\pi \frac{|\mathbf{k}_{\rm cm}| s\ \sigma^{\rm exp}_{\gamma N\to VN}(s)}{\Phi_2(\sqrt{s})} \tag{9.12}$$

where Φ_2 stands for the two-body phasespace integral

$$\Phi_2(\sqrt{s}) = \int\limits_{m_\pi^2}^{(\sqrt{s}-m_N)^2} dW^2 \mathcal{A}_V(W, n_N = 0)|\mathbf{q}_{\rm cm}(W)| \tag{9.13}$$

evaluated at zero density. The total cross section $\sigma_{\gamma N\to VN}$ has been measured with SAPHIR at ELSA [268], see also Fig. 9.7 below. In order to describe the photoproduction of ω mesons with masses W below the pole mass $m_V^o = 782$ MeV we follow the idea in Ref. [270] and extend the matrix element to subthreshold energies by defining a new invariant, namely the free energy

$$Q(W) = \sqrt{s_0(m_V^o)} - \sqrt{s_0(W)} + \sqrt{s} \equiv \sqrt{s} + m_V^o - W \tag{9.14}$$

Here, $\sqrt{s_0(m_V^o)}$ is the threshold energy for the production of ω mesons of mass $m_V^o = 782$ MeV and $\sqrt{s_0(W)}$ is the threshold energy for the production of ω mesons of mass W.

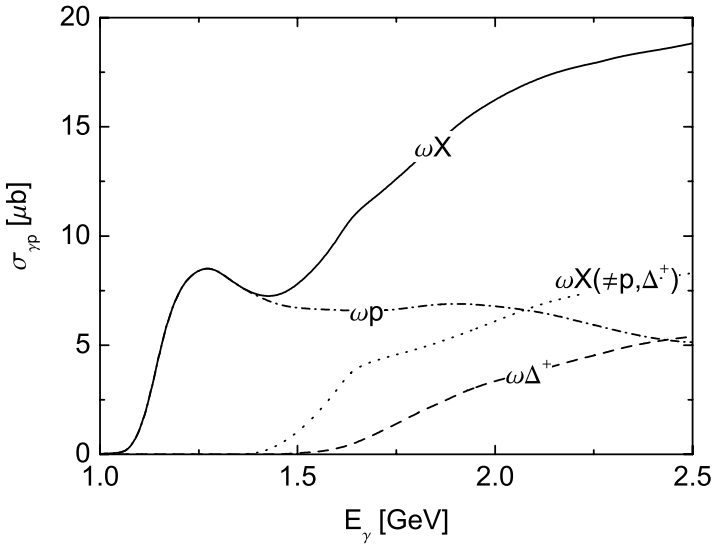

Figure 9.8: Total cross section for inclusive ω photoproduction channels off the proton.

In Eq. (9.11) the matrix element is evaluated at the energy $Q(W)$ instead of $\sqrt{s}$. Note, that in vacuum the main contribution to the integral comes at $Q(W) = Q(m_V^o) = \sqrt{s}$ due to the weight factor given by the ω spectral function.

In Fig. 9.7 the resulting total cross section is shown. If in addition to purely density dependent effects also a momentum dependence is introduced in the spectral function, the calculation of the cross section becomes more involved. This is for instance the case, when the collisional width calculated according to the low density theorem (8.26) is included. The calculation of the cross section for this case is explained in Appendix F. The in-medium curves shown in Fig. 9.7 are calculated at normal nuclear matter density including an average over the nucleon momentum distribution. We assume different scenarios of medium modifications. The cross section acquires large values at subthreshold energies in case of the attractive ω mass shift due to the low mass components in the spectral function that is integrated over in Eq. (9.11).

9.3.4 The γN $\to$ ωX reaction

Inclusive particle production in high energy photon-nucleon collisions is implemented in our Monte Carlo code by means of the event generators FRITIOF and PYTHIA, see Refs. [39, 43] and Appendix A. Below the threshold energy $\sqrt{s} = 2.0$ GeV the only inclusive production channel is $\gamma N \to \omega \pi N$. The matrix element for this process is adjusted such that a continuous transition from the low-energy to the high-energy regime is obtained, see Refs. [100, 166]. Analogous to the case of inclusive ϕ meson production the reaction $\gamma N \to \omega \Delta$ is treated independently of the high-energy event generators.

Here, we use the following parametrization:

$$\sigma_{\gamma N\to\omega\Delta} = \frac{1}{16\pi s|\mathbf{k}_{\rm cm}|}\int\limits_{m_\pi^2}^{(\sqrt{s}-m_N-m_\pi)^2} dW_V^2\mathcal{A}_V(W_V,n_N)\int\limits_{(m_N+m_\pi)^2}^{(\sqrt{s}-W_V)^2} dW_\Delta^2\mathcal{A}_\Delta(W_\Delta) \quad (9.15)$$

$$\times|\mathbf{q}_{\rm cm}(W_V,W_\Delta)|\frac{A}{(\sqrt{s}-M)^2+\Gamma^2/4}, \quad (9.16)$$

where the constants A, M and Γ are fitted to the experimental cross section of Ref. [271]. We obtain $A = 2.38$ mb GeV^2, $M = 2.3$ GeV and $\Gamma = 1.8$ GeV. We parametrize the angular distribution as follows:

$$\frac{d\sigma_{\gamma N\to\omega\Delta}}{dt} \propto \exp(Bt), \quad (9.17)$$

with $B = 6.0$ GeV^{-2}. For both the exclusive process $\gamma N \to \omega N$ and $\gamma N \to \omega\Delta$ we assume the cross section on the neutron to be the same as on the proton. The total ω photoproduction cross sections on a proton target are shown in Fig. 9.8.

9.4 The research program – Exploring the ω properties

The means to determine the ω in-medium properties from the $\pi^0\gamma$ photoproduction reaction on nuclei proposed in this Chapter slightly deviate from the historical progress on this issue. First, we will discuss the final state interactions in the semi-hadronic $\omega \to \pi^0\gamma$ decay channel. Then we will discuss the sensitivity of the observables to the imaginary and the real part of the in-medium ω self energy. On the basis of this discussion and the experimental data situation we will finally establish a method to extract the ω in-medium properties.

9.4.1 Final state interactions

One of the most critical arguments against studying the in-medium ω spectrum via the $\omega \to \pi^0\gamma$ decay channel is the strong final state interaction of the π^0. In a πN scattering event the π^0 alters its direction and energy, thus the information about the initial ω meson is essentially lost. We are able to study this effect quantitatively by means of our Monte Carlo transport model. Fig. 9.9 shows the $\pi^0\gamma$ invariant mass W versus the kinetic energy of the π^0 in the final state from the process γNb $\to \pi^0\gamma X$ at $E_\gamma = 1.2$ GeV. The background from π^0 rescattering processes is spread over a wide invariant mass range with a dominant contribution around $W = 0.4$ GeV. This is also visualized in Fig. 9.10 where the corresponding mass distributions are shown.

In a πN scattering event the π^0 looses quite an amount of its kinetic energy. Therefore those events appear at much smaller energies, see Fig. 9.9. As already pointed out in [260] this energy loss can be exploited to suppress the rescattering background successfully by applying a lower cut on the pion kinetic energy. In Fig. 9.9 such a cut on the π^0 kinetic

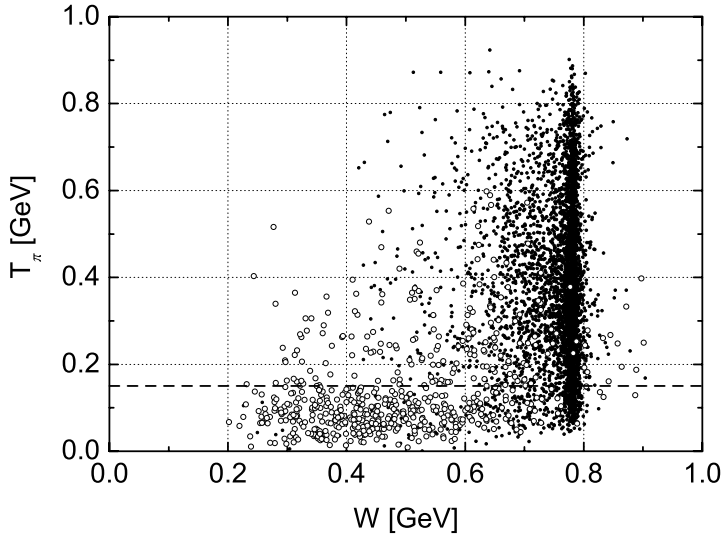

Figure 9.9: Pion kinetic energy T_π versus $\pi^0\gamma$ invariant mass W in the process $\gamma\mathrm{Nb} \to \pi^0\gamma X$ at $E_\gamma = 1.2$ GeV including collisional broadening and a lowering of the in-medium ω mass with $\alpha = -0.16$. *Full symbols*: ω events without rescattering, *open symbols*: events where the π^0 scattered elastically.

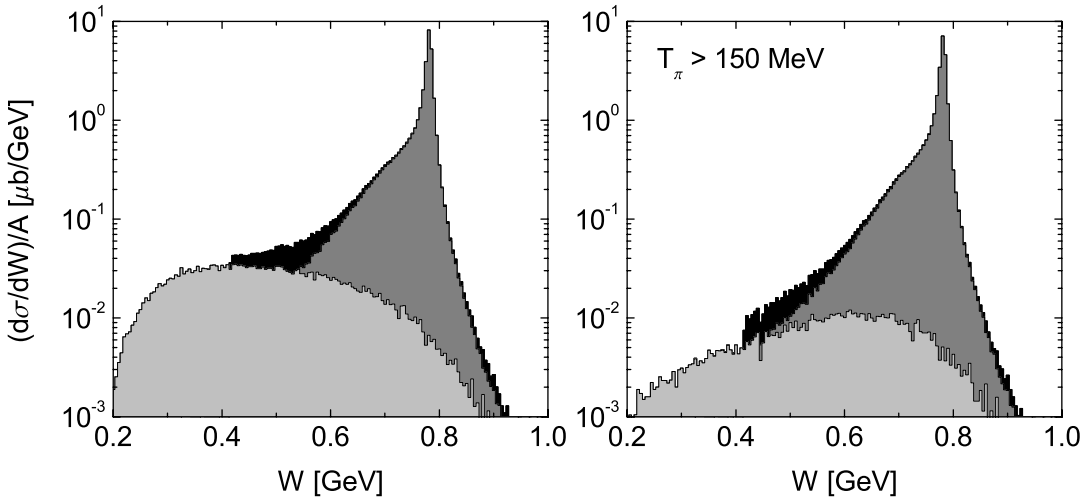

Figure 9.10: Differential cross sections for the reaction $\gamma\mathrm{Nb} \to \pi^0\gamma X$ at $E_\gamma = 1.2$ GeV. *Black area*: total spectrum, *dark gray area*: $\omega \to \pi^0\gamma$ spectrum without rescattering, *light gray area*: rescattering background.

energy is indicated by the dashed horizontal line at $T_\pi = 150$ MeV. By cutting away those events with $T_\pi < 150$ MeV one does not loose much of the actual ω signal. The effect of this cut on the invariant mass spectrum is demonstrated in the right panel of Fig. 9.10. Obviously the dominant part of the rescattering background can be eliminated

whereas the ω signal remains almost unchanged.

9.4.2 The ω width in nuclei

In the following we discuss the possibility to learn about the ω width in nuclei via the $\gamma \to \omega \to \pi^0\gamma$ reaction chain. As a matter of principle this is possible if the two following conditions are fulfilled:

1. The experimental resolution is high enough in order to allow the extraction of the generic width of the ω spectrum;
2. The $\pi^0\gamma$ spectrum is sensitive to variations of the ω collisional width.

The first point is fulfilled only if the broadening of the $\pi^0\gamma$ distribution exceeds the experimental mass resolution. In case of the CBELSA/TAPS measurement the resolution amounts to $\simeq 55$ MeV. Via photoexcitation one can only probe densities smaller than n_0. Moreover, one is sensitive only to the low-momentum tail of the ω spectrum for which the in-medium broadening is expected to be smaller than for the high-momentum part. Thus, we do not expect to observe a significant larger width of the ω spectrum measured from finite nuclei as compared to the vacuum situation. However, one can hope that future experiments will obtain data with resolutions superior to the CBELSA/TAPS measurement.

In order to study the sensitivity of the $\pi^0\gamma$ spectrum to the ω collision width we employ the semi-analytical Glauber model, see Appendix B. Here we use the eikonal expression for the invariant mass differential photoproduction cross section which takes into account the spontaneous vector meson decay, the density dependence of the spectral function and absorption by means of the low density theorem (B.42). Neglecting Fermi motion and Pauli blocking, the collision width and the total vector meson nucleon cross section are thus connected via

$$\Gamma_{\rm coll}(\mathbf{r}) = \Gamma_0 \frac{n_N(\mathbf{r})}{n_0} = \frac{|\mathbf{q}|}{W} n_N(\mathbf{r}) \sigma_{VN}^{\rm inel} \tag{9.18}$$

where $\mathbf{q}$ is the vector meson three-momentum, W is its invariant mass and n_N is the nuclear density. In the case at hand we consider absorptive vector meson nucleon collisions only. To study the dependence of the invariant mass differential cross section on the ω collision width we use $\Gamma_{\rm coll}$ as an input parameter which, thus, also defines the ωN absorption strength. Absorption of the vector meson decay products is not taken into account. In the following we vary Γ_0 in Eq. (9.18) in the range from $0 - 100$ MeV. The observable to be studied is the total width of the invariant mass differential photoproduction cross section from nuclei. We define this observable as the width parameter $\Gamma_{\rm BW}$ of a Breit-Wigner distribution fitted to the calculated cross section. As a showcase we choose a ^{40}Ca nucleus as target and ω mesons of 100 MeV momentum. We consider the following scenarios:

• *Uniform density distribution, instantaneous decay*: The nuclear density distribution is taken to be a step function, n_0 inside and zero outside. All ω mesons decay right at the place and time where they have been created. This scenario is trivial and therefore not

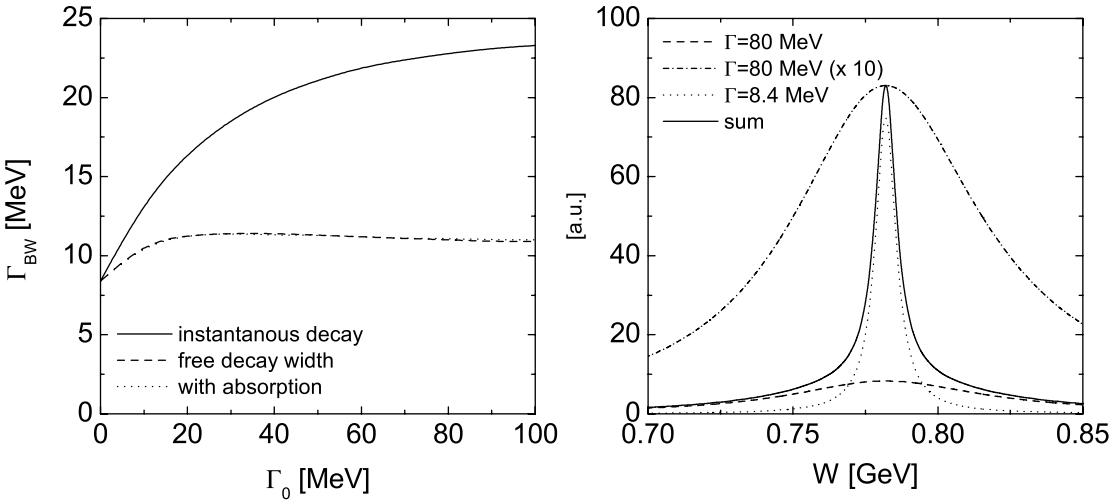

Figure 9.11: *Left*: Breit-Wigner widths $\Gamma_{\rm BW}$ of the invariant mass differential cross sections off Calcium according to the different scenarios discussed in the text, *right*: relativistic Breit-Wigner distributions with equal integrated strength. The summed spectrum has a fitted Breit-Wigner width of 11.8 MeV.

shown in Fig. 9.11. In this case $\Gamma_{\rm BW}$ exactly follows the input width Γ_0. The average probed density is $\bar{n}_N = n_0$.

• *Woods-Saxon density distribution, instantaneous decay*: The average density of the considered Calcium nucleus is much smaller than normal nuclear matter density, most nucleons are sitting at densities of $n_0/2$ and thus $\bar{n}_N = 0.65\, n_0$ and $\Gamma_{\rm BW} < \Gamma_0$. For large collision widths the decays at high density contribute as a background to the Breit-Wigner like distribution. If the width of the in-medium component becomes very large then in turn the height of its peak becomes small since the integrated strength does not increase. This is demonstrated in the right panel of Fig. 9.11 where we have added two relativistic Breit-Wigner distributions with widths $\Gamma = 8.4$ MeV and $\Gamma = 80$ MeV and equal integrated strengths (this corresponds to an amount of 50% of in-medium decays with total width $\Gamma = 80$ MeV, a more than optimistic scenario!). The width of the summed spectrum amounts to 11.8 MeV. A similar effect was found earlier for the case of nucleon resonance photoexcitation in Ref. [272].

• *Woods-Saxon density distribution, free decay width*: Here the ω mesons decay according to their vacuum decay width but no absorption is included. Since the decay width of the ω is small, most ω mesons decay outside the nucleus. The average probed density is constant at $\bar{n}_N = 0.43\, n_0$. The observed width quickly saturates at values of roughly 11 MeV. If Γ_0 becomes large, the in-medium decays contribute as a background to the mass distribution and do not further enhance $\Gamma_{\rm BW}$.

• *Woods-Saxon density distribution, full (in-medium) width*: Now also ω absorption is included. Consequently, the average density goes down from $\bar{n}_N = 0.43\, n_0$ with $\Gamma_0 = 0$ to $\bar{n}_N = 0.35\, n_0$ with $\Gamma_0 = 100$ MeV since more flux is lost in the early stages of the reaction. As we do not consider the absorption of the final state π^0 it is not surprising that the

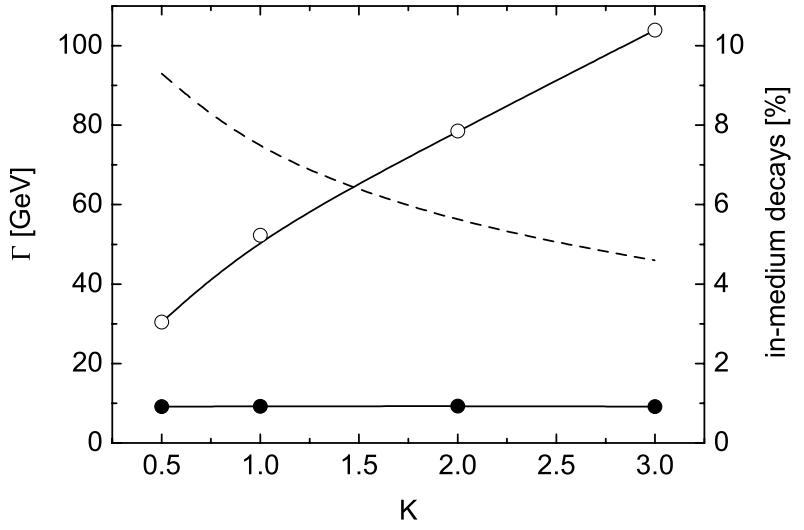

Figure 9.12: Fitted Breit-Wigner (BW) width of the $\pi^0\gamma$ spectrum from transport simulations at $E_\gamma = 1.5$ GeV using ^{40}Ca as target material. *Full symbols – left axis*: BW-width of full spectrum, *open symbols – left axis*: BW-width of mass spectrum taking into account in-medium ($n_N \geq 0.1\, n_0$) decays only, *dashed line – right axis*: fraction of in-medium decays.

result is almost identical to the previous case. Due to ω absorption, contributions from decays inside the nucleus are suppressed but also less vacuum decays occur. Moreover, as Γ_0 goes up, the decay vertices are pushed out of the nucleus and the probed densities go down.

Very similar results are obtained by a full transport calculation of ω photoproduction. In Fig. 9.12 the results of such a calculation are shown. The simulations have been performed at $E_\gamma = 1.5$ GeV using again Calcium as target material. The collisional width is varied in terms of an inelastic $K-$factor that is multiplied to our canonical parametrization of the ω in-medium width

$$\tilde{\Gamma}_{\rm coll} = K_{\rm inel} \cdot \Gamma_{\rm coll}. \tag{9.19}$$

According to the low density theorem this modification of the collisional width goes along with an analogous change of the total ωN cross section. In the present calculations, we put this modification entirely into the absorptive part of the ωN interaction

$$\tilde{\sigma}^{\rm inel}_{VN} = K_{\rm inel} \cdot \sigma^{\rm tot}_{VN} - \sigma^{\rm inel}_{VN}, \tag{9.20}$$

$$\tilde{\sigma}^{\rm el}_{VN} = \sigma^{\rm el}_{VN}\ , \tag{9.21}$$

where $\sigma_{\rm tot}$ is the sum of the elastic and inelastic VN cross sections. The total Breit-Wigner width of the obtained mass spectrum is almost constant at 10 MeV, whereas the width of the in-medium decay spectrum ($n_N > 0.1\, n_0$) increases almost linearly with the collisional width. On the other hand, at the same time the relative amount of in-medium

decays goes down due to the larger ω absorption rate (dashed line and right vertical axes in Fig. 9.12).

In summary, we have found that the Breit-Wigner width of the observed $\pi^0\gamma$ spectrum is only weakly sensitive to the collisional width of the ω meson. This statement is more or less independent of details of the calculation as the initial production process and final state interactions. A large collisional width contributes a background like distribution to the $\pi^0\gamma$ mass distribution that does not significantly enhance the width of the observed mass spectrum. This contribution is only significant on a logarithmic scale, compare Fig. 9.10 where a broadening and an in-medium mass shift of the ω has been considered. Such an effect, however, would require high experimental statistics that allows to produce meaningful spectra over a range of more than one order of magnitude.

A different means to obtain information on at least the absorptive part of the (on-shell) ω self energy is the attenuation measurement as introduced in the previous Chapter for the case of ϕ photoproduction. A detailed discussion of ω attenuation in nuclei will follow in Section 9.5. To this end the total production cross section has to be determined experimentally. Whereas this measurement is less sensitive to the tails of the spectral distribution (and, thus, less sensitive to the background subtraction) the overall normalization has to be determined with high accuracy. As opposed to the $\pi^0\gamma$ mass spectrum that is sensitive to the low-momentum tail of the ω spectrum the attenuation measurement probes the ω spectrum over its entire momentum range. As the centroid of the momentum spectrum is located at rather high ω momenta the transparency ratio without any cuts on the energy of the detected ω mesons provides information on the high-momentum part of the absorptive ω self energy in the vicinity of the actual peak of the mass distribution. Theoretical information about the ω in-medium properties at these energies is hardly available.

9.4.3 The ω mass in nuclei

In the following we address the question of how an in-medium shift of the ω mass manifests itself in the $\pi^0\gamma$ mass spectrum.

In Fig. 9.13 we show the results of transport simulations using various scenarios of ω in-medium properties as input. We consider the cases with either vacuum properties, collisional broadening or collisional broadening plus an additional mass shift. We use either $\alpha = -0.16$, which results in a very strong attractive ω potential, or $\alpha = 0.04$ which roughly corresponds to the moderate upwards shift found in the $K-$matrix analysis. The calculations have been done for the photon energy range from 900 MeV to 1200 MeV using ^{40}Ca as target. Note that the vacuum threshold for photoproduction of on-shell ω mesons lies at $E_{\rm thr} = 1.1$ GeV. Comparing the scenarios with vacuum properties and collisional broadening a moderate enhancement at masses below the vacuum peak can be observed. Including the attractive ω potential we encounter a huge enhancement of the cross section for small masses. In order to understand the mechanism behind this effect we have to go into some details of the calculations.

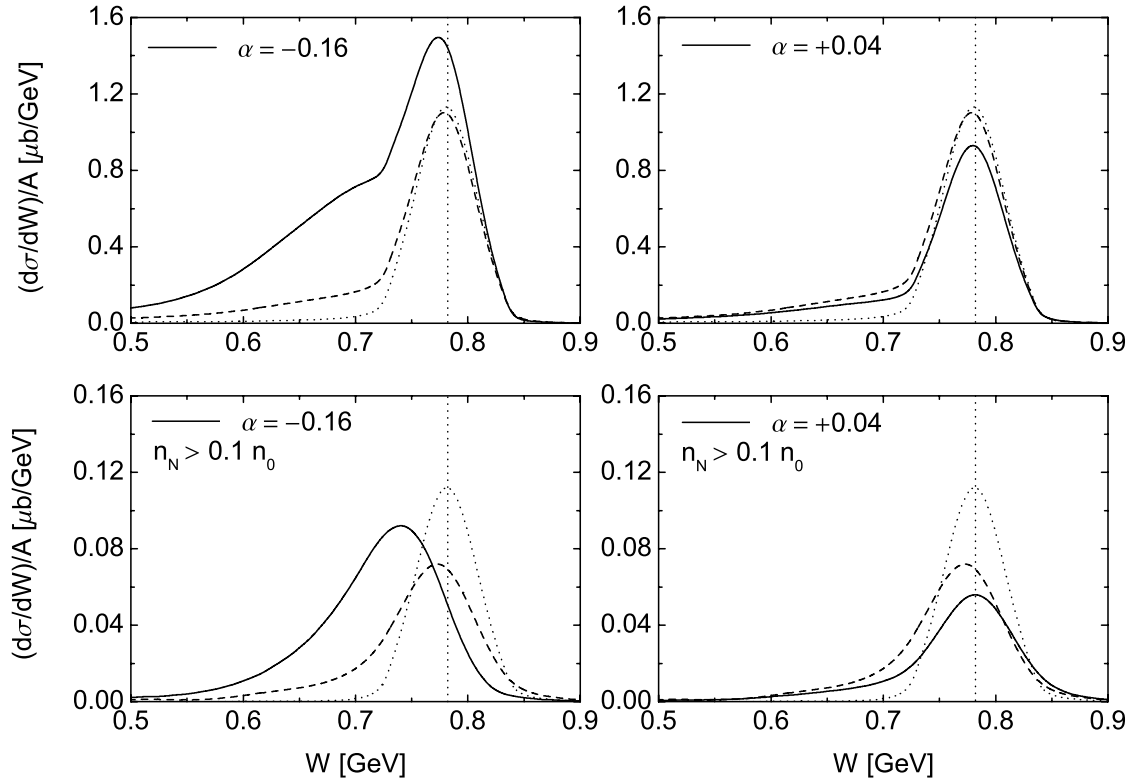

Figure 9.13: $\pi^0\gamma$ mass distribution obtained from a simulation of the reaction $\gamma\mathrm{Ca} \to \pi^0\gamma X$ at $E_\gamma = (900 - 1200)$ MeV including an experimental resolution of $\delta W = 25$ MeV and a weighting $\sim 1/E_\gamma$. *Dotted line*: vacuum properties, *dashed line*: with collisional broadening, *solid line*: with broadening and mass shift. Left panels are calculated with an attractive shift ($\alpha = -0.16$) and the right ones are calculated with a repulsive shift ($\alpha = 0.04$). The curves in the lower row give the contribution of in-medium ($n_N > 0.1\, n_0$) decays. The dotted vertical line indicates the physical ω mass.

According to Eq. (9.11) the mass differential cross section for the exclusive process $\gamma N \to VN$ is given by

$$\begin{aligned} \frac{d\sigma_{\gamma N \to VN}}{dW} &= \sigma_{\gamma N \to VN} \cdot \chi(W) \\ &= \frac{1}{16\pi s |\mathbf{k}_{\mathrm{cm}}|} \overline{|\mathcal{M}_{\gamma N \to VN}|^2}\, \mathcal{A}_V(W) |\mathbf{q}_{\mathrm{cm}}(W)| 2W \end{aligned} \tag{9.22}$$

where the squared matrix element in the second line is averaged over the probability distribution $\chi(W)$. Here we use the averaged matrix element since our Monte Carlo procedure works such, that in the photon-nucleon interaction first the types of the final state particles (e. g. ωN) are determined. This is done by Monte Carlo sampling according to the total production cross sections that are proportional to the averaged squared matrix elements. In a second step the energies and momenta of the final state particles are determined from the probability distribution $\chi(W)$. It is given by

$$\chi(W) = I^{-1} \mathcal{A}_V(W) |\mathbf{q}_{\mathrm{cm}}(W)| 2W \tag{9.23}$$

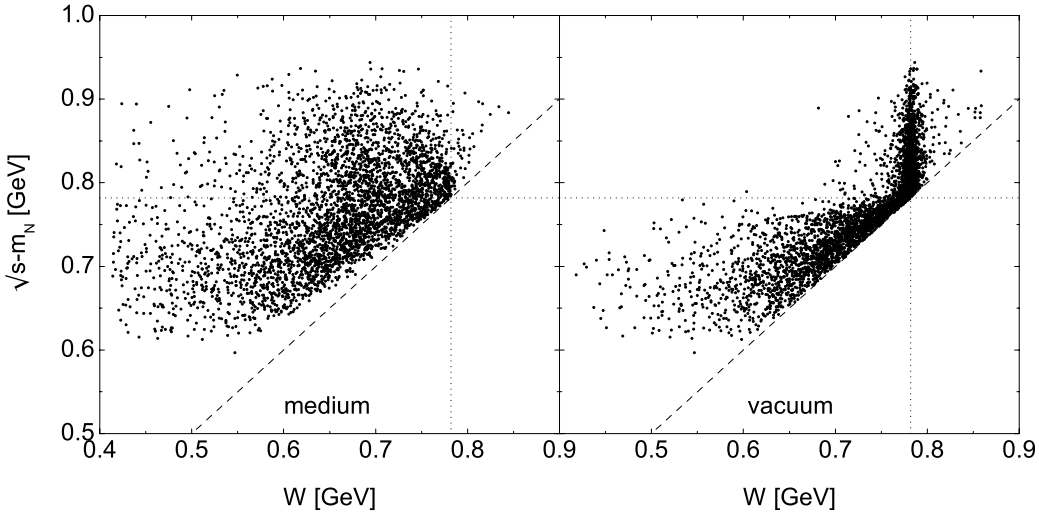

Figure 9.14: Free invariant energy (minus nucleon mass) versus the ω in-medium and vacuum masses determined by Monte Carlo sampling from the probability distribution (9.23) in the reaction $\gamma\mathrm{Ca} \to \omega X$ at $E_\gamma = 1.1$ GeV including collisional broadening and an attractive mass shift with $\alpha = -0.16$. *Solid line*: ω vacuum mass, *dashed line*: kinematical limit $\sqrt{s} = W + m_N$.

where I is chosen such that $\chi(W)$ is normalized to one. The distribution $\chi(W)$ completely governs the dependence of the cross section on the vector meson mass W. The phasespace factor $\mathbf{q}_{\mathrm{cm}}$ goes to zero as the vector meson mass reaches $W = \sqrt{s} - m_N$. In the Monte Carlo simulation the averaged squared matrix element and the flux factors go into the testparticle weights, whereas the product of spectral function and phasespace factor contained in $\chi(W)$ determine the mass distribution of the produced testparticles. The off-shell potential of a given test particle is defined by the difference of the vector meson in-medium and vacuum masses (see Eq. (A.10)). The vacuum mass is determined by Monte Carlo sampling according to the product of vacuum spectral function and phasespace factor $\mathbf{q}_{\mathrm{cm}}(W)$; the analytical from of the latter one is identical for both the vacuum and in-medium situations since apart from the vector meson invariant mass it depends on the available energy only.

In case of an attractive potential, the in-medium probability distribution $\chi_{\mathrm{med}}(W)$ can take high values for masses below the nominal vector meson mass. Thus, the production of vector mesons also at subthreshold energies $\sqrt{s} < m_N + m_V$ becomes likely. In this case also the normalized vacuum probability distribution $\chi_{\mathrm{vac}}(W)$ becomes sizable for small vector meson masses since the phasespace factor $\mathbf{q}_{\mathrm{cm}}$ cuts away the higher mass contributions. A test particle produced at subthreshold energies in the medium propagates to its vacuum mass as it escapes the nucleus. This mass still is smaller than the generic vector meson peak mass due to the limitation of phasespace. This is demonstrated in Fig. 9.14 where the available invariant energy minus the nucleon mass versus the sampled in-medium and vacuum ω masses in the reaction $\gamma\mathrm{Ca} \to \omega X$ at $E_\gamma = 1.1$ GeV is shown. Events below the solid horizontal line are subthreshold with respect to the free ω peak mass. For a given invariant energy $\sqrt{s}$ the dashed line

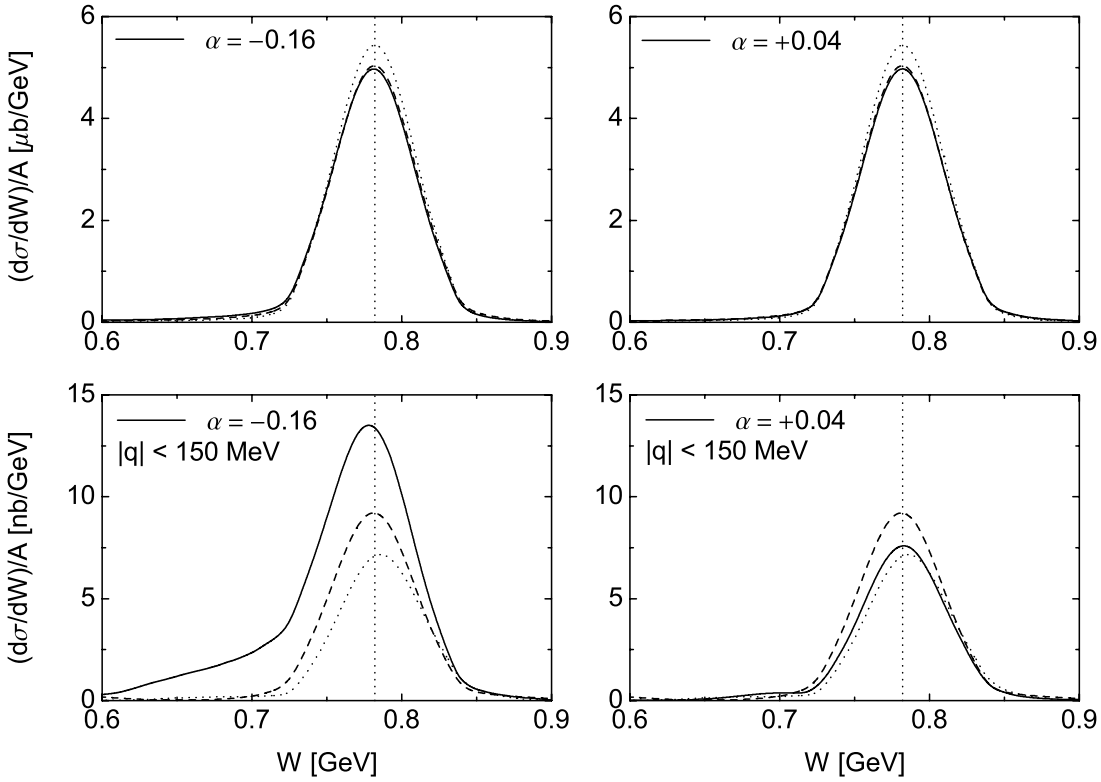

Figure 9.15: $\pi^0\gamma$ mass spectrum from the reaction $\gamma\mathrm{Ca} \to \pi^0\gamma X$ at $E_\gamma = (1500 - 2000)$ MeV including an experimental resolution of $\delta W = 25$ MeV and a weighting $\sim 1/E_\gamma$. *Dotted line*: vacuum properties, *dashed line*: with collisional broadening, *solid line*: with broadening and mass shift. Left panels are calculated with an attractive shift ($\alpha = -0.16$) and the right ones are calculated with a repulsive shift ($\alpha = 0.04$). Curves in the lower row contain a three-momentum cutoff $|\mathbf{q}| < 150$ MeV. The dotted vertical line indicates the physical ω mass.

$\sqrt{s} = W + m_N$ indicates the maximal possible ω mass. Above threshold the vacuum masses are close to the ω peak mass since the probability distribution $\chi(W)$ becomes sizable there. Below threshold the factor $\mathbf{q}_{\mathrm{cm}}(W)$ goes to zero at $W = \sqrt{s} - m_N < m_\omega$ and, thus, the vacuum masses are limited to the low-mass region.

This phasespace enhancement is the reason for the substantial effects which can be observed in Fig 9.13. Note, however, that this signal is created by a modification of phasespace of the elementary production process. The component of in-medium ($n_N > 0.1\, n_0$) decays alone (lower panels in Fig. 9.13) cannot account for the enhancement below the physical ω mass. Such a change can also be sensitive to details of the production mechanism as excited nucleon resonances, rescattering processes in the ωN final state and interferences. This can not be controlled without a complete understanding of the ω photoproduction process. According to the above arguments we do not observe such a strong medium effect for higher incident beam energies that are explicitly above the free ωN threshold. This can be seen in Fig. 9.15 where the same cross sections for beam

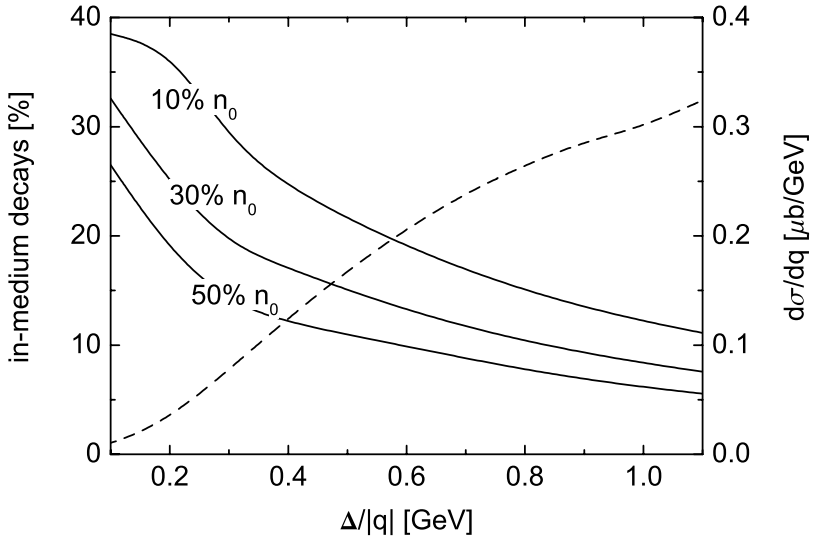

Figure 9.16: *Solid lines – left axis*: Relative contribution of in-medium decays depending on the three-momentum cutoff value $\Delta > |\mathbf{q}|$, *dashed line – right axis*: momentum differential photoproduction cross section. Both observables are evaluated in the reaction $\gamma\mathrm{Ca} \to \pi^0\gamma X$ at $E_\gamma = (1500 - 2000)$ MeV including a weighting $\sim 1/E_\gamma$. Different solid lines correspond to various limiting decay densities $n_N > (0.1,\, 0.3,\, 0.5)\, n_0$.

energies of $E_\gamma = (1.5 - 2.0)$ GeV are shown. Here the available energy is high enough in order to allow the ω mesons to propagate back to the free ω peak mass $m_\omega = 782$ MeV. Thus, in-medium effects can only be observed if the ω mesons decay at finite densities. The phasespace enhancement is also absent for the case of a repulsive ω potential. Thus, the mass spectra are only weakly sensitive to such an upwards shift of the ω mass. This can be seen in the right panels of both Figs. 9.13 and 9.15.

As discussed in an earlier Section 7.2.1 the contribution of events where the vector meson decay happens inside the nucleus can be raised by using a sensible three-momentum cutoff on the total $\pi^0\gamma$ momentum. In Fig. 9.16 we show the relative contribution of ω decays in the medium depending on the momentum cutoff value $\Delta > |\mathbf{q}| = |\mathbf{k}_\pi + \mathbf{k}_\gamma|$ for the beam energy range $E_\gamma = (1.5 - 2.0)$ GeV. Here, the interior of the nucleus is defined as the region where the density is larger than $n_N = 0.1\, n_0$, $0.3\, n_0$ or $0.5\, n_0$, respectively. For densities lower than $0.1\, n_0$ the average distance of the nucleons becomes larger than the inverse pion wave length that defines the long-range part of the nuclear force. Asymptotically the contribution of in-medium decays amounts to 7.5% only. With lower cutoff values this contribution can be raised up to almost 40%. This magnifies the observable in-medium effects. On the other hand, this comes at the price of much reduced counting rates since the ω photoproduction cross section drops substantially for low ω momenta. This is also indicated in Fig. 9.16 via the dashed line which shows the momentum differential ω photoproduction cross section of Calcium in the considered energy interval. The $\pi^0\gamma$ mass spectra including such a three-momentum cutoff are also shown in Fig. 9.15, lower panels. Imposing an attractive mass shift the in-medium

changes are again substantial. The advantage now is, that this effect is less sensitive to details of the inital production process. The only significant effect of the repulsive mass shift is a slight reduction of the total cross section which is due to phasespace suppression.

Even a symmetric broadening of the ω in-medium spectrum has observable consequences that are more substantial on the low-mass side of the free ω peak. The reason for this effect is on the one hand the phasespace factor (9.23), which depends on the total available energy, and on the other hand the branching ratio to the $\pi^0\gamma$ final state, that also can depend on the nuclear density. Consequently, a repulsive shift of the ω in-medium peak will be much harder to verify than an attractive shift. The phasespace enhancement in the threshold region as discussed for the attractive shift is absent in this case. High statistics data with a sensible three-momentum cutoff are necessary to either rule out or verify such a change of the in-medium ω spectrum. Moreover, we emphasize that even the mass spectrum of ω mesons produced inside finite nuclei and decaying in vacuum can strongly deviate from the mass spectrum of ω mesons produced on a proton target. The reason is that in general also the population processes depend on the ω invariant mass and, thus, on the in-medium spectral function. In particular if the photon energy is close to the ωN threshold, ω mesons with low mass are produced which cannot propagate to the free ω mass due to the limitation of phasespace. This has to be taken care of in the analysis of experimental data.

9.4.4 Analysis procedure

On the basis of the knowledge obtained in our previous studies and the available experimental data we propose the following method to extract the ω in-medium properties. It consists of three steps:

1. **Extraction** of the inelastic ωN cross section $\sigma_{\omega N}^{\text{inel}}$ from the attenuation measurement. Within the present data situation this can be done only for the integrated ω momentum spectrum at the photon energy of $E_\gamma = 1.5$ GeV where attenuation data are available. It would be desirable to do this also for various ω momentum bins in order to extract the momentum dependence of the inelastic ωN cross section.

2. **Extrapolation** of the inelastic cross section to low momenta and relation to the (imaginary part) of the in-medium self energy. The extrapolation can be done by either fitting the parameters of a microscopic model to the results obtained from (1.) or by rescaling a reasonable parametrization in order to describe the data. Ideally complementary information from vacuum scattering processes and/or other nuclear experiments is used in addition. The collisional width (the imaginary part of the on-shell self energy) can be obtained by means of the low-density theorem.

3. **Evaluation** of $\pi^0\gamma$ mass spectra from nuclear targets using the results from (1.) and (2.) as input. Employing the Monte Carlo transport model we will analyze the differential experimental data in view of an unshifted ω mass or an extra shift of spectral strength, either in form of a displacement of the in-medium ω peak or the creation of additional branches in the ω spectral function. Again it would be

desirable to do this for various bombarding energies and in different ω momentum bins.

In the next Sections we will follow this recipe resulting in the most sensible acquisition of information on the ω in-medium properties possible on the basis of the present data situation.

9.5 Total cross section and transparency

As a measure for the ω width in nuclei we use the nuclear transparency ratio as already introduced in Section 7.2.2. In order to minimize the ambiguities concerning a modification of the initial production process when going from the vacuum to finite nuclear systems we introduce a second ratio

$$T_{A,B} = \frac{B\sigma_{\gamma A \to VX}}{A\sigma_{\gamma B \to VX}} \tag{9.24}$$

where A and B are the mass numbers of different nuclear targets. One would have to use symmetric nuclei only in order to be free of the uncertainties in the difference of the proton and neutron cross sections. We will normalize to ^{12}C, the lightest target material used in the CBELSA/TAPS experiment. For $B = 1$ the ratio $T_{A,B}$ again reduces to the previously used transparency ratio. As before we normalize to the nuclear mass number and, thus, do not impose any assumption on the ω absorption strength.

9.5.1 Transport results

First we will discuss some general properties of the nuclear transparency ratio that can be studied quantitatively by means of our Monte Carlo model. At the end of this Section the inelastic ωN cross section will be extracted from the CBELSA/TAPS data.

Inclusive excitation function. To begin with we show in Fig. 9.17 the total $\pi^0\gamma$ photoexcitation function off various nuclei over the entire considered photon energy range as obtained from a BUU transport calculation. Here, we have included collisional broadening but no mass shift. Up to energies of $E_\gamma \simeq 1.3$ GeV the reaction is completely dominated by the exclusive ω production process. The resonance like structure at about $E_\gamma \simeq 1.2$ GeV can indeed be ascribed to the non-resonant $t-$channel pion exchange graph, see Fig. 9.5. Above energies of 1.3 GeV the inclusive production channels open. In this energy regime the theoretical error bars become more substantial since the inclusive channels have not even in vacuum been tested against experiment due to the lack of data. The right panel in Fig. 9.17 shows the $A-$scaling of the total ω yield. Close to the production threshold the inclusive cross section scales according to $\sigma \sim A^{2/3}$ whereas for higher energies the exponent α according to $\sigma \sim A^\alpha$ increases. This scaling behavior indicates strong ω absorption at small energies and weakening absorption for higher energies. It is created by the smoothly dropping ωN cross sections for increasing ω kinetic energies according to Eqs. (9.1) and (9.2).

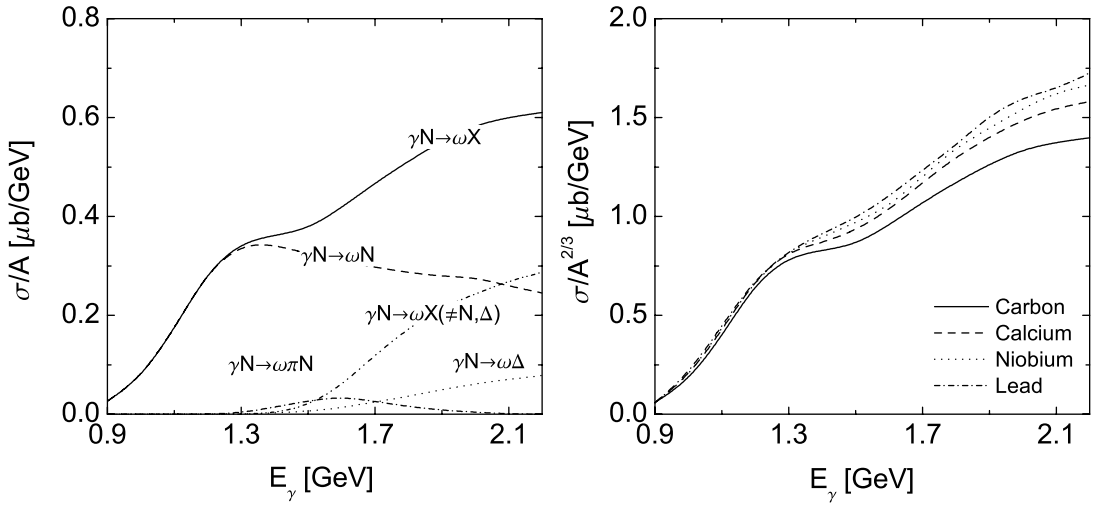

Figure 9.17: Total $\gamma A \to \pi^0 \gamma X$ photoproduction cross section off various nuclei. *Left panel*: Cross section from Carbon normalized by A and its decomposition into the various ω sources, *Right panel*: cross section normalized by $A^{2/3}$ off different target nuclei.

Transparency ratio. In order to systematically explore the imaginary part of the ω nucleus potential, we perform calculations at the fixed photon beam energy of $E_\gamma = 1.5$ GeV. On one hand, this energy is well above the free production threshold $E_{\rm th} = 1.1$ GeV so that here one is essentially free of any threshold effects such as medium modifications of the elementary cross section for instance due to the in-medium broadening of excited nucleon resonances. Also the sensitivity to a density-dependent shift of the ω pole mass becomes small for this beam energy as we will show in the following Section. On the other hand, the chosen energy is low enough so that any inclusive production channels $\gamma N \to V X$ with $X \neq N$ are of minor importance, see Fig. 9.17. Moreover, events from the dominant inclusive channel $\gamma N \to V \pi^0 X$ can easily be suppressed experimentally. Thus, ambiguities due to the elementary production process are minimized for the chosen beam energy of 1.5 GeV.

The BUU calculations have been performed for the targets ^{12}C, ^{40}Ca, ^{93}Nb, ^{120}Sn, and ^{208}Pb. In Fig. 9.18 we show results for the transparency ratio obtained within the standard scenario, i. e. using the cross sections as given by Eqs. (9.1), (9.2) and including collisional broadening of the ω as a medium modification only. In the experimental analysis one tries to get rid of pions that rescattered in the medium since these $\pi^0\gamma$ pairs essentially lose all information about their source. This can be done easily by applying a cut on the kinetic energy of the π^0 as discussed earlier, i. e. $T_\pi > 150$ MeV. Removing the pions that interacted via quasi elastic collisions from the total flux, we obtain the dashed line in Fig. 9.18. Only a small reduction of the transparency ratio is observed. This becomes immediately clear if one realizes that most of the observable ω mesons decay outside the nucleus and therefore the probability for the pion to scatter from the target nucleons is small. If, in addition, restrictions on the $\pi^0\gamma$ invariant mass are imposed in order to gate on the ω decay component in the $\pi^0\gamma$ spectrum, only a slight reduction

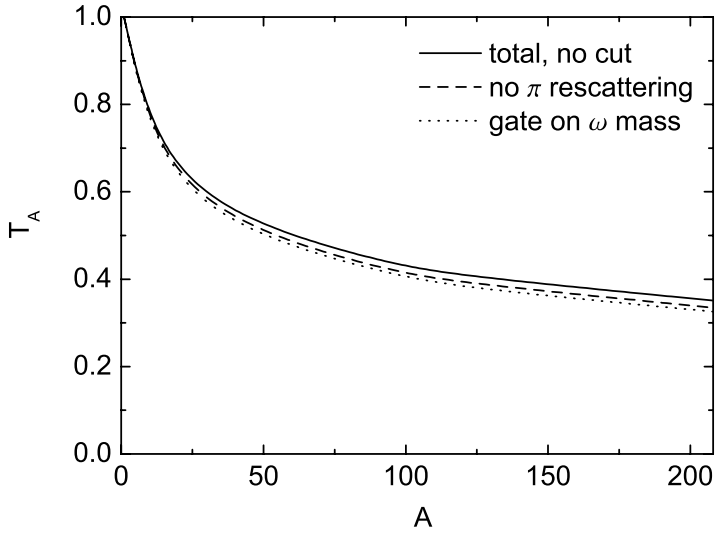

Figure 9.18: Nuclear transparency ratio from BUU calculations as function of the target mass number for the photon energy $E_\gamma = 1.5$ GeV. *Solid line*: no restrictions on energy and momentum of the $\pi^0\gamma$ pair, *dashed line*: pions that interacted via a quasi elastic collision are removed from the flux, *dotted line*: as dashed line but with invariant mass cut 0.75 GeV $\leq W \leq$ 0.81 GeV.

can be observed. This is shown by the dashed curve in Fig. 9.18, where the condition 0.75 GeV $\leq W \leq$ 0.81 GeV has been imposed. Again the reason for this marginal effect is the only tiny contribution of ω decays in the medium where the ω spectral distribution becomes broad.

Real part of the ωA potential. In the threshold region the total ω production cross section and therewith the transparency ratio are also sensitive to the real part of the ω nucleus potential. This is shown in Fig. 9.19, where the total cross section with and without a density dependent shift of the ω pole mass for the targets ^{12}C and ^{208}Pb are shown. We parametrize the real part of the ω in-medium self energy by the attractive mass shift as given in Eq. (9.3) with the canonical strength parameter $\alpha = -0.16$ [9, 200]. At low photon energy the cross section including the dropping ω mass shows a pronounced excess over the standard calculation due to the lowering of the ωN threshold in the medium. Note, however, that also the diminishing recoil due to coherent ω production would lead to a shift of the threshold with the mass number A. This shift, however, does not show up in the quasielastic events considered here. Also the in-medium broadening of the ω spectral function and the energy smearing caused by Fermi motion cause a lowering of the in-medium production threshold ($E_\gamma^{\rm th} \simeq 1.1$ GeV in vacuum) for finite nuclear targets.

The production of ω mesons at energies below the free production threshold is dominated by the low-energy tail of the ω in-medium spectral function. Such ω mesons far off-shell the free ω mass are difficult to identify experimentally, but they do contribute

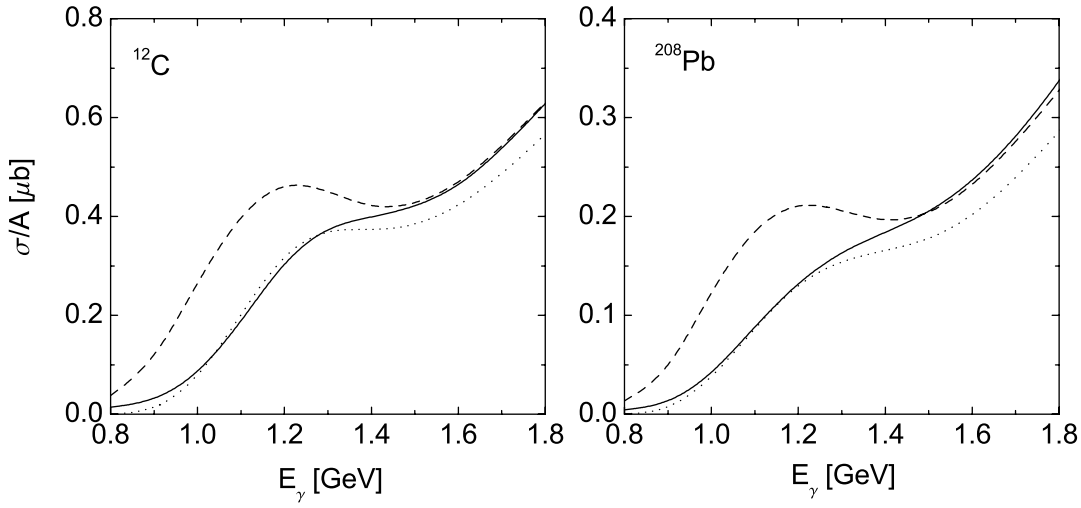

Figure 9.19: Total ω photoproduction cross section from ^{12}C and ^{208}Pb as function of the photon beam energy. *Solid line*: no potential, *dashed line*: attractive potential, *dotted line*: attractive potential and 0.75 GeV $\leq W \leq$ 0.81 GeV.

to the total ω yield and thus influence the transparency ratio. Therefore, we again show results with the condition 0.75 GeV $\leq W \leq$ 0.81 GeV. Imposing this restriction on the $\pi^0\gamma$ mass, the component of low-mass ω mesons in the final particle yield is discarded. However strong the threshold enhancement shows up, an extraction of the real part of the in-medium self energy from the total cross section has to rely on theoretical assumptions for the elementary ω photoproduction process as a baseline. The total cross section and the transparency are sensitive to the interference of the individual contributions to the ω photoproduction amplitude, see Appendix E. In-medium the interference pattern could change along with the ω and the excited resonance properties. Thus, a complete understanding of the elementary production process is required. Theoretical efforts towards such a complete description of ω photoproduction from elementary targets are, however, underway [249]. At present, a unique mapping of the observed effects to particular medium modifications turns out to be difficult as the relevant contributions to the ω photoproduction process have not yet been resolved. More important to our present calculations is, that the total cross section and the ratios T_A and $T_{A,B}$ are invariant under changes in the real part of the ω nucleus potential for energies above $E_\gamma = 1.4$ GeV.

In-medium decay width. In Fig. 9.20 we show the nuclear transparency with and without including the modification of the $\omega \to \rho\pi$ decay width according to Eq. (8.6) on top of the ω collisional width. The dropping ρ and ω masses alone have no effect on the transparency ratio as the photon energy is well above threshold where the change in the phasespace factors becomes small. Including the modified $\rho\pi$ decay width, more ω mesons decay to that channel due to the opening of the $\rho\pi$ phasespace at non-zero nuclear density. Hence more ω mesons are taken out of the total flux inside the nucleus. This leads to a further but small reduction of the transparency ratio.

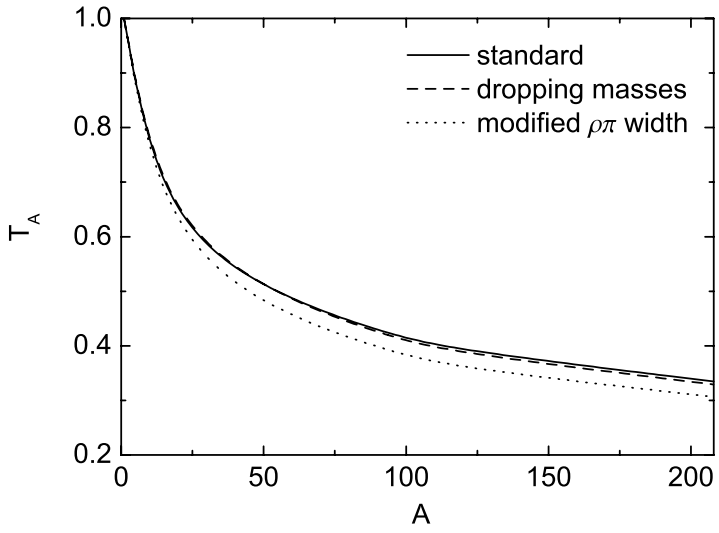

Figure 9.20: Nuclear transparency ratio at $E_\gamma = 1.5$ GeV. *Solid line*: collisional broadening (CB) only, *dashed line*: CB and dropping ρ and ω masses (DM), *dotted line*: CB, DM and medium modification of the $\omega \to \rho\pi$ decay width.

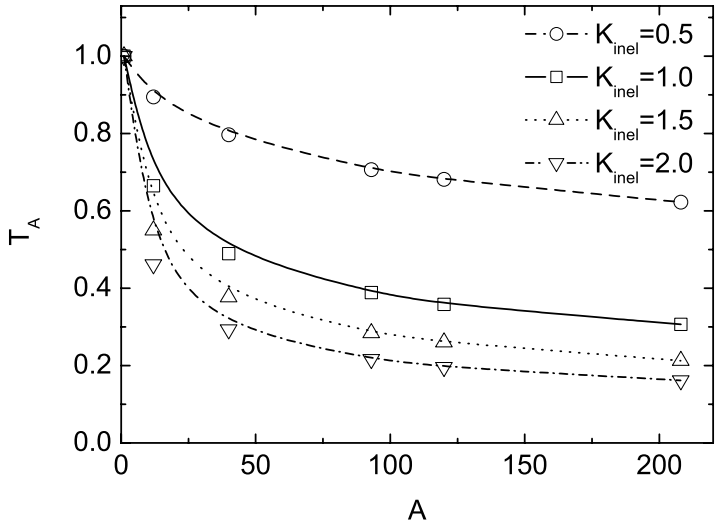

Figure 9.21: Nuclear transparency ratio obtained from BUU transport simulations as function of the target mass number. Calculations have been done for different inelastic $K-$factors. The photon energy is $E_\gamma = 1.5$ GeV. No acceptance corrections have been applied.

Absorption. We test the sensitivity of the nuclear transparency ratio to the inelastic ωN cross section by varying the inelastic ωN cross section in terms of the $K-$factor $K_{\rm inel}$ as defined in Eq. (9.20). The results are shown in Fig. 9.21. Besides the results obtained

with the canonical value for the ω collisional width ($K_{\rm inel} = 1.0$, $\Gamma_{\rm coll}(\mathbf{p} = 0) = 37$ MeV), curves with $K_{\rm inel} = 0.5$, $K_{\rm inel} = 1.5$ and $K_{\rm inel} = 2.0$ are shown. We also include the dropping ρ and ω masses as well as the modified $\rho\pi$ decay width as discussed previously. The results from our transport calculations show an obvious lowering of the nuclear transparency ratio as the ω width goes up and, hence, the mean free path of the ω shrinks to smaller values. The transparency ratio decreases in a non-linear way with the increasing ω width. Whereas the absolute size of the transparency ratio yields important information about the ω collisional width, its $A-(N-, Z-)$ scaling in principle is also sensitive to the isospin dependence of the production and absorption cross sections.

Elastic scattering. Finally, we explore the influence of different assumptions for the ωN elastic scattering cross section on the nuclear transparency. Again we use a constant normalization factor $K_{\rm el}$ that we now multiply to the elastic scattering cross section

$$\tilde{\sigma}^{\rm el}_{VN} = K_{\rm el} \cdot \sigma^{\rm el}_{VN} \tag{9.25}$$

$$\tilde{\sigma}^{\rm tot}_{VN} = \tilde{\sigma}^{\rm el}_{VN} + \sigma^{\rm inel}_{VN}. \tag{9.26}$$

Elastic scattering processes do not lead to a loss of flux and, thus, do not directly influence the total nuclear cross section and the transparency. On the other hand, such scattering processes change the ω momentum distribution. The stopping of the ω mesons in nuclear matter due to elastic ωN scattering is particularly large as the mass of the ω is comparable to the nucleon mass which leads to a relatively high energy loss of the ω in these collisions.

Indeed a change of the ω momentum spectrum for different elastic $K-$factors can be observed. ω mesons from the high-momentum part of the spectrum are shuffled to the low-momentum tail. On one hand, these ω mesons stay in the medium for a longer time where they have the chance to get absorbed in inelastic ωN collisions. On the other hand, the ωN absorption cross sections are particularly large at low energies due to the open phasespace at the ωN threshold for processes like $\omega N \to \pi N$, $\omega N \to \pi\pi N$ etc. Hence, the nuclear transparency is slightly reduced for increasing values of the elastic ωN cross section. This reduction, however, becomes significant only for very large $K-$factors and, thus, is accompanied by a rather drastic change of the elastic scattering cross section as compared to our standard estimate.

The ωN absorption cross section. We calculate the cross section ratio $T_{A,12}$ according to Eq. (9.24) using our Monte Carlo transport code. In these calculations we use $K_{\rm el} = 1$ (standard interaction strength for elastic ωN collisions), $\alpha = 0$ (no real ω potential) and collisional broadening that is connected to the total ωN cross section via the low-density theorem. The inelastic $K-$factor $K_{\rm inel}$ is varied unless agreement with the experimental data is obtained. The value that yields the best fit to the experimental data is

$$K_{\rm inel} = 1.25 \tag{9.27}$$

The result for the cross section ratio $T_{A,12}$ from this calculation is shown in Fig. 9.22.

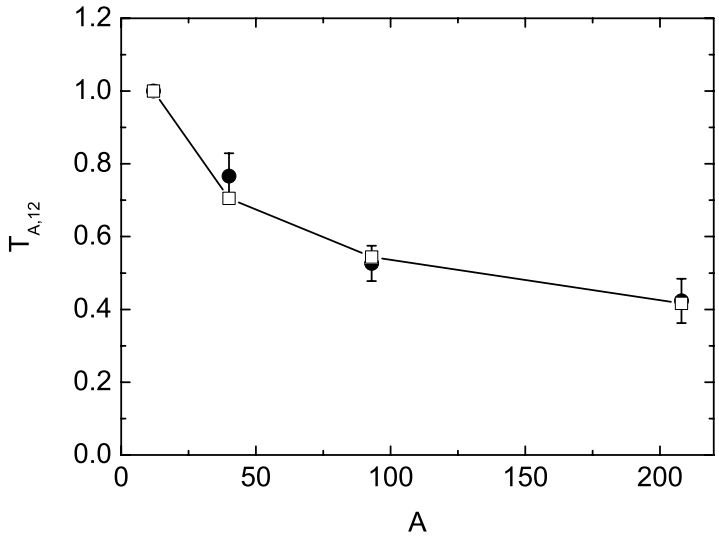

Figure 9.22: Cross section ratio according to Eq. (9.24) obtained from transport simulation of the process $\gamma A \to \omega X$ at $E_\gamma = 1.5$ GeV. An inelastic $K-$factor of $K_{\rm inel} = 1.25$ has been used. Experimental data from [19].

9.5.2 Glauber analysis

In this Section we will discuss ω photoproduction in the semi-analytical Glauber picture as a very simple means to extract the inelastic ωN cross section. In the Glauber-eikonal approximation, neglecting Fermi motion, Pauli blocking, coupled channel effects, nuclear shadowing and quasi elastic scattering processes, the incoherent single meson photoproduction cross section can be written in factorized form as

$$\sigma_{\gamma A} = A_{\rm eff}\, \sigma_{\gamma N} \tag{9.28}$$

where $\sigma_{\gamma N}$ is the vector meson photoproduction cross section on a single nucleon. A possible density dependence of the elementary photoproduction cross section is ignored. The effective mass number is given by

$$A_{\rm eff} = \frac{2\pi}{\sigma_{VN}^{\rm inel}} \int_0^\infty bdb \left(1 - \exp\left[-\sigma_{VN}^{\rm inel} \int_{-\infty}^{+\infty} dz'\; n_N(\mathbf{b}, z') \right] \right) \tag{9.29}$$

where n_N is the nuclear density and $\sigma_{VN}^{\rm inel}$ is the total vector meson-nucleon absorption cross section. This expression is derived in Appendix B. The cross section ratio $T_{A,B}$ is given by

$$T_{A,B} = \frac{BA_{\rm eff}}{AB_{\rm eff}}. \tag{9.30}$$

Equation (9.29) assumes that the vector meson goes forward with respect to the incoming photon beam direction. This assumption is well justified at sufficiently high photon

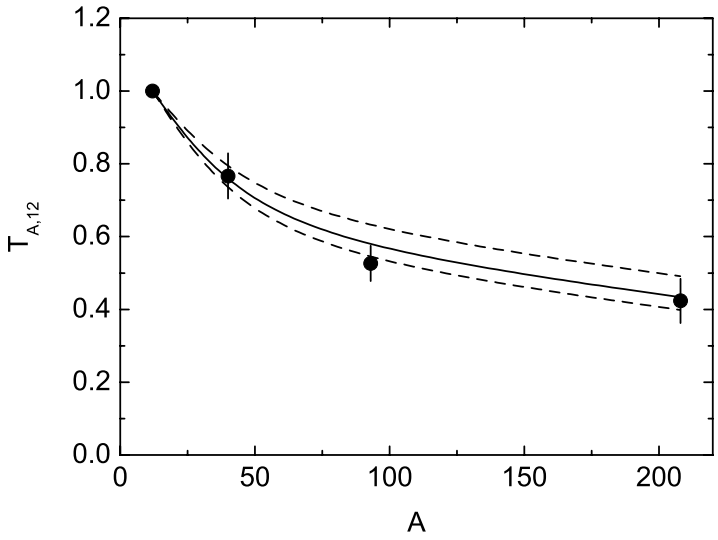

Figure 9.23: Cross section ratio $T_{A,12}$ according to Eq. (9.24) calculated within the Glauber model using the inelastic ωN cross section (9.31). Experimental data from [19]. *Dashed lines*: Error estimates from the spread of the data points.

energies. In addition, vector meson photoproduction cross sections are peaked in forward direction, see Fig. 9.6. Thus, the applicability of the eikonal approximation is rather well justified for the case at hand.

From the analysis of the CBELSA/TAPS experiment the cross section ratio $T_{A,12}$ has been obtained in the photon energy range $E_\gamma = (1.45 - 1.55)$ GeV [19]. We fit the ratio calculated by means of the expression (9.29) to the experimental values by a variation of the inelastic cross section $\sigma_{VN}^{\rm inel}$. This procedure yields

A	$T_{A,12}$	$\sigma_{VN}^{\rm inel}$[mb]
12	1	–
40	0.766 ± 0.062	22^{+14}_{-8}
93	0.526 ± 0.049	41^{+20}_{-12}
208	0.423 ± 0.061	36^{+23}_{-11}

The results are still connected with considerable error bars. Combining the values obtained from the different nuclear targets we find for the inelastic ωN cross section

$$\sigma_{\omega N}^{\rm inel}(|\bar{\mathbf{q}}|) = (33 \pm 10) \text{ mb} \tag{9.31}$$

Here, the bar indicates an average over the complete ω momentum spectrum. From our transport simulations in the previous Section we have extracted the averaged ω momentum. We find $|\bar{\mathbf{q}}| = (885 \pm 11)$ MeV. The error emerges from the slightly different

momentum spectra for the different target nuclei. Due to Fermi motion, Pauli blocking and elastic scattering processes the momentum spectra slightly soften for heavier targets. Inserting these values into the defining equation for the inelastic $K-$factor (9.20) and using the parametrizations for the elastic and inelastic ωN cross section from Eqs. (9.1) and (9.2), we find from the Glauber analysis

$$K_{\rm inel} = 1.23\,. \tag{9.32}$$

This is in perfect agreement with our BUU results ($K_{\rm inel} = 1.25$). In Fig. 9.23 the cross section ratio $T_{A,12}$ as obtained from the Glauber analysis is shown. Thus, the experimental data on the transparency ratio for ω photoproduction off nuclei suggest an inelastic ωN cross section roughly 30% larger than the estimate obtained in [261] from an interpolation of microscopic results and a valence quark model. This can possibly be ascribed to an only insufficient description of the ωN scattering dynamics via the rather simple model constructed in [261]. On the other hand, the more sophisticated $K-$matrix analysis discussed in the previous Chapter yields a total ωN cross section which is comparable in size to the one from [261] (see Ref. [249]). Aside from the ωN vacuum interaction, the additional absorption strength needed could also indicate a breakdown of the low density theorem already at the rather moderate densities inside ordinary nuclei.

Momentum dependence In general, the nuclear transparency ratio and the cross section ratio $T_{A,B}$ depend on the ω three-momentum. This momentum dependence can be exploited in order to obtain information on the momentum dependence of the inelastic ωN cross section. This is demonstrated in Fig. 9.24 where the cross section ratio $T_{A,12}$ as function of the ω three-momentum is shown. The effective mass numbers have been calculated according to Eq. (9.29). As a showcase, we have assumed three different scenarios:

1. Constant inelastic cross section $\sigma = 33$ mb (dotted line). In this case also the ratio $T_{A,12}$ does not depend on the ω momentum as can be seen immediately from Eq. (9.29).

2. Constant collisional width in the ω rest frame $\Gamma_{\rm coll} = 100\ {\rm MeV} n_N/n_0$ (solid line). This is equivalent to a rising absorption probability for low ω momenta. Thus, the cross section ratio goes down for low momenta and rises for high momenta.

3. Cross section parametrization (9.2) with $K_{\rm inel} = 1.25$ (dashed line). This scenario interpolates between cases (1.) and (2.) since the inelastic cross section rises for low momenta and levels of for high ω momenta.

This opens a possibility to study the momentum dependence of the inelastic ωN cross section. In Fig. 9.24 in addition preliminary data points from [273] are shown. They tend to favor the scenario of a constant collisional width. Physically, this could be generated by a strong momentum dependence of the ωN total cross section or, alternatively, a breakdown of the low density theorem. In particular at low energies three-body processes could become important similar as in the case of pion propagation in matter, see for instance Chapter 3. One should also keep in mind, that for low ω momenta Fermi

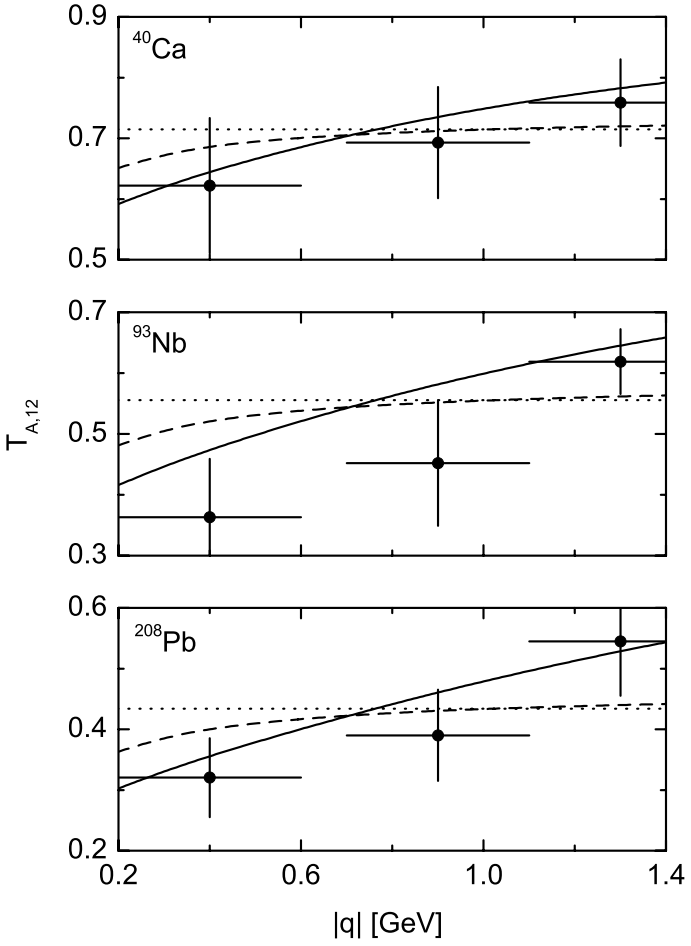

Figure 9.24: Cross section ratio $T_{A,12}$ for $A = 12, 93, 208$ as function of the ω three-momentum. Preliminary data from [273]. *Dotted line*: constant inelastic cross section, case (1.), *solid line*: constant inelastic width, case (2.), *dashed line*: cross section parametrization (9.2), case (3.).

motion and Pauli blocking can play a role. Moreover, the applied eikonal approximation is not valid for low ω energies. This, however, can be cured easily either by extending the simple Glauber formula (9.29) or by even using the coupled channel transport model. In addition, elastic scattering processes have to be considered here; they tend to reduce the high- and to enhance the low-momentum components of the ω momentum spectrum. Compare also to the discussion in Sec. 5.5.1 for the case of η photoproduction. These processes can not be treated within the Glauber approach. Qualitatively, the deviation of the data from the constant cross section scenario is expected to be even more substantial in nature due to the reshuffling of strength in the ω momentum spectrum.

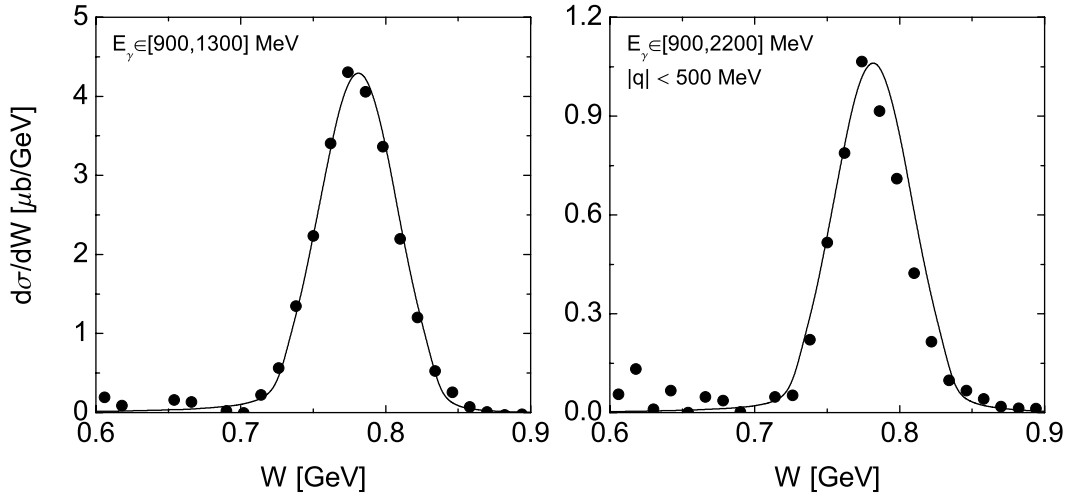

Figure 9.25: $\pi^0\gamma$ mass spectrum from proton target including a $\sim 1/E_\gamma$ weighting and a mass resolution of $\delta W = 55$ MeV. *Left*: $E_\gamma \in [900, 1300]$ MeV, *right*: $E_\gamma \in [900, 2200]$ MeV and $|\mathbf{q}| < 500$ MeV. Data from [19]. The data is normalized to the peak value of the calculated curve.

9.6 Differential cross sections

Now we investigate the $\pi^0\gamma$ mass distributions by means of our Monte Carlo model. Genuine sources of $\pi^0\gamma$ pairs in our calculations are the direct decay of the vector mesons $\omega \to \pi^0\gamma$ and $\rho \to \pi^0\gamma$. The $\rho \to \pi^0\gamma$ decay is suppressed by two orders of magnitude as compared to the ω decay and, thus, this component only marginally affects the spectra. For all our calculations from nuclear targets we now use the previously determined interaction strength according to Eq. (9.2) and (9.1) with $K_{\text{inel}} = 1.25$.

Experimentally the ^{1}H data serve as a reference measurement in order to verify any change of the ω line shape for nuclear targets. These data sets, shown in Fig. 9.25 for two different cuts on beam energy and ω momentum, are consistent with our calculations for proton targets. Including the Gaussian smearing according to Eq. (7.15) with $\delta W = 25$ MeV (corresponding to FWHM$\simeq$ 55 MeV) and a weighting $\sim 1/E_\gamma$ according to the bremsstrahlungs photon spectrum, the width of the mass distribution in the energy range $E_\gamma \in [900, 1300]$ MeV is reproduced with high precision whereas the experimental distribution in the energy range $E_\gamma \in [900, 2200]$ MeV with an upper cut on the ω three-momentum $|\mathbf{q}| < 500$ MeV exhibits a slightly smaller width. However, within the statistical uncertainty (error bars have not been given in [19]) the agreement is good and, thus, we will include the same resolution for all nuclear targets.

The left plot in Fig. 9.26 shows the $\pi^0\gamma$ mass distribution from proton and ^{40}Ca targets including all ordinary nuclear effects but no medium modifications of the ω meson. The ^{40}Ca curve has been divided by the nuclear mass number in order to allow the comparison of the normalization of both curves. Final state interactions yield a reduction of the total $\pi^0\gamma$ yield by more than a factor of two. The ω line shape is not affected by these trivial

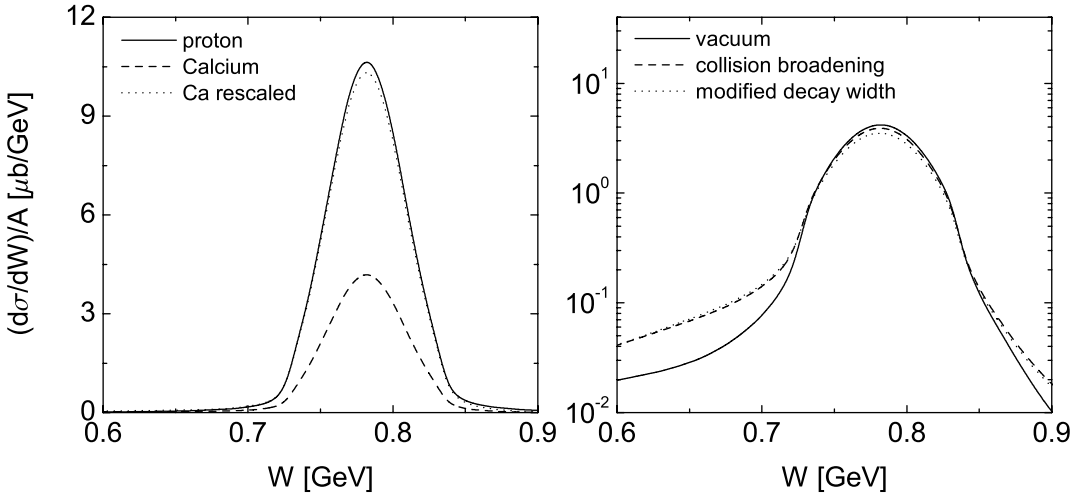

Figure 9.26: $\pi^0\gamma$ mass distribution from ^{1}H and ^{40}Ca targets in the energy range $E_\gamma \in [900, 2200]$ MeV. *Left*: proton target (*solid line*), ^{40}Ca target without medium modifications (*dashed line*), the same as before but scaled up to (almost) the proton curve (*dotted line*); *right*: ^{40}Ca target without medium modifications (*solid line*), with collisional broadening (*dashed line*), with collisional broadening and modified $\omega \to \rho\pi$ decay (*dotted line*).

final state effects. This is exactly what was expected since π^0 rescattering only marginally affects the $\pi^0\gamma$ mass spectrum in the mass range of the ω meson. The right panel of Fig. 9.26 shows the effect of collisional broadening of the ω (7.31) and the modified $\omega \to \rho\pi$ decay width (8.6) due to the in-medium changes of the ρ meson. Note, that here the spectrum is shown on a logarithmic scale. As discussed previously, the width of the ω peak does almost not increase when collisional broadening is included. Only the height of the peak and the tails of the $\pi^0\gamma$ spectrum are affected. The modified $\omega \to \rho\pi$ width also slightly reduces the total yield. This is due to the larger inelastic width of the ω in the medium, thus more ω mesons decay inside the target nucleus to unobserved final states. Again the spectral shape around the peak value is almost unaffected by this medium modification. Experimentally the observation of modifications of the tails of the mass distribution requires high statistics data that are not available at the time.

As discussed previously for the case of ϕ meson production in Chapter 7, the relative amount of in-medium decays in the data sample can be enhanced by gating on ω mesons with low momenta. These ω mesons travel shorter distances during their lifetimes and, thus, the probability that they decay inside the target nucleus is higher as compared to ω mesons with high momentum. This can be achieved either by restricting the beam energies to the near threshold region or by gating directly on the reconstructed ω three-momentum. In the experimental analysis [19] different scenarios have been considered:

- $E_\gamma \in [900, 1300]$ MeV
- $E_\gamma \in [900, 2200]$ MeV and $|\mathbf{q}| < 500$ MeV

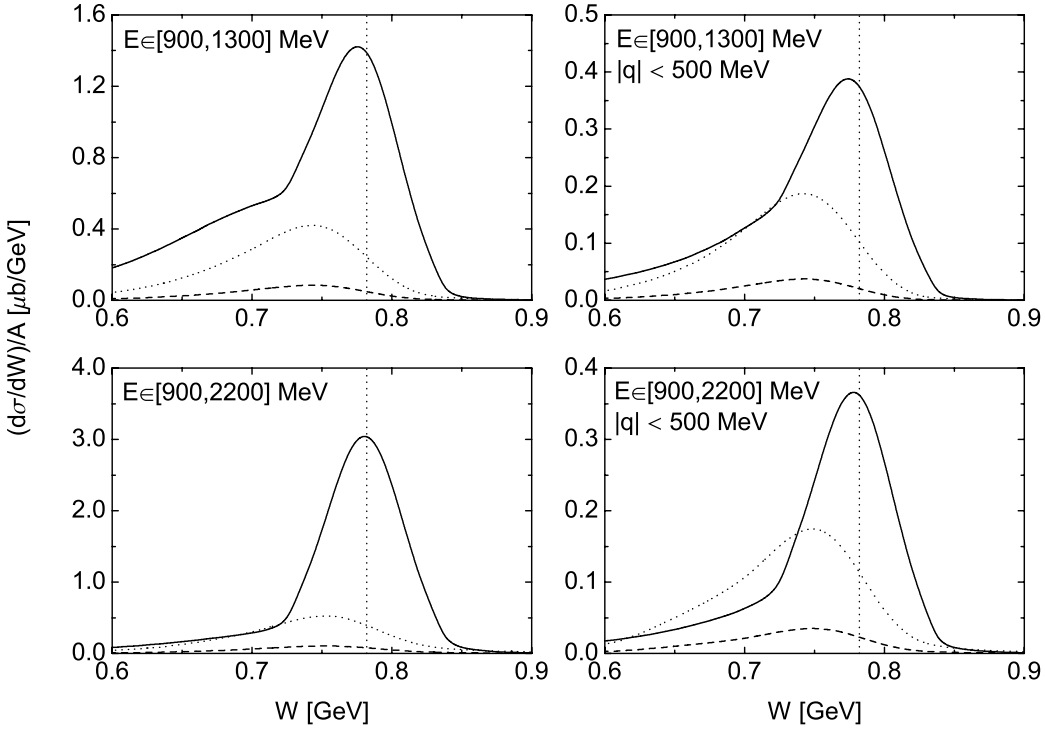

Figure 9.27: $\pi^0\gamma$ mass distributions for the Niobium target and different beam energy ranges. *Solid line*: total yield, *dashed line*: ω decays at $n_N/n_0 > 0.1$, *dotted line*: the same but multiplied with the artificial factor of 5 for visualization. The dotted vertical line indicates the physical ω mass.

- $E_\gamma \in [900, 1300]$ MeV and $|\mathbf{q}| < 500$ MeV
- $E_\gamma \in [900, 1300]$ MeV and $|\mathbf{q}| < 500$ MeV and $T_\pi > 150$ MeV.

In the last case in addition the kinetic energy cut with the aim to suppress the π^0 rescattering background has been applied. It has only little impact on the results since the rescattering background anyway is small in the studied $\pi^0\gamma$ mass interval [19]. This can be taken as indication that the observed effects are definitely not created by trivial FSI.

In Fig. 9.27 we show results of our BUU transport calculations applying the different possibilities to amplify the aimed at in-medium signal. To this end we have considered a medium sized Niobium target and have imposed the most substantial in-medium changes, namely collisional broadening according to Eq. (7.31) and a strongly attractive mass shift according to Eq. (9.3) with $\alpha = -0.16$. The medium modifications are most substantial in the case where the beam energy range is restricted to the near threshold region due to the previously discussed phasespace enhancement. Most of the ω mesons in the low mass tail do not even decay inside the nucleus. Nonetheless they are hindered to propagate to the free ω mass due to the too low total energy available. This effect is much smaller if the photon beam range is enlarged to $E_\gamma \in [900, 2200]$ MeV. Imposing an additional three-momentum cutoff the relative amount of ω decays inside the nucleus indeed rises as can

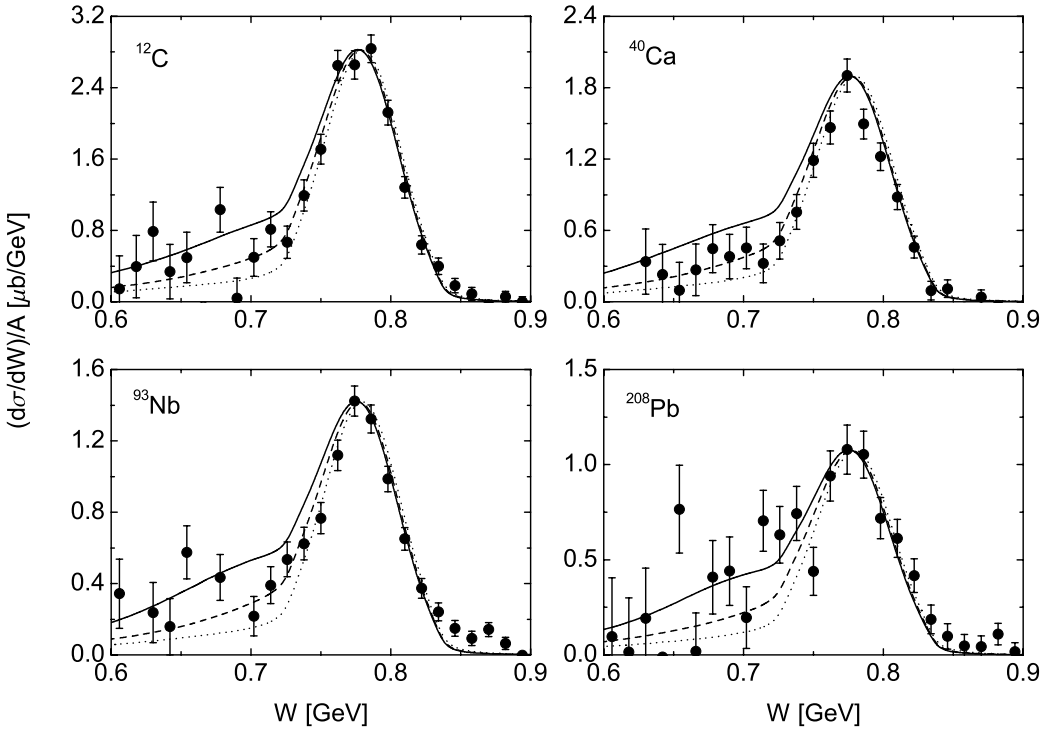

Figure 9.28: $\pi^0\gamma$ mass distributions for different targets in the photon energy range $E_\gamma \in [900, 1300]$ MeV. *Dotted line*: collisional broadening, *dashed line*: broadening and dropping mass with $\alpha = -0.08$, *solid line*: broadening and dropping mass with $\alpha = -0.16$. Data from [19]. The data and the dashed and dotted curves are normalized to the peak value of the solid curves.

be observed in Fig. 9.27 when going from the left to the right panels. This effect is more pronounced in case of the higher photon energies. The in-medium spectra are shifted to the low mass side and are substantially broadened as compared to the total distribution including a large component of ω mesons decaying in vacuum. The broadening is created not only by the collisional width but also by the attractive ω nucleus potential which has different values depending on the density that is integrated over to obtain the nuclear observables.

In the following we only study two of the above scenarios, namely the photon energy range close to threshold $E_\gamma \in [900, 1300]$ MeV without any three-momentum cutoff and the full energy interval $E_\gamma \in [900, 2200]$ MeV with a momentum cutoff of $|\mathbf{q}| < 500$ MeV. The experimental results from [19] corresponding to both scenarios are compared to our Monte Carlo results in Figs. 9.28 and 9.29. In all Figures three different curves corresponding to different scenarios of medium modifications of the ω meson are shown. Using different parameterizations for the real part of the ω nucleus potential one can hope to be able to judge if a particular situation is preferred by the experimental data. Since the data seem to suggest a downward shift of the in-medium ω mass we first consider the following cases:

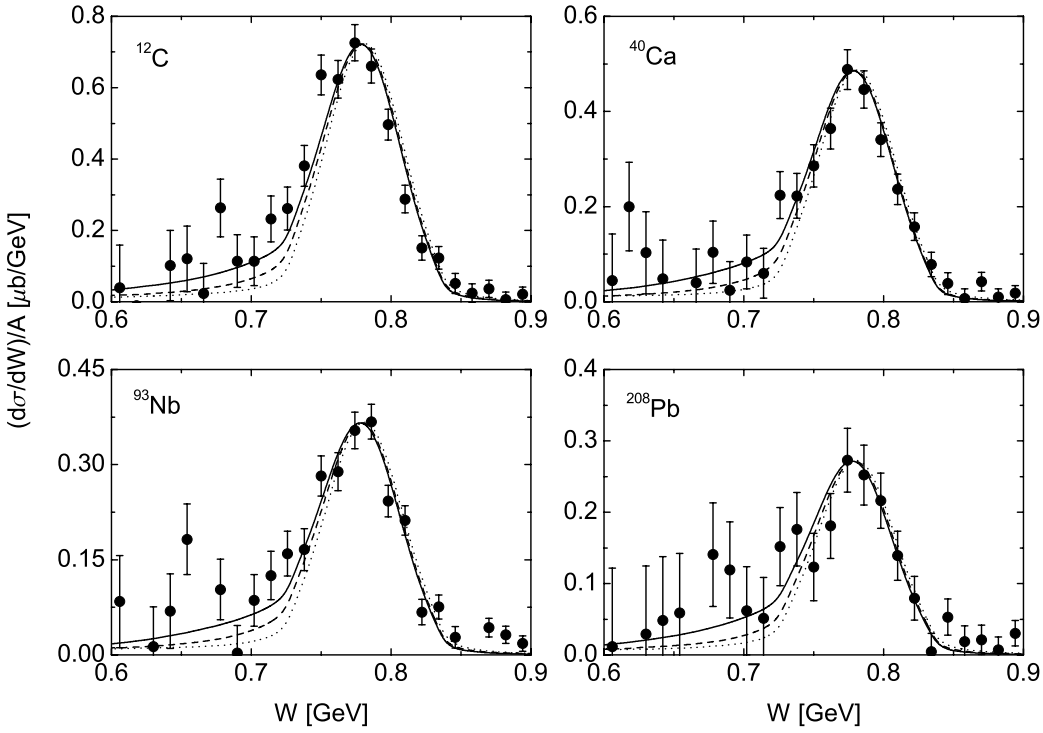

Figure 9.29: $\pi^0\gamma$ mass distributions for different targets in the photon energy range $E_\gamma \in [900, 2200]$ MeV with an upper cut on the ω three-momentum $|\mathbf{q}| < 500$ MeV. *Dotted line*: collisional broadening, *dashed line*: broadening and dropping mass with $\alpha = -0.08$, *solid line*: broadening and dropping mass with $\alpha = -0.16$. Data from [19]. The data and the dashed and dotted curves are normalized to the peak value of the solid curves.

(a) collisional broadening (7.31), no mass shift

(b) collisional broadening (7.31) and mass shift (9.3) with $\alpha = -0.08$

(c) collisional broadening (7.31) and mass shift (9.3) with $\alpha = -0.16$.

In all calculations we use the previously determined interaction strength with $K_{\rm inel} = 1.25$ in Eq. (9.20). Since the experimental data have been given without normalization, we chose their normalization in Figs. 9.28 and 9.29 such, that the peak values coincide with our calculations imposing the most attractive ω potential (scenario (c)). Furthermore, we also normalize our calculations using the parameter sets (a) and (b) in the same way in order to facilitate the comparison of the different calculations and the data.

In all cases spectral strength accumulates at the left hand side of the ω peak. This effect increases with the (input) mass shift parameter $\alpha = -(0...0.16)$. Theoretically the largest effects are observed in the case where the photon energy is limited to the near threshold region due to the previously discussed phasespace enhancement in the medium. If one enlarges the photon energy interval as done in Fig. 9.29 the relative importance of the phasespace enhancement decreases and, consequently, the observable effect is much

reduced. Experimentally the shifted strength seems to increase with increasing mass number. This $A-$dependence of the $\pi^0\gamma$ line shape is weaker in the theoretical curves. For the small nuclear targets ^{12}C and ^{40}Ca the calculation with $\alpha = -0.08$ seems to be favored by the data whereas for the heavy targets ^{93}Nb and ^{208}Pb a more drastic downward shift of the in-medium ω pole is needed. However, definite conclusions are hampered by the low statistics of the data. At this stage the following conclusions can be drawn: The experimental data indicate the accumulation of additional spectral strength at masses below the ω pole. This behavior cannot be reproduced by a broadening of the in-medium spectral function, even if the ω in-medium width becomes very large. Assuming a single peak structure of the ω in nuclear matter, an attractive mass shift of $(8-16)\%$ at normal nuclear matter density is needed to account for the accumulation of strength at low $\pi^0\gamma$ masses. Again we note, that all the above statements certainly depend on the experimental background subtraction. As long as this issue leaves room for experimental improvements, robust conclusions can hardly be drawn.

In Fig. 9.30 we compare our results to the data published earlier in [18]. Note, this data set slightly deviates from the one shown in Fig. 9.29 for the Niobium target. In the top the invariant mass differential cross sections normalized to the peak values, defined via

$$\frac{dN}{dW} = \left(\frac{d\sigma(W)}{dW}\right)\left(\frac{d\sigma(W_0)}{dW}\right)^{-1}_{\max} \tag{9.33}$$

are shown. The agreement of the calculations and the data is rather poor. Such a pronounced structure as seen experimentally can hardly be obtained with the scenarios of medium modifications considered here. Aside from the differential cross sections themeselves we illustrate the in-medium changes in two alternative ways. In the middle of Fig. 9.30 the difference of the cross sections from the Niobium and the proton target is shown, again for different assumptions on the ω in-medium changes. Before subtracting the cross sections they have been normalized to the same peak values. The lower panel shows the ratio of the same cross sections. In spite of the fact that the quantitative features of the measurement are not reproduced, it is quite astonishing that both the difference and the ratio of the cross sections possess the same qualitative properties as the data. This, however, is dominantly driven by the experimental mass resolution. As mentioned earlier, the CBELSA/TAPS mass resolution amounts to roughly FWHM= 55 MeV. Consequently, significant effects are only to be expected a certain distance in the order of 55 MeV away from the physical ω pole. The position of the observed effects in the difference and the ratio of the calculated cross sections shown in the lower panels of Fig. 9.30 are thus determined by the experimental resolution. Therefore the qualitative agreement is not necessarily generated by a correct description of the in-medium ω properties.

Concerning the comparison to the data from [18, 19] additional subtleties have to be considered carefully: The main in-medium effect in our calculations comes from the phasespace enhancement at the near and subthreshold energies treated in the present analysis, see Fig. 9.27 which shows the component of ω in-medium decays in the mass spectra. Thus, the results become sensitive to details of the ω production mechanism in the medium that are hardly assessable at all. A cleaner – albeit weaker – signal could be obtained by excluding such low photon energies in the data sample and gating

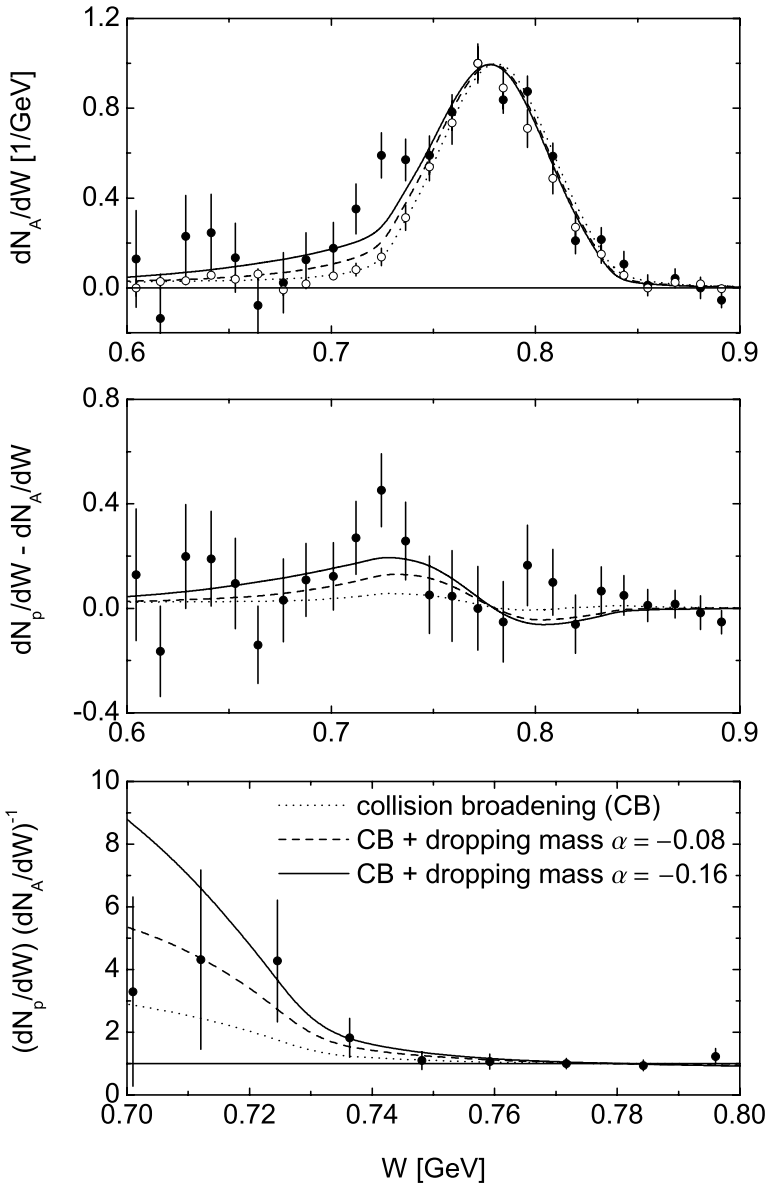

Figure 9.30: Results for the $\gamma\mathrm{Nb} \to \pi^0\gamma X$ and $\gamma p \to \pi^0\gamma X$ reactions in the photon energy interval $E_\gamma \in [900, 2200]$ MeV with an upper cut on the $\pi^0\gamma$ three-momentum $|\mathbf{q}| < 500$ MeV. Data from Ref. [18], *solid symbols*: Niobium target, *open symbols*: proton target. *Top*: invariant mass differential cross section normalized to the peak value, *middle*: difference of normalized cross sections from Niobium and proton, *bottom*: ratio of normalized cross sections from Niobium and proton. The various line styles correspond to different scenarios of medium modifications.

on small ω three-momenta. The assumption that the ω exhibits a one peak structure in the medium might most probably not be justified. In Refs. [174, 241, 249] sizable couplings of the ω to nucleon resonances have been found. We have demonstrated in the previous Chapter that such resonance-hole components can create additional peaks in the

ω in-medium spectral function. Whereas in principle resonance-hole excitations could produce such an effect as observed experimentally, in the actual analysis the positions of the additional peaks are found at much lower invariant mass. Since in addition the positions of resonance-hole components in the spectral function are almost independent of density, they can hardly affect the spectrum in the vicinity of the generic ω peak. Moreover, in the present study we have not included the energy variation of the ωN off-shell scattering amplitude. The ωN interaction strength can be much different for off-shell ω mesons as compared to ω mesons sitting on their mass shell. Further we note, that the interaction strength determined from the attenuation measurement is valid for ω momenta of around 900 MeV whereas the $\pi^0\gamma$ mass spectrum is sensitive only to the low momentum part of the in-medium ω spectrum. Thus, the results also depend on the extrapolation of the interaction strength to low ω momenta which in the present study was done only in a phenomenological way.

9.7 Experiment versus microscopic calculations

In this final Section we want to comment on a confrontation of our results for the ω in-medium spectral function obtained from the microscopic calculation presented in the previous Chapter and the experimental results discussed here. First we note that a consistent implementation of the microscopically calculated ω spectral function and self energy into the transport model is numerically expensive and cannot be done without approximations. However, the gross features of the theoretical results obtained from the $K-$matrix coupled channel calculation can be summarized in compact form: the peak of the ω spectral distribution moves slightly upwards in energy whereas the broadening becomes quite substantial already at normal nuclear matter density. At zero three-momentum the on-shell width of the ω amounts to roughly 60 MeV which is in agreement to the experimentally determined width extrapolated to small three-momenta of roughly 50 MeV at nuclear saturation density. In addition, our theoretical model produces rather weak low-lying resonance-hole components in the ω spectrum. The consistency of the experimentally observed spectral enhancement below the physical ω mass and the results of the coupled channel calculation is thus questionable.

In order to examine the compatibility of the data with a weak repulsive mass shift we show in Fig. 9.31 results for the $\pi^0\gamma$ mass spectrum from a transport simulation without any mass shift and a small upwards shift of the ω mass according to Eq. (9.3) with $\alpha = 0.04$. Collisional broadening is included in both cases according to Eq. (7.31) and using the experimentally determined interaction strength $K_{\rm inel} = 1.25$. This is roughly in agreement with the ω width predicted from the $K-$matrix calculation. On the high mass edge of the ω peak the consensus of the data and our Monte Carlo calculation is not spoiled by the small attractive mass shift. The only visible effect on the linear scale is a slight reduction of the total cross section which is due to phasespace suppression. Both the smallness of the upwards shift and the missing phasespace enhancement substantially reduce the sensitivity of the $\pi^0\gamma$ spectrum to this in-medium change. Consequently, the data do not rule out the small repulsive shift of the genuine ω peak which is found in our microscopic $K-$matrix calculations.

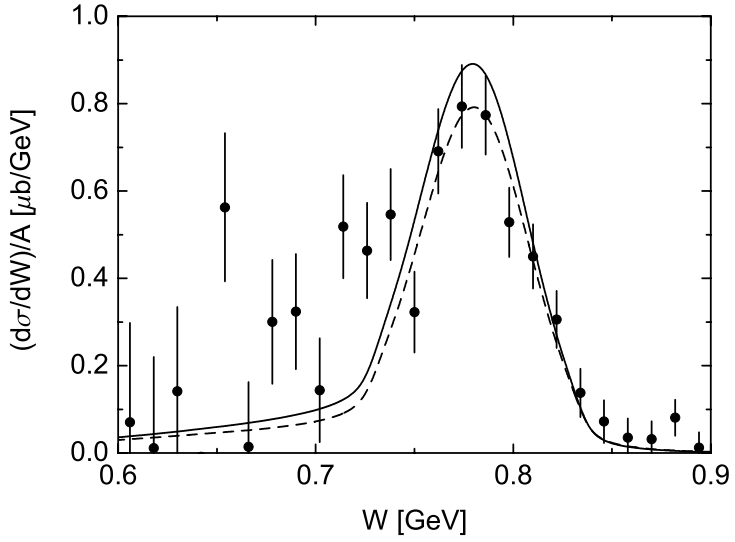

Figure 9.31: $\pi^0\gamma$ mass distributions for the Niobium target in the photon energy range $E_\gamma \in [900, 1300]$ MeV. *Solid line*: collisional broadening, no mass shift, *dashed line*: collisional broadening and repulsive mass shift according to Eq. (9.3) with $\alpha = 0.04$. The data is freely normalized.

The situation is different for the mass range below the ω peak. The question arises if such weak resonance-hole components as obtained theoretically can account for the experimentally observed low-mass enhancement. We note, however, that the observed mass spectrum cannot be compared directly to the spectral function calculated here since the experimental results represent a product of the spectral function with the branching ratio into the $\pi^0\gamma$ channel. The dominant vacuum decay branch $\omega \to \rho\pi$ increases with mass whereas that for the $\pi^0\gamma$ decay is much flatter as a function of the ω mass, see Fig. 8.1. In addition, the in-medium contributions to the total width have to be considered in order to obtain the relevant branching ratios. This effect has not been taken into account in the experimental analysis of the CBELSA/TAPS results. On the other hand, it is automatically contained in our BUU transport simulations. This issue is discussed in Appendix A.4. Moreover, the branching ratio is also sensitive to the ρ meson properties as discussed earlier in Section 9.3. We also note that the effect observed experimentally obviously depends on the background subtraction, see also [259].

In Fig. 9.32 the vacuum and in-medium branching ratios of the ω to the $\pi^0\gamma$ final state are shown. The in-medium curves are calculated with the ω in-medium self energy from our microscopic coupled channel calculation, presented in detail in Chapter 8, evaluated at zero three-momentum. The branching ratio is given by

$$BR_{\rm med}(\omega \to \pi^0\gamma) = \frac{\Gamma_{\omega\to\pi\gamma}(W)}{\Gamma_{\rm vac}(W) + \Gamma_{\rm coll}(W, |\mathbf{q}| = 0)} \tag{9.34}$$

where $\Gamma_{\rm vac}$ is the total spontaneous ω decay width to vacuum decay channels (2π, 3π, $\pi^0\gamma$) and $\Gamma_{\rm coll} = -\mathcal{I}{\rm m}\Pi_{\rm med}(W, |\mathbf{q}| = 0)/W$ is the in-medium contribution which arises

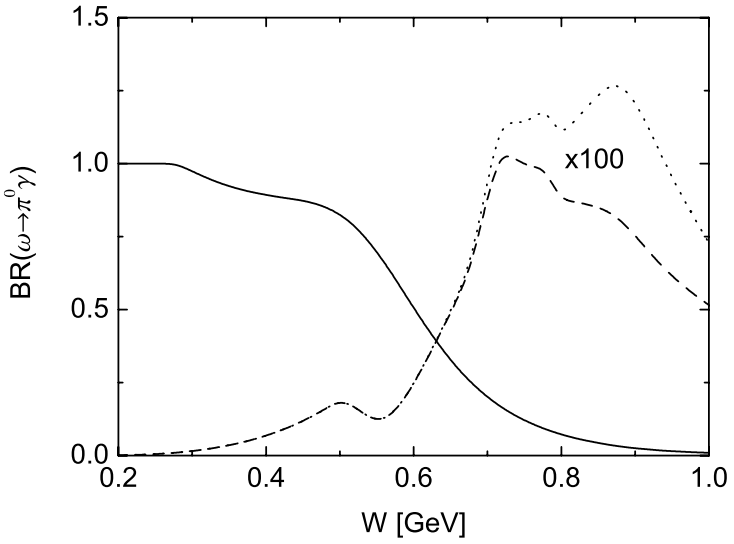

Figure 9.32: In-medium branching ratio $\omega \to \pi^0\gamma$ at $|\mathbf{q}| = 0$. *Solid line*: vacuum branching ratio, *dotted line (÷100)*: in-medium branching ratio calculated with vacuum ρ properties, *dashed line (÷100)*: in-medium branching ratio with in-medium ρ properties.

through ωN collisions. In addition, one curve is shown which includes also medium modifications of the ρ meson properties as introduced in Section 9.3, i. e. collisional broadening ($\Gamma_{\rm coll}(n_0) = 100$ MeV) and a strongly attractive mass shift similar to Eq. (9.3) with $\alpha_\rho = -0.16$. The vacuum and in-medium curves show an almost opposite energy dependence. This general trend of the in-medium curves was already observed in Section 9.3.1 where we used a phenomenological parametrization of the ω collision width independent of the ω invariant mass. Here, the structures of the in-medium branching ratios are generated by various resonance-hole components in the self energy which are strongly energy dependent. Note, that the in-medium branching ratio is about two orders of magnitude smaller than the vacuum one. This is due to the additional in-medium decay channels of the ω into resonance-hole states. In particular the opening of the $\rho\pi$ phasespace at low energies is not visible in the in-medium curves. This has to be ascribed to the fact that the in-medium width at low energies is dominated by nuclear decay channels including nucleon-hole configurations such as $\omega \to \pi N h$. At low energies these contributions are orders of magnitude larger than the spontaneous decay widths, thus the energy dependencies of the latter ones are not relevant for the in-medium branching ratio. The dropping ρ mass in the medium has the consequence that the $\omega \to \rho\pi$ width rises more quickly with energy. Thus, even more ω mesons decay to this channel reducing the flux going into the $\pi^0\gamma$ final state. Accordingly, the $\pi^0\gamma$ decay branching ratio goes down when the $\rho\pi$ threshold is lowered.

To get a more quantitative feeling of how the resonance-hole strength affects the $\pi^0\gamma$ mass spectrum, we calculate the $\pi^0\gamma$ rate in nuclear matter. Using vector meson dominance the four-fold momentum differential $\pi^0\gamma$ rate can be related to the isospin-0 current-current correlator. The current-current correlator can in turn be rewritten in terms of

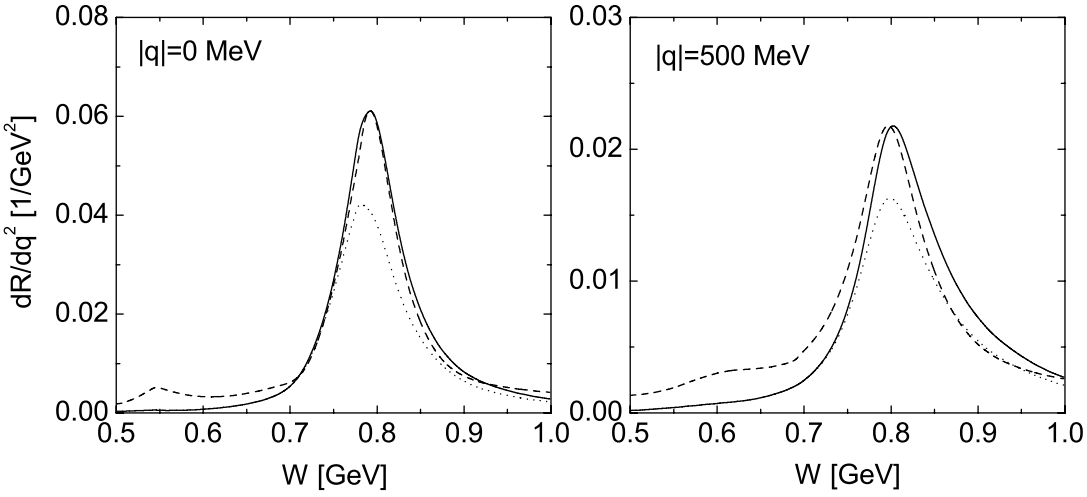

Figure 9.33: Differential $\pi^0\gamma$ production rate at $n_N = n_0$. *Solid line*: $\pi^0\gamma$ rate with vacuum ρ properties, *dashed line*: ω spectral function (renormalized), *dotted line*: $\pi^0\gamma$ rate at $n_N = n_0$ with modified ρ properties, see text for details.

the transverse and longitudinal components of the ω spectral function. One obtains

$$\frac{dR_{\pi\gamma}}{dq^2}(q) \sim \left[\frac{1}{3}\mathcal{A}_\omega^L(q_0,\mathbf{q}) + \frac{2}{3}\mathcal{A}_\omega^T(q_0,\mathbf{q})\right] \frac{\Gamma_{\omega\to\pi\gamma}(q)}{\Gamma_{\rm tot}(q)} \tag{9.35}$$

with the partial and total ω widths $\Gamma_{\omega\to\pi\gamma}$ and $\Gamma_{\rm tot}$ whose quotient forms the (in-medium) branching ratio discussed previously; q is the ω four-momentum with $q^2 = W^2$. Note, that Eq. (9.35) in particular applies to nuclear reactions with elementary projectiles. In this case the population processes are (at least roughly) known and are – at sufficiently low energies – dominated by one exclusive channel (γNh, πNh, ...). This is in contrast to heavy-ion reactions where the $\pi^0\gamma$ final state can be radiated from a thermal ω meson gas. In this case the population probability is again proportional to the – via the inverse decay processes – total ω width $\Gamma_{\rm tot}$ which, thus, cancels with the width in the denominator of Eq. (9.35).

In Fig. 9.33 we present results for the $\pi^0\gamma$ rates according to (9.35) at normal nuclear matter density using the spectral function obtained in the $K-$matrix framework and the in-medium branching ratio shown in Fig. 9.32. Whereas the spectral function shows some enhancement at low energies due to the resonance-hole components, the $\pi^0\gamma$ rate shows a much smoother behavior. This is due to the fact that the imaginary part of the in-medium self energy in the numerator of the spectral function cancels with the total (in-medium) width in the denominator by multiplication with the branching ratio. For large three-momenta the production rate is shifted towards high energies as compared to the spectral function. This comes because the (in-medium) branching ratio increases with the invariant mass, see Fig. 9.32. If the mass of the ρ meson drops in the medium more of the ω flux goes into the $\rho\pi$ channel. Consequently, the $\pi^0\gamma$ channel is depleted for energies above the $\rho\pi$ threshold.

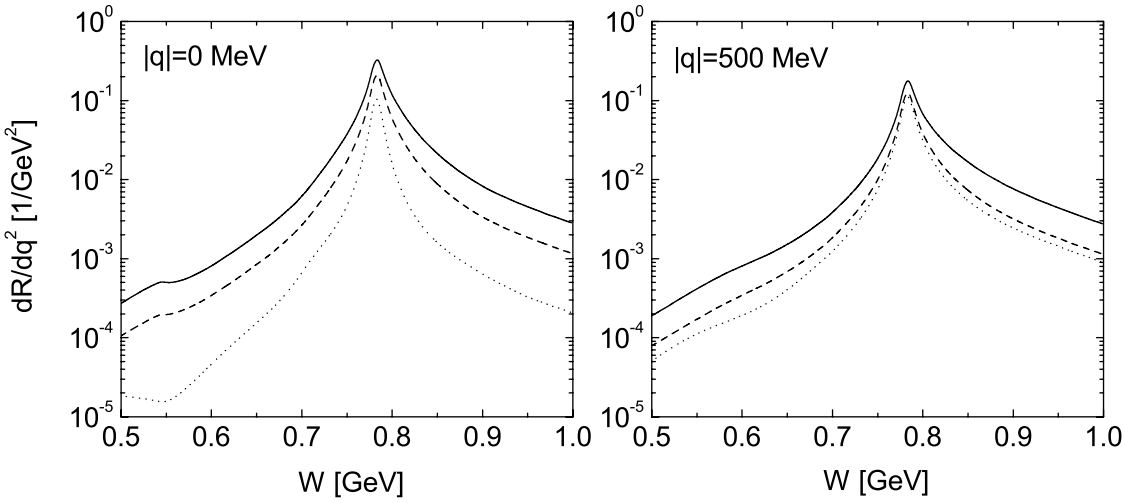

Figure 9.34: Differential $\pi^0\gamma$ production rate convoluted with Woods-Saxon density profile (^{40}Ca). *Solid line*: without absorption, *dashed line*: with ω absorption according to Eq. (9.36) and constant cross section, *dotted line*: with ω absorption according to (off-shell) self energy.

In order to come closer to experimental observables the $\pi^0\gamma$ rate has to be convoluted with the nuclear density profile. This is shown in Fig. 9.34 again for two different three-momenta imposing vacuum ρ meson properties. Employing the semi-analytical Glauber model (Appendix B) it is now straightforward to also include ω absorption. From the single meson production cross section (B.10) we obtain for the differential $\pi^0\gamma$ rate

$$\frac{d\mathcal{R}_{\pi\gamma}}{dq^2} \sim \int d^3r\, n_N(\mathbf{r}) \left[\frac{1}{3}\mathcal{A}_\omega^L(q_0,\mathbf{q}) + \frac{2}{3}\mathcal{A}_\omega^T(q_0,\mathbf{q})\right] \frac{\Gamma_{\omega\to\pi\gamma}(q)}{\Gamma_{\rm tot}(q)} \exp\left[\int_z^\infty dz' P(z')\right] \tag{9.36}$$

where $P(z)$ is the probability of absorption per unit length. Here, we use two different approaches for $P(z)$: first, we use a constant ω absorption cross section

$$P(z) = -\sigma_{\omega N} n_N(\mathbf{b}, z) \tag{9.37}$$

with $\sigma_{\omega N} = 33$ mb which has been extracted from the nuclear transparency measurement. This recipe relies on the low density theorem. Second, we use the complete (off-shell) self energy of the ω determined from the coupled channel analysis

$$P(z) = \frac{1}{|\mathbf{q}|}\mathcal{I}\mathrm{m}\Pi_\omega(q_0, \mathbf{q}, n_N(\mathbf{b}, z)) \tag{9.38}$$

which, at least in principle could include effects going beyond the two-body collisions contained in $\sigma_{\omega N}$. Results using both recipes are shown in Fig. (9.34). Inserting the constant ω absorption cross section the overall normalization of the curve is reduced whereas its shape is only slightly affected. This is clear because all regions of the spectrum are attenuated equally. Nevertheless a slight change in the spectral shape can be observed

due to the suppression of contributions from high densities where also the absorption probability becomes large. Using the total off-shell self energy of the ω in the exponential of Eq. (9.36) the various components of the spectral function are absorbed differently according to the energy variation of the self energy. This becomes apparent particularly in the upper plot of Fig. 9.34 where at low energies the $S_{11}(1535)$ resonance-hole component in the ω spectral function is visible. Since for this particular combination of $(q_0, \mathbf{q})$ the self energy has a maximum, also the absorption probability becomes very large. Consequently, the observable $\pi^0\gamma$ spectrum shows a depletion rather than a peak due to the resonance-hole excitation. Note, however, that in Eq. (9.38) we have assumed that the total self energy is due to ω absorption processes. Since generally this assumption is not realized in nature, the effect of absorption will be smaller in reality whereas the qualitative features of our considerations hold.

This situation shows that such an effect as observed experimentally can only hardly be generated by low-lying resonance-hole excitations that leave the position of the generic ω peak almost untouched. Much more substantial in-medium effects than those obtained in the present analysis are needed in order to explain the low-mass enhancement in the CBELSA/TAPS data. Due to the still evolving experimental situation as far as the ω coupling to nucleon resonances is concerned in particular the real part of the ω self energy still is associated with large error bars. High statistics data at photon energies clearly above threshold are needed to investigate the nature of the ω in-medium changes. On the other hand, both experiment and theory roughly agree on the in-medium broadening of the ω meson. The data points above the physical ω mass do not contradict the small repulsive mass shift of the generic ω peak found theoretically. In summary, we state that – provided the data is confirmed – there exists a distinct discrepancy between the ω properties suggested by elementary scattering data and the ω in-medium properties consistent with the $\pi^0\gamma$ photoproduction data. This contradiction has to be resolved in future investigations.

Chapter 10

Summary

In this work we have studied the properties of mesons inside a medium of strongly interacting matter. This was motivated by the expectation to learn about the interactions of these particles with nuclear matter on one hand and the close relation to the onset of chiral symmetry restoration in nuclei on the other hand. To this end we have approached the issue of in-medium changes from two different viewpoints: One approach was the microscopic calculation of in-medium spectral functions using our knowledge on elementary meson nucleon interactions. Whereas the level of sophistication of this type of model can be very high, the actual comparison to experimental data often is difficult and, thus, conclusions remain controversial. Alternatively, we have calculated observables in nuclear reactions and, in particular, have studied their sensitivity to the in-medium changes of meson properties. Moreover, we have investigated carefully the origin of experimentally observed effects regarding traditional nuclear effects such as Fermi motion and final state interactions or modifications of in-medium particle properties related for instance to changes of quark and gluon condensates.

Chiral symmetry is an approximate symmetry of the QCD Lagrangian in the sector of the light quarks. Unlike the Lagrangian the QCD ground state does not show this symmetry which is known as its spontaneous breakdown in vacuum. This is strongly suggested by the non-existence of parity duplets in the hadron spectrum, hadrons with equal mass and spin but opposite parity. As a consequence of the spontaneous symmetry breaking a massless mode appears which in the flavor SU(2) sector is to be identified with the pion isospin triplet. The only candidate to be the parity partner of the pion is the scalar σ meson that in vacuum is observed at most as a broad resonant structure in the two pion channel with its width being almost as large as its mass of roughly $m_\sigma \approx 500$ MeV. Due to partial symmetry restoration the σ properties are expected to change inside nuclear media. In Section 2.4 we have demonstrated that these changes and, thus, the onset of chiral symmetry restoration at moderate densities, are dominantly driven by the pion nucleon interaction. Due to the suppression of the two pion phasespace the σ spectrum develops a pronounced peak in the medium close to the $\pi\pi$ threshold. This enhancement as compared to the vacuum situation can at least in principle be observed in $\pi\pi$ production experiments inside nuclear targets. However, the pion nucleon interaction as well gives rise to traditional incoherent final state interactions of the outgoing pions which, consequently, can also generate observable effects in the $\pi\pi$ spectra.

Modifications of hadron properties at finite nuclear densities are most effectively studied in nuclear production experiments using elementary projectiles. Only then the nuclear

background is close to its equilibrium state which is an extremely useful basis for a theoretical treatment. Also the possibility to disentangle particular effects is easier in this case as only the impact of finite densities is encountered in contrast to heavy ion experiments where new states of matter are produced and particle properties at various temperatures are probed. In this respect, in particular electromagnetic projectiles are to be preferred as they illuminate the entire target almost homogeneously which is an advantage regarding the observation of density dependent effects. However, still the observables in nuclear production experiments contain various effects of the medium that can hamper the observation of generic particle properties. These are for instance Fermi motion, Pauli blocking, nuclear mean field potentials and final state interactions. The only means to study these effects in an at least semi quantitative way in intermediate and high energy photon and hadron induced nuclear reactions is semi classical transport theory. Transport models provide a transparent and intuitive interpretation of nuclear reactions and, consequently, allow to trace back observable effects to particular nuclear mechanisms or in-medium changes. In the present work we prefer the former over the latter ones as their existence is well established and, hence, their impact is non-negligible. Only after having ruled out the creation of the observable signals by such well-established effects we have introduced medium modifications in order to be able to explain the experimental data.

With this aim nuclear $\pi\pi$ production with low energy photons has been studied in Chapter 3. Whereas in principle questionable, the application of our transport model to such low energy pions has been tested and validated by the comparison of mean free path calculations to quantum mechanical results and the reproduction of nuclear pion absorption data. Experimentally an enhancement close to the 2π threshold has been found in the $\gamma \rightarrow \pi^0\pi^0$ channel but not in the $\pi^0\pi^\pm$ channel which has been interpreted as an indication for the renormalization of the σ mode generated by the presence of the medium [31]. In the present study, however, we have let the elementary production amplitudes untouched, thus maintaining the σ vacuum properties. In contrast, we have taken into account the full final state interactions of the outgoing pions. To this end we have compared two quite different means to implement the pion final state interaction, namely the pion optical potential calculated microscopically using many-body techniques and, in the spirit of classical transport theory, vacuum pion nucleon cross sections fitted to experimental data. Whereas quite different in size, the qualitative features of the differential cross sections came out very similar using both recipes. Driven by quasi elastic and charge exchange pion nucleon collisions a redshift of the two pion mass spectra has been found that becomes more sizable for heavy nuclear targets. Whereas the overall normalization of the cross sections in some cases disagrees with the experimental data, the shapes of the differential distributions are qualitatively well reproduced. The apparently different absorption of pions in the $\gamma \rightarrow \pi^0\pi^\pm$ channel as compared to the $\gamma \rightarrow \pi^0\pi^0$ channel is still an unsolved problem both from the experimental and theoretical point of view. However, our explanation of the observed downward shift of the invariant mass spectrum follows completely well established nuclear physics effects, that, even if a complete understanding of $\pi\pi$ photoproduction off complex nuclei is not yet possible, have to be accounted for in any serious calculation. We therefore conclude that, given our present understanding, the observed target mass dependence of the $\pi^0\pi^0$ mass spectrum does not provide an unmistakable evidence for the modification of the $\pi\pi$ interaction or,

respectively, the properties of the σ meson at finite nuclear densities.

In order to test the persistence of our results from photon nucleus reactions we have calculated pion induced double pion production in nuclei in Chapter 4. Also the pion nucleus data show a serious enhancement close to the 2π threshold in the $\pi^+ \to \pi^+\pi^-$ reaction but not in the $\pi^+ \to \pi^+\pi^+$ one that has been interpreted earlier along the very same lines as in the photon induced case [29, 30]. In a different experiment the $\pi^- \to \pi^0\pi^0$ channel has been measured that does not exhibit a strong enhancement at threshold but nevertheless shows a nuclear mass number dependence [54]. In particular the calculation of differential cross sections in nuclear reactions requires some knowledge on the elementary multi-differential distributions which serve as input to our incoherent transport calculations. To this end we have constructed the $\pi N \to \pi\pi N$ transition amplitude in a tree-level isobar model including $\pi(138)$, $\rho(770)$, $N(938)$, $\Delta(1232)$ and $N^*(1440)$ intermediate states. This model has been tested in elementary collisions as well as against Deuterium data using a simple spectator model. In both cases the level of agreement was high recalling that no parameters had been fitted to the data. Going to heavier nuclear targets we have again found a softening of strength in the $\pi\pi$ spectra generated by Fermi motion, the electromagnetic potential and, in particular, quasi elastic and charge exchange πN collisions. The collisions strongly modify the phasespace distributions of the pions in the $\pi^+\pi^-$ channel but only moderately in the $\pi^+\pi^+$ channel. This is due to the strong anisotropy of the initial distribution in the $\pi^+\pi^-$ channel and the almost homogeneous filling of the allowed phasespace area in the $\pi^+\pi^+$ channel. These results are qualitatively in agreement with experiment. Albeit smoother the mass number dependence in the $\pi^- \to \pi^0\pi^0$ reaction could not be obtained correctly using the $\pi \to \pi\pi$ isobar model as input to BUU simulations. In this channel the nuclear cross sections are rather reproduced using isotropic phasespace distributions as input. Taking the data as well as the isobar model for granted, this situation indeed seems to point into the direction of a serious in-medium change of the $(\pi, \pi\pi)$ transition amplitude.

Motivated by recent measurements [37, 152, 157], photoproduction of η mesons off complex nuclei has been investigated in Chapter 5. This was mainly driven by the expectation to obtain information on the η nucleus final state interaction and the in-medium properties of the $S_{11}(1535)$ resonance whose excitation saturates the $\gamma N \to \eta N$ cross section at low photon energies. Calculations of η photoproduction off Deuterium show that the data require a strong resonance coupling in the $\gamma n \to \eta n$ reaction channel at energies of $\sqrt{s} \simeq 1.7$ GeV which is not present in the $\gamma p \to \eta p$ channel. On the other hand, our calculations also require the cross section for the inclusive production channel $\gamma n \to \eta\Delta^0$ on neutrons to be roughly zero in order to not overestimate the total η yield. This is in contrast to the $\gamma p \to \eta\Delta^+$ reaction which has been determined experimentally [164] and has a sizable cross section. Moreover, an additional contribution to the η excitation function from Deuterium not seen from proton targets is needed in order to reproduce the data at intermediate energies $E = (1 - 1.3)$ GeV. From the differential η production data off nuclei the total ηN cross section has been extracted. This was done by means of the Glauber formalism. The total ηN cross section was found to amount to about 30 mb at η kinetic energies of 300 MeV and to drop smoothly to about 10 mb at kinetic energies of 1.2 GeV. The total and elastic ηN cross sections obtained in the coupled channel framework [170] have proven to yield reasonable results for both the total and differential η photoproduction cross sections when implemented into the semiclassical

BUU model. Consistent with the calculations presented earlier in [149], we found no sensitivity of the observables to an in-medium broadening of the $S_{11}(1535)$ resonance. The slight shift and broadening of the resonance structure as seen in the η excitation function off nuclei is created exclusively by Fermi motion and the energy dependence of the η absorption cross section. Also the real part of the η nucleus potential as calculated in [66, 70] has only very little impact on the η photoproduction reaction off nuclei.

The second part of this work has been devoted to the properties of the light neutral vector mesons. They are of special interest as their coupling to dilepton pairs opens a unique possibility to learn about their in-medium spectral distributions. However, even if the lepton spectra are not distorted by final state interactions, their differential distributions do not directly resemble the vector meson spectral functions. In fact, the partial decay widths of the vector mesons to the dilepton channel strongly modify these spectra, an issue that has to be accounted for carefully in all analysis. In spite of the various background sources and the electromagnetic nuclear potential even in photon nucleus reactions substantial effects can be expected if the properties of the vector mesons change in the medium. These in-medium changes are related to modifications of various quark and gluon condensates in the strongly interacting environment. This issue is most effectively addressed with the QCD sum rule approach. Due to the onset of chiral symmetry restoration at finite baryon density the scalar quark condensate, that serves as an order parameter for the symmetry breaking, substantially drops already in ordinary nuclei; an effect that gives rise to observable modifications of the vector meson in-medium spectral functions.

In Chapter 7 nuclear ϕ meson photoproduction related to different possibilities to learn about its in-medium changes has been studied. From very simple arguments such as the extremely small cross section, the low fraction of in-medium decays and the distortion of the events generated by the electromagnetic potential it is clear that no valuable information can be obtained from kaon-antikaon invariant mass measurements. A second more promising observable is the nuclear transparency ratio that is related to the inelastic vector meson nucleon cross section. By and large we find that the observed attenuation of the ϕ meson yield from finite nuclei [213] can not be explained by standard nuclear effects. Also the nuclear kaon mean field potentials that tend to reduce the nuclear cross sections are not sufficient to reproduce the experimental data. Considering all additional medium effects as being due to ϕ meson absorption, we found that a value of $\sigma_{\rm tot} \simeq 27$ mb is needed to obtain agreement with the data. This value is substantially larger than usual quark model estimates for the ϕN cross section in vacuum. The nuclear transparency ratio and the $A-$dependence of the total yield can be reproduced with high accuracy by adopting this value for the ϕN cross section and including a proper relativistic treatment of the kaon potentials in our BUU simulations. Uncertainties arise from the fact, that in principle not only the ϕ absorption process but also its decay width, the kaon final state interactions and the initial production cross sections could experience modifications in the medium. We, therefore, conclude that all nuclear effects as well as the kaon renormalization in the medium have to be considered carefully when the attempt is made to learn about the ϕ in-medium properties whereas the information that can be obtained is limited due to the large number of unknown parameters involved. The measurement [213] at least gives a hint towards the direction of additional in-medium modifications as

even thoroughly performed simulations using vacuum properties as input are not able to reproduce the magnitude of the observed attenuation effect.

In Chapter 8 we have calculated the ω meson spectral function at finite nuclear density and zero temperature in a microscopic framework using the low density theorem. The ωN forward scattering amplitude was constructed within a unitary coupled-channel effective Lagrangian model previously applied to the analysis of pion and photon induced reactions on the nucleon. The resulting amplitude was taken from the updated solution of the coupled channel problem in the energy region $\sqrt{s} \leq 2$ GeV [249]. To obtain the spectral function of the ω meson we have extended this approach to allow for arbitrary masses and three momenta of the asymptotic ω meson while the intermediate ω and all other mesons maintain their vacuum properties. This is in line with the low density approximation. As a general outcome of our investigations we found that coupled channel effects and resonance contributions play an important role and cannot be neglected when one aims at a reliable calculation of the ω in-medium properties. At normal nuclear density and zero ω momentum we found a significant broadening of about 60 MeV of the ω spectral function but only a small upwards shift of the ω peak relative to the physical ω mass. Furthermore, our results suggest an explicitly different momentum dependence of the transversal and longitudinal modes of the in-medium ω meson. The question of an in-medium mass shift remains to some extent an open issue due to the $2\pi N$ state that in [237] has been found to be responsible for a strong attractive mass shift. Unfortunately up to the present three-body states cannot be treated in a rigorous way within coupled channel rescattering models.

The experimental results presented in [18, 19] provide a unique source of information on the production of ω mesons in a nuclear medium. Both the $\pi^0\gamma$ invariant mass spectrum and the nuclear transparency ratio have been measured with the aim to learn about the ω in-medium properties. Whereas in principle valuable, the experimental information obtained from the $\pi^0\gamma$ invariant mass is limited due to statistical uncertainties and ambiguities concerning the background subtraction. Final state interactions of the outgoing pion do not hamper the observation of the spectral shape in the ω channel and can even be suppressed additionally by an appropriate kinematical cut. Medium modifications of the ω are significant on a level that cannot be obtained with present experiments or, in turn, induce effects on the production mechanism which cannot be controlled theoretically in a well-defined way. By and large the results seem to indicate a substantial downward shift of the in-medium ω mass, however, again assuming the background subtracted data to be correct. In contrast, a dispersion analysis of the ωN forward scattering amplitude rather suggests an unshifted or even slightly upwards shifted ω mass in the range of finite three momenta that are tested experimentally. The nuclear transparency ratio, however, is less sensitive to the experimental background subtraction and details of the theoretical treatment. Both calculations using again the transport approach and employing the semi analytical Glauber model suggest an inelastic ωN cross section of $\sigma \simeq 32$ mb which is roughly 30% larger than hitherto used estimates. Apart from an insufficent understanding of the ωN dynamics this could also indicate a breakdown of the low density theorem for the ω meson at the rather moderate densities inside common nuclei. However, similar as in the case of the ϕ meson uncertainties arise through possible in-medium changes of the production amplitude. Using measurements of the momentum differential cross section in principle also an extraction of the momentum

dependence of the in-medium ωN cross section is possible. The obvious contradiction of these results and the microscopic determination of the ω spectral function concerning an in-medium shift of the ω mass is a standing problem which asks for further experimental and theoretical investigations.

Finally, we want to discuss some improvements and possible extensions of our studies. Again we start with some issues related to double pion production in nuclei. Concerning the controversial situation in the case of photon induced double pion production it would be desirable to improve our understanding of the dynamics of low energy pions in nuclear matter. The observables have proven to be particularly sensitive to the Δ self energy in the medium. Consequently, it would be helpful to find further observables that could constrain this quantity. In the pion induced case a better understanding of the initial production process is required. This has to be tested against multi differential cross sections from elementary targets. It could also be interesting to study the medium modification of nucleon resonances on the $\pi \to \pi\pi$ transition amplitude. On top of the included final state interactions the medium modification of the $\pi\pi$ rescattering kernel could possibly improve the agreement with the data. This, however, should be done in a consistent model accounting both for the pion final state interaction and the dressing of the intermediate $\pi\pi$ propagators on the very same theoretical basis.

Now we turn to the photoproduction of vector mesons in nuclei. With the aim to improve the method to extract the inelastic vector meson nucleon cross section, one should study the in-medium changes of the initial production amplitude. This could be done very well for the ω meson where in the particular energy range considered here ($E_\gamma = 1.5$ GeV) the production process is expected to be dominated by $t-$channel $\pi-$exchange. The inclusion of the π polarization function as well as short-range correlations could possibly explain the strong depletion of the total yield when going from protons to nuclear targets as seen experimentally [19]. The effect of these mechanisms is, however, not intuitive but should be accounted for since the extraction of the inelastic vector meson cross section can be sensitive to it. Moreover, the elementary production amplitude can be very well tested against coherent ω production data that is sensitive to the excited resonances as the $\pi-$exchange background is expected to vanish for nuclear targets with an equal number of protons and neutrons. This is also an issue in the case of the ϕ meson. In addition, if the large ϕ attenuation cross section is confirmed, theoretical models have to find an explanation for this huge effect. In-medium cross sections with dressed kaon propagators indeed could give rise to changes of ϕ meson absorption in nuclei.

Finally, also the calculation of the ω spectral function in matter could be further improved. Exotic reactions as $\omega N \to 2\pi N$ should be constrained by data as much as possible – in particular if it turns out that such a channel is important for in-medium modifications. This, however, is not possible via direct measurements but can be obtained only by means of coupled channel analyses. The inclusion of this three-body final state including its decomposition in the $\Delta\pi$, ρN and σN channels into coupled channel $K-$matrix calculations is a highly non-trivial task that should be subject to future investigations. Concerning in-medium properties it could be interesting to also include Pauli blocking in the self energies of the intermediate nucleon resonances. The development of a separate code that mimics the rescattering mechanism via the inclusion of broad resonances would open the possibility to extend the model to coupled channels

concerning the in-medium scattering processes. Only then higher order density effects could be calculated and short range correlations as well as mean field potentials could be included. At the same time the in-medium self energies of all involved mesons and baryon resonances could be obtained in a consistent scheme. Moreover, the microscopically calculated spectral function has to be tested against experimental data by means of consistently performed transport calculations. In particular, full off-shell absorption and rescattering cross sections have to be calculated from the very same potential and implemented into the simulations. In this way the in-medium spectral information can simultaneously be constrained from elementary and nuclear reaction data.

Connected with fundamental properties of the underlying theory of strong interactions, the changes of meson properties in nuclear matter are striking phenomena of hadron physics. However, they are hard to approach both theoretically and experimentally. Theoretically, the number of unknown parameters is still large as compared to the amount of constraints which have to be obtained from experiment. Experimentally, the complete understanding of the nuclear processes including a full reconstruction of the backgrounds is challenging. Thus, new theoretical concepts and experiments will be needed in order to improve our present understanding of the physics of strongly interacting matter.

Appendix A

Transport Code

A.1 General Concept

Our Monte Carlo transport code is based upon that developed by Hombach, Teis, and Effenberger [146, 274, 275, 276, 277]. The version that has been used in the present work is in its main features identical to the one applied and developed further in [100] where a detailed description of the physical concepts and numerical aspects of the model can be found. The code was first applied to the description of relativistic heavy ion collisions at SIS energies [278, 279]. Later it has been extended to the calculation of observables in photon- end pion-induced nuclear reactions [110, 280, 281, 282] with the aim to have a model at hand that allows for the description of all kinds of nuclear reactions with the very same physical input. Recently, it has been applied to photon- and electron-induced reactions in the resonance region [283, 284], high energy reactions of protons, photons and leptons [166] and low-energy pion absorption [36, 84]. There also some special concepts and extensions of the model have been discussed.

The Giessen BUU transport code uses Monte Carlo methods to follow the individual destinies of sample testparticles through the nucleonic matter from the moment of their creation to their absorption or escape through the outer boundaries of the nucleus. In the present work, the nuclear environment is assumed to be spherically symmetric and static. The testparticles are characterized by their discrete quantum numbers and continuous energies, momenta, spatial positions and specific weight factors proportional to their total production cross sections. They are produced initially through incoherent photon or pion nucleon interactions. The rates of testparticle interactions with the nucleons of the nuclear medium are evaluated according to their total cross sections predetermined from vacuum processes. Unstable particles decay according to their life-times proportional to their inverse widths. Actual scattering and decay processes are simulated by taking into account Pauli blocking effects according to the local phasespace distributions of nucleons.

The target nuclei are modeled according to the static Woods-Saxon density distribution and applying a local density approximation [284]. The nucleons and baryon resonances move inside a local, density dependent mean field that is parametrized according to the Skyrme-type potential from Welke et al. [285, 286]. The parameters of this potential have been fitted to the saturation properties of nuclear matter and the momentum dependence known from proton nucleus scattering [287]. Isospin-3/2 resonances are assumed to feel

a reduced potential according to the phenomenological value of the $\Delta(1232)$ potential obtained from pion nucleus scattering [63]. If not mentioned differently, mesons do not feel any potential. Since most of our results only weakly depend on the Coulomb potential it is usually neglected in our calculations. In the present work the potentials and Pauli blocking factors are calculated from equilibrium nucleon distributions instead of the actual computed phasespace distributions of testparticles. This is well justified as the nuclei are supposed to stay close to their ground state in the considered photon- and pion-induced reactions.

At the start of each simulation, about 20.000 test-nucleons are initialized according to the local equilibrium distributions. Each physical particle is represented by a certain number of testparticles. Then the initialization of the elementary photon nucleon or pion nucleon interactions takes place. One such interaction is considered on each test-nucleon, the individual final states are sorted according to probabilities given by the differential cross sections for the individual channels. The reaction products are initialized by the determination of mass, momentum and moving direction of the final state particles. A statistical weight proportional to the total photon or pion nucleon cross section is assigned to each produced particle. Then transport is started. The transport part of our model is based upon a numerical solution of the semiclassical **B**oltzmann-**U**ehling-**U**hlenbeck (BUU) equation. The simulation of the collisional integral is done by means of the parallel ensemble method [100]. In order to enhance statistics and to further reduce computing times we rely on the so-called perturbative particle method [288, 289] that is frequently used to simulate nuclear reactions with elementary projectiles as photons, electrons and pions. These numerical concepts will be introduced briefly later in this Appendix.

During the simulation the path of each testparticle through the nuclear medium is followed by Monte Carlo sampling. The time step is kept fixed at $\Delta t = 0.5$ fm/c. With random numbers and tabulated cross sections initialized before the start of the actual simulation we decide at the beginning of each time step whether a particle moves freely or interacts. If it interacts it can scatter elastically or it can be absorbed; the final state testparticles of these interactions are initialized according to their differential cross sections if these are known or are distributed randomly in phasespace otherwise. In case of an unstable particle we decide if this particle decays according to the decay probability determined from its inverse (vacuum) decay width. Between collisions the testparticles are propagated according to Hamilton's equation of motion. The simulation is truncated at $t = 40$ fm/c. After this time interval most of the reaction products have left the nucleus and the interaction rate goes to zero. Finally the observables are calculated from the final particle yield and the individual testparticle weights. Differential cross sections are obtained by projection on the individual kinematical variables.

A.2 Structure of the code

Target initialization. In one simulation up to 1.500 target nuclei are considered in parallel. The nucleons of the target are initialized in position space according to a

Woods-Saxon density distribution:

$$n_N(\mathbf{r}) = n_0 \left[1 + \exp \frac{|\mathbf{r}| - r_0}{\alpha}\right]^{-1} \tag{A.1}$$

where n_0, r_0 and α are parameters that have been fitted to the density distributions known from electron nucleus scattering [287]. In momentum space the testparticles are initialized according to a local Thomas-Fermi approximation

$$f_0(\mathbf{r}, \mathbf{p}) = 4\,\Theta\left(p_F(\mathbf{r}) - |\mathbf{p}|\right) \tag{A.2}$$

where p_F is the local Fermi momentum. It is given by

$$p_F(\mathbf{r}) = \left(\frac{3}{2}\pi^2 n_N(\mathbf{r})\right)^{\frac{1}{3}}. \tag{A.3}$$

Particle species. Our model contains the particle species listed in Table A.1.

Elementary interactions. Within the perturbative particle method, we initialize on each target nucleon one photon nucleon or pion nucleon interaction. The individual final state is sorted with random numbers. The probability of an individual final state is given by the total cross section for that individual channel divided by the total photon or pion nucleon cross section. For the testparticles moving in the mean field potential, the cross sections are calculated as function of the free invariant energy:

$$\sqrt{s}_f \equiv \sqrt{m_1^{*2} + \mathbf{q}^2} + \sqrt{m_2^{*2} + \mathbf{q}^2}, \tag{A.4}$$

where m_i^* are the effective masses of the colliding particles and $\mathbf{q}$ is their CM momentum. The final state momenta are obtained by an iterative method taking into account the momentum dependent mean field. Photon nucleus cross sections are corrected for nuclear shadowing by means of an energy and coordinate dependent shadowing factor calculated within the Glauber approach [166, 290, 291]. The calculated shadowing factor is multiplied to the elementary photon nucleon cross section and enters the statistical weight of the produced testparticles.

Inclusive particle production. To determine the outcome of high-energy photon hadron and hadron hadron collisions we use the Monte Carlo simulation programs PYTHIA [292, 293] and FRITIOF [262, 294, 295] which rely on the Lund formalism. The Lund models are used for inclusive particle production for CM energies above $\sqrt{s} = 2.0$ GeV (photon hadron collisions), $\sqrt{s} = 2.2$ GeV (meson baryon collisions) and $\sqrt{s} = 2.6$ GeV (baryon baryon collisions). They determine the final state of inclusive reactions and initialize the outgoing particles in momentum space. The basic concept of the Lund formalism relies on a two-step process. First, two excited states with the quantum numbers of the incoming hadrons are produced (string excitation). In the second step the breakup of these strings into hadrons is described by means of the JETSET package

mesons	S	J	
	0	0	$\pi, \eta, \sigma, \eta', \eta_c$
	0	1	$\rho, \omega, \phi, J/\psi, D^*, \bar{D}^*$
	+1	0/1	K, K^*, D_s, D_s^*
	−1	0/1	$\bar{K}, \bar{K}^*, \bar{D}_s, \bar{D}_s^*$
baryons	S	I	
	0	1/2	$N(938), P_{11}(1440), S_{11}(1535), S_{11}(1650), S_{11}(2090),$ $D_{13}(1520), D_{13}(1700), D_{13}(2080), D_{15}(1675),$ $G_{17}(2190), P_{11}(1710), P_{11}(2100), P_{13}(1720), P_{13}(1879),$ $F_{15}(1680), F_{15}(2000), F_{17}(1990)$
	0	3/2	$P_{33}(1232), S_{31}(1620), S_{31}(1900),$ $D_{33}(1700), D_{33}(1940), D_{35}(1930), D_{35}(2350),$ $P_{31}(1744), P_{31}(1910), P_{33}(1600), P_{33}(1920),$ $F_{35}(1752), F_{35}(1905), F_{37}(1950)$
	−1		$\Lambda(1116), \Sigma(1189), P_{13}(1385), S_{01}(1405), D_{03}(1520),$ $P_{01}(1600), P_{11}(1660), S_{01}(1670), D_{13}(1670), D_{03}(1690),$ $S_{11}(1750), D_{15}(1775), S_{01}(1800), P_{01}(1810), F_{05}(1820),$ $D_{05}(1830), P_{03}(1890), F_{15}(1915), F_{17}(2030), G_{07}(2100),$ $F_{05}(2110)$
	else		$\Xi, \Xi^*, \Omega, \Lambda_c, \Sigma_c, \Sigma_c^*, \Xi_c, \Xi_c^*, \Omega_c$
photon			γ
leptons			e^+, e^-

Table A.1: Particle species in the BUU model.

(fragmentation). A brief introduction into the basic ideas of the Lund formalism can be found in [166].

In case of a photon hadron collision the vector meson dominance model (VMD) is used. Thus, the photon hadron interaction is reduced to the elastic or inelastic collision of the virtual hadronic components of the photon and hadron. According to probabilities given by the phenomenological vector meson photon couplings the incoming photon is replaced by either a ρ, ω or ϕ meson:

$$|\gamma\rangle \to \sum_{\rho,\omega,\phi} \frac{e}{g_V} |V\rangle. \tag{A.5}$$

Details on this recipe can be found in Refs. [290, 291].

Transport. The central part of our model relies upon a numerical solution of the semi-classical BUU equation. In short-hand notation it takes the following form:

$$(\partial_t + \partial_{\mathbf{p}}\mathcal{H}_i\partial_{\mathbf{r}} - \partial_{\mathbf{r}}\mathcal{H}_i\partial_{\mathbf{p}}) = G_i\mathcal{S}_i(1 \pm F_i) - L_iF_i \tag{A.6}$$

where F_i is the so-called spectral phasespace density. It is given as a product of the ordinary quasiparticle phasespace density f_i and the spectral function $\mathcal{S}_i$:

$$F_i(\mathbf{r}, \mathbf{p}, W, t) = f_i(\mathbf{r}, \mathbf{p}, t)\mathcal{S}_i(W, \mathbf{r}, \mathbf{p}). \tag{A.7}$$

The definition of the spectral function $\mathcal{S}_i$ slightly deviates from the commonly used definition, it is given by the product of the usual spectral function $\mathcal{A}_i$ times two times the particle mass W. Thus, $\mathcal{S}_i$ directly gives the probability that a particle of species i with momentum $\mathbf{p}$ at position $\mathbf{r}$ is found with mass W

$$\mathcal{S}_i(W, \mathbf{r}, \mathbf{p}) = \mathcal{A}_i(W, \mathbf{r}, \mathbf{p})2W = \frac{2}{\pi}\frac{W^2\Gamma_{\rm tot}(W, \mathbf{r}, \mathbf{p})}{(W^2 - m_i^2)^2 + W^2\Gamma_{\rm tot}^2(W, \mathbf{r}, \mathbf{p})}. \tag{A.8}$$

The Hamilton function $\mathcal{H}_i$ is given by the relativistic expression for the single particle energy

$$\mathcal{H}_i(\mathbf{r}, \mathbf{p}) = \sqrt{(W_i + U_i(\mathbf{r}, \mathbf{p}, f_0))^2 + \mathbf{p}_i^2} \tag{A.9}$$

where U_i is the coordinate and momentum dependent mean field that in the present work depends on the position and momentum of the testparticle and the equilibrium nucleon distribution (A.2). The structure and numerical implementation of the right hand side of the BUU equation (A.6) will be discussed in the next Section.

Off-shell transport. The dynamical treatment of density and momentum dependent spectral functions has been established by Effenberger *et al.* [159, 296]. This *ad hoc* method has been introduced in order to obtain the correct behavior of the mass spectra of particles that acquire a collisional width in the medium when these particles move through an environment with non-uniform nucleon density. The off-shellness of a given testparticle is absorbed in a scalar potential defined as

$$U_i(\mathbf{r}_i) = (W_i^* - W_i^o)\,\frac{n_N(\mathbf{r}_i)}{n_N(\mathbf{r}_i^*)} \tag{A.10}$$

where the asterisk refers to quantities determined at the instant of the creation of the testparticle; W_i^o is a mass chosen randomly according to its vacuum spectral function. This potential enters the single particle Hamilton function as an usual scalar potential, thus guaranteeing energy conservation. The effective mass of the testparticle is given as

$$W_i(\mathbf{r}) = W_i^o + U_i(\mathbf{r}) \tag{A.11}$$

which obviously yields the correct asymptotic value of the testparticle mass. Thus, the mass spectrum of a physical particle, represented by a bunch of testparticles, takes the

form of the vacuum spectral function (times phasespace factors due to the production processes) when all testparticles have escaped the nuclear environment.

This method has been justified theoretically *a posteriori* by the works [297, 298]. Their transport equations go over into our off-shell prescription by assuming that the collisional width is proportional to the nucleon density (this is exact when the low-density theorem is applied), its momentum dependence is weak (this is in general not the case), and the off-shellness is small as compared to the particle mass (this is true for instance for ω and ϕ mesons but not for ρ mesons).

A.3 Collision integral

The so-called collision term forms the right hand side of the BUU equation and influences the time evolution of the phasespace densities via the creation and destruction of particles in scattering and decay processes. In the quasiparticle limit ($\mathcal{S}_i \to 1$ and $F_i \to f_i$) the transport equation reads

$$\frac{df_i}{dt} = G_i(1 \pm f_i) - L_i f_i \tag{A.12}$$

where $(1 \pm f_i)$ is a Pauli blocking or Bose enhancement factor for the case where the particle i is a fermion or boson, respectively. In the following we attach a short discussion of the structure of the collision term and its numerical implementation into the transport simulation.

Collision term. The collision term can be separated into a gain and a loss term. This is already indicated in Eq. (A.12) where G_i stands for the gain and L_i for the loss term, respectively. In the following we will concentrate on the loss term and disregard the gain term which, however, has a similar form. In addition we restrict ourselves to $2 \to 2$ collisions in order to keep the formulas manageable. The loss term can then be written as

$$\begin{aligned} L_i(\mathbf{r}, \mathbf{p}_i, t) &= \frac{1}{(2\pi)^3} \sum_j \sum_{ab} \int d^3p_j \int d\Omega_{\rm cm} \frac{d\sigma_{ij\to ab}}{d\Omega_{\rm cm}} v_{ij} f(\mathbf{r}, \mathbf{p}_j, t) \mathcal{P}_a \mathcal{P}_b \\ &\quad + \sum_{cd} \int d\Omega_{\rm cm} \frac{d\Gamma_{i\to cd}}{d\Omega_{\rm cm}} \mathcal{P}_c \mathcal{P}_d \end{aligned} \tag{A.13}$$

where $d\sigma_{ij\to ab}/d\Omega_{\rm cm}$ and $d\Gamma_{i\to cd}/d\Omega_{\rm cm}$ are the angular differential cross sections and decay widths for the processes $ij \to ab$ and $i \to cd$, respectively. The terms $\mathcal{P}_X = 1 - f(\mathbf{r}, \mathbf{p}_X, t)$ with $X = a, b, c, d$ introduce Pauli blocking of the final states in the case where a, b, c, d are fermions or $\mathcal{P}_X = 1$ otherwise. v_{ij} is the relative velocity of the collision partners i and j. The final states ab and cd and the collision partners j are summed over in order to obtain the total loss rate.

Full ensemble method. The BUU equation can be solved numerically by means of a testparticle ansatz, where the single particle density is replaced by a discrete sum over δ-functions:

$$f_i(\mathbf{r},\mathbf{p},t) = \frac{(2\pi)^3}{N}\sum_{i=1}^{A\times N}\delta\left[\mathbf{r}-\mathbf{r}_i(t)\right]\delta\left[\mathbf{p}-\mathbf{p}_i(t)\right]. \tag{A.14}$$

Here A denotes the number of physical particles and N is the number of testparticles which collectively represent one physical particle. Between collisions the testparticle coordinates $\mathbf{r}_i$ and $\mathbf{p}_i$ obey the Hamilton equations of motion. This is obtained by plugging the testparticle ansatz into the left hand side of the BUU equation (A.6) and setting $df/dt = 0$. Using the testparticle ansatz with the loss term (A.13) we obtain the change of the phasespace densities per unit time in terms of collision and decay probabilities. This has been detailed for instance in Ref. [99]. The probability of a collision between the particles i and j is proportional to the infinitesimal volume element $\Delta V_{ij} = \sigma_{ij} v_{ij} \Delta t/N$ where Δt is the time step size. If particle j is located outside the volume element ΔV_{ij}, no collision can happen. Consequently, in the limit $N \to \infty$ the loss term becomes purely local. This solution of the collision term is known as the *full ensemble method*.

Parallel ensemble method. The full ensemble method is numerically expensive since all particles are allowed to scatter with each other. Thus, computing time scales according to $\sim N^2$. A common approximation is the *parallel ensemble method*. Here, one sets $N = 1$ and performs $\tilde{N}$ runs at the same time. The results as well as the particle densities needed to evaluate the mean field potentials are averaged over all parallel runs. Consequently, the computing time scales $\sim \tilde{N}$. On the other hand this scheme does not exactly provide a solution to the transport equation since the originally local collision term becomes non-local. Even in the limit $\tilde{N} \to \infty$ locality is not restored since the volume element which now reads $\Delta V_{ij} = \sigma_{ij} v_{ij} \Delta t$ does not converge. However, in several studies it has been shown that no great deviations to the exact full ensemble solution are to be expected [99, 100, 299]. More details on the numerical simulation of the collision integral and a comparison of the full and parallel ensemble solutions can be found in [99]. The results presented in this work are calculated with $\Delta t = 0.5$ fm and a typical number of ensembles of $\tilde{N} = 100 - 1500$ depending on the size of the target nucleus.

Perturbative particles. For the special case of photon and pion induced nuclear reactions the concept of *perturbative particles* has proven to be very useful. A perturbative particle is defined as a testparticle which is influenced by the real particles but which in turn does not influence the real particles. Thus, this approximation corresponds to the assumption that the impact of the produced particles on the nuclear background can be disregarded. The perturbative particles undergo the very same interactions as the real particles but do not interact with each other. In photon- and pion-induced reactions we initialize the products of the elementary projectile target interaction as perturbative particles corresponding to the assumption that the nucleus remains in its ground state. Each perturbative particle carries a weight which is proportional to the cross section with which it has been populated. The perturbative particle method allows to intialize

one photon- or pion-nucleon event on each target nucleon and, thus, saves additional computing time. This method is described in more detail in Ref. [100]. It can be used both together with the full and the parallel ensemble method.

In the case when calculations with perturbative particles are performed the real testparticles move freely inside their mean field potential. However, the phasespace distribution of nucleons moving inside the Skyrme type potential implemented in the BUU model is not perfectly constant in time. This is due to the fact that the initialized Woods-Saxon distribution does not exactly resemble the ground state of the nuclear potential. Consequently, the initial nucleon distribution slowly dissolves. This was demonstrated in [100]. Therefore it is reasonable to keep the density which is used to calculate the mean field potentials and gradients fixed according to the initial Woods-Saxon distribution. In this case also Pauli blocking is accounted for via blocking factors calculated from the analytical density functional rather than by means of the actual testparticle distribution. At the end of this Chapter we will comment briefly on the validity of these assumptions.

Optical potential. In the case of perturbative particle production the loss term (A.13) can even be simplified further. In this case only one particle species exists with which the perturbative particles may collide, namely the nucleons which form the target nucleus. Neglecting the isospin degree of freedom, Eq. (A.13) can then be recast into the form

$$L_i(\mathbf{r},\mathbf{p},t) = n_N(\mathbf{r})\langle v\tilde{\sigma}\rangle + \tilde{\Gamma} \tag{A.15}$$

where the parenthesis indicate an average over the nucleon momentum distribution, n_N is the local nucleon density, and the tilde indicates the hidden Pauli blocking factors. The first term now exactly has the form of a collisional width. Neglecting the gain term, the BUU equation (A.12) can be rewritten as

$$\frac{df_i}{dt} = -(\tilde{\Gamma}_{\rm coll} + \tilde{\Gamma}_{\rm vac})f_i \tag{A.16}$$

where $\tilde{\Gamma}_{\rm coll}$ and $\tilde{\Gamma}_{\rm vac}$ are the Pauli blocked collision and vacuum decay widths of the particle species i in the nuclear rest frame. This equation can be solved easily. We find

$$f_i(t) = f_0 \exp\left[-(\tilde{\Gamma}_{\rm coll} + \tilde{\Gamma}_{\rm vac})(t-t_0)\right] \tag{A.17}$$

where f_0 is the phasespace density at the time $t = t_0$. Numerically, the solution (A.17) can be simulated by just erasing particles from the flux in each time step with the fixed probability $w = \Gamma\Delta t$. This recipe corresponds to perturbative particles moving inside a complex valued optical potential whose imaginary part is given by

$$\mathcal{I}{\rm m}V_{\rm opt} = \frac{\mathcal{I}{\rm m}\Pi}{2E} = -\frac{\tilde{\Gamma}_{\rm coll} + \tilde{\Gamma}_{\rm vac}}{2} \tag{A.18}$$

where E is the particle energy in the nuclear rest frame and Π is the complex self energy. This treatment can be useful whenever the reaction products of any collision of the perturbative testparticles with the real particles do not contribute to further particle production and are not detected themselves. The essential advantage of this scheme is

the possibility to include nuclear effects going beyond the two particle collisions which are accounted for by means of the semiclassical collision term. Throughout this work this modus operandi is referred to as the optical model (OM) approach in contrast to the coupled channel (CC) modus which involves the explicit simulation of collisions. By default an optical potential is used only for the $\Delta(1232)$ resonance because of the importance of three-body collisions $\Delta NN \to \Delta NN/NNN$. This is discussed in Section 3.4.

A.4 Resonance decay

In the nuclear medium the total widths of hadronic resonances (e. g. vector mesons) change for instance due to the opening of additional decay channels containing nucleon-hole configurations. Thus, also the decay branching ratios are modified. This effect, however, is automatically contained in the numerical simulation of the BUU collision term and the decay rates. Since this issue is not as obvious, we discuss it briefly in the following by means of a simplified model. We consider the resonance creation and subsequent decay process

$$X \to R \to f \tag{A.19}$$

in infinite nuclear matter. The population of the resonance R via the initial state X may not be specified further. Using elementary Feynman rules the differential rate of the observed final state f (which itself does not undergo FSI, e. g. $f = e^+e^-$) is given by

$$\frac{d\mathcal{N}}{dW} = \mathcal{N}_0 \left|D_R\right|^2 \Gamma_{R\to f} \tag{A.20}$$

where D_R is the resonance propagator, $\Gamma_{R\to f}$ is the partial decay width of the resonance to the final state f and W is the invariant resonance mass. The prefactor $\mathcal{N}_0$ may contain all effects of the population including the density of particles X and the $R \to X$ partial width. Inserting explicitly the resonance propagator (neglecting any spin degrees of freedom) this Equation takes the form

$$\frac{d\mathcal{N}}{dW} = \mathcal{N}_0 \left|\frac{1}{k_R^2 - m_R^2 - \Sigma_R(k)}\right|^2 \Gamma_{R\to f} \tag{A.21}$$

where $k_R = (k_0, \mathbf{k})$ is the four-momentum of the resonance, m_R is the resonance rest mass and Σ_R is the resonance self energy containing vacuum and in-medium components. By rewriting the squared propagator and using $\Sigma_R = -iW\Gamma_{\text{tot}}$ we find

$$\frac{d\mathcal{N}}{dW} = \tilde{\mathcal{N}_0}\mathcal{A}_R \frac{\Gamma_{R\to f}}{\Gamma_{\text{tot}}} \tag{A.22}$$

where $\mathcal{A}_R = -1/\pi\, \mathcal{I}\text{m}D_R$ is the resonance spectral function, $\tilde{\mathcal{N}_0} = \mathcal{N}_0\pi W$, and $\Gamma_{\text{tot}} = \Gamma_{R\to X} + \Gamma_{\text{coll}}$ is the total resonance width which is given as a sum of the free decay width $\Gamma_{R\to X}$ and the collision width Γ_{coll} arising through collisions in the medium. The latter one is given by the first term of the right hand side of Eq. (A.15). Note, that the total

width appearing in the denominator of the decay branching ratio $\Gamma_{R\to f}/\Gamma_{\rm tot}$ and the width entering the spectral function are identical.

Let us now turn to the BUU simulation. Resonances are erased from the flux both due to their spontaneous decay as well as due to resonance nucleon collisions. In practical simulations, the spontaneous decay probability of any resonance in a time interval Δt is given by

$$p = \frac{\Gamma_{R\to X}}{\gamma}\Delta t \tag{A.23}$$

where $\Gamma_{R\to X}$ is the total vacuum decay width of the resonance and $\gamma = k_0/W$ is a Lorentz factor which transforms the decay width from the rest frame of the resonance to the nuclear rest frame. The final state f is determined by Monte Carlo sampling from the vacuum decay branching ratios

$$b = \frac{\Gamma_{R\to f}}{\Gamma_{R\to X}}. \tag{A.24}$$

We restrict the interactions of the resonance with the medium to purely absorptive collisions and, thus, neglect any coupled channel effects. As discussed in the previous Section, the collision rates introduced via the right hand side of the BUU equation are then equivalent to an optical potential. Thus, according to Eqs. (A.7) and (A.17), the resonance spectral phasespace density can be written as

$$F_R(\mathbf{r},\mathbf{p},t,W) = f_0(\mathbf{r},\mathbf{p})2W\mathcal{A}_R(W)e^{-\tilde{\Gamma}_{\rm tot}t} \tag{A.25}$$

where f_0 is the phasespace density at time $t = 0$ with the normalization

$$\int d^3r\frac{d^3p}{(2\pi)^3}f_0(\mathbf{r},\mathbf{p}) = \mathcal{N}_0 \tag{A.26}$$

and $\mathcal{N}_0$ again contains all effects of the population. Furthermore, $\mathcal{A}_R$ is the resonance spectral function and $\tilde{\Gamma}_{\rm tot}$ is the total resonance width in the nuclear rest frame, i. e. $\tilde{\Gamma}_{\rm tot} = \Gamma_{\rm tot}W/E$. The total width $\Gamma_{\rm tot}$ also enters both the numerator and denominator of the spectral function.

The asymptotic rate of any observed final state is then given by

$$\frac{d\mathcal{N}}{dW} = \int_0^\infty dt\int d^3r\frac{d^3p}{(2\pi^3)}F_R(\mathbf{r},\mathbf{p},t,W)\tilde{\Gamma}_{R\to f} \tag{A.27}$$

where $\tilde{\Gamma}_{R\to f}$ is the partial decay width of the resonance R to the final state f in the nuclear rest frame. Using Equations (A.25) and (A.26) the integrations can be carried out explicitly

$$\frac{d\mathcal{N}}{dW} = \int_0^\infty dt\int d^3r\frac{d^3p}{(2\pi^3)}f_0(\mathbf{r},\mathbf{p})2W\mathcal{A}_R(W)\tilde{\Gamma}_{R\to f}e^{-\tilde{\Gamma}_{\rm tot}t} \tag{A.28}$$

$$= \mathcal{N}_0\int_0^\infty dt\,2W\mathcal{A}_R(W)\tilde{\Gamma}_{R\to f}e^{-\tilde{\Gamma}_{\rm tot}t} \tag{A.29}$$

$$= \mathcal{N}_0 2W\mathcal{A}_R(W)\frac{\tilde{\Gamma}_{R\to f}}{\tilde{\Gamma}_{\rm tot}} = \tilde{\mathcal{N}}_0\mathcal{A}_R(W)\frac{\Gamma_{R\to f}}{\Gamma_{\rm tot}} \tag{A.30}$$

with $\tilde{\mathcal{N}_0} = 2W\mathcal{N}_0$. Thus, the correct expression (A.22) is retrieved. The total width appearing in the decay branching ratio $\Gamma_{R\to f}/\Gamma_{\text{tot}}$ contains both components from the free resonance decays and the in-medium collisional contributions. Thus, consistency of the decay branching ratio and the total width of the spectral function is guaranteed via the inclusion of the very same collision rates in the BUU collision integral as in the width of the spectral function. Only then the widths in the denominator of the branching ratio and in the numerator of the spectral function cancel each other and the correct rates are obtained.

The situation becomes more subtle in the case where the nuclear density is not constant any more. According to Eq. (A.20) the total width in the numerator of the spectral function and the denominator of the branching ratio still have to cancel each other since they are only introduced mathematically in order to rewrite Eq. (A.20) in terms of the resonance spectral function. In the transport simulation the resonance can propagate to smaller or higher nuclear densities before it eventually decays either via its spontanous decay width or via collisions with the medium. The decay branching ratio is – at least ideally – local and, thus, depends on the actual local nucleon density. The consistency of spectral function and branching ratio is thus conserved only if also the evolution of the spectral function follows the propagation of the resonance to different densities. For the case of the vector mesons this is guaranteed by means of the use of the scalar off-shell potential U_i (A.10). Thus, according to our semiclassical picture, the correct decay rates are automatically included in the space-time evolution of the vector meson phasespace densities.

A.5 Target excitation

Throughout this work the perturbative particle method is applied to the solution of the collision integral. Moreover, the nucleon densities, calculated according to analytical Woods-Saxon parameterizations, are kept constant in time. Both issues have been introduced previously. They rely on the assumption that the excitation of the nuclear background can be neglected for the case of the investigated photon and pion nucleus reactions. We attach a short discussion on the validity of this assumption.

Even if the target is excited with elementary probes such as pions or photons a certain amount of energy and momentum is transferred to the hit nucleon. This nucleon propagates through the medium and distributes its energy via secondary collisions among the other nuclei. If the energy transfer in these secondary collisions is high enough more particles can be produced. Moreover, the momentum distribution of the nucleons in the nucleus changes which, thus, is not in its ground state any more. This in turn can have an impact on the final state interactions of the initially produced particles. Applying the perturbative particle method any impact of the elementary collisions on the nuclear background is discarded.

A useful observable which contains information about the non-equilibrium of the target nucleons is the nucleon momentum distribution. As introduced briefly in a previous

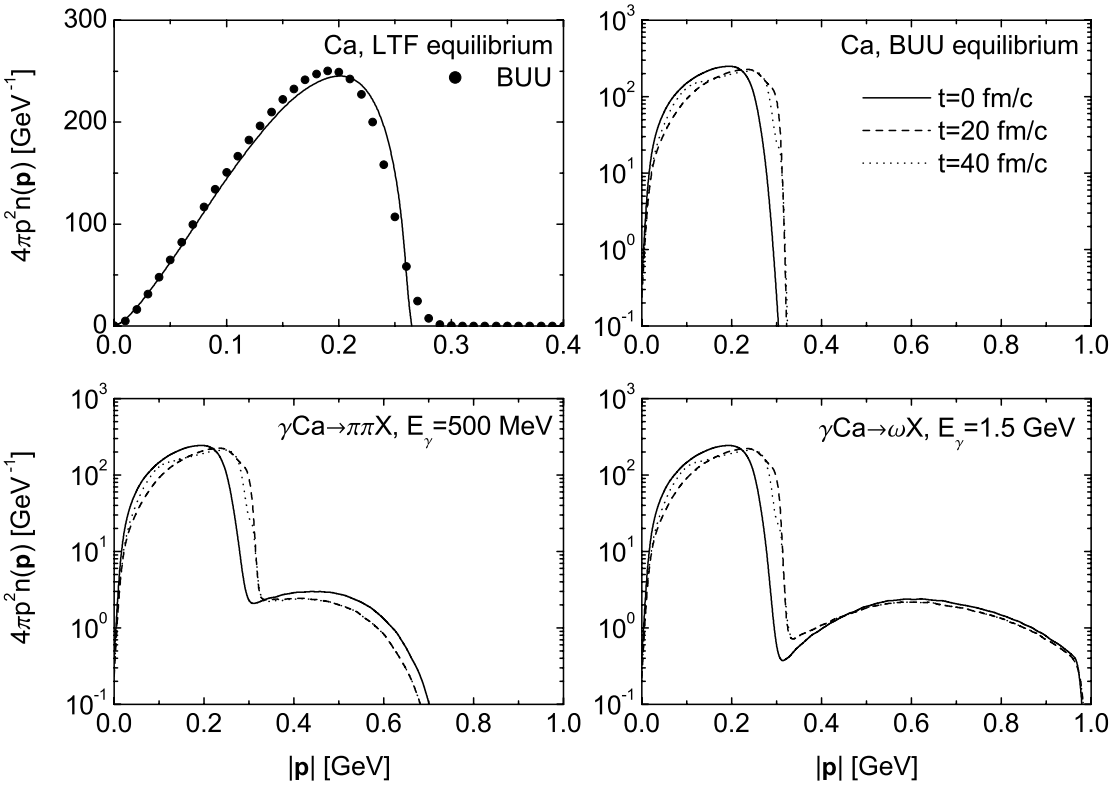

Figure A.1: Time evolution of the nucleon momentum distribution in BUU transport simulations. *Top left*: nucleon momentum distribution in ^{40}Ca according to the local Thomas-Fermi (LTF) model compared to the BUU initialization, *top right*: time evolution of the momentum distribution in a BUU ground state calculation, *bottom left*: double π^0 photoproduction at $E_\gamma = 500$ MeV, *bottom right*: ω photoproduction at $E_\gamma = 1.5$ GeV. BUU calculations have been done in the parallel ensemble mode without perturbative particles.

Section, we apply a local Thomas-Fermi method in order to initialize the target nucleus in coordinate and momentum space. The momentum distribution

$$4\pi \mathbf{p}^2 n(\mathbf{p}) = 16\pi^2 \mathbf{p}^2 \int_0^\infty r^2 dr f_N(\mathbf{r}, \mathbf{p}) \tag{A.31}$$

with $f(\mathbf{r}, \mathbf{p})$ given by Eq. (A.2) for the case of a Calcium nucleus is shown in the top left of Fig. A.1. In the top right panel of the same Figure we show the time evolution of this distribution in the actual BUU simulation. The ground state distribution is not perfectly constant in time. This has to be ascribed to the fact that the initial Woods-Saxon distribution does not exactly resemble the ground state of the implemented mean field nucleon potential. This issue and possible improvements have been investigated quite in detail in Refs. [100, 284].

In order to study the variation of this momentum distribution throughout the time evolution of a photon nucleus reaction we perform BUU calculations without applying

the perturbative particle method. Thus, the projectile directly influences the target nucleus via the transfer of energy and momentum to the hit nucleon. In doing so we use the parallel ensemble method and initialize one photon nucleon event for each ensemble. This corresponds to the physical situation where one photon reacts with one target nucleon. The time $t = 0$ is fixed to the instant right after the first elementary photon nucleon interaction. Before this, the nucleon momentum distribution is always identical to the one shown in the upper left panel of Fig. A.1.

Results for the nucleon momentum distribution can be seen in the lower panels of Fig. A.1. We have chosen two showcases, namely double π^0 photoproduction at $E_\gamma = 500$ MeV and ω photoproduction at $E_\gamma = 1.5$ GeV. In both cases the momentum distribution develops a long high-momentum tail whose range scales with the projectile energy. However, due to the fact that only one nucleon in each ensemble is initially hit, the strength sitting in this tail is relatively small. Compared to the nucleons which are still conform with the initial equilibrium distribution the high-momentum components are suppressed by two orders of magnitude. During the time evolution this tail only changes marginally which means that the other nucleons obviously stay close to their initial ground state configuration. Thus the perturbation of the nuclear background by the electromagnetic excitation is indeed negligible, in particular recalling the fluctuations of the momentum distribution which suffers from shortcomings in the implemented mean field potential. Consequently, it is more than reasonable to keep the initial momentum distribution fixed (upper left corner in Fig. (A.1)) at the expense of neglecting the impact of the high momentum tail (lower panels in Fig. A.1) on secondary interactions.

Appendix B

Glauber formalism

In this Section we give a short introduction to Glauber theory. Glauber theory is used to describe the interactions of high energetic particles with nuclei. Applying certain approximations that will be discussed briefly below, Glauber theory reduces the interaction with the nucleus to the more fundamental interactions with single nucleons. It has been derived first in Refs. [300, 301] where it was applied to calculations of hadron nucleus reactions. Later it has been used to calculate photon nucleus cross sections [143, 302] and, in particular, to study the effects of nuclear shadowing [143, 144, 303, 304] and color transparency [305, 306]. A comprehensive derivation and discussion can also be found in [307] and [166].

B.1 Theoretical basis

Here, we restrain to give a complete derivation of the formalism and refer the interested reader to the literature given above. Rather, we describe the general concept and the approximations which enter the formulas used in this work.

Incoming particles are described as plane waves. The interaction with a single nucleon distorts this wave such that behind the nucleon the wave function can be considered as a superposition of the original wave and a negative plane wave confined to the shadow region

$$\psi(\mathbf{b}, z) = (1 - \Gamma(\mathbf{b}))\, e^{ikz} \tag{B.1}$$

where $\mathbf{b}$ is the two dimensional coordinate perpendicular to the incoming beam direction which defines the z axis. The assumption that the scattered wave can again be cast into the form of a plane wave is already an approximation which is expected to hold in the case of high beam energies [307]. In this Equation we have introduced the nucleon profile function Γ. In [307] it was shown that via Fourier transformation it can be expressed in terms of the elastic scattering amplitude f

$$\Gamma(\mathbf{b}) = \frac{1}{2\pi i k} \int d^2 q_T e^{-i\mathbf{q}_T \cdot \mathbf{b}} f(\mathbf{q}_T). \tag{B.2}$$

where k is the total three momentum of the projectile. Here, $\mathbf{q}_T$ denotes the transverse momentum transfer in the scattering process. In turn, the scattering amplitude can

be obtained by the inverse transformation. The scattering amplitude is related to the differential cross section

$$\frac{d\sigma_{\rm el}}{d\Omega} = |f(\mathbf{q}_T)|^2. \tag{B.3}$$

The extension to nuclear targets is achieved by considering the nucleus as an assembly of non-interacting nucleons. The incoming wave now becomes modified by the presence of A nucleons. According to the ansatz (B.1) we can define the nuclear profile function as a product of distortion factors given by the nucleonic profile functions

$$1 - \Gamma_A(\mathbf{b}, \mathbf{s}_i) = \prod_{i=1}^{A} [1 - \Gamma(\mathbf{b} - \mathbf{s}_i)] \tag{B.4}$$

where $\mathbf{s}_i$ is the impact parameter space coordinate of the particular nucleon. The nuclear profile function is regarded as an operator which may induce transitions between the ground state $|0\rangle$ and an arbitrary excited state $|f\rangle$. Thus, we can write

$$\Gamma_A^{f0}(\mathbf{b}, \mathbf{s}_i) = \delta_{f0} - \langle f| \prod_{i=1}^{A} [1 - \Gamma(\mathbf{b} - \mathbf{s}_i)] \, |0\rangle. \tag{B.5}$$

Having found the nuclear profile function, the nuclear scattering amplitude at momentum transfer $\mathbf{q}_T$ for the excitation of the nucleus from its ground state $|0\rangle$ into an excited state $|f\rangle$ in analogy to Eq. (B.2) is given by

$$F_A^{0\to f}(\mathbf{q}_T) = \frac{ik}{2\pi} \int d^2b e^{i\mathbf{q}_T\cdot\mathbf{b}} \langle f|\Gamma_A^{f0}(\mathbf{b}, \mathbf{r}_i)|0\rangle \tag{B.6}$$

Using relation (B.3), the completeness relation $\sum_f |f\rangle\langle f| = 1$, and $d\Omega \simeq d^2q_T/k^2$ one finds for the total incoherent nuclear cross section

$$\sigma_{\rm inc} = \int d^2b \left\{ \langle 0| \left|\Gamma_A(\mathbf{b}, \mathbf{r}_i)\right|^2 |0\rangle - |\langle 0|\Gamma_A(\mathbf{b}, \mathbf{r}_i)|0\rangle|^2 \right\} \tag{B.7}$$

The second term is the coherent part that has to be subtracted from the total one in order to arrive at an expression for incoherent processes. This cross section eventually can be compared to our incoherent transport results.

B.2 Single meson production

The photoproduction of a single meson is regarded as a two step process. First, the incoming photon interacts with a single nucleon and produces a meson. Second, this meson can by absorbed via collisions with nucleons sitting on its path. According to this simple picture, the nuclear profile function for the single meson production process can be written as follows

$$\Gamma_A^{\gamma m}(\mathbf{b}) = \sum_i^A \Gamma_{\gamma m}(\mathbf{b} - \mathbf{s}_i) \left\{ \prod_{j\neq i}^{A} [1 - \Gamma_{mN}(\mathbf{b} - \mathbf{s}_j)\Theta(z_j - z_i)] \right\} e^{iq_L z_i}. \tag{B.8}$$

Here, $\Gamma_{\gamma m}$ and Γ_{mN} are the elementary profile functions for the processes $\gamma N \to mN$ and $mN \to X$, defined via the respective scattering amplitudes according to Eq. (B.2), and

$$q_L = k - \sqrt{k^2 - m^2} \tag{B.9}$$

is the longitudinal momentum transfer (neglecting recoil) due to the production of a meson with mass m. The Θ function appears because only nucleons sitting downstream with respect to the elementary production vertex contribute to the absorption of the meson in the final state. In a more elaborate approach, expression (B.8) could be modified by allowing the photon to first scatter into a vector meson that in a second step produces the observed meson [143]. For the case of vector meson production this has been considered in [307]. Via interference with the direct process considered here, this two step amplitude would give rise to nuclear shadowing.

In order to obtain the total meson production cross section, the profile function (B.8) has to be inserted in (B.7). This expression can then be worked out applying the following approximations:

- the nuclear ground state density is a product of one particle densities (independent particle model)

$$|\psi_0(\mathbf{r}_1, ..., \mathbf{r}_A)|^2 = \rho_A(\mathbf{r}_1, ..., \mathbf{r}_A) \simeq \prod_{i=1}^{A} n_N(\mathbf{r}_i)$$

- the transverse size of the nucleon profile function is small

$$n_N(\mathbf{s}, z) \to n_N(\mathbf{b}, z)$$

- the number of target nucleons is large $A \gg 1$

$$(1 - x)^A \to \exp(-x).$$

Finally, one arrives at the following expression for the single meson photoproduction cross section:

$$\sigma_A = \sigma_N \int d^2b \int_{-\infty}^{+\infty} dz\, n_N(\mathbf{b}, z)\, e^{-\sigma_{mN} \int_z^\infty dz' n_N(\mathbf{b}, z')}. \tag{B.10}$$

Here, σ_N is the meson production cross section on a single nucleon and σ_{mN} is the total meson nucleon cross section. Since elastic processes do not lead to a loss of flux, in general only the inelastic cross section has to be inserted here. This, however, can depend on the exact experimental situation. In the following Section, we describe some extensions and applications of the formalism to meson photoproduction off nuclei. All the formulas derived below rely on Eq. (B.10) as a baseline.

B.3 Useful formulae

Particles produced inside a nucleus not necessarily go in forward direction. The absorption probability depends on their exact path since larger or smaller parts of the nuclear volume have to be crossed. Moreover, in general the absorption probability does not have to satisfy the low density theorem. Regarding these considerations, Eq. (B.10) can be cast into a more general form accounting also for Fermi motion and Pauli blocking

$$\sigma_A = \int d^3r \int \frac{d^3p}{(2\pi)^3} f_0(\mathbf{r},\mathbf{p}) \int d\Omega_{\rm cm} \frac{d\sigma_N}{d\Omega_{\rm cm}} \Theta(p_F - |\mathbf{p}'|)\, e^{-T(\mathbf{r},q)} \tag{B.11}$$

where f_0 is the ground state nucleon phasespace density given by Eq. (A.2), p_F is the local Fermi momentum according to Eq. (A.3), $\mathbf{p}'$ is the nucleon LA three-momentum in the final state and T is a nuclear transmission factor

$$T(\mathbf{r},q) = \int_0^\infty \frac{dl}{\lambda(|\mathbf{r}'|,q)} \tag{B.12}$$

where $q = (q_0, \mathbf{q})$ is the four-momentum of the produced meson, λ is its mean free path and

$$\mathbf{r}' = \mathbf{r} + l\frac{\mathbf{q}}{|\mathbf{q}|}. \tag{B.13}$$

At sufficiently high beam energies, the influence of the initial nucleon momentum on the differential cross section and the Pauli blocking factor may be neglected. In this case, the momentum integration can be carried out and we obtain the simpler result

$$\sigma_A = \int d^3r\, n_N(\mathbf{r}) \int d\Omega_{\rm cm} \frac{d\sigma_N}{d\Omega_{\rm cm}}\, e^{-T(\mathbf{r},q)} \tag{B.14}$$

where n_N is the nuclear density. Because of rotational symmetry, the square of the coordinate $\mathbf{r}'$ can be expressed in cylindrical coordinates as

$$|\mathbf{r}'|^2 = (b + l\sin\theta\cos\varphi)^2 + (l\sin\theta\sin\varphi)^2 + (z + l\cos\theta)^2 \tag{B.15}$$

where φ and θ are the polar and azimuthal CM angles of the meson with respect to the $z-$axis defined via the incoming photon direction. The mean free path of the meson can be related to the imaginary part of the meson self energy via

$$\lambda(|\mathbf{r}'|,q) = -\frac{|\mathbf{q}|}{\mathcal{I}\mathrm{m}\Pi(|\mathbf{r}'|,q)} \tag{B.16}$$

which contains all processes that take the observed mesons out of the flux. Using again the low density theorem $\mathcal{I}\mathrm{m}\Pi = n_N|\mathbf{q}|\sigma_{\rm abs}(q)$, the mean free path reduces to

$$\lambda(|\mathbf{r}'|,q) = \frac{1}{n_N(\mathbf{r}')\sigma_{\rm abs}(q)} = \frac{v}{\Gamma(\mathbf{r}',q)} \tag{B.17}$$

where $\sigma_{\rm abs}(q)$ is the total meson absorption cross section. In the following we restrict the discussion to on-shell particles. Consequently, the reabsorption cross section is a function of one suitable energy variable only $\sigma_{\rm abs} \equiv \sigma_{\rm abs}(E)$. The extension to off-shell particles is, however, straightforward.

Kinetic energy differential cross section

Relativistically, the kinetic energy of any particle is given by

$$T = q_0 - m = \sqrt{m^2 + \mathbf{q}^2} - m \tag{B.18}$$

where m is the particle mass and $q = (q_0, \mathbf{q})$ is its four-momentum. In the LA frame, the target nucleon is at rest and the photon energy is k_0. Via a Lorentz transformation from the LA to the photon-nucleon CM frame with

$$\beta = \frac{k_0}{k_0 + m_N} \quad \text{and} \quad \gamma = \frac{k_0 + m_N}{\sqrt{s}} \tag{B.19}$$

we find for the LA kinetic energy of the meson in the final state

$$T = \frac{(k_0 + m_N)\sqrt{m^2 + \mathbf{q}_{\rm cm}^2} + k_0 |\mathbf{q}_{\rm cm}| \cos\theta_{\rm cm}}{\sqrt{s}} - m \tag{B.20}$$

where $\mathbf{q}_{\rm cm}$ is the CM momentum of meson and nucleon. Consequently, the elementary LA kinetic energy differential cross section is given by

$$\frac{d\sigma}{dT} = 2\pi \frac{\sqrt{s}}{k_0 |\mathbf{q}_{\rm cm}|} \frac{d\sigma}{d\Omega_{\rm cm}}. \tag{B.21}$$

In the nuclear case, the transmission factor $T(\mathbf{r}, q)$ in the exponential of Eq. (B.14) also depends on the meson emission angles. The azimuthal angle θ translates into the kinetic energy whereas the polar angle φ must be integrated over. We thus find

$$\frac{d\sigma_A}{dT} = \frac{\sqrt{s}}{k_0 |\mathbf{q}_{\rm cm}|} \int d^3r \, n_N(\mathbf{r}) \int_0^{2\pi} d\varphi \, \frac{d\sigma_N}{d\Omega_{\rm cm}} \, e^{-T(\mathbf{r},E)} \tag{B.22}$$

with the transmission factor $T(\mathbf{r}, E)$ according to Eq. (B.12).

High-energy (eikonal) limit

In high energy photon nucleon reactions, the reaction products go dominantly in forward direction. This implies $\cos\theta \simeq 1$ and $\sin\theta \simeq 0$ and, thus,

$$|\mathbf{r}'| \simeq \sqrt{b^2 + (z + l)^2} \equiv \sqrt{b^2 + z'^2}. \tag{B.23}$$

As a consequence, the transmission factor $T(\mathbf{r}, q)$ does not longer depend on the meson emission angles and, thus, the φ integration can be carried out:

$$\frac{d\sigma_A}{dT} = 2\pi \frac{\sqrt{s}}{k_0 |\mathbf{q}_{\rm cm}|} \frac{d\sigma_N}{d\Omega_{\rm cm}} \int d^3r \, n_N(\mathbf{r}) \, e^{-T(\mathbf{r},E)} \tag{B.24}$$

$$= \frac{d\sigma_N}{dT} \int d^3r \, n_N(\mathbf{r}) \, e^{-T(\mathbf{r},E)} \tag{B.25}$$

$$= \frac{d\sigma_N}{dT} \cdot A_{\rm eff} \tag{B.26}$$

where in the last step we have defined the effective mass number A_{eff}. It can be interpreted as the effective number of nucleons which participate in the nuclear meson photoproduction process. A_{eff} implicitly depends on the energy and momentum of the produced mesons via the absorptive meson self energy which – via (B.16) – enters the transmission factor $T(\mathbf{r}, E)$.

Applying again the low density theorem $\lambda = (n_N(\mathbf{r}) \cdot \sigma_{\text{abs}})^{-1}$, the effective mass number can be recast in the following way:

$$A_{\text{eff}} = \int d^3r\, n_N(\mathbf{r}) e^{-T(\mathbf{r},E)} \tag{B.27}$$

$$= 2\pi \int bdb \int dz\, n_N(\mathbf{r}) \exp\left(-\sigma_{\text{abs}}(E) \int_z^\infty dz' n_N(\mathbf{b}, z')\right) \tag{B.28}$$

$$= 2\pi \int bdb \int_{-\infty}^{\infty} dz \frac{1}{\sigma_{\text{abs}}(E)} \frac{\partial}{\partial z} \exp\left(-\sigma_{\text{abs}}(E) \int_z^\infty dz' n_N(\mathbf{b}, z')\right) \tag{B.29}$$

$$= \frac{2\pi}{\sigma_{\text{abs}}(E)} \int bdb \left[1 - \exp\left(-\sigma_{\text{abs}}(E) \int_{-\infty}^{+\infty} dz' n_N(\mathbf{b}, z')\right)\right]. \tag{B.30}$$

Note, that this expression depends on the meson energy and momentum only via the absorption cross section $\sigma_{\text{abs}}(E)$. This simplifies the numerical analysis of differential photoproduction cross sections. One can evaluate (B.30) as function of the meson nucleon cross section $\sigma_{\text{abs}}(E)$ and compare it to the data at different values of the meson kinetic energy. In this way the energy dependence of $\sigma_{\text{abs}}(E)$ can be obtained from the data, see Chapters 5 and 9 for the cases of η and ω photoproduction off nuclei.

Limit $\sigma_{\text{abs}} \longrightarrow 0$

This limit is rather trivial. The mean free path becomes infinitely long and, thus, the transmission factor $T(\mathbf{r}, q)$ vanishes. From Eq. (B.27) we find

$$A_{\text{eff}} \longrightarrow A \tag{B.31}$$

and, thus, the nucleus becomes completely transparent. The nuclear photoproduction cross section is $\sigma_A = A \cdot \sigma_N$.

Limit $\sigma_{\text{abs}} \longrightarrow \infty$

This limit can be discussed most intuitively in the approximation of a homogeneous nucleus of constant density. This approximation allows us to carry out the remaining integrals explicitly. For the density distribution we write

$$n_N(\mathbf{r}) = n_0 \Theta(|\mathbf{r}| - R) = \frac{3A}{4\pi R^3} \Theta(|\mathbf{r}| - R), \tag{B.32}$$

where R is the nuclear radius that we parametrize according to $R = r_0 \cdot A^{1/3}$. For the radius parameter r_0 we use the numerical value $r_0 = 1.143$ fm in order to be consistent with $n_0 = 0.16$ fm^{-3}. At this stage we introduce one further abbreviation, namely

$$\lambda_0 = \frac{1}{\sigma_{\rm abs} n_0} \tag{B.33}$$

which is the mean free path of the meson at normal nuclear matter density with respect to meson absorption. Evaluating Eq. (B.30) further we obtain

$$A_{\rm eff} = \frac{2\pi}{\sigma_{\rm abs}} \int_0^R b\, db \left\{ 1 - \exp\left[-\frac{1}{\lambda_0} \int_{-\infty}^{+\infty} dz' \Theta(\sqrt{b^2 + z'^2} - R) \right] \right\} \tag{B.34}$$

$$= \frac{\pi R^2}{\sigma_{\rm abs}} \left\{ 1 - \frac{2}{R^2} \int_0^R b db \exp\left[-2 \frac{\sqrt{R^2 - b^2}}{\lambda_0} \right] \right\}. \tag{B.35}$$

Carrying out the remaining integral, we finally obtain the following expression for the effective mass number:

$$A_{\rm eff} = \frac{\pi R^2}{\sigma_{\rm abs}} \left\{ 1 + \left(\frac{\lambda_0}{R} \right) \exp\left[-2 \frac{R}{\lambda_0} \right] + \frac{1}{2} \left(\frac{\lambda_0}{R} \right)^2 \left(\exp\left[-2 \frac{R}{\lambda_0} \right] - 1 \right) \right\}. \tag{B.36}$$

In the limit where the absorption cross section becomes very large $\sigma_{\rm abs} \to \infty$ and, thus, the mean free path becomes small as compared to the nuclear radius $\lambda_0 / R \to 0$ this expression just reduces to

$$A_{\rm eff} \longrightarrow \frac{\pi R^2}{\sigma_{\rm abs}} = \frac{\pi r_0^2}{\sigma_{\rm abs}} A^{2/3}. \tag{B.37}$$

The nuclear photoproduction cross section now strictly scales according to $\sigma_A \sim A^{2/3}$ independent of the meson absorption cross section $\sigma_{\rm abs}$ as long as the latter one is large.

In Fig. B.1 the effective nuclear mass number divided by $A^{2/3}$ according to Eq. (B.30) for various nuclei is shown. In particular for heavy target nuclei it is quite sensitive to the meson nucleon absorption cross section. This sensitivity, however, is essentially lost for very large meson nucleon cross sections. As discussed previously, in this limit the effective mass number scales like $A_{\rm eff} \sim A^{2/3}$. Furthermore, one can observe in Fig. (B.1) that for low values of the meson nucleon cross section the scaling of the nuclear photoproduction cross section substantially deviates from $\sigma_A \sim A^{2/3}$. This scaling behavior is retrieved only for large meson nucleon cross sections $\sigma_{\rm abs} > 40$ mb.

Resonances

Finally, we want to obtain an expression for the invariant mass differential cross section for the case where the produced particle is unstable. To this end we both rely on the high energy eikonal approximation and the low density theorem, i. e. our starting point

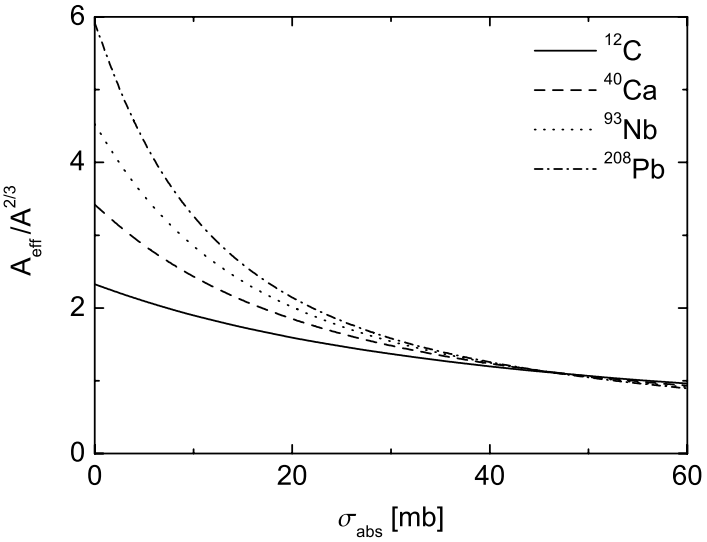

Figure B.1: Effective mass number A_{eff} normalized by $A^{2/3}$ as function of the meson nucleon cross section σ_{abs} according to Eq. (B.30) for various nuclei.

is again the single meson production cross section as given by Eq. (B.10). For the elementary invariant mass differential cross section we write

$$\frac{d\sigma_{\gamma N\to RN}}{dW} = 2W\mathcal{A}_R(W)\sigma_{\gamma N\to RN} \tag{B.38}$$

where W is the invariant resonance mass, $\mathcal{A}_R$ is the spectral function, and $\sigma_{\gamma N\to RN}$ is the total resonance photoproduction cross section from a single nucleon. Since the produced resonance decays, we only observe its decay products. The cross section for a particular channel f is given by

$$\frac{d\sigma_{\gamma A\to f}}{dW} = \frac{d\sigma_{\gamma N\to RN}}{dW}\frac{\Gamma_{R\to f}}{\Gamma_{R\to X}} \tag{B.39}$$

where $\Gamma_{R\to f}$ and $\Gamma_{R\to X}$ are the partial and total spontaneous decay widths of the resonance R in the resonance rest frame. The resonance interactions in the medium cause a density dependence of the spectral function. Thus, the actual width of the observable distribution of the particles in the final state f varies depending on the actual density at the decay coordinates. Moreover, the resonance can only be absorbed up to the point where it eventually decays. A complete expression including all these effects has the following form

$$\begin{aligned}\frac{d\sigma_{\gamma A\to f}}{dW} &= \sigma_{\gamma N\to RN}\frac{\Gamma_{R\to X}}{\gamma}2\pi\int_0^\infty dt\exp\left[-\frac{\Gamma_{R\to X}}{\gamma}t\right]\int_0^\infty bdb\int_{-\infty}^{+\infty}dz\,2W\mathcal{A}_R(W,n_N(\mathbf{r}'))\\ &\quad\times\frac{\Gamma_{R\to f}}{\Gamma_R^{\text{tot}}(\mathbf{b},z+\beta t)}n_N(\mathbf{b},z)\exp\left[-\sigma_{\text{abs}}(E)\int_z^{z+\beta t}dz'\,n_N(\mathbf{b},z')\right]\end{aligned} \tag{B.40}$$

where $\Gamma_R^{\rm tot}$ is the total resonance width in the resonance rest frame including its spontaneous decay width and collisional contributions arising through interactions with the medium:

$$\Gamma_R^{\rm tot}(\mathbf{r}) = \Gamma_{R\to X} + \frac{|\mathbf{q}|}{W}\sigma_{\rm abs}(E)n_N(\mathbf{r}). \tag{B.41}$$

Moreover, $\beta = |\mathbf{q}|/q_0$ is the resonance velocity and $\gamma = q_0/W$ is a Lorentz factor for the transformation from the LA to the resonance rest frame. Equation (B.40) can be recast into the following form that highlights the equivalence of the ω absorption processes to the opening of additional inelastic nuclear decay channels:

$$\begin{aligned}\frac{d\sigma_{\gamma A\to f}}{dW} &= \sigma_{\gamma N\to RN}\frac{\Gamma_{V\to X}}{\gamma}\int_0^\infty bdb\int_{-\infty}^{+\infty}dz\, n_N(\mathbf{b},z)\int_0^\infty dt\exp\left[-\int_0^t\frac{dt'}{\gamma}\Gamma_R^{\rm tot}(\mathbf{b},z+\beta t')\right]\\ &\quad\times 4\pi W\mathcal{A}_R(W,\mathbf{b},z+\beta t)\frac{\Gamma_{R\to f}}{\Gamma_R^{\rm tot}(\mathbf{b},z+\beta t)}.\end{aligned} \tag{B.42}$$

Appendix C

Pion nucleon scattering

We consider the scattering process

$$\pi(p_1) + N(p_2) \to \pi(p_3) + N(p_4). \tag{C.1}$$

The πN scattering amplitude is defined by its relation to the angular differential cross section

$$\frac{d\sigma}{d\Omega} = \frac{1}{2}\sum_{\text{spins}} |f_{\pi N\to\pi N}|^2, \tag{C.2}$$

that is averaged over the initial and summed over the final nucleon spins. The amplitude can be decomposed in two parts, namely a part where the spin of the nucleon remains unchanged and a part where the spin flips:

$$f_{\pi N\to\pi N}(s,\theta) = g(s,\theta) + ih(s,\theta)\boldsymbol{\sigma}\cdot\mathbf{n}. \tag{C.3}$$

Here, $\mathbf{n}$ is a unit-vector normal to the scattering plane and $\boldsymbol{\sigma}$ is the spin$-1/2$ transition operator. The functions g and h have isoscalar and isovector parts:

$$g = g_s + g_v\mathbf{t}\cdot\boldsymbol{\tau} \tag{C.4}$$

$$h = h_s + h_v\mathbf{t}\cdot\boldsymbol{\tau} \tag{C.5}$$

where $\mathbf{t}$ is the isospin of the pion and $\boldsymbol{\tau}$ is the isospin analogue to $\boldsymbol{\sigma}$. g and h obey the partial wave expansions

$$g_{s,v} = \sum_l \left[(l+1)f^{s,v}_{l_+} + l f^{s,v}_{l_-}\right] P_l(\cos\theta) \tag{C.6}$$

$$h_{s,v} = \sin\theta\sum_l \left[f^{s,v}_{l_+} - f^{s,v}_{l_-}\right] P'_l(\cos\theta) \quad \text{with} \quad l_\pm = J \mp \frac{1}{2} \tag{C.7}$$

where P_l and P'_l are the Legendre polynomials and their derivatives, respectively. The amplitudes $f^{s,v}_{l_\pm}$ can be isospin decomposed yielding

$$f^s_{l_\pm} = \frac{2f_{\frac{3}{2},l_\pm} + f_{\frac{1}{2},l_\pm}}{3} \tag{C.8}$$

$$f^v_{l_\pm} = \frac{f_{\frac{3}{2},l_\pm} - f_{\frac{1}{2},l_\pm}}{3}. \tag{C.9}$$

For each partial wave the isospin amplitudes $f_{I,l_\pm}$ are related to the complex phase shifts $\delta_{I,l_\pm}$ and inelasticity parameters $\eta_{I,l_\pm} = \exp(-2\mathcal{I}\mathrm{m}\delta_{I,l_\pm})$ by

$$f_{I,l_\pm} = \frac{1}{2i|\mathbf{q}|}\left(\eta_{I,l_\pm} e^{2i\mathcal{R}\mathrm{e}\delta_{I,l_\pm}} - 1\right). \tag{C.10}$$

The phase shifts $\delta_{I,l_\pm}$ and inelasticities $\eta_{I,l_\pm}$ have been determined experimentally by means of the SAID analysis [109]. More details on the phenomenology of πN scattering can be found for instance in [63].

Appendix D

Amplitudes for the $\pi\mathrm{N} \longrightarrow \pi\pi\mathrm{N}$ reaction

D.1 Cross section

We consider the process $\pi(p_1)N(p_2) \rightarrow N(p_3)\pi(p_4)\pi(p_5)$ with $p_i = (E_i, \mathbf{p}_i)$ the four-momenta of the particles. The multi-fold differential cross section can be written as [58]

$$d\sigma = \frac{S}{(2\pi)^5} \frac{m_N^2}{\lambda^{1/2}(s, m_\pi^2, m_N^2)} \prod_{i=3}^{5} \frac{d^3p_i}{2E_i} \frac{1}{2} \sum_{s_i} \sum_{s_f} |\mathcal{M}|^2 \delta^{(4)}(p_1 + p_2 - p_3 - p_4 - p_5) \quad \text{(D.1)}$$

where m_N and m_π are the masses of nucleon and pion, respectively, and $\frac{1}{2}\sum\sum|\mathcal{M}|^2$ stands for the amplitude squared, summed and averaged over the final and initial nucleon spin orientations. S is a symmetry factor

$$S = \prod_l k_l! \quad \text{(D.2)}$$

for k_l identical particles of species l in the final state. Depending on the isospin channel, S can take the values 1 or 2 in our case. The Kallen-function λ has the form

$$\lambda(x, y, z) = x^2 + y^2 + z^2 - 2(xy + xz + yz). \quad \text{(D.3)}$$

Working out the phase space one obtains for the total cross section [97]

$$\begin{aligned} \sigma &= \frac{m_N^2}{\lambda^{1/2}(s, m_\pi^2, m_N^2)} \frac{S}{4(2\pi)^4} \times \\ &\int_{E_4^-}^{E_4^+} d\omega_4 \int_{E_5^-(\omega_4)}^{E_5^+(\omega_4)} d\omega_5 \int_{-1}^{+1} d(\cos\theta_4) \int_0^{2\pi} d\phi_{45} \Theta(1 - \cos^2\theta_{45}) \frac{1}{2} \sum\sum |\mathcal{M}|^2 \end{aligned} \quad \text{(D.4)}$$

where ω_4 and ω_5 are the energies of the final state pions and s is the total CM energy squared. ϕ_{45} and θ_{45} are the azimuthal and polar angles of $\mathbf{p}_4$ with respect to $\mathbf{p}_5$ and

θ_4 is the angle of $\mathbf{p}_4$ with the $z-$direction defined by the incoming pion momentum $\mathbf{p}_1$. The integration boundaries are given by

$$E_4^- = m_\pi \tag{D.5}$$

$$E_4^+ = \frac{s + m_\pi^2 - (m_N + m_\pi)^2}{2\sqrt{s}} \tag{D.6}$$

$$E_5^- = \frac{s + m_\pi^2 - s_{24}^+}{2\sqrt{s}} \tag{D.7}$$

$$E_5^+ = \frac{s + m_\pi^2 - s_{24}^-}{2\sqrt{s}} \tag{D.8}$$

with

$$s_{24}^\pm = m_N^2 + m_\pi^2 - \frac{(s_{25} - s - m_\pi^2)(s_{25} + m_N^2 - m_\pi^2) \mp \lambda^{\frac{1}{2}}(s_{25}, s, m_\pi^2)\lambda^{\frac{1}{2}}(s_{25}, m_N^2, m_\pi^2)}{2s_{25}} \tag{D.9}$$

$$s_{25} = s + m_\pi^2 - 2\sqrt{s}\omega_4 \tag{D.10}$$

The remaining four-dimensional integral in Eq. (D.4) is solved numerically by means of a Gaussian quadrature method. Useful formulas concerning the calculation of total and differential cross section for the case of many-body final states can for instance be found in [308].

D.2 Lagrangians, propagators and widths

The diagrams 1(a), 1(b), 2(a) and 2(c) in Fig. 4.3 require the following pion nucleon Lagrangians [129, 139]:

$$\mathcal{L}_{\pi NN} = \frac{f}{m_\pi}\psi^\dagger \sigma_i (\partial_i \boldsymbol{\phi})\boldsymbol{\tau}\psi \tag{D.11}$$

$$\mathcal{L}_{\pi\pi\pi\pi} = -\frac{1}{4f_\pi^2}\left[\boldsymbol{\phi}^2(\partial^\mu \boldsymbol{\phi})^2 - \frac{m_\pi^2}{2}(\boldsymbol{\phi}^2)^2\right] \tag{D.12}$$

$$\mathcal{L}_{\pi\pi\pi NN} = -\frac{f}{m_\pi}\frac{1}{4f_\pi^2}\psi^\dagger \sigma_i (\partial_i \boldsymbol{\phi})\boldsymbol{\phi}^2\boldsymbol{\tau}\psi \tag{D.13}$$

$$\mathcal{L}_{\pi\pi NN} = -4\pi\left[\frac{\lambda_1}{m_\pi}\bar{\psi}\boldsymbol{\phi}\cdot\boldsymbol{\phi}\psi + \frac{\lambda_2^2}{m_\pi^2}\bar{\psi}\boldsymbol{\tau}(\boldsymbol{\phi}\times\partial_0\boldsymbol{\phi})\psi\right]. \tag{D.14}$$

The coupling constant f in (D.11) and (D.13) is given by $f = g_\pi m_\pi/(2m_N)$ with $g_\pi = 13.26$. In (D.12) the weak pion decay constant enters, taken to be $f_\pi = 87$ MeV. The parameters λ_1 and λ_2 in (D.14) are related to the $s-$wave pion nucleon scattering lengths. They have the values $\lambda_1 = 0.0075$ and $\lambda_2 = 0.053$. We also consider the coupling of the two pions in relative $p-$wave via an intermediate ρ meson. The Lagrangians needed for these contributions are

$$\mathcal{L}_{\rho\pi\pi} = -f_\rho \boldsymbol{\phi}_i \cdot (\boldsymbol{\phi}\times\partial_i\boldsymbol{\phi}) \tag{D.15}$$

$$\mathcal{L}_{\rho NN} = \sqrt{C_\rho}\frac{f}{m_\pi}\psi_N^\dagger \epsilon_{ijk}\sigma_i(\partial_j\boldsymbol{\rho}_k)\boldsymbol{\tau}\psi_N \tag{D.16}$$

where the scaling factor C_ρ is related to the usual coupling constants used in pion nucleon scattering via

$$\sqrt{C_\rho} = \left(\frac{f_{\Delta N\rho}}{m_\rho}\right)\left(\frac{f^*}{m_\pi}\right)^{-1}. \tag{D.17}$$

Here we use $C_\rho = 2$ and $f_\rho = 6.14$. The diagrams 3(a)–(c) in addition include the excitation of $\Delta(1232)$ resonances. The corresponding Lagrangians are given by

$$\mathcal{L}_{\Delta N\pi} = \frac{f^*}{m_\pi}\psi^\dagger_\Delta S^\dagger_i(\partial_i\boldsymbol{\phi})\mathbf{T}^\dagger\psi_N + h.c. \tag{D.18}$$

$$\mathcal{L}_{\Delta N\rho} = \sqrt{C_\rho}\frac{f^*}{m_\pi}\psi^\dagger_\Delta\epsilon_{ijk}S^\dagger_i\left(\partial_j\boldsymbol{\rho}_k\right)\mathbf{T}^\dagger\psi_N + h.c. \tag{D.19}$$

$$\mathcal{L}_{\pi\Delta\Delta} = \frac{f_\Delta}{m_\pi}\psi^\dagger_\Delta S_{\Delta i}\left(\partial_i\boldsymbol{\phi}\right)\mathbf{T}_\Delta\psi_\Delta. \tag{D.20}$$

We use $f^* = 2.13$ and $f_\Delta = (4/5)f$. Finally, we also include the $N^*(1440)$ resonance in the intermediate states. It can be coupled into our model by adding the phenomenological Lagrangians

$$\mathcal{L}_{N^*N\pi\pi} = -C\psi^\dagger_{N^*}\boldsymbol{\phi}\cdot\boldsymbol{\phi}\psi_N + h.c. \tag{D.21}$$

$$\mathcal{L}_{N^*N\pi} = \frac{\tilde{f}}{m_\pi}\psi^\dagger_{N^*}\sigma_i\left(\partial_i\boldsymbol{\phi}\right)\boldsymbol{\tau}\psi + h.c. \tag{D.22}$$

$$\mathcal{L}_{N^*\Delta\pi} = \frac{g_{N^*\Delta\pi}}{m_\pi}\psi^\dagger_\Delta S^\dagger_i\left(\partial_i\boldsymbol{\phi}\right)\mathbf{T}^\dagger\psi_{N^*} + h.c. \tag{D.23}$$

with $C = -2.29/m_\pi$, $\tilde{f} = 0.477$ and $g_{N^*\Delta\pi} = 2.07$. For the mass and width of the N^* resonance we have $m_{N^*} = 1.462$ GeV and $\Gamma_{N^*} = 0.235$ GeV.

In addition to the couplings we also need to specify the propagators of the intermediate particles. The non-relativistic π and ρ propagators are given by

$$\mathcal{D}_\pi(q) = \frac{1}{q_0^2 - \mathbf{q}^2 - m_\pi^2} \tag{D.24}$$

$$\mathcal{D}_\rho(q) = \frac{1}{q_0^2 - \mathbf{q}^2 - m_\rho^2 + im_\rho\Gamma_\rho} \tag{D.25}$$

Here, Γ_ρ is the total width of the ρ meson. It is almost saturated by the ρ decay width into two pions

$$\Gamma_{\rho\to\pi\pi}(W) = \frac{1}{6\pi}f_\rho^2\frac{|\mathbf{p}_{\rm cm}|^3}{W^2}\Theta(W - 2m_\pi) \tag{D.26}$$

where $|\mathbf{p}_{\rm cm}|$ is the CM momentum of the pions and W is the invariant mass of the ρ. For the non-relativistic nucleon propagator we take

$$\mathcal{G}_N(p) = \frac{1}{\sqrt{p_0^2 - \mathbf{p}^2} - m_N} \tag{D.27}$$

and for the Δ resonance we have

$$\mathcal{G}_\Delta(k) = \frac{1}{\sqrt{k_0^2 - \mathbf{k}^2} - M_\Delta + \frac{1}{2}i\Gamma_\Delta(W)} \tag{D.28}$$

with $k = (k_0, \mathbf{k})$ the momentum of the resonance, $W = \sqrt{k^2}$ and $\Gamma_\Delta(W)$ its total width that can be taken approximately equal to the partial $\Delta \to N\pi$ decay width. From the Lagrangian (D.18) one obtains

$$\Gamma_\Delta(W) = \frac{1}{6\pi}\left(\frac{f_\Delta}{m_\pi}\right)^2 \frac{m_N}{W}|\mathbf{q}_{\rm cm}|^3\Theta(W - m_N - m_\pi). \tag{D.29}$$

The step function denotes the fact that the width is zero for masses below the $N\pi$ threshold; W is the Δ invariant mass and $\mathbf{q}_{\rm cm}$ the pion momentum in the rest frame of the resonance as given by Eq. (E.5). Finally, we also need the Roper propagator. It is given by

$$\mathcal{G}_{N^*}(k) = \frac{1}{\sqrt{k_0^2 - \mathbf{k}^2} - m_{N^*} + \frac{1}{2}i\Gamma_{N^*}(W)} \tag{D.30}$$

with the total Roper width Γ_{N^*}. In our model the Roper has three decay channels, namely $N^* \to N\pi$, $N^* \to N(\pi\pi)_{s-\rm wave}$ and $N^* \to \Delta\pi$. The latter one has been discussed in Section 4.3.2. For the $N\pi$ decay we find

$$\Gamma_{N^*\to N\pi}(W) = \frac{3}{2\pi}\left(\frac{\tilde{f}}{m_\pi}\right)^2 \frac{m_N}{W}|\mathbf{q}_{\rm cm}|^3\Theta(W - m_N - m_\pi). \tag{D.31}$$

and for the decay into $s-$wave pions we take

$$\Gamma_{N^*\to N(\pi\pi)_{s-\rm wave}}(W) = \frac{3}{16\pi^3}C^2\frac{m_N}{W^2}\int\limits_{4m_\pi^2}^{(W-m_N)^2} dx \frac{\sqrt{\lambda(W^2, x, m_\pi^2)\lambda(x, m_\pi^2, m_\pi^2)}}{x} \tag{D.32}$$

where λ is the Kallen function given in Eq. (D.3).

D.3 Spin and isospin relations

Proton and neutron form a SU(2) isospin douplet. Their isospin wave functions are

$$|p\rangle \equiv \chi_p = \begin{pmatrix}1\\0\end{pmatrix} \qquad |n\rangle \equiv \chi_n = \begin{pmatrix}0\\1\end{pmatrix}. \tag{D.33}$$

The isospin$-1/2$ operator which induces transition between these two states forms a vector in isospin space

$$\boldsymbol{\tau} = \begin{pmatrix}\tau_1\\\tau_2\\\tau_3\end{pmatrix} \tag{D.34}$$

where the τ_i are represented by the Pauli matrices

$$\tau_1 = \begin{pmatrix}0 & 1\\1 & 0\end{pmatrix}, \quad \tau_2 = \begin{pmatrix}0 & -i\\i & 0\end{pmatrix}, \quad \tau_3 = \begin{pmatrix}1 & 0\\0 & -1\end{pmatrix}. \tag{D.35}$$

Proton and neutron are isospin eigenstates of τ_3

$$\tau_3|p\rangle = |p\rangle \qquad \tau_3|n\rangle = -|n\rangle. \tag{D.36}$$

The isospin raising and lowering operators are defined in the charge basis as

$$\tau_\pm = \frac{\tau_1 \pm i\tau_2}{2} \tag{D.37}$$

and thus

$$\tau_-|p\rangle = |n\rangle \qquad \tau_+|n\rangle = |p\rangle. \tag{D.38}$$

The pion has isospin 1 and, thus, is itself a vector in isospin space. In a cartesian basis in analogy to (D.34) the pion field is defined as

$$\boldsymbol{\phi} = \begin{pmatrix} \phi_1 \\ \phi_2 \\ \phi_3 \end{pmatrix}. \tag{D.39}$$

In the charge basis it, however, takes the form

$$\phi_\pm = \frac{\phi_1 \pm i\phi_2}{\sqrt{2}} \qquad \phi_0 = \phi_3. \tag{D.40}$$

In the language of second quantization, ϕ_+ creates a π^+ or destroys a π^- and vice versa for ϕ_-. With the above definitions, we find the following relations

$$\boldsymbol{\tau}\cdot\boldsymbol{\phi} = \sqrt{2}\tau_+\phi_- + \sqrt{2}\tau_-\phi_+ + \tau_3\phi_0 \tag{D.41}$$

$$\boldsymbol{\phi}^2 = \phi_0\phi_0 + 2\phi_+\phi_-. \tag{D.42}$$

In the following we give some relations which are important in the evaluation of the actual amplitudes when summing over the spin of the intermediate Δ resonances. In the spin (isospin) 3/2 sector $\mathbf{S}^\dagger(\mathbf{T}^\dagger)$ are the spin (isospin) $1/2 \to 3/2$ transition operators, defined such that their matrix elements simply become Clebsh-Gordan coefficients

$$\langle \tfrac{3}{2}s'|S^\dagger_\lambda|\tfrac{1}{2}s\rangle = (\tfrac{1}{2}s1\lambda|\tfrac{3}{2}s') \tag{D.43}$$

and follow the closure sum

$$\sum_s S_i|\tfrac{3}{2}s\rangle\langle\tfrac{3}{2}s|S^\dagger_j = \delta_{ij} - \frac{1}{3}\sigma_i\sigma_j = \frac{2}{3}\delta_{ij} - \frac{1}{3}i\epsilon_{ijk}\sigma_k \tag{D.44}$$

where σ_i is the spin (isospin) 1/2 operator represented by the Pauli matrices (D.35). Explicitely, the spin (isospin) $1/2 \to 3/2$ operator is given by

$$S_0 = \frac{|\mathbf{k}|}{m}\begin{pmatrix} 0 & \sqrt{2/3} & 0 & 0 \\ 0 & 0 & \sqrt{2/3} & 0 \end{pmatrix} \tag{D.45}$$

$$S_1 = \begin{pmatrix} -\sqrt{1/2} & 0 & \sqrt{1/6} & 0 \\ 0 & -\sqrt{1/6} & 0 & \sqrt{1/2} \end{pmatrix} \tag{D.46}$$

$$S_2 = i\begin{pmatrix} \sqrt{1/2} & 0 & \sqrt{1/6} & 0 \\ 0 & \sqrt{1/6} & 0 & \sqrt{1/2} \end{pmatrix} \tag{D.47}$$

$$S_3 = \frac{k_0}{|\mathbf{k}|}S_0 \tag{D.48}$$

For the hermitean conjugate of the spin (isospin) 3/2 operator in the charge basis we thus have

$$S_+^\dagger = -S_- \qquad S_-^\dagger = -S_+ \qquad S_0^\dagger = S_0 \tag{D.49}$$

and the product of the isospin $1/2 \to 3/2$ and the pion field operator in the charge basis is given by

$$\boldsymbol{\phi} \cdot \mathbf{T} = \phi_+ T_- - \phi_- T_+ + \phi_0 T_0. \tag{D.50}$$

Furthermore, $\mathbf{S}_\Delta(\mathbf{T}_\Delta)$ is the spin (isospin) 3/2 operator. It is defined such that

$$\langle \tfrac{3}{2} s' | S_{\Delta\lambda} | \tfrac{3}{2} s \rangle = \frac{1}{\sqrt{2(3/2)+1}} (\tfrac{3}{2} s 1 \lambda | \tfrac{3}{2} s') \langle \tfrac{3}{2} \| S_\Delta \| \tfrac{3}{2} \rangle \tag{D.51}$$

with

$$\frac{1}{\sqrt{2(3/2)+1}} \langle \tfrac{3}{2} \| S_\Delta \| \tfrac{3}{2} \rangle = \sqrt{\frac{3}{2}\left(\frac{3}{2}+1\right)} = \frac{\sqrt{15}}{2}. \tag{D.52}$$

When summing over polarizations of the intermediate Δ states, it is useful to implement the following closure relationship

$$\sum_{s,s'} S_i | \tfrac{3}{2} s' \rangle \langle \tfrac{3}{2} s' | S_{\Delta j} | \tfrac{3}{2} s \rangle \langle \tfrac{3}{2} s | S_k^\dagger = \frac{5}{6} i\epsilon_{ijk} - \frac{1}{6}\delta_{ij}\sigma_k + \frac{2}{3}\delta_{ik}\sigma_j - \frac{1}{6}\delta_{jk}\sigma_i. \tag{D.53}$$

D.4 Amplitudes

In Eq. (D.34) we need the summed and squared amplitude $\frac{1}{2}\sum |\mathcal{M}|^2$. In our non-relativistic model the ampitude is a 2×2 matrix due to the spin structure of the external particles. Thus, the summed and squared amplitude is given by

$$\frac{1}{2}\sum_s \sum_r |\mathcal{M}|^2 = \frac{1}{2}\mathrm{Tr}\,\mathcal{M}^\dagger \mathcal{M} = \frac{1}{2}\left(\mathcal{M}_{11}^\dagger \mathcal{M}_{11} + \mathcal{M}_{22}^\dagger \mathcal{M}_{22}\right) \tag{D.54}$$

where the sums run over the initial and final nucleon spin orientations. The amplitude depends on the four-momenta of the external particles. Using the notation invented previously we have

$$\mathcal{M} = \mathcal{M}(p_1, p_2, p_3, p_4, p_5). \tag{D.55}$$

In the following we give the amplitudes for the processes shown in diagrams 4a−c of Fig. 4.3 which have not been included in Ref. [129]. For each diagram we take into account all possible time orderings. Ω is an isospin factor that will be specified further below. Together with the amplitudes evaluated in [129], also taking into account their various time orderings, our model includes 74 different amplitudes. Their coherent sum represents our complete model.

Diagram 4(a):

$$
\begin{aligned}
\mathcal{M}_{4a}^{(a)} &= -iC\frac{\tilde{f}}{m_\pi}\Omega_{4a}^{(a)}(\boldsymbol{\sigma}\cdot\mathbf{p}_1)\,\mathcal{G}_{N^*}(p_1+p_2)\\
\mathcal{M}_{4a}^{(b)} &= -iC\frac{\tilde{f}}{m_\pi}\Omega_{4a}^{(b)}(\boldsymbol{\sigma}\cdot\mathbf{p}_1)\,\mathcal{G}_{N^*}(p_2-p_4-p_5)\\
\mathcal{M}_{4a}^{(c)} &= -iC\frac{\tilde{f}}{m_\pi}\Omega_{4a}^{(c)}(\boldsymbol{\sigma}\cdot\mathbf{p}_4)\,\mathcal{G}_{N^*}(p_2-p_4)\\
\mathcal{M}_{4a}^{(d)} &= -iC\frac{\tilde{f}}{m_\pi}\Omega_{4a}^{(d)}(\boldsymbol{\sigma}\cdot\mathbf{p}_4)\,\mathcal{G}_{N^*}(p_1+p_2-p_5)\\
\mathcal{M}_{4a}^{(e)} &= -iC\frac{\tilde{f}}{m_\pi}\Omega_{4a}^{(e)}(\boldsymbol{\sigma}\cdot\mathbf{p}_5)\,\mathcal{G}_{N^*}(p_2-p_5)\\
\mathcal{M}_{4a}^{(f)} &= -iC\frac{\tilde{f}}{m_\pi}\Omega_{4a}^{(f)}(\boldsymbol{\sigma}\cdot\mathbf{p}_5)\,\mathcal{G}_{N^*}(p_1+p_2-p_4)
\end{aligned}
$$

Diagram 4(b):

$$
\begin{aligned}
\mathcal{M}_{4b}^{(a)} &= -i\frac{\tilde{f}}{m_\pi}\frac{g_{N^*\Delta\pi}f^*}{m_\pi^2}\frac{1}{3}\Omega_{4b}^{(a)}(\boldsymbol{\sigma}\mathbf{p}_4)\cdot[2\mathbf{p}_1\mathbf{p}_5-i(\mathbf{p}_1\times\mathbf{p}_5)\boldsymbol{\sigma}]\\
&\qquad \mathcal{G}_\Delta(p_1+p_2)\,\mathcal{G}_{N^*}(p_1+p_2-p_5)\\
\mathcal{M}_{4b}^{(b)} &= -i\frac{\tilde{f}}{m_\pi}\frac{g_{N^*\Delta\pi}f^*}{m_\pi^2}\frac{1}{3}\Omega_{4b}^{(b)}\,[2\mathbf{p}_1\mathbf{p}_5-i(\mathbf{p}_1\times\mathbf{p}_5)\boldsymbol{\sigma}]\cdot(\boldsymbol{\sigma}\mathbf{p}_4)\\
&\qquad \mathcal{G}_{N^*}(p_2-p_4)\,\mathcal{G}_\Delta(p_1+p_2-p_4)\\
\mathcal{M}_{4b}^{(c)} &= -i\frac{\tilde{f}}{m_\pi}\frac{g_{N^*\Delta\pi}f^*}{m_\pi^2}\frac{1}{3}\Omega_{4b}^{(c)}(\boldsymbol{\sigma}\mathbf{p}_4)\cdot[2\mathbf{p}_1\mathbf{p}_5+i(\mathbf{p}_1\times\mathbf{p}_5)\boldsymbol{\sigma}]\\
&\qquad \mathcal{G}_\Delta(p_2-p_5)\,\mathcal{G}_{N^*}(p_1+p_2-p_5)\\
\mathcal{M}_{4b}^{(d)} &= -i\frac{\tilde{f}}{m_\pi}\frac{g_{N^*\Delta\pi}f^*}{m_\pi^2}\frac{1}{3}\Omega_{4b}^{(d)}\,[2\mathbf{p}_1\mathbf{p}_5+i(\mathbf{p}_1\times\mathbf{p}_5)\boldsymbol{\sigma}]\cdot(\boldsymbol{\sigma}\mathbf{p}_4)\\
&\qquad \mathcal{G}_{N^*}(p_2-p_4)\,\mathcal{G}_\Delta(p_2-p_4-p_5)\\
\mathcal{M}_{4b}^{(e)} &= -i\frac{\tilde{f}}{m_\pi}\frac{g_{N^*\Delta\pi}f^*}{m_\pi^2}\frac{1}{3}\Omega_{4b}^{(e)}(\boldsymbol{\sigma}\mathbf{p}_1)\cdot[2\mathbf{p}_4\mathbf{p}_5-i(\mathbf{p}_4\times\mathbf{p}_5)\boldsymbol{\sigma}]\\
&\qquad \mathcal{G}_\Delta(p_2-p_4)\,\mathcal{G}_{N^*}(p_2-p_4-p_5)\\
\mathcal{M}_{4b}^{(f)} &= -i\frac{\tilde{f}}{m_\pi}\frac{g_{N^*\Delta\pi}f^*}{m_\pi^2}\frac{1}{3}\Omega_{4b}^{(f)}\,[2\mathbf{p}_4\mathbf{p}_5-i(\mathbf{p}_4\times\mathbf{p}_5)\boldsymbol{\sigma}]\cdot(\boldsymbol{\sigma}\mathbf{p}_1)\\
&\qquad \mathcal{G}_{N^*}(p_1+p_2)\,\mathcal{G}_\Delta(p_1+p_2-p_4)\\
\mathcal{M}_{4b}^{(g)} &= -i\frac{\tilde{f}}{m_\pi}\frac{g_{N^*\Delta\pi}f^*}{m_\pi^2}\frac{1}{3}\Omega_{4b}^{(g)}(\boldsymbol{\sigma}\mathbf{p}_1)\cdot[2\mathbf{p}_4\mathbf{p}_5+i(\mathbf{p}_4\times\mathbf{p}_5)\boldsymbol{\sigma}]\\
&\qquad \mathcal{G}_\Delta(p_2-p_5)\,\mathcal{G}_{N^*}(p_2-p_4-p_5)
\end{aligned}
$$

$$
\begin{aligned}
\mathcal{M}_{4b}^{(h)} &= -i\frac{\tilde{f}}{m_\pi}\frac{g_{N^*\Delta\pi}f^*}{m_\pi^2}\frac{1}{3}\Omega_{4b}^{(h)}\,[2\mathbf{p}_4\mathbf{p}_5 + i(\mathbf{p}_4\times\mathbf{p}_5)\boldsymbol{\sigma}]\cdot(\boldsymbol{\sigma}\mathbf{p}_1) \\
&\qquad \mathcal{G}_\Delta(p_2-p_5)\,\mathcal{G}_{N^*}(p_2-p_4-p_5) \\
\mathcal{M}_{4b}^{(i)} &= -i\frac{\tilde{f}}{m_\pi}\frac{g_{N^*\Delta\pi}f^*}{m_\pi^2}\frac{1}{3}\Omega_{4b}^{(i)}(\boldsymbol{\sigma}\mathbf{p}_5)\cdot[2\mathbf{p}_1\mathbf{p}_4 - i(\mathbf{p}_1\times\mathbf{p}_4)\boldsymbol{\sigma}] \\
&\qquad \mathcal{G}_\Delta(p_1+p_2)\,\mathcal{G}_{N^*}(p_1+p_2-p_4) \\
\mathcal{M}_{4b}^{(j)} &= -i\frac{\tilde{f}}{m_\pi}\frac{g_{N^*\Delta\pi}f^*}{m_\pi^2}\frac{1}{3}\Omega_{4b}^{(j)}\,[2\mathbf{p}_1\mathbf{p}_4 - i(\mathbf{p}_1\times\mathbf{p}_4)\boldsymbol{\sigma}]\cdot(\boldsymbol{\sigma}\mathbf{p}_5) \\
&\qquad \mathcal{G}_{N^*}(p_2-p_5)\,\mathcal{G}_\Delta(p_1+p_2-p_5) \\
\mathcal{M}_{4b}^{(k)} &= -i\frac{\tilde{f}}{m_\pi}\frac{g_{N^*\Delta\pi}f^*}{m_\pi^2}\frac{1}{3}\Omega_{4b}^{(k)}(\boldsymbol{\sigma}\mathbf{p}_5)\cdot[2\mathbf{p}_1\mathbf{p}_4 + i(\mathbf{p}_1\times\mathbf{p}_4)\boldsymbol{\sigma}] \\
&\qquad \mathcal{G}_\Delta(p_2-p_4)\,\mathcal{G}_{N^*}(p_1+p_2-p_4) \\
\mathcal{M}_{4b}^{(l)} &= -i\frac{\tilde{f}}{m_\pi}\frac{g_{N^*\Delta\pi}f^*}{m_\pi^2}\frac{1}{3}\Omega_{4b}^{(l)}\,[2\mathbf{p}_1\mathbf{p}_4 + i(\mathbf{p}_1\times\mathbf{p}_4)\boldsymbol{\sigma}]\cdot(\boldsymbol{\sigma}\mathbf{p}_5) \\
&\qquad \mathcal{G}_{N^*}(p_2-p_5)\,\mathcal{G}_\Delta(p_2-p_4-p_5)
\end{aligned}
$$

Diagram 4(c):

$$
\begin{aligned}
\mathcal{M}_{4c}^{(a)} &= -if\frac{\tilde{f}^2}{m_\pi^3}\Omega_{4c}^{(a)}\,[(\mathbf{p}_1\mathbf{p}_5)(\boldsymbol{\sigma}\mathbf{p}_4) + (\mathbf{p}_4\mathbf{p}_5)(\boldsymbol{\sigma}\mathbf{p}_1) - (\mathbf{p}_1\mathbf{p}_4)(\boldsymbol{\sigma}\mathbf{p}_5) \\
&\qquad +i(\mathbf{p}_5\times\mathbf{p}_1)\mathbf{p}_4]\,\mathcal{G}_{N^*}(p_1+p_2-p_5)\mathcal{G}_N(p_1+p_2) \\
\mathcal{M}_{4c}^{(b)} &= -if\frac{\tilde{f}^2}{m_\pi^3}\Omega_{4c}^{(b)}\,[(\mathbf{p}_4\mathbf{p}_5)(\boldsymbol{\sigma}\mathbf{p}_1) + (\mathbf{p}_1\mathbf{p}_5)(\boldsymbol{\sigma}\mathbf{p}_4) - (\mathbf{p}_1\mathbf{p}_4)(\boldsymbol{\sigma}\mathbf{p}_5) \\
&\qquad +i(\mathbf{p}_5\times\mathbf{p}_4)\mathbf{p}_1]\,\mathcal{G}_{N^*}(p_2-p_4)\mathcal{G}_N(p_2-p_4-p_5) \\
\mathcal{M}_{4c}^{(c)} &= -if\frac{\tilde{f}^2}{m_\pi^3}\Omega_{4c}^{(c)}\,[(\mathbf{p}_1\mathbf{p}_4)(\boldsymbol{\sigma}\mathbf{p}_5) + (\mathbf{p}_4\mathbf{p}_5)(\boldsymbol{\sigma}\mathbf{p}_1) - (\mathbf{p}_1\mathbf{p}_5)(\boldsymbol{\sigma}\mathbf{p}_4) \\
&\qquad +i(\mathbf{p}_4\times\mathbf{p}_1)\mathbf{p}_5]\,\mathcal{G}_{N^*}(p_1+p_2-p_4)\mathcal{G}_N(p_1+p_2) \\
\mathcal{M}_{4c}^{(d)} &= -if\frac{\tilde{f}^2}{m_\pi^3}\Omega_{4c}^{(d)}\,[(\mathbf{p}_4\mathbf{p}_5)(\boldsymbol{\sigma}\mathbf{p}_1) + (\mathbf{p}_1\mathbf{p}_4)(\boldsymbol{\sigma}\mathbf{p}_5) - (\mathbf{p}_1\mathbf{p}_5)(\boldsymbol{\sigma}\mathbf{p}_4) \\
&\qquad +i(\mathbf{p}_4\times\mathbf{p}_5)\mathbf{p}_1]\,\mathcal{G}_{N^*}(p_2-p_5)\mathcal{G}_N(p_2-p_4-p_5) \\
\mathcal{M}_{4c}^{(e)} &= -if\frac{\tilde{f}^2}{m_\pi^3}\Omega_{4c}^{(e)}\,[(\mathbf{p}_1\mathbf{p}_4)(\boldsymbol{\sigma}\mathbf{p}_5) + (\mathbf{p}_1\mathbf{p}_5)(\boldsymbol{\sigma}\mathbf{p}_4) - (\mathbf{p}_4\mathbf{p}_5)(\boldsymbol{\sigma}\mathbf{p}_1) \\
&\qquad +i(\mathbf{p}_1\times\mathbf{p}_4)\mathbf{p}_5]\,\mathcal{G}_{N^*}(p_2-p_4)\mathcal{G}_N(p_1+p_2-p_4)
\end{aligned}
$$

$$
\begin{aligned}
\mathcal{M}_{4c}^{(f)} &= -if\frac{\tilde{f}^2}{m_\pi^3}\Omega_{4c}^{(f)}\left[(\mathbf{p}_1\mathbf{p}_5)(\boldsymbol{\sigma}\mathbf{p}_4)+(\mathbf{p}_1\mathbf{p}_4)(\boldsymbol{\sigma}\mathbf{p}_5)-(\mathbf{p}_4\mathbf{p}_5)(\boldsymbol{\sigma}\mathbf{p}_1)\right.\\
&\qquad \left.+i(\mathbf{p}_1\times\mathbf{p}_5)\mathbf{p}_4\right]\mathcal{G}_{N^*}(p_2-p_5)\mathcal{G}_N(p_1+p_2-p_5)\\
\mathcal{M}_{4c}^{(g)} &= -if\frac{\tilde{f}^2}{m_\pi^3}\Omega_{4c}^{(g)}\left[(\mathbf{p}_1\mathbf{p}_5)(\boldsymbol{\sigma}\mathbf{p}_4)+(\mathbf{p}_4\mathbf{p}_5)(\boldsymbol{\sigma}\mathbf{p}_1)-(\mathbf{p}_1\mathbf{p}_4)(\boldsymbol{\sigma}\mathbf{p}_5)\right.\\
&\qquad \left.+i(\mathbf{p}_5\times\mathbf{p}_1)\mathbf{p}_4\right]\mathcal{G}_N(p_1+p_2-p_5)\mathcal{G}_{N^*}(p_1+p_2)\\
\mathcal{M}_{4c}^{(h)} &= -if\frac{\tilde{f}^2}{m_\pi^3}\Omega_{4c}^{(h)}\left[(\mathbf{p}_4\mathbf{p}_5)(\boldsymbol{\sigma}\mathbf{p}_1)+(\mathbf{p}_1\mathbf{p}_5)(\boldsymbol{\sigma}\mathbf{p}_4)-(\mathbf{p}_1\mathbf{p}_4)(\boldsymbol{\sigma}\mathbf{p}_5)\right.\\
&\qquad \left.+i(\mathbf{p}_5\times\mathbf{p}_4)\mathbf{p}_1\right]\mathcal{G}_N(p_2-p_4)\mathcal{G}_{N^*}(p_2-p_4-p_5)\\
\mathcal{M}_{4c}^{(i)} &= -if\frac{\tilde{f}^2}{m_\pi^3}\Omega_{4c}^{(i)}\left[(\mathbf{p}_1\mathbf{p}_4)(\boldsymbol{\sigma}\mathbf{p}_5)+(\mathbf{p}_4\mathbf{p}_5)(\boldsymbol{\sigma}\mathbf{p}_1)-(\mathbf{p}_1\mathbf{p}_5)(\boldsymbol{\sigma}\mathbf{p}_4)\right.\\
&\qquad \left.+i(\mathbf{p}_4\times\mathbf{p}_1)\mathbf{p}_5\right]\mathcal{G}_N(p_1+p_2-p_4)\mathcal{G}_{N^*}(p_1+p_2)\\
\mathcal{M}_{4c}^{(j)} &= -if\frac{\tilde{f}^2}{m_\pi^3}\Omega_{4c}^{(j)}\left[(\mathbf{p}_4\mathbf{p}_5)(\boldsymbol{\sigma}\mathbf{p}_1)+(\mathbf{p}_1\mathbf{p}_4)(\boldsymbol{\sigma}\mathbf{p}_5)-(\mathbf{p}_1\mathbf{p}_5)(\boldsymbol{\sigma}\mathbf{p}_4)\right.\\
&\qquad \left.+i(\mathbf{p}_4\times\mathbf{p}_5)\mathbf{p}_1\right]\mathcal{G}_N(p_2-p_5)\mathcal{G}_{N^*}(p_2-p_4-p_5)\\
\mathcal{M}_{4c}^{(k)} &= -if\frac{\tilde{f}^2}{m_\pi^3}\Omega_{4c}^{(k)}\left[(\mathbf{p}_1\mathbf{p}_4)(\boldsymbol{\sigma}\mathbf{p}_5)+(\mathbf{p}_1\mathbf{p}_5)(\boldsymbol{\sigma}\mathbf{p}_4)-(\mathbf{p}_4\mathbf{p}_5)(\boldsymbol{\sigma}\mathbf{p}_1)\right.\\
&\qquad \left.+i(\mathbf{p}_1\times\mathbf{p}_4)\mathbf{p}_5\right]\mathcal{G}_N(p_2-p_4)\mathcal{G}_{N^*}(p_1+p_2-p_4)\\
\mathcal{M}_{4c}^{(l)} &= -if\frac{\tilde{f}^2}{m_\pi^3}\Omega_{4c}^{(l)}\left[(\mathbf{p}_1\mathbf{p}_5)(\boldsymbol{\sigma}\mathbf{p}_4)+(\mathbf{p}_1\mathbf{p}_4)(\boldsymbol{\sigma}\mathbf{p}_5)-(\mathbf{p}_4\mathbf{p}_5)(\boldsymbol{\sigma}\mathbf{p}_1)\right.\\
&\qquad \left.+i(\mathbf{p}_1\times\mathbf{p}_5)\mathbf{p}_4\right]\mathcal{G}_N(p_2-p_5)\mathcal{G}_{N^*}(p_1+p_2-p_5)
\end{aligned}
$$

D.5 Isospin coefficients

In Tables D.1, D.2 and D.3, we give all isospin coefficients needed to calculate the amplitudes as given above for a specific process. The columns are labelled as follows:

$$
\begin{aligned}
\mathbf{A} &= \pi^- p\to\pi^+\pi^- n & \mathbf{E} &= \pi^- p\to\pi^-\pi^0 p\\
\mathbf{B} &= \pi^+ p\to\pi^+\pi^+ n & \mathbf{F} &= \pi^+ n\to\pi^+\pi^- p\\
\mathbf{C} &= \pi^- p\to\pi^0\pi^0 n & \mathbf{G} &= \pi^- n\to\pi^-\pi^0 n\\
\mathbf{D} &= \pi^+ p\to\pi^+\pi^0 p & \mathbf{H} &= \pi^+ n\to\pi^+\pi^0 n.
\end{aligned}
$$

	A	**B**	**C**	**D**	**E**	**F**	**G**	**H**
(a)	$-2\sqrt{2}i$	0	$-2\sqrt{2}i$	0	0	$-2\sqrt{2}i$	0	0
(b)	$-2\sqrt{2}i$	0	$-2\sqrt{2}i$	0	0	$-2\sqrt{2}i$	0	0
(c)	$2\sqrt{2}i$	$2\sqrt{2}i$	0	$2i$	0	0	0	0
(d)	$2\sqrt{2}i$	$2\sqrt{2}i$	0	$2i$	0	0	0	0
(e)	0	$2\sqrt{2}i$	0	0	$2i$	$2\sqrt{2}i$	$-2i$	$-2i$
(f)	0	$2\sqrt{2}i$	0	0	$2i$	$2\sqrt{2}i$	$2\sqrt{2}i$	$-2i$

Table D.1: Isospin coefficients needed for the calculation of diagrams 4(a) in Fig. 4.3.

	A	**B**	**C**	**D**	**E**	**F**	**G**	**H**
(a)	$\sqrt{2}/3i$	$\sqrt{2}i$	$-\sqrt{2}/3i$	i	$2/3i$	0	0	$-2/3i$
(b)	$\sqrt{2}i$	$\sqrt{2}/3i$	$\sqrt{2}/3i$	i	0	0	$2/3i$	0
(c)	$\sqrt{2}i$	$\sqrt{2}/3i$	$\sqrt{2}/3i$	$i/3$	$-2/3i$	0	0	$2/3i$
(d)	$\sqrt{2}/3i$	$\sqrt{2}i$	$-\sqrt{2}/3i$	$i/3$	0	0	$-2/3i$	0
(e)	$\sqrt{2}/3i$	0	$2\sqrt{2}/3i$	$-\sqrt{2}/3i$	0	$\sqrt{2}i$	$-2/3i$	0
(f)	$\sqrt{2}i$	0	$2\sqrt{2}/3i$	0	$-2/3i$	$\sqrt{2}/3i$	0	$2/3i$
(g)	$\sqrt{2}i$	0	$2\sqrt{2}/3i$	$2/3i$	0	$\sqrt{2}/3i$	$2/3i$	0
(h)	$\sqrt{2}/3i$	0	$2\sqrt{2}/3i$	0	$2/3i$	$\sqrt{2}i$	0	$-2/3i$
(i)	0	$\sqrt{2}i$	$-\sqrt{2}/3i$	0	$1/3i$	0	$-i$	$-1/3i$
(j)	0	$\sqrt{2}/3i$	$\sqrt{2}/3i$	$\sqrt{2}/3i$	$1/3i$	$\sqrt{2}i$	$-i$	$-1/3i$
(k)	0	$\sqrt{2}/3i$	$\sqrt{2}/3i$	0	i	$\sqrt{2}i$	$-1/3i$	$-i$
(l)	0	$\sqrt{2}i$	$-\sqrt{2}/3i$	$\sqrt{2}/3i$	i	$\sqrt{2}/3i$	$-1/3i$	$-i$

Table D.2: Isospin coefficients needed for the calculation of diagrams 4(b) in Fig. 4.3.

	A	**B**	**C**	**D**	**E**	**F**	**G**	**H**
(a)	$2\sqrt{2}i$	0	$\sqrt{2}i$	0	$-2i$	0	0	$2i$
(b)	$2\sqrt{2}i$	0	$\sqrt{2}i$	$2i$	0	0	$2i$	0
(c)	0	0	$\sqrt{2}i$	0	$2i$	$2\sqrt{2}i$	0	$-2i$
(d)	0	0	$\sqrt{2}i$	$-2i$	0	$2\sqrt{2}i$	$-2i$	0
(e)	0	$2\sqrt{2}i$	$-\sqrt{2}i$	0	0	0	$-2i$	0
(f)	0	$2\sqrt{2}i$	$-\sqrt{2}i$	$2i$	$2i$	0	0	$-2i$
(g)	$2\sqrt{2}i$	0	$\sqrt{2}i$	0	$-2i$	0	0	$2i$
(h)	$2\sqrt{2}i$	0	$\sqrt{2}i$	$2i$	0	0	$2i$	0
(i)	0	0	$\sqrt{2}i$	0	$2i$	$2\sqrt{2}i$	0	$-2i$
(j)	0	0	$\sqrt{2}i$	$-2i$	0	$2\sqrt{2}i$	$-2i$	0
(k)	0	$2\sqrt{2}i$	$-\sqrt{2}i$	0	0	0	$-2i$	0
(l)	0	$2\sqrt{2}i$	$-\sqrt{2}i$	$2i$	$2i$	0	0	$-2i$

Table D.3: Isospin coefficients needed for the calculation of diagrams 4(c) in Fig. 4.3.

Appendix E

Vector meson photoproduction amplitudes

E.1 Cross section formulae

In the following we use the notation

$$\gamma(k) + N(p_1) \to V(q) + N(p_2) \tag{E.1}$$

where k, p_1, q and p_2 are the four momenta of the photon, incoming nucleon, vector meson and outgoing nucleon, respectively. The angular differential cross section in the CM frame is given by [58, 141]

$$\frac{d\sigma}{d\Omega} = \frac{1}{64\pi^2 s}\frac{|\mathbf{k}_{cm}|}{|\mathbf{q}_{cm}|}|\mathcal{M}(s,t)|^2 \tag{E.2}$$

where $s = (k+p_1)^2$ is the total CM energy squared and $t = (k-q)^2$ is the four momentum transfer squared. The momentum transfer can be related to the scattering angle and, consequently, one can write

$$\frac{d\sigma}{dt} = \frac{1}{64\pi s}\frac{1}{|\mathbf{q}_{cm}|^2}|\mathcal{M}(s,t)|^2. \tag{E.3}$$

A third kinematical quantity which can be used as independent variable is the LA momentum of the vector meson. For the momentum differential cross section we obtain [211]

$$\frac{d\sigma}{d|\mathbf{q}|} = \frac{1}{32\pi\sqrt{s}}\frac{|\mathbf{q}|}{|\mathbf{k}_{cm}|E_V E_\gamma}|\mathcal{M}(s,t)|^2 \tag{E.4}$$

where q_l is the absolute value of the vector meson three momentum, k_l is the photon three momentum and q_{l0} is the energy of the vector meson. The subscript refers to the LA frame. The CM three momentum in a two particle system with masses m_1 and m_2 and total energy W is

$$|\mathbf{q}_{\rm cm}| = \frac{\sqrt{(W^2 - m_1^2 - m_2^2)^2 - 4m_1^2 m_2^2}}{2W}. \tag{E.5}$$

In all above equations, $\mathcal{M}$ is the invariant Feynman amplitude. Its derivation for the case at hand will be discussed in the following.

E.2 Lagrangians and propagators

Our model for the ω and ϕ photoproduction amplitudes contains the processes shown in Figs. 7.3 and 9.5. In order to evaluate the $t-$channel meson exchange diagrams the following Lagrangians are needed

$$\mathcal{L}_{V\varphi\gamma} = e\frac{g_{V\varphi\gamma}}{m_V}\epsilon^{\mu\nu\alpha\beta}\partial_\mu V_\nu \partial_\alpha A_\beta \varphi \tag{E.6}$$

$$\mathcal{L}_{\varphi NN} = \frac{g_{\varphi NN}}{2m_N}\bar{u}_N\gamma_\mu\gamma_5 u_N \partial^\mu \varphi. \tag{E.7}$$

Here, V_μ is the vector meson field operator and $\varphi = \pi^0, \eta$. The $s-$ and $u-$channel nucleon exchange (Born) diagrams require the Lagrangians

$$\mathcal{L}_{\gamma NN} = -e\bar{u}_N\left(\gamma^\mu - \frac{\kappa_N}{2m_N}\sigma^{\mu\nu}\partial_\nu\right)A_\mu u_N \tag{E.8}$$

$$\mathcal{L}_{VNN} = -g_{VNN}\bar{u}_N\left(\gamma^\mu - \frac{\kappa_V}{2m_N}\sigma^{\mu\nu}\partial_\nu\right)V_\mu u_N. \tag{E.9}$$

For the case of ω photoproduction we also consider the excitation of the $P_{11}(1710)$ resonance. It has total spin 1/2 and positive parity. The Lagrangians which describe its coupling to the photon nucleon and vector meson nucleon channels we adopt from [158, 248]

$$\mathcal{L}_{RN\gamma} = e\frac{g_{RN\gamma}}{2m_N}\bar{u}_R\sigma_{\mu\nu}\partial_A^\nu u_N A^\mu \tag{E.10}$$

$$\mathcal{L}_{RNV} = \bar{u}_R\frac{g_{RNV}}{2m_N}\sigma_{\mu\nu}\partial_V^\nu u_N V^\mu \tag{E.11}$$

which ensure gauge invariance for the photon and vector meson fields alike by construction. The diagrams 7.3 and 9.5 require intermediate pseudoscalar meson, nucleon and resonance propagators (the Pomeron contribution will be treated seperately). These are given by

$$\mathcal{D}_\varphi(q) = \frac{i}{t - m_\varphi^2} \tag{E.12}$$

$$\mathcal{G}_N(p) = i\frac{\not{p} + m_N}{p^2 - m_N^2} \tag{E.13}$$

$$\mathcal{G}_R(k) = i\frac{\not{k} + m_R}{k^2 - m_R^2 - \langle\Sigma(k)\rangle} \tag{E.14}$$

where $\langle\Sigma(k)\rangle$ is the averaged resonance self energy that is related to the total width of the resonance via $\langle\Sigma(k)\rangle = -i\sqrt{k^2}\Gamma_R(k)$. Here, we simplify the treatment of the resonance in the fact that we consider only two decay channels, namely $R \to \omega N$ and $R \to 2\pi N$. The latter one gives the dominant contribution to the P_{11} self energy in the coupled channel analysis [158, 248].

The resonance width in its rest frame is given by [141]

$$\Gamma(k) = \frac{1}{8\pi}\frac{|\mathbf{p}_{\rm cm}|}{k^2}\frac{1}{2}\sum_{r,s}|\mathcal{M}(s)|^2 \tag{E.15}$$

vertex	g	Λ[GeV]	$\kappa_{p(n)}$	ξ
πNN	12.85	0.7		
$\omega\pi\gamma$	1.78	1.0		
ωNN	3.94	0.96	-0.94	0.6
γNN	e		1.79(-1.91)	
$RN\gamma$	0.284	1.69		0.5
$RN\omega$	8.162	4.0		0.5

Table E.1: Parameters needed for the evaluation of the ω photoproduction cross section.

where $\mathbf{p}_{\rm cm}$ is the CM momentum of the final state particles as given in Eq. (E.5) and $\mathcal{M}$ is the invariant amplitude for the decay process. The factor 1/2 originates from the average over the resonance spin orientations. From the Lagrangian (E.11) we find for the decay into the vector meson nucleon channel

$$\Gamma_{R\to NV} = \frac{1}{64\pi} g_{RNV}^2 \left(\frac{m_V}{m_N}\right)^2 \frac{\mathbf{p}_{\rm cm}}{\sqrt{s}} \left(4E_N - m_N\right) \tag{E.16}$$

where $E_N = \sqrt{m_N^2 + \mathbf{p}_{\rm cm}^2}$ is the CM energy of the nucleon in the final state. This expression allows to determine the coupling constant g_{RNV} at the physical resonance mass $m_R = 1.749$ GeV, that is given explicitely in Table E.1. The partial decay width to the $N\omega$ channel was obtained in [158, 248] and amounts to $\Gamma_{R\to\omega N}(m_R) = 60$ MeV. The coupling to scalar meson nucleon channels is described by the Lagrangian [248]

$$\mathcal{L}_{RN\zeta} = -\frac{g_{RN\zeta}}{m_R - m_N} \bar{u}_R i\gamma_\mu u_N \partial^\mu \zeta. \tag{E.17}$$

This vector coupling leads to the decay width

$$\Gamma_{R\to N\zeta} = \frac{1}{4\pi} \left(\frac{g_{RN\zeta}}{m_R - m_N}\right)^2 \frac{\mathbf{p}_{\rm cm}}{\sqrt{s}} (E_N + m_N) \left(\sqrt{s} - m_N\right)^2 \tag{E.18}$$

using the same notation as above. The scalar ζ channel is in [158, 248] invented in order to absorb all the inelasticity that goes to final states consisting of more than two particles. This recipe requires to use $m_\zeta = 2m_\pi$ for the mass of this effective mutli-pion state. We chose the coupling constant such that the $R \to N\varsigma$ accounts for the rest of the total resonance width which amounts to $\Gamma_R = 445$ MeV at the physical resonance mass.

With all the ingredients described above the $s-$, $t-$ and $u-$channel meson and baryon exchange contributions to the Feynman amplitude of our model can be calculated. To this end we use standard Feynman rules as for instance given in [58, 66]. The parameters needed to evaluate the amplitude numerically are given in Tables E.1 and E.2.

vertex	g	Λ[GeV]	$\kappa_{p(n)}$	ξ
πNN	13.26	0.7		
ηNN	3.53	1.0		
$\phi\pi\gamma$	-0.141	0.77		
$\phi\eta\gamma$	-0.707	0.9		
ϕNN	-0.24	1.87	0.2	0.9
γNN	e		1.79(-1.91)	

Table E.2: Parameters needed for the evaluation of the ϕ photoproduction cross section.

E.3 Regge amplitude

In the case of ϕ meson photoproduction the amplitude is dominated by the exchange of the Pomeron trajectory. This process is understood as the $t-$channel exchange of two interacting gluons and is invented in the framework of Regge theory, see for instance Refs. [166, 211] and references therein. For the Pomeron exchange it is assumed that the photon first converts into a quark-antiquark pair which then exchanges a Pomeron with the nucleon before recombining into the outgoing ϕ meson. The amplitude for this process can be written in factorized form as

$$T_{\mathbb{P}} = \bar{u}_N B \epsilon^*_\mu \mathcal{M}^{\mu\nu} \epsilon_\nu u_N. \tag{E.19}$$

The Dirac structure of the amplitude is obtained by assuming that the Pomeron coupling is photon-like. One finds

$$\mathcal{M}^{\mu\nu} = \gamma^\nu k^\mu - \not{k} g^{\mu\nu}. \tag{E.20}$$

The function B takes the conventional form of the Regge amplitude

$$B = CF(s,t) G_{\mathbb{P}}(t) e^{-i\frac{\pi}{2}\alpha_{\mathbb{P}}(t)} \left(\alpha'_{\mathbb{P}}(s - s_1)\right)^{\alpha_{\mathbb{P}}(t)} \tag{E.21}$$

with the parametrization of the trajectory

$$\alpha_{\mathbb{P}}(t) = \alpha_{\mathbb{P}}(0) + \alpha'_{\mathbb{P}} t = 1.08 + 0.25t \tag{E.22}$$

where the Regge intercept $\alpha_{\mathbb{P}}(0) \approx 1$ indicates the exchange of an (approximately) massless spin-0 boson (gluon ladder). The parameters have been fixed in [217] to $s_1 = 1.6$ GeV^2 and $C = 2.09$. The form factor $G_{\mathbb{P}}(t)$ is a product of the form factors from both vertices that are given explicitly in the following paragraph. The so-called correcting function $F(s,t)$ contains a trace over the nucleon spin matrices and serves to divide out the s and t dependence of the amplitude $\bar{u}_N \epsilon^*_\mu \mathcal{M}^{\mu\nu} \epsilon_\nu u_N$. Consequently, the momentum dependence of the amplitude $T_{\mathbb{P}}$ is given exclusively by the Regge factor (E.21) whereas its Dirac structure takes the conventional form of the $t-$channel vector exchange amplitude. The function $F(s,t)$ is given explicitly in Ref. [217].

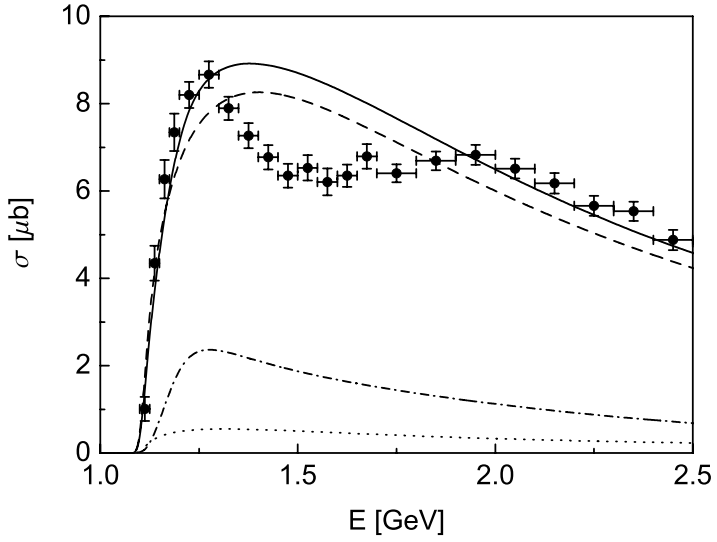

Figure E.1: Total exclusive ω photoproduction cross section. *Solid line*: coherent sum of all amplitudes, *dashes line*: only pion exchange, *dotted line*: nucleon exchange diagrams, *dash-dotted lines*: resonance contribution. Data from Ref. [268].

E.4 Parameters and cutoffs

All vertices in the diagrams 7.3 and 9.5 must be regularized by appropriate form factors. For these we use standard parameterizations:

$$F_{V\varphi\gamma}(t) = F_{\varphi NN}(t) = \frac{\Lambda^2 - m_\varphi^2}{\Lambda^2 - t} \tag{E.23}$$

$$F_{VNN}(s,u) = \xi f(s) + (1-\xi) f(u) \tag{E.24}$$

$$f(z) = \frac{\Lambda^4}{\Lambda^4 + (z - m_N^2)^2} \tag{E.25}$$

Note, that both the $s-$ and $u-$channel diagrams are multiplied with the same composite form factor F_{VNN} [218]. This recipe ensures gauge invariance since only the sum of the $s-$ and $u-$channel terms fulfills the Ward identity $k^\mu \mathcal{M}_\mu \equiv 0$ [58]. The same parametrization is used for the vertices including the P_{11} resonance with the replacement $m_N \to m_R$. The Pomeron vertices are regularized by the following form factors

$$F_{\mathbb{P}NN}(t) = \frac{4m_N^2 - 2.79t}{4m_N^2 - t} \left(\frac{1}{1 - t/0.71} \right)^2 \tag{E.26}$$

$$F_{\phi\gamma\mathbb{P}}(t) = \exp\left[\frac{1}{2} B (t - t_{\max}) \right] \tag{E.27}$$

with $B = 1.7$ GeV^2. We give all parameters of our model in Tables E.1 and E.2. The squared amplitudes are obtained as a coherent sum of all contributions described above. In the actual calculations the summed amplitude is obtained by means of the `Mathematica` package `Feyncalc` [254].

Finally, we show in Fig. E.1 the total ω photoproduction cross section that emerges from the described model and its decomposition into the different contributions. The $t-$channel pion exchange contribution clearly dominates the reaction in the considered energy range. In the energy interval $E_\gamma = (1.3 - 1.9)$ GeV the cross section is even overestimated by the pion exchange alone. This is in line with the results obtained in Ref. [249]. However, in [249] important contributions from the spin$-5/2$ sector in the D_{15} and F_{15} partial waves were found. Even if their relative contribution to the ω photoproduction cross section has turned out to be rather small, they strongly affect the cross section because of the destructive interference pattern between the pion exchange and the resonance contributions.

Appendix F

Photoproduction cross section at finite density

The total cross sections for photoproduction of vector mesons are calculated according to Eq. (9.11), taking into account the finite vector meson width. Inside nuclear matter, however, the vector meson spectral function on top of the vector meson mass depends on the nuclear density and the vector meson three-momentum, see also Chapter 8. These dependencies require an additional integration over the angular distributions, taking into account the impact of the varying momentum on the spectral function. Since the evaluation of the photoproduction cross section becomes numerically expensive, we calculate it on a two-dimensional grid for various values of the incident photon energy and the nuclear density. The total cross section including already an average over the Fermi sea is given by the following expression:

$$\begin{aligned}\sigma_{\gamma N\to VN}(E_\gamma, n_N) &= \frac{4}{n_N}\int_0^{p_F}\frac{d^3p}{(2\pi)^3}\int_{W^2_{\min}}^{(\sqrt{s}-m_N)^2} dW^2 \int_0^{4\pi} d\Omega_{\rm cm}\mathcal{A}_V(W,|\mathbf{q}|,n_N)\times \\ &\quad \times\frac{1}{64\pi^2 s}\frac{|\mathbf{p}_{\rm cm}(\sqrt{s},W,m_N)|}{|\mathbf{k}_{\rm cm}(\sqrt{s},m_N,0)|}\frac{1}{4}\sum_{r,s}|\mathcal{M}|^2 \end{aligned} \tag{F.1}$$

where n_N is the nuclear density and p_F is the local Fermi momentum as given by Eq. (A.3). The threshold mass $W_{\min}$ is either $W_{\min} = 2m_\pi$ for the case of the ρ meson or $W_{\min} = 3m_\pi$ for the case of the ω and ϕ mesons. Here, $|\mathbf{k}_{\rm cm}|$ is the initial CM momentum and $|\mathbf{p}_{\rm cm}|$ is the CM momentum in the final VN system as given by Eq. (E.5). The in-medium spectral function $\mathcal{A}_V$ is defined by Eq. (A.8). The vector meson momentum in the LA frame is given by

$$q = (q_0, \mathbf{q}) = \mathcal{L}\cdot\mathcal{R}\cdot q_{\rm cm} \tag{F.2}$$

with the CM three-momentum

$$q_{\rm cm} = \begin{pmatrix} \sqrt{W^2+\mathbf{p}^2_{\rm cm}} \\ |\mathbf{p}_{\rm cm}|\cos\phi\sin\theta \\ |\mathbf{p}_{\rm cm}|\sin\phi\sin\theta \\ |\mathbf{p}_{\rm cm}|\cos\theta \end{pmatrix} \tag{F.3}$$

where θ and ϕ are the azimuthal and polar CM angles of the vector meson which are integrated over in Eq. (F.1). The matrix $\mathcal{R}$ performs a rotation such that the angle of the vector meson is measured with respect to the incoming photon momentum. It is given by

$$\mathcal{R} = \begin{pmatrix} 1 & 0 & 0 & 0 \\ 0 & \cos\theta_R \cos\phi_R & -\sin\phi_R & \sin\theta_R \cos\phi_R \\ 0 & \cos\theta_R \sin\phi_R & \cos\phi_R & \sin\theta_R \sin\phi_R \\ 0 & -\sin\theta_R & 0 & \cos\theta_R \end{pmatrix} \tag{F.4}$$

with the rotation angles

$$\theta_R = \arccos \frac{p'_z}{|\mathbf{p}'|} \tag{F.5}$$

$$\phi_R = \arctan \frac{p'_y}{p'_x}. \tag{F.6}$$

Here, $\mathbf{p}'$ is the initial CM momentum of the nucleon. Finally, the rotated vector meson momentum has to be transformed to the LA frame. This is achieved by multiplication with the Lorentz matrix

$$\mathcal{L} = \left(\begin{array}{c|ccc} \gamma & -\gamma\boldsymbol{\beta} & & \\ \hline & 1+\eta\beta_x^2 & \eta\beta_x\beta_y & \eta\beta_x\beta_z \\ -\gamma\boldsymbol{\beta} & \eta\beta_y\beta_x & 1+\eta\beta_y^2 & \eta\beta_y\beta_z \\ & \eta\beta_z\beta_x & \eta\beta_z\beta_y & 1+\eta\beta_z^2 \end{array}\right) \tag{F.7}$$

with the abbreviations

$$\eta = \frac{\gamma^2}{1+\gamma} \tag{F.8}$$

$$\gamma = \frac{1}{\sqrt{1-\boldsymbol{\beta}^2}} \tag{F.9}$$

$$\boldsymbol{\beta} = -\frac{\mathbf{P}}{P_0} \tag{F.10}$$

where P is the total initial LA momentum $P = k + p$ with $P^2 = s$.

Appendix G

Forward ωN scattering amplitude

G.1 Relativistic Lagrangians

In order to evaluate the ωN forward scattering amplitude we consider its coupling to spin$-1/2$ and spin$-3/2$ resonances. The relativistic Lagrangians for the spin$-1/2$ case are [248]

$$\mathcal{L}_{RNV} = -\bar{u}_R \begin{pmatrix} 1 \\ -i\gamma_5 \end{pmatrix} \left(g_1 \gamma_\mu - \frac{g_2}{2m_N} \sigma_{\mu\nu} \partial_V^\nu \right) u_N V^\mu \tag{G.1}$$

and for the spin$-3/2$ resonances we have [248]

$$\mathcal{L}_{RNV} = \bar{u}_R^\mu \begin{pmatrix} i\gamma_5 \\ 1 \end{pmatrix} \left(\frac{g_1}{2m_N} \gamma^\alpha + i \frac{g_2}{4m_N^2} \partial_N^\alpha + i \frac{g_3}{4m_N^2} \partial_V^\alpha \right) \left(\partial_\alpha^V g_{\mu\nu} - \partial_\mu^V g_{\alpha\nu} \right) u_N V^\nu. \tag{G.2}$$

In both equations the upper operator corresponds to a positive and the lower one to a negative parity resonance. The first coupling ($\sim g_1$) in the $J^P = (1/2)^+$ Lagrangian is not current conserving. Thus, we rewrite it in the following way

$$\mathcal{L}_{RNV}^1 = -\frac{g_1}{m_V^2} \bar{u}_R \gamma_\mu \partial_\nu^V V^{\mu\nu} u_N \tag{G.3}$$

which on-shell is equivalent to the g_1 part of (G.1). Here, $V_{\mu\nu}$ is the antisymmetrized vector meson field tensor, defined as $V_{\mu\nu} = \partial_\mu V_\nu - \partial_\nu V_\mu$. The equivalence can be seen as follows:

$$\begin{aligned} \frac{g_1}{m_V^2} \gamma_\mu \partial_\nu V^{\mu\nu} &= \frac{g_1}{m_V^2} \gamma_\mu \partial_\nu \left(\partial^\mu g^{\nu\alpha} - \partial^\nu g^{\mu\alpha} \right) V_\alpha & \text{(G.4)} \\ &= \frac{g_1}{m_V^2} \gamma_\mu \left(\partial_\nu \partial^\mu V^\nu - \partial_\nu \partial^\nu V^\mu \right) & \text{(G.5)} \\ &= g_1 \gamma_\mu V^\mu. & \text{(G.6)} \end{aligned}$$

Here, $g_{\mu\nu}$ is the metric tensor. Going from line two to three the first term vanishes if we impose Lorentz gauge:

$$\partial_\nu V^\nu = 0. \tag{G.7}$$

The second term has been recast using the Proca equation

$$\left(\partial_\nu \partial^\nu + m_V^2\right) V_\mu = 0. \tag{G.8}$$

In the following we will work with the Lagrangian (G.3) which indeed ensures current conservation by construction.

In order to calculate the matrix elements for the resonance decay widths their coupling to scalar and pseudoscalar meson nucleon channels is needed. We use

$$\begin{aligned} \mathcal{L}_{RN\varphi} &= \frac{f}{m_\varphi} \bar{u}_R \gamma^\mu \left\{ \begin{array}{c} i\gamma_5 \\ 1 \end{array} \right\} u_N \partial_\mu \varphi \qquad J^P = \tfrac{1}{2}^\pm \\ \mathcal{L}_{RN\varphi} &= \frac{f}{m_\varphi} \bar{u}^\mu_R \left\{ \begin{array}{c} 1 \\ i\gamma_5 \end{array} \right\} u_N \partial_\mu \varphi \qquad J^P = \tfrac{3}{2}^\pm \end{aligned} \tag{G.9}$$

where in both Equations in the case of pseudoscalar mesons the upper operator corresponds to positive and the lower one to negative parity resonances and vice versa for the case of scalar mesons.

G.2 Relativistic Traces

The Lagrangians are used to calculate analytic expressions for both the vector meson nucleon forward scattering amplitude and the resonance decay widths. The traces arising in both calculations are of the same generic form. For the case of the vector meson nucleon channel the expression to be evaluated has been given in Eqs. (8.36) and (8.37). Owing to the fact that the relativistic RNV Lagrangians include various couplings with different Lorentz structures the analytic structure of the corresponding traces is rather involved and therefore not given explicitly here.

For the pseudoscalar meson nucleon decay one needs to calculate

$$\Omega_{1/2} = \mathrm{Tr}\left[\mathcal{V}(\not{k} + \sqrt{k^2})\mathcal{V}^\dagger(\not{p} + m_N)\right] \tag{G.10}$$

$$\Omega_{3/2} = \mathrm{Tr}\left[\mathcal{V}_\mu(\not{k} + \sqrt{k^2})P^{\mu\nu}_{3/2}\mathcal{V}^\dagger_\nu(\not{p} + m_N)\right] \tag{G.11}$$

where we have used the spin$-3/2$ projector

$$P^{\mu\nu}_{3/2} = g^{\mu\nu} - \frac{1}{3}\gamma^\mu\gamma^\nu - \frac{1}{3k^2}\left(\not{k}\gamma^\mu k^\nu + k^\mu \gamma^\nu \not{k}\right). \tag{G.12}$$

with k the four-momentum of the resonance. Using the Lagrangians from Eq. (G.9) the traces can be calculated analytically. They are given in Table G.1.

$\Omega^{\varphi}_{1/2}$	$J^P = \frac{1}{2}^{+(-)}$	$4\sqrt{s}\,(q^2\,(E_N - m_N) + 2\sqrt{s}\,\mathbf{q}^2_{\rm cm})$
$\Omega^{\varphi}_{1/2}$	$J^P = \frac{1}{2}^{-(+)}$	$4\sqrt{s}\,(q^2\,(E_N + m_N) + 2\sqrt{s}\,\mathbf{q}^2_{\rm cm})$
$\Omega^{\varphi}_{3/2}$	$J^P = \frac{3}{2}^{+(-)}$	$\frac{8}{3}\sqrt{s}\,\mathbf{q}^2_{\rm cm}(E_N + m_N)$
$\Omega^{\varphi}_{3/2}$	$J^P = \frac{3}{2}^{-(+)}$	$\frac{8}{3}\sqrt{s}\,\mathbf{q}^2_{\rm cm}(E_N - m_N)$

Table G.1: Relativistic traces for the resonance decay into pseudoscalar (scalar) meson nucleon channels in the CM frame. E_N is the CM nucleon energy, q is the vector meson four-momentum and $\mathbf{q}_{\rm cm}$ is the CM momentum in the vector meson nucleon system as given by Eq. (E.5).

G.3 Non-relativistic Lagrangians

In Section (8.2.3) we have shown for one particular case how to obtain a non-relativistic reduction of the relativistic RNV Lagrangians. In all following expressions $q = (q_0, \mathbf{q})$ is the vector meson momentum and $p = (p_0, \mathbf{p})$ is the nucleon momentum. For spin$-1/2$ resonances the Lagrangians are given by

$$\begin{aligned} J^P = \tfrac{1}{2}^+ : \qquad \mathcal{L}_1 &= -\frac{g_1}{m_V^2}\bar{\psi}^\dagger_R \psi_N \partial_i \left(\partial_0 V_i - \partial_i V_0\right) \\ \mathcal{L}_2 &= -\frac{g_2}{2m_N}\psi^\dagger_R \psi_N \epsilon_{ijk}\sigma_k \partial_j V_i \end{aligned} \tag{G.13}$$

and

$$\begin{aligned} J^P = \tfrac{1}{2}^- : \qquad \mathcal{L}_1 &= \frac{g_1}{m_V^2} q_0 \psi^\dagger_R \sigma_i \psi_N \left(\partial_0 V_i - \partial_i V_0\right) \\ \mathcal{L}_2 &= -\frac{g_2}{2m_N}\psi^\dagger_R \sigma_i \psi_N \left(\partial_0 V_i - \partial_i V_0\right). \end{aligned} \tag{G.14}$$

For the spin$-3/2$ resonances we obtain

$$\begin{aligned} J^P = \tfrac{3}{2}^+ : \qquad \mathcal{L}_1 &= -i\frac{g_1}{2m_N}\psi^\dagger_R S^\dagger_i \psi_N \sigma_j \left(\partial_j V_i - \partial_i V_j\right) \\ \mathcal{L}_2 &= \frac{g_2}{4m_N^2} p_0 \psi^\dagger_R S^\dagger_i \frac{\boldsymbol{\sigma}\mathbf{p}}{2m_N}\psi_N \left(\partial_0 V_i - \partial_i V_0\right) \\ \mathcal{L}_3 &= \frac{g_3}{4m_N^2} q_0 \psi^\dagger_R S^\dagger_i \frac{\boldsymbol{\sigma}\mathbf{p}}{2m_N}\psi_N \left(\partial_0 V_i - \partial_i V_0\right) \end{aligned} \tag{G.15}$$

$\Omega^{\varphi}_{1/2}$	$J^P = \frac{1}{2}^+$	$8m_N m_R \mathbf{q}^2$
$\Omega^{\varphi}_{1/2}$	$J^P = \frac{1}{2}^-$	$8m_N m_R q_0^2$
$\Omega^{\varphi}_{3/2}$	$J^P = \frac{3}{2}^+$	$\frac{16}{3} m_N m_R \mathbf{q}^2$
$\Omega^{\varphi}_{3/2}$	$J^P = \frac{3}{2}^-$	$\frac{16}{3} m_N m_R \mathbf{q}^4$

Table G.2: Non-relativistic traces for the resonance decay into pseudoscalar meson nucleon channels.

and

$$\begin{aligned} J^P = \tfrac{3}{2}^- : \quad \mathcal{L}_1 &= -\frac{g_1}{2m_N} \psi_R^\dagger S_i^\dagger \psi_N \left(\partial_0 V_i - \partial_i V_0\right) \\ \mathcal{L}_2 &= i\frac{g_2}{4m_N^2} p_0 \psi_R^\dagger S_i^\dagger \psi_N \left(\partial_0 V_i - \partial_i V_0\right) \\ \mathcal{L}_3 &= i\frac{g_3}{4m_N^2} q_0 \psi_R^\dagger S_i^\dagger \psi_N \left(\partial_0 V_i - \partial_i V_0\right). \end{aligned} \tag{G.16}$$

The non-relativistic Lagrangians for the pseudoscalar meson decay take the form

$$\begin{aligned} J^P = \tfrac{1}{2}^+ : \quad \mathcal{L}_{RN\varphi} &= i\frac{f}{m_\varphi} \psi_R^\dagger \sigma_i \psi_N \partial_i \varphi \\ J^P = \tfrac{1}{2}^- : \quad \mathcal{L}_{RN\varphi} &= \frac{f}{m_\varphi} \psi_R^\dagger \psi_N \partial_0 \varphi \\ J^P = \tfrac{3}{2}^+ : \quad \mathcal{L}_{RN\varphi} &= \frac{f}{m_\varphi} \psi_R^\dagger S_i^\dagger \psi_N \partial_i \varphi \\ J^P = \tfrac{3}{2}^- : \quad \mathcal{L}_{RN\varphi} &= i\frac{f}{2m_N m_\varphi} \psi_R^\dagger S_i^\dagger \sigma_j (\partial_j \psi_N) \partial_i \varphi. \end{aligned} \tag{G.17}$$

G.4 Non-relativistic Traces

Non-relativistically the trace for the decay of a resonance to the pseudoscalar nucleon channel is given by

$$\Omega = 4m_N m_R \mathrm{Tr}\left[\mathcal{V}^\dagger \mathcal{V}\right] \tag{G.18}$$

where the vertex factor $\mathcal{V}$ is given by the interaction Lagrangian. For the case of a $J^P = 1/2^+$ resonance we have

$$\mathcal{V} = -i\boldsymbol{\sigma} \cdot \mathbf{q} \tag{G.19}$$

Ω_L^V	$J^P = \frac{1}{2}^+$	$4m_N \left(\frac{g_1}{m_V^2}\right)^2 q^2 \mathbf{q}^2$
Ω_T^V	$J^P = \frac{1}{2}^+$	$4m_N \left(\frac{g_2}{2m_N}\right)^2 \mathbf{q}^2$
Ω_L^V	$J^P = \frac{1}{2}^-$	$-4m_N \left(q_0 \frac{g_1}{m_V^2} - \frac{g_2}{2m_N}\right)^2 q^2$
Ω_T^V	$J^P = \frac{1}{2}^-$	$4m_N \left(q_0 \frac{g_1}{m_V^2} - \frac{g_2}{2m_N}\right)^2 q_0^2$
Ω_L^V	$J^P = \frac{3}{2}^+$	$-\frac{8}{3} m_N \left(\frac{g_1}{2m_N}\right)^2 q^2 \mathbf{q}^2$
Ω_T^V	$J^P = \frac{3}{2}^+$	$\frac{8}{3} m_N \left(c_1^2 \mathbf{q}^2 + c_2^2 \mathbf{q}^2 q_0^2 + c_1 c_2 q_0 \mathbf{q}^2\right)$
Ω_L^V	$J^P = \frac{3}{2}^-$	$\frac{8}{3} m_N \left(\frac{g_1}{2m_N} + p_0 \frac{g_2}{4m_N^2} + q_0 \frac{g_3}{4m_N^2}\right)^2 q^2$
Ω_T^V	$J^P = \frac{3}{2}^-$	$\frac{8}{3} m_N \left(\frac{g_1}{2m_N} + p_0 \frac{g_2}{4m_N^2} + q_0 \frac{g_3}{4m_N^2}\right)^2 q_0^2$

Table G.3: Non-relativistic traces for the resonance decay into vector meson nucleon channels. We have used the abbreviations $c_1 = g_1/(2m_N)$ and $c_2 = (g_2 p_0 + g_3 q_0)/(8m_N^3)$.

where we have omitted the coupling constants and masses in the Lagrangian. Explicit expression for the traces are given in Table G.2. In order to calculate the vector meson nucleon decay width and the forward scattering amplitude we need

$$\Omega_{T/L} = 2m_N P_{T/L}^{\mu\nu} \mathrm{Tr}\left[\mathcal{V}_\mu^\dagger \mathcal{V}_\nu\right] \tag{G.20}$$

where $P_{T/L}$ is the three-longitudinal/transversal projector for the vector meson field. For the case of nuclear matter at rest, the longitudinal projector has been given in Eq. (8.10). For $J^P = 1/2^-$ resonances the vertex factor is given by

$$\mathcal{V}_\mu = i\left(\boldsymbol{\sigma} \cdot \mathbf{q}, q_0 \sigma_i\right) \tag{G.21}$$

where we have used the notation $\mu = (0, i)$ and again have neglected all coupling constants, masses and momenta which are just real numbers. Explicit expressions for the vector meson nucleon traces are given in Table G.3.

Appendix H

Scattering length

The definition of the scattering length in the present work differs from the definitions used in [249] and [241]. There a decomposition of the ωN helicity amplitudes with respect to the total angular momentum of the ωN system has been performed. In the present work, however, we define the scattering length as done in [237], what is consistent with the evaluation of the self energy as given by Eqs. (8.10), (8.11) and (8.27):

$$a_{\omega N} = \frac{m_N}{4\pi(m_N + m_\omega)} T_{\omega N}(q_0 = m_\omega), \tag{H.1}$$

where $T_{\omega N}$ is the spin- and helicity-averaged ωN forward scattering amplitude at threshold:

$$T_{\omega N}(m_\omega) = \frac{1}{2}\left(T_{+1+\frac{1}{2}}(m_\omega) + T_{+1-\frac{1}{2}}(m_\omega)\right) = T_{0+\frac{1}{2}}(m_\omega). \tag{H.2}$$

The lower indices stand for the ω and nucleon helicities. The amplitudes in the right-hand side of the Eq. (H.2) are obtained from the partial wave decomposition [173]

$$\begin{aligned} T_\lambda(m_\omega) &= \frac{4\pi(m_N + m_\omega)}{k_{\rm cm}\, m_N} \sum_J \left(J + \frac{1}{2}\right) d^J_{\lambda\lambda'}(0) \left(T^{J+}_{\lambda'\lambda}(m_N + m_\omega) + T^{J-}_{\lambda'\lambda}(m_N + m_\omega)\right) \\ &= \frac{4\pi(m_N + m_\omega)}{|\mathbf{k}_{\rm cm}|\, m_N} \left(T^{\frac{1}{2}^-}_{\lambda\lambda}(m_N + m_\omega) + 2T^{\frac{3}{2}^-}_{\lambda\lambda}(m_N + m_\omega)\right), \end{aligned} \tag{H.3}$$

where $\mathbf{k}_{\rm cm}$ is the ωN CM momentum and $\lambda = \lambda_\omega + \lambda_N$. Note, that only the $J^P = \frac{1}{2}^-$ and $J^P = \frac{3}{2}^-$ partial waves contribute close to the ωN threshold.

With the definition (H.2), the classical interpretation of the scattering length similar as for spinless particles holds:

$$\sigma(\sqrt{s} = m_N + m_\omega) = \sigma^{\frac{1}{2}} + \sigma^{\frac{3}{2}} = 4\pi\left(3|a^{\frac{1}{2}^-}_{\omega N}|^2 + \frac{3}{2}|a^{\frac{3}{2}^-}_{\omega N}|^2\right) \tag{H.4}$$

where σ is the usual spin- and helicity-averaged total ωN elastic cross section at threshold. With this definition the following formula for the on-shell mass shift applies:

$$\Delta m = -\frac{2\pi n_N}{m_\omega}\left(1 + \frac{m_\omega}{m_N}\right) \mathcal{R}e\; a_{\omega N}. \tag{H.5}$$

Using the amplitude obtained from the coupled channel calculation in Chapter 8, we find an on-shell mass shift of $\Delta m \simeq 15$ MeV. Note, however, that the shift of the ω peak in the spectral function is somewhat smaller since the real part of the self energy is reduced for q^2 values slightly above the ω pole mass, see Fig. 8.12.

Bibliography

[1] E. G. Drukarev and E. M. Levin, *The QCD sume rules and nuclear matter*, Nucl. Phys. **A511** (1990) 679.

[2] T. D. Cohen, R. J. Furnstahl and D. K. Griegel, *Quark and gluon condensates in nuclear matter*, Phys. Rev. **C45** (1992) 1881.

[3] G.-Q. Li and C. M. Ko, *Quark condensate in nuclear matter*, Phys. Lett. **B338** (1994) 118.

[4] R. Brockmann and W. Weise, *The Chiral condensate in nuclear matter*, Phys. Lett. **B367** (1996) 40.

[5] T. A. Armstrong *et al.*, *Total hadronic cross section of γ rays in hydrogen in the energy range $E = (0.265 - 4.215)$ GeV*, Phys. Rev. **D5** (1972) 1640.

[6] T. A. Armstrong *et al.*, *The total photon deuteron hadronic cross section in the energy range $E = (0.265 - 4.215)$ GeV*, Nucl. Phys. **B41** (1972) 445.

[7] N. Bianchi *et al.*, *Absolute total photoabsorption cross sections on nuclei in the nucleon resonance region*, Phys. Lett. **B325** (1994) 333.

[8] G. E. Brown and M. Rho, *Scaling effective Lagrangians in a dense medium*, Phys. Rev. Lett. **66** (1991) 2720.

[9] T. Hatsuda and S. H. Lee, *QCD sum rules for vector mesons in nuclear medium*, Phys. Rev. **C46** (1992) 34.

[10] G. Agakishiev *et al.*, *Enhanced production of low mass electron pairs in 200 GeV/u S-Au collisions at the CERN SPS*, Phys. Rev. Lett. **75** (1995) 1272.

[11] G. Agakishiev *et al.*, *Low-mass e^+e^- pair production in 158 AGeV Pb Au collisions at the CERN SPS, its dependence on multiplicity and transverse momentum*, Phys. Lett. **B422** (1998) 405, nucl-ex/9712008.

[12] B. Lenkeit *et al.*, *Recent results from Pb Au collisions at 158 GeV/c per nucleon obtained with the CERES spectrometer*, Nucl. Phys. **A661** (1999) 23, nucl-ex/9910015.

[13] J. P. Wessels *et al.*, *Latest results from CERES/NA45*, Nucl. Phys. **A715** (2003) 262, nucl-ex/0212015.

[14] M. Masera, *Dimuon production below mass* 3.1 GeV *in pW and SW interactions at 200 AGeV/c*, Nucl. Phys. **A590** (1995) 93c.

[15] K. Ozawa *et al.*, *Observation of rho/omega meson modification in nuclear matter*, Phys. Rev. Lett. **86** (2001) 5019, nucl-ex/0011013.

[16] T. Tabaru *et al.*, *Nuclear mass number dependence of inclusive production of omega and phi mesons in 12 GeV $p + A$ collisions* nucl-ex/0603013.

[17] F. Sakuma *et al.*, *Study of nuclear matter modification of decay widths in $\phi \to e^+e^-$ and $\phi \to K^+K^-$ channels* nucl-ex/0606029.

[18] D. Trnka *et al.*, *First observation of in-medium modifications of the omega meson*, Phys. Rev. Lett. **94** (2005) 192303, nucl-ex/0504010.

[19] D. Trnka, *Investigation of in-medium properties of the ω meson in photonuclear reactions*, Ph.D. thesis, Universitaet Giessen (2006).

[20] S. Zschocke, O. P. Pavlenko and B. Kämpfer, *In-medium spectral change of omega mesons as a probe of QCD four-quark condensate*, Phys. Lett. **B562** (2003) 57, hep-ph/0212201.

[21] R. Thomas, S. Zschocke and B. Kämpfer, *Evidence for in-medium changes of four-quark condensates*, Phys. Rev. Lett. **95** (2005) 232301, hep-ph/0510156.

[22] S. Leupold, *Factorization and non-factorization of in-medium four-quark condensates*, Phys. Lett. **B616** (2005) 203, hep-ph/0502061.

[23] B. Steinmueller and S. Leupold, *Weighted finite energy sum rules for the omega meson in nuclear matter*, Nucl. Phys. **A778** (2006) 195, hep-ph/0604054.

[24] P. Schuck, W. Norenberg and G. Chanfray, *Bound two pion cooper pairs in nuclei?*, Z. Phys. **A330** (1988) 119.

[25] Z. Aouissat, R. Rapp, G. Chanfray, P. Schuck and J. Wambach, *S-wave $\pi\pi$ correlations in dense nuclear matter*, Nucl. Phys. **A581** (1995) 471, nucl-th/9406010.

[26] H. C. Chiang, E. Oset and M. J. Vicente-Vacas, *Chiral nonperturbative approach to the isoscalar s-wave $\pi\pi$ interaction in a nuclear medium*, Nucl. Phys. **A644** (1998) 77, nucl-th/9712047.

[27] D. Jido, T. Hatsuda and T. Kunihiro, *In-medium $\pi\pi$ correlation induced by partial restoration of chiral symmetry*, Phys. Rev. **D63** (2001) 011901, hep-ph/0008076.

[28] P. Camerini, N. Grion, R. Rui and D. Vetterli, *Threshold behavior of the $\pi^+\pi^-$ invariant mass in nuclei*, Nucl. Phys. **A552** (1993) 451.

[29] F. Bonutti *et al.*, *A dependence of the $(\pi^+, \pi^+\pi^\pm)$ reaction near the $2m_\pi$ threshold*, Phys. Rev. Lett. **77** (1996) 603.

[30] F. Bonutti *et al.*, *Pion induced pion production in nuclei*, Phys. Rev. **C55** (1997) 2998.

[31] J. G. Messchendorp *et al.*, *In-medium modifications of the $\pi\pi$ interaction in photon-induced reactions*, Phys. Rev. Lett. **89** (2002) 222302, nucl-ex/0205009.

[32] E. Oset and L. L. Salcedo, *Delta self energy in nuclear matter*, Nucl. Phys. **A468** (1987) 631.

[33] P. Muehlich, L. Alvarez-Ruso, O. Buss and U. Mosel, *Low-energy $\pi\pi$ photoproduction off nuclei*, Phys. Lett. **B595** (2004) 216, nucl-th/0401042.

[34] L. Alvarez-Ruso, P. Muehlich, O. Buss and U. Mosel, *Low energy double-pion photoproduction in nuclei*, Int. J. Mod. Phys. **A20** (2005) 578.

[35] O. Buss, L. Alvarez-Ruso, P. Muehlich, U. Mosel and R. Shyam, *Low-energy pions in nuclear matter and $\pi\pi$ photoproduction within a BUU transport model* nucl-th/0502031.

[36] O. Buss, L. Alvarez-Ruso, P. Muhlich and U. Mosel, *Low-energy pions in nuclear matter and $\pi\pi$ photoproduction within a BUU transport model*, Eur. Phys. J. **A29** (2006) 189, nucl-th/0603003.

[37] B. Krusche, T. Mertens, I. Jaegle *et al.*, to be published.

[38] L. Alvarez-Ruso, T. Falter, U. Mosel and P. Muehlich, *In-medium properties of hadrons: Observables 2*, Prog. Part. Nucl. Phys. **55** (2005) 71, nucl-th/0412084.

[39] P. Muehlich *et al.*, *Photoproduction of ϕ mesons from nuclei*, Phys. Rev. **C67** (2003) 024605, nucl-th/0210079.

[40] P. Muhlich and U. Mosel, *Attenuation of ϕ mesons in γA reactions*, Nucl. Phys. **A765** (2006) 188, nucl-th/0510078.

[41] P. Muehlich, V. Shklyar, S. Leupold, U. Mosel and M. Post, *The spectral function of the omega meson in nuclear matter from a coupled-channel resonance model*, Nucl. Phys. **A780** (2006) 187, nucl-th/0607061.

[42] K. Gallmeister *et al.*, *In-medium hadrons: Properties, interaction and formation* nucl-th/0608025.

[43] P. Muehlich, T. Falter and U. Mosel, *Inclusive ω photoproduction off nuclei*, Eur. Phys. J. **A20** (2004) 499, nucl-th/0310067.

[44] T. Falter, J. Lehr, U. Mosel, P. Muehlich and M. Post, *In-medium properties of hadrons: Observables*, Prog. Part. Nucl. Phys. **53** (2004) 25, nucl-th/0312093.

[45] P. Muehlich, T. Falter and U. Mosel, *In-medium properties of the ω meson through ω photoproduction in nuclei* nucl-th/0402039.

[46] P. Muehlich and U. Mosel, *In-medium properties of the ω meson in photon induced nuclear reactions* nucl-th/0502029.

[47] P. Muhlich and U. Mosel, *Omega attenuation in nuclei*, Nucl. Phys. **A773** (2006) 156, nucl-th/0602054.

[48] L.-H. Chan and R. W. Haymaker, *Closed-loop corrections to the $SU(3) \times SU(3)$ sigma model - one- and two-point functions*, Phys. Rev. **D7** (1973) 402.

[49] T. Hatsuda, T. Kunihiro and H. Shimizu, *Precursor of chiral symmetry restoration in the nuclear medium*, Phys. Rev. Lett. **82** (1999) 2840.

[50] T. Hatsuda and T. Kunihiro, *The sigma meson and $\pi\pi$ correlation in hot/dense medium: Soft modes for chiral transition in QCD* nucl-th/0112027.

[51] J. Wambach, Z. Aouissat and P. Schuck, *Chiral fluctuations in nuclei*, Nucl. Phys. **A690** (2001) 127.

[52] G. Chanfray, D. Davesne, M. Ericson and M. Martini, *Two pion production processes, chiral symmetry and NN interaction in the medium*, Eur. Phys. J. **A27** (2006) 191.

[53] F. Bonutti *et al.*, *The $\pi\pi$ interaction in nuclear matter from a study of the $\pi^+ A \to \pi^+\pi^\pm A'$ reactions*, Nucl. Phys. **A677** (2000) 213, nucl-ex/0007017.

[54] A. Starostin *et al.*, *Measurement of $\pi^0\pi^0$ production in the nuclear medium by π^- interactions at* 0.408 GeV, Phys. Rev. Lett. **85** (2000) 5539.

[55] P. Camerini *et al.*, *General properties of the pion production reaction in nuclear matter*, Nucl. Phys. **A735** (2004) 89, nucl-ex/0401018.

[56] J. A. Oller and E. Oset, *Chiral symmetry amplitudes in the s-wave isoscalar and isovector channels and the sigma, f0(980), a0(980) scalar mesons*, Nucl. Phys. **A620** (1997) 438, hep-ph/9702314.

[57] M. J. Vicente Vacas and E. Oset, *Nuclear medium effects on the sigma mass and width* nucl-th/0112048.

[58] M. E. Peskin and D. V. Schroeder, *An Introduction to quantum field theory*, Addison-Wesley, Reading, USA (1995).

[59] U. Mosel, *Fields, symmetries, and quarks*, McGraw-Hill, Hamburg, Germany (1989).

[60] V. Koch, *Aspects of chiral symmetry*, Int. J. Mod. Phys. **E6** (1997) 203, nucl-th/9706075.

[61] J. Goldstone, *Broken symmetries*, Phys. Rev. Lett. **127** (1962) 965.

[62] W. Weise, *Quarks, hadrons and dense nuclear matter* Given at Les Houches Summer School on Theoretical Physics, Session 66: Trends in Nuclear Physics, 100 Years Later, Les Houches, France, 30 Jul - 30 Aug 1996.

[63] T. E. O. Ericson and W. Weise, *Pions and Nuclei*, *The international series of monographs on physics*, volume 74, Clarendon, Oxford, UK (1988).

[64] M. Gell-Mann and M. Levy, *The axial vector current in beta decay*, Nuovo Cim. **16** (1960) 705.

[65] J. D. Bjorken and S. D. Drell, *Relativistic quantum field theory*, volume 101, BI Hochschultaschenbuecher, Mannheim (1967).

[66] M. Post, *Hadronic spectral functions in nuclear matter*, Ph.D. thesis, Universitat Giessen (2003), http://theorie.physik.uni-giessen.de/documents/dissertation/post.pdf.

[67] T. Kunihiro, *The sigma meson and chiral transition in hot and dense matter*, AIP Conf. Proc. **619** (2002) 315, hep-ph/0111121.

[68] M. K. Volkov, A. E. Radzhabov and N. L. Russakovich, *sigma meson in hot and dense matter*, Phys. Atom. Nucl. **66** (2003) 997, hep-ph/0203170.

[69] D. Cabrera, E. Oset and M. J. Vicente Vacas, *Evaluation of the $\pi\pi$ scattering amplitude in the sigma channel at finite density*, Phys. Rev. **C72** (2005) 025207, nucl-th/0503014.

[70] M. Post, S. Leupold and U. Mosel, *Hadronic spectral functions in nuclear matter*, Nucl. Phys. **A741** (2004) 81, nucl-th/0309085.

[71] T. Hatsuda and T. Kunihiro, *Chiral symmetry restoration and the sigma meson* hep-ph/0010039.

[72] S. Ishida *et al.*, *Possible existence of the sigma meson and its implications to hadron physics. Proceedings, Workshop, Sigma Meson 2000, Kyoto, Japan, June 12-14, 2000* Prepared for YITP Workshop on Possible Existence of the sigma meson and it Implications to Hadron Physics (sigma-meson 2000), Kyoto, Japan, 12-14 Jun 2000.

[73] G. Chanfray and M. Ericson, *Critical fluctuations of the quark density in nuclei*, Eur. Phys. J. **A16** (2003) 291, nucl-th/0106069.

[74] G. Chanfray and D. Davesne, *Pion interaction in nuclear matter and chiral symmetry restoration*, Nucl. Phys. **A646** (1999) 125.

[75] M. J. Vicente Vacas and E. Oset, *Scalar isoscalar pion pairs in nuclei and the $A(\pi, \pi\pi)X$ reaction*, Phys. Rev. **C60** (1999) 064621, nucl-th/9907008.

[76] L. Roca, E. Oset and M. J. Vicente Vacas, *The sigma meson in a nuclear medium through two pion photoproduction*, Phys. Lett. **B541** (2002) 77, nucl-th/0201054.

[77] V. Bernard, U. G. Meissner and I. Zahed, *Properties of the scalar σ meson at finite density*, Phys. Rev. Lett. **59** (1987) 966.

[78] S. Schadmand, *Medium modifications of hadrons studied with photonuclear reactions*, Acta Phys. Polon. **B33** (2002) 873.

[79] S. Schadmand, *Nucleon resonances and meson production with TAPS at MAMI*, Acta Phys. Polon. **B31** (2000) 2431.

[80] V. Metag, *Are properties of hadrons changed in the nuclear medium? Experimental observations*, Nucl. Phys. **A690** (2001) 140.

[81] F. Bloch *et al.*, *$2\pi^0$ photoproduction from nuclei*, AIP Conference Proceedings **717** (2004) 372.

[82] S. Schadmand, *Two pion production in photon induced reactions* nucl-ex/0505023.

[83] S. Schadmand, *Double pion photoproduction from nuclei* nucl-ex/0504012.

[84] O. Buss, *Low-energy pions in a Boltzmann-Uehling-Uhlenbeck transport simulation*, Diploma thesis, Universitat Giessen (2004), http://theorie.physik.uni-giessen.de/documents/diplom/buss.pdf.

[85] E. Oset, L. Roca, M. J. Vicente Vacas and J. C. Nacher, *Two pion photoproduction on nucleons and nuclei in the rho and sigma regions* nucl-th/0112033.

[86] V. Metag and R. S. Simon, *Technical proposal for a two-arm photon spectrometer (TAPS)* 31, gSI Report GSI 87-19.

[87] S. Schadmand, *Photoproduction from nuclei in the resonance region*, Habilitation thesis Universitaet Giessen.

[88] H. Shimizu, T. Matsumura and T. Yorita, 2π *production experiments at SPring-8* Prepared for YITP Workshop on Possible Existence of the sigma meson and its implications to Hadron Physics (sigma-meson 2000), Kyoto, Japan, 12-14 Jun 2000.

[89] H. Shimizu, T. Matsumura, P. Shagin and T. Yorita, *Photoproduction of* $2\pi^0$ *with nuclear targets* Prepared for International Workshop on Physics with GeV Electrons and Gamma Rays, Sendai, Japan, 13-15 Feb 2001.

[90] T. Matsumura *et al.*, $2\pi^0$ *photoproduction experiment at SPring-8*, Nucl. Phys. **A721** (2003) 723.

[91] A. Braghieri *et al.*, *Total cross-section measurement for the three double pion production channels on the proton*, Phys. Lett. **B363** (1995) 46.

[92] A. Zabrodin *et al.*, *Total cross section measurement of the* $\gamma n \to p\pi^-\pi^0$ *reaction*, Phys. Rev. **C55** (1997) 1617.

[93] V. Kleber *et al.*, *Double* π^0 *photoproduction from the deuteron*, Eur. Phys. J. **A9** (2000) 1.

[94] M. Wolf *et al.*, *Photoproduction of neutral pion pairs from the proton*, Eur. Phys. J. **A9** (2000) 5.

[95] M. Kotulla *et al.*, *Double* π^0 *photoproduction off the proton at threshold*, Phys. Lett. **B578** (2004) 63, nucl-ex/0310031.

[96] A. Zabrodin, P. Pedroni *et al.*, private communication.

[97] J. C. Nacher, E. Oset, M. J. Vicente and L. Roca, *The role of* $\Delta(1700)$ *excitation and* ρ *production in double pion photoproduction*, Nucl. Phys. **A695** (2001) 295, nucl-th/0012065.

[98] J. A. Gomez Tejedor and E. Oset, *Double pion photoproduction on the nucleon: Study of the isospin channels*, Nucl. Phys. **A600** (1996) 413, hep-ph/9506209.

[99] O. Buss, L. Alvarez-Ruso, A. B. Larionov and U. Mosel, *Pion induced double charge exchange reactions in the Delta resonance region*, Phys. Rev. **C74** (2006) 044610, nucl-th/0607016.

[100] M. Effenberger, *Eigenschaften von Hadronen in einem vereinheitlichten Transportmodell*, Ph.D. thesis, Universitaet Giessen (1999), http://theorie.physik.uni-giessen.de/documents/dissertation/effenberger.ps.gz.

[101] J. Nieves, E. Oset and C. Garcia-Recio, *Many body approach to low-energy pion nucleus scattering*, Nucl. Phys. **A554** (1993) 554.

[102] C. Garcia-Recio, E. Oset, L. L. Salcedo, D. Strottman and M. J. Lopez, *Pion nucleus elastic scattering in the microscopic local Δh model*, Nucl. Phys. **A526** (1991) 685.

[103] J. Nieves, E. Oset and C. Garcia-Recio, *A Theoretical approach to pionic atoms and the problem of anomalies*, Nucl. Phys. **A554** (1993) 509.

[104] R. A. Mehrem, H. M. A. Radi and J. O. Rasmussen, *Behavior of pions incident on a slab of uniform complex nuclear material*, Phys. Rev. **C30** (1984) 301.

[105] P. Hecking, *Pion mean free path in nuclear matter*, Phys. Lett. **B103** (1981) 401.

[106] K. Nakai *et al.*, *Measurements of cross sections for pion absorption by nuclei*, Phys. Rev. Lett. **44** (1980) 1446.

[107] L. Roca, E. Oset and M. J. Vicente Vacas, private communication.

[108] R. A. Arndt, I. I. Strakovsky, R. L. Workman and M. M. Pavan, *Updated analysis of πN elastic scattering data to* 2.1 GeV*: The Baryon spectrum*, Phys. Rev. **C52** (1995) 2120, nucl-th/9505040.

[109] R. A. Arndt, I. I. Strakovsky and R. L. Workman, *The SAID PWA program*, Int. J. Mod. Phys. **A18** (2003) 449.

[110] A. Engel, W. Cassing, U. Mosel, M. Schafer and G. Wolf, *Pion-nucleus reactions in a microscopic transport model*, Nucl. Phys. **A572** (1994) 657, nucl-th/9307008.

[111] F. Bloch, B. Krusche *et al.*, Eur. Phys. J. **A**, to be published, nucl-ex/0703037.

[112] R. Rapp *et al.*, *Enhancement of $\pi A \to \pi\pi A$ threshold cross sections by in-medium $\pi\pi$ final state interactions*, Phys. Rev. **C59** (1999) 1237, nucl-th/9810007.

[113] R. Rapp, J. W. Durso and J. Wambach, *Chirally constraining the $\pi\pi$ interaction in nuclear matter*, Nucl. Phys. **A596** (1996) 436, nucl-th/9508026.

[114] F. Bonutti *et al.*, *$\pi^+ \to \pi^+\pi^\pm$ on deuterium at $T(\pi^+) = 283$* MeV, Nucl. Phys. **A638** (1998) 729.

[115] V. V. Vereshagin *et al.*, *Analysis of data on low-energy $\pi N \to \pi\pi N$ reaction. 1. Total cross-sections*, Nucl. Phys. **A592** (1995) 413, hep-ph/9504361.

[116] M. Kermani *et al.*, *Exclusive measurements of $\pi^\pm p \to \pi^+\pi^\pm n$ near threshold*, Phys. Rev. **C58** (1998) 3419.

[117] S. Prakhov *et al.*, *Measurement of $\pi^- p \to \pi^0\pi^0 n$ from threshold to $p(\pi^-) =$* 750 MeV, Phys. Rev. **C69** (2004) 045202.

[118] G. R. Smith *et al.*, *The CHAOS spectrometer for pion physics at TRIUMF*, Nucl. Instrum. Meth. **A362** (1995) 349.

[119] S. Prakhov *et al.*, *Search for the CP forbidden decay $\eta \to 4\pi^0$*, Phys. Rev. Lett. **84** (2000) 4802.

[120] S. A. Bunyatov *et al.*, *The investigation of $\pi^- p \to \pi^0\pi^0 n$ and $\pi^- p \to \pi^0\gamma n$ reactions at* 270 MeV, Sov. J. Nucl. Phys. **25** (1977) 177.

[121] A. A. Belkov *et al.*, *The investigation of the $\pi^- p \to \pi^0\pi^0 n$ reaction near the threshold*, Sov. J. Nucl. Phys. **31** (1980) 96.

[122] C. W. Bjork *et al.*, *Measurement of $\pi^- p \to \pi^-\pi^+ n$ near threshold and chiral symmetry breaking*, Phys. Rev. Lett. **44** (1980) 62.

[123] G. Kernel *et al.*, *Cross section measurement of $\pi^- p \to \pi^-\pi^+ n$ reaction near threshold*, Phys. Lett. **B216** (1989) 244.

[124] G. Kernel *et al.*, *Measurement of the reaction $\pi^+ p \to \pi^+\pi^+ n$ near threshold*, Z. Phys. **C48** (1990) 201.

[125] M. E. Sevior *et al.*, *Measurement of the $H(\pi^+, \pi^+\pi^+)n$ cross section near threshold and chiral symmetry*, Phys. Rev. Lett. **66** (1991) 2569.

[126] J. Lowe *et al.*, *$\pi^- p \to \pi^0\pi^0 n$ near threshold and chiral symmetry breaking*, Phys. Rev. **C44** (1991) 956.

[127] K. Craig *et al.*, *Dynamics of the $\pi^- p \to \pi^0\pi^0 n$ reaction for $p(\pi^-) < 750$ MeV*, Phys. Rev. Lett. **91** (2003) 102301.

[128] N. Grion *et al.*, *The $\pi \to \pi\pi$ process in nuclei and the restoration of chiral symmetry*, Nucl. Phys. **A763** (2005) 80, nucl-ex/0508028.

[129] E. Oset and M. J. Vicente-Vacas, *A model for the $\pi^- p \to \pi^+\pi^- n$ reaction*, Nucl. Phys. **A446** (1985) 584.

[130] V. Sossi, N. Fazel, R. R. Johnson and M. J. Vicente-Vacas, *$H(\pi, 2\pi)$ cross sections with $\pi\pi$ scattering derived from chiral Lagrangians*, Phys. Lett. **B298** (1993) 287.

[131] N. Fazel, R. R. Johnson and V. Sossi, *$\pi N \to \pi\pi N$ cross sections near threshold using the Oset-Vicente-Vacas model, and derivation of the chiral symmetry breaking parameter*, PiN Newslett. **7** (1992) 53.

[132] J. Beringer, *$\pi N \to \pi\pi N$ scattering in chiral perturbation theory*, PiN Newslett. **7** (1992) 33.

[133] O. Jaekel and M. Dillig, *Chiral symmetry and the near threshold pion induced 2π production on the nucleon. 3: Perturbative estimate of initial and final state interactions*, Nucl. Phys. **A561** (1993) 557.

[134] V. Bernard, N. Kaiser and U.-G. Meissner, *The reaction $\pi N \to \pi\pi N$ above threshold in chiral perturbation theory*, Nucl. Phys. **A619** (1997) 261, hep-ph/9703218.

[135] N. Fettes, V. Bernard and U. G. Meissner, *One-loop analysis of the reaction $\pi N \to \pi\pi N$*, Nucl. Phys. **A669** (2000) 269, hep-ph/9907276.

[136] H. Kamano and M. Arima, *The $\pi N \to \pi\pi N$ reaction around N*(1440) energy*, Phys. Rev. **C73** (2006) 055203, nucl-th/0601057.

[137] S. Schneider, S. Krewald and U.-G. Meissner, *The reaction $\pi N \to \pi\pi N$ in a meson-exchange approach* nucl-th/0603040.

[138] M. G. Olsson, U.-G. Meissner, N. Kaiser and V. Bernard, *On the interpretation of $\pi N \to \pi\pi N$ data near threshold*, PiN Newslett. **10** (1995) 201, hep-ph/9503237.

[139] L. Alvarez-Ruso, *Excitation of baryonic resonances induced by nucleons and leptons*, Ph.D. thesis, Universidad de Valencia (1999), ific.uv.es/nucth/thesis_alvarezruso.ps.

[140] V. Bernard, N. Kaiser and U.-G. Meissner, *Determination of the low-energy constants of the next-to- leading order chiral pion nucleon Lagrangian*, Nucl. Phys. **A615** (1997) 483, hep-ph/9611253.

[141] S. Eidelman *et al.*, *Review of particle physics*, Phys. Lett. **B592** (2004) 1.

[142] L. Hulthen and M. Sugawara, volume 39, Springer, Berlin (1957).

[143] T. H. Bauer, R. D. Spital, D. R. Yennie and F. M. Pipkin, *The hadronic properties of the photon in high-energy interactions*, Rev. Mod. Phys. **50** (1978) 261.

[144] T. Falter, S. Leupold and U. Mosel, *Low energy onset of nuclear shadowing in photoabsorption*, Phys. Rev. **C62** (2000) 031602, nucl-th/0002062.

[145] S. Teis *et al.*, *Probing nuclear expansion dynamics with π^-/π^+ spectra*, Z. Phys. **A359** (1997) 297, nucl-th/9701057.

[146] S. Teis, *Transporttheoretische Beschreibung von relativistischen Schwerionenkollisionen bei SIS-Energien*, Ph.D. thesis, Universitat Giessen (1997), http://theorie.physik.uni-giessen.de/documents/dissertation/promotion_s_teis.ps.gz.

[147] W. Greiner, *Mechanik*, Springer, Frankfurt (1989).

[148] M. Alqadi and W. R. Gibbs, *Final state interactions in pion production from nuclei* nucl-th/0208031.

[149] J. Lehr, M. Post and U. Mosel, *In-medium modifications of the $S_{11}(1535)$ resonance and η photoproduction*, Phys. Rev. **C68** (2003) 044601, nucl-th/0306024.

[150] D. M. Manley and E. M. Saleski, *Multichannel resonance parametrization of πN scattering amplitudes*, Phys. Rev. **D45** (1992) 4002.

[151] M. Effenberger and A. Sibirtsev, *The energy dependence of the in-medium ηN cross section evaluated from η photoproduction*, Nucl. Phys. **A632** (1998) 99, nucl-th/9710054.

[152] B. Krusche, I. Jaegle and T. Mertens, *Photoexcitation of baryon resonances on nucleons and nuclei*, Eur. Phys. J. **A**, proceedings of the IV International Conference on Quarks and Nuclear Physics, Madrid, Spain, 5. - 10. June 2006, in press.

[153] M. Roebig-Landau *et al.*, *Near threshold photoproduction of η mesons from complex nuclei*, Phys. Lett. **B373** (1996) 45.

[154] T. Yorita *et al.*, *Observation of $S_{11}(1535)$ resonance in nuclear medium via the $^{12}C(\gamma,\eta)$ reaction*, Phys. Lett. **B476** (2000) 226.

[155] H. Yamazaki *et al.*, *Study of S_{11} resonance in nuclei through (γ,η) reactions*, Nucl. Phys. **A670** (2000) 202.

[156] I. Jaegle, private communication.

[157] T. Mertens, *Photoproduction of η mesons from nuclei*, Ph.D. thesis, Universitaet Basel (2006).

[158] G. Penner and U. Mosel, *Vector meson production and nucleon resonance analysis in a coupled channel approach for energies $m_N < \sqrt{s} < 2$ GeV. II: Photon induced results*, Phys. Rev. **C66** (2002) 055212, nucl-th/0207069.

[159] M. Effenberger, E. L. Bratkovskaya and U. Mosel, *e^+e^- pair production from γA reactions*, Phys. Rev. **C60** (1999) 044614, nucl-th/9903026.

[160] V. Crede *et al.*, *Photoproduction of η mesons off protons for* 0.75 GeV $< E_\gamma <$ 3 GeV, Phys. Rev. Lett. **94** (2005) 012004, hep-ex/0311045.

[161] B. Krusche *et al.*, *New threshold photoproduction of η mesons off the proton*, Phys. Rev. Lett. **74** (1995) 3736.

[162] J. W. Price *et al.*, *Eta meson photoproduction on hydrogen near threshold*, Phys. Rev. **C51** (1995) 2283.

[163] V. Crede, *Photoproduction of $\gamma p \to p\pi^0\eta$ at ELSA in Bonn* Prepared for NSTAR 2002 Workshop on the Physics of Excited Nucleons, Pittsburgh, Pennsylvania, 9-12 Oct 2002.

[164] V. Crede, *Investigation of $\gamma p \to p\pi^0\eta$ at ELSA in Bonn*, AIP Conf. Proc. **717** (2004) 236.

[165] W.-T. Chiang, S.-N. Yang, L. Tiator and D. Drechsel, *An isobar model for η photo- and electroproduction on the nucleon*, Nucl. Phys. **A700** (2002) 429, nucl-th/0110034.

[166] T. Falter, *Nuclear reactions of high energy protons, photons, and leptons*, Ph.D. thesis, Universitat Giessen (2004), http://theorie.physik.uni-giessen.de/documents/dissertation/falter_phd.pdf.

[167] R. M. Brown *et al.*, *Differential cross sections for the reaction $\pi^-p \to \eta n$ between* 724 MeV *and* 2723 MeV, Nucl. Phys. **B153** (1979) 89.

[168] H. R. Crouch *et al.*, *Cross sections for $\pi^-p \to (1-5)\pi^0 N$ and $\pi^-p \to \eta(\to 2\gamma)N$ for incident pion momenta between* 1.3 GeV *and* 3.8 GeV, Phys. Rev. **D21** (1980) 3023.

[169] S. Prakhov *et al.*, *Measurement of $\pi^-p \to \eta n$ from threshold to $p_{\pi^-} = 747$* MeV, Phys. Rev. **C72** (2005) 015203.

[170] V. Shklyar, H. Lenske and U. Mosel, *Eta photoproduction in the resonance energy region* nucl-th/0611036.

[171] T. P. Vrana, S. A. Dytman and T. S. H. Lee, *Baryon resonance extraction from πN data using a unitary multichannel model*, Phys. Rept. **328** (2000) 181, nucl-th/9910012.

[172] T. Feuster and U. Mosel, *A unitary model for meson nucleon scattering*, Phys. Rev. **C58** (1998) 457, nucl-th/9708051.

[173] G. Penner and U. Mosel, *Vector meson production and nucleon resonance analysis in a coupled channel approach for energies* $m_N < \sqrt{s} < 2$ GeV. *I: Pion induced results and hadronic parameters*, Phys. Rev. **C66** (2002) 055211, nucl-th/0207066.

[174] V. Shklyar, G. Penner and U. Mosel, *Spin-5/2 resonance contributions to the pion-induced reactions for energies* $\sqrt{s} \leq 2$ GeV, Eur. Phys. J. **A21** (2004) 445, nucl-th/0403064.

[175] B. Krusche *et al.*, *Near threshold photoproduction of eta mesons from the deuteron*, Phys. Lett. **B358** (1995) 40.

[176] J. Weiss *et al.*, *Exclusive measurements of quasifree eta photoproduction from deuterium*, Eur. Phys. J. **A16** (2003) 275, nucl-ex/0210003.

[177] V. Hejny *et al.*, *Near threshold photoproduction of eta mesons from* ^{4}He, Eur. Phys. J. **A6** (1999) 83.

[178] R. A. Arndt, Y. I. Azimov, M. V. Polyakov, I. I. Strakovsky and R. L. Workman, *Nonstrange and other unitarity partners of the exotic* Θ^+ *baryon*, Phys. Rev. **C69** (2004) 035208, nucl-th/0312126.

[179] R. C. Carrasco and E. Oset, *Interaction of real photons with nuclei from* 100 MeV *to* 500 MeV, Nucl. Phys. **A536** (1992) 445.

[180] M. Effenberger, A. Hombach, S. Teis and U. Mosel, *Photoabsorption on nuclei*, Nucl. Phys. **A613** (1997) 353, nucl-th/9607005.

[181] R. L. Walker, *Phenomenological analysis of single pion photoproduction*, Phys. Rev. **182** (1969) 1729.

[182] T. Mertens, private communication.

[183] R. Arnaldi *et al.*, *First measurement of the rho spectral function in high- energy nuclear collisions*, Phys. Rev. Lett. **96** (2006) 162302, nucl-ex/0605007.

[184] R. Rapp and J. Wambach, *Chiral symmetry restoration and dileptons in relativistic heavy-ion collisions*, Adv. Nucl. Phys. **25** (2000) 1, hep-ph/9909229.

[185] http://www-dapnia.cea.fr/Sphn/Clas/CLASDet.

[186] G.-Q. Li, C. M. Ko and G. E. Brown, *Enhancement of low mass dileptons in heavy ion collisions*, Phys. Rev. Lett. **75** (1995) 4007, nucl-th/9504025.

[187] W. Cassing, W. Ehehalt and C. M. Ko, *Dilepton production at SPS energies*, Phys. Lett. **B363** (1995) 35, hep-ph/9508233.

[188] W. Cassing, W. Ehehalt and I. Kralik, *Analysis of the HELIOS-3* $\mu^+\mu^-$ *Data within a Relativistic Transport Approach*, Phys. Lett. **B377** (1996) 5, hep-ph/9601214.

[189] E. L. Bratkovskaya and W. Cassing, *Dilepton production from AGS to SPS energies within a relativistic transport approach*, Nucl. Phys. **A619** (1997) 413, nucl-th/9611042.

[190] L. Bergstrom, *Rare decay of a pseudoscalar meson into a lepton pair: a way to detect new interactions?*, Zeit. Phys. **C14** (1982) 129.

[191] T. E. Browder *et al.*, *A new upper limit on the decay* $\eta \to e^+e^-$, Phys. Rev. **D56** (1997) 5359, hep-ex/9706005.

[192] J. Weil and U. Mosel, Independent Studies Project, Universitaet Giessen (2006), http://www.stud.uni-giessen.de/~su5092/bh/bethe-heitler.pdf.

[193] S. Leupold and U. Mosel, *On QCD sum rules for vector mesons in nuclear medium*, Phys. Rev. **C58** (1998) 2939, nucl-th/9805024.

[194] D. B. Kaplan and A. E. Nelson, *Strange goings on in dense nucleonic matter*, Phys. Lett. **B175** (1986) 57.

[195] J. Schaffner, J. Bondorf and I. N. Mishustin, *In-medium kaon production at the mean-field level*, Nucl. Phys. **A625** (1997) 325, nucl-th/9607058.

[196] T. Waas and W. Weise, *S-wave interactions of* $\bar{K}$ *and* η *mesons in nuclear matter*, Nucl. Phys. **A625** (1997) 287.

[197] M. Lutz, *Nuclear kaon dynamics*, Phys. Lett. **B426** (1998) 12, nucl-th/9709073.

[198] A. Ramos and E. Oset, *The properties of* $\bar{K}$ *in the nuclear medium*, Nucl. Phys. **A671** (2000) 481, nucl-th/9906016.

[199] L. Tolos, A. Ramos and A. Polls, *The antikaon nuclear potential in hot and dense matter*, Phys. Rev. **C65** (2002) 054907, nucl-th/0202057.

[200] F. Klingl, N. Kaiser and W. Weise, *Current correlation functions, QCD sum rules and vector mesons in baryonic matter*, Nucl. Phys. **A624** (1997) 527, hep-ph/9704398.

[201] F. Klingl, T. Waas and W. Weise, *Modification of the* ϕ *meson spectrum in nuclear matter*, Phys. Lett. **B431** (1998) 254, hep-ph/9709210.

[202] E. Oset and A. Ramos, *Phi decay in nuclei*, Nucl. Phys. **A679** (2001) 616, nucl-th/0005046.

[203] D. Cabrera and M. J. Vicente Vacas, *Phi meson mass and decay width in nuclear matter*, Phys. Rev. **C67** (2003) 045203, nucl-th/0205075.

[204] D. Cabrera, L. Roca, E. Oset, H. Toki and M. J. Vicente Vacas, *Mass dependence of inclusive nuclear* ϕ *photoproduction*, Nucl. Phys. **A733** (2004) 130, nucl-th/0310054.

[205] E. Oset, M. J. Vicente Vacas, H. Toki and A. Ramos, *Test of* ϕ *renormalization in nuclei through* ϕ *photoproduction*, Phys. Lett. **B508** (2001) 237, nucl-th/0011019.

[206] B. Povh, C. Scholz, K. Rith and F. Zetsche, *Particles and nuclei: An introduction to the physical conceptions. (In German)*, Springer, Berlin (1993).

[207] A. Donnachie and P. V. Landshoff, *Exclusive vector photoproduction: Confirmation of Regge theory*, Phys. Lett. **B478** (2000) 146, hep-ph/9912312.

[208] H. J. Besch *et al.*, *Photoproduction of* ϕ *mesons on protons at 2.0 GeV*, Nucl. Phys. **B70** (1974) 257.

[209] E. Anciant *et al.*, *Photoproduction of $\phi(1020)$ mesons on the proton at large momentum transfer*, Phys. Rev. Lett. **85** (2000) 4682, hep-ex/0006022.

[210] *Photoproduction of meson and baryon resonances at energies up to 5.8 GeV*, Phys. Rev. **175** (1968) 1669.

[211] P. Muehlich, *Photoproduktion von ϕ Mesonen an Kernen*, Diploma thesis, Universitaet Giessen (2001), http://theorie.physik.uni-giessen.de/documents/diplom/muehlich.pdf.

[212] H. Alvensleben *et al.*, *Photoproduction of neutral ρ mesons from complex nuclei*, Phys. Rev. Lett. **24** (1970) 786.

[213] T. Ishikawa *et al.*, *ϕ photo-production from Li, C, Al, and Cu nuclei at $E_\gamma = (1.5 - 2.4)$ GeV*, Phys. Lett. **B608** (2005) 215.

[214] T. Nakano *et al.*, *Multi-GeV laser electron photon project at SPring-8*, Nucl. Phys. **A684** (2001) 71.

[215] T. Nakano *et al.*, *Observation of $S = +1$ baryon resonance in photo-production from neutron*, Phys. Rev. Lett. **91** (2003) 012002, hep-ex/0301020.

[216] R. G. T. Zegers *et al.*, *Beam polarization asymmetries for the $p(\gamma, K^+)\Lambda$ and $p(\gamma, K^+)\Sigma^0$ reactions at $E_\gamma = (1.5 - 2.4)$ GeV*, Phys. Rev. Lett. **91** (2003) 092001, nucl-ex/0302005.

[217] A. I. Titov, T. S. H. Lee, H. Toki and O. Streltsova, *Structure of the ϕ photoproduction amplitude at a few GeV*, Phys. Rev. **C60** (1999) 035205.

[218] H. Haberzettl, C. Bennhold, T. Mart and T. Feuster, *Gauge-invariant tree-level photoproduction amplitudes with form factors*, Phys. Rev. **C58** (1998) 40, nucl-th/9804051.

[219] H. J. Behrend *et al.*, *Elastic and inelastic ϕ photoproduction*, Nucl. Phys. **B144** (1978) 22.

[220] G. A. Schuler and T. Sjostrand, *Low and high mass components of the photon distribution functions*, Z. Phys. **C68** (1995) 607, hep-ph/9503384.

[221] G. A. Schuler and T. Sjostrand, *Parton distributions of the virtual photon*, Phys. Lett. **B376** (1996) 193, hep-ph/9601282.

[222] J. J. Sakurai, *Theory of strong interactions*, Annals Phys. **11** (1960) 1.

[223] M. Gell-Mann and F. Zachariasen, *Form-factors and vector mesons*, Phys. Rev. **124** (1961) 953.

[224] Y. S. Golubeva, L. A. Kondratyuk and W. Cassing, *Medium effects in the production and decay of vector mesons in pion nucleus reactions*, Nucl. Phys. **A625** (1997) 832, nucl-th/9710071.

[225] A. Sibirtsev, W. Cassing and U. Mosel, *Heavy meson production in proton nucleus reactions with empirical spectral functions*, Z. Phys. **A358** (1997) 357, nucl-th/9607047.

[226] F. Klingl, N. Kaiser and W. Weise, *Effective Lagrangian approach to vector mesons, their structure and decays*, Z. Phys. **A356** (1996) 193.

[227] C. Fuchs, D. S. Kosov, A. Faessler, Z. S. Wang and T. Waindzoch, *Consequences of covariant kaon dynamics in heavy ion collisions*, Phys. Lett. **B434** (1998) 245, nucl-th/9801048.

[228] A. E. Nelson and D. B. Kaplan, *Strange condensate realignment in relativistic heavy ion collisions*, Phys. Lett. **B192** (1987) 193.

[229] G. E. Brown and M. Rho, *From chiral mean field to Walecka mean field and kaon condensation*, Nucl. Phys. **A596** (1996) 503, nucl-th/9507028.

[230] A. B. Larionov and U. Mosel, *Kaon production and propagation at intermediate relativistic energies*, Phys. Rev. **C72** (2005) 014901.

[231] A. B. Larionov and U. Mosel, *Kaon production and propagation at SIS energies* nucl-th/0504023.

[232] J. Schaffner-Bielich, V. Koch and M. Effenberger, *Medium modified cross sections, temperature and finite momentum effects for antikaon production in heavy-ion collisions*, Nucl. Phys. **A669** (2000) 153, nucl-th/9907095.

[233] C. L. Korpa and M. F. M. Lutz, *Kaon and antikaon properties in cold nuclear medium*, Acta Phys. Hung. **A22** (2005) 21, nucl-th/0404088.

[234] V. Bernard and U. G. Meissner, *Properties of vector and axial vector mesons from a generalized Nambu-Jona-Lasinio Model*, Nucl. Phys. **A489** (1988) 647.

[235] J. C. Caillon and J. Labarsouque, *The Omega meson mass in nuclear matter with a density dependent relativistic NN interaction*, J. Phys. **G21** (1995) 905.

[236] B. Friman, *Meson nucleon scattering and vector mesons in nuclear matter*, Acta Phys. Polon. **B29** (1998) 3195, nucl-th/9808071.

[237] F. Klingl, T. Waas and W. Weise, *Nuclear bound states of omega mesons*, Nucl. Phys. **A650** (1999) 299.

[238] K. Saito, K. Tsushima, A. W. Thomas and A. G. Williams, *Sigma and omega meson propagation in a dense nuclear medium*, Phys. Lett. **B433** (1998) 243, nucl-th/9804015.

[239] K. Saito, K. Tsushima, D. H. Lu and A. W. Thomas, *Omega nucleus bound states in the Walecka model*, Phys. Rev. **C59** (1999) 1203, nucl-th/9807028.

[240] M. Post and U. Mosel, *Coupling of baryon resonances to the N omega channel*, Nucl. Phys. **A688** (2001) 808, nucl-th/0008040.

[241] M. F. M. Lutz, G. Wolf and B. Friman, *Scattering of vector mesons off nucleons*, Nucl. Phys. **A706** (2002) 431, nucl-th/0112052.

[242] A. K. Dutt-Mazumder, *omega meson propagation in dense nuclear matter and collective excitations*, Nucl. Phys. **A713** (2003) 119, nucl-th/0207070.

[243] T. Renk and A. Mishra, *Dilepton emission rates from hot hadronic matter*, Phys. Rev. **C69** (2004) 054905, nucl-th/0312039.

[244] A. T. Martell and P. J. Ellis, *Properties of the omega meson at finite temperature and density*, Phys. Rev. **C69** (2004) 065206, nucl-th/0404057.

[245] F. Riek and J. Knoll, *Self-consistent description of vector-mesons in matter*, Nucl. Phys. **A740** (2004) 287.

[246] A. K. Dutt-Mazumder, R. Hofmann and M. Pospelov, *Rho omega mixing in asymmetric nuclear matter via QCD sum rule approach*, Phys. Rev. **C63** (2001) 015204, hep-ph/0005100.

[247] T. Feuster and U. Mosel, *Photon and meson induced reactions on the nucleon*, Phys. Rev. **C59** (1999) 460, nucl-th/9803057.

[248] G. Penner, *Vector meson production and nucleon resonance analysis in a coupled channel approach*, Ph.D. thesis, Universitaet Giessen (2002), http://theorie.physik.uni-giessen.de/documents/dissertation/penner.pdf.

[249] V. Shklyar, H. Lenske, U. Mosel and G. Penner, *Coupled-channel analysis of the omega meson production in πN and γN reactions for CM energies up to 2 GeV*, Phys. Rev. **C71** (2005) 055206, nucl-th/0412029.

[250] W. Peters, M. Post, H. Lenske, S. Leupold and U. Mosel, *The spectral function of the rho meson in nuclear matter*, Nucl. Phys. **A632** (1998) 109, nucl-th/9708004.

[251] M. Post, S. Leupold and U. Mosel, *The rho spectral function in a relativistic resonance model*, Nucl. Phys. **A689** (2001) 753, nucl-th/0008027.

[252] S. Leupold and M. Post, *QCD sum rules at finite density in the large-N_c limit: The coupling of the ρ-nucleon system to the $D_{13}(1520)$*, Nucl. Phys. **A747** (2005) 425, nucl-th/0402048.

[253] L. Jahnke, *Complete Relativistic Description of the $N^*(1520)$*, Diploma thesis, Universitat Giessen (2005), http://theorie.physik.uni-giessen.de/documents/diplom/jahnke.pdf.

[254] R. Mertig and F. Orellana, *FeynCalc: Tools and Tables for Quantum Field Theory Calculations*, http://www.feyncalc.org, mathematica package, version 4.1.1.

[255] C. L. Korpa, *Complete spin structure of the pion nucleon loop Delta self-energy*, Heavy Ion Phys. **5** (1997) 77, hep-ph/9703339.

[256] L. M. Barkov *et al.*, *Measurement of the properties of the ω meson witha cryogenic magnetic detector*, JETP Lett. **46** (1987) 164.

[257] S. I. Dolinsky *et al.*, *Summary of experiments with the neutral detector at the e^+e^- storage ring VEPP-2M*, Phys. Rept. **202** (1991) 99.

[258] F. Eichstaedt, *In-medium properties of ω mesons*, Diploma thesis, Universitat Giessen (2006), http://theorie.physik.uni-giessen.de/documents/diplom/eichstaedt.pdf.

[259] M. Kaskulov, E. Hernandez and E. Oset, *Inclusive omega photoproduction from nuclei and omega in the nuclear medium* nucl-th/0610067.

[260] J. G. Messchendorp, A. Sibirtsev, W. Cassing, V. Metag and S. Schadmand, *Studying the omega mass in-medium in $\gamma + A \to \pi^0\gamma X$ reactions*, Eur. Phys. J. **A11** (2001) 95, hep-ex/0106041.

[261] G. I. Lykasov, W. Cassing, A. Sibirtsev and M. V. Rzyanin, *Omega N final state interactions and omega meson production from heavy-ion collisions*, Eur. Phys. J. **A6** (1999) 71, nucl-th/9811019.

[262] B. Andersson, G. Gustafson and H. Pi, *The FRITIOF model for very high-energy hadronic collisions*, Z. Phys. **C57** (1993) 485.

[263] V. L. Eletsky and B. L. Ioffe, *Meson masses in nuclear matter*, Phys. Rev. Lett. **78** (1997) 1010, hep-ph/9609229.

[264] L. A. Kondratyuk, A. Sibirtsev, W. Cassing, Y. S. Golubeva and M. Effenberger, *Rho meson properties at finite nuclear density*, Phys. Rev. **C58** (1998) 1078, nucl-th/9801055.

[265] H. Alvensleben *et al.*, *Determination of the photoproduction phase of ρ^0 mesons*, Phys. Rev. Lett. **25** (1970) 1377.

[266] H. Alvensleben *et al.*, *Determination of the photoproduction phase of ϕ mesons*, Phys. Rev. Lett. **27** (1971) 444.

[267] P. J. Biggs, D. W. Braben, R. W. Clifft, E. Gabathuler and R. E. Rand, *Determination of the real part of the rho-nucleon forward scattering amplitude and the relative rho-omega production phase*, Phys. Rev. Lett. **27** (1971) 1157.

[268] J. Barth *et al.*, *Low-energy of photoproduciton of omega mesons*, Eur. Phys. J. **A18** (2003) 117.

[269] J. Ballam *et al.*, *Vector meson production by polarized photons at 2.8 GeV, 4.7 GeV, and 9.3 GeV*, Phys. Rev. **D7** (1973) 3150.

[270] A. B. Larionov and U. Mosel, *The $NN \to N\Delta$ cross section in nuclear matter*, Nucl. Phys. **A728** (2003) 135, nucl-th/0307035.

[271] D. P. Barber *et al.*, *A study of the reactions $\gamma p \to \omega p$ and $\gamma p \to \omega\Delta^+$*, Z. Phys. **C26** (1984) 343.

[272] J. Lehr and U. Mosel, *In-medium broadening of nucleon resonances*, Phys. Rev. **C64** (2001) 042202, nucl-th/0105054.

[273] D. Trnka, M. Kotulla and V. Metag, private communication.

[274] A. Hombach, A. Engel, S. Teis and U. Mosel, *Pion and eta photoproduction in nuclei*, Z. Phys. **A352** (1995) 223, nucl-th/9411025.

[275] S. Teis *et al.*, *Pion-production in heavy-ion collisions at SIS energies*, Z. Phys. **A356** (1997) 421, nucl-th/9609009.

[276] A. Hombach, W. Cassing, S. Teis and U. Mosel, *Analysis of flow effects in relativistic heavy-ion collisions within the CBUU approach*, Eur. Phys. J. **A5** (1999) 157, nucl-th/9812050.

[277] M. Effenberger, A. Hombach, S. Teis and U. Mosel, *Photoproduction of pions and etas in nuclei*, Nucl. Phys. **A614** (1997) 501, nucl-th/9610022.

[278] B. Blaettel, V. Koch and U. Mosel, *Transport theoretical analysis of relativistic heavy ion collisions*, Rept. Prog. Phys. **56** (1993) 1.

[279] G. Wolf, W. Cassing and U. Mosel, *Eta and dilepton production in heavy ion reactions*, Prog. Part. Nucl. Phys. **30** (1993) 273.

[280] A. Engel, *Untersuchung der Pion-Kern-Reaktion in einer erweiterten BUU Simulation*, Ph.D. thesis, Universitat Giessen (1993).

[281] A. Hombach, *Photoproduktion von Pionen und Eta-Mesonen an Kernen*, Diploma thesis, Universitat Giessen (2004).

[282] M. Effenberger, *Gammaabsorption an Kernen*, Diploma thesis, Universitat Giessen (1996).

[283] J. Lehr, *Elektroproduktion von Mesonen an Kernen*, Diploma thesis, Universitat Giessen (1999), http://theorie.physik.uni-giessen.de/documents/diplom/lehr.ps.gz.

[284] J. Lehr, *In-Medium-Eigenschaften von Nukleonen und Nukleonresonanzen in einem semiklassischen Transportmodell*, Ph.D. thesis, Universitat Giessen (2003), http://theorie.physik.uni-giessen.de/documents/dissertation/lehr.pdf.

[285] G. M. Welke, M. Prakash, T. T. S. Kuo, S. Das Gupta and C. Gale, *Azimuthal distributions in heavy ion collisions and the nuclear equation of state*, Phys. Rev. **C38** (1988) 2101.

[286] C. Gale, G. M. Welke, M. Prakash, S. J. Lee and S. Das Gupta, *Transverse momenta, nuclear equation of state and momentum dependent interactions in heavy ion collisions* Print-89-0570 (Chalk River).

[287] H. Lenske, private communication.

[288] E. L. Bratkovskaya, W. Cassing, R. Rapp and J. Wambach, *Dilepton production and m(T)-scaling at BEVALAC/SIS energies*, Nucl. Phys. **A634** (1998) 168, nucl-th/9710043.

[289] T. Weidmann, E. L. Bratkovskaya, W. Cassing and U. Mosel, *e^+e^- pairs from π^-A reactions*, Phys. Rev. **C59** (1999) 919, nucl-th/9711004.

[290] T. Falter and U. Mosel, *Hadron formation in high energy photonuclear reactions*, Phys. Rev. **C66** (2002) 024608, nucl-th/0203052.

[291] T. Falter, K. Gallmeister and U. Mosel, *Incoherent ρ^0 electroproduction off nuclei*, Phys. Rev. **C67** (2003) 054606, nucl-th/0212107.

[292] T. Sjostrand *et al.*, *High-energy-physics event generation with PYTHIA 6.1*, Comput. Phys. Commun. **135** (2001) 238, hep-ph/0010017.

[293] T. Sjostrand, L. Lonnblad and S. Mrenna, *PYTHIA 6.2: Physics and manual* hep-ph/0108264.

[294] B. Andersson, G. Gustafson and B. Nilsson-Almqvist, *A model for low P_T hadronic reactions, with generalizations to hadron-nucleus and nucleus-nucleus collisions*, Nucl. Phys. **B281** (1987) 289.

[295] H. Pi, *An Event generator for interactions between hadrons and nuclei: FRITIOF version 7.0*, Comput. Phys. Commun. **71** (1992) 173.

[296] M. Effenberger and U. Mosel, *Off-shell effects on particle production*, Phys. Rev. **C60** (1999) 051901, nucl-th/9906085.

[297] S. Leupold, *Towards a test particle description of transport processes for states with continuous mass spectra*, Nucl. Phys. **A672** (2000) 475, nucl-th/9909080.

[298] W. Cassing and S. Juchem, *Semiclassical transport of particles with dynamical spectral functions*, Nucl. Phys. **A665** (2000) 377, nucl-th/9903070.

[299] G. Welke, R. Malfliet, C. Gregoire, M. Prakash and E. Suraud, *Collisional relaxation in simulations of heavy ion collisions using Boltzmann like equations*, Phys. Rev. **C40** (1989) 2611.

[300] R. J. Glauber, *High energy collision theory*, *Lectures in theoretical physics*, volume 1, Wiley Intersience, New York, USA (1959).

[301] R. J. Glauber, *Theory of high energy hadron-nucleus collisions*, High-Energy Physics and Nuclear Structure, Plenum, New York (1970).

[302] D. R. Yennie, *Interaction of high energy photons with nuclei as a test of vector meson dominance*, Interactions of Electrons and Photons, Academic, New York, USA (1971).

[303] T. Renk, G. Piller and W. Weise, *Coherence effects in diffractive electroproduction of rho mesons from nuclei*, Nucl. Phys. **A689** (2001) 869, hep-ph/0008109.

[304] T. Falter, S. Leupold and U. Mosel, *Nuclear shadowing at low photon energies*, Phys. Rev. **C64** (2001) 024608, nucl-th/0102058.

[305] B. Z. Kopeliovich, J. Nemchick, N. N. Nikolaev and B. G. Zakharov, *Decisive test of color transparency in exclusive electroproduction of vector mesons*, Phys. Lett. **B324** (1994) 469, hep-ph/9311237.

[306] B. Z. Kopeliovich, J. Nemchik, A. Schafer and A. V. Tarasov, *Color transparency versus quantum coherence in electroproduction of vector mesons off nuclei*, Phys. Rev. **C65** (2002) 035201, hep-ph/0107227.

[307] T. Falter, *Der Abschattungseffekt im nuklearen Photoabsorptionsquerschnitt*, Diploma thesis, Universitat Giessen (2000), http://theorie.physik.uni-giessen.de/documents/diplom/falter.ps.gz.

[308] E. Byckling and K. Kajantie, *Particle kinematics*, Wiley, London (1973).

Deutsche Zusammenfassung

Das zentrale Thema dieser Arbeit ist die Untersuchung der Eigenschaften von Hadronen, insbesondere Mesonen, in stark wechselwirkender Materie. Motivation hierfür ist einerseits die Möglichkeit etwas über die elementaren Wechselwirkungen der Mesonen mit Kernmaterie zu lernen und andererseits die enge Verbindung mesonischer in-Medium Eigenschaften mit dem Einsetzen der Restaurierung der chiralen Symmetrie, einer fundamentalen Symmetrie der starken Wechselwirkung. In der vorliegenden Arbeit untersuchen wir Mediummodifikationen im wesentlichen auf zwei unterschiedliche Weisen: Erstens berechnen wir mesonische Spektralfunktionen in kalter Kernmaterie innerhalb eines mikroskopischen Modells unter Verwendung experimentell gewonnener Informationen über elementare Meson-Nukleon Wechselwirkungen. Zwar können Modelle dieser Art ein hohes Maß an Ausgereiftheit und Komplexität erreichen, allerdings bleibt ein Vergleich mit tatsächlichen experimentellen Daten oft schwierig und definitive Aussagen sind daher häufig schwer zu treffen. Zweitens berechnen wir Observablen in Kernreaktionen mit elementaren Projektilen und untersuchen insbesondere deren Sensitivität auf die Änderungen von Teilcheneigenschaften im Kern. Besonderen Wert legen wir auf die Untersuchung der Ursachen experimentell beobachteter Effekte, wobei wir hier insbesondere traditionelle Mechanismen wie etwa die Fermibewegung der Nukleonen und Endzustandswechselwirkungen von mit fundamentalen Symmetrieeigenschaften verbundenen Änderungen der intrinsischen Teilcheneigenschaften bei endlicher Kerndichte trennen.

Die chirale Symmetrie ist eine näherungsweise Symmetrie der QCD Lagrangedichte im Bereich der leichten Quarks. Im Gegensatz zur Lagrangedichte weist der Vakuumgrundzustand der QCD diese Symmetrie nicht auf. Dies bezeichnet man als das spontane Zusammenbrechen der chiralen Symmetrie im Vakuum. Ein experimenteller Beweis dieser Eigenschaft der starken Wechselwirkung ist das offensichtliche Fehlen entarteter Zustände entgegengesetzter Parität im hadronischen Teilchenspektrum. Als Konsequenz der spontanen Symmetriebrechung finden sich nahezu masselose Teilchen im QCD Grundzustand, welche im SU(2) Sektor mit den Pionen identifiziert werden. Als möglicher chiraler Partner des Pions mit entgegengesetzter Parität wird das skalare σ Meson diskutiert, welches im Vakuum als breite Resonanz mit einer Breite etwa gleich groß seiner Masse von etwa $m_\sigma \approx 500$ MeV in der $\pi\pi$ Streuamplitude beobachtet wird. Verbunden mit der teilweisen Restaurierung der chiralen Symmetrie erwartet man, dass sich die Eigenschaften des σ Mesons in Kernmaterie ändern. In dieser Arbeit demonstrieren wir, dass diese Änderungen der in-Medium Eigenschaften im Bereich hadronischer Freiheitsgrade vor allem durch die Pion-Nukleon Wechselwirkung induziert werden. Durch die Unterdrückung des Phasenraumes für den Zerfall des σ Mesons in zwei Pionen entwickelt die spektrale Verteilung des σ Mesons im Medium ein ausgeprägtes Maximum nahe der Zweipionenschwelle. Zumindest prinzipiell kann diese Verstärkung des Zweipionenspektrums in $\pi\pi$ Produktionsexperimenten am Kern beobachtet werden. Allerdings

generiert die Pion-Nukleon Wechselwirkung nicht nur eine spektrale Verschiebung der Stärke im σ Kanal, sondern insbesondere auch traditionelle Endzustandswechselwirkungen, welche somit auch observable Effekte auf die zu messenden $\pi\pi$ Spektren erzeugen.

In-Medium Eigenschaften von Hadronen bei endlicher Kerndichte können sehr effektiv untersucht werden mittels Kernreaktionen mit elementaren Projektilen. Nur in dieser Art von Reaktion bleibt die Kernmaterie nahe ihres Grundzustandes. Diese Tatsache macht eine saubere theoretische Behandlung überhaupt erst möglich. Insbesondere verlangt die Zuordnung bestimmter beobachteter Effekte nach einem möglichst transparenten Reaktionsverlauf, was im Falle von Schwerionenkollisionen schwerlich der Fall ist, da hier eine Reihe von Nichtgleichgewichtszuständen mit verschiedenen Dichten und Temperaturen durchlaufen werden. In diesem Zusammenhang sind elektromagnetische Sonden von besonderem Interesse, da sie den gesamten Kern annähernd gleichmäßig erfassen, was von großem Vorteil für die Untersuchung dichteabhängiger Effekte ist. Dennoch enthalten die Observablen zahlreiche Kerneffekte, welche die Untersuchung von Teilcheneigenschaften stören können. Das sind insbesondere die Fermibewegung, Pauli Blocking, hadronische Potentiale und Endzustandswechswelwirkungen. Bislang ist die einzige Möglichkeit den Einfluß dieser Effekte auf hochenergetische photon- und hadroninduzierte Kernreaktionen quantitativ zu untersuchen die Verwendung semiklassischer Transportmodelle. Transportmodelle bieten eine transparente und intuitive Interpretation von Kernreaktionen an und bieten somit die Möglichkeit beobachtete Effekte auf bestimmte nukleare Mechanismen oder Mediummodifikationen zurückzuführen. In der vorliegenden Arbeit fokussieren wir auf die erste Klasse von Kerneffekten, da ihre Existenz unbestritten ist und ihr Einfluß somit nicht vernachlässigt werden kann. Erst nachdem alle Möglichkeiten bestimmte beobachtete Effekte durch konventionelle Prozesse zu erklären ausgeschöpft sind, führen wir Mediummodifikationen ein mit dem Ziel die experimentellen Daten zu beschreiben und im Umkehrschluss die Art und Stärke der Mediummodifikation zu bestimmen.

Mit dieser Absicht untersuchen wir die Produktion von korrelierten Pionenpaaren mittels niederenergetischer Photonen. Obwohl die Anwendung unseres Transportmodells auf niederenergetische Pionen im Prinzip fragwürdig erscheint, bestätigt der Vergleich mit Berechnungen der mittleren freien Weglänge innerhalb quantenmechanischer Modelle und die gute Beschreibung nuklearer Pionabsorptionsdaten die Möglichkeit, die relevanten Mechanismen auch bei niedrigen Energien beschreiben zu können. Experimentell ist von einer deutliche Erhöhung des Zweipionenspektrums nahe der Massenschwelle in der $\gamma \rightarrow \pi^0\pi^0$ Reaktion berichtet worden, welche nicht in dem ebenfalls untersuchten Kanal $\gamma \rightarrow \pi^0\pi^\pm$ gefunden wurde. Diese Tatsache ist als Mediummodifikation des σ Mesons interpretiert worden. In dieser Arbeit führen wir Berechnungen durch, bei denen wir die in-Medium Eigenschaften des σ Mesons gegenüber seinen Vakuumeigenschaften nicht verändern. Andererseits berücksichtigen wir die inkohärenten Endzustandswechselwirkungen der auslaufenden Pionen mit den Nukleonen des Targetkerns. Das wird auf verschiedene Weise gemacht, einerseits mittels eines mikroskopischen optischen Potentials für die Pionen und andererseits, im Geiste der klassischen Transporttheorie, mittels Pion-Nukleon Wirkungsquerschnitten, welche an die Pion-Nukleon Streuung im Vakuum angepasst wurden und welche eine gekoppelte Kanal Behandlung der Endzustandswechselwirkungen erlauben. Obwohl beide Rezepte Photon-Kern Wirkungsquerschnitte liefern, die sich in ihrer absoluten Größe deutlich unterscheiden, sind die qualitativen Eigenschaften der

Ergebnisse gleich. Verursacht durch elastische Stöße und Ladungsaustauschreaktionen beobachten wir eine Rotverschiebung der $\pi\pi$ Massenspektren, welche im Falle schwere Targetkerne an Deutlichkeit zunimmt. Trotz der teilweisen Diskrepanz der absoluten Größe der Wirkungsquerschnitte mit den Daten, weisen die Konturen der differentiellen Verteilungen ein hohes Maß an Übereinstimmung mit dem Experiment auf. Die offensichtlich verschiedene Absorptionsstärke in den $\gamma \to \pi^{\pm}\pi^0$ und $\gamma \to \pi^0\pi^0$ Reaktionen ist sowohl theoretisch als auch experimentell unverstanden. Unabhängig davon folgt unsere Erklärung der beobachteten Rotverschiebung etablierten nuklearen Effekten, welche in jeder ernst zu nehmenden Rechnung berücksichtigt werden müssen. Wir schließen daraus, dass die beobachtete Kernmassenabhängigkeit der Zweipionenspektren keine Evidenz für eine Mediummodifikation des σ Mesons liefert.

Um die Allgemeinheit dieses Schlusses zu testen, berechnen wir desweiteren pioninduzierte Zweipionenproduktion. Auch die pioninduzierten Daten zeigen eine deutliche Erhöhung des Zweipionenspektrums nahe der Massenschwelle, welches in dem Kanal $\pi^+ \to \pi^+\pi^-$ aber nicht im $\pi^+ \to \pi^+\pi^+$ Kanal beobachtet worden ist. Analog zu den photoinduzierten Resultaten ist diese Rotverschiebung als ein Effekt der einsetzenden chiralen Restaurierung erklärt worden. Später ist auch die Reaktion $\pi^- \to \pi^0\pi^0$ gemessen worden, welche zwar kein deutliches Maximum an der Zweipionenschwelle aber dennoch eine Kernmassenabhängigkeit aufweist. Insbesondere die Berechnung von differentiellen Wirkungsquerschnitten am Kern verlangt eine gewisse Präzision bezüglich der elementaren differentiellen Produktionsquerschnitte, welche in die Transportrechnungen eingehen. Aus diesem Grund konstruieren wir ein mikroskopisches Modell für die $\pi N \to \pi\pi N$ Übergangsamplituden, welches $\pi(138)$, $\rho(770)$, $N(938)$, $\Delta(1232)$ und $N^*(1440)$ Zwischenzustände enthält. Wir überprüfen dieses Modell mittels einer Konfrontation mit Daten zur elementaren $\pi\pi$ Produktion sowohl am Proton als auch an Deuterium und finden ein hohes Maß an Übereinstimmung insbesondere wenn man berücksichtigt, dass keine Parameter an die Daten angepasst wurden. An endlichen Kernen finden wir wiederum eine Rotverschiebung der Massenspektren generiert durch Fermibewegung, das elektromagnetische Potential des Kerns und, insbesondere, elastische Pion-Nukleon Stöße und Ladungsaustauschreaktionen. Die Kollisionen im Kern verändern die Phasenraumverteilung der Pionen im $\pi^+\pi^-$ Kanal deutlich, wohingegen die Änderungen im $\pi^+\pi^+$ Kanal nur gering sind. Das ist zurückzuführen auf die starke Anisotropie der Anfangsverteilung im $\pi^+\pi^-$ Kanal und die andererseits homogene anfängliche Füllung des Phasenraums im $\pi^+\pi^+$ Kanal. Die Resultate aus unseren BUU Rechnungen sind qualitativ im Einklang mit dem Experiment. Obwohl experimentell weniger deutlich ausgeprägt, kann die Kernmassenabhängigkeit der Zweipionenspektren in der $\pi^- \to \pi^0\pi^0$ Reaktion nicht durch unsere BUU Rechnungen im Zusammenhang mit dem vorher beschriebenen Modell für die elementaren $\pi \to \pi\pi$ Amplituden wiedergegeben werden. Im Gegensatz dazu beschreibt eine BUU Rechnung, bei der die Pionen anfangs isotrop im Phasenraum verteilt werden, die Daten recht gut. Sollte unser Modell der $\pi \to \pi\pi$ Amplitude also dem in der Natur realisierten Prozess hinreichend entsprechen, weisen die Ergebnisse in der Tat auf eine Mediummodifikation der $\pi \to \pi\pi$ Übergangsamplitude hin.

Unlängst ist die Photoproduktion von η Mesonen am Kern experimentell gemessen worden mit der Erwartung, Informationen sowohl über die Eigenschaften der $S_{11}(1535)$ Nukleonresonanz, welche den elementaren η Photoproduktionsquerschnitt bei kleinen

Energien saturiert, als auch über die $\eta-$Kern Endzustandswechselwirkungen zu erhalten. Resonanzmodellanalysen der η Produktion an Deuterium zeigen eine deutliche Resonanzstruktur bei Schwerpunktsenergien von etwa $\sqrt{s} \simeq 1.7$ GeV im $\gamma n \to \eta n$ Kanal, welche am Proton nicht beobachtet wird. Ausserdem zeigen unsere Rechnungen, dass der inklusive Produktionskanal $\gamma n \to \eta \Delta^0$ annähernd verschwinden muß, um eine Übereinstimmung mit den Deuterium Daten zu ermöglichen. Das steht in starkem Gegensatz zu dem Wirkungsquerschnitt für die Reaktion $\gamma p \to \eta \Delta^+$, welcher experimentell bestimmt wurde und von vergleichbarer Größe wie der exklusive Kanal ist. Andererseits zeigt die inklusive Anregunsfunktion an Deuterium, dass ein inklusiver Kanal am Neutron bereits bei relativ niedrigen Photonenergien, wo der inklusive Querschnitt am Proton noch sehr klein ist, beiträgt. Aus den experimentellen Daten für den kinetischen Energie differentiellen η Photoproduktionsquerschnitt am Kern extrahieren wir den totalen ηN Wirkungsquerschnitt mittels des Glauber Modells. Bei niedrigen Energien finden wir einen totalen Querschnitt von etwa 30 mb welcher langsam zu höheren Energien hin abfällt und schließlich bei einer kinetischen Energie von 1.2 GeV etwa 10 mb beträgt. Der totale und elastische ηN Querschnitt, welcher im Rahmen einer gekoppelten Kanal $K-$Matrix Rechnung aus elementaren Photon- und Pion-Nukleon Streudaten extrahiert wurde, liefert bei Verwendung innerhalb des BUU Modells eine recht gute Übereinstimmung mit den totalen und differentiellen η Photoproduktionsdaten am Kern. Ausserdem zeigen unsere Rechnungen, dass die η Produktion am Kern nur schwach sensitiv ist auf die in-Medium Eigenschaften der S_{11} Resonanz. Sowohl die leichte Energieabsenkung der Resonanzstruktur in der η Anregungsfunktion am Kern als auch ihre Verbreiterung werden ausschließlich durch die Fermibewegung und die Energieabhängigkeit des η Absorptionsquerschnittes generiert. Der Realteil des $\eta-$Kern Potentials hat nur einen vernachlässigbaren Einfluß auf die Observablen.

Verbunden mit der Erwartung Informationen über seine in-Medium Eigenschaften zu gewinnen berechnen wir die nukleare Photoproduktion von ϕ Mesonen. Einfache Argumente wie zum Beispiel der kleine Wirkungsquerschnitt, der sehr kleine Anteil von ϕ Zerfällen innerhalb des Targetkerns und die Zerstörung der Korrelationen der ϕ Zerfallsprodukte sowohl durch starke als auch durch elektromagnetische Endzustandswechselwirkungen, machen klar, dass keine brauchbaren Informationen aus einer Messung von Kaon-Antikaon invarianten Massenspektren erhalten werden können. Andererseits stellt das nukleare Transparenzverhältnis eine vielversprechende Observable dar, welche in unmittelbarer Beziehung zu dem Imaginärteil des $\phi-$Kern Potentials steht. Im großen Ganzen liefern unsere Untersuchungen das Ergebnis, dass die beobachtete Reduktion der ϕ Transmission an endlichen Kernen nicht durch traditionelle Kerneffekte allein erklärt werden kann. Auch die starken nuklearen Potentiale der Kaonen, welche in der Tat die ϕ Transmission reduzieren, können die Daten nicht hinreichend erklären. Nimmt man an, dass die gesamte Reduktion des Transparenzverhältnisses auf die Absorption von ϕ Mesonen zurückgeführt werden kann, liefern unsere Rechnungen einen totalen ϕN Wirkungsquerschnitt von etwa 27 mb. Dieser Wert ist deutlich größer als übliche Abschätzungen des ϕN Querschnittes im Vakuum. Sowohl die Transmissionsdaten als auch die $A-$Abhängigkeit der ϕ Anregungsfunktion werden mit hoher Präzision durch das BUU Modell wiedergegeben sofern wir einen totalen Wirkungsquerschnitt von 27 mb und eine relativistisch korrekte Behandlung der Kaon- und Antikaon-Kern Potentiale implementieren. Unsicherheiten entstehen vor allem durch die Möglichkeit, dass auch

die spontane Zerfallsbreite der ϕ Mesonen, die Endzustandswechselwirkungen der Kaonen als auch der elementare ϕ Photoproduktionsprozess Mediummodifikationen im Kern erfahren könnten. Die experimentelle Bestimmung der ϕ Transmission liefert zumindest einen deutlichen Hinweis auf weitere in-Medium Effekte, da auch eine komplette Rechnung mit Vakuumeigenschaften nicht in der Lage ist, die Transmissionsdaten zu beschreiben.

Die in-Medium Spektralfunktion des ω Mesons bei endlichen Dichten und verschwindender Temperatur berechnen wir mittels eines mikroskopischen Modells. Dazu extrahieren wir die ωN Vorwärtsstreuamplitude aus einer unitären gekoppelten Kanal Rechnung auf der Basis einer effektiven Lagrangedichte, welche zuvor auf die Berechnung photon- und pioninduzierter Reaktionen am Nukleonen angewendet wurde. Die resultierende Amplitude wird aus einer aktuellen Analyse des gekoppelten Kanal Problems im Energiebereich bis $\sqrt{s} = 2$ GeV gewonnen. Um die ω Spektralfunktion zu erhalten, erweitern wir das Modell durch die Einführung eines neuen Kanals, welcher die Berechnung der ω Streuamplitude für beliebige Massen und Impulse des externen ω Mesons erlaubt, wohingegen die hadronischen Zwischenzustände ihre Vakuumeigenschaften beibehalten. Diese Vorgehensweise entspricht der Niedrigdichtenäherung. Als ein generelles Resultat zeigen unsere Rechnungen, dass sowohl Resonanzbeiträge als auch Rückstreueffekte eine wichtige Rolle für die ω Selbstenergie spielen. Bei normaler Kerndichte und verschwindendem ω Impuls finden wir eine Verbreiterung der ω Spektralfunktion auf etwa 60 MeV und nur eine sehr kleine Verschiebung der ω Masse zu höheren Werten relativ zur freien ω Masse. Desweiteren zeigen unsere Ergebnisse eine deutlich unterschiedliche Impulsabhängigkeit der Selbstenergien des transversalen und longitudinalen Freiheitsgrades. Die Frage nach einer Verschiebung der ω Masse im Medium bleibt teilweise offen aufgrund des wichtigen Beitrages des $\omega N \to \pi\pi N$ Kanals. Unglücklicherweise können drei Teilchen Endzustände nur mit deutlichen Näherungen innerhalb gekoppelter Kanal Rechnungen berücksichtigt werden.

Die experimentellen Ergebnisse der CBELSA/TAPS Kollaboration stellen eine bislang einzigartige Quelle an Informationen über die Produktion von ω Mesonen am Kern dar. Mit der Absicht die ω Eigenschaften im Kern zu untersuchen sind sowohl $\pi^0\gamma$ invariante Massenspektren als auch nukleare Transmissionsdaten gemessen worden. Obwohl prinzipiell von hohem Wert, ist die experimentelle Information, welche in den gemessenen $\pi^0\gamma$ Massenspektren enthalten ist, aufgrund der niedrigen Statistik der Datensätze und den Unsicherheiten bei der Subtraktion des experimentellen Hintergrundes begrenzt. Pion-Nukleon Endzustandswechselwirkungen behindern nicht die Bestimmung der spektralen Verteilung der ω Mesonen und können sogar weiter unterdrückt werden durch das Einführen einer einfachen Bedingung an die Impulse der auslaufenden Teilchen. Allerdings sind die Effekte der Mediummodifikationen des ω Mesons nur auf einem Level signifikant, welches schwerlich mit heutigen Experimenten erreicht werden kann. Andererseits werden zum Teil beobachtbare Effekte induziert, welche theoretisch nur schwer kontrolliert werden können. Im großen Ganzen deuten die Ergebnisse in die Richtung einer starken Massenabsenkung des ω Mesons bei endlicher Dichte, wenn man voraussetzt, dass die experimentelle Hintergrundsubtraktion korrekt vorgenommen wurde. Im Gegensatz dazu liefert eine Dispersionsanalyse der ωN Vorwärtsstreuamplitude eine nahezu konstante oder sogar leicht angehobene in-Medium ω Masse im Bereich der endlichen Dreierimpulse, welche experimentell gemessen werden. Die nukleare Transmission ist

weniger sensitiv sowohl auf die Subtraktion des experimentellen Hintergrundes als auch auf die theoretische Behandlung. Rechnungen sowohl innerhalb des BUU Transportmodells als auch im Glauber Modell liefern einen inelastischen ωN Querschnitt, welcher etwa 30% größer ist als übliche theoretische Abschätzungen. Abgesehen von einer ungenügenden Beschreibung der ωN Dynamik mittels der herkömmlichen Modelle könnte dieses Ergebnis auch ein Zusammenbrechen des Niedrigdichtetheorems für das ω Meson bereits bei den moderaten Dichten innerhalb gewöhnlicher Kerne anzeigen. Ähnlich wie bei der Analyse der ϕ Photoproduktion enstehen allerdings auch im Falle des ω Mesons Unsicherheiten durch mögliche Mediummodifikationen der Produktionsamplitude. Mit Hilfe von Daten des impulsdifferentiellen ω Photoproduktionsquerschnittes am Kern ist es prinzipiell auch möglich die Impulsabhängigkeit des ωN Wirkungsquerschnittes zu studieren. Der offensichtliche Widerspruch der ω Eigenschaften, insbesondere bezüglich einer möglichen Verschiebung der in-Medium ω Masse, welche aus den Photoproduktionsdaten extrahiert wurden, und unserer mikroskopischen Rechnung stellt ein bislang ungelöstes Problem dar, welches durch weiterführende theoretische und experimentelle Untersuchungen gelöst werden muß.

Durch die Verbindung mit fundamentalen Symmetrieeigenschaften der zugrunde liegenden Theorie der starken Wechselwirkung stellen die in-Medium Eigenschaften von Mesonen in Kernmaterie faszinierende Phänomene der Hadronenphysik dar. Allerdings sind hadronische in-Medium Eigenschaften sowohl theoretisch als auch experimentell nur schwer zugänglich. Auf der theoretischen Seite stellt sich vor allem das Problem, dass die Anzahl der unbekannten Parameter groß ist gegenüber den Bedingungen, welche aus Experimenten erhalten werden können. Auf experimenteller Seite stellt das Verständins und die Rekonstruktion der Hintergrundprozesse eine der schwierigsten Herausforderungen dar. Neue theoretische Konzepte und Experimente müssen entwickelt werden, um unser heutiges Wissen über die Physik stark wechselwirkender Materie zu erweitern.